GEOLOGICALLY-CONSTRAINED MINERAL POTENTIAL MAPPING

Examples from the Philippines

EMMANUEL JOHN M. CARRANZA

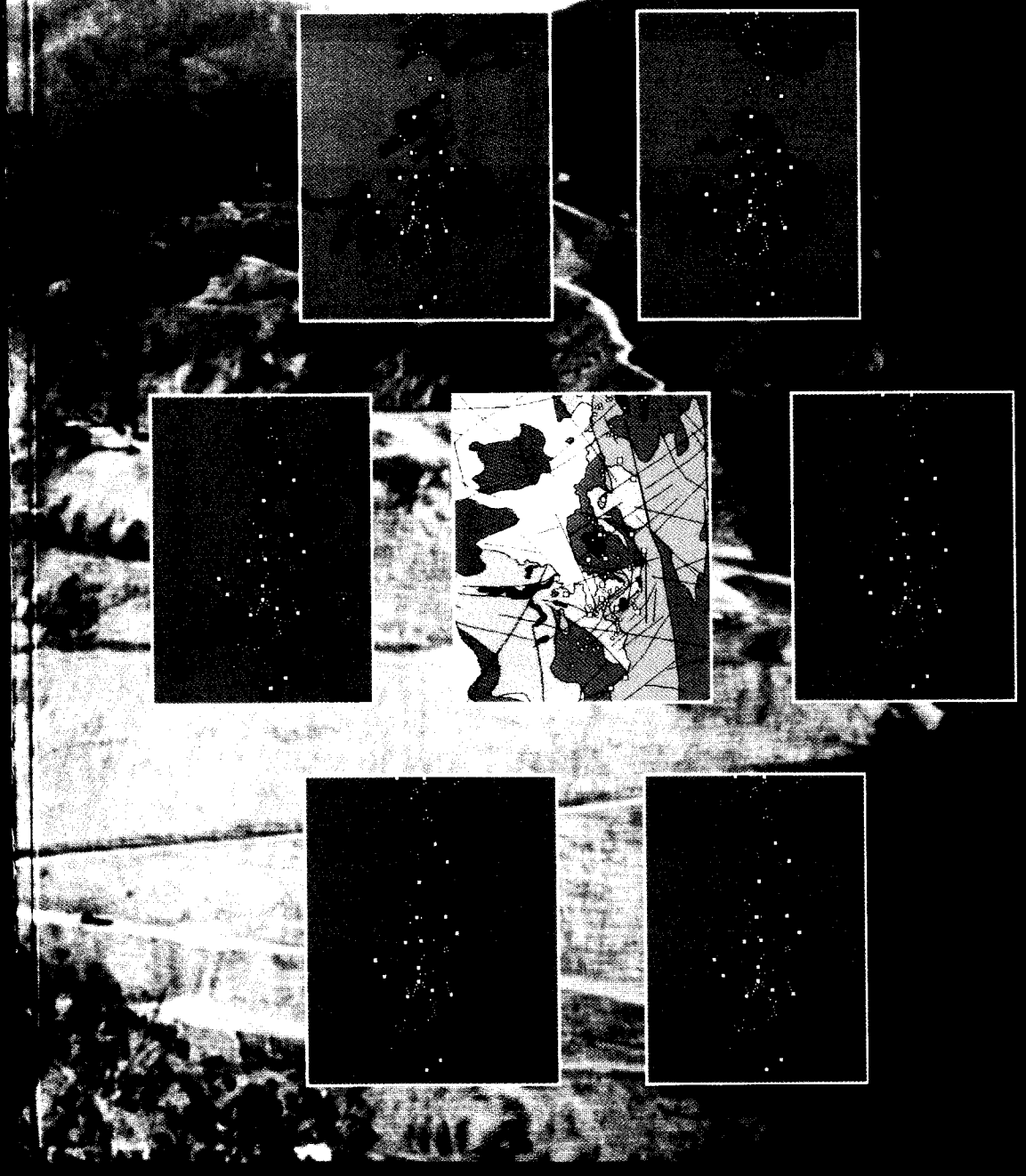

3813
TR 3813

GEOLOGICALLY-CONSTRAINED MINERAL POTENTIAL MAPPING

(Examples from the Philippines)

Proefschrift

ter verkrijging van de graad van doctor
aan de Technische Universiteit Delft,
op gezag van Rector Magnificus Prof. dr. ir. J.T. Fokkema,
voorzitter van het College voor Promoties,
in het openbaar te verdedigen op 4 februari 2002 om 13.30 uur.

BIBLIOTHEEK TECHNISCHE UNIVERSITEIT
Promotheusplein 1
DELFT

door

Emmanuel John Muico CARRANZA
Master of Science in Mineral Exploration, ITC Delft
geboren te Legazpi City, Philippines

Dit proefschift is goedgekeurd door de promotor:

Prof. dr. M. Hale

Samenstelling promotiecommissie:

Rector Magnificus, voorzitter
Prof. dr. M. Hale, Technische Universiteit Delft en ITC, promotor
Prof. dr. S.B. Kroonenberg, Technische Universiteit Delft
Prof. dr. F.D. van der Meer, Technische Universiteit Delft en ITC
Prof. dr. A.K. Turner, Technische Universiteit Delft en Colorado School of Mines
Prof. dr. S.M. de Jong, Rijks Universiteit Utrecht
Dr. H. de Boorder, Rijks Universiteit Utrecht
Dr. G.F. Bonham-Carter, Geological Survey of Canada en University of Ottawa

ISBN 90-6164-203-5
ITC Publication Number 86
International Institute for Aerospace Survey and Earth Sciences (ITC)
Hengelosestraat 99, 7514 AE Enschede, The Netherlands

Copyright © 2002 by E.J.M. Carranza

All rights reserved. No part of the material protected by this copyright notice may be reproduced or utilised in any form or by any means, electronic or mechanical, including photocopying, recording or by any information storage and retrieval system, without any written permission from the copyright owner.

Cover photo and design: John Carranza
Cover shows in the background the defunct Antamok gold mine in Baguio district, Philippines and in the foreground the geological and gold occurrence map of Baguio district used in mapping gold potential and the six geologically-constrained predictive maps of gold potential (depicting the six different methods developed in this thesis).

Dedicated to Ephie

Preface

To be an author, one has to be a student.
Anonymous

Why did I undertake this thesis? In many Third World countries, the lack of complete geoexploration datasets ideally required for mineral potential mapping is an impediment to development. The problem is exacerbated in national geological surveys of these countries because the use of computer-based quantitative techniques in mineral potential mapping is not yet routine due in part to the lack of financial resources to acquire computer hardware/software and in part to the reluctance of many geologists to use such techniques. An example is in the Philippine Mines and Geosciences Bureau (MGB), my employer since 1983, which is faced with the problem that prospective areas may be alienated to mineral resource development by land-use policies arising from the lack of input mineral potential maps due to a deficiency of geoexploration datasets other than lithological and structural maps (and mineral occurrence data). I undertook research on **geologically-constrained mineral potential mapping** to determine the usefulness of lithological and structural maps (and mineral occurrence data) in mapping mineral potential using computer-based geographic information systems (GIS). Behind this objective is not to question the importance of geochemical and geophysical data in mineral potential mapping but to investigate the value of mineral potential maps generated from only lithological and structural maps (and mineral occurrence data).

What do I present in this thesis? The quantitative techniques for geologically-constrained mineral potential mapping I present here are either new or modifications of established GIS-based methods for integrating diverse geoexploration datasets to map mineral potential. These quantitative techniques can be conceptually complicated to many non-mathematical geologists. Simplifying the application of the mathematical concept behind each of these techniques was therefore the principle I used in developing, modifying and explaining new quantitative techniques in order to make their use more appealing. To test the limitations of GIS-based geologically-constrained mineral potential mapping, I consider not just one but five study areas with different numbers of known mineral deposits of different types. I show quantitative methods to map mineral potential using lithological and structural map data and location of mineral deposits (i.e., data-driven methods) and using only lithological and structural map data (i.e., knowledge-driven methods). To prove the efficacy of these methods, I validate the geologically-constrained predictive mineral potential models against locations of mineral deposits not used in generating the predictive models and against integrated geochemical-geological predictive models of mineral potential. (A validation against integrated geophysical-geochemical-geological predictive models of mineral potential would have been even better; however, geophysical data were lacking). The most suitable methods found for geologically-constrained mineral potential mapping can now be applied to other areas where mineral potential maps are needed but where complete geoexploration datasets are lacking except lithological and structural maps (and mineral occurrence data). I hope that the methods presented here will be accepted by and prove beneficial to mineral explorationists, mathematical or not, and that the ideas generated here will stimulate geoscientists to develop further research in this field.

Who do I acknowledge for their support in producing this thesis? I am indebted to Professor dr Martin Hale who accepted me as his promovendus, guided and scrutinised the science of my work and managed the overall research process. I am grateful to ITC and DGIS (Dutch Agency for International Cooperation) for the fellowship to undertake this doctoral research. I thank several staff members of ITC: Dr Phil Westerhof, Dr Ed Sides (now at GE Smallworld), Drs Joop Dessauvagie (now retired), Drs Boudewijn de Smeth and Drs Frank van Ruitenbeek, who adopted me as a 'junior' staff member of the Mineral Exploration Division; Dr Elisabeth Kosters, Ineke Theussing and Loes Colenbrander, who provided administrative support; Gerard Reinink, who provided, from the ITC archives, the Landsat TM data in Baguio/Benguet; Dienke Maas-Geesteranus, Henk Wilbrink and Aiko Mulder, who provided computer hardware/software support; Bish Kewaaldar and Wim Zuiderwijk, who provided materials/facility support; Willie Engelen, Margaret Vrolijk, Barnette Stern and Carla Gerritsen, who provided library/secretariat support.; and Frank van Ruitenbeek, who translated to Dutch the summary of and propositions accompanying this thesis. I thank several people in MGB: Neoman de la Cruz (Director, MGB - Cordillera Administrative Region or CAR), Faye Apil (Chief Geologist, MGB-CAR) and Romeo Almeda (Chief Geologist, MGB - Central Office), who provided logistic support for my fieldwork in Baguio district and Benguet province; Jerrysal Mangaoang (Chief of Mining Division, MGB - Region 2), who provided the geoexploration data in Isabela area; Ed Avila (Cartographer, MGB - Region 5), who accompanied me in my 1st fieldwork and reproduced some of the geological maps I used in this research; and Gabriel Dulnuan (Cartographer, MGB-CAR), who accompanied me in my 2nd fieldwork. I thank certain local people in areas I visited in Benguet province for their hospitality. I thank Newmont Philippines Incorporated for the Benguet province stream sediment data, which I acquired through Ben Espejo (Geologist, MGB-CAR); Philex Mining Corporation, Benguet Mining Corporation and Lepanto Consolidated Mining Corporation for some useful data and for accommodation during my fieldwork; and NAMRIA (National Mapping and Resource Information Authority of the Philippines) for the topographic maps in the five study areas and the Landsat TM data in Catanduanes. I thank Dr Hooshang Asadi Harouni, my roommate in ITC-Delft, for some collaborative work during his doctoral research; and Zhu Sicai, my roommate in ITC-Enschede, for his caring support when I was writing this thesis. I acknowledge several Filipinos (a list of them would be long and impractical as I would be prone to forget some of them) who came to study at ITC and other institutions in The Netherlands or who are now Dutch nationals with whom I had good friendly acquaintances. Most especially, I am affectionately grateful to Ephie for many things - material and otherwise. I thank Coleen and Faye for their prayers. I thank the anonymous reviewers and editors of peer-reviewed journals who accepted for publication the papers I submitted. Most of all, my heartfelt gratitude goes to Him from whom I received innate abilities and further blessings.

JOHN CARRANZA
Delft, 2002

Samenvatting

Carranza, E.J.M., 2002. Geologically-Constrained Mineral Potential Mapping. PhD Thesis, Delft University of Technology, The Netherlands, 480 pp.

Het in kaart brengen van het minerale delfstoffenpotentieel is problematisch wanneer de beschikbare exploratie gegevens beperkt zijn tot geologische kaarten en stallietbeelden. Om deze eventuele problemen op te lossen zijn methoden ontwikkeld voor (i) het op afstand detecteren van de aanwezigheid van mineralisaties; (ii) het kwantificeren van de ruimtelijke samenhang tussen minerale afzettingen en geologische kenmerken; en (iii) het karteren van het minerale delfstoffen potentieel met behulp van geologische informatie alleen. De ontwikkelde methoden zijn toegepast op testgebieden in de Philippijnen: De Benguet provincie en het Abra gebied voor het in kaart brengen van porpfirisch koper; het Beguio district en het Catanduanes eiland voor epithermal goud (en koper); en het Isabela gebied voor het nikkellateriet potentieel.

Een methode voor het detecteren van omzettingsmineralogie was ontwikkeld. Hierbij werd een ratio van twee Landsat Tm beelden gebruikt in een principiële componenten analyse voor het verwijderen van spectrale vegetatie-effecten en voor het creëren van beelden van verschillende hydrothermale omzettingsmineralen. De mineraalbeelden, een digital hoogte model, en trainingspixels van de bekende hydrothermale omzettingseenheden zijn gebruikt in een supervised classificatie voor het inkaart brengen van de hydrothermale omzettingen. De resulterende kaarten hebben een nauwkeurigheid van 82% in het Baguio district en 73% in het Benguet provincie.

Voor het kwantificeren van de ruimtelijke samenhang tussen de mineralisaties en geologische patronen, een belangrijk onderdeel in het karteren van het minerale delfstoffenpotentieel, is een nieuwe manier bedacht. Deze manier, de zogenaamde afstandscorrelatie bepaling, doet geen aanname over de waarschijnlijkheidsverdeling van de mineralisaties en heeft daarom voordelen boven de gangbare ruimtelijke correlatie methode, die uitgaat van van een Poisson verdeling. De nieuwe methode is niet gevoelig voor het aantal mineralisaties dat is gebruikt in de analyse en daarom te prefereren boven de gangbare weights of evidence methode, die een groot aantal mineralisaties vereist voor de bepaling van een statistisch significante ruimtelijke correlatie. De afstandscorrelatie bepaling is een bevredigende methode; ze produceert statistisch significante resultaten ook als de waarschijnlijkheidsverdeling van de mineralisaties onbekend is en wanneer slechts een aantal mineralisaties bekend is.

Verschillende methoden voor het in kaart brengen van het minerale delfstoffenpotentieel met alleen geologische informatie zijn ontwikkeld met behulp van (1) eenvoudige kaart algebra, (2) weights of evidence modelleren, (3) de theorie over evidential belief, (4) de fuzzy set theorie, (5) logistic regressie en (6) principiële componenten analyse voor een wildcat methode. De toepassing van eenvoudige kaart algebra en weights of evidence modelleren maakt gebruik van binaire voorspellingspatronen van geologische kenmerken. De toepassing van de theorie over evidential belief, de theorie van fuzzy sets, logistic regressie en de principiële componenten analyse maken gebruik van uit meervoudige klassen bestaande voorspellings patronen van geologische kenmerken. De gekwantifiseerde ruimtelijk samenhang tussen de mineralisaties en de curvi-lineaire en puntvormige geologische patronen waren zeer bruikbaar voor het transformeren van

deze geologische kenmerken in binaire of uit meerdere klassen bestaande voorspellingspatronen en het karteren van het minerale delfstoffenpotentieel.

De op gegevens gebaseerde methoden van modelleren zoals de weights of evidence, evidential belief, en logistic regressie kunnen effectiever zijn dan op kennis gebaseerde modellen wanneeer het aantal mineralisaties dat is gebruikt in de voospelling groter is dan 20. Op kennis gebaseerde modellen zoals eenvoudige kaart algebra en de toepassing van de theorie van fuzzy sets zijn effectiever dan puur op gegevens gebaseerde modellen wanneeer het aantal mineralisaties gebruikt in de voorspelling kleiner is dan 20. Wanneer alleen de geologie bekend is en er geen locaties van mineralisaties bekend zijn dan geven op kennis gebaseeerde modellen zoals eenvoudige map algebra, de theorie van evidential belief, de fuzzy set theorie en wildcat karteren het beste resultaat.

De verschillende methoden voor het voorspellen van het minerale delfstoffen potentieel met alleen geologische gegevens indiceren dat 23% van de Benguet provincie potentieel heeft voor het voorkomen van porfirische koper afzettingen, ongeveer 22% van het Baguio district potentieel heeft voor epithermale goud voorkomens, ongeveer 23% van Abra potentieel heeft voor porfirische koper afzettingen, en ongeveer 22% van Catanduanes eiland potentieel heeft voor hydrothermale afzettingen. De gemiddelde success-rate van de voorspellingskaarten van Benguet, Baguio, Abra, en Catanduanes eiland is tenminste 60%.

In het Isabela gebied heeft gemiddeld 50% van de ultramafische gesteenten heeft een groot potentieel voor het voorkomen van nikkellaterieten, terwijl 33% van het gebied met bekende nikkellaterietvoorkomens een groot potentieel heeft voor dit type voorkomen. Het gedeelte met bekende nikkellateriet voorkomens is dus minder prospectief dan andere gedeelten in het ultramafische gesteente. Echter de gedeelten met groter potentieel liggen in een gebied dat is beschermt tegen de winning van minerale delfstoffen. De ban op de winning van minerale delfstoffen, die was opgelegd voordat de kaarten met het minerale delfstoffen potentieel gegenereerd waren, wordt niet in twijfel getrokken. Echter de resultaten laten zien dat kaarten van het minerale delfstoffen potentieel een belangrijke input levert bij de besluitvorming voor optimaal landgebruik.

De resultaten laten de doelmatigheid zien van de verschillende methoden die ontwikkeld zijn voor het karteren van het minerale delfstoffen potentieel met alleen geologische informatie. De ontwikkeling van zulke methoden kunnen overheidsdiensten, in landen waar geen systematische en volledige geo-exploratie gegevens aanwezig zijn, helpen bij het definieren van prospectief land, het afwegen van het minerale delfstoffen potentieel tegen de vraag van andere typen landgebruik, en het stimuleren van investeringen in de exploratie van mineralen in gebieden met een groot minerale delfstoffenpotentieel.

Summary

Carranza, E.J.M., 2002, Geologically-Constrained Mineral Potential Mapping. PhD Thesis, Delft University of Technology, The Netherlands, 480 pp.

Mineral potential mapping poses a problem when the geoexploration data available are limited to geological maps and satellite imagery. To address this problem, methods were developed for (i) remote detection of indications of mineralisation; (ii) quantifying spatial associations between mineral deposits and geological features; and (iii) geologically-constrained mineral potential mapping. The methods developed were applied in areas in the Philippines: Benguet province and Abra area to map porphyry copper potential; Baguio district and Catanduanes Island to map epithermal gold(-copper) potential; and Isabela area to map nickeliferous-laterite potential.

A mineral imaging method using two Landsat TM band ratio images in principal components analysis to remove the spectral effects of vegetation and create mineral images of each of the predominant hydrothermal alteration minerals was developed. The mineral images, a digital elevation model image and training pixels of the known hydrothermal alteration units were used in a supervised classification to map hydrothermal alterations. The resulting maps have an accuracy of 82% for Baguio district and 73% for Benguet province.

In order to quantify spatial association between mineral deposits and geological features, which is important in mineral potential mapping, a new distance correlation method was devised. It has no assumption of the probability distribution of the mineral deposits and thus advantageous over the established distance distribution method, which assumes a Poisson distribution for mineral deposits. It is not sensitive to the number of mineral deposit points used in the analysis and thus advantageous over the over the established weights of evidence method, which needs a fairly large number of mineral deposit points for the quantified spatial association to be statistically significant. The distance correlation method is a satisfactory method; it produces statistically-significant results when the probability distribution of the mineral deposits is unknown and when only a few mineral deposits are known.

Different methods for geologically-constrained predictive mineral potential mapping were developed using (1) simple map algebra, (2) weights of evidence modeling, (3) the theory of evidential belief, (4) the theory of fuzzy sets, (5) logistic regression and (6) principal components analysis. The applications of simple map algebra and weights of evidence modeling involve binary predictor patterns of geological features. The applications of the theory of evidential belief, the theory of fuzzy sets, logistic regression and principal components analysis involve multi-class predictor patterns of geological features. The quantified spatial associations between the mineral deposits and curvi-linear or point geological features were useful in transforming these geological features into binary or multi-class predictor patterns to map mineral potential.

Data-driven methods such as weights of evidence modeling, the application of the theory of evidential belief and logistic regression can be more effective than knowledge-driven methods when the number of mineral deposits used in the predictive modeling is at least 20. Combined data-driven and knowledge-driven methods such as simple map algebra and the application of the theory of fuzzy sets can be more effective than purely data-

driven methods when the number of mineral deposits used in the predictive modeling is at most 20. The wildcat mapping method is useful when the geology is known but mineral deposits are unknown.

The different methods for geologically-constrained predictive mineral potential mapping indicate that about 25% of Benguet province has potential for porphyry copper deposits, about 23% of Baguio district has potential for epithermal gold deposits, about 23% of Abra has potential for porphyry copper deposits and about 22% of Catanduanes Island has potential for hydrothermal deposits. For Benguet province, Baguio district, Abra area and Catanduanes Island, the average success rates of the predictive maps are at least 60%.

For Isabela area, an average of 50% of the ultramafic terrane has high potential for nickeliferous-laterite whilst an average of 33% of the section with known nickeliferous-laterite deposits has high potential for this type of deposit. The section with known nickeliferous-laterite deposits is less prospective than other sections in the ultramafic terrane. However, the more prospective sections are within a portion of the Isabela area that is protected from mineral resources development. The prohibition on mineral resources development, which was imposed prior to the generation of the geologically-constrained predictive maps, is not being disputed. Nevertheless, the results demonstrate that mineral potential maps are important inputs for optimum land-use decision-making.

The results demonstrate the efficacy of the different methods developed for geologically-constrained predictive mineral potential mapping. Development of such methods can help public service organisations of countries, where systematic and comprehensive geoexploration are lacking, to define prospective land, weigh mineral potential against competing demands for land-use other than mineral resource development and stimulate exploration investment through non-alienation of prospective areas.

Contents

Preface v
Samenvatting vii
Summary ix
Contents xi

Chapter 1 - Introduction 1
1.1 Description of the problem 1
1.2 Rationale for the research 2
1.3 Objectives of the research 3
1.4 Definition of mineral potential 3
1.5 Methodology 4
1.6 Organization of the thesis 5

Chapter 2 - Study Areas and Geoexploration Datasets 9
2.1 Background on philippine geology 9
2.1.1 Generalised tectonic setting 9
2.1.2 Major mineral deposits 12
2.1.3 The study areas 14
2.2 Benguet Province 15
2.2.1 Geology and porphyry copper mineralisation 15
2.2.2 Geological map data 15
2.2.3 DEM-derived structural geoinformation 18
2.2.4 Stream sediment geochemical data 20
2.3 Baguio district 23
2.3.1 Geology and epithermal gold mineralisation 23
2.3.2 Geological map data 24
2.3.3 Stream sediment geochemical anomalies 25
2.4 Abra area 27
2.4.1 Geology and copper mineralisation 27
2.4.2 Geological map data 30
2.4.3 DEM-interpreted faults/fractures 30
2.4.4 Stream sediment geochemical data 31
2.5 Catanduanes island 33
2.5.1 Geology and mineralisation 33
2.5.2 Geological map data 36
2.5.3 DEM-interpreted faults/fractures 36
2.5.4 Stream sediment geochemical anomalies 37
2.6 Isabela area 40
2.6.1 Geology and mineralisation 40
2.6.2 Geological map data 41
2.6.3 DEM-derived geoinformation 41
2.6.4 Stream sediment geochemical data 43
2.7 Concluding remarks 44

Chapter 3 - Remote Sensing of Indications of Mineral Deposits in Heavily-Vegetated Terranes 45
3.1 Introduction 45
3.2 State-of-the-Art: Remote detection of indications of mineralisation 46

3.2.1 Remote detection of hydrothermally-altered rocks....47
3.2.2 Remote detection of vegetation stress....50
3.3 Remote detection of hydrothermally-altered rocks in the presence of vegetation using Landsat TM data....55
3.3.1 Baguio district: hydrothermal alteration, vegetation and Landsat TM data....59
3.3.2 Application of the Crósta technique to Baguio district....63
3.3.3 Application of the software defoliant technique to Baguio district....65
3.3.4 Discussion of results of the Crósta and the software defoliant techniques....66
3.3.5 Mineral imaging methodology using Landsat TM data....67
3.3.6 Mineral imaging method applied to Baguio district....70
3.3.7 Mineral imaging method applied to Mankayan district....78
3.3.8 Mineral imaging method applied to Benguet province....85
3.3.9 Discussion of the mineral imaging method....89
3.4 Remote detection of geochemically-stressed vegetation using Landsat TM data....90
3.4.1 Classification of land cover types....92
3.4.2 Vegetation spectra and stream sediment geochemistry relationship....94
3.4.3 Spectral characteristics of vegetation in Zn-enriched catchment basins....97
3.4.4 Spectral characteristics of vegetation around mineralised zones....99
3.4.5 Remote detection of vegetation-covered Zn-enriched and mineralised zones....100
3.4.6 Discussion....103
3.4 Conclusions....104

Chapter 4 - Spatial Association of Mineral Deposits and Geological Features... 107
4.1 Introduction.... 107
4.2 Methods....110
4.2.1 Observed vs. predicted distance distribution method.... 111
4.2.2 Weights of evidence method....112
4.2.3 Distance correlation method....114
4.2.4 Map operations....116
4.2.5 Presentation and interpretation of results....117
4.3 Application to Benguet province....117
4.3.1 Theoretical considerations....117
4.3.2 Porphyry plutons vs. strike-slip fault discontinuities....120
4.3.3 Porphyry copper deposits vs. strike-slip fault discontinuities....122
4.3.4 Porphyry copper deposits vs. porphyry plutons....123
4.3.5 Porphyry plutons vs. batholithic pluton margins....125
4.3.6 Porphyry copper deposits vs. batholithic pluton margins....127
4.3.7 Discussion....129
4.4 Application to Baguio district....131
4.4.1 Gold deposits vs. northeast-trending faults/fractures....131
4.4.2 Gold deposits vs. northwest-trending faults/fractures....133
4.4.3 Gold deposits vs. batholithic pluton margins....134
4.4.4 Gold deposits vs. porphyry pluton contacts....136
4.4.5 Discussion....138
4.5 Application to Abra area....140
4.5.1 Porphyry copper deposits vs. granodiorite margins....140
4.5.2 Porphyry copper deposits vs. quartz diorite margins....142
4.5.3 Porphyry copper deposits vs. porphyry pluton centroids....144
4.5.4 Porphyry copper deposits vs. north-trending faults/fractures....146

4.5.5 Porphyry copper deposits vs. northeast-trending faults/fractures 148
4.5.6 Porphyry copper deposits vs. northwest-trending faults/fractures 150
4.5.7 Porphyry copper deposits vs. intersections of regional faults 152
4.5.8 Discussion 154
4.6 Application to Catanduanes island 156
4.6.1 Gold-copper deposits vs. Batalay Intrusive contacts 156
4.6.2 Gold-copper deposits vs. north-trending faults/fractures 158
4.6.3 Gold-copper deposits vs. east-trending faults/fractures 160
4.6.4 Gold-copper deposits vs. northeast-trending faults/fractures 162
4.6.5 Gold-copper deposits vs. northwest-trending faults/fractures 164
4.6.6 Batalay Intrusive centroids vs. north-trending faults/fractures 166
4.6.7 Batalay Intrusive centroids vs. northeast-trending faults/fractures 168
4.6.8 Batalay Intrusive centroids vs. northwest-trending faults/fractures 170
4.6.9 Discussion 172
4.7 General Discussion 173
4.8 Conclusions 176

Chapter 5 - Geologically-Constrained Mineral Potential Mapping: Application of Deposit Exploration Models 177
5.1 Introduction 177
5.2 Methodology 178
5.3 Mapping porphyry copper potential 180
5.3.1 General characteristics of porphyry copper deposits 180
5.3.2 General characteristics of Philippine porphyry copper deposits 184
5.3.3 Geologic criteria for porphyry copper potential mapping 185
5.3.4 Porphyry copper potential mapping, Benguet province 186
5.3.4 Porphyry copper potential mapping, Abra area 188
5.4 Mapping epithermal gold potential 192
5.4.1 General characteristics of epithermal deposits 192
5.4.2 General characteristics of Philippine epithermal gold deposits 194
5.4.3 Geologic criteria for epithermal gold potential mapping 196
5.4.4 Epithermal gold potential mapping, Baguio district 196
5.4.5 Epithermal gold mineral potential mapping, Catanduanes Island 200
5.5 Mapping nickeliferous-laterite potential 203
5.5.1 General characteristics of nickeliferous-laterite deposits 203
5.5.2 General characteristics of Philippine nickeliferous-laterite deposits 204
5.5.3 Geologic criteria for nickeliferous-laterite potential mapping 205
5.5.4 Nickeliferous-laterite potential mapping, Isabela area 205
5.6 Conclusions 207

Chapter 6 - Geologically-Constrained Probabilistic Mapping of Mineral Potential 209
6.1 Introduction 209
6.2 Bayesian probability model 210
6.2.1 Conditional probability of mineral deposit: single binary pattern 210
6.2.2 Conditional probability of mineral deposit: multiple binary patterns 212
6.3 Bayesian probability modeling using GIS 214
6.3.1 Data inputs 214
6.3.2 Generation of binary predictor patterns 214
6.3.3 Combining binary predictor patterns 215
6.3.4 Pairwise test of conditional independence 215

6.3.5 Overall test of conditional independence 219
6.3.6 Data integration and validation of results 220
6.4 Application to Benguet province 220
6.4.1 Spatial association of porphyry copper deposits with geologic features ...221
6.4.2 Spatial association of porphyry plutons with geologic features 222
6.4.3 Probabilistic mapping of porphyry copper potential 223
6.4.4 Probabilistic mapping of zones of porphyry pluton emplacement 224
6.5 Application to Baguio district 226
6.5.1 Spatial association of gold deposits with geological features 226
6.5.2 Probabilistic mapping of epithermal gold mineral potential 227
6.6 Application to Abra area 233
6.6.1 Spatial association of porphyry copper deposits with geological features 234
6.6.2 Probabilistic mapping of porphyry copper potential 235
6.7 Application to Catanduanes Island 241
6.7.1 Spatial association of gold-copper deposits with geological features 242
6.7.2 Probabilistic mapping of gold-copper potential 243
6.8 Discussion 246
6.9 Conclusions 248

Chapter 7 - Evidential Belief for Mapping Mineral Potential 251
7.1 Introduction 251
7.2 Dempster-Shafer evidential belief function 252
7.3 Application of evidential belief functions using GIS 254
7.3.1 Data inputs 254
7.3.2 Belief function representation of geological map data 254
7.3.3 Generation of belief functions 258
7.3.4 Integration of belief function maps 258
7.3.5 Generation and validation of mineral potential maps 260
7.4 Application to Benguet province 260
7.4.1 Belief functions of spatial evidences of porphyry copper potential 260
7.4.2 Evidential belief mapping of porphyry copper potential 261
7.4.3 Discussion 266
7.5 Application to Baguio district 267
7.5.1 Belief functions of spatial evidences of epithermal gold potential 267
7.5.2 Evidential belief mapping of epithermal gold potential 268
7.5.3 Discussion 275
7.6 Application to Abra area 276
7.6.1 Belief functions of spatial evidences of porphyry copper potential 276
7.6.2 Evidential belief mapping of porphyry copper potential 277
7.6.3 Discussion 281
7.7 Application Catanduanes island 282
7.7.1 Belief functions of spatial evidences of gold-copper potential 283
7.7.2 Evidential belief mapping of gold-copper potential 283
7.7.3 Discussion 288
7.8 Application to Isabela area 289
7.8.1 Belief functions of spatial evidences of nickeliferous-laterite potential 290
7.8.2 Evidential belief mapping of nickeliferous-laterite potential 290
7.8.3 Discussion 294
7.9 Discussion 295
7.10 Conclusions 296

Chapter 8 - Geologically-Constrained Fuzzy Mapping of Mineral Potential 299
8.1 Introduction 299
8.2 Fuzzy sets 300
8.3 Application of fuzzy sets in a GIS environment 303
8.3.1 Data inputs 303
8.3.2 Generation of fuzzy sets 303
8.3.3 Integration of fuzzy sets 305
8.4 Application to Benguet province 305
8.4.1 Fuzzy sets of evidences of porphyry copper potential 305
8.4.2 Integration of fuzzy sets of evidences of porphyry copper potential 307
8.4.3 Fuzzy predictive mapping of porphyry copper potential 308
8.4.4 Discussion 311
8.5 Application to Baguio district 313
8.5.1 Fuzzy sets of evidences of epithermal gold potential 313
8.5.2 Integration of fuzzy sets of evidences of epithermal gold potential 316
8.5.3 Fuzzy predictive mapping of epithermal gold potential 317
8.5.4 Discussion 323
8.6 Application to Abra area 325
8.6.1 Fuzzy sets of evidences of porphyry copper potential 325
8.6.2 Integration of fuzzy sets of evidences of porphyry copper potential 327
8.6.3 Fuzzy predictive mapping of porphyry copper potential 328
8.6.4 Discussion 330
8.7 Application to Catanduanes island 332
8.7.1 Fuzzy sets of evidences of gold-copper potential 332
8.7.2 Integration of fuzzy sets of evidences of gold-copper potential 333
8.7.3 Fuzzy predictive mapping of gold-copper potential 335
8.7.4 Discussion 339
8.8 Application to Isabela area 340
8.8.1 Fuzzy sets of spatial evidences of nickeliferous-laterite potential 340
8.8.2 Integration of fuzzy sets of evidences of nickeliferous-laterite potential 343
8.8.3 Fuzzy predictive mapping of nickeliferous-laterite potential 343
8.8.4 Discussion 344
8.9 General discussion 345
8.10 Conclusions 347

Chapter 9 - Logistic Regression for Mineral Potential Mapping 349
9.1 Introduction 349
9.2 Logistic regression model 350
9.3 Application of logistic regression model using GIS 353
9.3.1 Data inputs 353
9.3.2 Data representation for logistic regression modeling 353
9.3.3 Logistic regression modeling 354
9.3.4 Presentation and validation of mineral potential maps 355
9.4 Application to Benguet province 356
9.4.1 Variables in logistic regression modeling 356
9.4.2 Predictors or porphyry copper potential 357
9.4.3 Predictive mapping of porphyry copper potential 357
9.4.4 Discussion 360
9.5 Application to Baguio district 360
9.5.1 Variables in logistic regression modeling 360
9.5.2 Predictors or epithermal gold potential 362

9.5.3 Predictive mapping of epithermal gold potential 363
9.5.4 Discussion 364
9.6 Application to Abra area 365
9.6.1 Variables in logistic regression modeling 365
9.6.2 Predictors or porphyry copper potential 366
9.6.3 Predictive mapping of porphyry copper potential 367
9.6.4 Discussion 369
9.7 Application to Catanduanes Island 369
9.7.1 Variables in logistic regression modeling 369
9.7.2 Predictors of gold-copper potential 371
9.7.3 Predictive mapping of gold-copper potential 372
9.7.4 Discussion 375
9.8 Discussion 375
9.9 Conclusions 377

Chapter 10 - Wildcat Mapping of Mineral Potential 379
10.1 Introduction 379
10.2 Wildcat model of mineral potential 380
10.3 Wildcat modeling of mineral potential using GIS 382
10.3.1 Data inputs 382
10.3.2 Representation of indicative geological variables 382
10.3.3 Generation and validation of wildcat favourability maps 383
10.4 Application to Benguet province 383
10.4.1 Degrees of favourability of indicative geological variables 384
10.4.2 Favourability function for porphyry copper potential 385
10.4.3 Wildcat mapping of favourability for porphyry copper potential 386
10.4.4 Discussion 387
10.5 Application to Baguio district 388
10.5.1 Degrees of favourability of indicative geological variables 388
10.5.2 Favourability function for epithermal gold potential 389
10.5.3 Wildcat mapping of favourability for epithermal gold potential 390
10.5.4 Discussion 391
10.6 Application to Abra area 392
10.6.1 Degrees of favourability of indicative geological variables 392
10.6.2 Favourability function for porphyry copper potential 396
10.6.3 Wildcat mapping of favourability for porphyry copper potential 395
10.6.4 Discussion 396
10.7 Application to Catanduanes island 397
10.7.1 Degrees of favourability of indicative geological variables 397
10.7.2 Favourability function for hydrothermal deposit potential 398
10.7.3 Wildcat mapping of favourability for hydrothermal deposit potential 399
10.7.4 Discussion 400
10.8 Application to Isabela area 401
10.8.1 Degrees of favourability of indicative geological variables 402
10.8.2 Favourability function for nickeliferous-laterite potential 403
10.8.3 Wildcat mapping of favourability for nickeliferous-laterite potential 403
10.8.4 Discussion 404
10.9 Discussion 405
10.10 Conclusions 406

Chapter 11 - Conclusions 409
11.1 Introduction 409
11.2 Methods for remote detection of indications of mineralisation using Landsat TM data 411
11.3 Methods for quantifying spatial association of mineral deposits and curvi-linear or point geological features 412
11.4 Methods for geologically-constrained predictive mineral potential mapping 414
11.4.1 General overview 414
11.4.2 Methods involving binary evidences 416
11.4.3 Methods involving multi-class evidences 417
11.4.4 Methods applied to different study areas 420
11.5 Comparison of mineral potential maps 421
11.5.1 Porphyry copper potential maps of Benguet province 422
11.5.2 Epithermal gold potential maps of Baguio district 423
11.5.3 Porphyry copper potential maps of Abra area 424
11.5.4 Gold-copper vein deposit potential maps of Catanduanes Island 424
11.5.5 Nickeliferous-laterite potential maps of Isabela area 425
11.5.6 Summary of comparison of mineral potential maps 426
11.6 Mineral prospectivity of the study areas 426
11.6.1 Porphyry copper potential of Benguet province 427
11.6.2 Epithermal gold potential of Baguio district 428
11.6.3 Porphyry copper potential of Abra area 430
11.6.4 Gold-copper vein deposit potential of Catanduanes Island 431
11.6.5 Nickeliferous-laterite potential of Isabela area 433
11.6 Recommendations for applying geologically-constrained mineral potential mapping elsewhere 434
11.7 Recommendations for further research 435

References 437

Curriculum Vitae 475

List of ITC PhD Dissertations 477

Chapter 1

Introduction

"Errors using inadequate data are much less than those using no data at all."

Babbage, Charles (1792-1871)

1.1 DESCRIPTION OF THE PROBLEM

Many Third World and developing countries rely mainly on the utilisation of their natural resources to sustain their economic development. In the Philippines in particular, the exploitation of mineral resources has traditionally been a significant component of the Philippine economy (Domingo, 1993). Minerals, however, are nonrenewable resources. One reason for the decline in economic development of many developing countries is depletion of known mineral reserves. Hence, sustainable mineral resource development requires comprehensive mineral-resource information. One of the conclusions of the International Conference on Development and Mining, Washington, D.C., June 1994, is that the lack of basic geological and mineral-resource data is a fundamental constraint on the development of many countries (Östensson, 1996). With the realisation of fundamental constraints on economic development of many countries, UNCTAD proposed a model framework that comprises four components, among which is the development of a geomanagement system – essentially a georeferenced management tool of natural-resource location and classification (Östensson, 1996).

The development of a comprehensive geomanagement system requires, among others, sufficient geoscience data. Geoscience data that are relevant to mineral resources development should include at least geological and mineral resource information (e.g., Mason and Arndt, 1996, Lewis, 1997). Geological information is important to determine which areas are favourable for the occurrence of particular types of mineralisation. Mineral resource information is important to determine, among others, the locations of potentially-mineralised areas. A vital component of a mineral resource information system is mineral potential assessment and classification (e.g., McCammon and Briskey, 1992; McLaren, 1992). The inherent problems of classifying or inventorying mineral resource potential (as opposed to known mineral resources), however, pose specific challenges.

Mineral potential assessment or classification is a multi-stage activity with the ultimate objective of delineating mineralised zones that can be exploited under prevailing economic conditions (Reeves et al., 1990). Ideally, during each stage, multivariate and multi-source geoexploration datasets are used to guide the

succeeding stages of mineral potential assessment and classification. At the small and medium-scale stage (i.e., regional to district scale ranging from 1:50,000 to 1:100,000), for example, the geoexploration datasets required should be derived from geological, geophysical and geochemical surveys. The increasing need to integrate geoexploration datasets arises from the fact that the easily-recognised mineral deposits have long been known and that more evidences and advanced methods are necessary to accurately assess and classify the mineral potential of a particular area (Bonham-Carter, 1997; Chinn and Ascough, 1997; Raines, 1997; Pan and Harris, 2000).

For many developing countries, however, there is a general lack of geoexploration data required for a reliable and comprehensive nationwide mineral potential assessment and classification. This lack of geoexploration data and nationwide comprehensive mineral potential assessment and classification have, in the Philippines for example, brought about conflicts and competing demands between land-uses that permit mineral resources development and those that promote protection of ecosystems (Domingo, 1993). The mineral potential assessment and classification of an area is critical for land-use policy-making so that prospective land is not alienated from mineral resources development in the future (McCammon and Briskey, 1992; McLaren, 1992). In order to achieve mineral potential assessment and classification despite the lack or incompleteness of systematic and comprehensive geoexploration datasets alternative methodologies are needed.

1.2 RATIONALE FOR THE RESEARCH

The geology of a particular area is the single most important indicator of its mineral potential. Comparing the geology of a particular area with conceptual mineral deposit and exploration models is among the initial steps undertaken to assess and classify its mineral potential. In addition, a qualitative knowledge of the spatial associations of known mineral deposits with the different geological features in well-explored areas is a factor in most exploration programs. This is encouraging because, for many countries, the geoexploration data available are more in the form of lithologic and structural maps. It is therefore hypothesised that there are ways to classify or map mineral potential when the geology is known but systematic and comprehensive geoexploration data are lacking. This hypothesis is tested through the development of methods for geologically-constrained mineral potential assessment and classification. The development of geologically-constrained mineral potential mapping techniques is motivated by the needs of public service organisations to outline prospective land, to weigh mineral potential against demands for land-use other than mineral resource development, and to encourage exploration investment through non-closure of areas likely to contain mineral deposits.

1.3 OBJECTIVES OF THE RESEARCH

The main objectives of this research are threefold.

1. To develop and demonstrate a methodology for remote-detection of indications of mineralisation in heavily-vegetated terranes to augment available geological data as inputs to geologically-constrained predictive mapping of mineral potential.

2. To develop and demonstrate a methodology for quantifying spatial associations between known mineral deposits and geological features as inputs to geologically-constrained predictive mapping of mineral potential.

3. To develop and demonstrate quantitative methodologies for geologically-constrained predictive mapping of mineral potential for areas where limited geological and mineral occurrence data are available.

1.4 DEFINITION OF MINERAL POTENTIAL

Mineral deposits, whether metalliferous or non-metalliferous, are accumulations or concentrations of one or more useful substances that are for the most part sparsely distributed in the Earth's crust (Bateman, 1951a). The geological processes that lead to the formation of mineral deposits are collectively called mineralisation (Bateman, 1951b).

Mineral potential, as used in this research, is the set of characteristics attributed to a particular area that describes the probability for the presence of mineral deposits or existence of mineralisation. Factors affecting economic viability of mineral deposits are not considered in this definition because the geological and mineral deposit data that are available are insufficient to determine sizes and grades of mineral deposits. Mineral potential is determined by how well the geological and mineral deposit data fit established mineral deposit models and existing knowledge about the mineralisation of a particular area. Mineral potential statements that arise from this research are estimates, rather than facts, because of the dynamic and variable nature of geological knowledge and the mineral exploration environment. It is, however, of prime importance that these statements establish the potential for the discovery of mineral deposits.

The geologically-constrained predictive mineral potential maps generated in this research are based on two factors: favourability and validity. Favourability is determined by integration of geological variables that are considered essential for mineral occurrence. Validity is determined by how well the predictive models delineate correctly known mineral deposits that were not used to generate the models. These two factors are important for assessing the efficacy of the methodologies developed for geologically-constrained predictive mapping of mineral potential.

1.5 METHODOLOGY

Figure 1.1 shows the 3-step methodology followed to undertake a geologically-constrained predictive mapping of mineral potential.

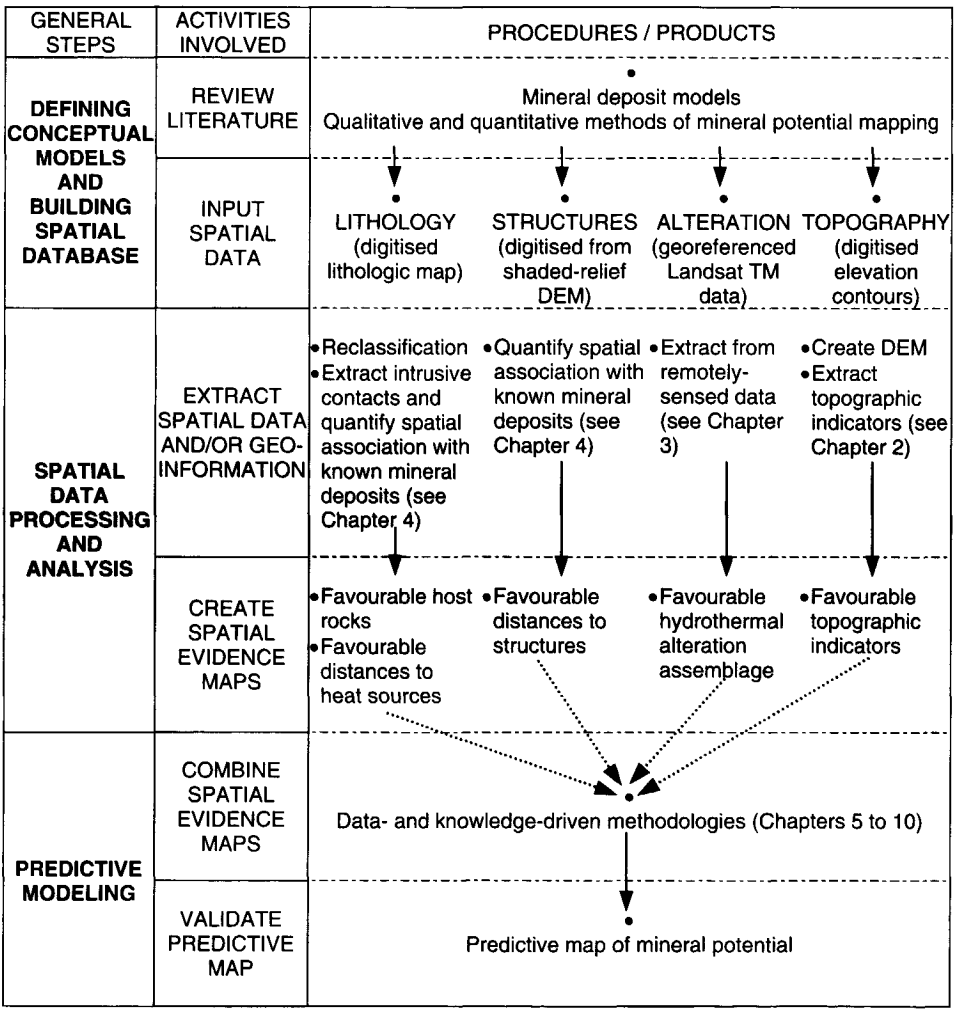

Figure 1.1. Flowchart of methodology for geologically-constrained predictive mapping of mineral potential.

The first step involves (a) review of literature pertinent to qualitative and quantitative methods of mineral potential mapping and (b) input of spatial data into a geographic information system (GIS). The four types of spatial data layers

indicated in the flowchart are not necessarily used together to map potential for a particular type of mineral deposit in a particular study area. This is the reason for the dashed arrows in the lower portion of the flowchart. The second step involves (a) procedures to extract spatial evidential data and/or spatial geoinformation about the relationship between known mineral deposits and geological features and (b) creation of derivative maps to be used as spatial evidences of mineralisation. The third step involves (a) integration of the spatial evidence maps to create a geologically-constrained predictive mineral potential map and (b) validation of the predictive map.

The general methodology is applied and demonstrated for mapping potential for porphyry copper, epithermal gold and nickeliferous-laterite mineralisation in five different study areas in the Philippines (see Chapter 2). There are two study areas for porphyry copper mineralisation; one is well-explored, the other is less-explored. There are two study areas for epithermal gold mineralisation; one is well-explored, the other is less-explored. There is one study area for nickeliferous-laterite mineralisation.

1.6 ORGANIZATION OF THE THESIS

This dissertation synthesises results of the research work to develop and demonstrate methodologies for geologically-constrained predictive mapping of mineral potential. This is an anthology of fifteen scientific papers published in peer-reviewed international geoscience journals and international geoscience conference proceedings since 1999. The contents of the different published scientific papers, however, were modified slightly in this thesis to avoid superfluity and achieve consistency between the different chapters. This thesis is also an omnibus of unpublished works, which fortify the robustness of the methodologies developed and described in the published works. This thesis consists of eleven chapters. A combined list of references cited in the different chapters is given at the end of the thesis.

The methodologies developed and described in this thesis are applied and demonstrated, in most cases, to all of the five study areas. To avoid repetition, the descriptions of the geology and mineralisation of the different study areas are put together in Chapter 2. The geological datasets input to the GIS are also described. The extraction of structural geoinformation from digital elevation models (DEM), to augment geological map data, is demonstrated. The processing and analysis of geochemical exploration datasets are described in Chapter 2 as well. Portions of Chapter 2 appear in the various scientific papers that were published.

Chapter 3 is about Mineral Imaging with Landsat TM Data for Hydrothermal Alteration Mapping in Heavily-Vegetated Terrane (Carranza and Hale, 2001d). It also concerned with Remote Detection of Vegetation Stress for Mineral

Exploration (Carranza and Hale, 2001f), which is described in detail as Remote Detection of Mineralization-Related Vegetation Stress Using Landsat TM Data, Catanduanes Island, Philippines (Carranza and Hale, 2001e). The remotely-detected hydrothermal alteration zones were used in the predictive mapping of porphyry copper and epithermal gold mineralisation potential.

Chapter 4 relates to the Spatial Association of Mineral Occurrences and Curvi-Linear Geological Features (Carranza and Hale, 2001g). It demonstrates two established methods and a new method for quantifying spatial associations between point features (e.g., mineral deposits) and linear features (e.g., faults/fractures). In addition, it presents a salient finding of this research that porphyry copper deposits are favourably emplaced near strike-slip fault discontinuities (Carranza and Hale, 1999d, 1999e). The quantified spatial associations between the known mineral deposits and geological features in the different study areas were applied in the geologically-constrained predictive mapping of mineral potential through the use of binary geological predictor patterns (Chapters 5 and 6) and multi-class geological predictor patterns (Chapters 7, 8 and 9).

Chapter 5 concerns the application of geologic criteria provided by deposit exploration models to create binary geological predictor patterns that are combined through simple map algebra to generate mineral potential maps. The binary evidences were assigned scores of 0 and 1 to indicate absence and presence, respectively, of a geological feature required by a particular deposit exploration model. Portions of Chapter 5 are based on Application of Mineral Exploration Models and GIS to Generate Mineral Potential Maps as Inputs for Optimum Land-Use Planning in the Philippines (Carranza et al., 1999a), which demonstrate a technique for areas with no known nickeliferous-laterite mineralisation. For areas with known mineral deposits, the results of the spatial association analyses are shown to be useful in the selection and creation of binary geological predictor patterns as demonstrated for predictive mapping of porphyry copper and epithermal gold potential.

Chapter 6 explains the application of a Bayesian probability model, otherwise known as weights of evidence modeling, for combining binary predictor patterns for geologically-constrained mineral potential mapping. It is based chiefly on Geologically Constrained Probabilistic Mapping of Gold Potential, Baguio, District, Philippines (Carranza and Hale, 1999b, 2000) and Where are Porphyry Copper Deposits Spatially Localized? A Case Study in Benguet Province, Philippines (Carranza and Hale, 2001h). The binary predictor patterns were assigned weights based on quantified spatial associations between known mineral deposits and geological features using the weights of evidence model.

Chapter 7 demonstrates an innovative technique for a data-driven application of the Dempster-Shafer theory of evidential belief to mineral potential mapping. The Dempster-Shafer theory of evidential belief is applied invariably to

knowledge-driven mineral potential mapping as shown by examples in the literature. In this work, modified equations were devised for data-driven estimation of probability assignments of multi-class geological predictor patterns, which are based on the spatial association analyses. The work presented here is based on Evidential Belief Functions for Geologically-Constrained Predictive Mapping of Gold Mineralization Potential, Baguio District, Philippines (Carranza and Hale, 2001a). The data-driven technique was also applied to geologically-constrained mapping of porphyry copper mineralisation potential. In addition, a knowledge-driven approach is shown for mapping nickeliferous-laterite potential.

Chapter 8 explains the application of the theory of fuzzy sets to geologically-constrained mineral potential mapping. Multi-class sets of patterns of lithologic units, hydrothermal alteration units, geochemical anomalies and proximity to curvi-linear or point geological features (based on the quantified spatial association models), were assigned subjective fuzzy weights and then combined by fuzzy operators using fuzzy logic as an inference engine. The work described is based on Geologically Constrained Fuzzy Mapping of Gold Mineralization Potential, Baguio District, Philippines (Carranza and Hale, 2001b). The fuzzy approach is also demonstrated for mapping porphyry copper potential. A fuzzy approach for mapping mineral potential in areas with no known mineral deposits is demonstrated for nickeliferous-laterite type of deposit.

Chapter 9 describes a logistic regression approach to geologically-constrained mineral potential mapping. Nominal map data such as lithologic units, hydrothermal alteration units, geochemical anomalies and proximity classes of curvi-linear or point features, based on the spatial association analyses, were quantified systematically and used as independent variables in logistic regression to predict the probability for presence or absence of mineralisation. The work described is based on Logistic Regression for Geologically-Constrained Mapping of Gold Mineralization Potential, Baguio District, Philippines (Carranza and Hale, 2001c). The logistic regression approach is also shown for mapping porphyry copper potential.

Chapter 10 demonstrates a 'wildcat' methodology for mapping mineral potential based on given geological map data alone. Favourability scores were defined for proximity classes of curvi-linear or point geological features, hydrothermal alteration units and/or geochemical anomalies, which were used in principal components analyses to extract a favourability function interpreted to represent mineral potential. The proximity maps were constructed without regard to the results of the spatial association analyses. The work presented is based on Wildcat Mapping of Gold Potential, Baguio District, Philippines (Carranza and Hale, 2001i). The 'wildcat' approach is also demonstrated for mapping potential for porphyry copper.

Chapter 11 presents the salient findings and major conclusions of the work vis-à-vis the research objectives and provides suggestions for further research.

Chapter 2

Study Areas and Geoexploration Datasets

Maps and Maidens -
They must be well-proportioned and not too plain;
Colour must be applied carefully and discretely;
They are more attractive if well dressed but not over-dressed;
They are very expensive things to dress up properly;
Even when they look good, they can mislead the innocent;
And unless they are well bred, they can be awful liars!

Willats, E.C., 1970. Maps and maidens.
Cartographic Journal, v. 7, no. 1, p. 50.

This Chapter describes the study areas. A brief background of the geology of and types of mineral deposits in the Philippines is given first. The geology and type of mineralisation studied in each of the study areas are then explained briefly. The geological map data inputs to the GIS are described next. Then, the extraction of structural geoinformation from digital elevation models (DEM) is demonstrated. Available geochemical exploration datasets and their processing to delineate geochemically anomalous zones are described next. Portions of this Chapter appear in the various published papers resulting from the studies that led to this thesis.

2.1 BACKGROUND ON PHILIPPINE GEOLOGY

2.1.1 Generalised tectonic setting

The Philippine archipelago is located in the Western Pacific (Figure 2.1). It is situated in a very active and complex tectonic region and represents an amalgamation of rock units that resulted from successive collages of exotic terranes (Rangin, 1991). It forms a roughly triangular area bounded by the Philippine Sea to the east, the South China Sea to the west, and the Celebes Sea to the south. The archipelago has the unique feature of being caught between two opposing convergent systems, the eastward-dipping Manila, Sulu-Negros, and Palawan Trenches; and the westward-dipping East Luzon and Philippine Trenches. With over 3,500 km of active subduction zones, the archipelago has morphological and geological features characteristic of island-arc systems (Mitchell and Balce, 1990). It consists of active and recently active arc systems; older Tertiary and Cretaceous arcs in which erosion has exposed plutons; ophiolitic and meta-igneous rocks mostly forming basement to superimposed arc systems; and areas of continental crust (Figure 2.2). Cutting through the central parts of the whole of the archipelago is the Philippine Fault

Zone, a left-lateral strike-slip fault system, which apparently controlled the morphological orientation of the various island groups (Mitchell et al., 1986). The Philippine Fault Zone resulted from the accommodation of the east-west compressive regimes due to the eastward subduction of the South China Sea oceanic crust beneath the Philippine Plate along the Manila and Sulu-Negros Trenches and the westward subduction of the Philippine Sea Plate beneath the Philippine Plate along the East Luzon and Philippine Trenches (Rangin, 1991; Aurelio, 1992; Ringenbach, 1992; Aurelio et al., 1994; Quebral, 1994; Aurelio et al., 1997).

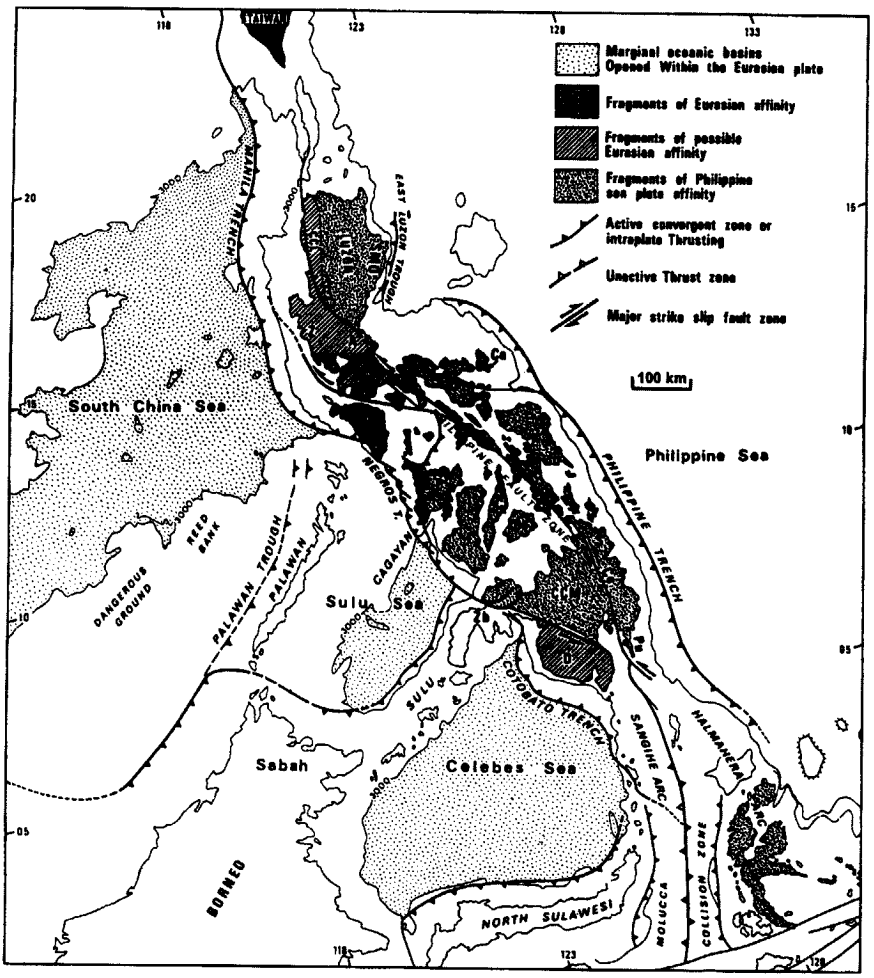

Figure 2.1. Geotectonic setting of the Philippine archipelago (from Rangin, 1991). CCL = Central Cordillera of Luzon; SMO = Sierra Madre Oriental; CCM = Central Cordillera of Mindanao.

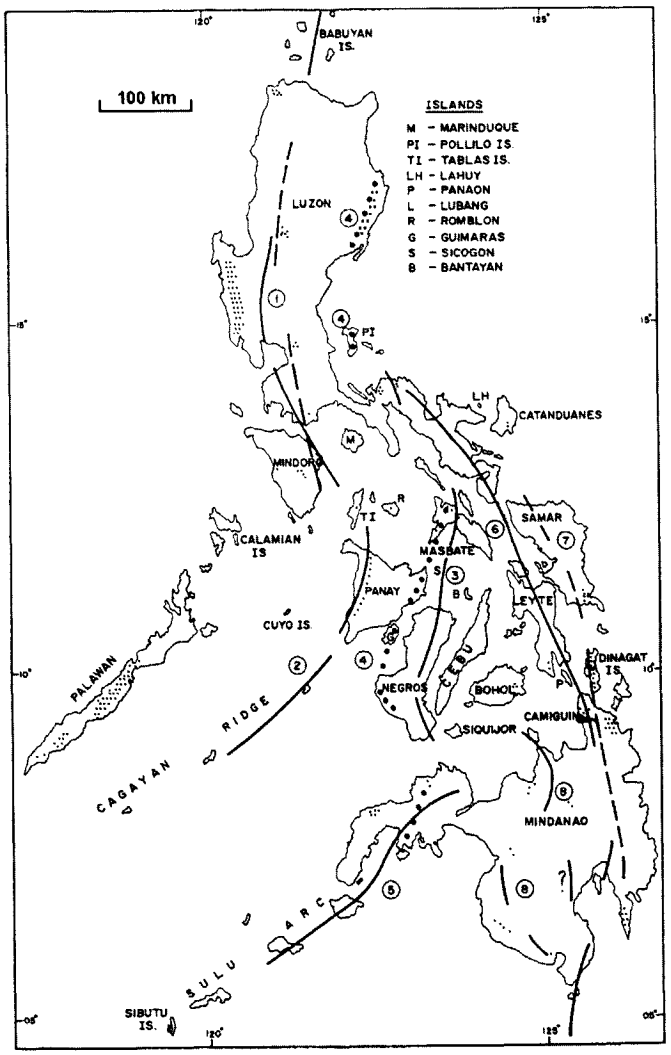

Figure 2.2. Distribution of some Cenozoic magmatic arcs in the Philippines. 1 = NW Luzon-SW Luzon-E Mindoro: broken line, early mid-Miocene, end upper Miocene in NW Luzon; solid line, Pliocene-Quaternary; 2 = W Panay-Cagayan ridge, early mid-Miocene; 3 = E Negros-Masbate-? SE Luzon (Paracale), early mid-Miocene, Pliocene-Quaternary, and in Negros also late Miocene; 4 = NE Luzon - Polillo Is. - Masbate - E Panay - SW Negros, late Eocene to Oligocene; 5 = Sulu-Zamboanga: solid line, mostly Quaternary; dotted line, Paleogene or early Miocene; 6 = SE Luzon - E Leyte - E Mindanao, Pliocene-Quaternary; 7 = Samar-E Mindanao, Miocene; 8 = N central and SW Mindanao, Pliocene and Quaternary. Stippled areas indicate larger ophiolitic bodies (from Mitchell and Balce, 1990).

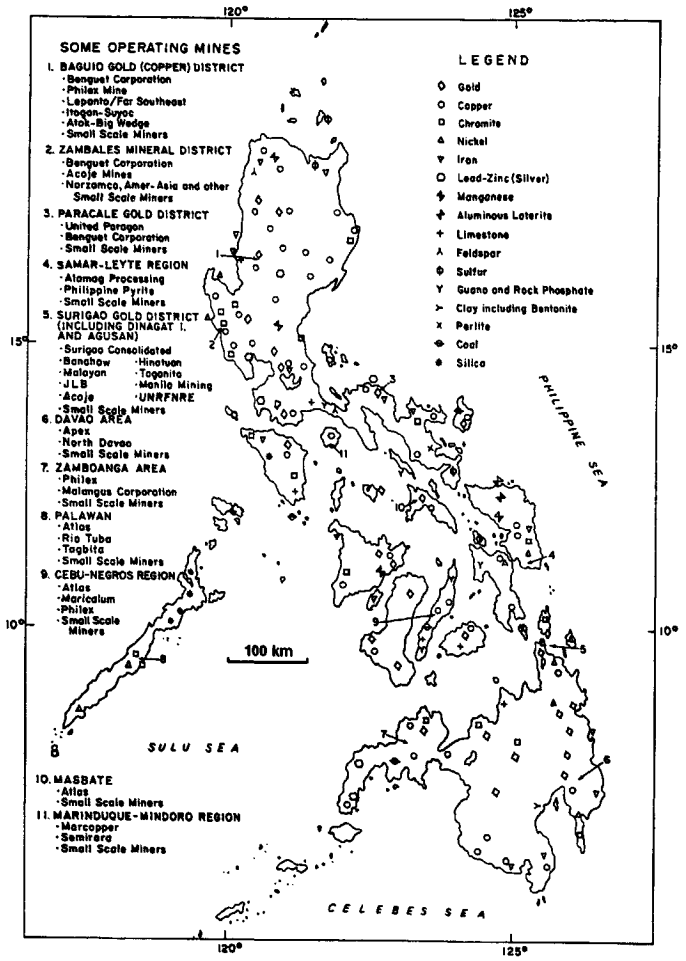

Figure 2.3. Distribution of some major Philippine mineral deposits (from Domingo, 1993).

2.1.2 Major mineral deposits

Philippine mineral resources include a variety of metalliferous and non-metalliferous minerals (Figure 2.3). The Philippines has a long, well-established history of major production from its mines and ranked previously among the world's top ten in the production of chromite, copper, nickel and gold (Domingo, 1993). As recently as 1998, copper and gold remain the backbone of the country's mineral industry (Lyday, 1998).

With an area of about 300,000 km^2 and in 1995 official gold production of at least 27 tonnes, the Philippines then had a higher gold production per unit land

area than any country except South Africa (Table 2.1). Almost 65% of the Philippines' official gold production comes from epithermal systems, the remainder coming from gold-rich porphyry copper deposits (Mitchell and Leach, 1991). The epithermal gold-silver vein deposits, particularly in the major mining districts, have a strong affinity with Neogene dioritic plutons and volcanic terranes. Some gold deposits in the country are characterised by the presence of skarns and base metal anomalies, which suggest gold-rich porphyry copper-skarn rather than epithermal deposits. In addition, there are gold deposits related to greenschist-facies metavolcanic and metasedimentary rocks and it is uncertain whether these deposits are of the epithermal or mesothermal type (Bureau of Mines and Geosciences, 1986).

Table 2.1. Top six gold producing countries in 1995*.

Country	Gold production (kg)	Area (km^2)	Gold production per unit area (kg/km^2)
South Africa	447,900	1,221,040	0.3668
United States of America	354,000	9,629,047	0.0368
Australia	307,900	7,682,292	0.0400
Canada	161,700	9,970,610	0.0162
China	155,500	9,571,300	0.0162
Indonesia	152,400	1,919,400	0.0794
Philippines**	27,144	300,000	0.0905

*Source: http://www.goldinstitute.org/worldprod.html
**Source: Mines and Geosciences Bureau, Philippines.

The most significant copper mineralisation is of the porphyry type. With a porphyry-type copper resource of at least 100 million tonnes (Bureau of Mines and Geosciences, 1986), the Philippine archipelago constitutes one of the world's premier porphyry copper provinces. The porphyry copper deposits occur within or adjacent to magmatic arc dioritic plutons (Domingo, 1993). Together with the copper deposits is some molybdenite mineralisation, especially in those deposits associated with Cretaceous-Paleogene dioritic intrusives (Sillitoe and Gappe, 1984).

Chromite deposits are of various types – podiform, residual and transported alluvial deposits (Bureau of Mines and Geosciences, 1986). These deposits are related to the ophiolitic terranes (Figure 2.2). In these ophiolitic terranes, nickeliferous-laterite deposits are found. The more economical of these nickeliferous-laterite deposits are found in Palawan and in northeastern Mindanao.

2.1.3 The study areas

Figure 2.4 shows the location of the study areas, namely: Benguet province; Baguio district, Abra area; Catanduanes Island; and Isabela area.

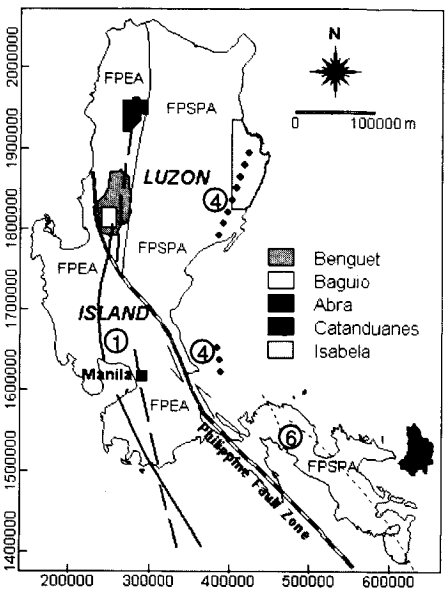

Figure 2.4. Location of study areas. FPSPA = Fragments of Philippine sea plate affinity; FPEA = Fragments of possible Eurasian affinity (Rangin, 1991; see Figure 2.1). See Figure 2.2 for explanation of numbered magmatic arcs.

Benguet province, Baguio district and Abra area are in the northwestern part of Luzon Island. These areas lie along a north-south trending magmatic arc, which is characterised by a mountainous belt known as the Central Cordillera of Luzon (Figures 2.1 and 2.2). Benguet province is well-explored for its epithermal gold and porphyry copper deposits. It is studied here for its porphyry copper deposits. The Baguio district is within Benguet province. It is the most productive among the mining districts in the Philippines. It has produced well in excess of 800 tonnes of gold, more than any other goldfield in the east Asia-western Pacific region (Mitchell and Leach, 1991). Although it also contains porphyry copper deposits, it is studied here for its epithermal gold deposits. The Abra area is less-explored; it is studied here for its known prospects for copper mineralisation.

Catanduanes Island province lies to the east of the southeastern leg of Luzon Island. It is uncertain to which magmatic arc the island is associated. Mitchell and Leach (1991), however, postulate a northeast Luzon – Polillo Island – Catanduanes Island magmatic arc that is associated with subduction in the East Luzon – Philippine Trenches (Figures 2.1 and 2.2). Catanduanes Island is not well-explored but is known to contain hydrothermal gold-copper deposits, which are studied here.

The Isabela area is in northeastern part of Luzon Island, which is characterised geologically by a magmatic arc adjacent to an ophiolitic terrane. The area has known copper and chromite deposits; but it is studied for nickeliferous-laterite mineralisation.

2.2 BENGUET PROVINCE

The administrative province of Benguet has two mineral districts, namely, Baguio (which is also studied in this work) and Mankayan. Both mineral districts are endowed with epithermal gold and gold-rich porphyry copper deposits (Mitchell and Leach, 1991; Garcia, 1991). For this reason, the province has been the subject of several mineral exploration programs and geological studies. Consequently, the geology of Benguet's neighbouring administrative provinces has been relatively little studied. The work presented in this thesis is therefore confined within the administrative jurisdiction of the province.

2.2.1 Geology and porphyry copper mineralisation

Benguet province lies at the southern end of the north-south trending regional geanticlinal mountain range known as the Central Cordillera of Luzon (Figures 2.1 and 2.4). This mountainous belt corresponds to a magmatic arc associated with the eastward subduction of the South China Sea oceanic crust beneath the Philippine Plate along the Manila Trench west of the archipelago (Balce et al., 1980). The province is underlain mostly by Cretaceous-Paleogene metavolcanic rocks that occupy the core of the regional geanticline (Figure 2.5). Batholithic plutons of Oligocene to Middle Miocene age intruded these metavolcanic rocks. Overlying these rocks are Eocene-Miocene volcaniclastic rocks that are also overlain by Middle Miocene reef and lagoonal limestones. Late Miocene to Pliocene clastic and volcanic rocks occupy the western part of the province along the western flank of the geanticline. The pre-existing rocks are intruded by Late Miocene to Pleistocene dioritic and andesitic/dacitic porphyry plutons.

There are 31 known porphyry copper deposits (Table 2.2; Figure 2.5). Many of these deposits are gold-rich. The deposits are associated with dioritic and andesitic/dacitic porphyry plutons and are hosted by Cretaceous-Paleogene metavolcanic rocks (Sillitoe and Gappe, 1984).

2.2.2 Geological map data

Geological data inputs to the GIS are derived and compiled from geologic maps of various scales (either wholly or partly covering Benguet province). The locations of porphyry copper deposits were digitised as points with UTM (Universal Transverse Mercator projection) coordinates. The contacts of mapped lithologic units were hand-digitised into vector (segment) format. Because the geologic maps were of different scales, there are differences in the positions of the lithologic contacts. To overcome the problem of choosing which contact is accurate and producing a 'unified' lithologic map of the province, a series of map overlay operations were performed (two segment maps at a time). The main criterion for choosing the 'accurate' contact is the original scale of the paper

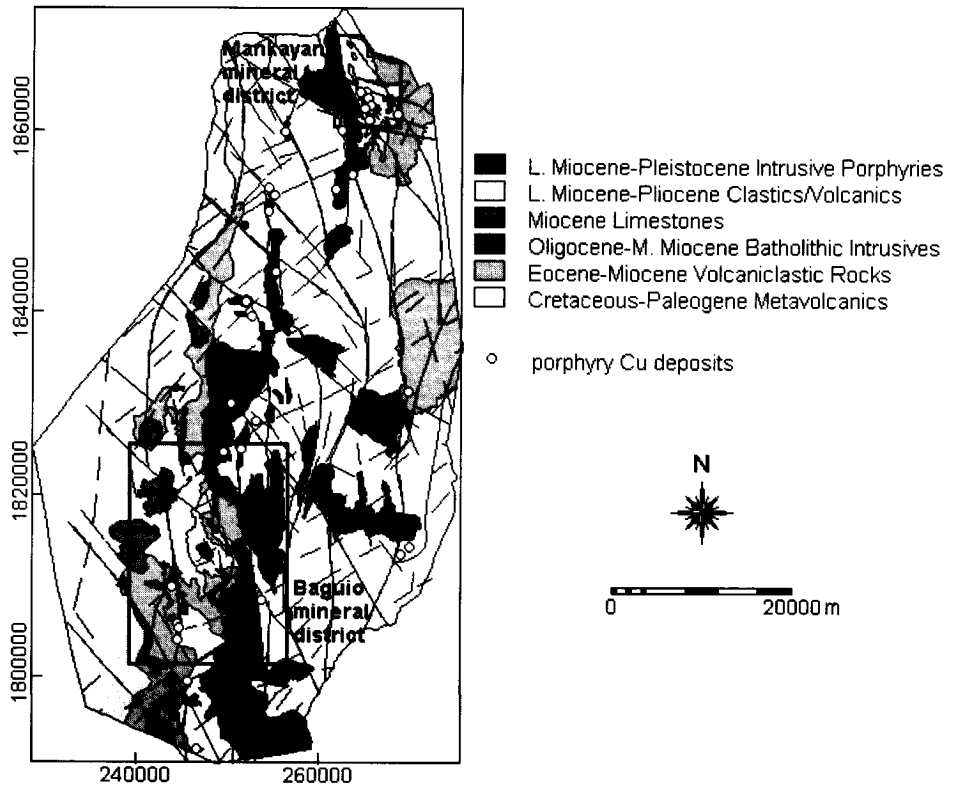

Figure 2.5. Simplified geological map of Benguet province. Linear features are inferred faults/fractures from shaded-relief images of DEM (see Section 2.2.3). Unfilled circles are locations of porphyry copper deposits. Map coordinates are in metres (UTM projection, zone 51).

map. Thus, lithologic contacts in maps with larger scale were chosen; the 'inaccurate' segments in the maps with smaller scales were cut and deleted. Manual adjustments of some segments were necessary so that respective contacts from the different maps join. The 'unified' segment map of lithologic contacts was then polygonised; each polygon was labeled according to the name of each litho-stratigraphic formation. A reclassification based on geologic age was undertaken to simplify the lithologic map. The lithologic map shown in Figure 2.5 is therefore a synthesis of the lithologic maps of MMAJ-JICA (1977), Balce et al. (1980) and several lithologic maps from various unpublished reports of the Philippine Bureau of Mines and Geosciences.

Table 2.2. Porphyry copper mines, explored deposits and prospects, Benguet province.

	Name	UTM Coordinates		Res. (Mt)	% Cu	g/t Au	Reference
		Northing	Easting				
Mines	Santo Tomas	245575	1799485	367	0.31	0.62	Baluda & Galapon, 1998
	Santo Niño*	249550	1824618	125	0.34	0.26	Sillitoe & Gappe, 1984
	Ullman*	251441	1824892	38	0.34	0.33	Sillitoe & Gappe, 1984
	Lobo*	251991	1841091	210	0.28	0.25	Sillitoe & Gappe, 1984
	Boneng*	252567	1839547	15	0.33	0.44	Sillitoe & Gappe, 1984
	Lepanto FSE	265029	1864106	356	0.73	1.24	Concepcion & Cinco, 1989
	Black Mountain*	243891	1809871	52	0.37	0.3	Sillitoe & Gappe, 1984
Explored Deposits	Suluakan	253122	1824892	123	0.35	0.13	Sillitoe & Gappe, 1984
	Polar	262567	1859903	100	0.4	0.4	Yumul, 1980
	Tirad	268451	1861717	500	0.4	0.4	Sillitoe & Angeles, 1985
	Buaki	264391	1864114	2	0.4	0.4	Garcia & Bongolan, 1989
	Palidan	265460	1861119	30	0.45	1.1	Yumul, 1980
	Tawi-tawi	269037	1813380	159	0.39	0.16	Sillitoe & Gappe, 1984
	Sinipsip	261913	1853432	8	0.51	<0.02	Sillitoe & Gappe, 1984
	San Antonio	254380	1851026	29	0.37	0.3	Sillitoe & Gappe, 1984
	Gambang	263622	1855126	55	0.35	0.01	Yumul, 1980
Prospects	Lepanto FSE-FW	265194	1863489				Concepcion & Cinco, 1989
	Bulalacao	265607	1862676				Concepcion & Cinco, 1989
	Nayak	264923	1862432				Concepcion & Cinco, 1989
	Masalin	256209	1859801				Yumul, 1980
	R & MSV claims	255092	1852895				Caculitan, 1987
	Sapiangao claims	250268	1829998				Yumul, 1980
	Regalian claims	254361	1853672				Yumul, 1980
	Gregorian claims	255291	1844436				Yumul, 1980
	Ansagan	246556	1792105				Yumul, 1980
	Zipporah claims	253819	1808384				Yumul, 1980
	Pugo claims	244458	1805814				Yumul, 1980
	Camp 4	244660	1805351				Yumul, 1980
	Twin Peaks	244436	1803969				Yumul, 1980
	Bolo claims	269937	1814293				Yumul, 1980
	Palansa	269818	1831297				Mendoza & Viaga, 1993

*defunct mines

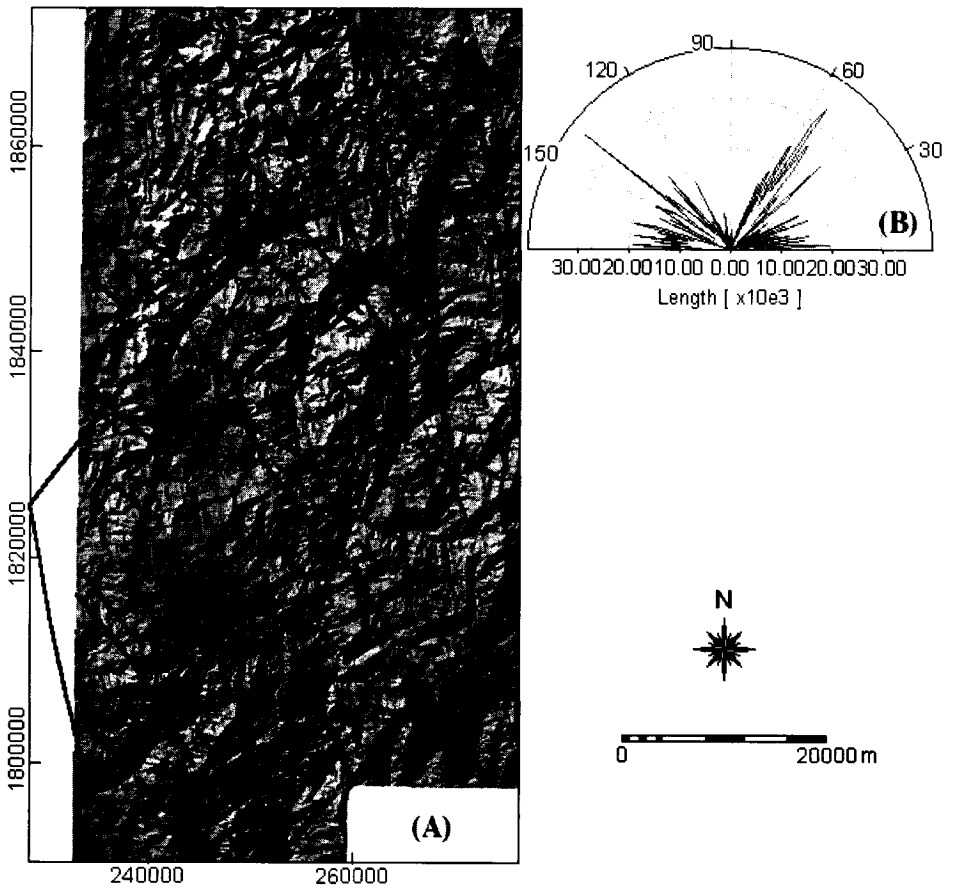

Figure 2.6. (A) Northwest-illuminated shaded-relief image of DEM of Benguet province and faults/fractures interpreted from different shaded-relief images of DEM. (B) Rose diagram of interpreted faults/fractures.

2.2.3 DEM-interpreted faults/fractures

Mining in Benguet dates back to the pre-Spanish colonial period. Continued exploration in the province resulted in several versions of structural maps of varying scales and hence varying accuracies. There is therefore a problem in choosing which structural map to use in the spatial data analyses. The problem was overcome by interpreting, from shaded-relief images of a digital elevation model (DEM) of the province, the regional fault/fracture patterns.

From the 1:50,000 scale topographic maps of the National Mapping Resource and Information Authority (NAMRIA, 1990a, 1990c, 1990d, 1990g, 1990j, 1990k, 1990m, 1990r), with elevation contours of 20 m intervals, contour lines of 100-m intervals were hand-digitised into vector (segment) format. Where necessary, intermediate 50-m interval contours were hand-digitised. Mountain peaks, ridge and hilltops were digitised as short segments. Each segment was assigned the elevation (in metres) as its spatial attribute. The digitised lines were rasterised and interpolations of elevations between rasterised contour lines were calculated automatically to generate the DEM.

Shaded-relief images were calculated from the DEM by applying directional filters. The directional filters were designed to provide illumination from eight different directions: N, N45E, E, S45E, S, S45W, W and N45W. The different illumination sources were necessary to highlight fault/fracture lineament patterns that strike in different directions. The shaded-relief image exhibited in Figure 2.6 is illuminated from N45W. Lineaments representing faults/ fractures (e.g., in Figure 2.6) were interpreted visually and digitised 'on-screen' from the different shaded-relief images. Linear features in the northwest portion outside Benguet province represent westerly dipping sedimentary strata; these linear features were not digitised. The rose diagram of the interpreted faults/fractures reflects the east-west compressive stress regimes that brought about structural deformation of the region (Figure 2.6; Balce et al., 1980).

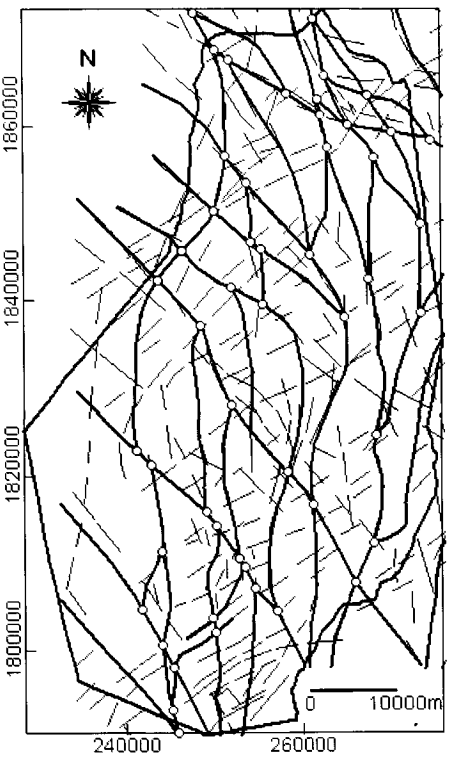

Figure 2.7. Regional fault/fracture systems based on fault/fracture lineaments interpreted from shaded-relief images of DEM of Benguet. Unfilled circles are inferred strike-slip fault discontinuities (see Section 3.3.1).

The regional fault systems were interpreted from the digitised fault/fracture lineaments (Figure 2.7). These regional faults that trend mainly northwest and north-south are believed to be horsetail splays of the sinistral strike-slip Philippine Fault system (Balce et al., 1980; Ringenbach et al., 1990). The northeast trending faults/fractures are interpreted as conjugate shears of the northwest and north-south trending left-lateral strike slip faults.

2.2.4 Stream sediment geochemical data

Stream sediment geochemical data, courtesy of Newmont Philippines, Inc., are available for some portions of the province. The geochemical data consist of Cu values determined by AAS (atomic absorption spectrophotometry) and Au values determined by BLEG (bulk cyanide leach extractable gold). The geochemical data pertain to the southeast-central and southwest-central portions of the province (Figure 2.8). There are 233 samples in the southeast-central area; these samples represent 319.7 km^2 of catchment basins. Thus, the mean sampling density in the southeast-central area is about one sample per 1.4 km^2. There are 56 samples in the southwest-central area; these samples represent 271.4 km^2 of catchment basins. Thus, the mean sampling density in the southwest-central area is about one sample per 4.8 km^2.

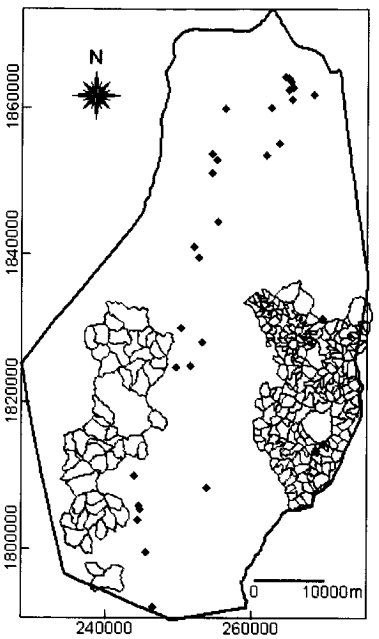

Figure 2.8. Stream sediment catchment basins, Benguet province. Filled diamonds = porphyry copper deposits.

Because the geochemical data pertain to areas that are underlain by different lithologies (see Figure 2.5), they are studied separately. Table 2.3 shows the elementary statistics of the raw geochemical data. As indicated by their skewness coefficients, all the element distributions are positively skewed. Asymmetry of the raw data distributions is effectively reduced after a $\log_e$-transformation. Histograms of the $\log_e$-transformed data are shown in Figure 2.9. The histogram for Au values in the southeast-central portion shows at least three populations (Figure 2.9a). The histogram for Au values in the southwest-central portion approximates a unimodal Gaussian distribution (Figure 2.9c). The histogram of the Cu values in the southeast-central portion approximates a unimodal Gaussian distribution (Figure 2.9b). The histogram of the Cu values in the southwest-central portion shows at least three populations (Figure 2.9d).

The $\log_e$-transformed data were assigned to four classes, namely, low background, high background, slightly anomalous, highly anomalous. For the $\log_e$-transformed Au data (southeast-central area) and Cu data (southwest-central area), natural breaks in the histograms were used in the classification scheme. For the $\log_e$-transformed Cu data (southeast-central area) and Au data (southwest-central area), which approximate Gaussian distributions, the mean and standard deviation were used in the classification scheme (Rose et al.,

1979). Values that are equal to or less than the mean are considered low background. Values between the mean and mean plus one standard deviation ($\bar{x}$ + s.d.) are high background. Values between $\bar{x}$ + s.d. and $\bar{x}$ + (2 * s.d.) are slightly anomalous. Values greater than $\bar{x}$ + (2 * s.d.) are highly anomalous.

Table 2.3. Elementary statistics of raw geochemical data and skewness of $\log_e$-transformed data, Benguet province.

Area	Element	Minimum	Maximum	Mean	Std. Dev.	Skewness	Skewness ($\log_e$)
Southeast-central	Au (ppb)	0.1	436	15	39	6.5	0.55
	Cu (ppm)	0.09	930	42	92	5.4	-0.19
Southwest-central	Au (ppb)	0.1	440	21	63	5.7	0.241
	Cu (ppm)	3.1	660	61	131	3.2	1.15

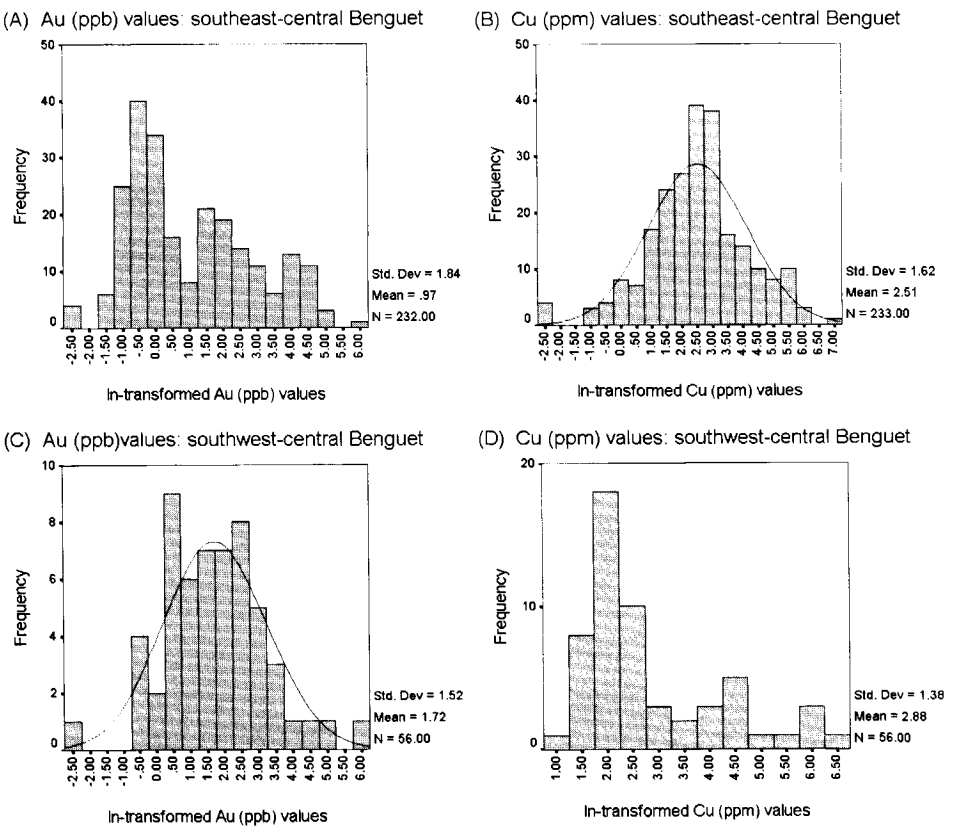

Figure 2.9. Histograms of Au and Cu geochemical data, Benguet province.

Shown in Figure 2.10 are presentations of the geochemical data as catchment basin anomaly maps (Carranza and Hale, 1997). The Cu and Au anomalies in the southeast-central area show spatial association with the known porphyry copper deposits. The Cu and Au anomalies in the southwest-central area lie along the belt of porphyry copper deposits in the province. The geochemical anomalies of Cu and Au are spatially coincident. The Pearson correlation coefficient for the Cu and Au values in the southeast-central area is 0.631; in the southwest-central area 0.772. These correlation coefficients are significant at the 0.01 probability level (Howarth, 1983). Copper and Au are, respectively, indicator and pathfinder elements for porphyry copper deposits (Learned and Boissen, 1973). These geochemical anomaly maps will be used to validate the results of the geologically-constrained predictive mineral potential mapping presented in the succeeding chapters.

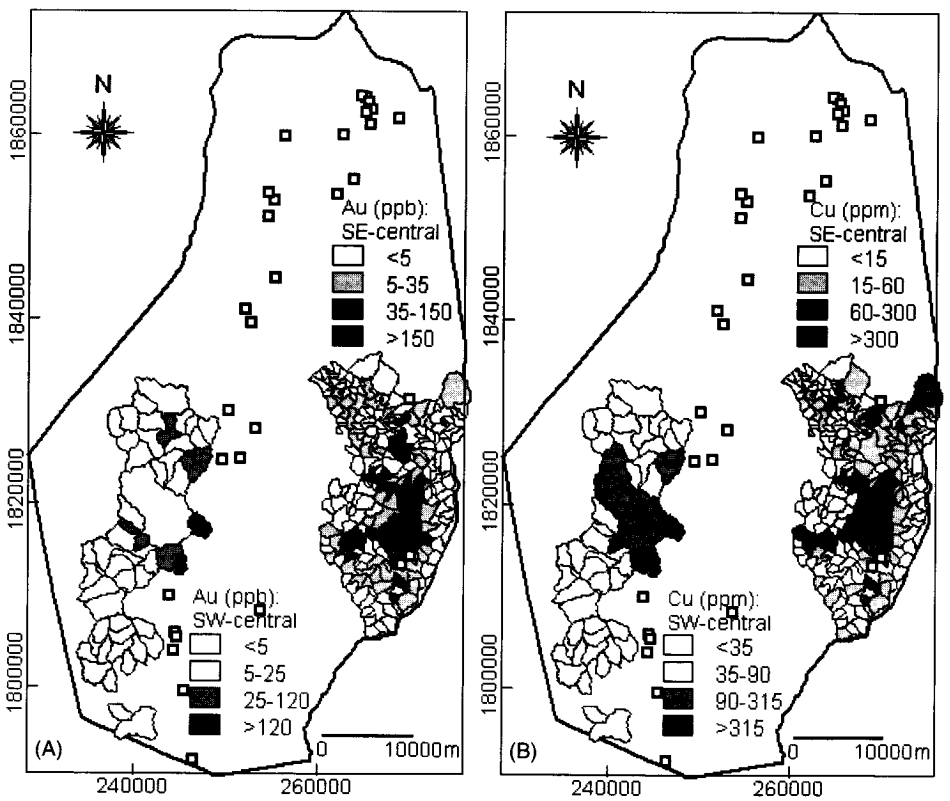

Figure 2.10. Stream sediment catchment basin geochemical anomaly maps for Benguet province: (A) Au; (B) Cu. Open squares = porphyry copper deposits.

2.3 BAGUIO DISTRICT

The Baguio district is located in Benguet province (Figure 2.4). It is a major mining district in the Philippines and has been subjected to numerous geoscientific investigations. It is studied here to demonstrate examples of geologically-constrained mineral potential mapping in a well-explored district. The district has produced well in excess of 800 tonnes of gold, more than any other gold-field in the east Asia-western Pacific region (Mitchell and Leach, 1991).

2.3.1 Geology and epithermal gold mineralisation

The district is underlain mainly by five lithologic units (Figure 2.11). The Pugo Formation of Cretaceous to Eocene age is a sequence of metavolcanic and metasedimentary rocks. The Zigzag Formation unconformably overlies the Pugo Formation. It consists largely of marine sedimentary rocks of Early to Middle Miocene age (Balce et al., 1980). However, it is intruded by andesite porphyry dated 15.0 ±1.6 Ma (Wolfe, 1981) or pre-Middle Miocene. Mitchell and Leach (1991) consider the Zigzag Formation to be largely Late Eocene, but it may include rocks of Early Miocene age. The Kennon Formation of Middle Miocene age conformably overlies the Zigzag Formation (Balce et al., 1980). It is composed of limestones that occur discontinuously along a north-south trending belt west of the district. The Klondyke Formation of Late Miocene age unconformably overlies all other formations (Balce et al., 1980; Wolfe, 1988; Mitchell and Leach, 1991). It consists mainly of clastic rocks that are very largely or entirely andesitic in composition. The other major lithologic unit is the Agno Batholith. Its bulk is composed mainly of hornblende quartz diorite. Radiometric dating indicates that the different rocks in the batholith were intruded in several phases. Wolfe (1981) cited an average age of 27 Ma for the earlier phases and a range of 12-15 Ma for the later phases. More recent workers contend that the Agno Batholith intruded mainly into the Pugo Formation (Balce et al., 1980) but earlier workers believed that it also intruded the Zigzag Formation (Peña, 1970; Sawkins et al., 1979). The Zigzag and Pugo Formations have also been intruded by younger dioritic, andesitic and dacitic porphyries that vary in age from Late Miocene to Pleistocene (Mitchell and Leach, 1991; Cooke et al., 1996).

Most of the gold in the district comes from epithermal systems that are confined to a north-trending zone about 7 km wide east of Baguio City (Fernandez and Damasco, 1979). There are 19 large-scale gold deposits in the district (Table 2.4). The epithermal veins are commonly fracture-controlled. The epithermal veins that are more productive trend northeasterly to easterly although there are some productive northwesterly trending veins (Mitchell and Leach, 1991). The auriferous veins are hosted mostly by the Zigzag and Pugo Formations and the Agno Batholith. Almost all known productive veins are found at the western

fringe of the contact zone between the Agno Batholith and the intruded rocks. Wolfe (1988) suggested that the Agno plutons are an important source of the gold. More recent workers, however, claim that the epithermal gold mineralisation is related to the younger intrusive complexes (Mitchell and Leach, 1991; Cooke et al., 1996).

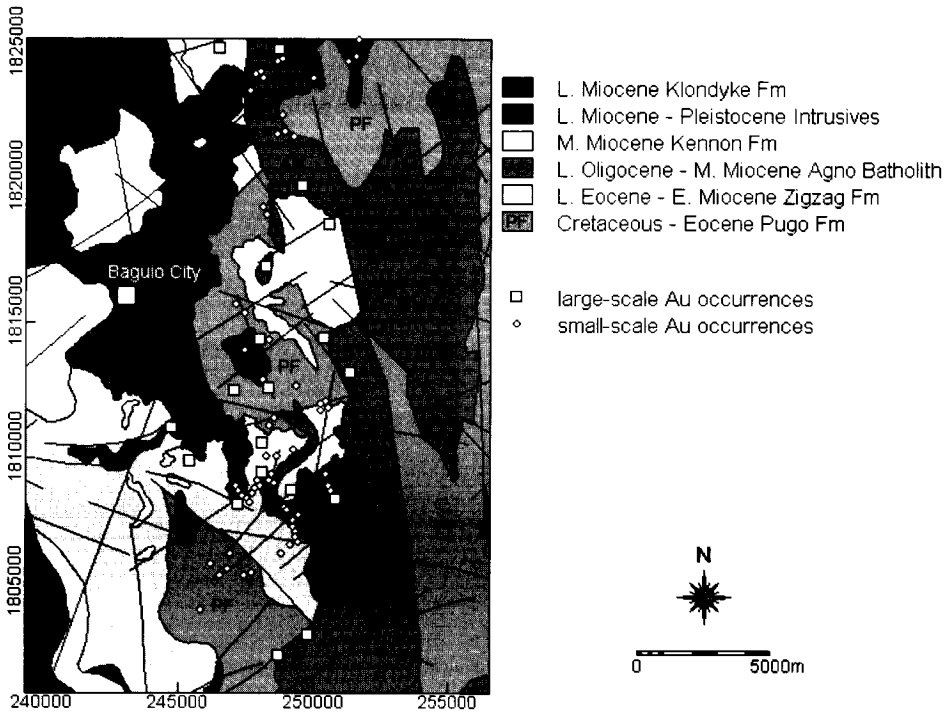

Figure 2.11. Simplified geological map of Baguio district (modified after MMAJ-JICA, 1977; Balce et al., 1980). Curvi-linear features are faults/fractures. Map coordinates are in metres (UTM projection, zone 51).

2.3.2 Geological map data

The map data of lithologic formations, faults/fractures and locations of large-scale and small-scale gold deposits (Figure 2.11), were derived from published works (Mitchell and Leach, 1991; MMAJ, 1996; MMAJ-JICA, 1977) and unpublished maps/reports in the Philippine Mines and Geosciences Bureau (MGB). The boundaries of lithologic units, fault/fractures and the locations of 19 large-scale gold deposits and 63 small-scale gold deposits were digitised from paper maps. The large-scale gold deposits are those that have been mined on a large-scale or have been explored extensively for development by private

companies (Table 2.4). The small-scale gold deposits are locations of small-scale workings for gold by local people.

Table 2.4. Large-scale gold deposits in Baguio district.

	Name	UTM coordinates		Ore reserve/ Status	Average Au grade	Reference
		Easting	Northing			
Mine (active or defunct)	Acupan	249154	1808773	>200 t Au produced since 1915	6.1 g/t	Cooke et al., 1996
	Antamok	250348	1814448	>300 t Au produced since 1907	4-5 g/t	Mitchell and Leach, 1991
	Baco	248308	1812596	0.36 Mt	7-17 g/t	Yumul, 1980; Mitchell and Leach, 1991
	Itogon	250784	1808478	4.123 Mt	4.1 g/t	Mitchell and Leach, 1991
	Macawiwili	249776	1803446	1.552 Mt	11 g/t	Yumul, 1980
	Camp 7	244728	1811100	0.026 Mt	30.5 g/t	Yumul, 1980
	Kelly	250347	1814356		4 g/t	Mitchell and Leach, 1991
	Keystone	251313	1813146		2-3 g/t	Yumul, 1980
	Omico	248668	1802690		10 g/t	Mitchell and Leach, 1991
	Chico	247030	1812488	0.689 Mt, closed since 1977	4.3 g/t	Yumul, 1980
	Baguio Gold	248217	1817087	Depleted	Up to 29 g/t	Yumul, 1980; Mitchell and Leach, 1991
	Cal Horr	248076	1810539	Depleted	2.5 g/t	Mitchell and Leach, 1991
	Sierra Oro	248064	1809462	Depleted	6-13 g/t	Mitchell and Leach, 1991
Prospect	Belle	250545	1818659	Explored deposit		Yumul, 1980
	Capunga	246466	1825165	Explored deposit	0.3-1.3 g/t	Yumul, 1980
	Demonstration	245396	1809862	Explored deposit		Yumul, 1980
	Gold Fields	249522	1820055	Explored deposit		Yumul, 1980
	King Solomon	248691	1825139	Explored deposit		Yumul, 1980
	Nagawa	247159	1808304	Explored deposit	2 g/t	Mitchell and Leach, 1991

2.3.3 Stream sediment geochemical anomalies

As part of a training program to improve the capability of the MGB of the Philippines in identifying areas of potential gold mineralisation, geochemical exploration work was carried out in the district (UNDP, 1987a). The total number of stream sediment samples collected in an area of 360 km^2 around Baguio (Figure 2.12) is 1087, or a mean sampling density of about 3 samples per km^2. As the sample locations and the raw geochemical data are unavailable to the author for (re-)analysis, the geochemical anomalies interpreted by UNDP (1987a) are adopted here. Figure 2.12 shows the spatial association of the major geochemical anomalies with the gold deposits. The gold anomalous zones (Figure 2.12a) are defined by stream sediment concentrations of $\geq$ 0.1 ppm Au, the silver anomalous zones (Figure 2.12b) by $\geq$ 0.5 ppm Ag, the arsenic anomalous zones (Figure 2.12c) by $\geq$ 5 ppm, and antimony anomalous zones (Figure 2.12d) by $\geq$ 0.3 ppm Sb. The geochemical anomalies cover an average of about 24% of the study area. The geochemical anomalies accurately reflect

the locations of about 68% of the known large-scale deposits. These geochemical anomalies will be used for comparing and validating the results of the spatial data analyses in the succeeding chapters.

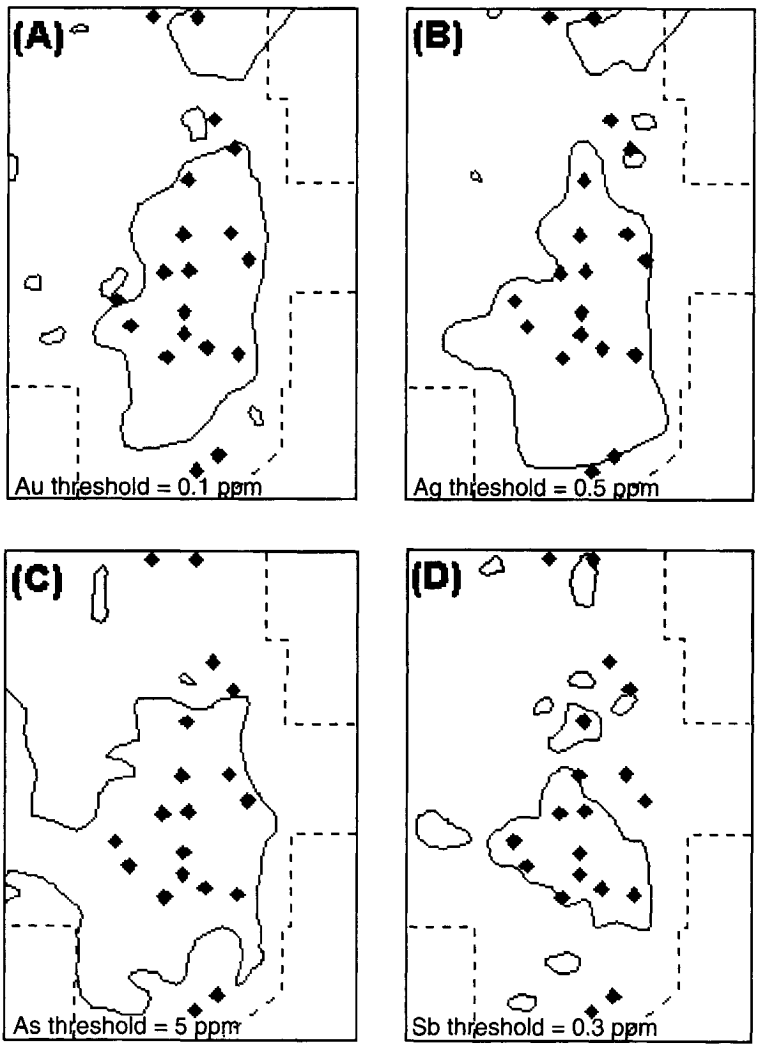

Figure 2.12. Geochemically anomalous zones for stream sediment contents, Baguio district (from UNDP, 1987a): (A) Au; (B) Ag; (C) As; and (D). Map area same as Figure 2.11. Solid line = outline of geochemical anomaly; dashed line = boundary of geochemical survey; filled diamonds = large-scale gold deposits.

2.4 ABRA AREA

The Abra area lies along the Central Cordillera of Luzon and is located to the north of Benguet province (Figures 2.1 and 2.4). The area has a similar geological setting to Benguet. The data presented below are derived from JICA (1980) except where stated otherwise.

2.4.1 Geology and copper mineralisation

The area is underlain mostly by the Licuan Group Formation II (Figure 2.13). It is made up of andesite lavas and andesitic pyroclastic rocks with intercalated limestone lenses. It is of Eocene age based on foraminiferal fossils (Bureau of Mines and Geosciences, 1982). The Licuan Group Formation II is overlain unconformably by the Tineg Formation. It is made up of dacitic lavas and dacitic pyroclastic rocks. Sandstone, mudstone and limestone intercalate with the pyroclastic rocks. The Tineg Formation is of Oligocene age based on foraminiferal fossils. Overlying unconformably the Tineg Formation is the Alava Formation. Its lower portions consist of tuffaceous siltstone and sandstone; its upper portions limestone. Foraminiferal fossils indicate Late Miocene to Pliocene age for this formation. Granodiorite and quartz diorite intrude mostly into the Licuan and Tineg Formations. These plutonic rocks collectively belong to the Agno Batholith (Bureau of Mines and Geosciences, 1982). Dykes and stocks of quartz diorite porphyry intrude into the pre-existing plutonic and volcano-sedimentary rocks.

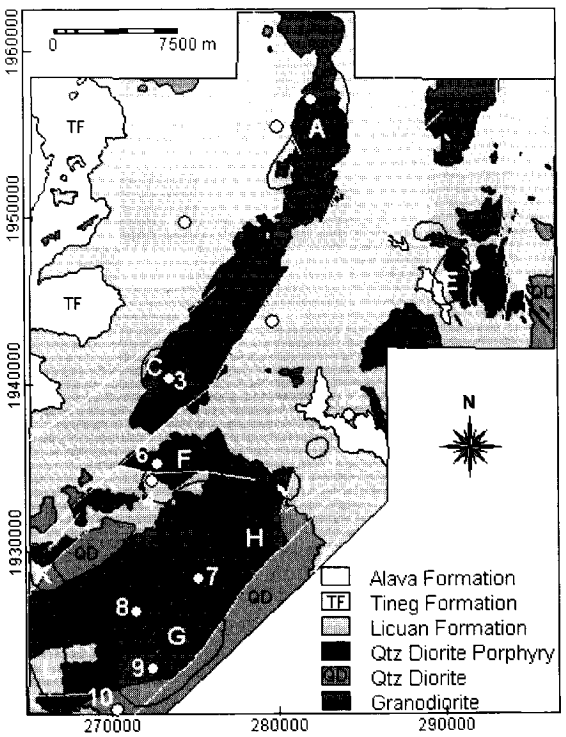

Figure 2.13. Simplified geologic map of Abra area (modified after JICA, 1980). White lines = faults; letter-identified polygons = mineralised zones (see Table 2.4); number-identified circles = copper deposits (see Table 2.5). Map coordinates are in metres (UTM projection, zone 51).

Table 2.5. Mineralised zones in Abra area (from JICA, 1980).

Zone[a]	Type of mineralisation[b]	Surface dimension (km x km)	Host rock	Ore minerals[c]	Alteration[d]	Remarks
A	Diss., stockworks, skarn	8 x 2	Granodiorite, Licuan Fm	Cp, Py, Mal, (Bor), Cc	Strong Sil, Arg, K-alt.	Consists of 4 sub-zones. Cu contents range: 0.05-2.78%
B	Diss., veinlets	1 x 1	Granodiorite, Licuan	Py, Mal	Sil, Ser	Consist of 4 outcrops. Cu value is 1.68%
C	Vein, diss.	1.5 x 0.5	Granodiorite, Licuan Fm	Py, Cp, Sph	Sil, Arg	Consists of Abra mine and 4 outcrops. Cu contents range: 0.73-14.87%
D	Diss.	0.8 x 0.8 km	Granodiorite, Licuan	Py, (Cp)	Sil, Arg	Many outcrops in contact with host rocks
E	Diss, vein	0.8 x 2	Granodiorite, Licuan Fm	Py, Cp, Mal	Sil, Ser, Arg	Consists of 5 outcrops. Cu contents range: 0.87-3.65%
F	Diss., stockwork	5 x 2	Granodiorite, quartz diorite porphyry, Licuan Fm	Cp, Py, Mal, (Bor), (Azu)	Sil, Ser, Arg	Consist of 3 sub-zones. Cu contents range: 1.46-3.51%. Explored by BMG in 1973 and 1974.
G	Diss., stockwork	5 x 9	Granodiorite, quartz diorite porphyry	Py, (Cp), (Mal)	Sil, (Ser), (Arg)	Consist of more than 20 mineralised outcrops. Low Cu contents (0.27%)
H	Diss., vein	1.3 x 1	Granodiorite	Py, Mal	Sil	Consists of 3 outcrops. Cu content 2.68%
I	Diss., skarn	1.5 x 1	Granodiorite, Licuan Fm	Py, Cp	Sil, skarn minerals	Consists of 3 outcrops. Cu contents: 0.02-0.53%
J	Vein	1 km along creek	Licuan Fm	Py, (Sph), (Ga)	Sil, (Ser)	Consist of 3 quartz veins
K	Diss.	0.6 x 1.5	Granodiorite, quartz diorite porphyry	Py, (Cp)	Sil	Consist of 6 weakly mineralised outcrops
L	Stockwork	1.5 x 4	Granodiorite, Licuan Fm	Py		Weakly mineralised veinlet stockworks

[a]Letter identifies mineralised zone in Figure 2.13.
[b]Diss. = disseminated.
[c]Py = pyrite; Cp = chalcopyrite, Mal = malachite, Bor = bornite, Sph = sphalerite; Cc = chalcocite; Azu = azurite; Ga = galena. Those in parentheses are present in minor amounts.
[d]Sil = silicification; Ser = sericitisation; Arg = argillisation; K-alt. = Potassic alteration. Those in parentheses are less intense alteration.

Table 2.6. Copper deposits in Abra area (from Bureau of Mines, 1976).

Mineral occ.[a]	Type of mineralisation[b]	Host rock(s)	Ore minerals[c]	Alteration[d]	Remarks
1	Diss., veinlets	Metavolcanics/ metasediments, diorite	Py, Cp, (Bor)	Sil, Arg	High-grade ore contains 40-96% Cu.
2	Diss., veinlets	Metavolcanics, diorite	Py, Cp, (Bor), (Cc)	Sil	Ore samples contain 0.06-15% Cu
3	Veinlets	Metavolcanics, diorite	Py, Cp, (Sph), (Ga)	Sil	
4	Diss., veinlets	Metavolcanics/ metasediments, diorite	Py, Cp, Bor	Sil	Ore samples contain 0.03-3.15% Cu
5	Skarn, stockworks, diss.	Metavolcanics/ metasediments, quartz diorite	Py, Cp, (Bor)	Sil, Chl	Ore samples contain 0.06-1.54% Cu
6	Stockworks, diss., veinlets	Metavolcanics, quartz diorite	Py, Cp, (Bor)	Sil, Ser, (Arg)	Ore samples contain 0.17-16.4% Cu
7	Veinlets, diss.,	Metavolcanics, quartz diorite	Py, Cp, (Bor)	Sil	
8	Diss.	Metavolcanics/ metasediments, quartz diorite	Py, Cp, Bor	Sil	
9	Diss., veinlets	Quartz diorite	Py, Cp, (Bor)	Sil, Arg, Ser	Ore samples contain 1.05-6.2% Cu
10	Stockworks, veinlets	Quartz diorite	Cp, Bor, Py, (Mal)	Sil, Arg, Ser, Chl	
11	Diss.	Diorite	Py, Cp, Bor	Sil	Ore samples contain 0.04-1.06% Cu
12	Veinlets	Metavolcanics, diorite	Py, Cp, Bor	Sil	Ore samples contain 0.04-1.06% Cu

[a]Number identifies mineral deposits in Figure 2.13.
[b]Diss. = disseminated.
[c]Py = pyrite; Cp = chalcopyrite; Bor = bornite; Sph = sphalerite; Ga = galena; Mal = malachite; Cc = chalcocite. Those in parentheses are present in minor amounts.
[d]Sil = silicification; Arg = argillisation; Chl = chloritisation; Ser = sericitisation. Those in parentheses are less intense alteration.

There are two major sets of faults in the area, the N-S trending and the NE-SW trending faults. The N-S trending faults are believed to be basement structures that controlled the intrusion of the Agno Batholith plutons. These faults are cut by NE-SW trending faults that are considered to have been formed by the plutonic intrusions. The E-W trending faults are observed in the southern half of the area; these are also cut by the NE-SW trending faults. There are also NNW-SSE trending faults, which are believed to be conjugate faults of the NE-SW trending faults; these faults are believed to have been formed by compressive stresses with E-W axial directions (Balce et al., 1980).

Twelve mineralised zones have been identified in the area (JICA, 1980; Figure 2.13; Table 2.5). Mineralisations in these zones are in the form of disseminations, stockworks and/or veinlets of sulphide minerals, commonly

pyrite and chalcopyrite. Many of the mineralised outcrops in the different zones have characteristics typical of porphyry copper deposits whilst a few have characteristics typical of contact metasomatic (or skarn) deposits.

2.4.2 Geological map data

The map data of lithologic formations, faults and mineralised zones are all derived from the 1:50,000 scale maps of JICA (1980). These were hand-digitised into vector format. The point map of copper deposits is derived from the 1:250,000 scale map of the Bureau of Mines (1976).

2.4.3 DEM-interpreted faults/fractures

The faults in Figure 2.13, which may have been mapped in the field, are a conservative representation of the faults and fractures in the Abra area. To determine the presence or indications of other faults or fractures in the area, a DEM was constructed. The DEM is derived from digitisation of 100-m interval contour lines in the 1:50,000 scale topographic maps of the National Mapping and Resource Information Authority (NAMRIA, 1990l, 1990p, 1990q). Shaded-relief images of the DEM, illuminated from eight different directions (NW, N, NE, E, SE, S, SW, W), reveal most of the faults mapped by JICA (1980) as shown in Figure 2.14; several other faults/ fractures are also indicated. The shaded-relief images of the DEM reflect mostly N-S and NE-SW trending fault/fracture lineaments. The N-S trending lineaments are probably extension fractures associated with the formation of the regional geanticline. The NE-SW trending lineaments are probably due to the E-W compressive stresses that act on the Philippine archipelago (Rangin, 1991; Ringenbach, 1992).

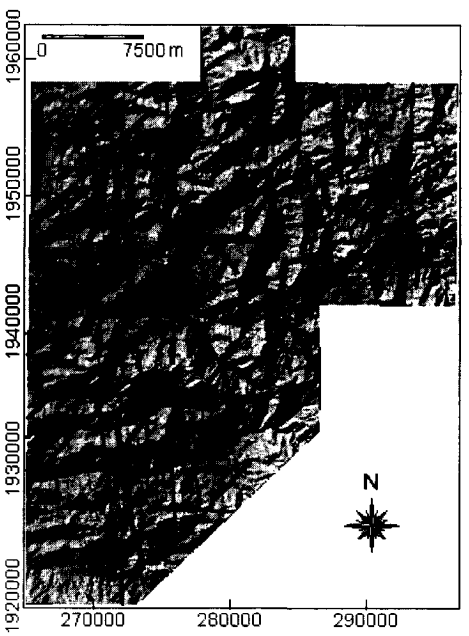

Figure 2.14. Northwest-illuminated shaded-relief image of DEM of Abra area. Black lines are inferred faults/fractures

2.4.4 Stream sediment geochemical data

Stream sediment samples (n=949) collected in the area were analysed only for Cu and Zn by AAS (JICA, 1980). The stream sediment samples represent 684.8 km^2 of sample catchment basins; the mean sampling density is about one sample per 0.72 km^2. The elementary statistics for the Cu and Zn data are given in Table 2.7. As indicated by their skewness coefficients, the element distributions are positively skewed. Asymmetry of the raw data distributions is effectively reduced by a log_e-transformation. The geochemical data for Cu and Zn both approximate unimodal Gaussian distributions after a log_e-transformation (Figure 2.15). Thus, the geochemical data are classified into background and anomalous classes after a log_e-transformation.

Table 2.7. Elementary statistics of raw geochemical data and skewness of log_e-transformed data, Abra area.

Element	Minimum	Maximum	Mean	Std. Dev.	Skewness	Skewness (log_e)
Cu* (ppm)	5	866	62	65	6.03	0.59
Zn (ppm)	5	2277	107	133	9.35	-0.19

*Four outliers of 1 ppm Cu have been removed after log_e-transformation of the data.

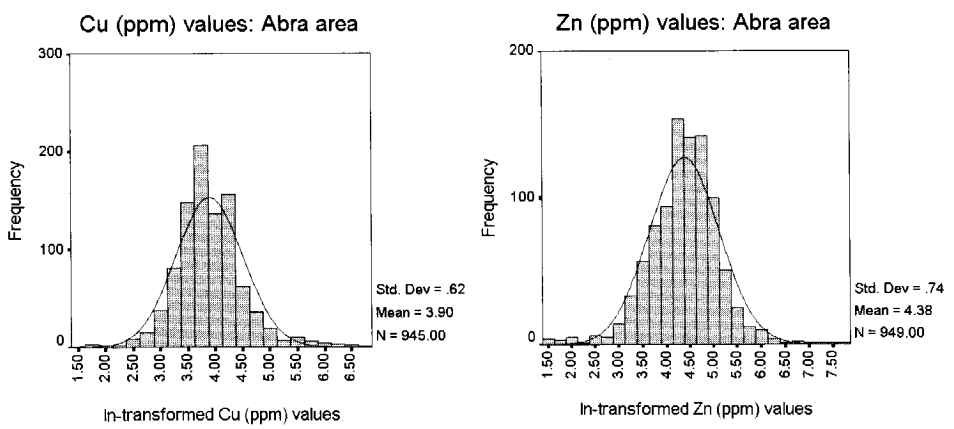

Figure 2.15. Histograms of log_e-transformed Cu and Zn stream sediment geochemical data, Abra area.

The $\log_e$-transformed data were assigned four classes, namely, low background, high background, slightly anomalous, highly anomalous. Values between the mean and mean plus one standard deviation ($\bar{x}$+s.d.) are high background. Values between $\bar{x}$+s.d. and $\bar{x}$+(2*s.d.) are slightly anomalous. Values greater than $\bar{x}$+(2*s.d.) are highly anomalous. Figure 2.16 shows the geochemical data as catchment basin anomaly maps (Carranza and Hale, 1997).

The geochemical anomalies for Cu and Zn are not spatially coincident (Figure 2.16). The Cu and Zn data have a low correlation coefficient of 0.280; however, it is significant statistically at the 0.01 probability level (Howarth, 1983). The significant yet low correlation coefficient is probably due to background Cu and Zn contents. Background values of both elements are spatially coincident. The non-coincident spatial patterns of the Cu and Zn geochemical anomalies are probably due to the differences in the mobility of these elements in the surficial environment. The geochemical anomalies for Cu reflect most of the mineralised zones delineated by JICA (1980) and show spatial association with the copper deposits mapped by the Bureau of Mines (1976); the Zn anomalies do not. These geochemical anomalies will be used to validate the results of geologically-constrained mineral potential mapping presented in the succeeding chapters.

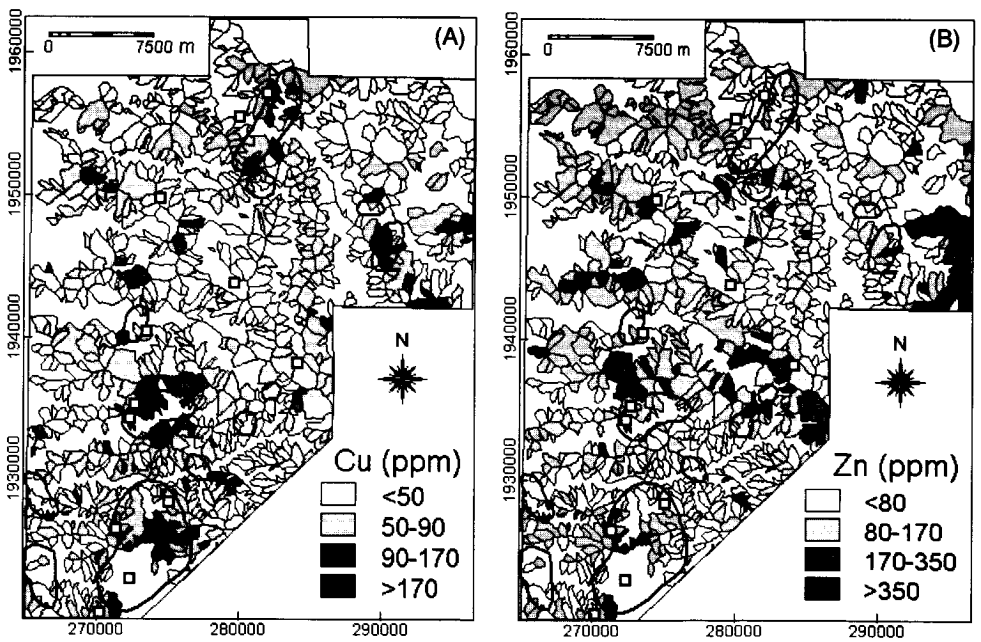

Figure 2.16. Catchment basin geochemical anomaly maps for Abra area: (A) Cu; (B) Zn. Polygons in heavy solid lines = mineralised zones (see Figure 2.13; Table 2.5). Unfilled squares = copper deposits.

2.5 CATANDUANES ISLAND

2.5.1 Geology and mineralisation

Figure 2.17 shows the geologic map of the island. The Catanduanes Formation forms the stratigraphic basement of the island. It consists mostly of strongly folded indurated sandstones and, in places, phyllitic schists and conglomerates. Its age is inferred to be Jurassic (Miranda and Vargas, 1967). Overlying unconformably the Catanduanes Formation is the Yop Formation. It underlies conformably and/or intertongues with the Bonagbonag Limestone. The Yop Formation is composed mainly of spilitic basaltic lavas with intercalations of tuffaceous volcaniclastic rocks. Its age is inferred to be Cretaceous (Miranda and Vargas, 1967). The Bonagbonag Limestone is composed of stratified limestone with minor shale and siltstone beds. It is of Cretaceous age based on fossil assemblages (Bureau of Mines and Geosciences, 1982). Overlying unconformably the Catanduanes, Yop and Bonagbonag Formations is the Payo Formation. It is composed of the Cabugao sandstone, the Hitoma-Payo coal measures and Sipi Limestone members. Miranda and Vargas (1967) inferred its age to be Eocene. The Sipi Limestone member was dated Late Eocene based on foraminiferal fossils (Bureau of Mines and Geosciences, 1982). Intruding the above volcano-sedimentary formations are the Batalay Intrusives. These intrusives include diorites, andesite porphyries, basalts and aplites that cut into the pre-existing rock formations mainly in the southern half of the island (Figure 2.17). Potassium-argon dating of samples of intrusive rocks from different

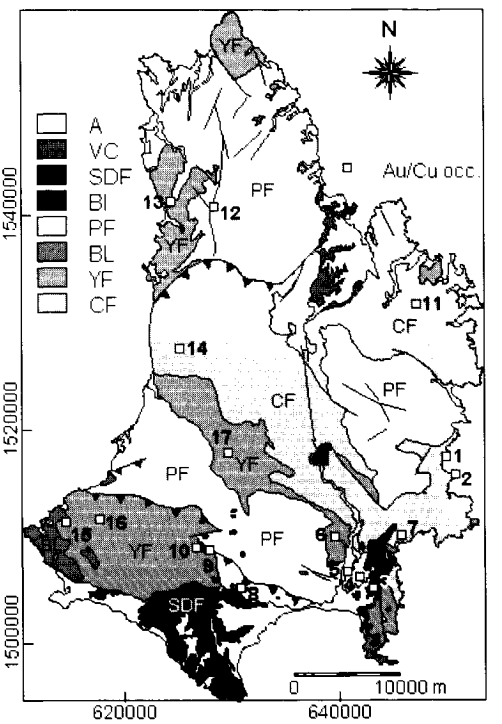

Figure 2.17. Simplified geologic map of Catanduanes Island (from JICA-MMAJ, 1994). A = alluvium; VC = Viga Conglomerate; SDF = Sto. Domingo Formation; BI = Batalay Intrusives; PF = Payo Formation; BL = Bonagbonag Limestone; YF = Yop Formation; CF = Catanduanes Formation. Curvi-linear features = faults; saw-teeth indicate up-thrusted block. Map coordinates are in metres (UTM projection, zone 51).

outcrops yielded ages of 30.2±1.0 to 39.5±0.9 Ma or Eocene to Oligocene period (JICA-MMAJ, 1994). Overlying unconformably the Catanduanes and Yop Formations in the southern part of the island is the Sto. Domingo Formation. It consists of sandy to marly limestone in its basal portions and tuffaceous to marly shale in its upper portions. The limestone yielded fossils of Late Miocene age; the shale yielded fossils of Pliocene age (Bureau of Mines and Geosciences, 1982). Overlying unconformably the Payo and Catanduanes Formations in the northeastern section is the Viga Conglomerate (Bureau of Mines and Geosciences, 1982). As its formational name implies, it consists mainly of conglomerates, with minor intercalations of sandstones and siltstones. It is dated Pleistocene (Bureau of Mines and Geosciences, 1982). Other lithologic formations that do not appear at the scale of Figure 2.17 are the Buti Hill Limestone and the San Vicente Formation, which occur in the southeastern parts of the island. The Buti Hill Limestone is of Miocene age, and overlies unconformably the Bonagbonag Limestone, Yop Formations and Batalay Intrusives (Bureau of Mines and Geosciences, 1982). The San Vicente Formation consists of conglomerates and sandstones that contain lithic fragments belonging to the pre-existing rocks in the island. It is dated Late Miocene (Bureau of Mines and Geosciences, 1982).

The island is divided geologically into northern, central and southern blocks by two thrust faults (JICA-MMAJ, 1994; Figure 2.17). The northern block is underlain mostly by the Yop and Payo Formations. It has relatively gentle hilly topographic features (Figure 2.18). The central block is thrusted over the northern block. The topographic expression of the thrust fault that divides the northern and central blocks is clearly visible from a southeast-illuminated shaded-relief DEM of the island (Figure 2.18). The central block is extensively underlain by the Catanduanes Formation and to a lesser extent by the Yop and Payo Formations. The central block is characterised by a rugged mountainous landscape. The southern block is thrusted over the central block. It is underlain by the Catanduanes, Yop, Payo and Sto. Domingo Formations. Variations in the landscape in this block can be attributed to the underlying lithologic formations (Figure 2.18).

Seventeen gold-copper deposits have been identified in the island province (Figure 2.17; Table 2.8; Miranda and Vargas, 1967; JICA-MMAJ, 1994). Field observations have shown that these gold-copper deposits are mostly vein type deposits although at least two skarn type deposits have been identified. There have been no detailed genetic studies of the gold-copper deposits although they are considered to be of hydrothermal origin and related to the Batalay Intrusives (Miranda and Vargas, 1967; JICA-MMAJ, 1994). The absence of pervasive hydrothermal alteration, except for silicification and pyritisation adjacent to veins, and the presence of calcite in the veins in several of the gold-copper deposits (JICA-MMAJ, 1994) suggest that the deposits are replacement vein-type deposits. The calcareous facies in the different host formations have probably

been replaced by silica (quartz) and re-crystallised to calcite accompanied by the deposition of precious and base metals. However, the gold-copper deposits probably represent the deepest portions of epithermal systems based on the general geological/geochemical characteristics of epithermal deposits in the Philippines (UNDP, 1987a; Mitchell and Balce, 1990; Mitchell and Leach, 1991), (see Chapter 5; Figure 5.11). Hence, the gold-copper deposits in the island can be classified tentatively as epithermal.

Table 2.8. Gold and/or copper prospects, Catanduanes Island (from JICA-MMAJ, 1994).

Mineral occ.[a]	Type of deposit[b]	Host rock(s)[c]	Ore minerals[d]	Alteration[e]	Remarks
1	Vein	CF, BI	Cp, Py, Mal	Sil	More than 10 veins 0.1-1.4 m wide; sample yield 0.06-1.445%Cu (JICA-MMAJ, 1994)
2	Vein, diss.	CF	Cp		Inaccessible gossanous outcrop on vertical sea cliff (JICA-MMAJ, 1994)
3	Vein	YF, BI	Cp, Py, (Mo)		Angular floats of quartz veins in cultivated area; samples yield max 0.474%Cu, 0.25g/t Au, 0.133% Mo (JICA-MMAJ, 1994)
4	Vein	CF, BI	Py, Cp	Py, Lim	3 samples: nil to 1g/t Au, 0.28-8.96% Cu, 5.5-41.5g/t Ag (Miranda & Vargas, 1967)
5	Skarn	PF, BI	P, Sph, Py, Hm		1 sample: 0.964 g/t Au, 22 g/t Ag, 1.35% Cu (JICA-MMAJ, 1994)
6	Vein	YF BI	Py	Arg	4 samples: nil to 0.03g/t Au, 0.022-0.033% Cu (JICA-MMAJ, 1994)
7	Vein (?)	CF, BI			Gold in stream sediment panned concentrates (JICA-MMAJ, 1994)
8	Skarn	CF, BI		Epi, Gar, skarn	5 samples: 0.63-5.93% Cu, nil to 2g/t Au, 5-24g/t Ag (Miranda & Vargas, 1967)
9	Veinlets	CF, PF, BI			Small-scale workings for Au by local people (JICA-MMAJ, 1994)
10	Vein	CF, PF, YF, BI	Mag, Cp, Py, (Sph)	Sil, Py	Small-scale workings for Au by local people (JICA-MMAJ, 1994)
11	Vein, diss.	CF	Py	Sil	5 samples: nil to 21.5 g/t Au, 0.03-0.08%Cu (Miranda & Vargas, 1967)
12	Veinlets, diss.	PF, BI	Py, (Cp)	Sil	Samples yield 0.06-6.8% Cu (Miranda & Vargas, 1967); 2 samples: 0.062 and 0.156 g/t Au (JICA-MMAJ, 1994)
13	Vein	YF	Native Cu, Mal	Sil, Epi	1 sample: 1.495% Cu (JICA-MMAJ, 1994)
14	Vein	CF		Arg	2 samples: 22.706 and 28.024 g/t Au (JICA-MMAJ, 1994)
15	Vein	YF			Pre-WW II small-scale workings
16	Vein	YF	Py	Sil, Py	2 samples: nil and 0.249 g/t Au, 0.007 and 0.026% Cu (JICA-MMAJ, 1994)
17	Vein	YF, CF			1 sample: 0.01% Cu (JICA-MMAJ, 1994)

[a]Number identifies mineral deposit in Figure 2.17.

[b]Diss. = disseminated.

[c]See Figure 2.17 caption for explanation of acronyms.

[d]Py = pyrite; Cp = chalcopyrite; Sph = sphalerite; Mal = malachite; Mag = magnetite; Hm = hematite; Mo = molybdenite. Those in parentheses are present in minor amounts.

[e]Sil = silicification; Arg = argillisation Py = pyritisation; Epi = epidotisation; Lim = limonitisation. Those in parentheses are less intense alteration.

2.5.2 Geological map data

The map data of lithologic formations, faults and mineral deposits (Figure 2.17) were derived from the 1:100,000 scale geological map of JICA-MMAJ (1994). The boundaries of lithologic units and the faults were digitised into vector format. The locations of the gold-copper deposits were digitised as points.

2.5.3 DEM-interpreted faults/fractures

Figure 2.17 shows a conservative representation of the faults or fractures present in the island of Catanduanes. To augment the available geological data, a DEM of the island was generated based on 20-m interval elevation contours of 1:50,000 scale topographic maps of the National Mapping and Resource Information Authority (NAMRIA, 1990b, 1990e, 1990f, 1990h, 1990i, 1990n, 1990o). Shaded-relief images of the DEM of the island, illuminated from eight different directions (NW, N, NE, E, SE, S, SW, W), were analysed visually for lineaments that are believed to represent faults/ fractures (Figure 2.18). Most of the faults mapped by JICA-MMAJ (1994) are recognisable in the shaded-relief images of the DEM. The presence of other faults/fractures is indicated.

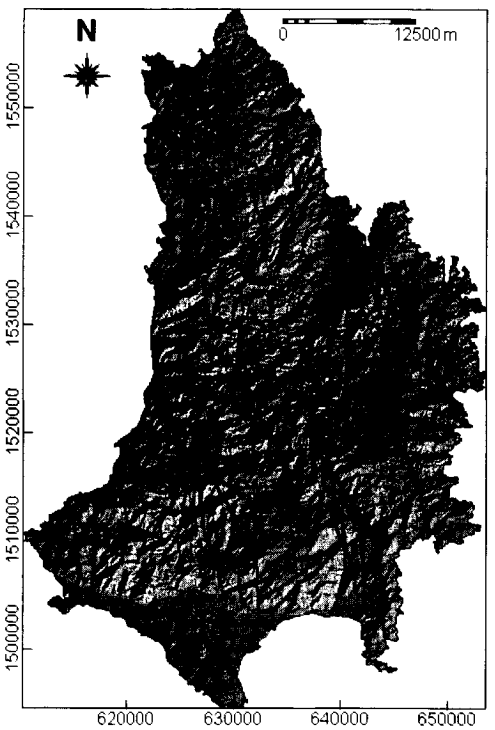

Figure 2.18. Southeast-illuminated shaded-relief DEM and inferred faults/fractures, Catanduanes Island.

The three different blocks recognised by JICA-MMAJ (1994) show different fault/fracture patterns. The northern block shows north-trending lineaments that apparently cut northwest-trending lineaments. The northeast-trending lineaments are probably conjugate shears of the northwest-trending lineaments. The central block shows mostly north-trending and northwest-trending lineaments. The north-trending lineaments form horsetail patterns with the northwest-trending lineaments. The southern block has few lineaments that are recognisable from the shaded-relief images of the DEM.

2.5.4 Stream sediment geochemical anomalies

Geochemical data for Au, Ag, As, Cu, Fe, Hg, Mo, Pb, S, Sb and Zn are available in JICA-MMAJ (1994). These data pertain to 717 stream sediment samples. Geochemical data for 694 stream sediment samples are used in this study. The samples not used have catchment basins that are not representable at the scale of the maps presented here. Among the suite of elements, Au, As, Cu, Fe, S and Zn are studied; the other elements are mostly below the analytical detection limits. Neutron activation analysis was used to determine Au, induction furnace combustion for S, and ICP-AES for As, Cu, Fe and Zn.

Listed in Table 2.9 are the elementary statistics of the raw data and skewness of the $\log_e$-transformed data. As indicated by their skewness coefficients, the raw data distributions are positively skewed. Asymmetry of the raw data distributions is effectively reduced by a $\log_e$-transformation. The $\log_e$-transformed uni-element data are used in the classification of geochemically anomalous sample catchment basins.

Table 2.9. Elementary statistics of raw geochemical data and skewness of $\log_e$-transformed data, Catanduanes Island.

Element	No. of samples	Minimum	Maximum	Mean	Std. Dev.	Skewness	Skewness ($\log_e$)
Au (ppb)	502	1	4510	156	496	5.49	0.93
As (ppm)	352	2	94	12	10	3.46	-0.29
Cu (ppm	694	24	425	104	38	1.28	-0.27
Zn (ppm	694	34	424	134	61	1.48	0.16
Fe (%)	566	2.78	16	10.34	3.63	0.32	-0.22
S (%)	658	0.001	1.25	0.023	0.076	10.69	0.976

In the Benguet province and Abra area, geochemically anomalous zones have been defined by classification of the uni-element data mainly because multi-element data are unavailable. For the area under review, geochemically-anomalous zones were defined by multivariate analysis of the data. Principal components (PC) analysis was performed to extract a multi-element association that characterises the known mineralisation in the area (Garrett et al., 1980). The loadings of the six principal components of the $\log_e$-transformed geochemical data are listed in Table 2.10.

The first principal component or PC1 (at least 30% of the variance) has high positive loadings for Zn and Fe, which suggest the scavenging effects of Fe oxides in the secondary environment. The Zn-Fe association is antipathetic with a Au-S-As association that has negative loadings. This latter association indicates presence of possible Au-As sulphide mineralisation. High PC1 scores, however, will reflect zones where the scavenging effects of Fe are predominant.

Table 2.10. Principal components analysis of the $\log_e$-transformed data, Catanduanes.

	PC1	PC2	PC3	PC4	PC5	PC6
Au	-0.299	-0.601	0.450	0.397	0.426	0.084
As	-0.239	0.458	0.634	0.415	-0.398	-0.022
Cu	0.021	0.836	0.110	-0.040	0.535	0.022
Zn	0.896	-0.017	0.245	-0.059	-0.068	0.360
Fe	0.879	-0.124	0.273	0.067	0.090	-0.354
S	-0.291	-0.122	0.603	-0.732	-0.010	-0.029
% Var.	30.10	21.69	18.56	14.61	10.65	4.39

At least 21% of the variance is explained by PC2. It has high positive loadings on Cu and As and high negative loadings on Au. The antipathetic associations reflect differences in the mobility of Au and the mobility of Cu and As in the surficial environment. The antipathetic association further implies anomalies of Cu and As that are spatially non-coincident with Au anomalies. Whilst these antipathetic associations also imply presence of mineralisation, high PC2 scores would also reflect zones of hydromorphic anomalies of Cu and As.

The third principal component or PC3 explains at least 18% of the variance and has positive loadings on all elements. The high positive loadings on As, Au and S imply gold-rich sulphide mineralisation while the low positive loadings on Fe, Zn and Cu indicate lithologic association. The positive loadings on all elements are interpreted to be a metallogenic association.

At least 14% of the variance is explained by PC4, which has positive loadings on As and Au, whilst PC5 explains at least 10% of the variance and has positive loadings on Cu and Au. These two PCs probably reflect at least two types of gold-rich mineralisation in the island. The fourth principal component or PC4 indicates spatially coincident geochemical anomalies of As and Au; PC5 of Cu and Au. These two PCs, although suggestive of presence of mineralisation, also indicate surficial geochemical processes (i.e., clastic dispersion); hence, these are not readily interpreted as due to mineralisation alone. The sixth principal component or PC6 is interpreted as reflecting zones where stream sediment contents of Zn are unrelated to scavenging effects of Fe; it does not reflect a metallogenic association.

All the principal components, except PC6, reflect multi-element associations that indicate presence of mineralisation; however, PC1, PC2, PC4 and PC5 also reflect multi-element associations that represent secondary geological processes. The third principal component or PC3 does not reflect associations that represent secondary geological processes; it is interpreted to reflect an anomalous As-S-Au-Fe-Zn-Cu geochemical signature that probably represents the gold-copper mineralisation in the island. The spatial distribution of PC3 scores will indicate geochemically-anomalous areas. The PC3 scores are calculated according to the formula (George and Bonham-Carter, 1989):

$$S_{ci} = \sum_{j=1}^{6} l_{cj} e_{ij} \quad (2\text{-}1)$$

where S_{ci} = score for sample i on component c; l_{cj} = loading of variable j on component c; and e_{ij} = concentration of element j for sample i. The PC3 scores are classified into four percentile classes (0-50, 50-75, 75-90 and 90-100) to depict zones with anomalous metallogenic association. The spatial distribution of the PC3 scores, represented as catchment basin anomalies, is shown in Figure 2.19. Catchment basins with anomalous PC3 scores (i.e., 75-100th percentiles) show close spatial association with the known gold-copper deposits. Eight of the 17 known gold-copper deposits are contained in catchment basins with anomalous PC3 scores. This multi-element geochemical anomaly map will be used in validating the results of predictive geologically-constrained mapping of mineral potential in the succeeding chapters.

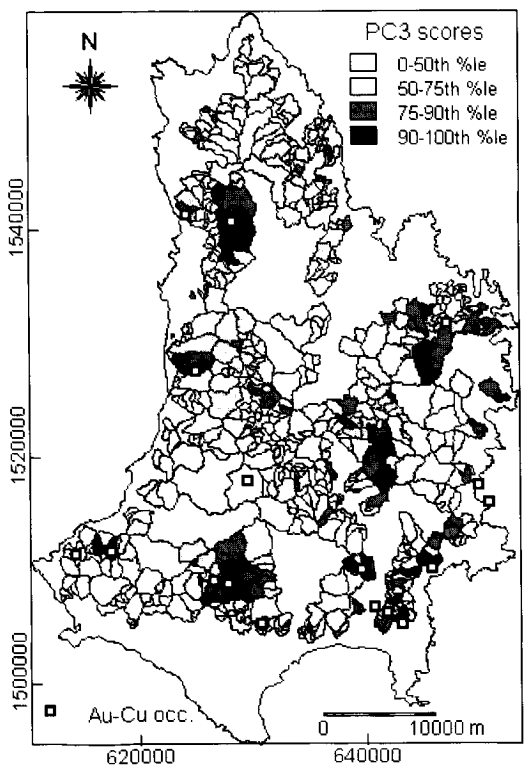

Figure 2.19. Stream sediment catchment basins characterised by an anomalous As-S-Au-Fe-Zn-Cu geochemical signature represented by high PC3 scores. Unfilled squares = gold-copper deposits.

2.6 ISABELA AREA

The Isabela area is studied to demonstrate potential mapping for nickeliferous-laterite deposits. There are, however, no known nickeliferous-laterite deposits in the area.

2.6.1 Geology and mineralisation

The Isabela Ultramafics, of possible Cretaceous age, form the basement rocks and are extensively exposed in the eastern part of the area (Figure 2.20). The ultramafic rocks are part of an ophiolitic suite that is believed to have been generated and formed in the Philippine Sea (JICA-MMAJ, 1987). They consist mainly of harzburgite with dunite lenses and massive to bedded gabbros. Associated with these ophiolitic ultramafic rocks are pillow basalts and cherts of Cretaceous age. The ultramafic rocks are thrusted over volcano-sedimentary rocks of Paleocene to Oligocene age that underlie the central to western parts of the area. These volcano-sedimentary rocks are intruded by dioritic plutons of late Oligocene age. In the east-central portions of the area, the Isabela Ultramafics are unconformably overlain by Miocene-Pliocene sedimentary rocks.

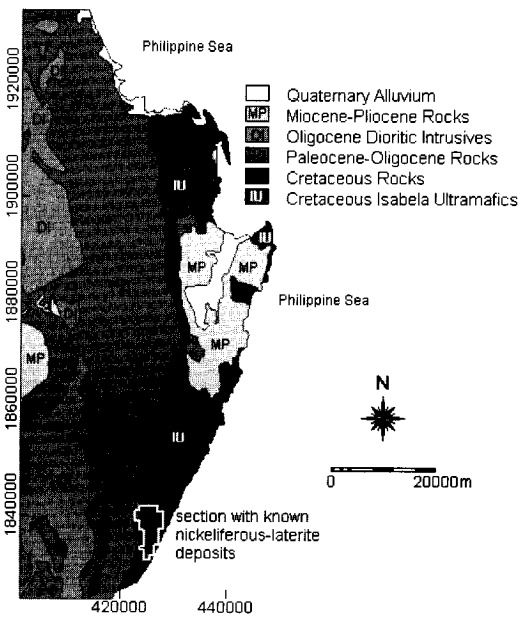

Figure 2.20. Simplified geologic map of Isabela area (from JICA-MMAJ, 1987). Map coordinates are in metres. (UTM projection, zone 51).

The mineral deposits mainly found in the area are orthomagmatic chromite deposits in the ultramafic rocks, stratabound manganese and massive sulphide deposits in pillow basalts and cherts, and epithermal veins and disseminations around dioritic plutons (Bureau of Mines and Geosciences, 1986). Nickeliferous-laterite deposits are known in only one section of the ultramafic terrane in the area (Figure 2.20). The portions of the area immediately north of the section with known nickeliferous-laterite deposits have been alienated to mineral exploration and development by existing land-use policies (Mangaoang, 1997).

2.6.2 Geological map data

The sources of geological map data are the 1:250,000 scale geologic maps of JICA-MMAJ (1987). The boundaries of the lithologic units were digitised and polygonised.

2.6.3 DEM-derived geoinformation

As will be shown in Chapter 5, there are two topographic indicators essential for the classification of nickeliferous-laterite potential. These two topographic indicators are (1) slopes of ≤20° and (2) plateau edges. The GIS procedures to extract these spatial features are discussed below.

Topographic data were derived from 100-m interval elevation contours of 1:250,000 scale topographic maps of the National Mapping and Resource Information Authority (NAMRIA, 1992a, 1992b). The elevation contours were hand-digitised and converted from vector (segment) to raster format. From the raster map of elevation contours, interpolation was carried out to produce a DEM of the area (Figure 2.21). To create a slope map, horizontal and vertical gradient filters were applied to the DEM. The slope map was re-classified into two map units, areas with slopes of >20° and of ≤20° (Figure 2.23a).

Figure 2.21. Northwest-illuminated shaded-relief DEM of Isabela area. Ultramafic terrane indicated by solid line.

To extract areas where plateau edges occur, a detailed analysis of the DEM was carried out. The analysis was confined to the area underlain by the Isabela Ultramafics because it is with ultramafic rocks that nickeliferous-laterites are known to be associated (see Section 5.5). Ranges of elevations where plateaus and plateau edges occur were estimated by graphically analysing the histogram of DEM pixels in the ultramafic terrane. For areas underlain by a single rock unit, the inter-contour distances are fairly uniform so that the 'steps' in the histogram of elevation ranges are also fairly uniform. Variations in the widths of the 'steps' indicate the presence of erosional surfaces, such as plateaus and plateau edges, in the landscape. Plateau edges are knickpoints that represent interruptions in the peneplanation history of the land. From the histogram of the DEM of the ultramafic terrane (Figure 2.22), it is possible to

define ranges of elevations where plateau edges occur by drawing lines that connect the 'steps' of the histogram. A long straight segment indicates ranges of elevations resulting from a long peneplanation history (i.e., plateaus are present). Short segments indicate ranges of elevations that result from interruptions in the peneplanation events (i.e., plateau edges are present). It is clear that there are three long segments that represent elevation ranges where plateaus are present (0-100, 200-700 and 800-1100 m) and there are two short segments that represent elevation ranges where plateau edges are present (100-200 and 700-800 m). The areas within the ultramafic terrane with elevation ranges of 100-200 and 700-800 m are shown in Figure 2.23b.

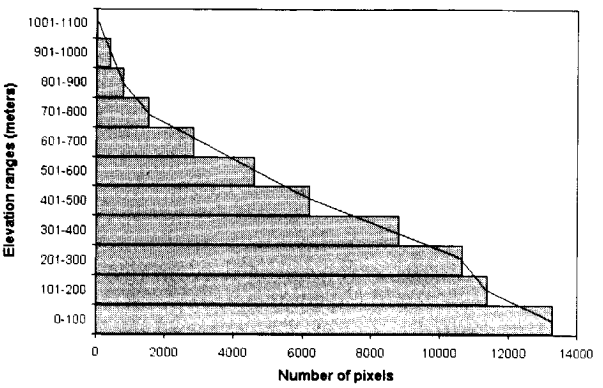

Figure 2.22. Histogram of pixel values (elevations) in DEM of ultramafic terrane, Isabela area.

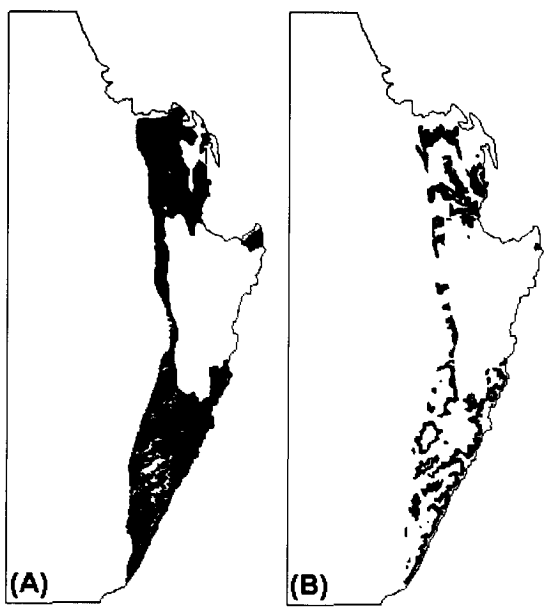

Figure 2.23. Areas of ultramafic terrane, Isabela area, with (A) slopes ≤20° and (B) plateau edges.

2.6.4 Stream sediment geochemical data

A subset of stream sediment geochemical data for Ni (JICA-MMAJ, 1987) was used to determine which portions of the ultramafic terrane are enriched in nickel. The histogram of the Ni data shows at least three populations (Figure 2.24). The population at the upper tail of the Ni data pertains to the ultramafic terrane. To depict the spatial distribution of the stream sediment contents of Ni (Figure 2.25), the Ni data were classified into five percentile classes: 0-75 %le (4-570 ppm); 75-80 %le (570-780 ppm); 80-90 %le (780-1600 ppm); 90-95 %le (1600-2500 ppm); and 95-100 %le (2500-4500 ppm). The stream sediment geochemical data for Ni will be used to validate the results of geologically-constrained predictive mapping of nickeliferous-laterite potential in the succeeding chapters.

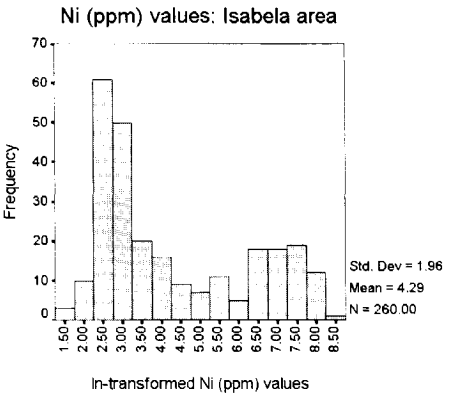

Figure 2.24. Histogram of Ni stream sediment geochemical data, Isabela area.

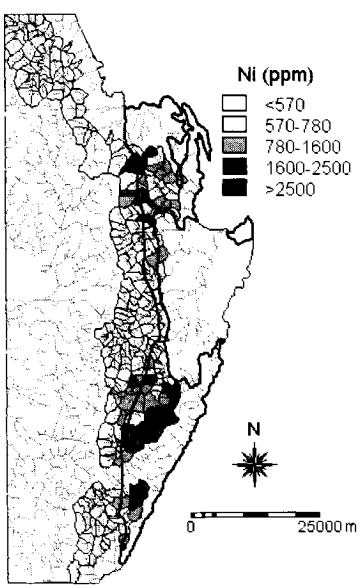

Figure 2.25. Spatial distribution of Ni stream sediment concentrations in catchment basins, Isabela area.

2.7 CONCLUDING REMARKS

Comprehensive geoexploration datasets pertaining to the study areas are unavailable. They are either non-existent, private domain or economically unobtainable. The present situation of unavailability of comprehensive geoexploration datasets simulates the scenario of general lack of comprehensive geoexploration datasets in many developing countries. The present situation provides an opportunity to test geologically-constrained mineral potential mapping as a methodology for mineral potential assessment and classification.

For the present study, the following geoexploration datasets are available: lithologic maps; locations of mineral deposits and/or mineralised zones; maps of faults/fractures; and stream sediment geochemical data. These geological datasets are derived from various published works and unpublished maps/reports of the Philippines Mines and Geosciences Bureau. In addition to these geoexploration datasets, structural and topographic geoinformation were derived from digital elevation models, which were generated from digitisation of elevation contours of topographic maps of the National Mapping and Resource Information Authority. This DEM-derived geoinformation augments the available geological (i.e., lithologic and structural) map data.

For Benguet province, Baguio district and Catanduanes Island, other available sources of geological information are Landsat Thematic Mapper (TM) data. For Benguet province and Baguio district, hydrothermal alteration zones will be remotely-sensed from the Landsat TM data. For Catanduanes Island, the Landsat TM data will be used to experiment remote detection of geochemically-stressed vegetation. The remote detection of indications of mineralisation is discussed in the next chapter.

The geological map data, the mineral deposit data, the DEM-derived geoinformation and (for Benguet province and Baguio district) remotely-detected hydrothermal alteration will be used in the geologically-constrained predictive mapping or modeling of mineral potential in the different study areas. The mineral deposit datasets or sub-datasets will be used to train the geological map and DEM-derived datasets for predictive modeling of mineral potential. The mineral deposit datasets or sub-datasets that are not used to generate the predictive models will be used to validate them.

The stream sediment geochemical datasets will be combined with the geological map and DEM-derived datasets to generate integrated geochemical-geological predictive models of mineral potential. These integrated geochemical-geological predictive models will be used to evaluate the efficacy of the geologically-constrained predictive models.

Chapter 3

Remote Sensing of Indications of Mineral Deposits in Heavily-Vegetated Terranes

"When there's nothing to see, look."

Dakota Indian saying

This Chapter deals with Image Processing and GIS for Hydrothermal Alteration Mapping (Carranza and Hale, 1999a), Mineral Imaging with Landsat TM Data for Hydrothermal Alteration Mapping in Heavily-Vegetated Terrane (Carranza and Hale, 2001d) and Remote Detection of Vegetation Stress for Mineral Exploration (Carranza and Hale, 2001f) and Remote Detection of Mineralization-Related Vegetation Stress Using Landsat TM Data, Catanduanes Island, Philippines (Carranza and Hale, 2001e).

3.1 INTRODUCTION

The presence of mineral deposits may be indicated by a lithological anomaly, a geochemical anomaly, or a geophysical anomaly. A lithological anomaly may be defined as an assemblage of minerals, in pre-existing rocks, that were formed because of later geological processes. Hydrothermally-altered rocks are a lithologic anomaly, which result from the chemical attack of pre-existing rocks by hydrothermal fluids (Pirajno, 1992). The spatial distribution of hydrothermally-altered rocks is a key to locating the main outflow zones of hydrothermal systems, which may lead to the recognition of mineral deposits (e.g., Lowell, 1991). A geochemical anomaly is a departure from the geochemical patterns that are normal for a given geochemical environment (Rose et al., 1979). An example of a geochemical anomaly is the variation in the normal characteristics and taxonomic distribution of plant species; it is a geobotanical anomaly (Brooks, 1972). Vegetation stress is a collective term that refers to changes in the normal characteristics and taxonomic distribution of plant species due to a number of factors, one of which is geochemically-anomalous concentrations of elements in the substrata (e.g., mineral deposits). A geophysical anomaly is a variation, relative to some normal background value, of a measured physical property of the Earth's upper crust (e.g., magnetism), which can be attributed to a localized subsurface zone such as a mineral deposit (Kearey and Brooks, 1984). An initial goal of many mineral exploration programmes is to map zones of indications of mineral deposits through one or a combination of various methods that include field geological surveys, geochemical surveys, field geophysical surveys and remote sensing (Evans, 1995). Remote sensing

methods include photogeological mapping, airborne geophysical surveys and interpretation of airborne/satellite imagery (Siegal and Gillespie, 1980; Drury, 1993; Sabins, 1996).

The objective of this Chapter is to demonstrate techniques pertinent to the remote detection and mapping, from satellite imagery, of hydrothermally-altered rocks and vegetation stress in heavily-vegetated terranes. A review of the state-of-the-art of remote detection and mapping of hydrothermally-altered rocks and vegetation stress is given first. Methodologies for the remote detection of hydrothermally-altered rocks and vegetation stress are then described. The results of the experiments are then described and discussed, from which conclusions are drawn.

3.2 STATE-OF-THE-ART: REMOTE DETECTION OF INDICATIONS OF MINERALISATION

The atmospheric transmittance of the different regions of the electromagnetic (EM) spectrum is illustrated in Figure 3.1. It is the basis of the design of remote sensing systems to study the surface of the Earth and its atmosphere. For example, the position of Landsat TM band 7 is potentially useful in geological mapping (Drury, 1993).

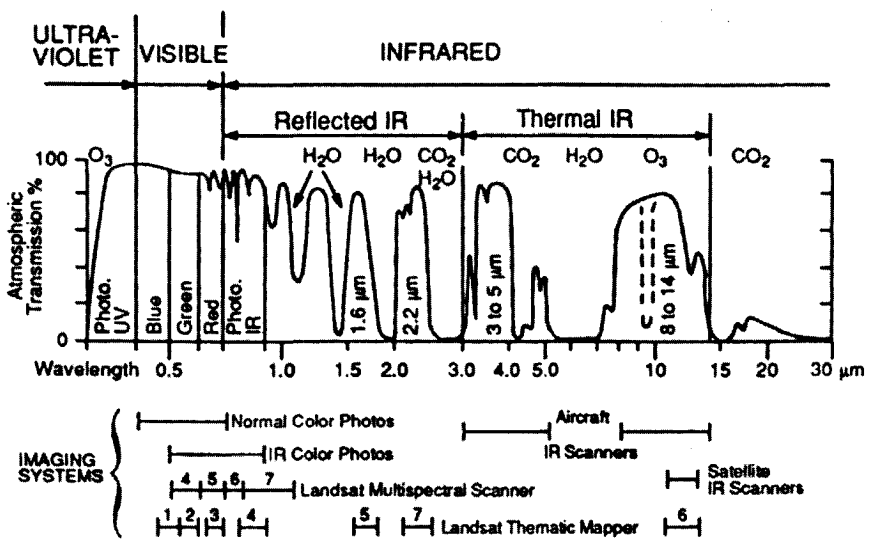

Figure 3.1. Atmospheric transmittance of different regions of a portion of the electromagnetic spectrum and the placement of some commonly used remote sensing systems (from Sabins, 1996).

3.2.1 Remote detection of hydrothermally-altered rocks

Certain alteration minerals associated with hydrothermal mineral deposits have diagnostic spectral features in the visible to the mid-infrared regions (i.e., between 0.35-3.5 μm) of the EM spectrum that permit their detection by EM sensors (Hunt, 1979; Hunt and Ashley, 1979; Buckingham and Sommer, 1983; Gladwell et al., 1983; Whitney et al., 1983; Lee and Raines, 1984; Feldman and Taranik, 1986; Clark et al., 1993). Clay minerals, for example, show a distinct absorption feature at approximately 2.2 μm (Figure 3.2). Consequently, conventional black-and-white aerial photography has little application to remote detection of hydrothermally-altered rocks due to their limited spectral information. Colour aerial/orbital photography, however, provides another dimension over black-and-white aerial photography, because inherent properties of materials, such as reflectance characteristics, can be used for identification and discrimination among similar-appearing rocks (Goetz et al., 1983). For example, Prost (1983) identified on Skylab colour and colour infrared photographs areas of red-ochre colours, which indicate iron-oxide alteration associated with manto deposits in the Weston Pass in Central Colorado. Still, aerial/orbital colour photographs are not widely used in remote detection and mapping of hydrothermally-altered rocks because the spectral data they represent are limited to the visible and photographic infrared regions of the EM spectrum (Figure 3.1). With the advancement in remote sensing technologies, airborne/spaceborne multispectral and hyperspectral data have found useful applications to the identification and mapping of hydrothermally-altered rocks (Goetz et al., 1985; Taranik and Crósta, 1996; Spatz, 1997).

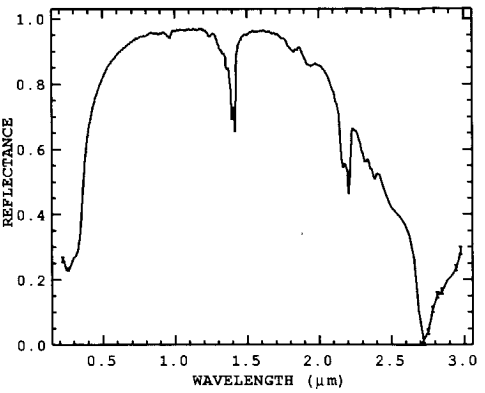

Figure 3.2. Reflectance spectra of kaolinite (from Clark et al., 1993).

Several investigators have demonstrated the useful applications of broad-band (i.e., >50 nm band width) airborne and/or spaceborne multispectral data to the detection and mapping of hydrothermally-altered rocks. Podwysocki et al. (1983) used airborne multispectral scanner images and identified previously unrecognized areas of argillic, alunitic and limonitic alteration in a mining area in Marysvale, Utah. Abrams et al. (1983) used airborne TM simulator data and were able to identify propylitic, phyllic and potassic alteration associated with porphyry copper deposits in southern Arizona. Segal (1983) and Lee (1985) used Landsat multispectral scanner (MSS) data and were able to delineate areas of limonitic alteration in the Butte-Dillon, Montana-Idaho area. Several

investigators have demonstrated the application of Landsat TM data for mapping hydrothermally-altered rocks, e.g., Huckberby et al. (1986), Magee et al. (1986), Fraser (1991), Ruiz-Armenta and Prol-Ledesma (1998). Borengasser and Taranik (1985) demonstrated the limitations of SPOT simulator data in comparison with Landsat MSS and TM data for the detection and mapping of hydrothermally-altered rocks in Goldfield-Cuprite, Nevada. Broad-band remote sensing systems thus provide tools that can detect groups of hydrothermal alteration minerals such as clays and iron oxides.

Early investigators, e.g., Abrams et al. (1977), Hunt (1979) and Ashley and Abrams (1980) have indicated that imaging spectrometers with higher spatial resolution and multispectral/hyperspectral capabilities are potentially more useful for detailed identification of hydrothermal alteration. Marsh and McKeon (1983) have shown the usefulness of the first operational airborne spectroradiometer for mapping specific types of hydrothermal alteration. The first operational airborne spectroradiometer, developed by the Geophysical Environmental Research Company in 1981, has a 20-m spatial resolution and records spectral data from 576 channels covering the 0.4-2.5 μm wavelength range (Collins et al., 1981). Goetz and Srivastava (1985), Goetz et al. (1985) and Kruse (1988) applied the Airborne Imaging Spectrometer (AIS) for identification of individual hydrothermal alteration minerals (e.g., alunite, kaolinite). The AIS is the first generation of imaging spectrometers developed by the Jet Propulsion Laboratory of NASA in 1983. It acquires data in 128 spectral bands in the 1.2-2.4 μm wavelength range (Vane et al., 1983). Kruse and Taranik (1989), Boardman and Kruse (1994), Crósta et al. (1996), Farrand (1997), Beratan et al. (1997) have demonstrated the usefulness of the Airborne Visible/Infrared Imaging Spectrometer (AVIRIS) for mapping and classifying specific types of hydrothermally-altered rocks. The AVIRIS is the second generation of NASA imaging spectrometers. It has a 20-m spatial resolution and records spectral data in 224 contiguous spectral bands of approximately 10 nm band widths within the 0.4-2.5 μm wavelength range (Porter and Enmark, 1987). Kierein-Young and Kruse (1989) and Kruse et al. (1990) have shown the usefulness of the Geophysical and Environmental Research Imaging Spectrometer (GERIS), the first commercial imaging spectrometer, for discriminating individual hydrothermal alteration minerals (e.g., alunite, kaolinite, hematite, zeolites, and buddingtonite). The GERIS has a 15-m spatial resolution and acquires spectral data from the 0.4-0.25 μm wavelength range in 63 channels with variable band widths (Collins and Chang, 1990). Resmini et al. (1997) applied the Hyperspectral Digital Imagery Collection Experiment (HYDICE) sensor for identifying individual hydrothermal alteration minerals such as alunite, kaolinite and calcite. The HYDICE, built by Hughes-Danbury Optical Systems, Inc. and operational in January 1995, acquires data from the 0.4-2.5 μm wavelength region in 210 channels. Mazzarini et al. (2001) used Multispectral Infrared and Visible Imaging Spectrometer (MIVIS) data for mapping argillic, advanced argillic and silicic hydrothermal alteration in Vulcano Island in Sicily. The MIVIS system, developed by Daedalus in 1994, collects

spectral data of variable spectral resolution from 102 channels covering the 0.4-2.5 μm and 8.2-12.7 μm of the EM spectrum. Airborne imaging spectrometer systems therefore make possible the identification of individual minerals (e.g., alunite, kaolinite, illite, goethite, etc.), which allow more detailed mapping of hydrothermal alteration minerals (e.g., Kruse and Hauff, 1989).

The application of data from the thermal infrared (TIR) region of the EM spectrum to the detection of hydrothermally-altered rocks also holds great potential because silicate minerals have distinctive emission minima within narrow band widths between 8.8 and 11.5 μm (Spatz, 1997). Sensors that measure in discrete bands across this wavelength interval are capable of discriminating rock types with basic or felsic tendencies (Lahren et al., 1988; Sabine et al., 1994). Hydrothermal silicification can therefore be identifiable with TIR sensors; however, hydrothermal alteration other than silicification causes a shift in absorption features toward shorter wavelengths in the TIR (Salisbury et al., 1987; Collins, 1989). For this reason, hydrothermal alteration could be confused with unaltered felsic rocks. This ambiguity can be compensated by synergy of TIR data with VNIR and SWIR data. For example, Kierein-Young (1997) demonstrated a synergistic application of TIR data (TIMS or Thermal Infrared Multispectral Scanner), AVIRIS data and synthetic aperture radar data (AIRSAR or Airborne Synthetic Aperture Radar) for a more accurate characterisation of mineralogy and morphology of surfaces in Death Valley, California.

In addition to the airborne imaging spectrometer systems mentioned above, the Advanced Spaceborne Thermal Emission and Reflectance Radiometer (ASTER) can have potential for hydrothermal alteration mapping. The ASTER is currently onboard Terra, a satellite launched in December 1999 as part of NASA's Earth Observing System (EOS). The ASTER was designed with three bands in the visible and near-infrared (VNIR) spectral regions, six bands in the short wave infrared (SWIR) regions, and five bands in the thermal infrared (TIR) regions (Kahle et al., 1991). The VNIR and SWIR bands of ASTER have a spectral resolution in the order of 10 nm and spatial resolutions of 15 m and 30 m, respectively; the TIR bands have a spatial resolution of 90 m. The ASTER has a swath width of 60 km with 136 km cross-track and a temporal resolution of 16 days. The application of ASTER to hydrothermal alteration mapping is still in its infancy (Abrams, 2000; Hewson et al., 2001; Yamaguchi et al., 2001). The Australian Resource Information and Environment Satellite (ARIES), scheduled for launch in 2002 (Huntington, 1998), can also have potential for remote detection of hydrothermally-altered rocks. The ARIES is designed for environmental and mineral applications, and will have 32 contiguous bands in the VNIR regions and 32 contiguous bands in the SWIR regions, and a panchromatic band. The imaging spectrometer and panchromatic imager of ARIES will have 30 m and 10 m spatial resolutions, respectively, with temporal resolution of 7 days and ground swath of 15 km.

Accurate remote detection and mapping of hydrothermally-altered rocks thus desirably require high spatial resolution and multispectral/hyperspectral airborne/satellite data. Among the desirable airborne/satellite data for remote detection and mapping of hydrothermally-altered rocks, Landsat TM data are the most widely used in many developing Third World countries because of low cost and availability. The application of Landsat TM data for the remote mapping of hydrothermally-altered rocks has also been more widely demonstrated not only in the arid and semi-arid regions but also in the tropical regions of the world (e.g., Crósta and Moore, 1989; Crósta and Rabelo, 1993; Almeida-Filho and Vitorello; 1997; Ruiz-Armenta and Prol-Ledesma, 1998). On the other hand, the application of hyperspectral data to hydrothermal alteration mapping in highly-vegetated terranes is not widely documented. Van der Meer (1995) demonstrated the inherent problems of hyperspectral data application to mineral mapping in a moderately vegetated area in Spain. In this study, Landsat TM data were used for detection and mapping of hydrothermally-altered rocks; it is the only remotely-sensed multispectral data available to this research.

3.2.2 Remote detection of vegetation stress

A variety of vegetation stress or response is triggered by anomalous substrate geochemical conditions due to natural causes (e.g., mineralisation) and/or anthropogenic causes (e.g., industrial pollution). There are three categories of vegetation response to anomalous substrate geochemical conditions, namely, taxonomic response, structural response and spectral response (Mouat, 1982; Milton and Mouat, 1989). Taxonomic response refers to growth or non-growth of certain plant species depending on substrate geochemical conditions. Structural responses include morphological, phenological and physiological changes in plants due to variations in substrate geochemical conditions. Morphological changes include dwarfism or stunted growth, gigantism, mottling and yellowing of leaves (chlorosis), and other colour changes, changes of flower colour and abnormal fruits. Phenological changes pertain to disturbances in the natural rhythmic senescence and timing of flowering/fruiting of plants. Physiological changes occur at the cellular level, where metals disrupt the normal functions of enzymes involved in chlorophyll synthesis (Lepp, 1981; Fitter and Hay, 1987; Van Assche and Clijsters, 1990). Spectral response refers to the effects that the taxonomic and structural responses have on the spectral characteristics of vegetation.

Areas with geochemically-anomalous substrata are invariably colonised by plant species that are tolerant of the anomalous concentrations of elements in the substrata (Shaulis and Lancaster, 1994). These plant species may be called indicator species – plant species that serve as a measure of the environmental conditions that exist in a given locale (Ricklefs, 1990) – and constitute the taxonomic response of vegetation to anomalous substrate geochemical conditions. Colonies of indicator plant species, depending on their areal

dimensions, can be delineated by remote sensing. Visual observations from a low-flying aircraft and aerial photography are viable methods for mapping colonies of indicator plants (Rose et al., 1979). Krohn et al. (1981) have observed, on Landsat MSS imagery, the distribution of Quercus prinus associated with hydrothermally-altered andesites in a deciduous forest in eastern United States. Elvidge (1982), using airborne TM data, recognised that plant species Mimosa biuncifera, Cercidium microphyllum, Calliandra eriophylla and Condalia spathulata occur preferentially on a mineralised zone whilst Acacia Greggii, Happlopappus sarothrae and Opuntia spinosior occur preferentially on non-mineralised areas in the Upper Sonoran Desert. Odhiambo et al. (1989), Odhiambo and Howarth (1993) and Payás et al. (1993), among others, demonstrated the application of Landsat TM data to the detection of colonies of various indicator plant species associated with different types of mineralisation. Milton (1983) used an airborne multispectral scanner with narrower spectral band-widths and 10x10 m spatial resolution and was able to identify a community of vegetation associated with hydrothermally-altered and potentially mineralised volcanic rocks in East Tintic mining district in Utah. The different studies based on airborne and/or spaceborne spectral data invariably showed that indicator plant species contain higher trace element contents and have distinctly higher reflectance than vegetation in surrounding non-mineralised areas. These studies also indicated that EM sensors with higher spatial and spectral resolutions are potentially useful in the detection of indicator plant species. Consequently, Clark et al., (1995) indicated the potential of imaging spectrometer data for mapping of individual plant species at a farmland scale.

Stunted or thinly-developed vegetation is a common indicator of anomalous substrate geochemical conditions. In serpentine and/or ultramafic areas, for example, vegetation is stunted or thinly-developed perhaps because of the unusually high contents of Ni, Co, Cr and other elements, deficiencies in K and other essential elements, or the poor drainage often associated with clay-rich overburden over these lithologic units (Rose et al., 1979). The characteristic stunted vegetation in serpentine and/or ultramafic areas is readily discernible in aerial photographs and in coarse spatial resolution and broad-band spectral resolution satellite imagery (Raines and Wynn, 1982; Milton and Mouat, 1984). For mineral exploration, Tolbert et al. (1971) provide an example of the successful application of locating stunted vegetation by aerial photography, which was instrumental to the discovery of the Serra dos Carajas iron deposits in Brazil. Small obvious areas of diminished vegetation growth can certainly be identified by aerial photography but not by coarse spatial resolution and broad-band spectral resolution satellite imagery. Bølviken et al. (1977) concluded that Landsat-1 MSS data are inadequate for mapping small patches of stunted vegetation due to Pb poisoning attributed to a certain mineral deposit in Snertingdal, Norway. They also reported, however, the usefulness of Landsat-1 MSS data to detect relatively large areas of sparse and naturally heavy-metal-poisoned vegetation on a Cu deposit in Karasjok, northern Norway. They also showed that the naturally heavy-metal poisoned vegetation have significantly

different spectral characteristics than the surrounding healthy vegetation. Milton (1983) avers that the differences between reflectance characteristics of thinly-vegetated mineralised zones and thickly-vegetated non-mineralised zones could be explained by vegetation density. Many workers, however, have shown that, notwithstanding seasonal changes, vegetation on mineralised zones invariably have higher reflectance in the visible wavelengths and lower reflectance in the infrared wavelengths as compared to vegetation on non-mineralised zones (Horler et al., 1980; Milton et al., 1983; Nash and McCoy, 1993).

Morphological changes in the greenness of vegetation that are not related to natural seasonal senescence of vegetation may or not be attributed to anomalous substrate geochemical conditions (Rose et al., 1979). Abnormal yellowing of leaves or chlorosis, for example, is caused by excessive concentrations of Ni, Cu, Co, Cr, Zn and Mn, which produce a deficiency in Fe essential to chlorophyll formation (Cannon, 1960). Aside from anomalous substrate geochemical conditions, chlorosis and other colour changes can result from other causes, including plant infections, improper drainage, and excess acidity in soil. Although abnormally-coloured leaves are non-specific guides to mineral deposits, they always deserve the attention of the mineral prospector inasmuch as chlorotic symptoms are common in mineralised areas. An apparent remote sensing technique to identify patches of vegetation that exhibit abnormal colours is through visual observations from low-flying airborne platforms. On the other hand, a number of measures have been developed to detect changes in the greenness of vegetation from remotely-sensed data. The most common of these measures are the various vegetation indices (Wickham et al., 1993). The simplest is the vegetation index (VI), sometimes called ratio vegetation index (RVI), which is the ratio of infrared to red radiation (Tucker, 1979). Several variations have emerged over the years, notably, the perpendicular vegetation index (PVI) proposed by Richardson and Wiegand (1977), the greenness index (GI) of Kauth and Thomas (1976), the soil adjusted vegetation index (SAVI) of Huete (1988), and the soil adjusted ratio vegetation index ($SAVI_2$) of Major et al., (1990), all of which were introduced to better account for background reflectance of soil. Another measure, the normalised difference vegetation index (NDVI), was proposed by Rouse et al. (1974) to minimise the sensitivity to noise. Although superficially different, there appears to be little functional difference among most of these vegetation indices (Perry and Lautenschlager, 1984). Demetriades-Shah et al. (1990), however, noted that whilst most of these vegetation indices reduce the contribution of soil to canopy spectral measure, they do not eliminate it. Adams et al. (1999) developed a 'yellowness index', which eliminates the effects of soil background to properly estimate leaf colour/chlorosis of geochemically-stressed vegetation from high resolution spectral data.

Phenological responses of vegetation to anomalous substrate geochemical conditions are detectable by using multi-temporal remote sensing datasets. Matsuoka et al. (1982) used multi-temporal Landsat TM images of the Virginia

Piedmont to study four heavily-vegetated sites (two mineralised sites and two non-mineralised control sites) with similar soil types, bedrock, hydrogeology, vegetation (Quercus alba) and vegetation density. They have observed that vegetation on the mineralised sites had higher reflectance in bands 3 and 5 than vegetation on the non-mineralised sites throughout the growing season, and that the spectral differences were even greater at the onset of and during autumn. They also found that vegetation on the mineralised sites has a later spring leaf-out and an earlier fall senescence than vegetation on the non-mineralised control sites. Darch and Barber (1983) used four temporal Landsat MSS datasets to study a colony of vegetation associated with the Dolfrwynog bog in the Coed y Brenin area in northern Wales. Vegetation over the bog, a copper geochemical anomaly of four hectares, was dominated by a copper indicator plant species Armenia maritima whereas vegetation surrounding the bog is a coniferous forest dominated by Picea sitchensis and permanent pastures. Darch and Barber (1983) concluded that the bog was detectable most clearly in May, during which the vegetation it supported always had lower visible and near-infrared reflectance than the surrounding coniferous forest and pastures. They did not indicate, however, whether vegetation density was a factor in the temporal differences in the spectral characteristics of vegetation on the bog and on the surrounding areas.

On a regional scale, phenological changes in vegetation, though not necessarily due to anomalous substrate geochemical conditions, have been studied by several workers using the Advanced Very High Resolution Radiometer or AVHRR data (e.g., Kasischke and French, 1997; França and Setzer, 1998; Duchemin et al., 1999; Schwartz and Reed, 1999). The AVHRR, onboard the National Oceanographic and Atmospheric Administration (NOAA) series of satellites, provides daily images with 1.1 km spatial resolution and spectral data taken from 5 non-contiguous channels (0.58-0.68 μm, 0.725-1.10 μm, 3.55-3.93 μm, 10.3-11.3 μm, 11.5-12.5 μm). The potential of AVHRR for spatio-temporal studies of phenological changes in vegetation in metallogenic provinces (e.g., the Iberian Pyrite Belt) has not been assessed yet.

The reflectance spectra of vegetation are unique compared to the reflectance spectra of most Earth surface materials (Wickham et al., 1993). Shown in Figure 3.3 is a generalised pattern of EM energy reflected by healthy and stressed vegetation. The abrupt increase in vegetation reflectance from the visible region to the near-infrared region (at approximately 0.7 μm) of the EM spectrum is referred to as the red-edge. The red-edge was first reported by Gates et al. (1965) and discussed in remote sensing literature by Knipling (1970). The position of the red-edge has been used as an indicator of vegetation stress and senescence (Collins, 1978; Horler et al., 1983; Rock et al., 1988; Hodcroft and Moore, 1988; Boochs et al, 1990). Vegetation stress, as indicated by changes in position of the red-edge, due to mineral deposits has been reported by, among others, Chang and Collins (1983), Collins et al. (1983), Curtiss and Maecher

(1991). Shifts in the red-edge position toward shorter wavelengths, or blue shift, are attributed to chlorophyll loss, whilst shifts in the red-edge position toward longer wavelengths, or red shift, is attributed to chloroplast damage (Curtiss and Maecher, 1991). Many other researchers have indicated that shifts in the position of the red-edge are associated with plant chlorophyll content (e.g., Horler et al., 1980; Lepp, 1981; Rock et al., 1988; Singhroy et al., 1989; Van Assche and Clijsters, 1990; Carter, 1994a). The most probable reason for associating variations in chlorophyll content to changes in the red-edge position is that, among the photosynthetic pigments (chlorophyll, xantophyll, and carotene), only chlorophyll absorbs in the red regions of the EM spectrum (Shaulis and Lancaster, 1994). Other researchers, however, recognised that atmospheric, canopy and illumination geometry effects also influence variations in the red-edge position (Chang and Collins, 1980; Schwaller, 1982; Collins et al., 1983; Shutt et al., 1984; Vanderbilt et al., 1985; Vanderbilt et al., 1988; Curtiss and Maecher, 1991).

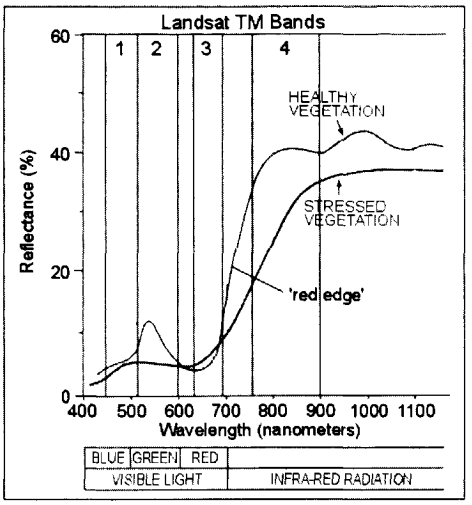

Figure 3.3. Schematic reflectance spectra of healthy and stressed vegetation in visible and infrared regions of EM spectrum (from Hodcroft and Moore, 1988).

Detection of vegetation stress from remote sensor data often employs techniques to locate the red-edge position (Horler et al., 1983; Bonham-Carter, 1988; Miller et al., 1990; Guyot et al., 1992; Chen and Elvidge, 1993; Railyan and Korobov, 1993; Danson and Plummer, 1995; Dawson and Curran, 1998). Shaulis and Lancaster (1994) indicated that remote detection of the position of the red-edge is possible only by using imaging spectrometer data. Leprieur (1989) and Elvidge et al. (1993) have shown the usefulness of AVIRIS data to discern vegetation red-edge. Lehman et al. (1991) used GERIS spectra to study the red-edge position of healthy and stressed vegetation. Yang et al. (2000) were able to identify changes in the position of red-edge from Modular Airborne Imaging Spectrometer (MAIS) data. Van der Meer et al. (2000) have indicated the potential application of Medium Resolution Imaging Spectrometer (MERIS) data to determine changes in the red-edge position. The MERIS will collect data from the European Space Agency's ENVISAT-1 satellite, which is scheduled for launch in October 2001 (http://envisat.esa.int/). The MERIS is designed to acquire data from the 390-1040 nm range of the EM spectrum in 15 spectral bands with variable band widths and positions (Rast et al, 1999).

Inasmuch as many researchers associate changes in the position of the red-edge to changes in chlorophyll content in plants, remote detection of chlorophyll content in plants has become the goal of many plant physiological and ecological studies. In some old and recent studies, vegetation reflectances near 550 nm and 700 nm have been found to show maximum sensitivity to a wide range of chlorophyll contents (Thomas and Gausman, 1977; Baret et al., 1992; Buschman and Nagel, 1993; Yoder and Waring, 1994; Gitelson and Merzlyak, 1996; Lichtenhaler et al., 1996). The red-edge position has also been found to be a sensitive indicator of chlorophyll content (Horler et al., 1983; Curran et al., 1991; Curran et al., 1992; Gitelson et al., 1996; Pinar and Curran, 1996). Because of the apparent very subtle changes in the position of the red-edge and/or chlorophyll content in plants, the accurate estimation of these parameters requires imaging spectrometry data (Boochs et al, 1990; Gitelson and Merzlyak, 1994, 1997; Zagolski et al., 1996; Blackburn, 1998; Datt, 1999). Dawson (2000) discusses the potential of MERIS for estimation of chlorophyll from vegetation. Broad-band remote sensing systems apparently are not potentially useful for estimation of chlorophyll content in plants; however, Landsat TM data have been reported to be useful in the determination of chlorophyll distribution in lake waters (Dekker and Peters, 1993; Brivio et al., 2001).

Accurate remote detection and mapping of stressed vegetation due to anomalous substrate geochemical conditions thus desirably require high spatial resolution and multispectral/hyperspectral airborne/satellite data. The limitations of remotely-sensed data from broad-band spaceborne systems, such as Landsat TM, for vegetation stress detection and mapping are apparently due to its low spatial and spectral resolutions. The higher spatial resolution of ASTER in the VNIR regions may provide useful application to vegetation stress detection and mapping. High spatial resolution and multispectral/hyperspectral remotely-sensed data, however, are not only expensive but also not readily available to many Third World countries. Nash and Hernandez (2001) demonstrate the cost-effectiveness of Landsat TM data in vegetation anomaly mapping for geothermal exploration. This is encouraging because Landsat TM data are most widely used in many developing Third World countries. In this study, Landsat TM data are used in experiments to detect and map vegetation stress associated with geochemically-anomalous and/or mineralised areas. Landsat TM data are the only remotely-sensed multispectral data available to this study.

3.3 REMOTE DETECTION OF HYDROTHERMALLY-ALTERED ROCKS IN THE PRESENCE OF VEGETATION USING LANDSAT TM DATA

Relative successes have been achieved in detecting hydrothermally-altered rocks using Landsat TM data. In arid and semi-arid regions, outcropping alteration zones are mineralogically conspicuous enough to be detected successfully from Landsat TM data (Podwysocki et al., 1984; Kepper et al., 1986; Mouat et al., 1986; Amos and Greenbaum, 1989; Rockwell, 1989; Tanaka

and Segal, 1989; Ashley, 1990a, 1990b; Fraser, 1991; John et al., 1991; Bennett, 1993; Barniak et al., 1996; Spatz, 1997). In tropical regions, however, high vegetation density can critically limit the successful application of Landsat TM data to the detection and mapping of hydrothermally-altered rocks (Siegal and Goetz, 1977; Adams and Adams, 1984; Fraser and Green, 1987; Schmidt et al., 1987). The main reason for the relatively poor successes in the application of Landsat TM data to the mapping of hydrothermal alteration in heavily-vegetated terranes is that vegetation obstructs the reflectance of the underlying substrate.

Where vegetation is dense, the 30x30 m Landsat TM pixels could represent purely vegetation spectra. Where vegetation is not dense enough and the spatial resolution of Landsat TM is inadequate to clearly 'see between the trees', the pixels represent a mixture spectra of different materials. In this latter case, techniques for image processing of Landsat TM data to detect and map hydrothermally-altered rocks are aimed at separating or reducing substantially the spectral effects of vegetation from the spectral effects of the underlying substrate (e.g., Adams and Adams, 1984; Fraser and Green, 1987). The process of separating the spectral effects of different materials is called spectral unmixing (Smith et al., 1985). Spectral unmixing endeavours to search for the abundances or fractions of pure spectral components, so-called end-members, that best explain the observed mixed pixel spectra. Spectral unmixing has been shown to very successful when applied to imaging spectrometry data (Boardman, 1993; Van der Meer, 1996). A major hindrance to the successful application of spectral unmixing of Landsat TM data is the low spectral resolution of the sensor, which results in few or no pure pixels (Van der Meer and De Jong, 2000). Apparently, the search for spectrally pure pixels of hydrothermally-altered rocks in Landsat TM data pertaining to heavily-vegetated areas and the application of spectral unmixing can be futile. Consequently, the application of spectral unmixing to mapping of hydrothermally-altered rocks in heavily-vegetated terranes using Landsat TM data has not been widely reported.

Techniques for digital enhancement of Landsat TM data to map hydrothermally-altered rocks commonly aim at the identification of clay and iron oxide (limonitic) alteration zones. The remote detection of iron oxide and clay zones in the presence of vegetation, however, is difficult due to similarities in the reflectance spectra of the materials (Figure 3.4). Iron oxides and vegetation have similar reflectance spectra in the wavelength regions covered by Landsat TM bands 1 and 2. These bands are, thus, together not very useful in distinguishing iron oxides in vegetated regions. Clay minerals have strong reflectance in the spectral region covered by Landsat TM band 5 and an absorption feature in the spectral region covered by Landsat TM band 7. Landsat TM bands 5 and 7 are thus potentially useful in detecting clay zones. However, similarities in shape and relative intensities of the reflectance curves of vegetation and clay minerals in the spectral regions covered by Landsat TM bands 5 and 7 make their differentiation difficult. In the spectral region covered by Landsat TM band 3, iron oxides and clays have high reflectance whilst vegetation has strong absorption.

In the spectral region covered by Landsat TM band 4, vegetation has strong reflectance whilst iron oxides and clays show absorption features. Landsat TM bands 3 and 4 can thus be used to differentiate areas of iron oxides and/or clays from areas of vegetation. For heavily-vegetated areas, remote identification of hydrothermally-altered rocks commonly uses Landsat TM bands 3, 4, 5 and 7. These bands are used in image enhancement techniques that include band ratio calculations (Segal, 1983), principal components analysis (Crósta and Moore, 1989), or a combination of both (Fraser and Green, 1987).

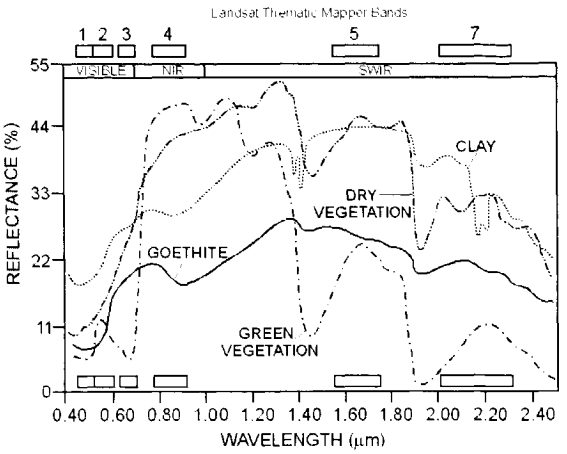

Figure 3.4. Typical reflectance spectra of vegetation, iron oxides and clays (from Fraser and Green, 1987).

A popular image enhancement technique based on principal components analysis is known as the Crósta technique (Crósta and Rabelo, 1993). The Crósta technique is based on the examination of principal components (PC) eigenvector loadings to decide which of the PC images will concentrate information related directly to the theoretical spectral signatures of specific target materials. The technique is able to predict whether the target material is represented by bright or dark pixels in the PC images according to the magnitude and sign of the eigenvectors. Limonitic alteration zones are mapped by using Landsat TM bands 1, 3, 4 and 5; clay alteration zones by Landsat TM bands 1, 4, 5 and 7 (Crósta and Rabelo, 1993; Ruiz-Armenta and Prol-Ledesma, 1998). Image processing is carried out on raw image data as Loughlin (1991) has shown that standardisation is unnecessary in the PC analysis.

An image enhancement technique based on band ratio calculations and principal components analysis is called the software defoliant technique (Fraser and Green, 1987). The software defoliant technique is a directed principal components (DPC) analysis of two band ratio images. The input band ratios are selected on the basis that one band ratio contains information related to the component of interest (e.g., hydrothermal alteration), the spectral response of which suffers interference from the spectral response of another component (i.e., vegetation). The second band ratio should thus contain information about this spectrally interfering component. Fraser and Green (1987) aver that the input band ratio images, which are computed from unstretched data, need to be standardised through a histogram equalisation stretch so that their range

extends from 0 to 255 and their means approximate 128. Once computed, the DPC that has loadings of similar signs on both input band ratio images explains the variance due to similarities in the spectral responses of the interfering component and the component of interest. The other DPC, whose loadings are of different signs on either of the input band ratio images, highlights contributions unique to each of the components. The sign of the loadings dictates whether the component of interest is represented as bright or dark pixels in the DPC image; a positive loading implies bright pixels, a negative loading implies dark pixels. Based on the generalised reflectance curves of selected cover types (Figure 3.4), band ratio 4:3 serves as an excellent vegetation indicator whilst band ratios of 3:1 and 5:7 are commonly used to enhance iron oxides and clays, respectively (Fraser and Green, 1987).

The Crósta technique and the software defoliant technique were applied to the Landsat TM data of Baguio district to identify limonitic and clay alteration zones. It will be demonstrated that these techniques are inadequate to map known hydrothermally-altered zones in the Baguio district. As an alternative, an innovative methodology was devised to map the known and unknown hydrothermal alteration zones in the test districts using Landsat TM data.

Image pre-processing of the Landsat TM data included only haze correction by a simple dark-object subtraction method (Richards, 1999). Haze is due to particulates present in the atmosphere, which obscures the spectral response of ground objects and has an additive noisy effect on the image brightness. The simple dark-objection subtraction method relies on the assumption that there should be black pixels (e.g., shadows) in an image and these pixels should have a DN (digital number) value of zero (i.e., no reflectance). Due to haze, however, these black or dark objects have DN values greater than zero. The simple dark-objection subtraction method thus involves subtracting a constant DN value from a certain digital image. This constant DN value is the lowest (i.e., pertaining to the darkest pixels) in a certain digital image and is determined from a histogram of the DN values of that image. The improved dark-object subtraction method of Chavez (1988) was not employed, as it requires an atmospheric scattering model that best represents the atmospheric conditions at the time of data collection. Because of the variable atmospheric conditions in tropical areas, a single atmospheric scattering model, notwithstanding the difficulties in determining such a model (Curico, 1961), is deemed inappropriate for haze removal in the Landsat TM data of the test district(s). The maximum noise fraction (MNF) method of Green et al., (1988) for noise removal was also not used. The MNF method was designed to perform noise removal from images whose principal components transforms do not show steadily decreasing image quality. The Landsat TM images of the test district(s), however, do not show this characteristic as will be illustrated below. Thus, only the simple dark-object subtraction method was applied to the Landsat TM data. Although the method assumes a constant haze value throughout an image, it does accomplish a first-order correction, which is better than no correction at all.

3.3.1 Baguio district: hydrothermal alteration, vegetation and Landsat TM data

The geology and mineralisation of the Baguio district are described in Chapter 2 (section 2.3.1). The district contains epithermal gold and porphyry copper deposits. The epithermal gold mineralisation is younger than the porphyry copper mineralisation (Mitchell and Leach, 1991). This implies that existing hydrothermal alteration patterns in the district reflect largely or totally the effects of the lower temperature epithermal systems due to overprinting upon the effects of the higher temperature porphyry systems (UNDP, 1987b). The major types of hydrothermal alterations genetically associated to the epithermal systems are propylitic, illitic and advanced argillic alterations (Mitchell and Leach, 1991; UNDP, 1987b). The known epithermal gold deposits are spatially associated with illitic (quartz-illite) alteration zones (Figure 3.5). The spatial distribution of the advanced argillic and illitic alteration zones mapped by UNDP (1987b) is largely due to geological mapping along stream traverses and not due to geological processes. Also indicated in Figure 3.5 are inferred boundaries of alteration zones identified by Benguet Corporation (unpublished data). The advanced argillic zone of UNDP (1987b) coincides spatially with the 'strongly argillised' zone of Benguet Corporation. Both groups of workers, however, recognise that propylitic alteration is widespread east of Baguio.

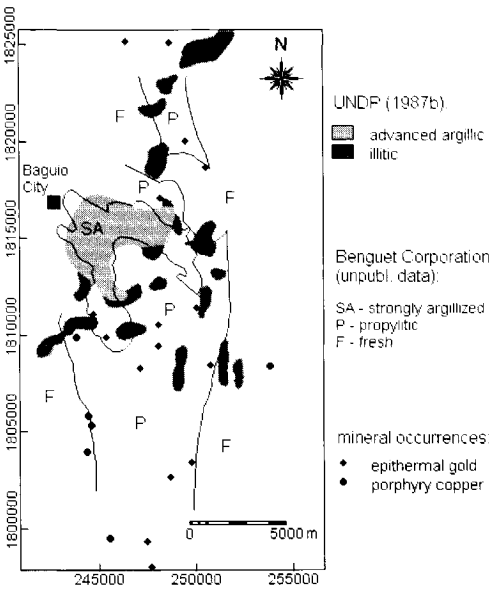

Figure 3.5. Hydrothermal alteration zones in the Baguio district.

In the field, propylitic alteration is characterised by the presence of green-grey rocks that are slightly silicified, usually contain chlorite and epidote, and locally calcareous. On XRD (x-ray diffraction) analysis, propylitised rocks are defined by predominant chlorite, presence of epidote, with or without quartz, illite and pyrite. In the field, illitic alteration is recognised by the presence of clay (illite) or more usually silica and clay (quartz + illite). Illitic alteration is defined on XRD analysis by the presence of predominant illite, with or without quartz, chlorite and pyrite. The XRD analyses indicate that the distinction between propylitic and illitic alteration is not always precise (UNDP, 1987b). Advanced argillic alteration was mapped east of Baguio as a crescent-shaped zone dominated by a quartz-alunite mineral assemblage (UNDP, 1987b). The XRD analysis shows that the altered rocks contain alunite and quartz with or without kaolinite.

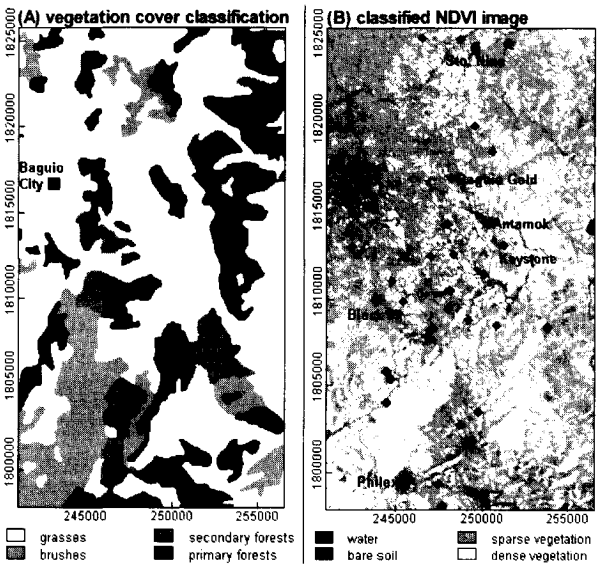

Figure 3.6. Baguio district: (a) vegetation cover map (from NAMRIA, 1989); (b) classified NDVI map.

Rugged topography and dense vegetation cover impede thorough mapping of the district's surface geology and hydrothermal alteration. A vegetation map of the district, based on interpretation of 1987-1988 SPOT multispectral data by the National Mapping and Resource Information Authority (NAMRIA, 1989), is shown in Figure 3.6a. At least 56% of the district is grassland, at least 13% is brushland, at least 23% is secondary growth pine (Pinus kesiya) forest and at least 6% is primary growth pine (Pinus kesiya) forest. Inspection of the natural colour composite (red channel = band 3, green channel = band 2, blue channel = band 1) of the Landsat TM data and NDVI image leads to a classified NDVI map of the district (Figure 3.6b). It indicates that 38% of the district is densely vegetated (i.e., pixels containing purely vegetation), 52% sparsely vegetated (i.e., pixels of mixed vegetation and bare soil) and 10% bare soil and water. Bare soil areas pertain to known mines (e.g., Philex, Black Mountain, Keystone, Antamok and Sto. Niño), urban areas and river channels. The rugged topography and examples of densely and sparsely vegetated areas are illustrated in Figure 3.7.

Landsat TM imagery Path 116 Row 049 acquired on 09 January 1989 was used in this study. Figure 3.8 shows the principal component images of a subscene of the Landsat TM imagery covering most of Benguet province where Baguio district is located. The images illustrate steadily decreasing image qualities with no or few indications of noise such as salt-and-pepper speckles and/or linear striping patterns. Hence, the Landsat TM data were de-hazed only by simple dark-object subtraction (Richards, 1999). A subscene of the Landsat TM imagery (522 pixels by 933 pixels) for the Baguio district covers 16°14'06" - 16°30'05" N latitudes and 120°34'30" - 120°43'07" E longitudes (Figure 3.8). The Landsat TM subscene of Baguio district is georeferenced using affine transformation and four control points representing stream junctions whose UTM coordinates were determined from 1:50,000 scale topographic maps. The resulting root mean square error for the georeferencing was 0.861 pixels.

Figure 3.7. Relative vegetation densities in Baguio district: dense (left); sparse (right).

The elementary statistics of the different spectral bands are given in Table 3.1. The bands (1, 2 and 3) in the visible range have higher minimum and maximum values than the bands (4, 5 and 7) in the infrared range; this is due to haze (Richards, 1999). On the basis of the reflectance spectra of vegetation in Figure 3.3, the lower maximum value in band 2 compared to the higher maximum value in band 3 could be an indication of vegetation stress, probably due to hydrothermal mineralisation and alteration in the district. Band 5 has the highest standard deviation due to large variations in spectral response of the various materials contained in the image. Band 2 has the lowest standard deviation, which is due to its low contrast.

Table 3.1. Elementary statistics of spectral bands of Landsat TM data, Baguio district.

	Band 1	Band 2	Band 3	Band 4	Band 5	Band 7
Minimum	54	17	12	7	4	1
Maximum	173	144	177	161	176	90
Mean	70.29	31.09	27.76	81.48	71	25.17
Std. Dev.	7.79	4.81	7.00	14.07	14.98	7.26

The spectral data in bands 1, 2 and 3 are highly correlated (Table 3.2) and hence much of their information is redundant. Good correlation exists between the spectral data in bands 5 and 7. Bands 5 and 7 are thus not useful to distinguish between areas of vegetation and hydrothermally-altered rocks because, as indicated in Figure 3.4, ratios of band 5 to 7 are similar for vegetation and clayey/limonitic materials. The data in band 4 is poorly correlated with the data in bands 1, 2 and 3. Bands 1, 2, 3 and 4 can thus be used to discriminate areas that contain vegetation from those that contain soil because, as indicated in Figure 3.4, ratios of band 4 to either band 1, 2 or 3 are higher for vegetation than for clayey/limonitic materials. The data in bands 4 and 7 are not well correlated; these bands can thus be used to differentiate areas that contain clay alteration from those that contain vegetation because, as indicated in Figure 3.4, ratios of band 4 to band 7 are lower for clay areas than for vegetation areas.

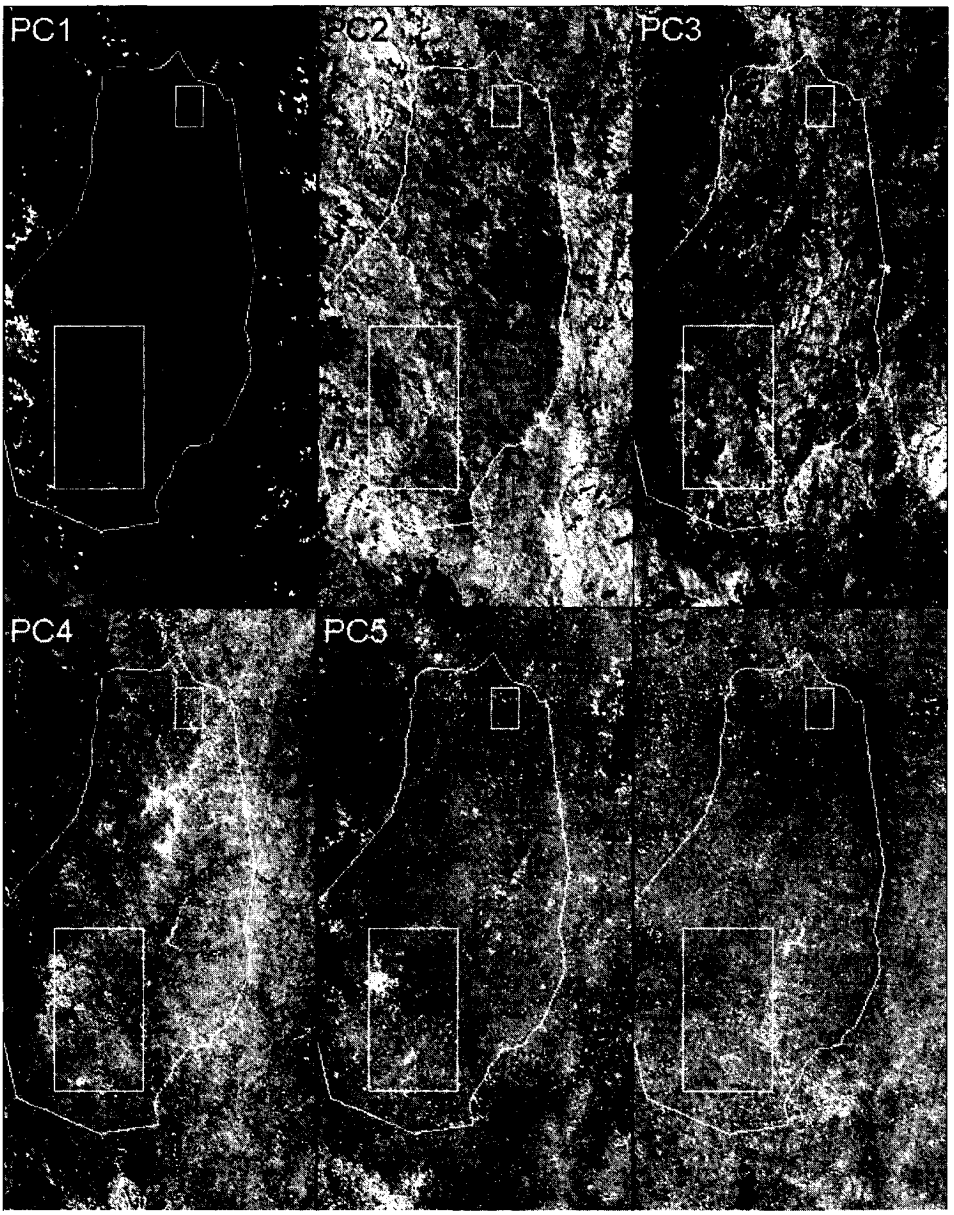

Figure 3.8. Decreasing quality of principal component images of a subscene of raw Landsat TM data use for Baguio district (larger box). Boundaries of Mankayan district (smaller box) and Benguet province (irregular polygon) are shown.

Table 3.2. Correlation matrix of spectral bands of Landsat TM data, Baguio district.

	Band 1	Band 2	Band 3	Band 4	Band 5	Band 7
Band 1	1.00					
Band 2	0.95	1.00				
Band 3	0.94	0.95	1.00			
Band 4	0.09	0.24	0.04	1.00		
Band 5	0.56	0.72	0.64	0.55	1.00	
Band 7	0.76	0.84	0.84	0.23	0.89	1.00

3.3.2 Application of the Crósta technique to Baguio district

Table 3.3 describes the PC transformation for limonitic alteration detection. All the input bands have positive loadings in PC1, which represents albedo and topographic information in the data. The PC2 has high and positive loadings for band 4; it represents vegetation. The contrast between the spectral data in the VNIR and SWIR regions of the EM spectrum is described in PC3. Limonitic alteration (characterised by high reflectance in band 3 and low reflectance in band 1) is explained by PC4 based on high loadings of opposite signs for bands 1 and 3. The positive sign on the loading on band 3 indicates that limonitic alteration is mapped as bright pixels (Figure 3.9a). The limonitic alteration component accounts for less than 1% of the total variance in the spectral data.

Table 3.3. Principal components analysis on four spectral bands of Baguio Landsat TM data for limonitic alteration detection by the Crósta technique. The principal component with loadings in bold indicates limonitic alteration.

Principal components	Eigenvectors				Eigenvalues (%)
	Band 1	Band 3	Band 4	Band 5	
PC1	0.225	0.210	0.583	0.752	66.38
PC2	-0.441	-0.441	0.720	-0.303	26.42
PC3	-0.641	-0.353	-0.366	0.575	6.72
PC4	**-0.587**	**0.798**	0.082	-0.112	0.43

The mapped limonitic alteration zones pertain to known mining areas (see Figure 3.6b). Several small patches of limonitic alteration are mapped southeast of Baguio City where many epithermal gold deposits occur. Larger patches of bare soil areas in and around Baguio City are indicated to be of limonitic character. Bright pixels along the river that drains Antamok and Keystone mines suggest iron oxide precipitates in the stream load. Many of the mapped limonitic zones do not coincide spatially with the known hydrothermal alteration zones.

The PC transformation for detecting clay alteration is described in Table 3.4. Inspection of the loadings for PC1, PC2 and PC3 yields interpretations that are analogous to those for detecting limonitic alteration. The PC1 represents albedo and topographic information, PC2 accounts for vegetation, and PC3 describes contrast between the spectral data in the VNIR and SWIR regions. Clay

alteration minerals are explained by PC4 based on high loadings with opposite signs for bands 5 and 7. The negative sign of the loading for band 5 indicates that the clay alteration will be mapped as dark pixels. By negating (i.e., multiplying by –1) PC4, clay alteration zones are mapped as bright pixels (Figure 3.9b). The clay alteration component accounts for less than 1% of the total variance in the spectral data.

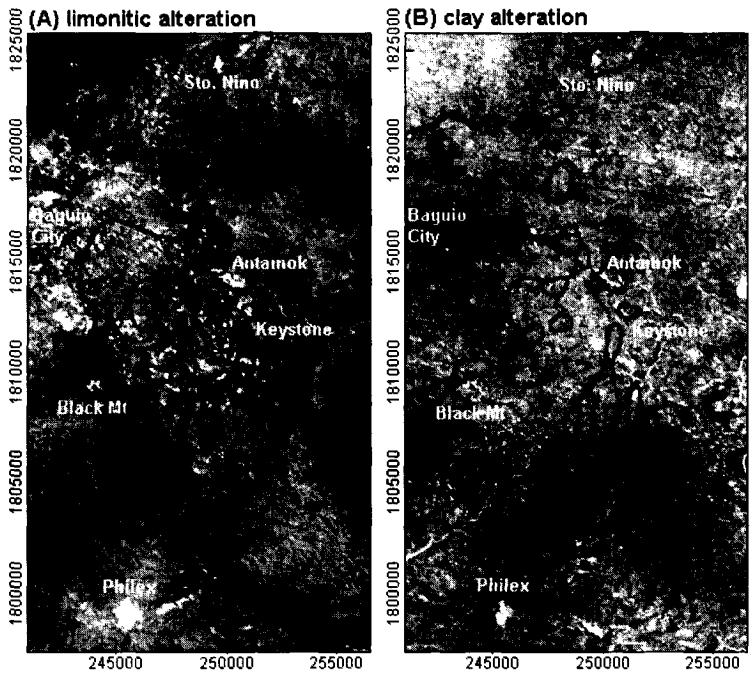

Figure 3.9. Alteration zones (bright pixels) mapped in the Baguio district by the Crósta technique: (a) limonitic and (b) clay. Polygons in black lines are hydrothermal alteration zones mapped by UNDP (1987b).

Table 3.4. Principal components analysis on four spectral bands of Baguio Landsat TM data for clay alteration detection by the Crósta technique. The principal component with loadings in bold indicates clay alteration.

Principal components	Eigenvectors				Eigenvalues (%)
	Band 1	Band 4	Band 5	Band 7	
PC1	0.217	0.557	0.744	0.299	69.05
PC2	-0.396	0.779	-0.321	-0.366	24.92
PC3	0.861	0.255	-0.441	-0.003	5.62
PC4	-0.235	0.135	**-0.387**	**0.881**	0.41

Clay alterations pertain to bare soil areas of some of the known mining areas (see Figure 3.6b). The area southeast of Baguio City where many epithermal gold deposits occur is indicated to contain clay alteration. Bright pixels along the river systems imply clayey materials in the stream load. Previously unknown clay alteration zones are identified to the north of Baguio City. Many of the bright pixels do not coincide spatially with the known hydrothermal alteration zones.

3.3.3 Application of the software defoliant technique to Baguio district

The DPC analysis on band ratio images 3:1 and 4:3 to map limonitic alteration is described in Table 3.5. The DPC1 accounts for the contrast between zones that contain iron oxides from those that contain vegetation. The DPC2 represent zones where the spectral responses due to vegetation and iron oxides cannot be differentiated. The DPC1 should thus map zones containing iron oxides. The negative sign of the loading on band ratio 3:1 suggests that the DPC1 image must be negated to represent zones of limonitic alteration as bright pixels (Figure 3.10a). Several zones of limonitic alteration are identified, which include known mining areas and, in the central part, the area of epithermal gold deposits. The preponderance of iron oxides is indicated in Baguio City and its vicinity. Other zones of limonitic alteration are mapped in zones where no known mineralisation and/or urbanisation are present. Several bright pixels coincide spatially with the known hydrothermal alteration zones.

Table 3.5. Directed principal components analysis of band ratio Landsat TM images for limonitic alteration detection in Baguio district by the software defoliant technique. The DPC with loadings in bold explains limonitic alteration.

Principal components	Eigenvectors		Eigenvalues (%)
	Band 3 : Band 1	Band 4 : Band 3	
DPC1	**-0.693**	**0.721**	55.32
DPC2	0.721	0.693	44.68

The DPC analysis on band ratio images 4:3 and 5:7 to map clay alteration is described in Table 3.6. The DPC1 depicts the strong similarity between the input images and represents zones in which the spectral responses of vegetation and clay alteration cannot be differentiated. The DPC2 represents clay alteration. The positive sign of the loading on band ratio 5:7 suggests that clay alteration is mapped as bright pixels (Figure 3.10b). Bright pixels are present southeast of Baguio City where epithermal gold deposits exist. Bright pixels are also present north of Baguio City and north of Antamok mine; these areas are not known to contain mineralisation.

Table 3.6. Directed principal components analysis of band ratio Landsat TM images for clay alteration detection in Baguio district by the software defoliant technique. The DPC with loadings in bold explains clay alteration.

Principal components	Eigenvectors		Eigenvalues (%)
	Band 4 : Band 3	Band 5 : Band 7	
DPC1	0.707	0.707	94.75
DPC2	**-0.707**	**0.707**	5.25

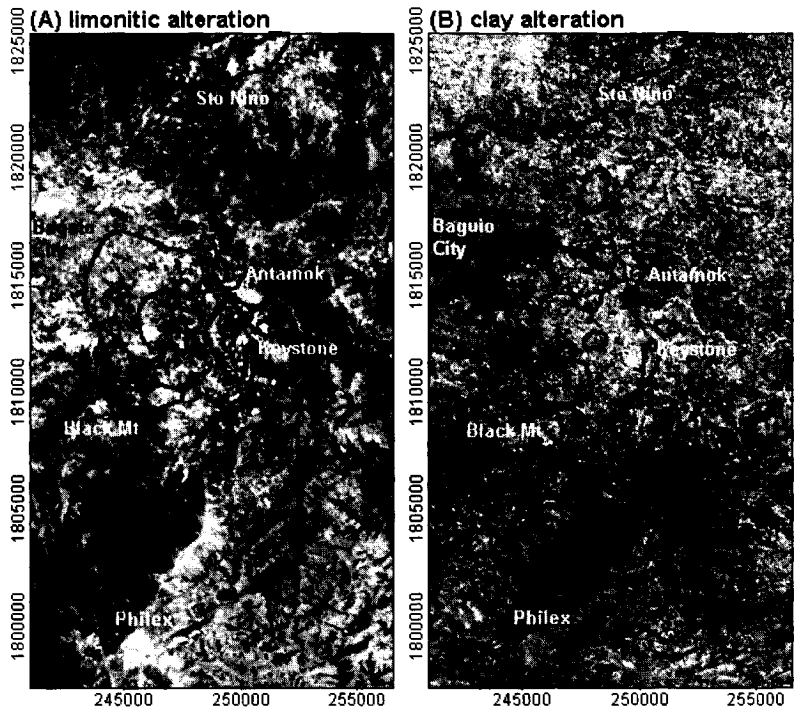

Figure 3.10. Alteration zones (bright pixels) mapped in the Baguio district by the software defoliant technique: (a) limonitic and (b) clay. Polygons in thick black lines are hydrothermal alteration zones mapped by UNDP (1987b)

3.3.4 Discussion of results of the Crósta and the software defoliant techniques

Inspection and comparison of Figures 3.9 and 3.10 with Figure 3.6 show that most of the limonitic and/or clay alteration zones mapped in the Baguio district by either the Crósta technique or the software defoliant technique pertain mostly to bare soil areas. The Crósta technique proved inadequate for remote mapping of hydrothermal alteration in areas of sparse vegetation. On the other hand, the software defoliant technique was able to map limonitic and clay alteration in areas of sparse vegetation. However, it is also inadequate for remote mapping

of hydrothermal alteration in the Baguio district because it failed to map clay alteration in bare soil areas and it was unable to highlight known mining areas where clay alteration is likely to be present.

The two techniques are not only inadequate but also inappropriate because the generalised reflectance spectra of the target materials (i.e., iron oxides and clay) are not characteristic of the hydrothermal alteration minerals in the Baguio district. The known hydrothermal alterations are composed of minerals whose reflectance spectra are different from the generalised reflectance spectra used as bases for the two techniques (Figure 3.4). Reflectance spectral data for the different hydrothermal alteration minerals in the Baguio district are lacking but published spectral data (Figure 3.11; Clark et al., 1993; USGS, 1998) clarify why direct applications of the two techniques to the present case prove inadequate. For example, the reflectance curves in Figure 3.11a to 3.11e are different from the generalised reflectance curve for clay minerals (Figure 3.4). Hence, using only bands 5 and 7, in combination with the vegetation indicator bands 3 and 4, to map clay alteration in the Baguio district is inadequate.

The different reflectance curves in Figure 3.11 suggest that different combinations of bands are needed to enhance the spectral response of the different hydrothermal alteration in the Baguio district. Unique reflectance spectra for each alteration mineral make detection of the individual alteration minerals appealing. Landsat TM bands, however, are too wide to allow detection of individual minerals that compose outcropping soils/rocks. In the Baguio district, however, where the hydrothermally-altered rocks are composed predominantly of two minerals, the usefulness of Landsat TM data in detecting these minerals to map hydrothermal alteration zones can be tested.

3.3.5 Mineral imaging methodology using Landsat TM data

A new methodology to map hydrothermal alteration using Landsat TM data was tested. The first step in this new methodology was to use the software defoliant technique to enhance the spectral response of each alteration mineral into a separate mineral image based on published reflectance spectra of minerals (Figure 3.11; Clark et al., 1993). The second step was to use GIS to extract training areas for known hydrothermal alteration zones. The third step was to carry out a supervised classification of the mineral images to map hydrothermally-altered zones. A fourth step was to incorporate DEM image for improving the results of the classification as will be explained and demonstrated below.

The principle of the software defoliant technique was applied to create separate images that portray the spatial distributions of each of the predominant hydrothermal alteration minerals. The predominant hydrothermal alteration minerals in the Baguio district are quartz and alunite for the advanced argillic

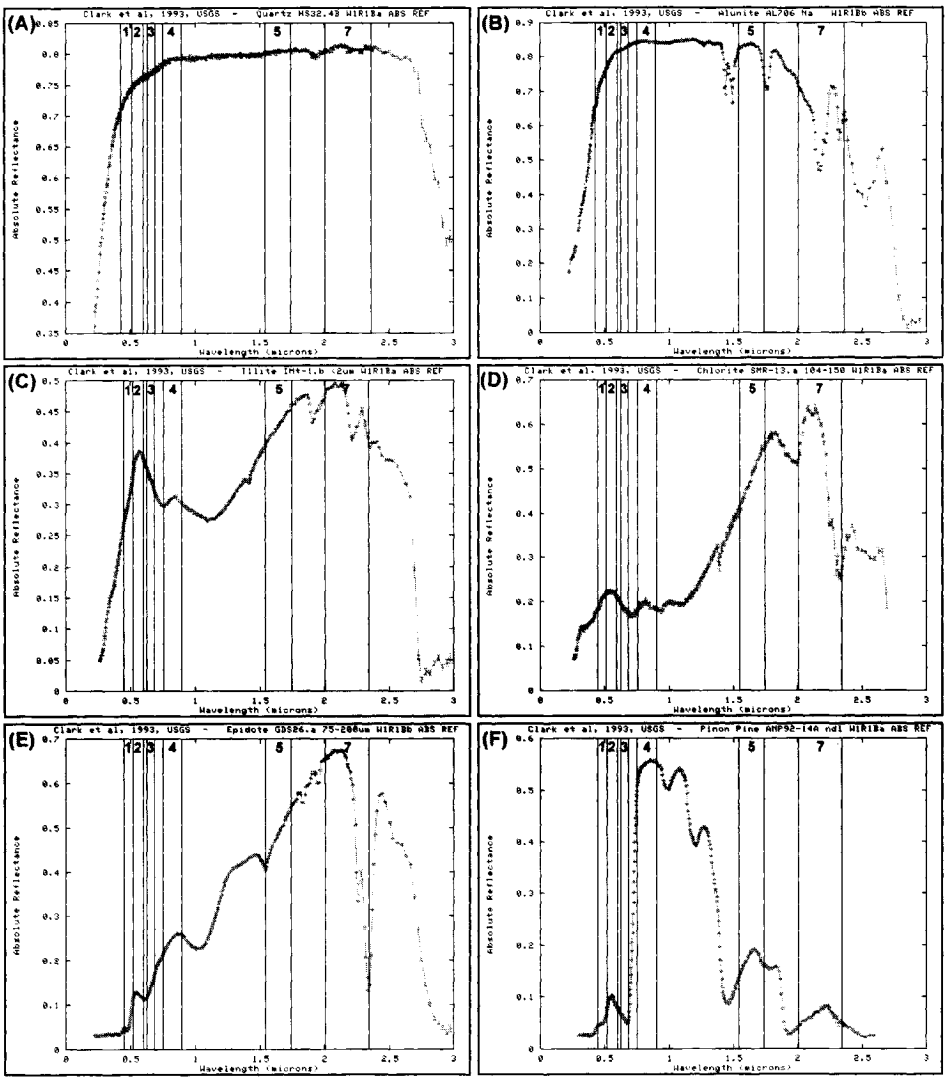

Figure 3.11. Laboratory reflectance spectra of (a) quartz, (b) alunite, (c) illite, (d) chlorite, (e) epidote and (f) green vegetation (from Clark et al., 1993). Wavelength coverages of Landsat TM spectral bands are indicated.

alteration, quartz and illite for the illitic alteration, and chlorite and epidote for the propylitic alteration. To enhance effectively the spectral response of each of these minerals in the presence of vegetation, two band ratio images were created. In both images, the band ratios for vegetation must be high (i.e., greater than 1) based on the spectral curve in Figure 3.11f, whereas the band ratios for a mineral considered must either be high (i.e., greater than 1) or low (i.e., less

than 1) based on the appropriate spectral curve in Figures 3.11a to 3.11e. To select the optimum bands for the band ratio images, the highest possible band ratios for vegetation based solely on Figure 3.11f and the highest and lowest possible band ratios for a particular mineral based solely on the appropriate spectral curves in Figure 3.11a to 3.11e were considered. No band ratio image was used twice in combination with another band ratio image, and a unique combination of band ratio images was sought for each mineral. Listed in Table 3.7 are the different optimum input band ratios that were used to create the mineral images. The selection of the optimum combination of band ratio images proved difficult for illite and chlorite due to their similar reflectance curves. Band ratios 5:1 and 7:1 can thus be used interchangeably for these minerals.

Table 3.7. Optimum band ratios to enhance spectral response of individual predominant mineral constituents of hydrothermal alteration zones in Baguio district.

Alteration mineral to map	Band ratio images input to DPC
Quartz	2/3; 7/1
Alunite	2/3; 5/1
Illite	4/2; 7/1
Chlorite	4/2; 5/1
Epidote	4/1; 5/7

A directed principal components analysis of the two band ratio images resulted in a 'vegetation' component and a 'mineral' component. The 'vegetation' component has positive loadings in both input images. It explains the variance due to similarities in the spectral response of vegetation and the mineral considered as indicated by one of the input images in which the band ratios for vegetation and the mineral considered are both high (i.e., greater than 1). The interference of vegetation on the spectral response of the mineral considered is also explained in the 'vegetation' component. The 'mineral' component has loadings of opposite signs. It explains the variance due to differences in the spectral response of vegetation and the mineral considered as indicated by one of the input images in which the band ratio for vegetation is high (i.e., grater than 1) whilst the band ratio for the mineral considered is low (i.e., less than 1). An image of the 'mineral' component was referred to as a mineral image. If the 'mineral' component' has positive loadings on the input image having a high ratio for a given mineral, then that mineral is mapped as bright pixels in the mineral image. If the 'mineral' component has negative loadings on the input image having a high ratio for a given mineral, then negation is needed to map that mineral as bright pixels in the mineral image. Separate mineral images were created for each of the different hydrothermal alteration minerals.

The pixels in the mineral images were then categorised using conventional supervised image classification approaches, namely: parallelepiped classifier, minimum-distance-to-mean classifier, and maximum-likelihood classifier (Richards, 1999). Training pixels were extracted from the known hydrothermal

alteration zones and used in the supervised classification. The results of the classification are expressed in so-called error or confusion matrix, from which the overall accuracy, the khat-statistic and the Z-statistic based were calculated to assess the significance and/or usefulness of the classification. Formulas to calculate the overall accuracy, the khat-statistic and the Z-statistic can be found either in Cohen (1960), Bishop et al. (1975), Rosenfield and Fitzpatrick-Lins (1986), Story and Congalton (1986), Congalton (1991), Bonham-Carter (1994) or Congalton and Green (1999) and are not repeated here. The minimum overall accuracy for acceptable results is 85% (Anderson et al., 1976). The khat-statistic (an estimate of the coefficient of agreement, kappa) is a measure of agreement between the classified image and the reference data (i.e., the known hydrothermal alteration zones). The levels of agreement between a classified image and reference data depend on the range of the khat values (Landis and Koch, 1977). Khat values greater than 0.8 represent strong agreement, values between 0.4 and 0.8 represent moderate agreement, and values below 0.4 represent poor agreement. The Z-statistic (i.e., standard normal deviate) is used to test the significance of the classification. Given the null hypothesis H_0: $K_1 = 0$ and the alternative H_1: $K_1 \neq 0$, H_0 is rejected if $Z \geq Z_{\alpha/2}$, where $\alpha/2$ is the confidence level of the two-tailed Z test and the degrees of freedom is assumed to be ∞ or infinity (Congalton and Green, 1999).

It will be shown later that the classification of hydrothermal alteration zones from the mineral images can be improved with the application of a DEM. Various applications of a DEM to geological remote sensing have been demonstrated by several researchers (e.g., Fraser et al., 1997; Saraf and Choudhury, 1998; Akman et al., 2001; Lundén et al., 2001; Ricchetti, 2001). The statistic for testing if two classification results are significantly different is expressed by a Z value computed from the khat values ($\hat{K}_1$ and $\hat{K}_2$) and their variances ($\hat{var}(\hat{K})_1$ and $\hat{var}(\hat{K})_2$) estimated from the error of confusion matrix of each classification (Congalton and Green, 1999). Given the null hypothesis H_0: $(\hat{K}_1 - \hat{K}2) = 0$, and the alternative H_1: $(\hat{K}_1 - \hat{K}_2) \neq 0$, H_0 is rejected if $Z \geq Z_{\alpha/2}$, where $\alpha/2$ is the confidence level of the two-tailed Z test and the degrees of freedom is assumed to be ∞ or infinity (Congalton and Green, 1999).

A district scale application of the mineral imaging method is demonstrated for the Baguio district and the Mankayan district. A provincial scale application of the mineral imaging method is demonstrated for the Baguio province.

3.3.6 Mineral imaging method applied to Baguio district

The mineral images are shown in Figure 3.12. The pixel brightness in the different mineral images is considered partly to indicate relative abundance of the different alteration minerals in the ground surface. However, because of the broad wavelength range of the Landsat TM bands and similarities in the

reflectance spectra of various materials, none of the mineral images pertains solely to a particular material. The pixel brightness in the different mineral images also indicates the degree to which the spectral responses of the ground surface are enhanced by the software defoliant technique. Many areas of dense vegetation (see Figure 3.6b) are mapped as dark pixels in the mineral images.

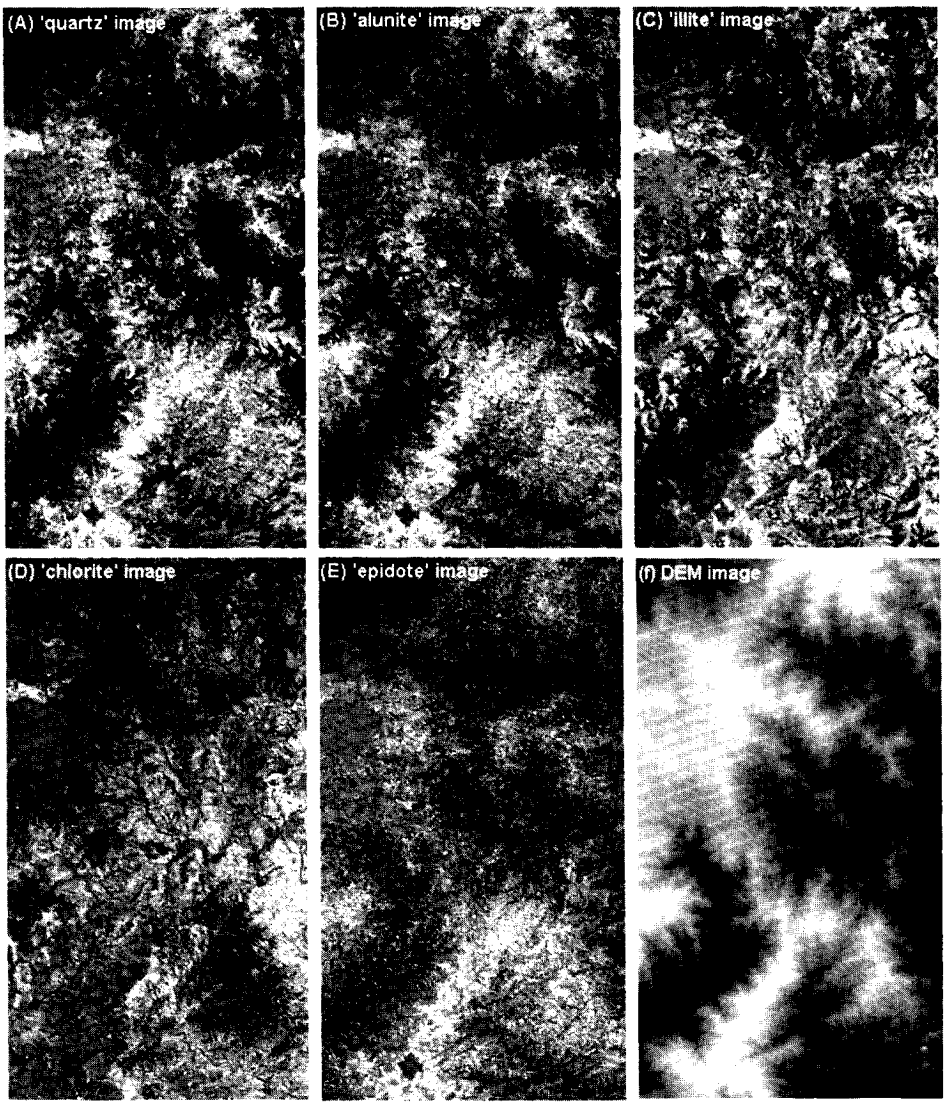

Figure 3.12. Baguio district: mineral images of (a) quartz, (b) alunite, (c) illite, (d) chlorite, and (e) epidote; and (f) DEM image. Pixel brightness in mineral images indicates relative abundance of mineral considered. Pixel bright in DEM image indicates elevation.

There are, however, areas of dense vegetation mapped as bright pixels in the mineral images; vegetation density in these areas is probably particularly low so that the spectral responses of the ground surface are enhanced. There are also areas of sparse vegetation (see Figure 3.6b) mapped as dark pixels in the mineral images; these areas are probably where the material sought is not present in sufficient abundance. Many of the bright pixels in the mineral images spatially coincide with the bright pixels (i.e., areas of high elevation) in the DEM image (Figure 3.12f). Many of these elevated areas are sparsely vegetated (see Figure 3.6b) so that the spectral responses of the ground surface are enhanced. Most dark pixels in the mineral images pertain to areas of lower elevations (Figure 3.12f). Water in the drainage systems and dense vegetation in areas of lower elevations probably strongly interfered with the spectral responses of the underlying materials. It could also be possible that, in areas of lower elevations, any of the minerals considered are not present in particularly sufficient abundance to be mapped adequately in the mineral images.

Provided that the mineral images can be considered indications of relative abundance of the different hydrothermal alteration minerals, the statistical parameters of training data of known hydrothermal alteration units can be used to compute the statistical probability of unknown pixels being members of specific hydrothermal alteration units can be computed. This was carried out through supervised classification (Richards, 1999). To carry out a supervised classification, training/testing pixels are required.

The training/testing pixels for the Baguio district were extracted from the integrated hydrothermal alteration maps of UNDP (1987b) and Benguet Corporation (unpublished data). The 'advanced argillic' of the former and the 'strongly argillised' of

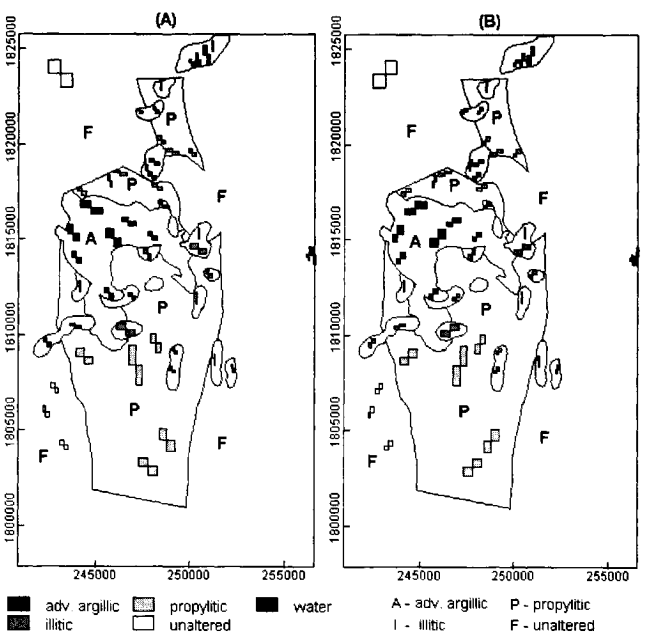

Figure 3.13. Two sets of pixels in Baguio district used in supervised classification and accuracy assessment of classification: (a) training pixels and (b) testing pixels. The irregular polygons represent combined alteration map of UNDP (1987b) and Benguet Corporation (unpublished data).

the latter are combined into one advanced argillic alteration unit. Training/testing areas for the different alteration units are extracted only for sparse vegetation and bare soil areas. For each of the known hydrothermal alteration zones, contiguous pixels are selected. It was ensured that the number of pixels selected per each hydrothermal alteration unit exceeded the recommended number of training pixels for statistically reliable supervised classification results. The recommended number of training pixels is at least 100 times the number of input images (Swain and Davis, 1979). Training/testing pixels for water areas were also extracted from the classified NDVI map (Figure 3.6b). The selected pixels are then split into two sets; each set is the mirror image of the other (Figure 3.13). Each set of the selected pixels was used interchangeably to train and classify the input mineral images and to test the accuracy of the classification. Hence, two sets of classified hydrothermal alteration maps were produced.

Among the conventional supervised classification approaches (Richards, 1999), the maximum-likelihood classifier provided the best results to map known hydrothermal alterations in the district. The hydrothermal alteration map in Figure 3.14a is the result of classification based on the training pixels in Figure 3.13a. The hydrothermal alteration map in Figure 3.14b is the result of classification based on the testing pixels in Figure 3.13b.

The overall accuracy, the khat-statistic and Z-statistic of the classification were estimated based on (1) the training/testing pixels not used in the classification, (2) the combined alteration map of UNDP (1987b) and Benguet Corporation (unpublished data) as shown in Figure 3.13, and (3) the alteration map of UNDP (1987b). To calculate the overall accuracy and khat-statistic of the classification against the combined alteration,

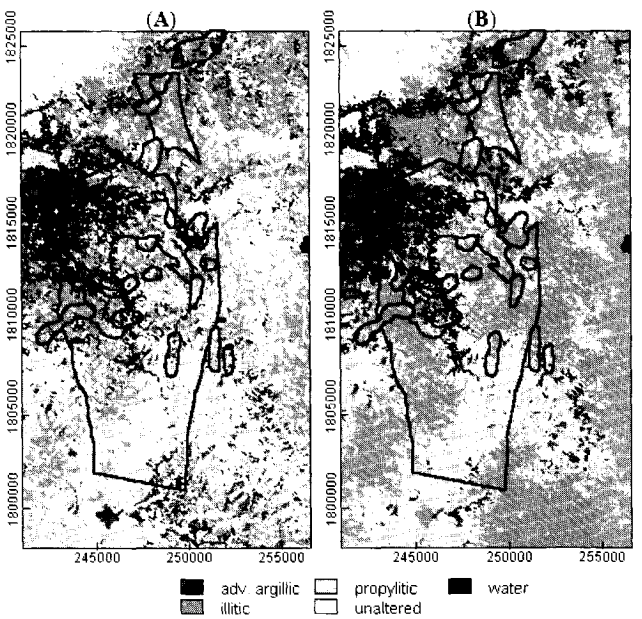

Figure 3.14. Classified hydrothermal alteration maps of the Baguio district using the mineral images and based on (a) training pixels in Figure 3.13a; (b) testing pixels in Figure 3.13b. Boundaries of combined hydrothermal alteration units (UNDP, 1987b; Benguet Corporation, unpublished data) are shown for reference.

the pixels labeled 'unaltered' in the classified images were excluded for two reasons. First, the accuracy and precision of field mapping of the fresh or unaltered rocks cannot be entirely relied upon due to incomplete mapping because of dense vegetation cover, rugged topography, and mapping by Benguet Corporation only within their property. The same reason holds true for the 'propylitised' rocks especially because mapping of this unit by Benguet Corporation is 'open-ended' (Figure 3.5), although it is here 'closed' for purposes of the accuracy assessment (Figure 3.13). Second, since the calculation of the khat-statistic assumes a square matrix, it is convenient to exclude the pixels labeled 'unaltered'. To calculate the overall accuracy and khat-statistic of the classification against the alteration map of UNDP (1987b), the pixels labeled 'propylitic' and 'unaltered' are excluded for the same reasons given above.

Summarized in Table 3.8 are the overall accuracy and khat values for the classified images in Figures 3.14. The results of the classification are unacceptable (i.e., overall accuracy of <85%) and there is poor agreement between the classified images and the reference data (i.e., khat values <0.4). The computed Z values, however, exceed the critical value of Z of 2.58 at the 99% confidence level, which implies that the khat values are significantly greater than zero (i.e., the results are better than a random classification).

The unacceptable and poor results of the classification stem from misclassification between the illitic and advanced argillic classes. UNDP (1987b) indicated that the advanced argillic alteration occur stratigraphically and topographically above the illitic alteration. Thus, the procedure was modified to include a DEM image of the Baguio district in the supervised classification to test whether topographic elevations can be an important aspect in remote mapping of the hydrothermal alteration zones. The values in

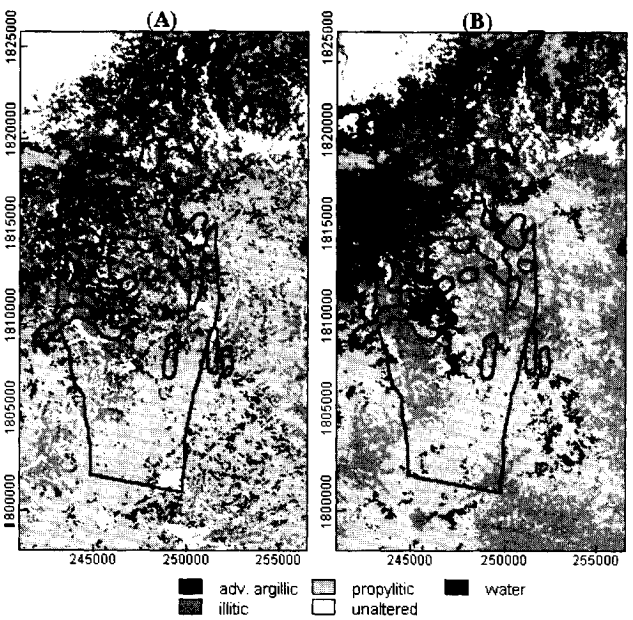

Figure 3.15. Classified hydrothermal alteration maps of the Baguio district using the mineral images and a DEM and based on: (a) training pixels in Figure 3.13a; (b) testing pixels in Figure 3.13b. Boundaries of combined hydrothermal alteration units (UNDP, 1987b; Benguet Corporation, unpublished data) are shown for reference.

the DEM, which range from 300 to 1900 m, were stretched by histogram equalisation to the 0-255 range like the other input images. The results are shown in Figure 3.15.

Table 3.8. Statistical indicators of accuracy of classification of hydrothermal alteration zones based on mineral images, Baguio district.

Statistical parameters	Based on training/testing pixels		Based on combined alteration map		Based on alteration map (UNDP, 1987b)	
	Fig. 3.14a	Fig 3.14b	Fig. 3.14a	Fig. 3.14b	Fig 3.14a	Fig 3.14b
Over accuracy (%)	54	52	51	51	67	69
Khat-statistic	0.40	0.37	0.22	0.24	0.34	0.39
Variance of Khat	0.000089	0.000098	0.000016	0.000014	0.000134	0.000117
Z-statistic	42.0	37.6	53.7	62.9	29.74	35.81

Summarized in Table 3.9 are the overall accuracy and khat-values for the classified images in Figure 3.15. The computed Z values exceed the critical value of Z value of 2.58 at the 99% confidence level, which implies that the classification results are better than a random classification. Based on the training/testing pixels, the classification results inclusive of the DEM are still unacceptable and there is poor agreement between the classified images and the reference data. Based on the alteration map of UNDP (1987b), however, the classification results approach the acceptable level of 85% and there is moderate agreement between the classified images and the alteration map. Comparison of Tables 3.8 and 3.9 reveals that, inclusive of the DEM, the classification results in a general increase in the overall accuracy and khat values. Inclusion of the DEM also results in a decrease in misclassification of advanced argillic and illitic classes. However, the results also show increase in misclassification of illitic and propylitic classes. There is probably no solution to improve differentiation between illitic and propylitic classes, as distinction between illitic and propylitic alteration in the field is also difficult probably due to overprinting of the hydrothermal alterations on one another (UNDP, 1987b).

Table 3.9. Statistical indicators of accuracy of classification of hydrothermal alteration zones based on mineral images and DEM, Baguio district.

Statistical parameters	Based on training/testing pixels		Based on combined alteration map		Based on alteration map (UNDP, 1987b)	
	Fig. 3.15a	Fig 3.15b	Fig. 3.15a	Fig. 3.15b	Fig 3.15a	Fig 3.15b
Over accuracy (%)	62	61	47	53	82	82
Khat-statistic	0.50	0.49	0.22	0.28	0.63	0.64
Variance of Khat	0.000075	0.00007	0.000012	0.000012	0.000045	0.000041
Z-statistic	58.1	56.1	65.9	80.3	94.39	100.18

The significance of inclusion of the DEM in the classification was evaluated statistically. Table 3.10 shows that the classifications results, exclusive and inclusive of the DEM, are significantly different. Computed Z values are mostly greater than the critical Z value of 2.58 at the 99% confidence level. These statistical tests imply that the DEM is a significant input, in addition to the mineral images, for the classification of hydrothermal alteration in the Baguio district.

Table 3.10. Computed Z values to test statistical difference between classification using mineral images and classification using mineral images and DEM, Baguio district.

	Classified images		
	Based on training/testing pixels	Based on combined alteration map	Based on alteration map (UNDP, 1987b)
Z_1	7.8	0	21.7
Z_2	9.1	7.8	19.9

Z_1, Z_2 are Z values to test statistical difference between classified images in Figures 3.14a and 3.15a and between classified images in Figures 3.14b and 3.15b, respectively.

Further work was carried out to examine whether the classification results using the mineral images alone and together with the DEM are statistically better than the results of a maximum-likelihood classification using the de-hazed Landsat TM data only. The classification results using the de-hazed Landsat TM data are shown in Figure 3.16 and the summary of the accuracy and acceptability assessment is given in Table 3.11.

The classified images in Figure 3.16 show similarities to Figures 3.14 and 3.15 in terms of the spatial distribution of the hydrothermal alteration units, particularly the advanced argillic and the unaltered units. However, the classified images based only on the de-hazed Landsat TM show the strong influence of the topography on the spectral data. The effects of topography in the data have been eliminated quite effectively in the mineral images by using the band ratio input images (Figure 3.12). Based on Tables 3.8 and 3.11, there seems to be little difference between the accuracy of the classification results using the mineral images alone and using the de-hazed Landsat TM bands. However, in a statis-

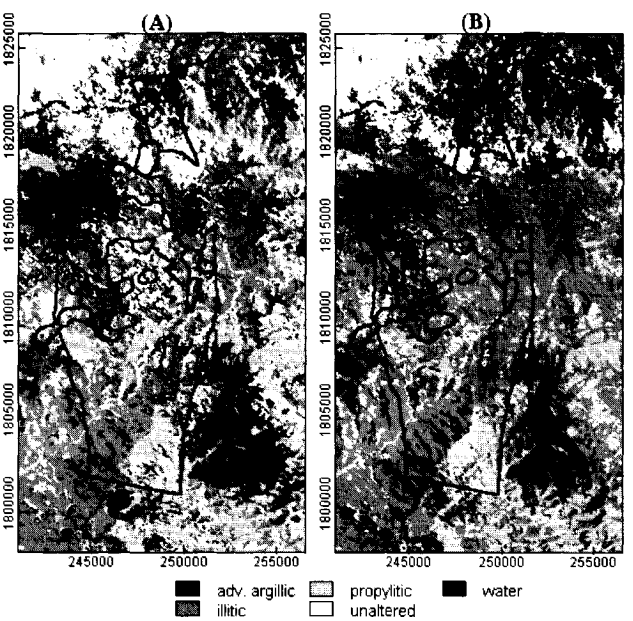

Figure 3.16. Classified hydrothermal alteration maps of the Baguio district using de-hazed Landsat TM data and based on: (a) training pixels in Figure 3.13a; (b) testing pixels in Figure 3.13b. Boundaries of combined hydrothermal alteration units (UNDP, 1987b; Benguet Corporation, unpublished data) are shown for reference.

Table 3.11. Statistical indicators of accuracy of classification of hydrothermal alteration based on de-hazed Landsat TM spectral bands, Baguio district.

Statistical parameters	Based on training/testing pixels		Based on combined alteration map		Based on alteration map (UNDP, 1987b)	
	Fig. 3.16a	Fig 3.16b	Fig. 3.16a	Fig. 3.16b	Fig 3.16a	Fig 3.16b
Over accuracy (%)	60	57	37	31	67	66
Khat-statistic	0.47	0.44	0.14	0.12	0.33	0.32
Variance of Khat	0.000084	0.000088	0.000012	0.000007	0.000141	0.000117
Z-statistic	51.4	46.5	40.4	45.1	27.79	29.78

tical comparison of these two sets of classification results, the computed Z values exceed the critical Z value of 2.58 at the 99% confidence level (Table 3.12). This implies that the classified hydrothermal alteration maps based on the mineral images are significantly different from the classification using the de-hazed Landsat TM bands.

Table 3.12. Computed Z values to test statistical difference between classification using mineral images and classification using de-hazed Landsat TM images, Baguio district.

	Classified images		
	Based on training/testing pixels	Based on combined alteration map	Based on alteration map (UNDP, 1987b)
Z_1	4.6	26.5	0
Z_2	3.7	43.6	2.0

Z_1, Z_2 are Z values to test statistical difference between classified images in Figures 3.14a and 3.16a and between classified images in Figures 3.14b and 3.16b, respectively.

Table 3.13 also indicates that the classification results using the mineral images and the DEM are significantly different from the classification using the de-hazed Landsat TM bands. The classification of the hydrothermal alteration in the Baguio district based on the mineral images and the DEM agree better with the known hydrothermal alteration zones and are thus more acceptable. Furthermore, based on the different statistical parameters, the classified hydrothermal alteration map in Figure 3.15b is better than the classified hydrothermal alteration map in Figure 3.15a (see Table 3.11). The former can serve as evidence for mapping potential for gold deposits in the district, although care must be exercised with its application.

Table 3.13. Z values for pairwise tests of statistical difference between classification using mineral images and DEM and classification using de-hazed Landsat TM spectral bands, Baguio district.

	Classified images		
	Based on training/testing pixels	Based on combined alteration map	Based on alteration map (UNDP, 1987b)
Z_1	1.6	20.4	11.0
Z_2	3.1	50.5	12.7

Z_1, Z_2 are Z values to test statistical difference between classified images in Figures 3.15a and 3.16a and between classified images in Figures 3.15b and 3.16b, respectively.

3.3.7 Mineral imaging method applied to Mankayan district

The geology and mineralisation of the Mankayan district has been summarised by Sillitoe and Angeles (1985), Garcia (1991) and Hedenquist et al. (1998). There are five lithologic units in the district (Figure 3.17): (1) the Cretaceous to Paleogene meta-volcanic rocks; (2) the Eocene to Miocene volcaniclastic rocks; (3) the Miocene batholithic plutons of tonalitic composition; (4) the Pliocene volcanic rocks of dacitic to andesitic composition; and (5) the Pleistocene intrusive porphyries of dacitic to andesitic composition. The Pliocene and Pleistocene volcanic rocks are chemically similar and were probably derived from a common parent magma (Hedenquist et al., 1998). Ore deposits in the district are spatially and temporally related to Pliocene to Pleistocene volcanic rocks of intermediate composition. Magmatism during formation of the deposits was mainly intrusive and significant volcanism resumed immediately after the Cu-Au mineralisation with the eruption of the Pleistocene porphyritic volcanics (Garcia, 1991; Hedenquist et al., 1998). Mineralisation in the district was accompanied by pervasive hydrothermal alteration.

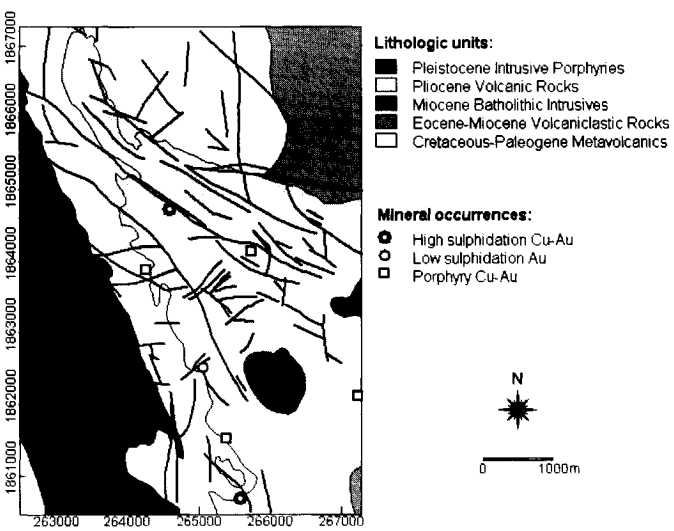

Figure 3.17. Simplified geologic map of Mankayan district, modified after Garcia (1991) and Lepanto Consolidated Mining Company (unpublished data). Curvi-linear features = faults/fractures.

The hydrothermal alteration zones mapped by Lepanto Consolidated Mining Company or LCMC (unpublished data) shown in Figure 3.18a are confined to areas of sparse or no vegetation (see Figure 3.19b) and areas of lower elevations (see Figure 3.20d). The potassic alteration is generally not exposed

and consists of biotite ± K-feldspar. The clay/kaolinite-pyrite alteration and the sericite-pyrite alteration are essentially similar to the sericite-clay-chlorite alteration described by Sillitoe and Angeles (1985) and to the illitic (or argillic) alteration of UNDP (1987b) and Hedenquist et al. (1998). To use the alteration map of LCMC as reference data in the classification of alteration zones, the clay/kaolinite-pyrite and sericite-pyrite alteration zones are re-classified into illitic alteration zones and the quartz-alunite alteration zones are re-classified into advanced argillic alteration zones (Figure 3.18b; Claveria, pers. comm.).

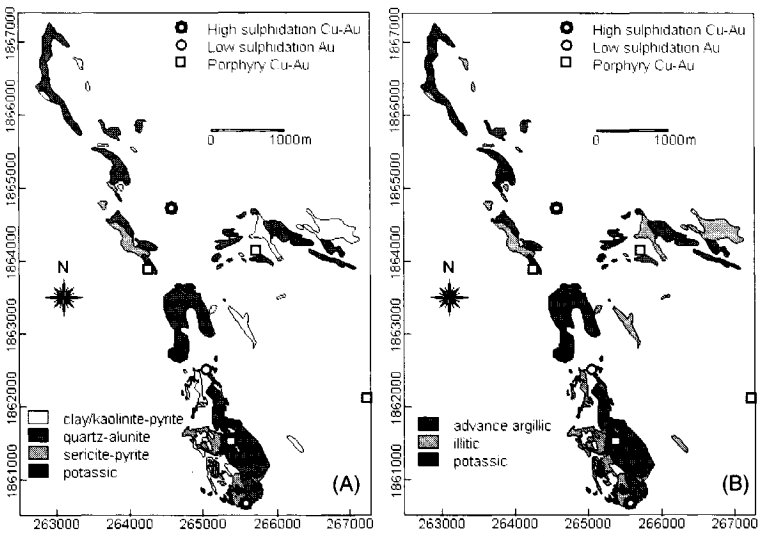

Figure 3.18. Mankayan district: (a) hydrothermal alteration zones (from LCMC, unpublished data); (b) re-classified hydrothermal alteration zones (see text).

Figure 3.19a shows the vegetation map of the district, based on interpretation of 1987-1988 SPOT data by the National Mapping and Resource Information Authority (NAMRIA, 1989). About 60% of the district is brushland, about 39% is grassland and about 1% is pine (Pinus kesiya) forest. Inspection of the natural colour composite of the Mankayan Landsat TM data and NDVI image leads to a classified NDVI map of the district (Figure 3.19b). It indicates that at least 71% of the district is densely vegetated (i.e., pixels containing purely vegetation), about 23% is sparsely vegetated (i.e., pixels of mixed vegetation and bare soil), about 3% is bare soil areas and about 3% is water areas.

A subscene (227 pixels by 160 pixels) of the same Landsat TM imagery used for the Baguio district was used (see Figure 3.8). The subscene represents the Mankayan district within 16°48'59" - 16°52'42" N latitudes and 120°46'17" - 120°48'56" E longitudes. The Landsat TM data in Mankayan district were

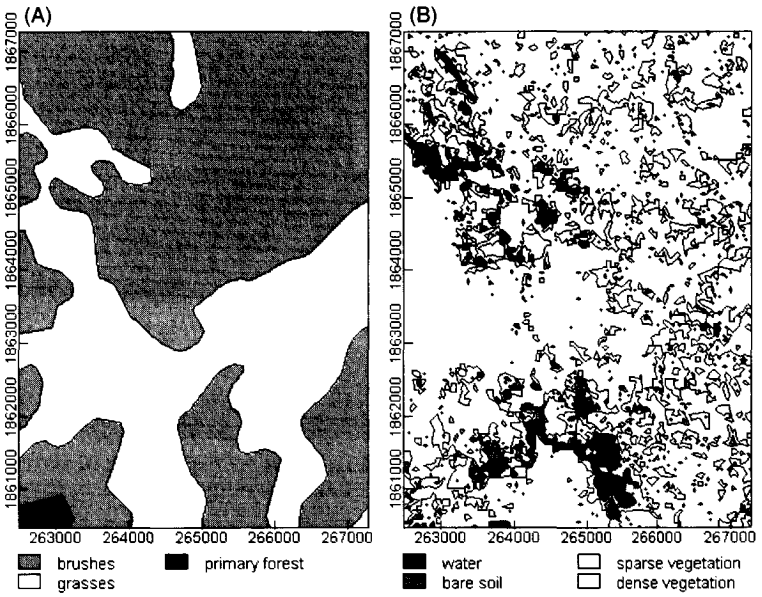

Figure 3.19. Mankayan district: (a) vegetation cover map (from NAMRIA, 1989); (b) classified NDVI map.

georeferenced using affine transformation and four control points representing stream junctions whose UTM coordinates were determined from 1:50,000 scale topographic maps. The resulting root mean square error for the georeferencing was 0.867 pixels.

The elementary statistics of the different spectral bands are given in Table 3.14. With reference to the reflectance spectra of selected materials shown in Figure 3.4, the ranges of DN values in the different spectral bands are apparently normal except in band 1, which has the highest minimum and maximum values. This implies that the data in band 1 are the most affected by haze (Richards, 1999). With reference to the reflectance spectra of vegetation in Figure 3.3, the lower maximum value in band 2 compared to the higher maximum value in band 3 could be an indication of the presence of stressed vegetation, probably due to hydrothermal mineralisation and alteration in the district.

Table 3.14. Elementary statistics of spectral bands of subscene of Landsat TM data, Mankayan district.

	Band 1	Band 2	Band 3	Band 4	Band 5	Band 7
Minimum	57	19	16	26	27	8
Maximum	138	71	80	128	126	69
Mean	68.36	29.99	27.27	76.79	65.25	22.89
Std. Dev.	5.97	3.98	5.84	13.55	12.13	5.47

The correlation coefficients of the spectral band data of the Mankayan Landsat TM subscene (Table 3.15) are similar to the correlation coefficients of the spectral band data of the Baguio Landsat TM subscene (Table 3.2). Therefore, the same deductions can be made about the applicability of the different spectral bands to the differentiation between areas of vegetation and areas of hydrothermally-altered rocks in the Mankayan district.

Table 3.15. Correlation matrix of spectral bands of Landsat TM data subscene, Mankayan district.

	Band 1	Band 2	Band 3	Band 4	Band 5	Band 7
Band 1	1.00					
Band 2	0.90	1.00				
Band 3	0.90	0.92	1.00			
Band 4	0.05	0.25	0.01	1.00		
Band 5	0.50	0.69	0.60	0.57	1.00	
Band 7	0.70	0.78	0.77	0.26	0.87	1.00

The predominant hydrothermal alteration minerals observable in the field are quartz, alunite and illite (LCMC, unpublished data; Sillitoe and Angeles, 1985; Hedenquist et al., 1998). Mineral images of these hydrothermal alteration minerals were created using the appropriate band ratio combinations indicated in Table 3.9. The mineral images are exhibited in Figure 3.20.

The mineral images of quartz and alunite are strongly similar. This demonstrates the association of these minerals in advanced argillic alteration. Quartz and alunite are indicated to be abundant mostly in areas of higher elevations in the southern half of the district (Figure 3.20d). In areas of lower elevations (e.g., along drainage systems), quartz- and/or alunite-bearing rocks are probably absent or scarcely present. It also probable that water and/or dense vegetation in areas of lower elevations strongly interfered with the spectral response of quartz- and/or alunite-bearing hydrothermally-altered rocks in the ground surface. The mineral image of illite shows clear similarities and differences with the mineral images of quartz and alunite. Illite is indicated to be abundant in areas of higher elevations in the southern half of the district. In contrast to quartz and alunite, illite is indicated, by the grey to light grey pixels, to be relatively more abundant in areas of lower elevations. In addition, illite is relatively more abundant than quartz and alunite in the northern half of the district. The spatial coincidence of bright pixels of quartz, alunite and illite probably indicates overprinting of advanced argillic alteration and illitic alteration over the other, which could render their remote identification and classification inaccurate.

The mineral images, exclusive and inclusive of the DEM image, were used in a supervised classification of hydrothermally-altered rocks in the district. Training pixels were extracted from the re-classified hydrothermal alteration map of LCMC (Figure 3.18b). Training pixels for water areas were not extracted as

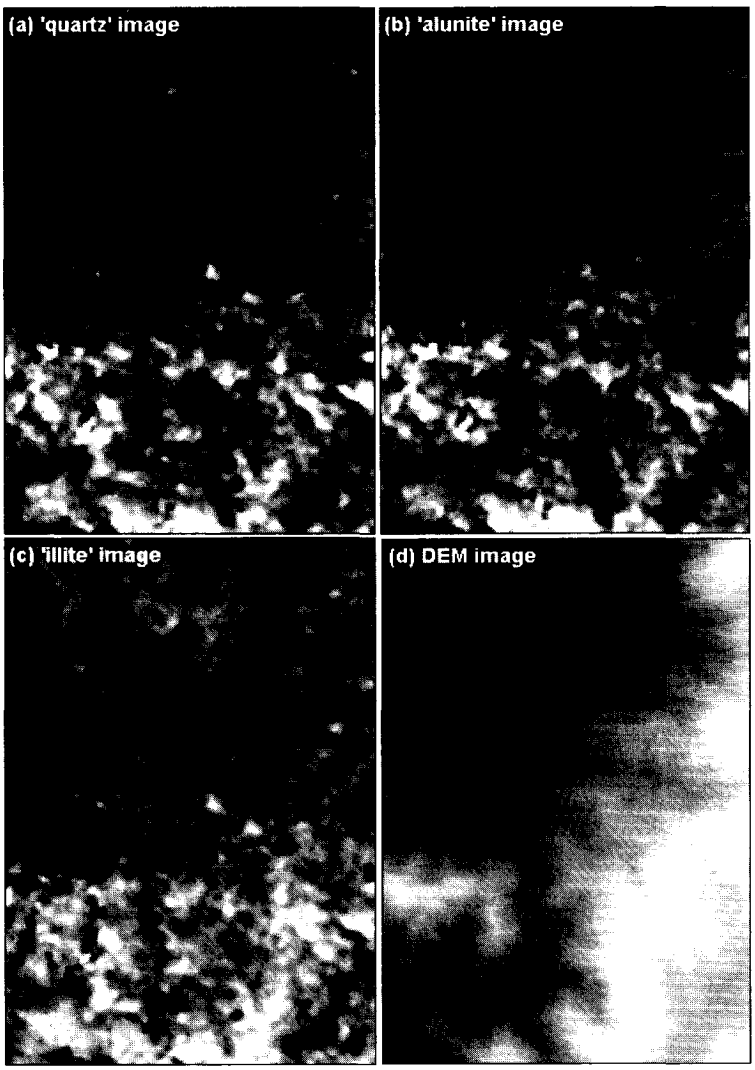

Figure 3.20. Mankayan district: mineral images of (a) quartz, (b) alunite and (c) illite; and (f) DEM image. Pixel brightness in the mineral images indicates relative abundance of mineral considered. Pixel brightness in the DEM image indicates elevation.

LCMC had, probably in the drier months, mapped hydrothermal alteration in some of these areas (see Figures 3.18b and 3.19b). Training pixels for advanced argillic and illitic alteration units were extracted only from areas of sparse vegetation and bare soil. Because areas of sparse vegetation and bare soil occupy less than 30% of the district, there is an insufficient number of training pixels that could be divided into two sets, one set for training/ classifying

the pixels in the mineral images and the other set for validating the classification. Hence, only one set of training pixels were extracted (Figure 3.21). The re-classified map of LCMC (Figure 3.18b) was used to validate the results of the supervised classification of hydrothermal alteration in the district.

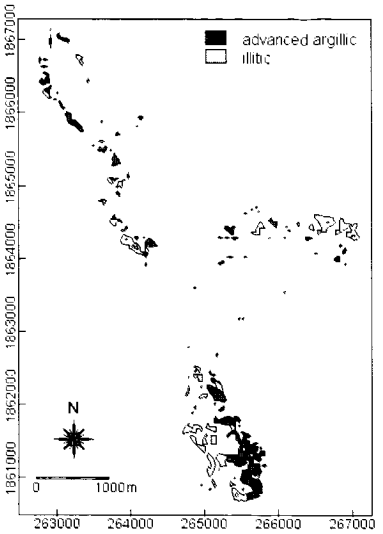

Figure 3.21. Training areas in Mankayan district used in supervised classification of mineral images.

The result of the classification of the hydrothermal alteration units using the mineral images is shown in Figure 3.22a. There is an apparent good spatial coincidence between the hydrothermal alteration units classified from the mineral images and the hydrothermal alteration units re-classified from the map of LCMC. It is also apparent that the known advanced argillic zones are better mapped than the known illitic alteration zones.

The summary of accuracy assessment of the classification shown in Figure 3.22a is given in Table 3.16, respectively. The classification is unacceptable (i.e., overall accuracy of <85%) but the agreement between the classified image and the re-classified map of LCMC is moderate (i.e., khat value between 0.4 and 0.8). The computed Z value exceeds the critical value of Z of 2.58 at the 99% confidence level, which implies that the classification is better than a random classification.

Table 3.16. Statistical indicators of accuracy of classification of hydrothermal alteration based on mineral images, Mankayan district.

Statistical parameters	Calculated values
Overall accuracy (%)	67
Khat-statistic	0.67
Variance of khat	0.001795
Z-statistic	15.8

The result of the classification of the hydrothermal alteration units using the mineral images and the DEM image is shown in Figure 3.22b. It shows good spatial coincidence between the hydrothermal alteration units classified from the mineral images and DEM image and the hydrothermal alteration units re-classified from the map of LCMC. It is noticeable that the known advanced argillic zones are better mapped than the known illitic alteration zones.

Table 3.17. Statistical indicators of accuracy of classification of hydrothermal alteration based on mineral images and DEM image, Mankayan district.

Statistical parameters	Calculated values
Overall accuracy (%)	69
Khat-statistic	0.69
Variance of khat	0.001351
Z-statistic	18.8

Summarised in Table 3.17 is the accuracy assessment of the classification results shown in Figure 3.22b. The classification is unacceptable (i.e., overall accuracy of <85%) but the agreement between the classified image and the re-classified map of LCMC is moderate (i.e., khat value between 0.4 and 0.8). The computed Z value exceeds the critical value of Z of 2.58 at the 99% confidence level, which implies that the classification is better than a random classification.

The classification of hydrothermal alteration in the Mankayan district based on the mineral images and the DEM image is better albeit slightly than the classification based on the mineral images alone. In a statistical comparison of these two classification results, the computed Z value is 0.71, which does not exceed the critical Z value of 2.58 at the 99% confidence level. Hence, there is

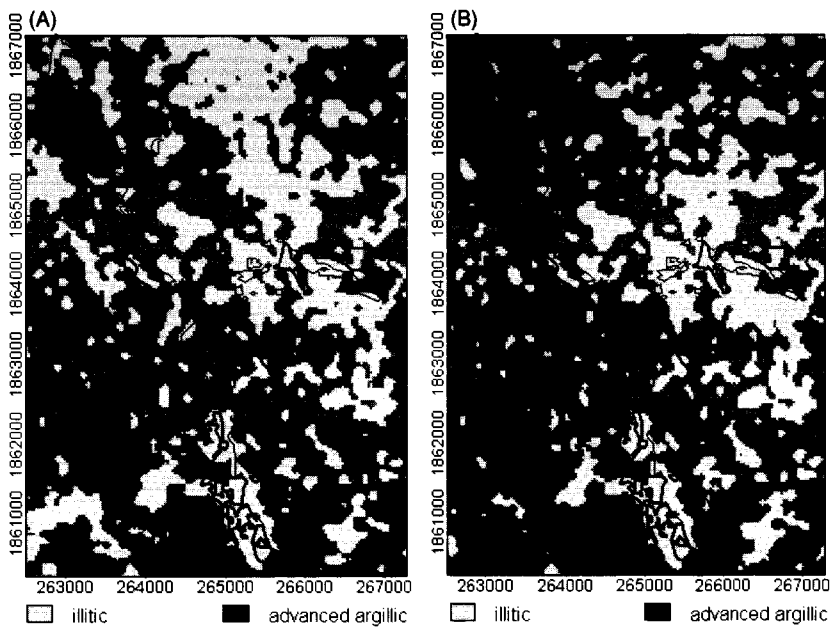

Figure 3.22. Classified hydrothermal alteration maps of Mankayan district: (a) based on mineral images; (b) based on mineral images and DEM image. Boundaries of known advanced argillic alteration (polygons in thin lines) and illitic alteration (polygons in thick lines) are shown for reference.

no statistically significant difference between the two classification results. The application of the DEM image, thus, did not contribute significantly to the classification of hydrothermal alteration in the district. Garcia (1991), however, observed that although advanced argillic rather than illitic alteration occurs mostly along ridges, the stratigraphic sequences of the different hydrothermal alteration units are, on the surface, hardly indistinguishable in some portions of the district. Notwithstanding the unacceptable accuracy of either classification result, their moderate agreement with the re-classified alteration map of LCMC suggests that they can be used as guides to mineral potential although care must be exercised with their application.

3.3.8 Mineral imaging method applied to Benguet province

Field mapping in Benguet province indicated that the Cretaceous-Paleogene metavolcanics are generally propylitised. The Eocene-Miocene volcaniclastic rocks and the Oligocene to Middle Miocene batholithic intrusives generally sustain illitic alteration. Portions of the Miocene limestones and the Late Miocene to Pliocene clastics/volcanics are unaltered or mainly sustain illitic alteration. The Late Miocene to Pleistocene intrusive porphyries sustain either propylitic or illitic alteration. The mineral imaging method was applied to the whole of Benguet province to test its applicability in mapping similar types of hydrothermal alteration, which may be used as evidence for mineral potential. The aim was to map zones of hydrothermal alteration similar to those mapped by UNDP (1987b) and Benguet Corporation (unpublished data) in the Baguio district and by LCMC in the Mankayan district.

A subscene (4152 pixels by 2175 pixels) of the same Landsat TM imagery used for the Baguio district and the Mankayan district was used (see Figure 3.8). The subscene represents an area of low percentage of cloud cover within 16°03'43" - 17°00'20" N latitudes and 120°29'59" - 120°59'58" E longitudes, which covers most of Benguet province (Figure 3.23). The elementary statistics of the spectral band data are given in Table 3.18.

Table 3.18. Elementary statistics of spectral bands of Landsat TM data, Benguet province.

	Band 1	Band 2	Band 3	Band 4	Band 5	Band 7
Minimum	45	12	9	3	2	0
Maximum	255	255	255	255	255	255
Mean	70.84	31.04	27.45	83.75	69.15	23.97
Std. Dev.	18.02	9.91	12.42	18.74	19.73	10.57

The data in bands 1, 2 and 3 have higher minimum values than the data in bands 4, 5 and 7; this is due to haze (Richards, 1999). All spectral bands have the same maximum values of 255; this is due to the clouds and bodies of water.

Band 5 has the highest standard deviation due to large variations in spectral response of different materials within this spectral range. Band 2 has the lowest standard deviation, which is due to low contrast in the spectral response of the various materials in this spectral range.

The correlation coefficients of the spectral data in the Landsat TM subscene of Benguet (Table 3.19) are similar to the correlation coefficients of the spectral data in the Baguio Landsat TM subscene (Table 3.2) and in the Mankayan Landsat TM subscene (Table 3.15). Therefore, the same deductions can be made about the usefulness of the different spectral bands to differentiate areas of hydrothermally-altered rocks from areas of vegetation in Benguet.

The Landsat TM data in Benguet were georeferenced using affine transformation and 14 ground control points representing stream junctions whose UTM coordinates were determined from 1:50,000 scale topographic maps. The resulting root mean square error for the georeferencing was 0.885 pixels.

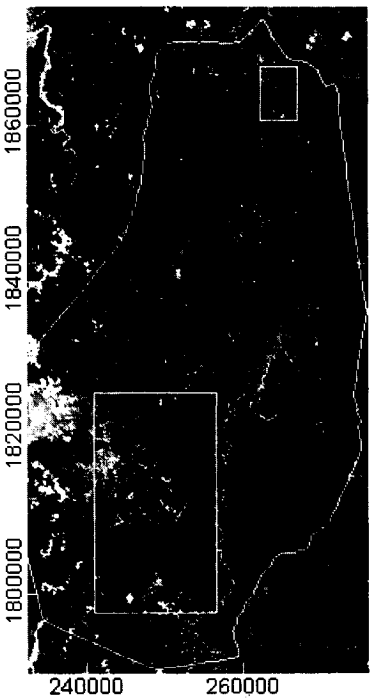

Figure 3.23. Spectral band 3 of Landsat TM subscene of Benguet province (irregular polygon). Larger box pertains to Baguio district; smaller box pertains to Mankayan district.

Table 3.19. Correlation matrix of spectral bands of Landsat TM data, Benguet province.

	Band 1	Band 2	Band 3	Band 4	Band 5	Band 7
Band 1	1.00					
Band 2	0.96	1.00				
Band 3	0.96	0.98	1.00			
Band 4	0.31	0.39	0.27	1.00		
Band 5	0.66	0.75	0.72	0.59	1.00	
Band 7	0.83	0.87	0.89	0.36	0.91	1.00

The optimum band ratios listed in Table 3.7 were used to create separate mineral images, for Benguet province, of each of the predominant minerals of the hydrothermal alteration units mapped in the Baguio and Mankayan districts. The DEM of Benguet province (see Figure 2.6) was stretched to the 8-bit range and used in the classification because in the Baguio and Mankayan districts inclusion of a DEM image in the classification produced better classification of

the hydrothermal alteration units. The testing pixels shown in Figure 3.13b, which produced the more accurate and more acceptable classification results in the Baguio district, and the training pixels used for the Mankayan district (Figure 3.21) were integrated and were used in the supervised classification. The test pixels shown in Figure 3.13a, the combined alteration maps of UNDP (1987b) and Benguet Corporation (unpublished data), the alteration map of UNDP (1987b) and the re-classified alteration map of LCMC (Figure 3.18b) were used to assess the accuracy and acceptability of the supervised classification.

The result of the supervised classification of the mineral images indicates that most of the rocks in the province are extensively hydrothermally altered (Figure 3.24). The spatial relationships or topology of the mapped hydrothermal alteration units conform to the known geological setting of the geanticlinal ridge that is the Central Luzon Cordillera where Benguet is situated. For example, the topology of the advanced argillic and the propylitic alteration units suggests that, within the geanticline, advanced argillic rocks occur stratigraphically on top of propylitised rocks. The core of the geanticlinal ridge, which is now exposed by erosion, is composed of propylitised rocks. The advanced argillic rocks occupy the limbs of the geanticlinal ridge. The topology of the mapped hydrothermal alteration units is probably influenced by inclusion of the DEM in the supervised classification. The results, however, are explicable by the geological setting of the province, which indicates the importance of the DEM in the classification.

The overall accuracy of the classified hydrothermal alteration map in Figure 3.24 ranges between 46% and 73% depending on which reference data it is compared with (Table 3.20). The classification is unacceptable (i.e., <85% accuracy). The classification has poor agreement with the combined alteration map of UNDP (1987b) and Benguet Corporation and with the re-classified map of LCMC. The classification has moderate agreement with the testing pixels not used in the classification and with the alteration map of UNDP (1987b). The computed Z values, however, exceed the critical Z value of 2.58 at the 99% confidence level. This implies that the classified hydrothermal alteration map in Figure 3.24 is better than a random classification.

Table 3.20. Statistical indicators of accuracy of classification of mineral images and DEM image, Benguet province.

Statistical parameters	Based on testing pixels (Figure 3.13a)	Based on combined alteration map of UNDP (1987b) and Benguet Corp. (see Figure 3.13)	Based on UNDP (1987b) alteration map (Figure 3.5)	Based re-classified alteration map of LCMC (Figure 3.18b)
Overall accuracy (%)	63	46	73	54
Khat-statistic	0.52	0.21	0.46	0.19
Variance of khat	0.000076	0.000021	0.000084	0.001447
Z-statistic	59.4	60.6	49.8	4.9

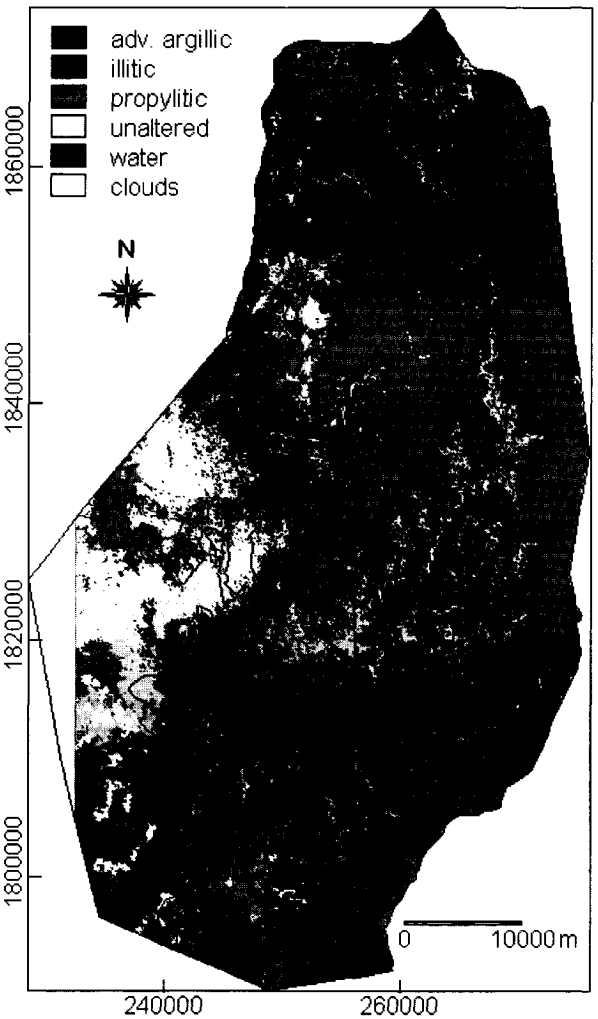

Figure 3.24. Classified hydrothermal alteration map of Benguet province. Thin lines are boundaries of litho-stratigraphic units. Polygons in thick lines are combined hydrothermal alteration units of UNDP (1987b) and Benguet Corporation (unpublished data). Box refers to Mankayan district.

The classified hydrothermal alteration map of Benguet is most accurate when compared with the hydrothermal alteration map of UNDP (1987b). The agreement between the two hydrothermal alteration maps is moderate. In comparison with the training pixels in Figure 3.13a, the accuracy of the classified hydrothermal alteration map of Benguet is similar to the accuracy of the classified hydrothermal alteration maps of Baguio shown in Figure 3.15 (see

Table 3.9). These observations suggest that the classified hydrothermal alteration map of Benguet can be used as a guide to potential for similar types of hydrothermal deposits found in Baguio. This is not to state, however, that the types of hydrothermal deposits in Baguio district and in Mankayan district are different; rather the styles of hydrothermal mineralisation and alteration in these districts are different. Therefore, the lower accuracy of the classified hydrothermal alteration map of Benguet and its poorer agreement with the re-classified hydrothermal alteration map of LCMC, suggest that care must be exercised with its application to mineral potential mapping. The classified hydrothermal alteration map of Benguet has lowest accuracy when validated against the combined alteration map of UNDP (1987b) and Benguet Corporation. These reference data represent different scales of mapping and field identification/nomenclature of hydrothermal alteration (see Figure 3.5). The differences in quality of reference data can therefore critically influence the results of the supervised classification of hydrothermal alteration units. This further accentuates that care must be exercised in the application of the classified hydrothermal alteration map to mineral potential mapping.

3.3.9 Discussion of the mineral imaging method

The mineral imaging method is robust in enhancing the spectral response of materials on the ground in the presence of sparse to dense vegetation. In contrast to the Crósta technique (Crósta and Moore, 1989) and the software defoliant technique (Fraser and Green, 1987), which were applied to mapping of limonitic and clay alteration, the mineral imaging method involves mapping of the specific predominant mineral constituents of hydrothermal alteration assemblages. The integration of ground data, however, is vital to the generation of mineral images from Landsat TM data. For example, knowledge of the predominant mineral constituent of a hydrothermal alteration unit is important for deciding which mineral image to create. Differences in the composition of the hydrothermal mineral assemblages and the field classification of these mineral assemblages, however, can be crucial to the application of the method. In the Mankayan district, for example, a re-classification of mapped alteration zones was made to conform to the more generalised classification (or nomenclature) of hydrothermal alteration.

The complex spatial (and temporal) relationships between the different hydrothermal alteration units, i.e., due to overprinting or telescoping, are also crucial in the application of the mineral imaging method. Where the topology, stratigraphically and/or topographically, of the different hydrothermal alteration units is distinct, as in the Baguio district, the application of a DEM improves the classification of hydrothermal alteration units based on the mineral images. In contrast, where the topology of the different hydrothermal alteration units is not clearly distinct, the application of DEM does not provide significant improvement in the classification of hydrothermal alteration units based of the mineral images.

What has not been dealt with in the application of the mineral imaging method is assessment of the accuracy of the supervised classification of hydrothermal alteration in regard to spatial autocorrelation (e.g., Campbell, 1981; Congalton, 1988). Spatial autocorrelation is a characteristic of spatial data (e.g., remotely-sensed data) in which the spatial attributes of objects exhibit higher degree of dependency or similarity to the spatial attributes of neighbouring objects than to the spatial attributes of objects that are farther away (Griffith, 1988). Congalton (1988) analysed the effect of spatial autocorrelation on remote sensing classification accuracy by generating binary difference image (showing pixels of non-agreement and agreement) between a classified image and a reference image and performing a join-count statistical analysis on the difference image. Join-count statistics is a method of spatial autocorrelation analysis for discrete, nominal or thematic variables (Cliff and Ord, 1981; Griffith and Amrhein, 1991; Bonham-Carter, 1994). The lack of a definitive reference data (i.e., an accurate field-based hydrothermal alteration map; see sub-section 3.3.1), however, did not warrant a proper analysis of the effect of spatial autocorrelation on the accuracy of the classified images similar to the analysis of Congalton (1988).

Aside from the factors mentioned already, the spectral and spatial resolution of Landsat TM data is probably the most critical factor that limits the generation of an acceptable classification of the mineral images. As mentioned earlier, the pixel brightness in the mineral images can only be considered partly to indicate relative abundance of a particular mineral because of the different materials contained in a 30x30 m area. Even the training/testing pixels are themselves not entirely composed of the materials they represent; hence, the accuracy of the classification results are unacceptable when assessed against the training/testing pixels. However, in contrast to the Crósta technique and the software defoliant technique, the mineral imaging method is able to map the known hydrothermal alteration zones in the Baguio district more adequately.

In this section, the spectral effects of vegetation were not used to detect hydrothermal alteration as an indicator of mineral deposits. In the next section, the spectral characteristics of vegetation are studied in relation to mineral deposits and/or geochemically-enriched zones.

3.4 REMOTE DETECTION OF GEOCHEMICALLY-STRESSED VEGETATION USING LANDSAT TM DATA

Multispectral data have limited application to the study of the spectral response of vegetation to anomalous substrate geochemical conditions because of the coarse spectral and spatial resolution of the sensor with which the data are collected (Shaulis and Lancaster, 1994). Bølviken et al. (1977), however, using Landsat-1 MSS data, had indicated that naturally heavy-metal poisoned vegetation on mineralised zones have significantly different spectral characteristics than healthier vegetation in surrounding areas. Nash and

Hernandez (2001) have also shown that vegetation anomaly mapping from Landsat TM data is not only feasible but also cost-effective. In this work, Landsat TM data are used to examine the spectral characteristics of vegetation in and around geochemically-enriched and mineralised zones.

In the previous section, the elementary statistics of the Landsat TM data in Baguio and Mankayan district indicated the presence of geochemically-stressed vegetation, probably due to hydrothermal mineralisation and alteration. However, to study the Landsat TM data of the Baguio district and/or the Mankayan district to determine the presence of geochemically-stressed vegetation due to mineral deposits can be futile. Mining, which started in the pre-Spanish colonial period, urban and industrial development could cause geochemical stress in vegetation in the Baguio and the Mankayan districts. As an alternative to the Baguio and the Mankayan districts, Catanduanes Island was chosen to study vegetation stress from Landsat TM data for three main reasons. First, Landsat TM data are available. Second, mineral development in the island has been minimal and old forest growths still prevail. Third, stream sediment geochemical data are available (see section 2.5.4). These attributes were considered adequate to contribute data for the detection of geochemically-stressed vegetation using Landsat TM data.

A subscene of Landsat TM imagery Path 114 Row 050 acquired on 18 February 1994 was used (Figure 3.25). The subscene was geo-referenced using affine trans-formation and 14 ground control points representing stream junctions and points (i.e., narrow land masses jutting into the sea) whose UTM coordinates were determined from 1:50,000 scale topographic maps. The resulting root mean square error for the georeferencing was 0.907 pixels. The Landsat TM data were de-hazed by the dark-object subtraction method (Richards, 1999). The study is confined to the southern portion of the island, over which there is the lowest percentage cloud cover in the Landsat TM data.

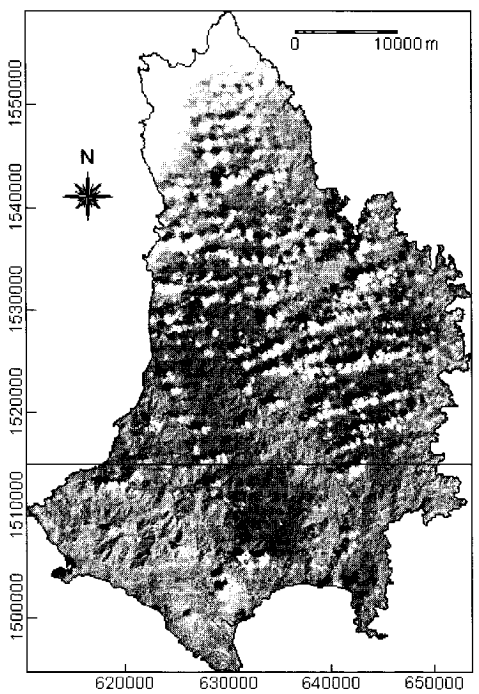

Figure 3.25. Spectral band 5 of Landsat TM subscene of Catanduanes Island. The portion in the lower box is the study area.

The analyses of the spectral characteristics of vegetation in and around the geochemically-enriched and mineralised zones were carried out in a number of steps. A

supervised maximum-likelihood classification was performed to map the different general land cover types. Training pixels were determined and chosen through visual examination of various RGB colour composites of the Landsat TM data. Areas of vegetation were extracted from the classified image. The NDVI [i.e., (band 4 – band 3) / (band 4 + band 3)] was also calculated. For each of the sample catchment basins (see Figure 2.19), the mean values of NDVI and mean DN values of the 'vegetation' pixels in the different spectral bands were determined as spectral spatial attributes. Correlation analysis of the geochemical and spectral attributes of the sample catchment basins was performed. Plots of mean DN values versus element concentration levels were constructed. Buffer zones of 30-m intervals were constructed around each of the gold-copper deposits (see Figure 2.19). The mean NDVI values for the 'vegetation' pixels and the mean DN values of the 'vegetation' pixels in each of the 30-m wide buffer zones were determined. Plots of mean NDVI values versus distance from mineral deposits were constructed. Plots of mean DN values of 'vegetation' pixels for the different spectral bands for each of the buffer zones were constructed.

3.4.1 Classification of land cover types

Ideally, ground information (e.g., spatial distribution of plant species) on vegetation cover is important to studies pertinent to the detection of vegetation stress (Shaulis and Lancaster, 1994). This information is lacking, however. The spatial distribution of vegetation-covered zones in the area was therefore extracted from the Landsat TM data through supervised maximum-likelihood classification. Various RGB colour composites of the Landsat TM data were inspected to decide on the training pixels used in the classification. The author's knowledge gained from geological fieldwork in the island was also incorporated into the selection of training pixels. The land cover types classified in the Landsat TM data are shown in Figure 3.26. About 62% of the area is covered by vegetation (mainly old forest growth), about 22% by bare soils or rocks (with or without sparse vegetation), about 7% by alluvial deposits and about 3% by water (i.e., rivers, swamps, beaches). The classification, based only on the chosen training pixels, is 99% accurate.

To verify further the accuracy of the land cover classification, the NDVI was calculated. The NDVI indicates the presence and condition of green vegetation (Wickham et al., 1993). Inspection of the NDVI image and the natural colour composite of the Landsat TM data led to a classified map of the NDVI (Figure 3.27). The classified NDVI map indicates that about 76% of the area contains green vegetation. Comparing the land cover classification map (Figure 3.26) with the classified NDVI map indicates that about 92% of the 'vegetated areas' are 'green vegetation areas'. This implies that about 8% of the 'vegetated areas' do not contain green but possibly stressed vegetation. Comparison of Figures 3.26 and 3.27 also indicates that about 23% of the 'green vegetation areas' are

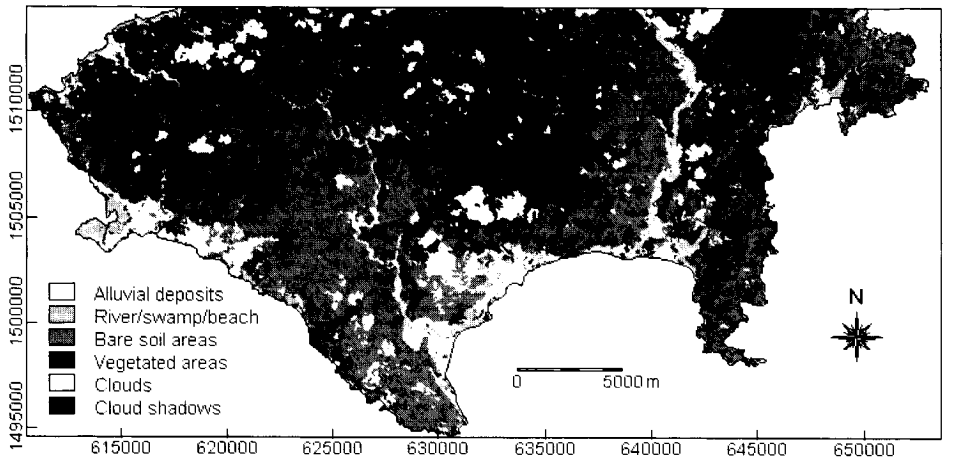

Figure 3.26. Land cover types classified from Landsat TM data, southern Catanduanes.

classified as 'bare soil areas'. This indication is accurate because the 'bare soil areas' are not purely bare but contain sparse vegetation characterised by grasses and shrubs. Thus, the accuracy of the land cover classification with respect to the classified NDVI map is acceptable.

The 'bare soil areas' pertain to lowlands (see Figure 2.18) that are usually disturbed anthropogenically. On the other hand, the 'vegetated areas' pertain to highlands characterised by rugged terrain that are relatively less disturbed anthropogenically. It can be expected that causes of vegetation stress in these

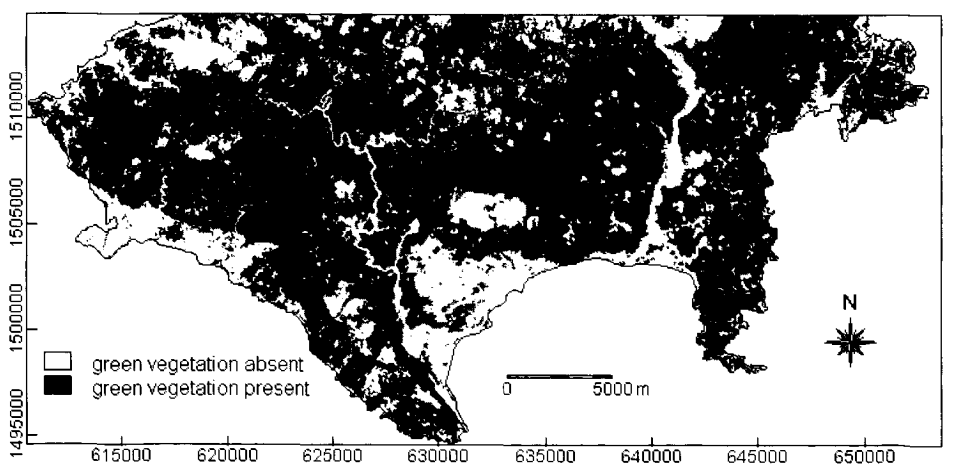

Figure 3.27. Classified NDVI map, southern Catanduanes.

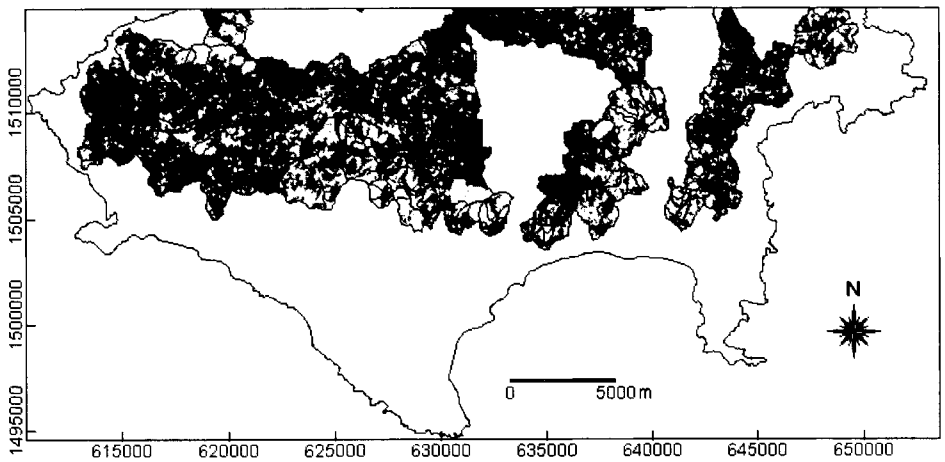

Figure 3.28. Vegetated areas in sample catchment basins, southern Catanduanes.

'vegetated areas' are natural causes (e.g., mineralised or geochemically-enriched zones) rather than anthropogenic causes. The analysis of spectral characteristics of vegetation was therefore confined to 'vegetated areas' in the different stream sediment sample catchment basins (Figure 3.28).

3.4.2 Vegetation spectra and stream sediment geochemistry relationship

Stream sediments are nature's closest approximation to a composite sample of the rocks and soils upstream from a sample site (Nichol et al., 1969). Although the relation between metal concentrations in stream sediments and soils is inexact (Moon, 1999), high-density stream sediment sampling can often provide information such as nature and contacts of the underlying soil and lithologic units (Levinson, 1974). Because the compositions of soils/rocks influence stream sediment geochemistry, and because the compositions of soils/rocks influence spectral characteristics of vegetation, there is usually an indirect or imprecise relationship between stream sediment geochemistry and vegetation spectra.

Information about the reflectance characteristics of vegetation is contained in the DN values of the pixels in the multispectral data. The elementary statistics of the DN values of de-hazed Landsat TM pixels pertaining to the 'vegetated areas' in the different sample catchment basins are given in Table 3.21. In comparison with vegetation spectra in Figures 3.3 and 3.11f, the maximum DN values in the de-hazed Landsat TM bands appear normal. The ranges of DN values listed in Table 3.21, however, were considered narrow to determine clear variations in the spectral characteristics of vegetation in the 'vegetated areas'. The ranges of DN values in the different bands were therefore linearly stretched to the 0-255

Table 3.21. Elementary statistics of DN values of de-hazed Landsat TM band pixels pertaining to 'vegetated areas' in different stream sediment sample catchment basins, southern Catanduanes.

	Band 1	Band 2	Band 3	Band 4	Band 5	Band 7
Minimum	0	0	0	22	13	3
Maximum	47	62	41	145	108	52
Mean	19.31	21.61	18.22	81.53	57.09	19.58
Std. Dev.	11.99	13.87	11.22	33.77	26.01	11.01

range without standardising the data (as in a histogram equalisation stretch) to maintain the shape of their histograms (Richards, 1999). The calculated NDVI values, which range from –1 to 1, were also linearly-stretched to the 0-255 range.

The mean DN and NDVI values of pixels of the 'vegetated areas' in the different sample catchment basins were calculated from the linearly-stretched de-hazed spectral bands of the Landsat TM data. These mean DN values were considered spectral spatial attributes of the sample catchment basins. The correlation coefficients between the geochemical and spectral attributes are given in Table 3.22. Arsenic data are available but were not studied because very few samples yielded detectable concentrations.

Table 3.22. Pearson linear correlation coefficient (r) matrix of the stream sediment geochemical data and the mean DN values of linearly-stretched spectral band data and mean NDVI values of 'vegetated areas'. Values in bold are statistically significant correlation coefficients. (Critical value of $r_{\alpha=0.05}$=0.135 for n=215; Howarth, 1983).

	Band 1	Band 2	Band 3	Band 4	Band 5	Band 7	NDVI
Fe	-0.038	-0.007	0.017	-0.054	-0.047	-0.048	-0.060
S	**-0.141**	-0.085	-0.101	0.076	-0.025	-0.073	**0.151**
Au	-0.059	0.004	-0.030	-0.004	0.002	-0.010	0.009
Cu	-0.086	-0.055	-0.042	0.072	0.047	0.005	0.083
Zn	**0.277**	**0.214**	**0.223**	0.066	**0.168**	**0.185**	**-0.234**

Before proceeding to explain the correlation coefficients in the table above, it is important to first describe typical vegetation spectra and the plant components that dominate the different regions of the EM spectrum (Figure 3.29). In the visible region of the EM spectrum, the photosynthetic pigments, chlorophyll, xantophyll, and carotene have a dominant impact on absorption and reflectance. While each pigment has absorption maxima in the 300-500 nm region, only chlorophyll absorbs in the red wavelengths, i.e., TM band 3 (Shaulis and Lancaster, 1994). Mostly the cell structure, the refractive properties, and the leaf water content influence the spectra of vegetation in the infrared regions of the EM spectrum. In general, plants display high reflectance in the near infrared (700 to 1200 nm) and high absorption in the middle-infrared (1300 to 2500 nm).

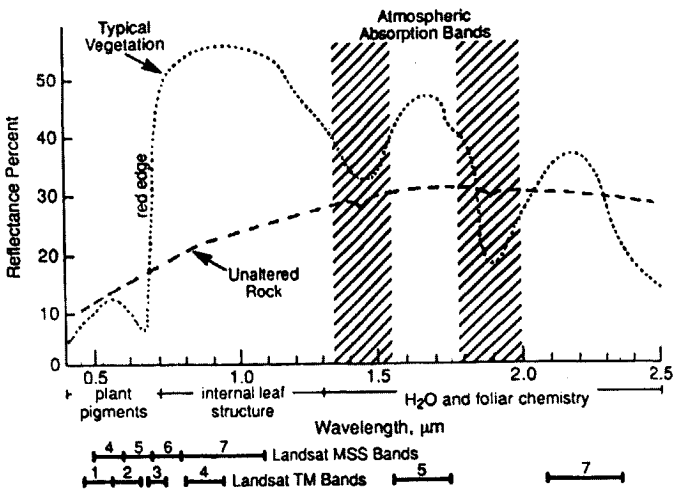

Figure 3.29. Typical vegetation reflectance spectra and dominant plant features affecting specific spectral regions (from Sabins, 1996).

Among the five elements in Table 3.21, Fe, Cu, S and Zn are essential elements for plant growth (Salisbury and Ross, 1969). Gold is chemically inert and is non-essential to plant growth, which explains its lack of correlation with the mean DN and NDVI values of vegetation. Of the essential elements for plant growth, Fe and Cu show lack of correlation with the spectral attributes whilst S and Zn show weak but significant correlation with a number of the spectral attributes. The lack of correlation of Fe and Cu with the spectral attributes suggests that their concentrations in the substrate are neither deficient nor sufficiently high to affect the spectral characteristics of vegetation in the area. The weak but significant correlations of S and Zn with a number of the spectral attributes need further explanation.

The weak negative correlation of sulphur with the mean DN values in band 1 implies that its concentrations in the substrate influence the vegetation's photosynthetic pigments that have absorption features in the 300-500 nm region (i.e., TM band 1). Its significant positive correlation with the mean NDVI values suggests that high sulphur values correspond to greener vegetation and low sulphur values to less green vegetation. The correspondence of low sulphur values to less green vegetation is normal because sulphur deficiency results in chlorosis (Resh, 1983). The correspondence of high sulphur values to greener vegetation, however, needs further elaboration because high concentrations of sulphur also cause chlorosis (Resh, 1983). It is probable that high sulphur stream sediment contents in the study area represent substances that are geoavailable but not bioavailable to vegetation. This is explained further below.

Geoavailability is defined as that portion of an element's or compounds' total content in an Earth material that can be liberated to the environment (or biosphere) through mechanical, chemical or biological processes (Smith et al., 1994). On the other hand, bioavailability can be defined as the degree to which a substance can be absorbed by living organisms and produce a physiological effect (McKinney and Rogers, 1992; John and Leventhal, 1995). The chemical form of sulphur that is bioavailable and essential to plants is water-soluble sulphate (Salisbury and Ross, 1969). In the stream sediment samples in the study area, however, the sulphur contents are probably due to pyrite. Pyrite is a sulphide mineral, which is not readily soluble in water and not bioavailable to plants. The high sulphur contents in the stream sediments, probably due to pyrite, apparently had no physiological effect(s) on the vegetation, which explains its correspondence with high NDVI values.

Zinc is positively correlated with the mean DN values in all spectral bands except band 4 and negatively correlated with NDVI. The positive correlation is higher with the mean DN values in bands 1, 2 and 3 than with the mean DN values in bands 5 and 7. This implies that Zn has more intense impact on the vegetation's pigments than their water and foliar chemistry (Figure 3.29). The lack of correlation of Zn with the mean DN values in band 4 implies that Zn has no influence on the vegetation's internal leaf structure. These observations are similar to the observations of Lehmann et al. (1991) who reported that reflectance of corn growing in their waste disposal test site showed significant positive correlation with Zn concentrations. The negative correlation of Zn with the mean NDVI indicates that high Zn values correspond to less green vegetation and low Zn values to greener vegetation. This observation conforms to the known chlorotic effects of Zn on plants (Lepp, 1981). The observed correlation between the Zn data and the spectral data is probably due to the high mobility of Zn in the surficial environment and Zn is probably in a chemical form that is bioavailable to plants.

3.4.3 Spectral characteristics of vegetation in Zn-enriched catchment basins

Shown in Figure 3.30 are the stream sediment sample catchment basins with >100 ppm Zn. A majority of the gold-copper mineral deposits shows close spatial association to the Zn-enriched catchment basins. This observation has two implications. The first implication is that the Zn anomalies are significant (i.e., they are related to mineralisation). The wide spatial distribution and lack of spatial coincidence of the Zn anomalies with some of the mineral deposits, however, is partly due to (a) its high mobility in the surficial environment, (b) the stream sediment sampling design and (c) the effect of presenting geochemical data using sample catchment basins. The second implication is that the spectral characteristics of vegetation related to Zn enrichment in the stream sediment is also related to mineralisation.

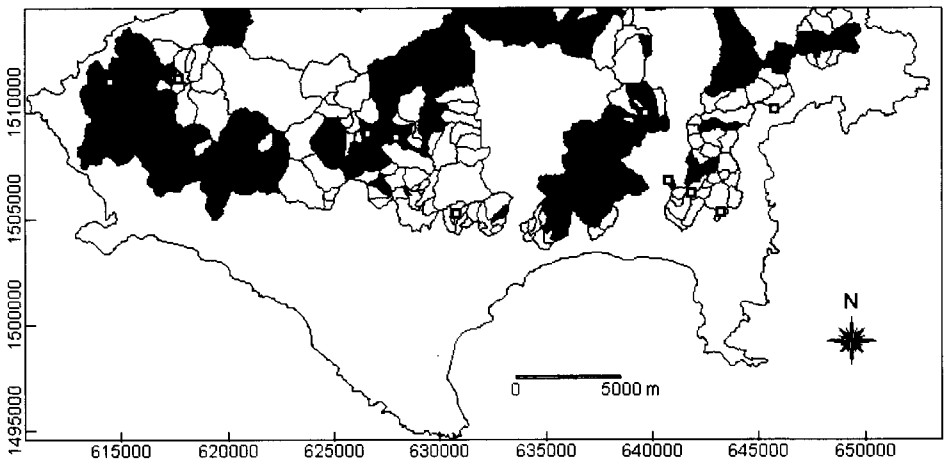

Figure 3.30. Sample catchment basins with stream sediment Zn contents >100 ppm. Open squares = gold-copper deposits.

Shown in Figure 3.31 are plots of mean DN values of 'vegetated areas' versus different levels of stream sediment Zn concentrations. For all spectral bands, the mean DN values for 'vegetated areas' with >200 ppm stream sediment Zn contents are distinctly higher than the mean DN values of 'vegetated areas' with lower Zn concentrations. The mean DN values for bands 1, 2 and 3 are also higher in 'vegetated areas' with stream sediment Zn contents >100 ppm than in 'vegetated areas with stream sediment Zn contents <100 ppm. The plots indicate a blue shift in the red-edge of spectra of vegetation in Zn-poor zones compared to the red-edge of spectra for vegetation in Zn-enriched zones.

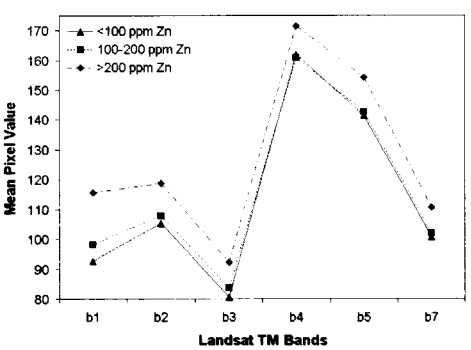

Figure 3.31. Mean DN values of vegetation in areas of different stream sediment Zn concentration levels

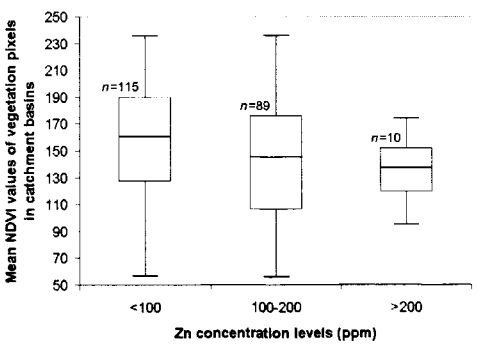

Figure 3.32. Boxplots of mean NDVI values of vegetation pixels in catchment basins of different Zn concentration levels.

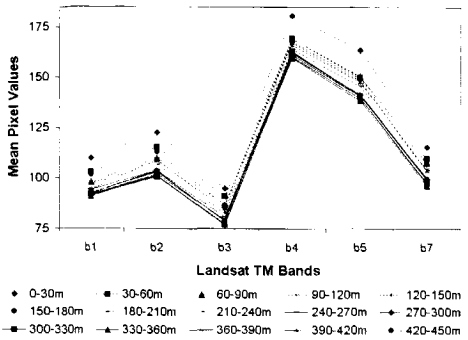

Figure 3.33. Mean DN values of vegetation in 30-m wide buffer zones around gold-copper deposits.

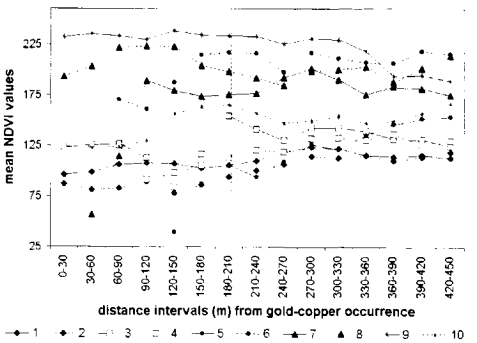

Figure 3.34. Mean NDVI values of vegetation as a function of distance from gold-copper deposits (nos. 1-10, shown by different symbols)

The mean NDVI values of vegetation are inversely proportional to the stream sediment Zn contents (Figure 3.32). This indicates that vegetation in the Zn-enriched zones is less green than vegetation in Zn-poor zones. This implies that vegetation in the Zn-enriched zones is stressed and furthermore that NDVI can indicate geochemically-stressed vegetation.

3.4.4 Spectral characteristics of vegetation around mineralised zones

Shown in Figure 3.33 are plots of the mean DN values of vegetation pixels in 30-m wide buffer zones around the gold-copper deposits in the different spectral bands of the Landsat TM data. The mean DN values of vegetation pixels within 180 m of the gold-copper deposits are distinctly higher than the mean DN values of vegetation beyond 240 m. In general, the mean DN values of vegetation within 240 m of the gold-copper deposits are higher than the mean pixel values of vegetation beyond 240 m. The plots indicate a blue shift in the red-edge of spectra for vegetation far from the mineralised zones compared to spectra of vegetation near the mineralised zones.

Figure 3.34 shows plots of mean NDVI values of vegetation pixels as a function of distance from the mineralised zones. Vegetation is absent within 60-120 m of two to four of the ten gold-copper deposits. Where vegetation is present within 300 m of the gold-copper deposits, the means of NDVI values show mostly a generally increasing trend. Within 300 m of the gold-copper deposits, the mean NDVI values are highly variable. Beyond 300 m of the gold-copper deposits, the mean NDVI values are relatively stable. These characteristics imply that the greenness of vegetation increases with distance away from most of the gold-copper deposits and that, within 300 m of most of the gold-copper deposits, vegetation is stressed. These findings imply furthermore that NDVI can indicate

vegetation stress due to mineralisation. The narrow zones (i.e., 300-m radius) of vegetation affected by most of the gold-copper deposits are reflecting vein-type mineralisation with narrow alteration halos.

3.4.5 Remote detection of vegetation-covered Zn-enriched and mineralised zones

Vegetation in the Zn-enriched and mineralised zones has lower NDVI values compared to vegetation in Zn-poor zones and zones further away from the mineralised zones. Thus, NDVI can be used to detect remotely indications of mineralisation. However, other remotely-sensed data layers need to be integrated because NDVI alone is not totally diagnostic of the vegetation characteristics in the Zn-enriched and mineralised zones as shown above. The plots in Figures 3.32 and 3.34 indicate the potential use of band ratios to discriminate stressed vegetation from healthy vegetation. Band ratios are more useful than single band data because the latter contain topographic effects (e.g., shadows) on the spectral characteristics of different materials. Band ratioing eliminates the effects of topography on the spectral data (Sabins, 1996).
It is appealing to use band ratios with band 3 as the denominator. As indicated above, Zn concentrations have more intense impact on the vegetation's pigments, which include chlorophyll and only chlorophyll absorbs in the red wavelengths (i.e., regions covered by band 3). If vegetation in and near the Zn-enriched and mineralised zones suffers from chlorosis and vegetation farther away from these zone does not, then band 3 DN values of vegetation in and near the Zn-enriched and mineralised zones can be expected to be lower than band 3 DN values of vegetation in Zn-poor and non-mineralised zones. This means that band ratios with band 3 as the denominator are higher for the latter and lower for the former.

The plots in Figure 3.35 show that band ratios (with band 3 as denominator) for vegetation are generally inversely proportional to stream sediment Zn contents. The only exceptions are for ratios band 1 : band 3 and band 7 : band 3, which show that the band ratios are directly proportional to stream sediment Zn contents. The mean of ratios band 7 : band 3, however, are slightly lower for Zn contents >200 ppm than for Zn contents of 100-200 ppm. The band ratios with band 3 as denominator (particularly with bands

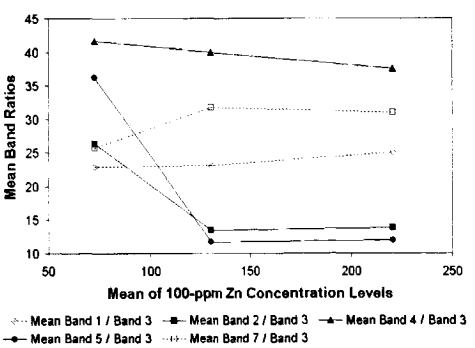

Figure 3.35. Plots of mean concentrations of Zn classes versus mean band ratios.

2, 4 and 5 as numerators) can thus be used with NDVI to map Zn-enriched zones, which may be related to mineralisation.

The plots in Figure 3.36 show that band ratios (with band 3 as denominator) for vegetation within 300 m of the gold-copper deposits are more variable than band ratios for vegetation beyond 300 m of the gold-copper deposits. The different plots all show a subtle but discernible fabric that slopes positively. The slopes of the fabric are steeper within 300 m of the gold-copper deposits and flatter beyond 300 m of the gold-copper deposits. The plots indicate that the band ratios within 300 m of the gold-copper deposits are lower than the band ratios beyond 300 m. Excluded in Figure 3.36 are plots for band 4 to band 3 ratios, as they look very similar to the NDVI plots (Figure 3.34). The NDVI is a special band ratio that involves bands 3 and 4. The band ratios with band 3 as denominator can thus be used with NDVI to detect vegetation-covered gold-copper mineralised zones.

Two sets of experiments were performed using different combinations of band ratio images and the NDVI image in a supervised maximum-likelihood

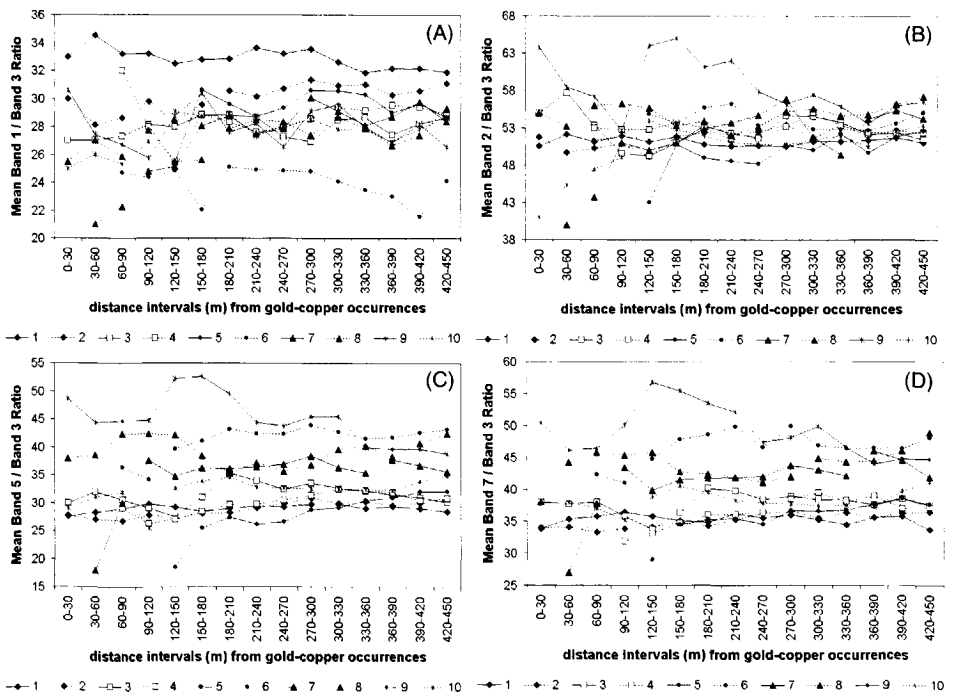

Figure 3.36. Plots of mean band ratios for 'vegetated areas' versus distance from gold-copper deposits, southern Catanduanes: (a) band 1 : band 3; (b) band 2 : band 3; (c) band 5 : band 3; (d) band 7 : band 3. Vertical dotted-line is boundary within and beyond 300 m of gold-copper deposits (nos. 1-10, shown by different symbols).

classification of stressed and healthy vegetation. One set of experiments was based on training pixels of 'vegetated areas' representing healthy vegetation in sample catchment basins with ≤100 ppm Zn contents and training of 'vegetated areas' representing stressed vegetation in sample catchment basins with >100 ppm Zn contents. The other set of experiments was based on training pixels of 'vegetated areas' representing healthy vegetation beyond 300 m of the gold-copper deposits and training pixels of 'vegetated areas' representing stressed vegetation within 300 m of the gold-copper deposits. The result of one set of experiments was cross-validated against the set of training pixels used in the other set of experiments. The results of the classification experiments with the highest cross-validation accuracy are very similar and were both generated using the NDVI image and band ratio images with band 3 as denominator and bands 1, 2, 5 and 7 as numerators (Figures 3.37 and 3.38). Areas other than the 'vegetated areas' and those areas underlain by lithologic units not associated with the known gold-copper deposits (see sub-section 2.5.1, Table 2.8) are masked out from the classified maps.

The overall accuracy of the classified map in Figure 3.37 is 53.9%, with respect to the training pixels used to create the classified map in Figure 3.38. The classified map in Figure 3.37 indicates that about 35% of vegetation in the 'vegetated areas' in the Zn-enriched sample catchment basins sustains geochemical stress. The overall accuracy of the classified map in Figure 3.38 is 52.5%, with respect to the training pixels used to create the classified map in

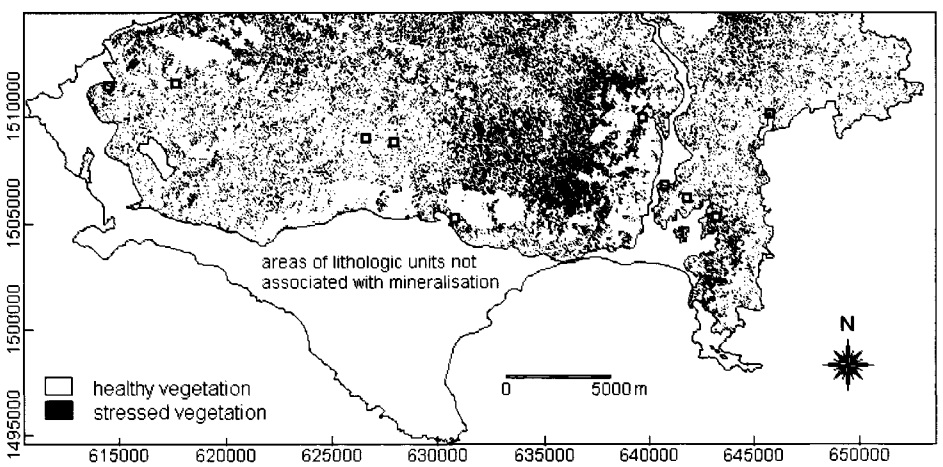

Figure 3.37. Classified zones of healthy and stressed vegetation in 'vegetated areas' underlain by lithologic units known to be associated with gold-copper deposits, southern Catanduanes. The map was created by supervised classification of NDVI image and band ratio images (with band 3 as denominator and bands 1, 2, 5 and 7 as numerators) using training pixels of healthy and stressed vegetation, respectively, in Zn-poor and Zn-enriched sample catchment basins. Open squares = gold-copper deposits.

Figure 3.37. The classified map in Figure 3.38 indicates that about 31% of vegetation in the Zn-enriched sample catchment basins sustains geochemical stress. Both of the classified maps indicate the presence of stressed vegetation at or near most of the gold-copper deposits and in the Zn-enriched catchment basins. An interesting feature indicated by both classified maps is the dense neighbourhood of stressed vegetation at the central part of the area. This zone of dense stressed vegetation pertains to the un-sampled watershed at the central part of the area (see Figure 3.28 or 3.30). East and north of this zone of dense stressed vegetation, on the other side of the drainage divide, are Zn-enriched sample catchment basins (Figure 3.30). This zone of dense stressed vegetation needs further field investigation.

3.4.6 Discussion

It has been shown that vegetation in and near mineralised and geochemically-enriched zones has lower mean NDVI and higher mean spectral band DN values than vegetation farther away from these zones. It is realised, however, that soil geochemical data would provide results that more accurately detect vegetation stress. In addition, ground spectrophotometer data from vegetation are more desirable for similar studies. Notwithstanding the lack of optimum data, the results of analysis indicate that geochemical stress in vegetation can be detected with a broad band spectral scanner like Landsat TM. The results of the

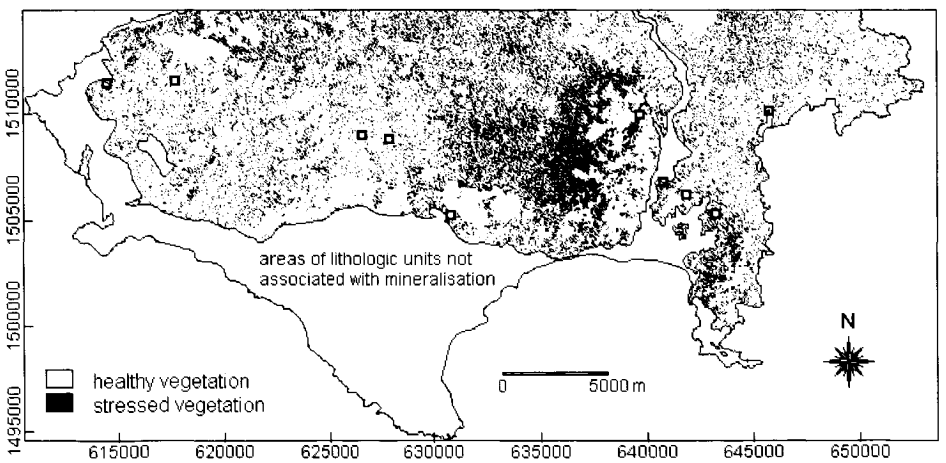

Figure 3.38. Classified zones of healthy and stressed vegetation in 'vegetated areas' underlain by lithologic units known to be associated with gold-copper deposits, southern Catanduanes. The map was created by supervised classification of NDVI image and band ratio images (with band 3 as denominator and bands 1, 2, 5 and 7 as numerators) using training pixels of stressed and healthy vegetation, respectively, within and beyond 300 m of the gold-copper deposits. Open squares = gold-copper deposits.

study therefore contradict the conclusion of Shaulis and Lancaster (1994) that shifts in the red-edge position, as an indicator of vegetation stress, are not observable in Landsat TM data. The increased spectral band DN values of vegetation in and near geochemically-enriched and mineralised zones as detected from the Landsat TM bands 2, 3 and 4 indicated a blue shift in the red-edge position of vegetation. The increased DN values of stressed vegetation as observed in bands 1, 2 and 3 are similar to increased reflectance of stressed vegetation as observed in the 400-700 nm range when using narrow-band imaging spectrometer data (Carter, 1994b). Whilst Carter (1994b) also showed that stressed vegetation is detectable from imaging spectrometer band ratios, particularly the 694 nm : 760 nm band ratio, the results of the study showed that stressed vegetation is detectable from Landsat TM NDVI image and band ratios, particularly band ratios with band 3 as denominator. Consequently, band ratios with band 3 as the denominator performed well in a supervised classification of stressed vegetation.

The main impact of mineralisation and surface geochemical enrichment in the area on the vegetation is chlorophyll loss, as indicated by the observed blue shift in the red-edge position. In addition, to explain the higher mean band 3 DN values of vegetation in mineralised and geochemically-enriched zones as due to chlorophyll loss is logical. However, to explain the higher mean band 2 DN values of the same vegetation as due to chlorophyll loss alone is illogical. High concentrations of chlorophyll in healthy vegetation are associated with high reflectance in band 2 (i.e., the green band). The results of analysis, however, agree with the work of Lehmann et al. (1991) and Curran et al. (1992) who showed that increasing reflectance in the visible bands is associated with increasing concentrations of Zn, Pb and Cu. The results of analysis also agree with the work of Buschman and Nagel (1993) and Gitelson and Merzlyak (1994) who showed that vegetation with lower chlorophyll contents can have higher reflectance in the green spectral band (i.e., band 2). These latter studies indicate that the incidence of higher reflectance in band 2 and lower chlorophyll contents is natural for certain plant species and during certain periods of senescence. These latter studies indicate further that if species reflectance differences and phenology are not considered, it may be possible to interpret healthy vegetation as being stressed.

The spectral anomalies of vegetation in the mineralised and geochemically-enriched zones could also be possibly due to taxonomic and/or structural changes in vegetation. Data are lacking to confirm this hypothesis, but if such were the case then geobotanical methods of mineral prospecting would be applicable to the area. Further investigation of the delineated dense neighbourhood of stressed vegetation in the central part of the area is needed to confirm its mineral exploration significance. In this area, the spectrally-anomalous vegetation is unlikely to be due to man-induced environmental contamination.

3.4 CONCLUSIONS

Remote detection of hydrothermally-altered zones in densely-vegetated terranes is rendered difficult because vegetation obscures the reflectance characteristics of the underlying substrate. The success of conventional remote detection of hydrothermal alteration associated with mineral deposits relies heavily on whether the spectral scanner is able to 'see between the trees'. Several techniques have been developed to reduce the effects of vegetation to detect limonitic and clay alteration. The use of band ratios and directed principal components analysis of Landsat TM data to detect limonitic and clay alteration in the presence of vegetation has proved successful in several locations. These methods, however, rely on the generalised spectral curves for iron oxides and clays. Remote detection of limonitic and clay alteration by such methods proves inadequate where the hydrothermal alteration mineral assemblages are not iron oxides and clays as in the Baguio district. The new mineral imaging methodology developed here proved more successful in mapping known hydrothermally-altered zones in heavily-vegetated areas. In the Baguio district, the accuracy of the classified hydrothermal alteration map reaches 82%. In the Mankayan district, the accuracy of the classified hydrothermal alteration map reaches 67%. For Benguet province, the accuracy of the classified hydrothermal alteration map reaches 73%. The classified hydrothermal alteration maps of Baguio district and Benguet province will be integrated with the other geological datasets (see Chapter 2) in the geologically-constrained predictive modeling of mineral potential of these areas.

Remote detection of vegetation stress has considerable potential for mineral exploration. Analyses of Landsat TM data indicate that, for the Catanduanes area, vegetation in and near gold-copper deposits and Zn-enriched catchment basins are geochemically-stressed. The results of the analyses are qualitative rather than quantitative but reflect an empirical relationship between anomalous geochemical conditions of the substrate and the anomalous spectral characteristics of vegetation growing over them. Optimum data are lacking, however, to determine whether the delineated vegetation spectral anomalies are due to structural and/or taxonomic vegetation response. Because ground information is needed to verify findings of this study and because the delineated spectral anomalies of vegetation pertain only to the southern parts of the island, these anomalies will not be integrated with the other geological datasets in the geologically-constrained predictive modeling of mineral potential of the whole island.

Chapter 4

Spatial Association of Mineral Deposits and Geological Features

> ". . . when you can measure what you are speaking about and express it in numbers, you know something about it; but when you cannot express it in numbers, your knowledge is of a meagre and unsatisfactory kind; it may be the beginning of knowledge, but you have scarcely in your thoughts advanced to the state of science, whatever the matter may be."
>
> Lord Kelvin

This Chapter aims to characterise quantitatively the spatial association between the known mineral deposits and the geological features in four of the five study areas described in Chapter 2. Two established methods for characterising quantitatively spatial association between mineral deposits and geological features are applied. A new method is demonstrated. The results of the different methods are compared and implications are drawn from them with regard to existing knowledge about the mineral deposits in the study areas and for predictive mapping of mineral potential. Portions of this chapter are published as Spatial Association of Mineral Occurrences and Curvi-Linear Geological Features (Carranza and Hale, 2001g).

4.1 INTRODUCTION

It has long been recognised that certain types of mineral deposits are spatially associated with certain curvi-linear geological features. The curvi-linear geological features dealt with here are those features that are faults or fractures, fault intersections, intrusive margins/contacts, lithologic units, etc.; physical and chemical properties of geological materials are not used. The spatial association between certain types of mineral deposits and curvi-linear geological features is due to the role of the latter in localising mineralisation. For example, faults/fractures provide channelways for mineralising fluids whilst igneous intrusions provide heat sources and cause chemical reactions with the intruded rocks that may bring about mineral deposition at or near the intrusive margins/contacts. Qualitative knowledge about the spatial association between certain mineral deposits and curvi-linear geological features is, in fact, the general basis of area selection in many mineral exploration programmes. However, the degrees of spatial associations of mineral deposits with curvi-linear geological features can be different from one area to another so that

qualitative knowledge alone is inadequate for assessing mineral potential. A quantitative knowledge of the spatial associations between known mineral deposits and curvi-linear geological features in a particular area is more important.

The spatial association dealt herewith refers to the distance or range of distances at which point features (e.g., mineral deposits) are preferentially located from curvi-linear geological features. The objective of this Chapter is to make a direct comparison between a set of points and a set of lines to characterise the spatial association between these two spatial data layers or themes. This spatial association can be regarded as spatial dependence, i.e., the locations of the points depend upon the lines; hence, it is assumed that mineral deposits are spatially associated to their nearest neighbour point on curvi-linear geological feature(s). Subjective characterisation of this spatial association or dependence simply by overlaying a map of mineral deposits on a map of lineaments, for example, can be misleading. A few points may lie on or near a number of lines, leading to biased interpretation. To avoid subjective bias, a quantitative characterisation is required, which has the advantage that the results can be tested for statistical significance.

The quantitative analysis and interpretation of the relationships between spatial data is spatial statistics (Ripley, 1981). Spatial statistics has three branches, namely, geostatistics, lattice statistics and point pattern analysis (Cressie, 1993). Geostatistics is usually applied to analyse the spatial variability of a given layer or theme of continuous quantitative spatial data, e.g., metal contents in soil (Matheron, 1963; Journel and Huijbregts, 1878; Stein et al., 1995). Hence, geostatistics is not applicable to quantify the spatial association between mineral deposits and curvi-linear geological features, which represent different discontinuous or discrete spatial data. Lattice statistics involves the analysis of univariate or multivariate continuous or discontinuous quantitative data observed at spatial sites called a lattice, which may be spatially regular or irregular (Besag, 1974). When a lattice of univariate continuous quantitative spatial data is analysed, then geostatistical methods also apply (Bonham-Carter, 1994). When a lattice of multivariate continuous or discontinuous data is involved, it is the spatial interaction(s) or (in)dependence between all the neighbouring (as opposed to nearest neighbour) variables that is(are) analysed (Ripley, 1981; Cressie, 1993). Hence, lattice statistics is not generally applicable to quantify the spatial association between mineral deposits and curvi-linear geological features, which represent different layers or themes of essentially qualitative data. In addition, although the curvi-linear geological features may be represented quantitatively (i.e., proximity to faults), the spatial association in question is between mineral deposits and nearest neighbour points on curvi-linear geological features. Point pattern analysis is the study of the dispersion and/or arrangement of a univariate or multivariate point, usually qualitative or categorical, data; that is, whether the pattern of a point data can be described by a complete spatial randomness or CSR, a cluster or a regular pattern (Diggle,

1983; Boots and Getis, 1988). Point pattern analysis is therefore applicable to the characterisation of the spatial association of mineral deposits to their nearest neighbour points on curvi-linear geological features.

Of the various methods of statistical analysis of multivariate spatial point patterns, the nearest neighbour distance distribution method described by Diggle et al., (1976) is appropriate to the present study. The theoretical model of an appropriate nearest neighbour distance distribution method is described by Berman (1977) and applied by Huntington and Green (1978), Simpson et al., (1980), Bonham-Carter et al. (1985), Bonham-Carter (1985) and Carranza and Hale (2001g) to quantify spatial association between mineral deposits and geological features. The most important limitation of the distance distribution method is that it assumes mineral deposits to have a Poisson distribution; however, mineral deposits can be related to a particular magmatic regime and therefore are not necessarily independent. Another limitation of the distance distribution method lies in the selection of optimum random (Poisson) points whose frequency distribution function of nearest distances to linear features is compared with the frequency distribution function of nearest distances between mineral deposits and linear features. In the case studies that follow, the optimum random points are (a) equal in number to the number of mineral deposits used in the analysis, i.e., the random points and the mineral deposits have equal point density in a study area, (b) confined only to lithologic units with which mineral deposits are known to be associated and (c) assume a condition of CSR.

A statistical method for quantifying spatial association between mineral deposits and curvi-linear geological features that avoids the limitations of the distance method is the weights of evidence method (Bonham-Carter et al., 1988, 1989; Watson and Rencz, 1989; Agterberg et al., 1990; Bonham-Carter, 1991,1994; Turner, 1997; Carranza and Hale, 1999b, 1999c, 1999d, 2000, 2001g). The weights of evidence method employs Bayesian conditional probability to determine the optimum binary pattern of a geological feature that shows spatial association with a set of mineral deposits. A certain distance to be determined in the modeling, which is used to buffer a curvi-linear geological feature to indicate its presence, defines the binary pattern. The major limitation of the weights of evidence method is that there should be a fairly large number of mineral deposits used in the modeling; otherwise, the quantified spatial association can be statistically not significant.

Though not necessarily overcoming the limitations of the distance distribution and weights of evidence methods, Agterberg and Fabbri (1972) used harmonic analysis to analyse the locations of gold and copper deposits in the Abitibi Belt in the Canadian Shield. They showed that the deposits lie along elongated clusters and concluded that the periodic regularities in the location of the deposits coincide with structures of different ages in the Archean. The analysis of Agterberg and Fabbri (1972) involved examination of the spatial patterns of lines and points independently, with subsequent comparison of periodicity and

clustering, instead of direct analysis of the spatial association between a set of points and a set of lines.

Quantitative methods of direct comparison between a set of points and a set of lines to quantify the spatial association between them are lacking. The lack of methods in question stems from the fact that mineral deposits and geological features are special types of spatial data so that the more commonly used spatial statistical methods are not generally applicable. In the following section, the methods used in this study are described.

4.2 METHODS

Of the three methods mentioned above, the distance distribution method and the weights of evidence method were used. The harmonic analysis of Agterberg and Fabbri (1972) was considered inappropriate to the present study because the mineral deposits in the study areas are associated mainly with one episode or at most two episodes of mineralisation in the Tertiary (Wolfe, 1981, 1988). To overcome the limitations of the distance distribution method and the weights of evidence method, a new method is introduced here, namely, the distance correlation method (Carranza and Hale, 2001g). The distance correlation method has no assumption of the probability distribution of the mineral deposits and its robustness in the case of a small number of points will be demonstrated. The results of these methods are compared and contrasted.

The underlying assumption behind each method is that mineral deposits are associated spatially with the curvi-linear geological feature of a particular type nearest to them. The assumption may not necessarily be the case considering that, on one hand, the locations of some mineral deposits indicated on maps are usually, if not always, the surface projections of their positions in subsurface 3D-space. On the other hand, the locations of geological features on the map are their 'true' surface locations. In addition, the amount and detail of map data, and hence the scale of the map, will influence significantly the quantitative characterisation of spatial association of mineral deposits and geological features in 2D surface space.

Consider a hypothetical case of a number of hydrothermal mineral deposits and that surface and subsurface observations indicate some of the deposits to be associated spatially with outcropping intrusive rocks whilst others are associated spatially with non-outcropping intrusive rocks. Consider further that some of the outcropping intrusive rocks are not mappable at a particular map scale. In this case, it is only the spatial association of the known hydrothermal mineral deposits and the mapped outcropping intrusive rocks that is characterised. It is thus important to realise that the quantified spatial association is pertinent only to the given geological map data and to the stage or scale of mapping the given map data represent. The ideal solution to the above problems would be 3D

characterisation of the spatial association; this, however, is beyond the scope of this work.

The three methods, which are described in detail below, were applied to quantify the spatial associations between the mineral deposits and the curvi-linear geological features in Benguet province, Baguio district, Abra area and Catanduanes Island.

4.2.1 Observed vs. predicted distance distribution method

Consider the nearest distance x between a point (in a set of points) and a line (in a set of lines) or another point (in another set of points). To compare observed or measured, $\hat{O}(x)$, and expected or predicted, $\hat{E}(x)$, cumulative frequency distributions of nearest distances x, Bonham-Carter et al. (1985) used a one-tailed test of the null hypothesis that a set of points and a set of lines or another set of points are spatially independent (i.e., lack of spatial association), by computing the Kolmogorov-Smirnov statistic $D = \max(\hat{O}(x) - \hat{E}(x))$. For a positive spatial association (i.e., within a given distance from a linear feature, there is a higher proportion of points than would be expected due to chance), the curve for $\hat{O}(x)$ is above or higher than the curve for $\hat{E}(x)$, i.e., $\hat{O}(x) > \hat{E}(x)$. For a negative spatial association (i.e., within a given distance from a linear feature, there is a lower proportion of points than would be expected due to chance), the curve for $\hat{O}(x)$ is below or lower than the curve for $\hat{E}(x)$, i.e., $\hat{O}(x) < \hat{E}(x)$. The statistical significance of the spatial association is tested by computing the quantity $\beta_{max} = 4D^2NM/(N+M)$, which is approximately distributed as χ^2 with 2 degrees of freedom (Goodman, 1954; Siegel, 1956), where M denotes the number of random points used to estimate $\hat{E}(x)$ and N is the number of points used to estimate $\hat{O}(x)$.

To estimate $\hat{O}(x)$ and $\hat{E}(x)$ and test the null hypothesis of spatial independence between a set of mineral deposits and a set of geological features, the following procedures were followed.

1. Digitise geological features as lines or points, as the case may be.
2. Rasterise line/point maps of geological features and generate maps portraying distances away from these features.
3. Digitise mineral deposits as points.
4. Rasterise point map of mineral deposits and determine distances x of each deposit to the nearest geological feature. Sort these distances into ascending order.
5. Calculate $\hat{O}(x) = i/N$ for i=1,2... N observed distances.
6. Generate random 'mineral deposit' points, equal in number to the mineral deposits (see below).
7. Repeat step 5 for randomly generated points.

8. Determine proportion of distances of M randomly generated 'mineral deposit' points that are less than or equal to each of the ordered distances of observed points; this is $\hat{E}(x)$.
9. Compute D, β and an upper confidence band $\hat{U}(x) = \hat{E}(x) + \{9.21(N+M)/4NM\}^{1/2}$, where 9.21 is the tabulated χ^2 value with 2 degrees of freedom at significance level α=0.01 (or other values for chosen α).
10. Create plots of $\hat{O}(x)$ and $\hat{E}(x)$ versus x and plots of β versus x.

To create a map of random 'mineral deposit' points, a random number generator was used to determine the northing and easting coordinates of these points within the limits of each of the study areas. Since the number of sets of randomly generated points is countless, two criteria were applied to select a set of optimum randomly generated points. First, the random points should not occur within lithologic formations that are not known to host the mineral deposits studied. Second, the random points must assume a condition of complete spatial randomness (CSR), i.e., no correlation exists between locations of points. To test for CSR, which is not elaborated here, expected frequencies of deposits of reflexive nearest neighbours were compared with expected frequencies of deposits in a condition of CSR (Boots and Getis, 1988).

4.2.2 Weights of evidence method

The weights of evidence method has been developed by Bonham-Carter et al. (1988, 1989). Because the mathematical formulation of this method is somewhat complex (see Chapter 6), the simplified and intuitive approach suggested by Turner (1997) was adopted in this Chapter. Given the presence or absence of a domain (e.g., a zone of proximity to a curvi-linear geological feature), a scoring or weighting can be performed between that domain and a set of points (e.g., mineral deposits). The weighting yields (1) W + weights within the domain (D_P), and (2) W – weights outside the domain (D_A). Note that $T = D_P + D_A$; T is the total area being studied. Because the areal coverage of a deposit is much smaller than the domain being considered, the weights of evidence are estimated by taking the natural logarithms ($\log_e$) of the probability ratios

$$W+ = \log_e ((\% \text{ deposits in } D_P) \div (\% \text{ of total area occupied by } D_P)); \quad (4\text{-}1)$$

$$W- = \log_e ((\% \text{ deposits in } D_A) \div (\% \text{ of total area occupied by } D_A)). \quad (4\text{-}2)$$

Equations 4-1 and 4-2 are numerically equal to Equations 6-6 and 6-7 (see Chapter 6), respectively. The weights W+ and W- represent unitless measures of the spatial association between the deposits and a given domain. (W+) > 0 and (W-) < 0 imply positive spatial association, (W+) < 0 and (W-) > 0, imply negative spatial association, and (W+) = (W-) = 0 imply no spatial association. The variances of the weights can be calculated (Bishop et al., 1975) as

$$s^2(W+) = \frac{1}{mD_P} + \frac{1}{bD_P} \text{ and} \quad (4\text{-}3)$$

$$s^2(W-) = \frac{1}{mD_A} + \frac{1}{bD_A}, \quad (4\text{-}4)$$

where mD_P and mD_A are respectively the number of pixels with mineral deposits inside and outside a given domain; bD_P and bD_A are respectively the number of pixels without mineral deposits inside and outside a given domain. Note that $D_P = mD_P + bD_P$ and $D_A = mD_A + bD_A$.

For each binary domain, the contrast C combines these weights into an overall measure of the spatial association with a set of points and is defined simply as

$$C = (W+) - (W-). \quad (4\text{-}5)$$

Equation 4-5 is numerically equal to Equation 6-12 (Chapter 6). Hence, for a positive spatial association, C will have positive values; C will have negative values in the case of negative spatial association. The maximum C usually gives the cutoff distance buffer at which there is optimal spatial association between a given domain and a set of points (Bonham-Carter et al., 1989). However, in cases of a small number of points (or deposits) such as the present cases, the uncertainty of the weights could be large so that C is meaningless. In cases of a small number of points, a useful measure to determine the most significant cutoff distance is to calculate the Studentised value of C (Bonham-Carter, 1994). The Studentised C, calculated as the ratio of C to its standard deviation, C/s(C), indicates the statistical significance of the spatial association. The standard deviation of C is calculated as:

$$s(C) = \sqrt{s^2(W+) + s^2(W-)}. \quad (4\text{-}6)$$

Ideally, a Studentised C greater than 2 suggests a statistically significant spatial association (Bonham-Carter, 1994). Due to the small number of mineral deposits in the study areas, the cutoff distance within which their spatial association with a given domain is optimal was chosen based on the maximum Studentised C.

From the discussion above, it is obvious that calculation of weights to estimate spatial association requires polygonal domains. Our test domains, however, are either point or curvi-linear geological features. To convert these point and curvi-linear domains into polygonal domains, distance buffering was performed. Determining the spatial associations of interest involved the following steps.

1. Digitise geological features as lines or points, as the case may be.

2. Rasterise the maps of curvi-linear or point geological features and generate maps portraying distances away from these features.
3. Re-classify maps portraying distances to geological features into a series of binary domains representing buffered corridors of distances away from the geologic features. The domain within a particular cumulative distance indicates presence of geological feature; the domain outside the cumulative distance indicates its absence.
4. Digitise mineral deposits as points.
5. Rasterise point map of mineral deposits.
6. Determine number of points within and outside a binary domain by crossing or overlaying each of the raster maps of the binary domains with the raster map of mineral deposits.
7. Calculate the weights according to Equations (4-2) and (4-3).
8. Determine C and Studentised C.

4.2.3 Distance correlation method

The concept of the new method established here for quantitative characterisation of spatial association between a set of points and a set of lines (or points) is illustrated in Figure 4.1. Consider points P_{jx} (j=1, 2,... n points) at nearest distances X_j from a nearest line L_i (i=1, 2,... m lines), their nearest neighbour points P_{j0} on line L_i, and an arbitrary point AP. Hence, there are two sets of measured distances, d_{jx} and d_{j0}, from AP to P_{jx} and P_{j0}, respectively. If all points P_{jx} lie exactly on L_i, then $d_{jx}= d_{j0}$ and the correlation coefficient $r_{d_{jx}d_{j0}}$ is unity, which implies a 'perfect' spatial association. However, if X_j is variable (as in the present cases of distances between mineral deposits and curvi-linear geological features), then $d_{jx} \neq d_{j0}$ and $r_{d_{jx}d_{j0}} \neq 1$. In this latter case, the spatial association can be qualified as 'imperfect' and needs to be characterised quantitatively.

Now consider points P_{jy}, along the line that passes through P_{jx} and P_{j0}, at equal distances Y_j from line L_i. The method endeavours to find a distance Y_j, at which $r_{d_{jx}d_{jy}}$ is highest (equal to 1 if points P_{jx} have equal distances X_j from nearest line L_i), and hereafter referred to as $Y_j max_r$. At $Y_j max_r$, the differences between d_{jy} and d_{jx} are minimal (i.e., P_{jx} and P_{jx} are close enough). This also implies that a majority of points P_{jx} lie about $Y_j max_r$ from line L_i. Hence, $Y_j max_r$ can be regarded as the distance at which a set of points is spatially associated with a set of lines.

Within a particular study area, there are several possible arbitrary points AP from which the spatial association between the mineral deposits and curvi-linear geological features can be characterised quantitatively. Experiments were performed using nine different arbitrary points AP within and along the map boundaries of the study areas. These arbitrary points are the centre, north

(midpoint of the north boundary of map), NE (northeast corner of map), east (midpoint of east boundary of map, SE (southeast corner of map), south (midpoint of south boundary of map), SW (southwest corner of map), west (midpoint of west boundary of map) and NW (northwest corner of map). These nine arbitrary points were selected to examine the spatial association between the mineral deposits and the curvi-linear features within and around the periphery of a particular study area because the distances d_{j0} and d_{jx} will vary with the position of an arbitrary point. Consequently, the experiments showed that Y_jmax_r is not the same for all the eight arbitrary points. Hence, not just one but many arbitrary points are necessary to examine properly the spatial association between the mineral deposits and the curvi-linear geological features. It was assumed that Y_jmax_r could be adequately determined using the nine arbitrary points.

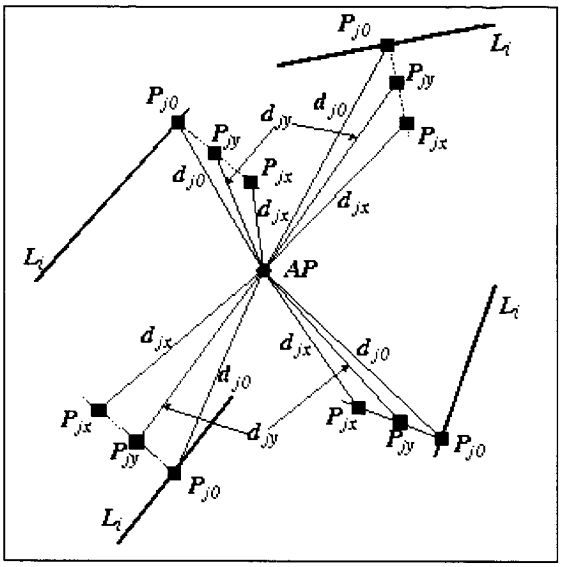

Figure 4.1. Diagram to illustrate concept of distance correlation method for quantitative characterisation of spatial association between a set of points and a set of lines (or points).

Among the nine Y_jmax_r determined, the Y_jmax_r with the highest frequency was considered optimum. However, in cases of an equal frequency, a triple-tie or a quadruple-tie in frequencies, the higher or highest Y_jmax_r was considered optimum. The reason for this is discussed later. For a positive spatial association, more P_{jx} points would lie within the optimum Y_jmax_r. Hence, it can be expected that the mean $r_{d_{jx}d_{jy}}$ within the optimum Y_jmax_r (or $mdcioY_jmax_r$) is greater than the mean $r_{d_{jx}d_{jy}}$ beyond the optimum Y_jmax_r (or $mdcooY_jmax_r$). For a negative spatial association, more P_{jx} points would lie beyond the optimum Y_jmax_r. Hence, it can be expected that the $mdcioY_jmax_r$ is less than the $mdcooY_jmax_r$.

The procedures below were carried out to characterise quantitatively the spatial association between the mineral deposits and geological features based on the concept presented above.

1. Digitise geological features as lines or points, as the case may be.
2. Digitise and rasterise an arbitrary point AP; generate a map portraying distances away from AP.
3. Digitise mineral deposits as points and determine d_{jx}.
4. On each line map of geological features, determine P_{j0} visually and digitise line segments of at least maximum X_j length starting from P_{j0} passing through P_{jx}. (In case the geological feature is a 'point', the 'point' becomes P_{j0}).
5. Create points P_{jy} along the line segments at regular intervals from P_{j0}. Hence P_{jy} and P_{j0} are the same when $Y_j = 0$.
6. For all points P_{jy}, determine d_{jy} using map of distances away from AP.
7. Determine $r_{d_{jx}d_{jy}}$ at regular intervals from P_{j0}. A t-test for the significance of $r_{d_{jx}d_{jy}}$ (Davis, 1973) is given by

$$t = \frac{r_{d_{jx}d_{jy}}\sqrt{n-2}}{\sqrt{1-(r_{d_{jx}d_{jy}})^2}} \qquad (4\text{-}7)$$

   which has n-2 degrees of freedom, where n is the number of P_{j0}, which is equal to the number of P_{jy}.

8. Repeat procedures 2-7 each time for different arbitrary points AP.
9. For the different arbitrary points, determine the optimum $Y_j max_r$.
10. For the arbitrary points AP with optimum $Y_j max_r$, calculate the mean of $r_{d_{jx}d_{jy}}$ as determined in step 7 for points P_{jy} within $Y_j max_r$; this mean is $mdcioY_j max_r$. Also calculate the mean of $r_{d_{jx}d_{jy}}$ as determined in step 7 for P_{jy} beyond $Y_j max_r$ up to $2Y_j marx_r$; this mean is $mdcooY_j max_r$. This step determines whether the spatial association within $Y_j max_r$ is positive or negative.

4.2.4 Map operations

Most of the procedures described above were carried out using ILWIS (Integrated Land and Water Information System) GIS software. A pixel size (or unit cell) of 100 m by 100 m was used in rasterising the digitised input data. This pixel size is chosen to ensure that only one mineral deposit is present in any given pixel; it is also a realistic average size of the mineral deposits in the study areas. Using this pixel size, the number of pixels in Benguet province is 259591 (equivalent to 2,595.91 km^2), in Baguio district 42039 (420.39 km^2), in Abra area 91963 (919.63 km^2) and in Catanduanes Island 144811 (1448.11 km^2).

4.2.5 Presentation and interpretation of results

In each of the subsequent four sections of this Chapter, the quantified spatial associations between mineral deposits and curvi-linear geological features using all three methods are described. The results obtained per method are summarised in paragraphs numbered 1-3, where
1 = results for observed vs. predicted distance distribution method
2 = results for weights of evidence method
3 = results for distance correlation method.

Variations in magnitude of quantified spatial associations between the mineral deposits and each of the different curvi-linear geological features reflect the strengths or weaknesses of the spatial associations. Comparison of the strength/weakness of spatial association of mineral deposits with different curvi-geological features was based on the distances at which the spatial association is optimal. The strength of a positive spatial association is inversely proportional to distance, i.e., short distances represent strong spatial associations and long distances represent weak spatial associations. On the other hand, the strength of a negative spatial association is directly proportional to distance, i.e., short distances represent weak negative spatial associations and long distances represent strong negative spatial associations. Hence, the comparison can be made only with similar types of spatial association, i.e., the strength of a positive spatial association cannot be compared with the strength of a negative spatial association.

4.3 APPLICATION TO BENGUET PROVINCE

Sillitoe and Gappe (1984) identified four spatial characteristics of the porphyry copper deposits in the Philippines (see Chapter 5). Based on these spatial characteristics, several districts in the Philippines become prime candidates for exploration for this type of deposit. To provide exploration guides in a district, the spatial association of porphyry copper deposits and geological features in Benguet are studied using the methods described.

4.3.1 Theoretical considerations

Porphyry copper deposits, in contrast to other hydrothermal deposits, are invariably associated genetically with porphyry plutons localised along island- and continental-arc strike-slip fault systems (Bryner, 1969; Field et al., 1974; Lowell, 1974; Laznicka, 1976; Hollister, 1974, 1978; Horton, 1978; Titley and Heidrick, 1978; Sillitoe, 1981; Titley, 1981; Titley and Beane, 1981; Sillitoe and Gappe, 1984; Pirajno, 1992). To investigate where porphyry plutons are emplaced along strike-slip fault systems, it is important to understand where magmatic fluids are focused within the crust. The migration of magmatic fluids

into favourable loci is governed by fluid-flow thermodynamics and mechanics (Johnson, 1992). Fluids generally flow from zones of higher pressure to zones of lower pressure and from zones of higher temperature to zones of lower temperature. According to Ryan (1990), it is the fault patterns and spatially varying stress patterns that regulate how and where magma will be focused in shallow storage and transport structures. Thus, an appreciation of fault mechanics is essential to studying where porphyry plutons are favourably emplaced.

In compressive stress regimes that lead to strike-slip faulting, the major stress axis, σ_1, and the least stress axis, σ_3, are contained in a (sub-) horizontal plane, and the intermediate stress axis, σ_2, lies on a (sub-)vertical plane (Freund, 1974; Mandl, 1988; Aurelio et al., 1997). A strike-slip fault develops when the differential stress (i.e., σ_1-σ_3) attains a certain critical value. When a strike-slip fault develops or reactivates, a permeable rupture zone is formed. If the faulting transects a zone of suprahydrostatic fluid pressure gradient (i.e., above an asthenospheric magmatic dome), the formation of structural permeability causes post-failure magmatic fluid discharge from the over-pressured region into the fault plane. The discharge of magmatic fluids into the fault plane continues until the hydraulic gradient reverts to hydrostatic or until the fault reseals (Sibson, 1981, 1990; Figure 4.2).

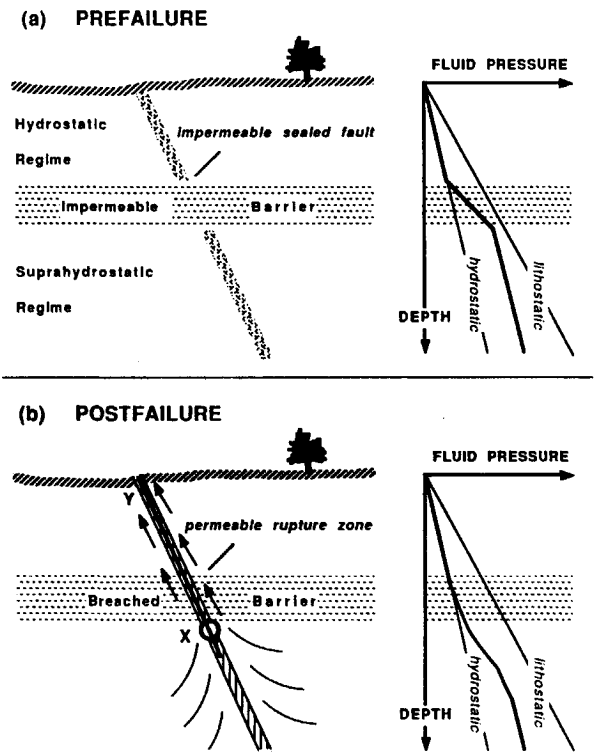

Figure 4.2. Post-failure magmatic discharge from overpressured regional into fault plane (from Sibson, 1990).

The simplistic expectation is that magmatic fluids flow upward through the fault. However, the shear stress conditions [i.e., $\frac{1}{2}(\sigma_1 - \sigma_3)$] along a strike-slip fault will focus the fluid-flow because the strain rate (rate of flow) of viscous fluids (e.g.,

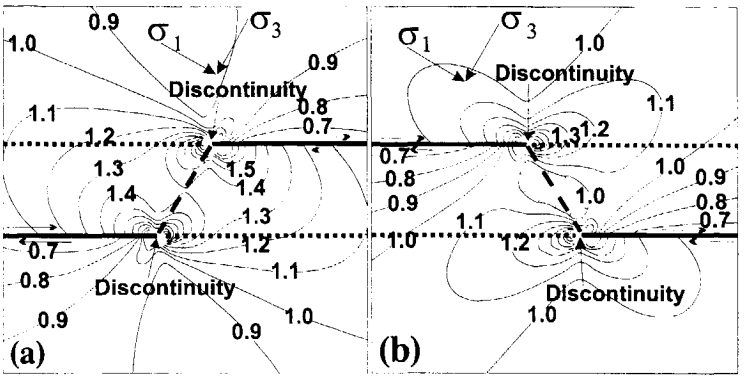

Figure 4.3. State of shear stress, ½(σ_1 - σ_3), near en echelon strike-slip faults: (a) left-stepping right-lateral; and (b) right-stepping left-lateral (modified after Segall and Pollard, 1980). Dotted lines are traces of original faults; dashed lines are traces of step-over faults.

magma) is directly proportional to the shear stress (White, 1974). Before the relaxation of the stress regimes, fluid-flow is focused into zones of high shear stress; these zones are where porphyry plutons are likely to be emplaced.

Strike-slip faults are discontinuous geologic features. At the discontinuities of strike-slip faults, the strike-slip displacement is accommodated by bending or splaying (Mandl, 1988). Discontinuities along strike-slip faults are those foci where the slip motion steps-over to a (sub)-parallel fault. Segall and Pollard (1980) have shown that high values of shear stress occur at or near zones of discontinuities of en echelon strike-slip faults (Figure 4.3). It is hypothesised, therefore, that zones around strike-slip discontinuities are where magmatic fluids are focused and are favourable loci for the emplacement of porphyry plutons. As a corollary, it is also hypothesised that zones that are favourable for porphyry pluton emplacement are favourable for porphyry copper mineralisation.

The hypotheses were tested by characterising quantitatively the spatial associations between (1) outcropping porphyry plutons and strike-slip fault discontinuities, (2) known porphyry copper deposits and strike-slip fault discontinuities and (3) known porphyry copper deposits and outcropping porphyry plutons. The centroids of the mapped porphyry plutons were considered focal points of emplacement and were digitised as points and used in the spatial data analyses. The strike-slip fault discontinuities have been interpreted from shaded-relief images of a DEM of the province (Figure 2.6; Section 2.2.3). These strike-slip fault discontinuities were digitised as points and used in the spatial data analyses. In addition, the spatial association of the porphyry plutons and the porphyry copper deposits with the batholithic pluton margins were characterised quantitatively. These latter quantifications could

provide insights about the role of the batholithic plutons in the emplacement of the porphyry plutons.

4.3.2 Porphyry plutons vs. strike-slip fault discontinuities

1. Most parts of the curve for the observed cumulative frequency distribution of nearest distances between the porphyry plutons and the strike-slip fault discontinuities are just above the predicted curve (Figure 4.4a). This implies positive spatial association, which, however, is not significant statistically (Figure 4.4b). The highest peak along the β curve suggests that the positive spatial association is optimal within 2400 m.

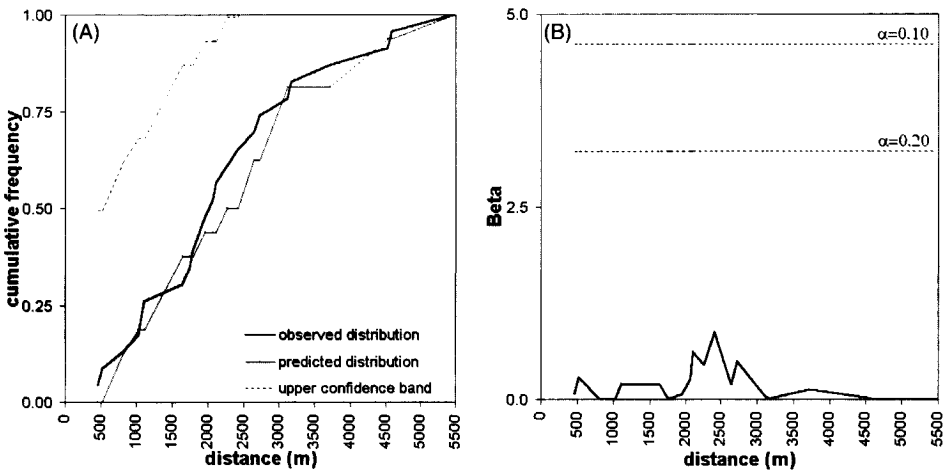

Figure 4.4. Porphyry plutons centroids and nearest strike-slip fault discontinuities in Benguet province: (a) distance distribution and (b) variation of β.

2. There is positive spatial association between the strike-slip fault discontinuities and the porphyry pluton centroids as indicated by the contrasts C (Table 4.1). The positive spatial association is statistically significant within 2000 to 4000 m; however, according to the highest Studentised C, it is optimal within 2750 m.

3. For the different arbitrary points, the Y_jmax_r varies between 1750 to 2750 m (Table 4.2). The t-test indicates that the measured correlation coefficients are significantly different from zero at the 99.9% significance level. The optimum Y_jmax_r is 2500 m, within which the spatial association is positive, i.e., $mdcioY_jmax_r > mdcooY_jmax_r$.

Table 4.1. Variation of weights and contrasts for cumulative distances from strike-slip fault discontinuities with respect to porphyry pluton centroids, Benguet province*.

Distance buffer (m)	No. of pixels in D_P**	No. of porphyry pluton centroids in D_P	W+	s(W+)	W-	s(W-)	C	s(C)	C/s(C)
500	3475	1	1.178	1.000	-0.031	0.213	1.209	1.023	1.182
1000	14135	3	0.874	0.577	-0.084	0.224	0.957	0.619	1.546
1500	31048	6	0.780	0.408	-0.175	0.243	0.955	0.475	2.011
2000	52362	11	0.863	0.302	-0.425	0.289	1.289	0.417	3.087
2250	64217	13	0.826	0.277	-0.549	0.316	1.375	0.421	3.269
2500	76758	15	0.791	0.258	-0.706	0.354	1.497	0.438	3.418
2750	**89286**	**17**	**0.765**	**0.243**	**-0.922**	**0.408**	**1.687**	**0.475**	**3.553**
3000	100733	17	0.644	0.243	-0.853	0.408	1.497	0.475	3.153
3250	113064	19	0.640	0.229	-1.177	0.500	1.818	0.550	3.304
3500	125127	19	0.539	0.229	-1.091	0.500	1.630	0.550	2.963
3750	136740	20	0.501	0.224	-1.289	0.577	1.790	0.619	2.891
4000	147844	20	0.423	0.224	-1.194	0.577	1.617	0.619	2.612
4500	168041	20	0.295	0.224	-0.995	0.577	1.290	0.619	2.083
5000	186137	22	0.288	0.213	-1.873	1.000	2.161	1.022	2.114
5500	200738	23	0.257	0.209					

*Table entries in bold pertain to optimal spatial association. **D_P = domain is present

The porphyry plutons are positively spatially associated with the strike-slip fault discontinuities. The distance distribution method and the distance correlation method indicate that the positive spatial association is optimal within 2400 and 2500 m, respectively. The weights of evidence method indicates that the positive spatial association is optimal within 2750 m.

Table 4.2. Results of distance correlation calculations to quantify spatial association between porphyry plutons and strike-slip fault discontinuities, Benguet province*.

AP	$Y_j max_r$ (m)	$r_{d_{jx}d_{jy}}$ at $Y_j max_r$	t-value for $r_{d_{jx}d_{jy}}$ at $Y_j max_r$	$mcdioY_j max_r$	$mcdooY_j max_r$
Centre	2000	0.99791	70.714**		
North	1750	0.99949	143.640**		
NE	**2500**	**0.99906**	**105.373****	**0.99819**	**0.99792**
East	2250	0.99268	37.663**		
SE	2250	0.99922	116.127**		
South	**2500**	**0.99899**	**102.751****	**0.99804**	**0.99728**
SW	2750	0.99892	98.449**		
West	2000	0.99421	42.387**		
NW	1750	0.99973	195.625**		

*Table entries in bold pertain to optimal spatial association.

**Calculated t-values are significantly different from zero; critical t-value at α=0.001 and ν=23-2=21 degrees of freedom is 3.527 (Davis, 1973).

4.3.3 Porphyry copper deposits vs. strike-slip fault discontinuities

1. As indicated in Figure 4.5, there is a statistically significant positive spatial association between the porphyry copper deposits and the strike-slip fault discontinuities. The positive spatial association is optimal within 2800 metres as indicated by the highest peak in the β curve.

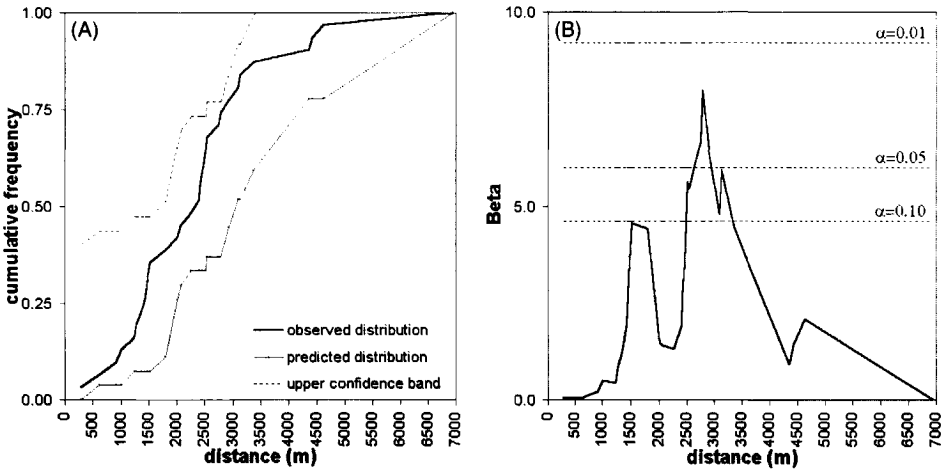

Figure 4.5. Porphyry copper deposits and nearest strike-slip fault discontinuities in Benguet province: (a) distance distribution and (b) variation of β.

2. The contrasts C indicate a positive spatial association between the strike-slip fault discontinuities with respect to the porphyry copper deposits (Table 4.3). The positive spatial association is significant statistically within 5500 m, but it is optimal within 3000 m as indicated by the highest Studentised C.

3. The distances between porphyry copper deposits and strike-slip fault discontinuities at which the measured values of $r_{d_{jx}d_{jy}}$ are highest vary between 2000 and 2500 m (Table 4.4). The t-test indicates that these measured correlation coefficients are significantly different from zero at the 99.9% significance level. The spatial association is optimal within 2250 metres. Within this distance, the spatial association is positive.

Table 4.3. Variation of weights and contrasts for cumulative distances from strike-slip fault discontinuities with respect to porphyry copper deposits, Benguet province*.

Distance buffer (m)	No. of pixels in D_P**	No. of porphyry copper occ. in D_P**	W+	s(W+)	W-	s(W-)	C	s(C)	C/s(C)
500	3475	1	0.880	1.000	-0.019	0.183	0.899	1.017	0.884
1000	14135	3	0.575	0.577	-0.046	0.189	0.621	0.608	1.022
1500	31048	10	0.992	0.316	-0.262	0.218	1.254	0.384	3.265
2000	52362	12	0.652	0.289	-0.264	0.229	0.916	0.369	2.485
2500	76758	18	0.675	0.236	-0.519	0.277	1.194	0.364	3.279
3000	**100733**	**24**	**0.691**	**0.204**	**-0.997**	**0.378**	**1.688**	**0.430**	**3.929**
3500	125127	27	0.591	0.192	-1.390	0.500	1.981	0.536	3.698
4000	147844	27	0.425	0.192	-1.205	0.500	1.630	0.536	3.042
4500	168041	29	0.368	0.186	-1.699	0.707	2.067	0.731	2.827
5000	183137	30	0.300	0.183	-2.172	1.000	2.472	1.017	2.431
5500	200738	30	0.224	0.183	-1.950	1.000	2.174	1.017	2.139
6000	211763	30	0.171	0.183	-1.743	1.000	1.913	1.017	1.882
6500	220779	30	0.129	0.183	-1.534	1.000	1.663	1.017	1.636
7000	227698	31	0.131	0.180					

*Table entries in bold pertain to optimal spatial association. **D_P = domain is present

The three methods indicate that, between the porphyry copper deposits and the strike-slip fault discontinuities, there is optimum positive spatial association, which varies between 2250 and 3000 m.

Table 4.4. Results of distance correlation calculations to quantify spatial association between porphyry copper deposits and strike-slip fault discontinuities, Benguet province*.

AP	Y_jmax_r (m)	$r_{d_{jx}d_{jy}}$ at Y_jmax_r	t-value for $r_{d_{jx}d_{jy}}$ at Y_jmax_r	$mcdioY_jmax_r$	$mcdooY_jmax_r$
Centre	**2250**	**0.99658**	**64.923****	**0.99360**	**0.97577**
North	**2250**	**0.99876**	**108.187****	**0.99748**	**0.99395**
NE	**2250**	**0.99870**	**105.707****	**0.99780**	**0.99529**
East	**2250**	**0.99410**	**49.361****	**0.98710**	**0.96516**
SE	2500	0.99837	94.330**		
South	2500	0.99869	104.969**		
SW	**2250**	**0.99907**	**124.446****	**0.99821**	**0.99513**
West	2000	0.99702	69.635**		
NW	**2250**	**0.99833**	**93.120****	**0.99656**	**0.98972**

*Table entries in bold pertain to optimal spatial association.
**Calculated t-values are significantly different from zero; critical t-value at α=0.001 and v=23-2=21 degrees of freedom is 3.527 (Davis, 1973).

4.3.4 Porphyry copper deposits vs. porphyry plutons

1. There is positive spatial association between the porphyry copper deposits and the porphyry pluton centroids, i.e., observed distribution curve is above predicted curve (Figure 4.6a). The positive spatial association is statistically significant up to 4000 m but is optimal within 1300 m (Figure 4.6b).

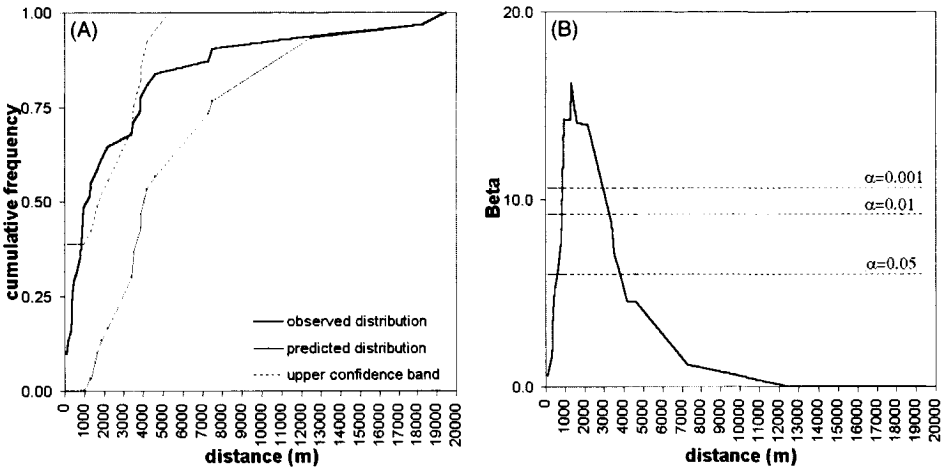

Figure 4.6. Porphyry copper deposits and nearest porphyry pluton centroids, Benguet province: (a) distance distribution and (b) variation of β.

2. Table 4.5 shows the variations in contrast C for cumulative distances from the porphyry plutons with respect to the porphyry copper deposits. The contrasts are mostly positive, which implies positive spatial association. The positive spatial association is statistically significant up to 10000 m but is optimal within 1000 m as indicated by the highest Studentised C.

Table 4.5. Variation of weights and contrasts for cumulative distances from porphyry plutons with respect to porphyry copper deposits, Benguet province*.

Distance buffer (m)	No. of pixels in D_P**	No. of porphyry copper occ. in D_P**	W+	s(W+)	W-	s(W-)	C	s(C)	C/s(C)
500	9782	8	1.925	0.354	-0.260	0.209	2.185	0.411	5.321
1000	**17783**	**15**	**1.956**	**0.258**	**-0.590**	**0.250**	**2.546**	**0.359**	**7.083**
1500	26777	17	1.671	0.243	-0.686	0.267	2.357	0.361	6.531
2000	36063	19	1.485	0.229	-0.800	0.289	2.284	0.369	6.194
3000	56615	20	1.085	0.224	-0.790	0.302	1.875	0.375	4.994
4000	80415	24	0.916	0.204	-1.117	0.378	2.034	0.430	4.734
5000	103719	26	0.742	0.196	-1.315	0.447	2.056	0.488	4.211
6000	122877	26	0.572	0.196	-1.183	0.447	1.756	0.488	3.595
8000	157581	28	0.397	0.189	-1.041	0.577	1.799	0.608	2.961
10000	185768	28	0.233	0.189	-1.078	0.577	1.311	0.608	2.158
12000	206612	28	0.126	0.189	-0.746	0.577	0.873	0.608	1.437
14000	224090	29	0.080	0.186	-0.751	0.707	0.832	0.731	1.138
16000	238054	29	0.020	0.186	-0.252	0.707	0.271	0.731	0.371
18000	249596	29	-0.027	0.186	0.516	0.707	-0.544	0.731	-0.744
19000	253721	30	-0.010	0.183	0.355	1.000	-0.365	1.017	-0.359
20000	256625	31	-0.011	0.180					

*Table entries in bold pertain to optimal spatial association. **D_P = domain is present.

3. Table 4.6 shows the distances between porphyry copper deposits and porphyry plutons at which the measured values of $r_{d_{jx}d_{jy}}$ are highest. The t-test indicates that these measured correlation coefficients are significantly different from zero at the 99.9% significance level. The spatial association varies between 2000 to 5000 m. The spatial association is optimal within 4000 m. Within this distance, the spatial association is positive.

Table 4.6. Results of distance correlation calculations to quantify spatial association between porphyry copper deposits and porphyry plutons, Benguet province*.

AP	$Y_j max_r$ (m)	$r_{d_{jx}d_{jy}}$ at $Y_j max_r$	t-value for $r_{d_{jx}d_{jy}}$ at $Y_j max_r$	$mcdioY_j max_r$	$mcdooY_j max_r$
Centre	3500	0.97355	22.994**		
North	2000	0.99723	69.766**		
NE	**4000**	**0.99428**	**50.116****	**0.99228**	**0.99092**
East	3500	0.93713	14.460**		
SE	2000	0.99489	53.076**		
South	**4000**	**0.99349**	**46.698****	**0.98942**	**0.98855**
SW	4500	0.98585	31.666**		
West	5000	0.90463	11.430**		
NW	2500	0.99411	49.389**		

*Table entries in bold pertain to optimal spatial association.
**Calculated t-values are significantly different from zero; critical t-value at α=0.001 and ν=23-2=21 degrees of freedom is 3.527 (Davis, 1973).

The porphyry copper deposits are positively spatially associated with the porphyry plutons. The distance distribution method and weights of evidence method indicate that the positive spatial association is optimal within 1000 and 1300 m, respectively. The distance correlation method indicates that the positive spatial association is optimum within 4000 m.

4.3.5 Porphyry plutons vs. batholithic pluton margins

1. The curve for the observed cumulative frequency distribution of nearest distances between the porphyry pluton centroids and the batholithic pluton margins fluctuates above and below the predicted curve (Figure 4.7a). It is above the predicted curve within 1100 m, below between 1100 and 2500 m, and above between 2500 and 4500 m. These results imply a tendency for a positive spatial association within 1100 m, a negative spatial association within 1100 to 2500 m, and a positive spatial association within 2500 to 4500 metres. The highest peak along the β curve at about 2100 m suggests a dominant negative spatial association, which is not significant statistically (Figure 4.7b).

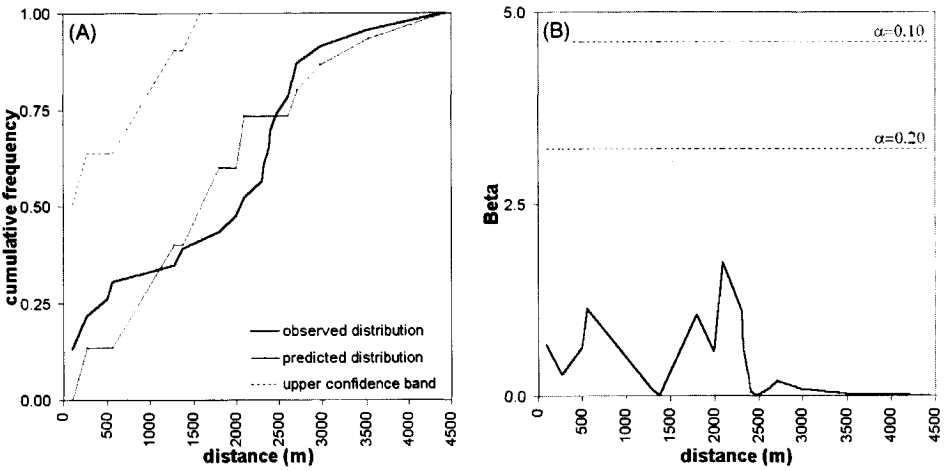

Figure 4.7. Porphyry plutons and nearest batholithic pluton margins, Benguet province: (a) distance distribution and (b) variation of β.

2. Table 4.7 shows the variations in contrast C for cumulative distances from the batholithic pluton margins with respect to the porphyry plutons. The contrasts within 2250 m are not significantly greater than zero, which implies lack of or negative spatial association within this distance range. Beyond 2250 m, there is positive spatial association, which is most statistically significant within 3000 m as indicated by the highest Studentised C.

Table 4.7. Variation of weights and contrasts for cumulative distances from batholithic pluton margins with respect to porphyry plutons, Benguet province*.

Distance buffer (m)	No. of pixels in D_P**	No. of porphyry pluton centroids in D_P**	W+	s(W+)	W-	s(W-)	C	s(C)	C/s(C)
500	40871	5	0.323	0.447	-0.074	0.236	0.396	0.506	0.784
1000	71950	7	0.094	0.378	-0.038	0.250	0.132	0.453	0.291
1500	96140	9	0.055	0.333	-0.034	0.267	0.089	0.427	0.208
2000	114561	11	0.080	0.302	-0.068	0.289	0.149	0.417	0.357
2250	122675	12	0.099	0.289	-0.098	0.302	0.197	0.417	0.472
2500	129745	17	0.391	0.243	-0.651	0.408	1.042	0.475	2.195
2750	136313	20	0.504	0.224	-1.292	0.577	1.797	0.619	2.902
3000	**171746**	**21**	**0.514**	**0.218**	**-1.653**	**0.707**	**2.167**	**0.740**	**2.928**
3250	147386	21	0.475	0.218	-1.604	0.707	2.079	0.740	2.809
3500	152738	21	0.439	0.218	-1.555	0.707	1.994	0.740	2.695
3750	157392	22	0.456	0.213	-2.203	1.000	2.659	1.022	2.601
4000	162238	22	0.426	0.213	-2.155	1.000	2.580	1.022	2.524
4500	171347	23	0.415	0.209					

*Table entries in bold pertain to optimal spatial association. **D_P = domain is present.

3. The distances Y_jmax_r vary between 1500 and 2250 m (Table 4.8). The t-test indicates that the measured correlation coefficients are significantly different from zero at the 99.9% significance level. The spatial association is optimal within 2000 m, within which the spatial association is negative, i.e., $mcdioY_jmax_r$ is less than $mcdooY_jmax_r$.

Table 4.8. Results of distance correlation calculations to quantify spatial association between porphyry plutons and batholithic pluton margins, Benguet province*.

AP	Y_jmax_r (m)	$r_{d_{jx}d_{jy}}$ at Y_jmax_r	t-value for $r_{d_{jx}d_{jy}}$ at Y_jmax_r	$mcdioY_jmax_r$	$mcdooY_jmax_r$
Centre	1750	0.99783	71.155**		
North	1750	0.99941	133.302**		
NE	1750	0.99953	148.673**		
East	1500	0.99539	47.555**		
SE	**2000**	**0.99768**	**67.107****	**0.99578**	**0.99640**
South	2250	0.99896	100.237**		
SW	**2000**	**0.99900**	**102.169****	**0.99842**	**0.99878**
West	**2000**	**0.99161**	**35.149****	**0.98315**	**0.98735**
NW	**2000**	**0.99899**	**101.916****	**0.99789**	**0.99789**

*Table entries in bold pertain to optimal spatial association.

**Calculated t-values are significantly different from zero; critical t-value at α=0.001 and ν=23-2=21 degrees of freedom is 3.527 (Davis, 1973).

The three methods indicate that there is negative spatial association between the porphyry plutons and the batholithic pluton margins within 2000 to 2250 m. The weights of evidence method further indicates that the porphyry plutons are positively spatially associated with the batholithic pluton margins within 3000 m.

4.3.6 Porphyry copper deposits vs. batholithic pluton margins

1. Most parts of the curve for the observed cumulative frequency distribution of nearest distances between the porphyry copper deposits and the batholithic pluton margins are below the predicted curve most conspicuously between 500 and 2000 m (Figure 4.8a). This implies negative spatial association, which, however, is not significant statistically (Figure 4.8b). The highest peak along the β curve shows that the negative spatial association is optimal within 1000 m.

2. Variations in contrast C for cumulative distances from the batholithic pluton margins with respect to the porphyry copper deposits are shown in Table 4.9. The contrasts within 1000 m are not significantly greater than zero, which indicates lack of or negative spatial association within this distance range. The contrasts beyond 1000 m are significantly positive, which imply positive spatial association. The positive spatial association is optimal within 2250 m as indicated by the highest Studentised C.

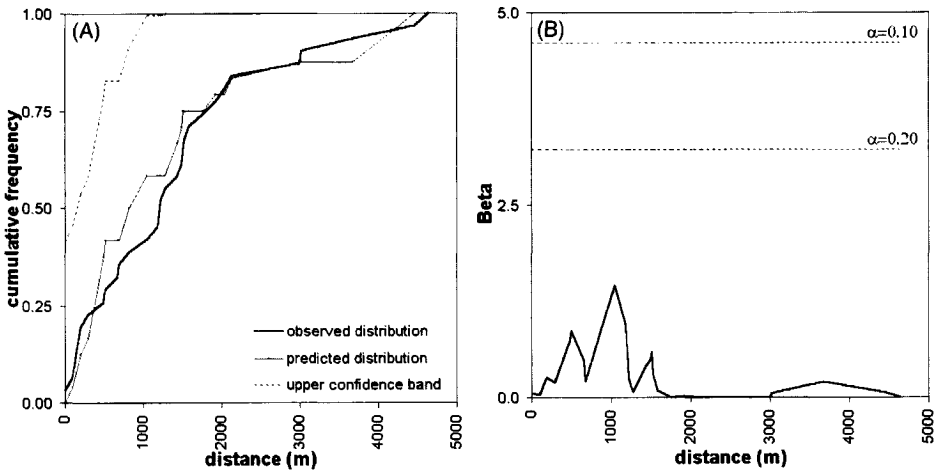

Figure 4.8. Porphyry copper deposits and nearest batholithic pluton margins, Benguet province: (a) distance distribution and (b) variation of β.

Table 4.9. Variation of weights and contrasts for cumulative distances from batholithic pluton margins with respect to porphyry copper deposits, Benguet province*.

Distance buffer (m)	No. of pixels in D_P**	No. of porphyry copper occ. in D_P**	W+	s(W+)	W-	s(W-)	C	s(C)	C/s(C)
500	40871	8	0.494	0.354	-0.127	0.209	0.621	0.410	1.514
1000	71950	12	0.334	0.289	-0.165	0.229	0.499	0.369	1.353
1500	96140	19	0.504	0.229	-0.487	0.289	0.990	0.369	2.686
1750	106006	22	0.553	0.213	-0.712	0.333	1.265	0.396	3.196
2000	114561	24	0.562	0.204	-0.906	0.378	1.468	0.430	3.418
2250	**122675**	**26**	**0.574**	**0.196**	**-1.185**	**0.447**	**1.759**	**0.488**	**3.601**
2500	129745	26	0.518	0.196	-1.132	0.447	1.650	0.488	3.378
2750	136313	26	0.468	0.196	-1.080	0.447	1.548	0.488	3.171
3000	41746	26	0.429	0.196	-1.035	0.447	1.464	0.608	2.998
3250	147386	28	0.464	0.189	-1.497	0.577	1.961	0.608	3.228
3500	152738	28	0.429	0.189	-1.448	0.577	1.876	0.731	3.089
4000	162238	29	0.403	0.186	-1.706	0.707	2.164	0.731	2.959
4500	171347	30	0.383	0.183	-2.355	1.000	2.738	1.017	2.693
4750	175763	31	0.390	0.180					

*Table entries in bold pertain to optimal spatial association. **D_P = domain is present.

3. The distances $Y_j max_r$ vary between 1250 and 2000 m (Table 4.10). The t-test indicates that the measured correlation coefficients are significantly different from zero at the 99.9% significance level. The spatial association between the porphyry copper deposits and the batholithic margins is optimal within 2000 metres. Within 2000 m, the spatial association is negative, i.e., $mcdioY_j max_r$ is less than $mcdooY_j max_r$.

Table 4.10. Results of distance correlation calculations to quantify spatial association between porphyry copper deposits and batholithic pluton margins, Benguet province*.

AP	$Y_j max_r$ (m)	$r_{d_{jx}d_{jy}}$ at $Y_j max_r$	t-value for $r_{d_{jx}d_{jy}}$ at $Y_j max_r$	$mcdioY_j max_r$	$mcdooY_j max_r$
Centre	**2000**	**0.99644**	**63.622****	**0.99350**	**0.99499**
North	1750	0.99900	120.345**		
NE	1500	0.99946	163.608**		
East	1500	0.99587	59.054**		
SE	1750	0.99864	103.291**		
South	**2000**	**0.99918**	**133.284****	**0.99863**	**0.99873**
SW	**2000**	**0.99915**	**130.233****	**0.99870**	**0.99871**
West	1250	0.99471	52.157**		
NW	1250	0.99905	123.243**		

*Table entries in bold pertain to optimal spatial association.

**Calculated t-values are significantly different from zero; critical t-value at α=0.001 and ν=23-2=21 degrees of freedom is 3.527 (Davis, 1973).

The porphyry copper deposits are generally negatively spatially associated with the batholithic pluton margins within 2000 m. The distance distribution method and the weights of evidence method indicate that the negative spatial association is optimal within 1000 m. The distance correlation method indicates that the negative spatial association is optimal within 2000 m. The weights of evidence method further indicates that the porphyry copper deposits are positively spatially associated with the batholithic pluton margins beyond 2000 m. The positive spatial association is optimal within 2250 m.

4.3.7 Discussion

The results of the analyses of the spatial associations are summarised in Table 4.11. The spatial associations of both the porphyry copper deposits and the porphyry plutons with the strike-slip fault discontinuities are significant statistically for similar distances (2250-3000 and 2400-2750 m, respectively). The porphyry copper deposits are spatially associated with the porphyry plutons within an average distance of 2100 m. These quantifications of spatial associations have at least two implications. First, the porphyry copper deposits are spatially, as they are genetically, associated with the porphyry plutons. Second, the porphyry plutons and the porphyry copper deposits are spatially localised within 3 km of the strike-slip fault discontinuities. This latter finding supports the hypothesis that zones around strike-slip discontinuities are where magmatic fluids are focused and are favourable loci for the emplacement of porphyry plutons. Consequently, these zones are favourable targets for exploration for porphyry mineralisation.

The results of the spatial analyses also indicate that both the porphyry copper deposits and the porphyry plutons are negatively spatially associated with the

batholithic pluton margins for similar distances (1000-2000 and 2000-2250 m, respectively). These observations imply that the porphyry copper deposits and the porphyry plutons tend not to be localised preferentially within 2250 m from the batholithic plutons. They tend to be localised preferentially between 2250 and 3000 m away from the batholithic plutons margins. The reason for emplacement of the porphyry plutons away from the batholithic plutons is not entirely clear. The batholithic plutons probably acted as effective buttresses to later ascent of magma (Sillitoe and Gappe, 1984). The later magmatic fluids, however, probably tended to be localised preferentially close to strike-slip fault discontinuities that tend not to cut the batholithic plutons.

Table 4.11. Summary of quantitative characterisation of spatial association between porphyry copper deposits and geological features in Benguet province.

Relation	Distance distribution method			Weights of evidence method			Distance correlation method		
	Spatial assn.	Dist. (m)	β	Spatial assn.	Dist. (m)	Studentised C	Spatial assn.	Dist. (m)	Mean $r_{d_{jx}d_{iy}}$
pp-ssfd[1]	positive	2400	0.874*	positive	2750	3.553	positive	2500	0.99902
pcd-ssfd[2]	positive	2800	7.969	positive	3000	3.929	positive	2250	0.99759
pcd-pp[3]	positive	1300	16.178	positive	1000	7.083	positive	4000	0.99388
pp-bpm[4]	negative	2100	1.734*	none positive	2250 3000	0.472* 2.928	negative	2000	0.99682
pcd-bpm[5]	negative	1000	1.459*	none positive	1000 2250	1.353* 3.601	negative	2000	0.99826

[1]pp-ssfd = porphyry plutons and strike-slip fault discontinuities
[2]pcd-ssfd = porphyry copper deposits and strike-slip fault discontinuities
[3]pcd-pp = porphyry copper deposits and porphyry plutons
[4]pp-bpm = porphyry plutons and batholithic pluton margins
[5]pcd-bpm = porphyry copper deposits and batholithic pluton margins
*not statistically significant

The mechanism of magmatic fluid migration may be attributed to seismic activity, e.g., earthquakes, during tectonic regimes that bring about magmatism (Gold and Soter, 1985; Sibson, 1987). One may speculate that the strike-fault systems were active during emplacement of porphyry intrusions although it is impossible to determine whether the seismic activities coincided precisely or not with these porphyry intrusions. Karig (1983) summarised evidences of tectonic activities of the northern sector of the Philippine Fault system during the last 15 Ma. By 15 Ma, plutonism had commenced in the southern portion of Luzon Central Cordillera with the first stage of batholithic plutons (Wolfe, 1988). Renewed magmatism during the period 10-8 Ma represented the first stage of porphyry copper mineralisation (Wolfe, 1988). Thus, there is substantial indirect evidence that the strike-slip fault systems were active during Neogene porphyry copper mineralisation in southern Luzon Central Cordillera.

4.4 APPLICATION TO BAGUIO DISTRICT

The epithermal gold deposits in the district are fault/fracture-controlled. The northeasterly trending veins are more productive than the northwesterly trending veins (Mitchell and Leach, 1991). Wolfe (1988) suggests that the batholithic plutons are important controls of the epithermal gold deposits. Cooke et al. (1996), however, claim that the epithermal gold mineralisation is related to the younger porphyry plutons. To reconcile the different claims, the spatial associations of the 19 large-scale epithermal gold deposits with the northeast-trending faults/fractures, northwest-trending faults/fractures, batholithic pluton margins and porphyry pluton contacts are characterised quantitatively.

4.4.1 Gold deposits vs. northeast-trending faults/fractures

1. The curve for the observed cumulative frequency distribution of nearest distances between the gold deposits and the northeast-trending faults/fractures is consistently above the predicted curve (Figure 4.9a). This implies positive spatial association. The calculated values of β indicate a statistically significant positive spatial association within 350 to 900 m. The positive spatial association is optimal within about 400 m (Figure 4.9b).

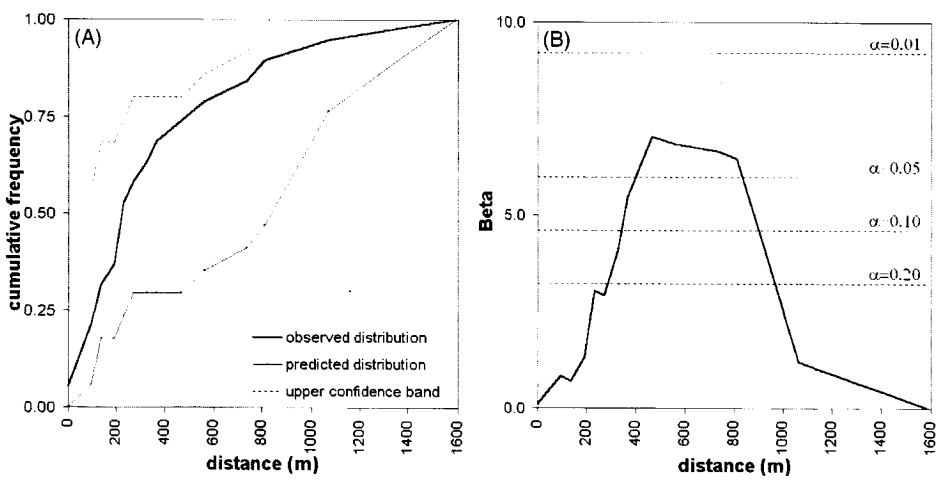

Figure 4.9. Gold deposits and nearest northeast-trending faults/fractures, Baguio district: (a) distance distribution and (b) variation of β.

Table 4.12. Variation of weights and contrasts for cumulative distances from northeast-trending faults/fractures with respect to gold deposits, Baguio district*.

Distance buffer (m)	No. of pixels in D_P**	No. of gold occ. in D_P**	W+	s(W+)	W-	s(W-)	C	s(C)	C/s(C)
100	4723	4	0.628	0.500	-0.117	0.258	0.746	0.563	1.325
200	7820	7	0.684	0.378	-0.254	0.289	0.938	0.476	1.971
300	11827	11	0.722	0.302	-0.535	0.354	1.257	0.465	2.704
400	**14641**	**13**	**0.676**	**0.277**	**-0.725**	**0.408**	**1.401**	**0.494**	**2.837**
500	17296	14	0.583	0.267	-0.805	0.447	1.388	0.521	2.664
600	20928	15	0.461	0.258	-0.870	0.500	1.331	0.563	2.365
700	23623	15	0.340	0.258	-0.733	0.500	1.071	0.563	1.907
800	25556	16	0.326	0.250	-0.910	0.577	1.236	0.629	1.964
900	27348	17	0.319	0.243	-1.200	0.707	1.519	0.748	2.032
1000	29321	17	0.249	0.243	-1.056	0.707	1.305	0.748	1.746
1100	31231	18	0.243	0.236	-1.586	1.000	1.830	1.027	1.781
1200	32752	18	0.196	0.236	-1.435	1.000	1.630	1.027	1.587
1300	33930	18	0.160	0.236	-1.299	1.000	1.459	1.027	1.420
1400	35191	18	0.124	0.236	-1.130	1.000	1.254	1.027	1.220
1500	36400	18	0.090	0.236	-0.936	1.000	1.026	1.028	0.998
1600	37254	19	0.121	0.229					

*Table entries in bold pertain to optimal spatial association. **D_P = domain is present.

2. The contrasts C for cumulative distances from the northeast-trending faults/fractures with respect to the gold deposits are positive, which indicates positive spatial association (Table 4.12). The highest Studentised C indicates that the positive spatial association is optimal within 400 m.

3. The distances Y_jmax_r vary between 350 and 600 m (Table 4.13). The t-test indicates that the measured correlation coefficients are significantly different from zero at the 99.9% significance level. The spatial association is optimal within 400 m, within which the spatial association is positive.

Table 4.13. Results of distance correlation calculations to quantify spatial association between gold deposits and northeast-trending faults/fractures, Baguio district*.

AP	Y_jmax_r (m)	$r_{d_{jx}d_{jy}}$ at Y_jmax_r	t-value for $r_{d_{jx}d_{jy}}$ at Y_jmax_r	$mcdioY_jmax_r$	$mcdooY_jmax_r$
Centre	350	0.99492	40.752**		
North	**400**	**0.99796**	**64.504****	**0.99731**	**0.99603**
NE	**400**	**0.99930**	**110.118****	**0.99892**	**0.99783**
East	600	0.99273	34.005**		
SE	500	0.99705	53.532**		
South	550	0.99879	83.712**		
SW	600	0.99916	100.379**		
West	350	0.99623	43.378**		
NW	**400**	**0.99667**	**50.429****	**0.99507**	**0.99151**

*Table entries in bold pertain to optimal spatial association.
**Calculated t-values are significantly different from zero; critical t-value at α=0.001 and v=19-2=17 degrees of freedom is 3.646 (Davis, 1973).

The gold deposits are positively spatially associated with the northeast-trending faults. The three methods indicate that the positive spatial association is optimal within 400 m.

4.4.2 Gold deposits vs. northwest-trending faults/fractures

1. The curve for the observed cumulative frequency distribution of nearest distances between the gold deposits and the northwest-trending faults/fractures is consistently below the predicted curve (Figure 4.10a). This implies negative spatial association, which is significant statistically within about 1000 metres (Figure 4.10b).

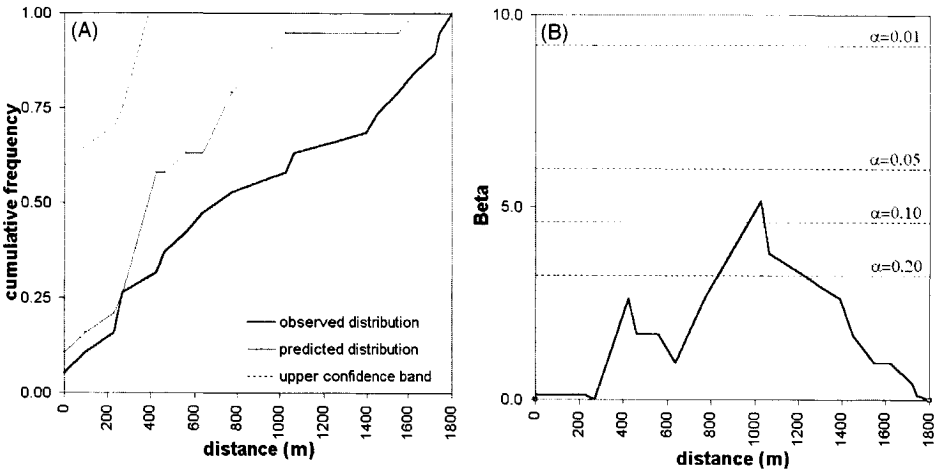

Figure 4.10. Gold deposits and nearest northwest-trending faults/fractures, Baguio district: (a) distance distribution and (b) variation of β.

2. For all successive cumulative distances away from the northwest-trending faults/fractures, the contrasts C are negative (Table 4.14); this implies negative spatial association. This negative spatial association is optimal within 1300 m as indicated by the most negative Studentised C.

3. The distances between the gold deposits and the northwest-trending faults/fractures at which the measured values of $r_{d_{jx}d_{jy}}$ are maximum vary from 800 to 1450 m (Table 4.15). The t-test indicates that these measured correlation coefficients are significantly different from zero at the 99.9% significance level. The spatial association is optimal within 850 m, within which the spatial association is negative, i.e., $mcdioY_jmax_r$ is less than $mcdooY_jmax_r$.

Table 4.14. Variation of weights and contrasts for cumulative distances from northwest-trending faults/fractures with respect to gold deposits, Baguio district*.

Distance buffer (m)	No. of pixels in D_P**	No. of gold occ. in D_P**	W+	s(W+)	W-	s(W-)	C	s(C)	C/s(C)
200	7812	2	-0.569	0.707	0.094	0.243	-0.663	0.748	-0.887
400	14151	5	-0.246	0.447	0.105	0.267	-0.351	0.521	-0.674
600	20218	8	-0.133	0.354	0.109	0.302	-0.242	0.465	-0.521
800	25254	9	-0.238	0.333	0.276	0.316	-0.514	0.460	-1.119
1000	29607	10	-0.291	0.316	0.471	0.333	-0.763	0.460	-1.660
1200	33401	12	-0.230	0.289	0.584	0.378	-0.814	0.476	-1.711
1300	**34666**	**12**	**-0.267**	**0.289**	**0.743**	**0.378**	**-1.010**	**0.476**	**-2.122**
1400	35911	13	-0.222	0.277	0.774	0.408	-0.996	0.494	-2.016
1600	37907	15	-0.133	0.258	0.762	0.500	-0.895	0.563	-1.590
1800	39414	19	-0.065	0.229					

*Table entries in bold pertain to optimal spatial association. **D_P = domain is present.

The gold deposits are negatively spatially associated with the northwest-trending faults/fractures. The distance distribution method and the weights of evidence method indicate that the negative spatial association is optimal within 1000 and 1300 m, respectively. The distance correlation method indicates that the negative spatial association is optimal within 850 m.

Table 4.15. Results of distance correlation calculations to quantify spatial association between gold deposits and northwest-trending faults/fractures, Baguio district*.

AP	$Y_j max_r$ (m)	$r_{d_{jx}d_{jy}}$ at $Y_j max_r$	t-value for $r_{d_{jx}d_{jy}}$ at $Y_j max_r$	$mcdioY_j max_r$	$mcdooY_j max_r$
Centre	**850**	**0.99168**	**31.753****	**0.98654**	**0.98721**
North	**850**	**0.99776**	**61.489****	**0.99622**	**0.99667**
NE	**850**	**0.99470**	**39.894****	**0.99075**	**0.99137**
East	800	0.98431	23.002**		
SE	1450	0.99911	97.910**		
South	950	0.99692	50.468**		
SW	800	0.99551	43.378**		
West	800	0.98558	24.018**		
NW	1050	0.99760	59.539**		

*Table entries in bold pertain to optimal spatial association.
**Calculated t-values are significantly different from zero; critical t-value at α=0.001 and ν=19-2=17 degrees of freedom is 3.646 (Davis, 1973).

4.4.3 Gold deposits vs. batholithic pluton margins

1. The curve for the observed cumulative frequency distribution of nearest distances between the gold deposits and the batholithic pluton margins is above the predicted curve within 800 m and below the predicted curve beyond 800 m (Figure 4.11a). This implies positive spatial association within 800 m and

negative spatial association beyond 800 m. The positive spatial association is optimal within 400 m (Figure 4.11b).

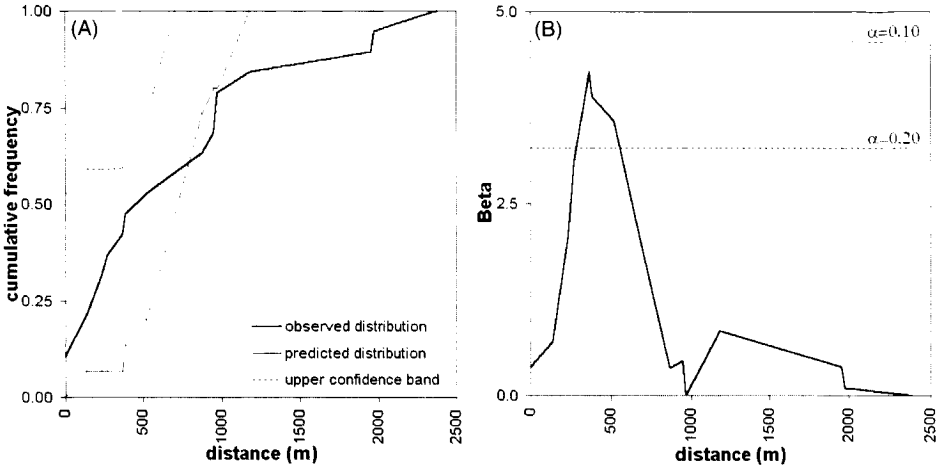

Figure 4.11. Gold deposits and nearest batholithic pluton margins, Baguio district: (a) distance distribution and (b) variation of β.

Table 4.16. Variation of weights and contrasts for cumulative distances from batholithic pluton margins with respect to gold deposits, Baguio district*.

Distance buffer (m)	No. of pixels in D_P**	No. of gold occ. in D_P**	W+	s(W+)	W-	s(W-)	C	s(C)	C/s(C)
250	5581	6	0.815	0.408	-0.229	0.277	1.044	0.494	2.114
500	10725	9	0.619	0.322	-0.347	0.316	0.967	0.460	2.103
750	14581	10	0.417	0.316	-0.321	0.333	0.739	0.460	1.607
1000	**17907**	**15**	**0.617**	**0.258**	**-1.003**	**0.500**	**1.621**	**0.563**	**2.880**
1250	20514	16	0.546	0.250	-1.177	0.577	1.723	0.629	2.738
1500	22898	16	0.436	0.250	-1.059	0.577	1.495	0.629	2.376
1750	24785	16	0.357	0.250	-0.956	0.577	1.312	0.629	2.085
2000	26186	18	0.420	0.236	-1.970	1.000	2.389	1.027	2.325
2250	27466	18	0.372	0.236	-1.885	1.000	2.257	1.027	2.197
2500	28441	19	0.391	0.229					

*Table entries in bold pertain to optimal spatial association. **D_P = domain is present.

2. The contrasts C for cumulative distances from the batholithic pluton margins with respect to the gold deposits contrasts are positive, which indicates positive spatial association (Table 4.16). The highest Studentised C indicates that the positive spatial association is optimal for a distance of 1000 m.

3. The distances $Y_j max_r$ vary between 650 and 950 m (Table 4.17). The t-test indicates that the measured correlation coefficients are significantly different

from zero at the 99.9% significance level. The spatial association is optimal within 950 metres. Within this distance, the spatial association is positive, i.e., $mcdioY_jmax_r$ is greater than $mcdooY_jmax_r$.

Table 4.17. Results of distance correlation calculations to quantify spatial association between gold deposits and batholithic pluton margins, Baguio district.

AP	Y_jmax_r (m)	$r_{d_{jx}d_{jy}}$ at Y_jmax_r	t-value for $r_{d_{jx}d_{jy}}$ at Y_jmax_r	$mcdioY_jmax_r$	$mcdooY_jmax_r$
Centre	650	0.99167	31.748**		
North	700	0.99747	57.867**		
NE	650	0.99624	47.425**		
East	**950**	**0.98458**	**23.201****	**0.98343**	**0.97323**
SE	550	0.99739	56.912**		
South	**950**	**0.99660**	**49.885****	**0.99603**	**0.99325**
SW	850	0.99624	47.438**		
West	550	0.97386	17.667**		
NW	**950**	**0.99476**	**40.099****	**0.99369**	**0.99031**

*Table entries in bold pertain to optimal spatial association.
**Calculated t-values are significantly different from zero; critical t-value at α=0.001 and v=19-2=17 degrees of freedom is 3.646 (Davis, 1973).

The distance distribution method indicates that there is positive spatial association between the gold deposits and the batholithic pluton margins within 800 m and that the positive spatial association is optimal within 400 m. The weights of evidence method and the distance correlation method indicate that the positive spatial association between the gold deposits and the batholithic pluton margins is optimal within 1000 and 950 m, respectively.

4.4.4 Gold deposits vs. porphyry pluton contacts

1. The curve for the observed cumulative frequency distribution of nearest distances between the gold deposits and the porphyry plutons is above the predicted curve (Figure 4.12a). This implies positive spatial association, which, however, is not statistically significant (Figure 4.12b). Nevertheless, the highest peak along the β curve suggests that the positive spatial association is optimal within about 2700 m.

2. The variations in contrast for cumulative distances from the batholithic pluton margins with respect to the gold deposits are shown in Table 4.18. The contrasts C for all cumulative distances are positive, which indicates positive spatial association. According to the maximum Studentised C, the positive spatial association is optimal within 2750 m.

3. The distances $Y_i max_r$ vary between 1500 and 2800 m (Table 4.19). The t-test indicates that the measured correlation coefficients are significantly different from zero at the 99.9 % significance level. The spatial association is optimal within 2800 m, within which the spatial association is positive.

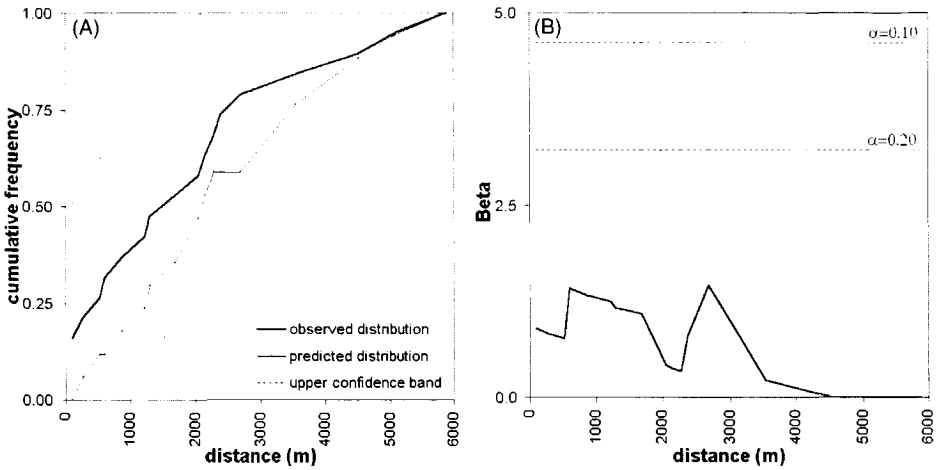

Figure 4.12. Gold deposits and nearest porphyry pluton contacts, Baguio district: (a) distance distribution and (b) variation of β.

Table 4.18. Variation of weights and contrasts for cumulative distances from porphyry pluton contacts with respect to gold deposits, Baguio district*.

Distance buffer (m)	No. of pixels in D_P**	No. of gold occ. in D_P**	W+	s(W+)	W-	s(W-)	C	s(C)	C/s(C)
500	2699	4	1.189	0.500	-0.170	0.258	1.359	0.563	2.413
1000	5051	7	1.121	0.378	-0.334	0.289	1.453	0.476	3.054
1500	7915	9	0.923	0.334	-0.433	0.316	1.357	0.460	2.952
2000	10748	10	0.723	0.316	-0.452	0.333	1.175	0.460	2.556
2500	13524	14	0.829	0.267	-0.947	0.447	1.776	0.521	3.409
2750	**14922**	**15**	**0.800**	**0.258**	**-1.120**	**0.500**	**1.920**	**0.563**	**3.411**
3000	16210	15	0.717	0.258	-1.071	0.500	1.788	0.563	3.178
3500	19096	15	0.553	0.258	-0.953	0.500	1.506	0.563	2.676
4000	22072	16	0.473	0.250	-1.102	0.577	1.574	0.629	2.502
4500	25212	16	0.340	0.250	-0.930	0.577	1.270	0.629	2.018
5000	28097	17	0.292	0.243	-1.148	0.707	1.440	0.748	1.926
5500	30688	18	0.261	0.236	-1.636	1.000	1.896	1.027	1.846
6000	32973	19	0.243	0.229					

*Table entries in bold pertain to optimal spatial association. **D_P = domain is present.

The gold deposits are positively spatially associated with the porphyry pluton contacts. The three methods indicate that the positive spatial association is optimal within similar distances of 2700, 2750 and 2800 m, respectively.

Table 4.19. Results of distance correlation calculations to quantify spatial association between gold deposits and porphyry pluton contacts, Baguio district*.

AP	Y_jmax_r (m)	$r_{d_{jx}d_{jy}}$ at Y_jmax_r	t-value for $r_{d_{jx}d_{jy}}$ at Y_jmax_r	$mcdioY_jmax_r$	$mcdooY_jmax_r$
Centre	**2800**	**0.91699**	**9.478****	**0.88145**	**0.88026**
North	**2800**	**0.97932**	**20.059****	**0.96911**	**0.96700**
NE	**2800**	**0.96317**	**14.769****	**0.94037**	**0.93890**
East	1700	0.87082	7.304**		
SE	1500	0.98449	23.135**		
South	2600	0.97337	15.508**		
SW	2200	0.97633	18.613**		
West	1700	0.86746	7.189**		
NW	1600	0.96368	14.878**		

*Table entries in bold pertain to optimal spatial association.

**Calculated t-values are significantly different from zero; critical t-value at α=0.001 and ν=19-2=17 degrees of freedom is 3.646 (Davis, 1973).

4.4.5 Discussion

The results of the quantitative characterisation of the spatial associations of the gold deposits with the different geological features using the three methods produced similar results (Table 4.20). The gold deposits are (a) positively spatially associated with the northeast-trending faults/fractures within 400 m, (b) negatively associated with the northwest-trending faults/fractures within 850-1300 m, (c) positively associated with the batholithic pluton margins within 400-1000 m, and (d) positively associated with the porphyry pluton contacts within 2700-2800 m. The positive spatial association between the gold deposits and the northeast-trending faults/fractures is strongest, between the gold deposits and the batholithic pluton margins it is intermediate and between the gold deposits and the porphyry pluton contacts it is weakest.

Table 4.20. Summary of results of quantitative characterisation of spatial association between gold deposits and geological features in Baguio district.

Relation	Distance distribution method			Weights of evidence method			Distance correlation method		
	Spatial assn.	Dist. (m)	β	Spatial assn.	Dist. (m)	Studentised C	Spatial assn.	Dist. (m)	Mean $r_{d_{jx}d_{jy}}$
gd-neff[1]	positive	400	7.034	positive	400	2.837	positive	400	0.99885
gd-nwff[2]	negative	1000	5.158	negative	1300	-2.122	negative	850	0.99471
gd-bpm[3]	positive	400	4.211	positive	1000	2.880	positive	950	0.99198
gd-ppc[4]	positive	2700	1.453*	positive	2750	3.411	positive	2800	0.95316

[1]gd-neff = gold deposits and northeast-trending faults/fractures

[2]gd-nwff = gold deposits and northwest-trending faults/fractures

[3]gd-bpm = gold deposits and batholithic pluton margins

[4]gd-ppc = gold deposits and porphyry pluton contacts

*not statistically significant

The strong positive spatial association between the gold deposits and the northeast-trending faults/fractures is consistent with field observations that the more productive auriferous epithermal quartz veins are associated with northeasterly trending faults/fractures (Mitchell and Leach, 1991). In the Baguio district, the northeast trending faults/fractures are conjugate shears of the northwest-trending strike-slip fault/fracture systems (Balce et al., 1980). The northeast-trending faults/fractures are extensional or 'open' structures whilst the northwest-trending faults/fractures are tensional or 'open' structures. Thus, the northeast-trending faults/fractures are more favourable for vein formation than the northwest-trending faults/fractures. The lower favourability of the 'closed' northwest-trending faults/fractures explains the negative spatial association between the gold deposits and the northwest-trending faults/fractures.

The intermediate positive spatial association between the gold deposits and the Agno Batholith margins is consistent with earlier findings, which suggest that the gold deposits are genetically associated with the Agno Batholith (Wolfe, 1988). The weak positive spatial association between the gold deposits and the porphyry intrusive contacts is inconsistent with the findings of Mitchell and Leach (1991) and Cooke et al. (1996) that the gold deposits are genetically associated with the younger intrusive porphyries. Whilst the findings of Mitchell and Leach (1991) and Cooke et al. (1996) are based on deposit-scale studies, the quantified spatial association between the gold deposits and the porphyry plutons is based on a district-scale map. The weak positive spatial association between the gold deposits and the porphyry plutons probably implies that whilst gold deposits are observed on the surface, they are associated with smaller bodies of porphyry plutons that are either non-outcropping or are not mappable at the scale of Figure 2.11. Larger scale maps may provide a more detailed characterisation of the spatial association between the gold deposits and the porphyry plutons. This implies that the scale of mapping is important in the characterisation of spatial associations between mineral deposits and geological features.

The positive spatial associations of the gold deposits with the Agno Batholith margins and the porphyry intrusive contacts suggest that both magmatic regimes acted as heat sources for the epithermal gold mineralisation in the area. Whilst previous workers suggest that the gold mineralisation in the study area is genetically associated with either the Agno Batholith or the porphyry intrusives (Wolfe, 1988; Mitchell and Leach, 1991; Cooke et al., 1996), the results of the study lead to a hypothesis that the gold deposits are genetically associated with both magmatic regimes. The intrusion of the Agno Batholith probably caused a first pulse of epithermal mineralisation, while the younger porphyry intrusives caused a second pulse of epithermal mineralisation and/or remobilisation of the epithermal deposits formed earlier.

4.5 APPLICATION TO ABRA AREA

JICA (1980) hypothesised the following geological episodes that brought about porphyry copper mineralisation in the Abra area. First, batholithic plutons (granodiorite and quartz diorite) intruded into the volcanic rocks along north-trending fault/fracture systems. Second, northeast-trending faults/fractures were formed following the intrusion of the batholithic plutons. Third, porphyry plutons (quartz diorite porphyry) intruded along north-trending and northeast-trending faults/fractures. Fourth, hydrothermal solutions related to porphyry pluton intrusions formed porphyry copper mineralisation. These hypotheses were based on field observations that (1) the porphyry copper deposits are distributed near and along the margins of batholithic plutons where porphyry plutons have been intruded and (2) they exhibit close spatial relationships with north-trending and northeast-trending faults/fractures.

To contribute to the understanding of the genesis of the porphyry copper deposits in the Abra area, quantitative characterisations are made of their spatial associations with (a) batholithic pluton margins, (b) porphyry pluton centroids, (c) north-trending faults/fractures, (d) northeast-trending faults/fractures. In addition, the spatial associations of the porphyry copper mineralisation with northwest-trending faults/fractures and with intersections of regional faults (i.e., north-trending and northeast-trending faults/fractures) are characterised quantitatively to determine indirectly whether these geological features played a genetic role in the porphyry copper mineralisation in the area. There are more northwest-trending faults/fractures than east-west trending faults/fractures mapped in the area (see Figures 2.13 and 2.14) so that the spatial association of the porphyry copper deposits with the latter are not studied. The intersections of regional north-trending and northeast-trending faults/fractures are interpreted as zones of greater rock permeability, which can favour hydrothermal fluid circulation; thus, the spatial association of the porphyry copper deposits with these geological features are studied.

4.5.1 Porphyry copper deposits vs. granodiorite margins

1. The curve for the observed cumulative frequency distribution of nearest distances between the porphyry copper deposits and the granodiorite margins is mainly below the predicted curve within 1100 m (Figure 4.13a). It is just above the predicted curve beyond 1100 m. A negative spatial association within 1100 m is thus implied which, however, is not statistically significant (Figure 4.13b). The highest peak along the β curve indicates that the negative spatial association is optimal within about 800 m.

2. The variations in contrast C for cumulative distances from the granodiorite margins with respect to the porphyry copper deposits are shown in Table 4.21. The contrasts within 1000 m are not significantly greater than zero, which

indicates lack of or negative spatial association. Beyond 1000 m up to 3000 m, the contrasts are positive, which indicates positive spatial association. The highest Studentised C indicates that the positive spatial association is optimal, but not statistically significant, within 1500 m.

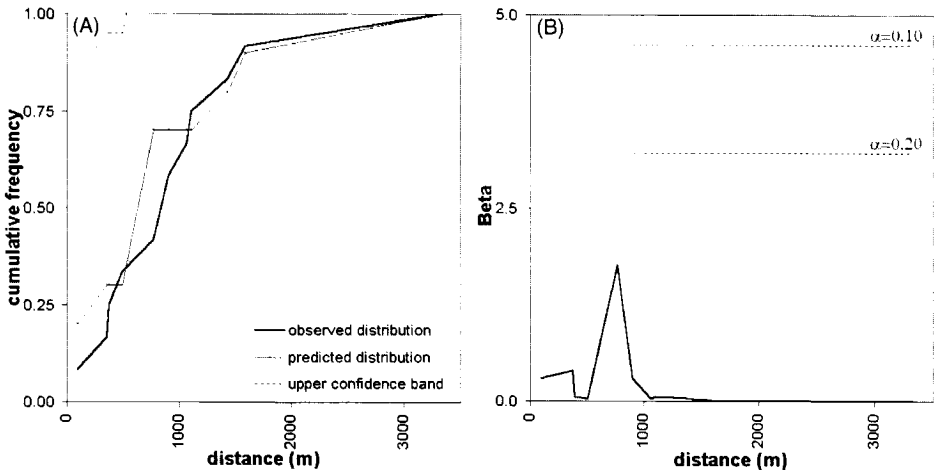

Figure 4.13. Porphyry copper deposits and nearest granodiorite margins, Abra area: (a) distance distribution and (b) variation of β.

Table 4.21. Variation of weights and contrasts for cumulative distances from granodiorite margins with respect to porphyry copper deposits, Abra area*.

Distance buffer (m)	No. of pixels in D_P**	No. of porphyry copper occ. in D_P**	W+	s(W+)	W-	s(W-)	C	s(C)	C/s(C)
500	25477	3	-0.103	0.577	0.037	0.333	-0.139	0.667	-0.209
1000	42892	7	0.224	0.378	-0.247	0.447	0.471	0.586	0.805
1250	49537	9	0.331	0.333	-0.613	0.577	0.944	0.667	1.416
1500	**55421**	**10**	**0.324**	**0.316**	**-0.869**	**0.707**	**1.193**	**0.775**	**1.540**
1750	60021	10	0.244	0.316	-0.734	0.707	0.979	0.775	1.264
2000	63774	11	0.279	0.302	-1.303	1.000	1.582	1.044	1.514
2500	69647	11	0.191	0.302	-1.069	1.000	1.260	1.044	1.206
3000	73204	11	0.141	0.302	-0.895	1.000	1.036	1.044	0.992
3500	75441	12	0.198	0.289					

*Table entries in bold pertain to optimal spatial association. **D_P = domain is present.

3. The distances between the porphyry copper deposits and the granodiorite margins at which the measured values of $r_{d_{jx}d_{jy}}$ are highest vary between 750 and 1250 m (Table 4.22). The t-test indicates that these measured correlation coefficients are significantly different from zero at the 99.9% significance level.

The spatial association is optimal within 1000 m, within which the spatial association is negative.

Table 4.22. Results of distance correlation calculations to quantify spatial association between porphyry copper deposits and granodiorite margins, Abra area.

AP	$Y_j max_r$ (m)	$r_{d_{jx}d_{jy}}$ at $Y_j max_r$	t-value for $r_{d_{jx}d_{jy}}$ at $Y_j max_r$	$mcdioY_j max_r$	$mcdooY_j max_r$
Centre	**1000**	**0.99660**	**38.007****	**0.99195**	**0.99536**
North	750	0.99983	169.919**		
NE	**1000**	**0.99873**	**62.657****	**0.99757**	**0.99791**
East	1250	0.99300	26.593**		
SE	**1000**	**0.99701**	**40.789****	**0.99415**	**0.99638**
South	**1000**	**0.99861**	**60.619****	**0.99735**	**0.99836**
SW	750	0.99971	130.760**		
West	1250	0.99497	31.416**		
NW	**1000**	**0.99864**	**30.618****	**0.99678**	**0.99760**

*Table entries in bold pertain to optimal spatial association.
**Calculated t-values are significantly different from zero; critical t-value at α=0.001 and ν=12-2=10 degrees of freedom is 4.144 (Davis, 1973).

The three methods indicate that the porphyry copper deposits are negatively spatially associated with the granodiorite margins within 800 to 1000 m. In addition, the weights of evidence method indicates that the porphyry copper deposits have positive spatial association with the granodiorite margins within 1500 m.

4.5.2 Porphyry copper deposits vs. quartz diorite margins

1. The curve for the observed cumulative frequency distribution of nearest distances between the porphyry copper deposits and the quartz diorite margins is mainly below the predicted curve within 5000 m (Figure 4.14a). It is just above the predicted curve beyond 5000 metres. A negative spatial association within 5000 m is thus implied which, however, is not significant statistically (Figure 4.14b). The highest peak along the β curve suggests that the negative spatial association is optimal within about 2600 m.

2. The contrasts C for cumulative distances from the quartz diorite margins with respect to the porphyry copper deposits are either negative or not significantly greater than zero (Table 4.23). This indicates negative or no spatial association. The most negative Studentised C indicates that the negative spatial association is optimal, yet not significant statistically, within 2500 m.

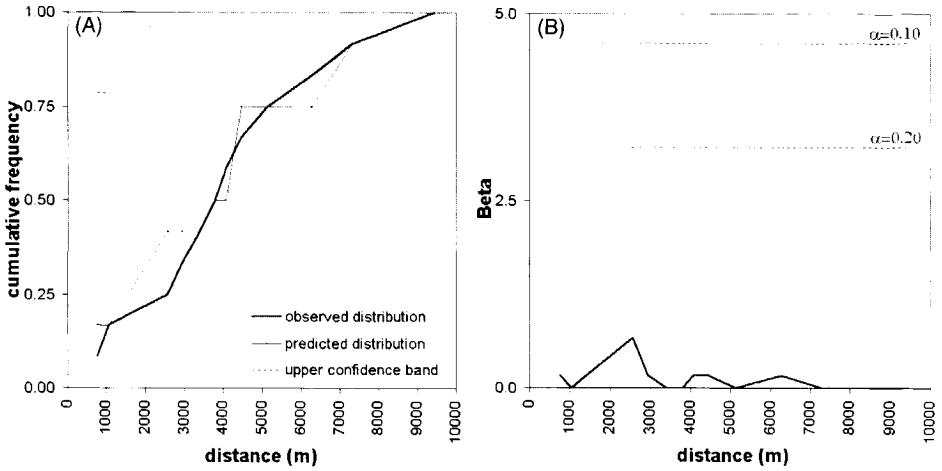

Figure 4.14. Porphyry copper deposits and nearest quartz diorite margins, Abra area: (a) distance distribution and (b) variation of β.

Table 4.23. Variation of weights and contrasts for cumulative distances from quartz diorite margins with respect to porphyry copper deposits, Abra area*.

Distance buffer (m)	No. of pixels in D_P**	No. of porphyry copper occ. in D_P**	W+	s(W+)	W-	s(W-)	C	s(C)	C/s(C)
1000	15177	1	-0.683	1.000	0.093	0.302	-0.777	1.045	-0.744
1500	21366	2	-0.332	0.707	0.082	0.316	-0.414	0.775	-0.535
2000	27181	2	-0.573	0.707	0.168	0.316	-0.741	0.775	-0.957
2500	**33205**	**2**	**-0.773**	**0.707**	**0.266**	**0.316**	**-1.039**	**0.775**	**-1.341**
3000	39475	4	-0.253	0.500	0.155	0.354	-0.408	0.612	-0.667
3500	46314	5	-0.190	0.447	0.161	0.378	-0.351	0.586	-0.599
4000	52535	6	-0.133	0.408	0.154	0.408	-0.287	0.577	-0.497
5000	63646	9	0.080	0.333	-0.208	0.577	0.289	0.667	0.433
6000	72988	10	0.049	0.316	-0.214	0.707	0.262	0.775	0.339
7000	80801	10	-0.053	0.316	0.317	0.707	-0.370	0.775	-0.478
8000	85758	11	-0.017	0.302	0.211	1.000	-0.228	1.045	-0.219
9000	89223	11	-0.057	0.302	1.029	1.000	-1.086	1.045	-1.039
10000	91609	12	0.004	0.289					

*Table entries in bold pertain to optimal spatial association. **D_P = domain is present.

3. The distances Y_jmax_r vary between 3000 and 7000 m (Table 4.24). The t-test indicates that the measured correlation coefficients are significantly different from zero at the 99.9% significance level. The spatial association is optimal within 5000 m. Within this distance, the spatial association is negative, i.e., $mcdioY_jmax_r$ is less than $mcdooY_jmax_r$.

Table 4.24. Results of distance correlation calculations to quantify spatial association between porphyry copper deposits and quartz diorite margins, Abra area*.

AP	Y_jmax_r (m)	$r_{d_{jx}d_{jy}}$ at Y_jmax_r	t-value for $r_{d_{jx}d_{jy}}$ at Y_jmax_r	$mcdioY_jmax_r$	$mcdooY_jmax_r$
Centre	3500	0.97702	14.494**		
North	**5000**	**0.98243**	**16.648****	**0.97774**	**0.97829**
NE	5500	0.97822	14.905**		
East	4500	0.97499	13.872**		
SE	**5000**	**0.95501**	**10.183****	**0.90690**	**0.91537**
South	**5000**	**0.97736**	**14.608****	**0.95190**	**0.96235**
SW	7000	0.98949	21.636**		
West	3000	0.98123	16.089**		
NW	4500	0.96200	11.142**		

*Table entries in bold pertain to optimal spatial association.
**Calculated t-values are significantly different from zero; critical t-value at α=0.001 and v=12-2=10 degrees of freedom is 4.144 (Davis, 1973).

The three methods indicate that the porphyry copper deposits are generally negatively spatially associated with the quartz diorite margins within 5000 m. The distance distribution method and the weights of evidence method indicate that the negative spatial association is optimal within 2600 and 2500 m, respectively. The distance correlation method indicates that the negative spatial association is optimal within 5000 m.

4.5.3 Porphyry copper deposits vs. porphyry pluton centroids

1. The curve for the observed cumulative frequency distribution of nearest distances between the porphyry copper deposits and the porphyry pluton centroids is mainly below the predicted curve particularly between 2600 and 6900 m (Figure 4.15a). This implies a negative spatial association. Figure 4.15b indicates that the negative spatial association is not significant statistically. The highest peak along the β curve suggests that the negative spatial association is optimal within about 5700 m.

2. The variations in contrast C for cumulative distances from porphyry pluton centroids with respect to the porphyry copper deposits are shown in Table 4.25. The contrasts between 2500 and 6000 m are not significantly greater than zero, which indicates lack of or negative spatial association. This lack of or negative spatial association is optimal within 5000 m, within which there is lowest contrast and Studentised C. The contrasts are significantly greater than zero within 2000 m, which indicates positive spatial association. The positive spatial association is optimal within 1500 m, as indicated by the highest Studentised C.

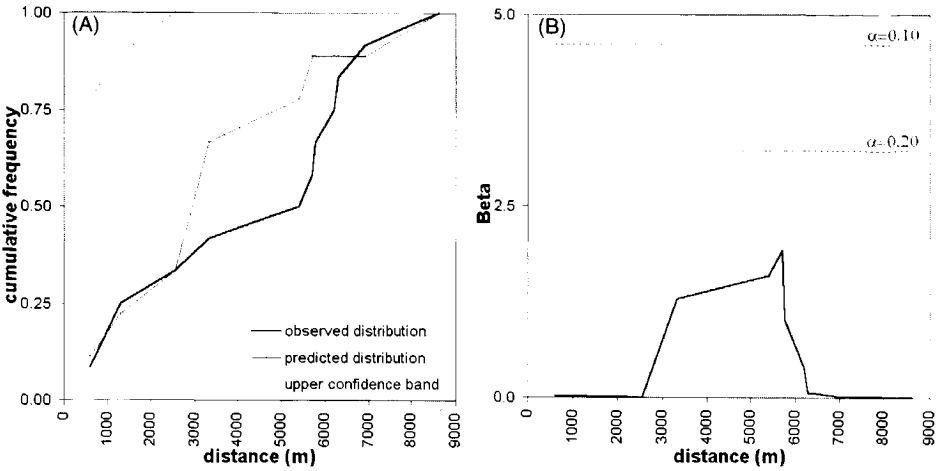

Figure 4.15. Porphyry copper deposits and nearest porphyry plutons, Abra area: (a) distance distribution and (b) variation of β.

Table 4.25. Variation of weights and contrasts for cumulative distances from porphyry pluton centroids with respect to porphyry copper deposits, Abra area*.

Distance buffer (m)	No. of pixels in D_P**	No. of porphyry copper occ. in D_P**	W+	s(W+)	W-	s(W-)	C	s(C)	C/s(C)
1000	3532	1	0.775	1.000	-0.048	0.302	0.823	1.045	0.787
1500	**6658**	**3**	**1.240**	**0.577**	**-0.213**	**0.333**	**1.452**	**0.667**	**2.178**
2000	10198	3	0.813	0.577	-0.170	0.333	0.983	0.667	1.475
2500	14063	3	0.492	0.577	-0.122	0.333	0.613	0.667	0.920
3000	17923	4	0.537	0.500	-0.189	0.354	0.725	0.612	1.185
3500	22074	5	0.552	0.447	-0.265	0.378	0.816	0.586	1.394
4000	26322	5	0.376	0.447	-0.202	0.378	0.577	0.586	0.986
4500	30801	5	0.218	0.447	-0.131	0.378	0.350	0.586	0.597
5000	**35508**	**5**	**0.076**	**0.447**	**-0.051**	**0.378**	**0.127**	**0.586**	**0.217**
5500	40424	6	0.129	0.408	-0.114	0.408	0.243	0.577	0.421
6000	45153	8	0.306	0.354	-0.423	0.500	0.729	0.612	1.191
7000	54831	11	0.430	0.302	-1.578	1.000	2.008	1.044	1.923
8000	63761	11	0.279	0.302	-1.303	1.000	1.582	1.044	1.515
9000	71114	12	0.257	0.289					

*Table entries in bold pertain to optimal spatial associations. **D_P = domain is present.

3. The distances between the porphyry copper deposits and the porphyry pluton centroids at which the measured $r_{d_{jx}d_{jy}}$'s are maximum vary between 3500 and 5500 m (Table 4.26). The t-test indicates that these measured correlation coefficients are significantly different from zero at the 99.9% significance level. The spatial association is optimal within 4000 m, within which the spatial association is negative.

Table 4.26. Results of distance correlation calculations to quantify spatial association between porphyry copper deposits and porphyry pluton centroids, Abra area*.

AP	Y_jmax_r (m)	$r_{d_{jx}d_{jy}}$ at Y_jmax_r	t-value for $r_{d_{jx}d_{jy}}$ at Y_jmax_r	$mcdioY_jmax_r$	$mcdooY_jmax_r$
Centre	**4000**	**0.95749**	**10.497****	**0.89742**	**0.93817**
North	**4000**	**0.99210**	**25.012****	**0.97782**	**0.98636**
NE	**4000**	**0.98898**	**21.127****	**0.97192**	**0.98126**
East	3500	0.96192	11.129**		
SE	**4000**	**0.96954**	**12.517****	**0.92674**	**0.94751**
South	5500	0.98934	21.482**		
SW	4500	0.98704	19.452**		
West	4500	0.95795	10.558**		
NW	4500	0.99312	26.827**		

*Table entries in bold pertain to optimal spatial association.

**Calculated t-values are significantly different from zero; critical t-value at α=0.001 and ν=12-2=10 degrees of freedom is 4.144 (Davis, 1973).

The porphyry copper deposits are mostly negatively spatially associated with the porphyry plutons. The distance distribution method and weights of evidence method indicate that the negative spatial association is optimal within 5700 and 5000 m, respectively. The distance correlation method indicates that the negative spatial association is optimal within 4000 m. The weights of evidence method further indicates that some of the porphyry copper deposits are positively spatially associated with the porphyry plutons within 1500 m.

4.5.4 Porphyry copper deposits vs. north-trending faults/fractures

1. The curve for the observed cumulative frequency distribution of nearest distances between the porphyry copper deposits and the north-trending faults/fractures is mostly above the predicted curve (Figure 4.16a). A positive spatial association is thus implied which, however, is not significant statistically (Figure 4.16b). The highest peak along the β curve suggests that the positive spatial association is optimal within about 1250 m.

2. The contrasts C for cumulative distances from north-trending faults/fractures with respect to the porphyry copper deposits are low yet significantly greater than zero mostly within 2000 m (Table 4.27). This indicates a tendency for a positive spatial association. The highest Studentised C indicates that the positive spatial association is optimal yet not significant statistically within 1500 m.

3. The distances Y_jmax_r vary between 750 and 2000 m (Table 4.28). The t-test indicates that the measured correlation coefficients are significantly different from zero at the 99.9% significance level. The spatial association is optimal within 1500 m, within which the spatial association is positive, i.e., $mcdioY_jmax_r$ is greater than $mcdooY_jmax_r$.

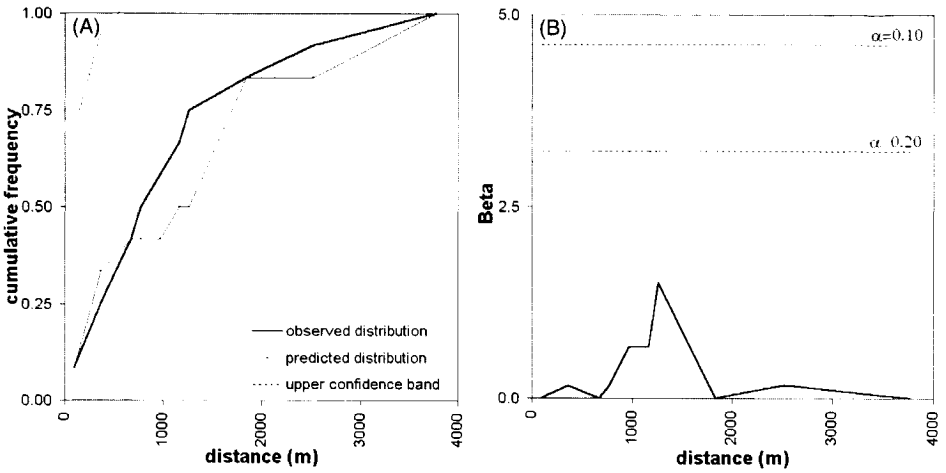

Figure 4.16. Porphyry copper deposits and nearest north-trending faults/fractures, Abrea area: (a) distance distribution and (b) variation of β.

Table 4.27. Variation of weights and contrasts for cumulative distances from north-trending faults/fractures with respect to porphyry copper deposits, Abra area*.

Distance buffer (m)	No. of pixels in D_P**	No. of porphyry copper occ. in D_P**	W+	s(W+)	W-	s(W-)	C	s(C)	C/s(C)
500	20237	3	0.128	0.577	-0.039	0.333	0.167	0.667	0.250
1000	37010	7	0.371	0.378	-0.361	0.447	0.732	0.586	1.250
1250	43201	8	0.350	0.354	-0.464	0.500	0.814	0.612	1.330
1500	**49849**	**9**	**0.325**	**0.333**	**-0.605**	**0.577**	**0.930**	**0.667**	**1.395**
1750	55453	9	0.218	0.333	-0.463	0.577	0.681	0.667	1.021
2000	59758	10	0.249	0.316	-0.743	0.707	0.991	0.775	1.280
2500	68394	10	0.114	0.316	-0.430	0.707	0.544	0.775	0.702
3000	75284	11	0.113	0.302	-0.778	1.000	0.891	1.045	0.853
3500	81704	11	0.031	0.302	-0.292	1.000	0.323	1.045	0.309
4000	85199	12	0.076	0.289					

*Table entries in bold pertain to optimal spatial association. **D_P = domain is present.

The porphyry copper deposits are positively spatially associated with the north-trending faults/fractures. The distance distribution method indicates that the positive association is optimal within 1250 m. The weights of evidence method and the distance correlation method indicate that the positive spatial association is optimal within 1500 m.

Table 4.28. Results of distance correlation calculations to quantify spatial association between porphyry copper deposits and north-trending faults/fractures, Abra area*.

AP	$Y_j max_r$ (m)	$r_{d_{jx}d_{jy}}$ at $Y_j max_r$	t-value for $r_{d_{jx}d_{jy}}$ at $Y_j max_r$	$mcdioY_j max_r$	$mcdooY_j max_r$
Centre	750	0.99869	61.777**		
North	1000	0.99964	117.397**		
NE	**1500**	**0.99885**	**66.012****	**0.99796**	**0.99676**
East	**1500**	**0.98671**	**19.200****	**0.97491**	**0.97399**
SE	1250	0.99290	26.405**		
South	1000	0.99908	73.599**		
SW	1250	0.99894	68.498**		
West	2000	0.98648	19.036**		
NW	**1500**	**0.99799**	**49.809****	**0.99586**	**0.99524**

*Table entries in bold pertain to optimal spatial association.
**Calculated t-values are significantly different from zero; critical t-value at α=0.001 and ν=12-2=10 degrees of freedom is 4.144 (Davis, 1973).

4.5.5 Porphyry copper deposits vs. northeast-trending faults/fractures

1. The curve for the observed cumulative frequency distribution of nearest distances between the porphyry copper deposits and the northeast-trending faults/fractures is mostly below the predicted curve (Figure 4.17a). A negative spatial association is thus implied, which, however, is not significant statistically (Figure 4.17b). The highest peak along the β curve suggests that the negative spatial association is optimal within about 950 metres.

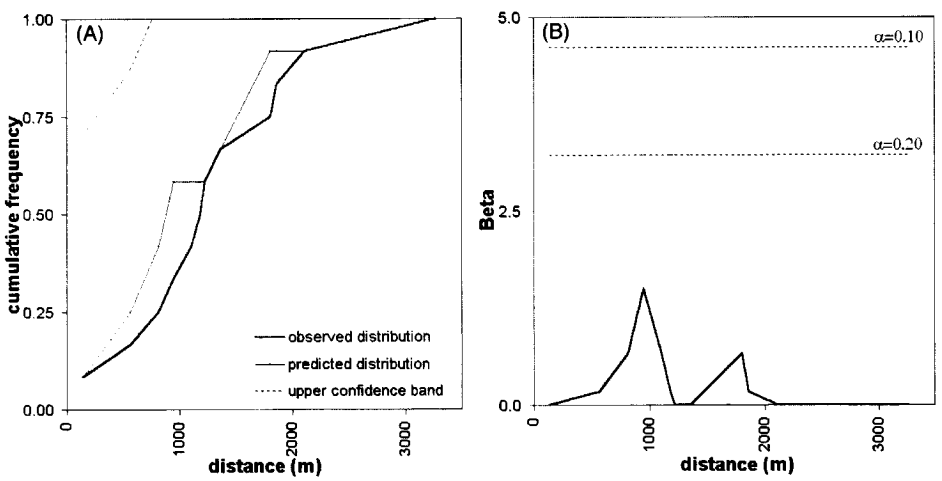

Figure 4.17. Porphyry copper deposits and nearest northeast-trending faults/fractures, Abra area: (a) distance distribution and (b) variation of β.

2. The variations in contrast C for cumulative distances from northeast-trending faults/fractures with respect to the porphyry copper deposits are shown in Table 4.29. The contrasts are mostly negative or not significantly greater than zero, which indicate a dominant negative spatial association particularly within 1500 m. The most negative Studentised C indicates that the negative spatial association is optimal, yet not significant statistically, within 750 m.

Table 4.29. Variation of weights and contrasts for cumulative distances from northeast-trending faults/fractures with respect to porphyry copper deposits, Abra area*.

Distance buffer (m)	No. of pixels in D_P**	No. of porphyry copper occ. in D_P**	W+	s(W+)	W-	s(W-)	C	s(C)	C/s(C)
250	12862	1	-0.518	1.000	0.064	0.302	-0.582	1.045	-0.557
500	24878	1	-1.178	1.000	0.228	0.302	-1.406	1.044	-1.346
750	**38487**	**2**	**-0.921**	**0.707**	**0.360**	**0.316**	**-1.281**	**0.775**	**-1.653**
1000	49406	4	-0.477	0.500	0.365	0.354	-0.842	0.612	-1.376
1250	58565	7	-0.088	0.378	0.137	0.447	-0.225	0.586	-0.385
1500	65229	8	-0.062	0.354	0.137	0.500	-0.199	0.612	-0.325
2000	74757	10	0.025	0.316	-0.116	0.707	0.140	0.775	0.181
2500	81087	11	0.039	0.302	-0.350	1.000	0.389	1.045	0.372
3000	85472	11	-0.014	0.302	0.166	1.000	-0.180	1.045	-0.172
3500	87853	12	0.046	0.289					

*Table entries in bold pertain to optimal spatial association. **D_P = domain is present.

3. The distances $Y_j max_r$ vary between 750 and 2000 m (Table 4.30). The t-test indicates that the measured correlation coefficients are significantly different from zero at the 99.9% significance level. The spatial association is optimal within 1250 m. Within this distance, the spatial association is negative, i.e., $mcdioY_j max_r$ is less than $mcdooY_j max_r$.

Table 4.30. Results of distance correlation calculations to quantify spatial association between porphyry copper deposits and northeast-trending faults/fractures, Abra area*.

AP	$Y_j max_r$ (m)	$r_{d_{jx}d_{jy}}$ at $Y_j max_r$	t-value for $r_{d_{jx}d_{jy}}$ at $Y_j max_r$	$mcdioY_j max_r$	$mcdooY_j max_r$
Centre	**1250**	**0.99463**	**30.405****	**0.98965**	**0.99279**
North	**1250**	**0.99839**	**55.700****	**0.98989**	**0.99813**
NE	2000	0.99921	79.692**		
East	**1250**	**0.99790**	**48.731****	**099337**	**0.99556**
SE	750	0.99435	29.630**		
South	750	0.99828	53.780**		
SW	1000	0.99955	105.103**		
West	1500	0.99441	29.786**		
NW	1000	0.99642	37.293**		

*Table entries in bold pertain to optimal spatial association.
**Calculated t-values are significantly different from zero; critical t-value at α=0.001 and ν=12-2=10 degrees of freedom is 4.144 (Davis, 1973).

The porphyry copper deposits are positively spatially associated with the northeast-trending faults/fractures. The distance distribution method and the weights of evidence method indicate that the positive spatial association is optimal within 950 and 750 m, respectively. The distance correlation method indicates that the positive spatial association is optimal within 1250 m.

4.5.6 Porphyry copper deposits vs. northwest-trending faults/fractures

1. The curve for the observed cumulative frequency distribution of nearest distances between the porphyry copper deposits and the northwest-trending faults/fractures is conspicuously below the predicted curve within 3500 m and between 500 and 7000 m (Figure 4.18a). This implies a negative spatial association; however, it is not significant statistically (Figure 4.18b). The highest peak along the β curve suggests that the negative spatial association is optimal within about 1600 m.

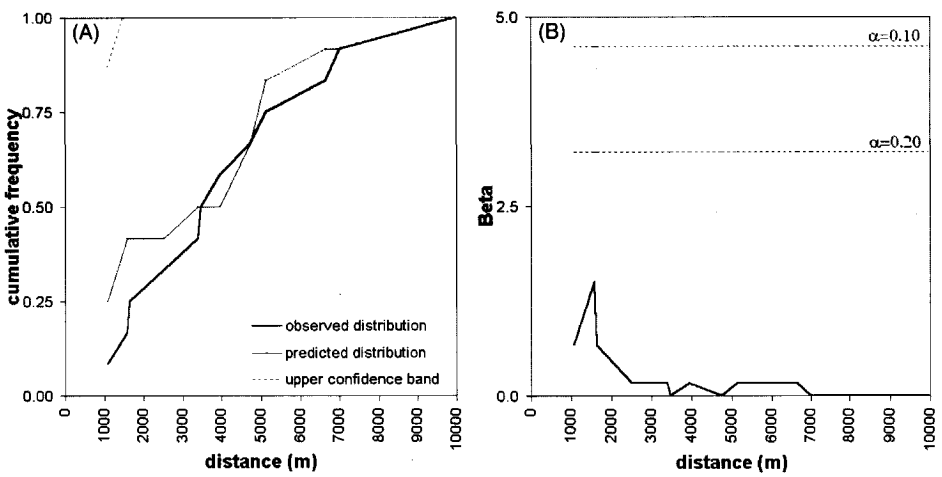

Figure 4.18. Porphyry copper deposits and nearest northwest-trending faults/fractures, Abra area: (a) distance distribution and (b) variation of β.

2. The variations in contrast C for cumulative distances from northwest-trending faults/fractures with respect to the porphyry copper deposits are shown in Table 4.31. The contrasts are mostly negative or not significantly greater than zero, which indicates a negative spatial association particularly within 6000 m. The most negative Studentised C indicates that the negative spatial association is optimal, but not significant statistically, within 1500 m.

Table 4.31. Variation of weights and contrasts for cumulative distances from northwest-trending faults/fractures with respect to porphyry copper deposits, Abra area*.

Distance buffer (m)	No. of pixels in D_P**	No. of porphyry copper occ. in D_P**	W+	s(W+)	W-	s(W-)	C	s(C)	C/s(C)
500	7729	0			0.088	0.289			
1000	15991	0			0.191	0.289			
1500	**24592**	**1**	**-1.166**	**1.000**	**0.224**	**0.302**	**-1.390**	**1.044**	**-1.331**
2000	32732	3	-0.353	0.577	0.152	0.333	-0.506	0.667	-0.758
2500	40020	3	-0.554	0.577	0.284	0.333	-0.838	0.667	-1.257
3000	45574	4	-0.397	0.500	0.279	0.354	-0.676	0.612	-1.103
4000	55147	7	-0.028	0.378	0.040	0.447	-0.068	0.586	-0.115
5000	63368	8	-0.033	0.354	0.070	0.500	-0.103	0.612	-0.168
6000	69877	9	-0.013	0.333	0.040	0.577	-0.053	0.667	-0.080
7000	75278	10	0.018	0.316	-0.085	0.707	0.103	0.775	0.133
8000	79614	11	0.057	0.302	-0.477	1.000	0.534	1.045	0.512
9000	83250	11	0.013	0.302	-0.128	1.000	0.141	1.045	0.135
10000	86357	12	0.063	0.289					

*Table entries in bold pertain to optimal spatial association. **D_P = domain is present.

3. The distances Y_jmax_r vary between 3500 and 5000 m (Table 4.32). The t-test indicates that the measured correlation coefficients are significantly different from zero at the 99.9% significance level. The spatial association is optimal within 3500 m. Within this distance, the spatial association is negative.

Table 4.32. Results of distance correlation calculations to quantify spatial association between porphyry copper deposits and northwest-trending faults/fractures, Abra area*.

AP	Y_jmax_r (m)	$r_{d_{jx}d_{jy}}$ at Y_jmax_r	t-value for $r_{d_{jx}d_{jy}}$ at Y_jmax_r	$mcdioY_jmax_r$	$mcdooY_jmax_r$
Centre	5000	0.97928	13.325**		
North	**3500**	**0.99117**	**23.636****	**0.98739**	**0.98992**
NE	4500	0.98420	17.578**		
East	**3500**	**0.93314**	**8.208****	**0.91533**	**0.92347**
SE	**3500**	**0.98420**	**17.576****	**0.97351**	**0.97784**
South	4000	0.99520	32.289**		
SW	4000	0.98434	17.658**		
West	4500	0.98103	16.002**		
NW	5000	0.99727	42.741**		

*Table entries in bold pertain to optimal spatial association.
**Calculated t-values are significantly different from zero; critical t-value at α=0.001 and ν=12-2=10 degrees of freedom is 4.144 (Davis, 1973).

The porphyry copper deposits are negatively spatially associated with the northwest-trending faults/fractures. The distance distribution method and the weights of evidence method indicate that the negative spatial association is

optimal within 1600 and 1500 m, respectively. The distance correlation indicates that the spatial association is optimal within 3500 m.

4.5.7 Porphyry copper deposits vs. intersections of regional faults

1. The curve for the observed cumulative frequency distribution of nearest distances between the porphyry copper deposits and the intersection of regional faults is mostly above the predicted curve (Figure 4.19a). A positive spatial association is thus implied, which, however, is not significant statistically (Figure 4.19b). The highest peak along the β curve suggests that the positive spatial association is optimal within about 1000 m.

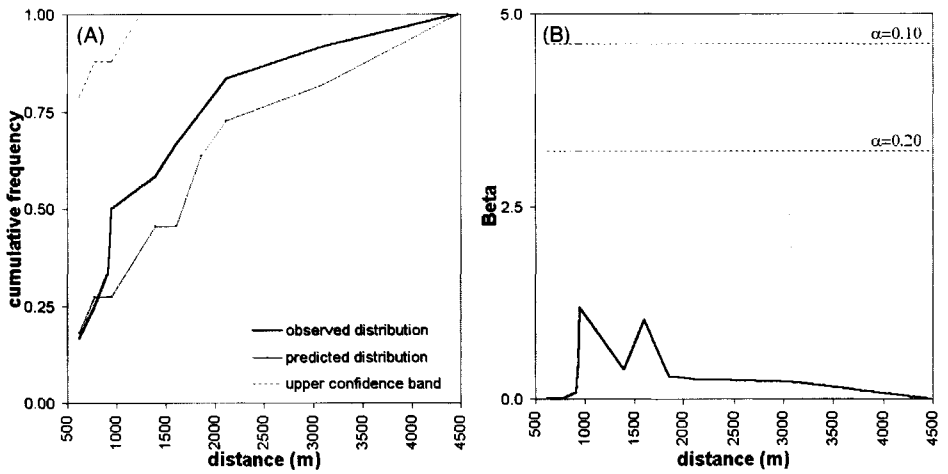

Figure 4.19. Porphyry copper deposits and nearest intersection of regional faults, Abra area: (a) distance distribution and (b) variation of β.

2. The contrasts C for cumulative distances from the intersection of regional faults with respect to the porphyry copper deposits are significantly positive within 2000 m, which indicates a positive spatial association within this distance range (Table 4.33). The highest Studentised C indicates that the positive spatial association is optimal within 1000 m.

3. The distances between the porphyry copper deposits and the intersection of regional faults at which the measured values of $r_{d_{jx}d_{iy}}$ are highest vary between 1000 and 2000 m (Table 4.34). The t-test indicates that these measured correlation coefficients are significantly different from zero at the 99.9% significance level. The spatial association is optimal within 2000 m. Within this distance, the spatial association is positive.

Table 4.33. Variation of weights and contrasts for cumulative distances from intersections of regional faults with respect to porphyry copper deposits, Abra area*.

Distance buffer (m)	No. of pixels in D_P**	No. of porphyry copper occ. in D_P**	W+	s(W+)	W-	s(W-)	C	s(C)	C/s(C)
500	3364	0			0.037	0.289			
750	7462	2	0.720	0.707	-0.098	0.316	0.818	0.775	1.055
1000	**12547**	**6**	**1.299**	**0.408**	**-0.547**	**0.408**	**1.846**	**0.577**	**3.196**
1250	18682	6	0.901	0.408	-0.466	0.408	1.367	0.577	2.367
1500	25176	7	0.757	0.378	-0.556	0.447	1.312	0.586	2.241
1750	31584	8	0.663	0.354	-0.678	0.500	1.341	0.612	2.190
2000	37681	9	0.605	0.333	-0.859	0.577	1.464	0.667	2.196
2500	48100	10	0.466	0.316	-1.052	0.707	1.517	0.775	1.959
3000	56210	10	0.310	0.316	-0.847	0.707	1.157	0.775	1.494
3500	63299	11	0.287	0.302	-1.319	1.000	1.606	1.044	1.537
4000	69374	11	0.195	0.302	-1.081	1.000	1.276	1.044	1.222
4500	74319	11	0.126	0.302	-0.834	1.000	0.960	1.044	0.919
5000	78486	11	0.071	0.302	-0.565	1.000	0.636	1.045	0.609
5500	82194	11	0.025	0.302	-0.243	1.000	0.268	1.045	0.257
6000	85216	11	-0.011	0.302	0.127	1.000	-0.138	1.045	-0.132
6500	87567	11	-0.038	0.302	0.556	1.000	-0.594	1.045	-0.569
7000	89230	12	0.030	0.289					

*Table entries in bold pertain to optimal spatial association. **D_P = domain is present.

The porphyry copper deposits are positively spatially associated with the intersection of regional faults (i.e., north-trending and northeast-trending faults/fractures). The distance distribution method and the weights of evidence method indicate that positive spatial association is optimal within 1000 m. The distance correlation method indicates that the positive spatial association is optimal within 2000 m.

Table 4.34. Results of distance correlation calculations to quantify spatial association between porphyry copper deposits and intersection of regional faults, Abra area*.

AP	Y_jmax_r (m)	$r_{d_{jx}d_{jy}}$ at Y_jmax_r	t-value for $r_{d_{jx}d_{jy}}$ at Y_jmax_r	$mcdioY_jmax_r$	$mcdooY_jmax_r$
Centre	1250	0.99693	40.248**		
North	**2000**	**0.99761**	**45.610****	**0.99613**	**0.99575**
NE	**2000**	**0.99636**	**36.972****	**0.99418**	**0.99242**
East	1000	0.99556	33.460**		
SE	1750	0.98867	20.828**		
South	1500	0.99555	33.405**		
SW	**2000**	**0.99840**	**55.847****	**0.99685**	**0.99373**
West	1500	0.98846	20.633**		
NW	1500	0.99370	28.031**		

*Table entries in bold pertain to optimal spatial association.
**Calculated t-values are significantly different from zero; critical t-value at α=0.001 and ν=12-2=10 degrees of freedom is 4.144 (Davis, 1973).

4.5.8 Discussion

The results of the distance distribution and the weights of evidence method are similar (Table 4.35). The results of the distance correlation method are similar to the results of either of the other two methods with respect to the spatial association of the porphyry copper deposits with the granodiorite margins and the north-trending faults/fractures. With respect to the spatial association of the porphyry copper deposits and the other geological features, the results of the distance correlation method are invariably greater than the results of the other two methods. The distances of optimal spatial association quantified by the distance correlation method are invariably larger but are similar to the maximum statistically significant distances determined by the other two methods. The ranges of distances and types of spatial association determined by the three methods are therefore similar; the difference being the distances within which the spatial associations are optimal.

Table 4.35. Summary of results of quantitative characterisation of spatial association between porphyry copper deposits and geological features in Abra area.

Relation	Distance distribution method			Weights of evidence method			Distance correlation method		
	Spatial assn.	Dist. (m)	β	Spatial assn.	Dist. (m)	Studentised C	Spatial assn.	Dist. (m)	Mean $r_{d_{jx}d_{jy}}$
pcd-gm[1]	negative	800	1.751*	negative positive	1000 1500	0.805* 1.540*	negative	1000	0.99792
pcd-qdm[2]	negative	2600	0.667*	negative	2500	-1.341*	negative	5000	0.97160
pcd-ppc[3]	negative	5700	1.921*	negative positive	5000 1500	0.217* 2.178	negative	4000	0.97703
pcd-nff[4]	positive	1250	1.500*	positive	1500	1.395*	positive	1500	0.99107
pcd-neff[5]	negative	950	1.500*	negative	750	-1.653*	negative	1250	0.99683
pcd-nwff[6]	negative	1600	1.500*	negative	1500	-1.390*	negative	3500	0.96590
pcd-irf[7]	positive	1000	1.186*	positive	1000	3.196	positive	2000	0.99746

[1] pcd-gm = porphyry copper deposits and granodiorite margins
[2] pcd-qdm = porphyry copper deposits and quartz diorite margins
[3] pcd-ppc = porphyry copper deposits and porphyry pluton centroids
[4] pcd-nff = porphyry copper deposits and north-trending faults/fractures
[5] pcd-neff = porphyry copper deposits and northeast-trending faults/fractures
[6] pcd-nwff = porphyry copper deposits and northwest-trending faults/fractures
[7] pcd-irf = porphyry copper deposits and intersection of regional faults
* not statistically significant

The porphyry copper deposits are positively spatially associated with the north-trending faults/fractures and the intersections of regional faults. The positive spatial association between the porphyry copper deposits and the intersection of regional faults (mean distance $\approx$ 1350 m) is stronger than the positive spatial association between the porphyry copper deposits and the north-trending faults/fractures (mean distance $\approx$ 1400 m). The positive spatial associations of

the porphyry copper deposits with the intersections of regional faults and the north-trending faults/fractures have a number of implications. First, structural (i.e., fault) controls played an important role in porphyry copper mineralisation. Second, the north-trending faults/fractures were likely precursors of later magmatic regimes that provided hydrothermal fluids for porphyry copper mineralisation in the area. Third, the intersections of regional faults (i.e., the north-trending and northeast-trending faults/fractures; see Figure 2.16) provided particularly favourable 'ground preparation' for those magmatic regimes. The question is then: Which magmatic regimes were responsible genetically for the porphyry copper mineralisation in the area?

The porphyry copper deposits are negatively spatially associated with the granodiorite margins, the quartz diorite margins, the porphyry pluton centroids, the northeast- and the northwest-trending faults/fractures. The negative spatial association between the porphyry copper deposits and the porphyry pluton centroids is strongest (mean distance $\approx$ 4900 m). The negative spatial association between the porphyry copper deposits and the quartz diorite margins is next strongest. The negative spatial association between the porphyry copper deposits and the northwest-trending faults/fractures is intermediate (mean distance $\approx$ 2200 m). The negative spatial association between the porphyry copper deposits and the northeast-trending faults/fractures is next weakest (mean distance $\approx$ 983 m). The negative spatial association between the porphyry copper deposits and the granodiorite margins is weakest (mean distance $\approx$ 935 m).

The negative spatial associations of the porphyry copper deposits with the quartz diorite margins, the granodiorite margins and the porphyry pluton centroids suggest that none of these magmatic regimes was associated genetically with the porphyry copper mineralisation. The quantifications of the spatial associations of the porphyry copper deposits with the margins and centroids of the different magmatic units in the area do no corroborate field observations that the porphyry copper deposits are associated genetically with the porphyry plutons. Nevertheless, the weights of evidence method in particular reveals two subtle features that can shed further light to answer the question above. First, the porphyry copper deposits tend to be positively spatially associated (albeit not significantly) with the granodiorite margins just beyond the zone of the negative spatial association between these features. Second, within the zone of negative spatial association between the porphyry copper deposits and the porphyry pluton centroids, (some of) the porphyry copper deposits are significantly statistically positively spatially associated with the porphyry pluton centroids. These results have two implications. First, the porphyry copper deposits are spatially distributed beyond 1000 m of the granodiorite margins and within 1500 m of the porphyry pluton centroids. Second, the quantified negative spatial association between the porphyry copper deposits and the porphyry pluton centroids probably implies that whilst porphyry copper deposits are

observed on the surface they are associated with non-outcropping porphyry plutons. Overall, the quantitatively characterised negative spatial associations of the porphyry copper deposits with the granodiorite and quartz diorite margins corroborate field observations. The subtle positive spatial association between the porphyry copper deposits and the porphyry pluton centroids revealed by the weights of evidence substantiates field observations regarding their genetic association.

The weaker negative spatial association of the porphyry copper deposits with the northeast-trending faults/fractures than with the northwest-trending faults/fractures implicates the former rather than the latter in porphyry copper mineralisation in the area. This finding further supports the genetic importance of the intersections of regional faults (mainly between north-trending and northeast-trending faults/fractures) to porphyry copper mineralisation in the area.

4.6 APPLICATION TO CATANDUANES ISLAND

The gold-copper deposits in the island have not been studied extensively (see Chapter 2). The deposits are probably due to hydrothermal activity related to the Batalay Intrusives. The fact that many of the deposits are vein-type deposits suggests structural control in their mode of formation. To contribute to the understanding of the mode of formation of the gold-copper deposits, their spatial associations are characterised quantitatively with (a) the Batalay Intrusive contacts, (b) north-trending faults/fractures, (c) east-trending faults/fractures, (d) northeast-trending faults/fractures and (e) northwest-trending faults/fractures. The spatial associations of the gold-copper deposits with the different sets of faults/fractures were studied because it is not well-known with which of these sets of structures the deposits are associated. In addition, the spatial associations of the centroids of the Batalay Intrusives with the more prominent faults/fractures (i.e., the north-trending, northeast-trending and northwest-trending faults/fractures) were analysed to determine indirectly whether the magmatic regime is structurally-controlled. These latter analyses were confined to the southern half of the island where the Batalay Intrusives have been mapped (see Figure 2.17); the number of pixels of the area studied is 69422.

4.6.1 Gold-copper deposits vs. Batalay Intrusive contacts

1. The curve for the observed cumulative frequency distribution of nearest distances between the gold-copper deposits and the Batalay Intrusive contacts is above the predicted curve within 14000 m (Figure 4.20a). A positive spatial association is implied, which is significant statistically within 5000 m (Figure 4.20b). The highest peak along the β curve suggests that the positive spatial association is optimal within 2400 m.

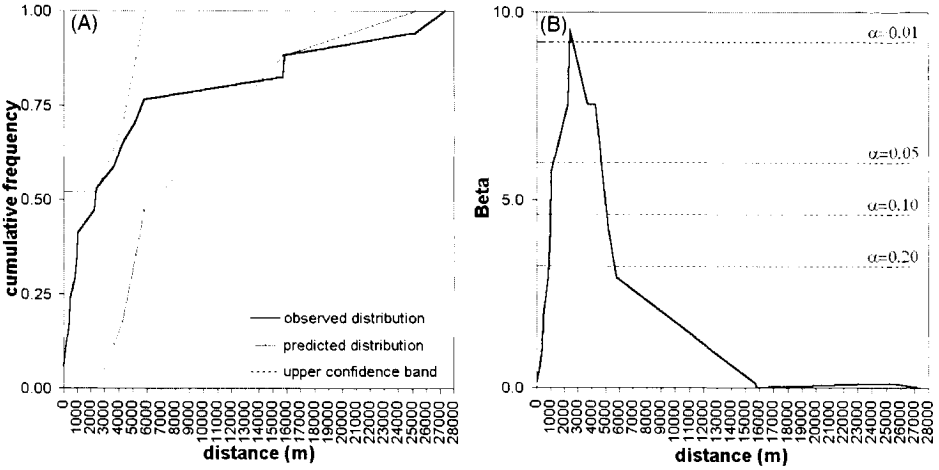

Figure 4.20. Gold-copper deposits and nearest Batalay Intrusive contacts, Catanduanes Island: (a) distance distribution and (b) variation of β.

2. The variations in contrast C for cumulative distances from the Batalay Intrusive contacts with respect to the gold-copper deposits are show in Table 4.36. The contrasts are statistically significant within 7500 m, which indicates positive spatial association within this distance range. The positive spatial association is optimal within 1000 m, as indicated by the highest Studentised C.

Table 4.36. Variation of weights and contrasts for cumulative distances from Batalay Intrusive contacts with respect to gold-copper deposits, Catanduanes Is.*

Distance buffer (m)	No. of pixels in D_P**	No. of gold/ copper occ. in D_P**	W+	s(W+)	W-	s(W-)	C	s(C)	C/s(C)
500	5747	4	1.780	0.500	-0.228	0.277	2.008	0.572	3.511
1000	**10815**	**6**	**1.553**	**0.408**	**-0.358**	**0.302**	**1.911**	**0.508**	**3.765**
1500	16269	7	1.299	0.378	-0.411	0.316	1.711	0.493	3.471
2000	21269	7	1.031	0.378	-0.372	0.316	1.403	0.493	2.846
3000	31068	9	0.903	0.333	-0.512	0.354	1.416	0.486	2.913
4000	40999	10	0.731	0.316	-0.555	0.378	1.286	0.493	2.609
5000	49584	11	0.637	0.302	-0.622	0.408	1.259	0.508	2.480
7500	66714	13	0.507	0.277	-0.830	0.500	1.336	0.572	2.337
10000	78839	13	0.340	0.277	-0.661	0.500	1.001	0.572	1.750
12500	88286	13	0.227	0.277	-0.506	0.500	0.733	0.572	1.282
15000	96852	13	0.134	0.277	-0.342	0.500	0.476	0.572	0.832
17500	105044	15	0.196	0.258	-0.848	0.707	1.044	0.753	1.386
20000	113182	15	0.121	0.258	-0.619	0.707	0.740	0.753	0.983
22500	119375	15	0.068	0.258	-0.401	0.707	0.469	0.753	0.623
25000	123841	15	0.031	0.258	-0.208	0.707	0.239	0.753	0.318
27500	127587	17	0.127	0.243					

*Table entries in bold pertain to optimal spatial association. **D_P = domain is present.

3. The distances between the gold-copper deposits and the Batalay Intrusive contacts at which the measured values of $r_{d_{jx}d_{jy}}$ are highest vary between 2000 and 5500 m (Table 4.37). The t-test indicates that these measured correlation coefficients are significantly different from zero at the 99.9% significance level. The spatial association is optimal within 3500 m, within which the spatial association is positive, i.e., $mcdioY_jmax_r$ is greater than $mcdooY_jmax_r$.

Table 4.37. Results of distance correlation calculations to quantify spatial association between gold-copper deposits and Batalay Intrusive contacts, Catanduanes Is.*

AP	Y_jmax_r (m)	$r_{d_{jx}d_{jy}}$ at Y_jmax_r	t-value for $r_{d_{jx}d_{jy}}$ at Y_jmax_r	$mcdioY_jmax_r$	$mcdooY_jmax_r$
Centre	**3500**	**0.78783**	**4.954****	**0.76731**	**0.76167**
North	2000	0.93674	10.365**		
NE	**3500**	**0.92403**	**9.361****	**0.90689**	**0.89207**
East	4000	0.86545	6.690**		
SE	5000	0.82557	5.666**		
South	2500	0.83975	5.990**		
SW	5500	0.89324	7.678**		
West	3000	0.93818	10.498**		
NW	2000	0.85940	6.510**		

*Table entries in bold pertain to optimal spatial association.
**Calculated t-values are significantly different from zero; critical t-value at α=0.001 and v=17-2=15 degrees of freedom is 3.733 (Davis, 1973).

The gold-copper deposits are positively spatially associated with the Batalay Intrusives. The three methods indicate that the positive spatial association extends beyond 5000 m of the Batalay Intrusive contacts. The distance distribution method and the weights of evidence method indicate that the positive spatial association is optimal within 2400 and 1000 m, respectively. The distance correlation method indicates that the positive spatial association is optimal within 3500 m.

4.6.2 Gold-copper deposits vs. north-trending faults/fractures

1. The curve for the observed cumulative frequency distribution of nearest distances between the gold-copper deposits and the north-trending faults/fractures is mostly above the predicted curve (Figure 4.21a). A positive spatial association is implied, which is significant to barely significant statistically within 3000 m (Figure 4.21b). The highest peak along the β curve suggests that the positive spatial association is optimal within 800 m.

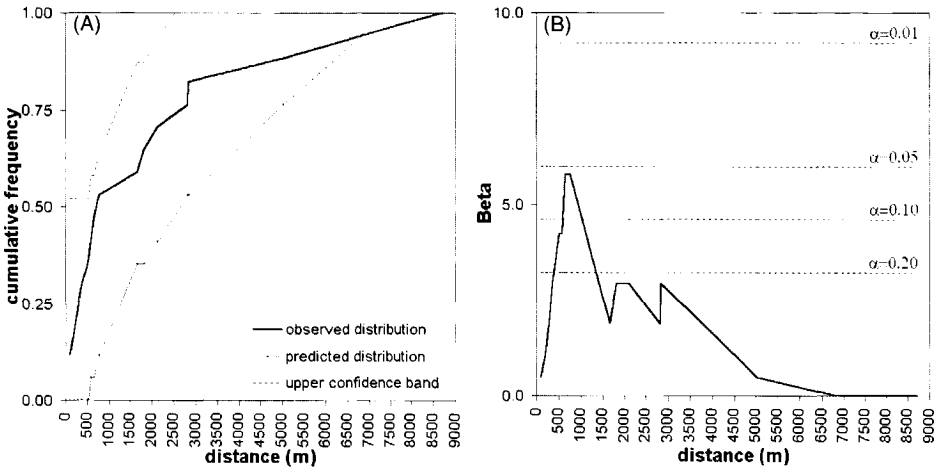

Figure 4.21. Gold-copper deposits and nearest north-trending faults/fractures, Catanduanes Island: (a) distance distribution and (b) variation of β.

2. The contrasts C for cumulative distances from the Batalay Intrusive contacts with respect to the gold-copper deposits are significantly positive within 3000 m, which indicates positive spatial association (Table 4.38). The positive spatial association is optimal within 750 m, as indicated by highest Studentised C

Table 4.38. Variation of weights and contrasts for cumulative distances from north-trending faults/fractures with respect to gold-copper deposits, Catanduanes Is.*

Distance buffer (m)	No. of pixels in D_P**	No. of gold/ copper occ. in D_P**	W+	s(W+)	W-	s(W-)	C	s(C)	C/s(C)
250	10469	3	0.893	0.577	-0.119	0.267	1.012	0.636	1.590
500	21938	5	0.664	0.447	-0.184	0.289	0.848	0.532	1.592
750	**30756**	**8**	**0.796**	**0.354**	**-0.397**	**0.333**	**1.193**	**0.486**	**2.455**
1000	40742	9	0.632	0.333	-0.423	0.354	1.056	0.486	2.173
2000	72225	11	0.260	0.302	-0.351	0.408	0.611	0.508	1.204
3000	94556	14	0.232	0.267	-0.676	0.577	0.908	0.636	1.428
4000	110385	14	0.077	0.267	-0.298	0.577	0.375	0.636	0.590
5000	122420	14	-0.026	0.267	0.132	0.577	-0.158	0.636	-0.249
6000	132539	15	-0.037	0.258	0.328	0.707	-0.365	0.753	-0.484
7000	138803	16	-0.018	0.250	0.349	1.000	-0.367	1.031	-0.356
8000	142507	16	-0.045	0.250	1.308	1.000	-1.352	1.031	-1.312
9000	144328	17	0.003	0.243					

*Table entries in bold pertain to optimal spatial association. **D_P = domain is present.

3. The distances $Y_j max_r$ vary between 1000 and 4000 m (Table 4.39). The t-test indicates that the measured correlation coefficients are significantly different from zero at the 99.9% significance level. The spatial association is optimal within 3000 m, within which the spatial association is positive.

Table 4.39. Results of distance correlation calculations to quantify spatial association between gold-copper deposits and north-trending faults/fractures, Catanduanes Is.*

AP	$Y_j max_r$ (m)	$r_{d_{jx}d_{jy}}$ at $Y_j max_r$	t-value for $r_{d_{jx}d_{jy}}$ at $Y_j max_r$	$mcdioY_j max_r$	$mcdooY_j max_r$
Centre	2000	0.98602	14.944**		
North	4000	0.99121	29.010**		
NE	**3000**	**0.99187**	**30.197****	**0.98777**	**0.98662**
East	1000	0.98827	25.058**		
SE	2750	0.98664	23.458**		
South	**3000**	**0.98910**	**26.023****	**0.98469**	**0.98451**
SW	1000	0.99762	56.085**		
West	1750	0.99076	28.287**		
NW	3250	0.99045	27.820**		

*Table entries in bold pertain to optimal spatial association.
**Calculated t-values are significantly different from zero; critical t-value at α=0.001 and v=17-2=15 degrees of freedom is 3.733 (Davis, 1973).

The gold-copper deposits are positively spatially associated with the north-trending faults/fractures. The three methods indicate that the positive spatial association generally extends up to 3000 m. The distance distribution method and the weights of evidence method indicate that the positive spatial association is optimal within 800 and 750 m, respectively. The distance correlation method indicates that the positive spatial association is optimal within 3000 m.

4.6.3 Gold-copper deposits vs. east-trending faults/fractures

1. The curve for the observed cumulative frequency distribution of nearest distances between the gold-copper deposits and the east-trending faults/fractures is below the curve for the predicted cumulative frequency distribution (Figure 4.22a). A negative spatial association is implied, which is significant statistically (Figure 4.22b). The highest peak along the β curve suggests that the negative spatial association is optimal within 11700 m.

2. The variations in contrast C for cumulative distances from the east-trending faults/fractures with respect to the gold-copper deposits are shown in Table 4.40. The contrasts are mostly negative, which indicates negative spatial association. The negative spatial association is optimal within 11250 m, as indicated by the most negative Studentised C.

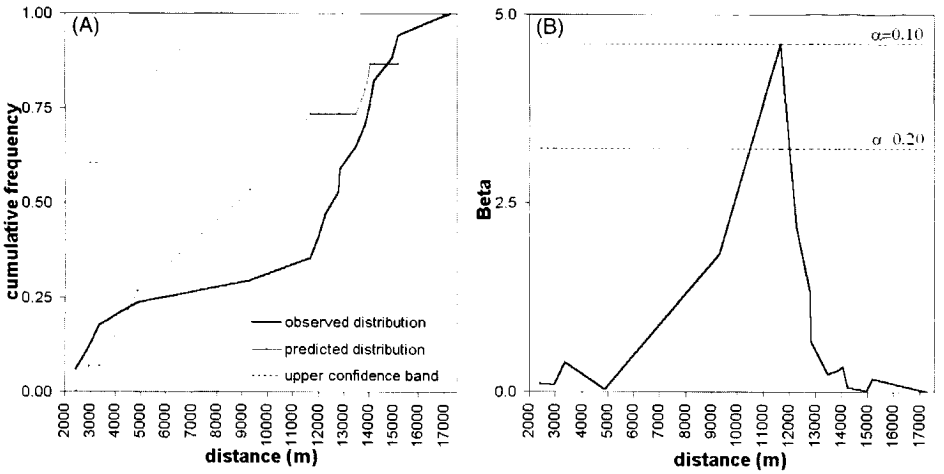

Figure 4.22. Gold-copper deposits and nearest east-trending faults/fractures, Catanduanes Island: (a) distance distribution and (b) variation of β.

Table 4.40. Variation of weights and contrasts for cumulative distances from east-trending faults/fractures with respect to gold-copper deposits, Catanduanes Is.*

Distance buffer (m)	No. of pixels in D_P**	No. of gold/ copper occ. in D_P**	W+	s(W+)	W-	s(W-)	C	s(C)	C/s(C)
2500	17710	1	-0.732	1.000	0.070	0.250	-0.802	1.031	-0.778
5000	37333	4	-0.091	0.500	0.030	0.277	-0.121	0.572	-0.212
7500	59094	4	-0.551	0.500	0.256	0.277	-0.807	0.572	-1.411
10000	80992	5	-0.643	0.447	0.471	0.289	-1.114	0.532	-2.093
11250	**90186**	**5**	**-0.750**	**0.447**	**0.627**	**0.289**	**-1.377**	**0.532**	**-2.587**
12500	98935	8	-0.373	0.354	0.514	0.333	-0.886	0.486	-1.824
15000	115602	15	0.100	0.258	-0.539	0.707	0.639	0.753	0.849
17500	128737	17	0.118	0.243					

*Table entries in bold pertain to optimal spatial association. **D_P = domain is present.

3. The distances Y_jmax_r vary between 6000 and 11000 m (Table 4.41). The t-test indicates that the measured correlation coefficients are significantly different from zero at the 99.9% significance level. The spatial association is optimal within 9000 m, within which the spatial association is negative, i.e., mcdioY_jmax_r is less than mcdooY_jmax_r.

The gold-copper deposits are negatively spatially associated with the east-trending faults/fractures. The three methods indicate that the negative spatial association extends beyond 10000 m. The distance distribution method and the weights of evidence method indicate that the negative spatial association is optimal within 11700 and 11250 m, respectively. The distance correlation indicates that the negative spatial association is optimal within 9000 m.

Table 4.41. Results of distance correlation calculations to quantify spatial association between gold-copper deposits and east-trending faults/fractures, Catanduanes Is.*

AP	$Y_j max_r$ (m)	$r_{d_{jx}d_{jy}}$ at $Y_j max_r$	t-value for $r_{d_{jx}d_{jy}}$ at $Y_j max_r$	$mcdioY_j max_r$	$mcdooY_j max_r$
Centre	7000	0.87711	7.073**		
North	7000	0.97051	15.593**		
NE	11000	0.97354	16.501**		
East	**9000**	**0.96498**	**14.274****	**0.86554**	**0.94501**
SE	8000	0.97331	16.424**		
South	8000	0.95960	13.209**		
SW	**9000**	**0.96536**	**14.328****	**0.84269**	**0.93128**
West	**9000**	**0.97722**	**17.833****	**0.92746**	**0.96257**
NW	6000	0.98570	21.652**		

*Table entries in bold pertain to optimal spatial association.

**Calculated t-values are significantly different from zero; critical t-value at α=0.001 and ν=17-2=15 degrees of freedom is 3.733 (Davis, 1973).

4.6.4 Gold-copper deposits vs. northeast-trending faults/fractures

1. The curve for the observed cumulative frequency distribution of nearest distances between the gold-copper deposits and the northeast-trending faults/fractures is above the predicted curve (Figure 4.23a). A positive spatial association is implied, but it is barely significant statistically (Figure 4.23b). The highest peak along the β curve suggests that the positive spatial association is optimal within 1000 m.

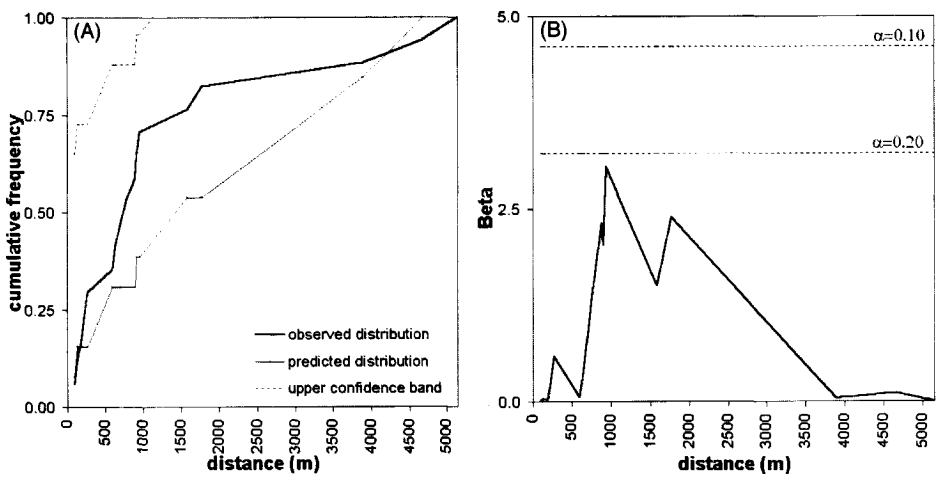

Figure 4.23. Gold-copper deposits and nearest northeast-trending faults/fractures, Catanduanes Island: (a) distance distribution and (b) variation of β.

2. The variations in contrast C for cumulative distances from the northeast-trending faults/fractures with respect to the gold-copper deposits are shown in Table 4.42. The contrasts are significantly positive within 2500 m, which indicate a positive spatial association. The positive spatial association is optimal within 1000 m.

Table 4.42. Variation of weights and contrasts for cumulative distances from northeast-trending faults/fractures with respect to gold-copper deposits, Catanduanes Is.*

Distance buffer (m)	No. of pixels in D_P**	No. of gold/ copper occ. in D_P**	W+	s(W+)	W-	s(W-)	C	s(C)	C/s(C)
500	26722	5	0.466	0.447	-0.144	0.289	0.611	0.532	1.147
750	41049	9	0.625	0.333	-0.420	0.354	1.045	0.486	2.151
1000	**53005**	**12**	**0.657**	**0.289**	**-0.768**	**0.447**	**1.425**	**0.532**	**2.677**
1250	63121	12	0.482	0.289	-0.651	0.447	1.133	0.532	2.129
1500	71430	14	0.513	0.267	-1.055	0.577	1.568	0.636	2.464
2000	84620	14	0.343	0.267	-0.857	0.577	1.200	0.636	1.886
2500	95427	14	0.223	0.267	-0.659	0.577	0.882	0.636	1.386
3000	104282	14	0.134	0.267	-0.461	0.577	0.595	0.636	0.936
3500	112177	15	0.130	0.258	-0.650	0.707	0.780	0.753	1.036
4000	119320	15	0.068	0.258	-0.403	0.707	0.471	0.753	0.626
4500	125970	16	0.079	0.250	-0.794	1.000	0.873	1.031	0.847
5000	131770	16	0.034	0.250	-0.426	1.000	0.460	1.031	0.446
5500	136401	17	0.060	0.243					

*Table entries in bold pertain to optimal spatial association. **D_P = domain is present.

3. The distances Y_jmax_r vary between 1000 and 1500 m (Table 4.43). The t-test indicates that the measured correlation coefficients are significantly different from zero at the 99.9% significance level. The spatial association is optimal within 1000 m, within which the spatial association is positive.

Table 4.43. Results of distance correlation calculations to quantify spatial association between gold-copper deposits and northeast-trending faults/fractures, Catanduanes Is.*

AP	Y_jmax_r (m)	$r_{d_{jx}d_{jy}}$ at Y_jmax_r	t-value for $r_{d_{jx}d_{jy}}$ at Y_jmax_r	$mcdioY_jmax_r$	$mcdooY_jmax_r$
Centre	**1000**	**0.98175**	**19.993****	**0.97585**	**0.96693**
North	**1000**	**0.99702**	**50.050****	**0.99637**	**0.99453**
NE	1500	0.99785	59.018**		
East	1500	0.99765	56.358**		
SE	**1000**	**0.99547**	**40.471****	**0.99401**	**0.99328**
South	1500	0.99568	41.523**		
SW	**1000**	**0.99964**	**145.055****	**0.99943**	**0.99870**
West	1500	0.98957	26.609**		
NW	**1000**	**0.99389**	**34.878****	**0.99209**	**0.99205**

*Table entries in bold pertain to optimal spatial association.
**Calculated t-values are significantly different from zero; critical t-value at α=0.001 and ν=17-2=15 degrees of freedom is 3.733 (Davis, 1973).

The gold-copper deposits are positively spatially associated with the northeast-trending faults/fractures. The three methods indicate that the positive spatial association is optimal within 1000 m.

4.6.5 Gold-copper deposits vs. northwest-trending faults/fractures

1. The curve for the observed cumulative frequency distribution of nearest distances between the gold-copper deposits and the northwest-trending faults/fractures is below the predicted curve within 3500 m (Figure 4.24a). A positive spatial association is implied, which is significant statistically (Figure 4.24b). The highest peak along the β curve suggests that the negative spatial association is optimal within 2000 m.

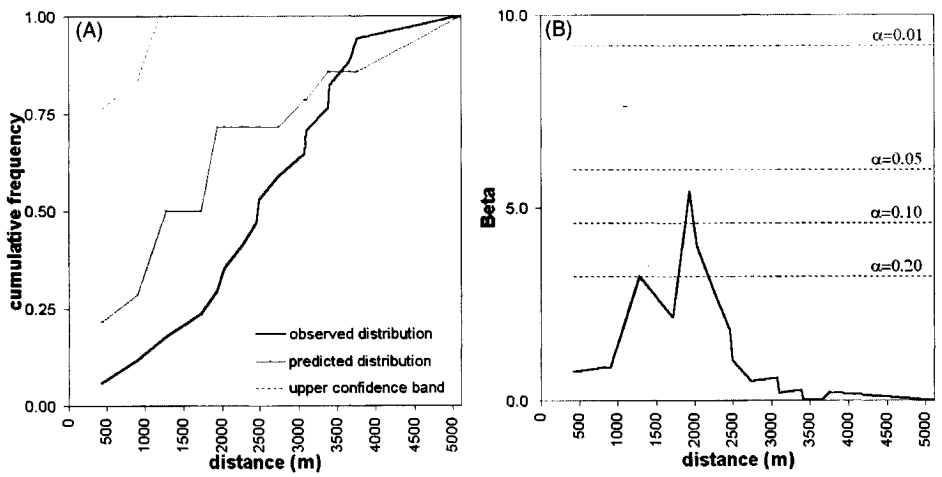

Figure 4.24. Gold-copper deposits and nearest northwest-trending faults/fractures, Catanduanes Island: (a) distance distribution and (b) variation of β.

2. The variations in contrast C for cumulative distances from the northwest-trending faults/fractures with respect to the gold-copper deposits are shown in Table 4.44. The contrasts are negative within 3500 m, which indicate negative spatial association. The most negative Studentised C indicates that the negative spatial association is optimal within 1500 m.

3. The distances between the gold-copper deposits and the northwest-trending faults/fractures at which the measured values of $r_{d_{jx}d_{jy}}$ are highest vary between 2000 and 3000 m (Table 4.45). The t-test indicates that these measured correlation coefficients are significantly different from zero at the 99.9% significance level. The spatial association is optimal within 2500 m. Within this

Table 4.44. Variation of weights and contrasts for cumulative distances from northwest-trending faults/fractures with respect to gold-copper deposits, Catanduanes Is.*

Distance buffer (m)	No. of pixels in D_P**	No. of gold/copper occ. in D_P**	W+	s(W+)	W-	s(W-)	C	s(C)	C/s(C)
500	19219	1	-0.814	1.000	0.082	0.250	-0.896	1.031	-0.869
1000	38903	2	-0.826	0.707	0.188	0.258	-1.013	0.753	-1.346
1500	**56260**	**3**	**-0.789**	**0.577**	**0.298**	**0.267**	**-1.087**	**0.636**	**-1.708**
2000	70975	5	-0.511	0.447	0.325	0.289	-0.836	0.532	-1.571
2500	83944	9	-0.091	0.333	0.113	0.354	-0.204	0.486	-0.419
3000	94401	10	-0.103	0.316	0.168	0.378	-0.271	0.493	-0.549
3500	102524	14	0.151	0.267	-0.504	0.577	0.655	0.636	1.029
4000	109513	16	0.219	0.250	-1.422	1.000	1.640	1.031	1.591
4500	115905	16	0.162	0.250	-1.222	1.000	1.384	1.031	1.343
5000	121542	16	0.115	0.250	-1.005	1.000	1.120	1.031	1.086
5500	126432	17	0.136	0.243					

*Table entries in bold pertain to optimal spatial association. **D_P = domain is present.

distance, the spatial association is negative, i.e., $mcdioY_jmax_r$ is less than $mcdooY_jmax_r$.

The gold-copper deposits are negatively spatially associated with the northwest-trending faults/fractures within 3000 m. The distance distribution method and the weights of evidence method indicate the negative spatial association is optimal within 2000 and 1500 m, respectively. The distance correlation method indicates that the negative spatial association is optimal within 2500 m.

Table 4.45. Results of distance correlation calculations to quantify spatial association between gold-copper deposits and northwest-trending faults/fractures, Catanduanes Is.*

AP	Y_jmax_r (m)	$r_{d_{jx}d_{jy}}$ at Y_jmax_r	t-value for $r_{d_{jx}d_{jy}}$ at Y_jmax_r	$mcdioY_jmax_r$	$mcdooY_jmax_r$
Centre	2000	0.98679	23.592**		
North	2000	0.99868	75.390**		
NE	**2500**	**0.99692**	**49.233****	**0.99035**	**0.99420**
East	**2500**	**0.99518**	**39.291****	**0.98754**	**0.99261**
SE	3000	0.99856	71.980**		
South	3000	0.99863	73.992**		
SW	**2500**	**0.99742**	**53.773****	**0.98999**	**0.99460**
West	2000	0.99741	53.721**		
NW	**2500**	**0.99924**	**99.608****	**0.99719**	**0.99808**

*Table entries in bold pertain to optimal spatial association.
**Calculated t-values are significantly different from zero; critical t-value at α=0.001 and ν=17-2=15 degrees of freedom is 3.733 (Davis, 1973).

4.6.6 Batalay Intrusive centroids vs. north-trending faults/fractures

1. The curve for the observed cumulative frequency distribution of nearest distances between the Batalay Intrusive centroids and the north-trending faults/fractures is above the predicted curve and exceeds the upper confidence band (Figure 4.25a). A positive spatial association is implied, which is significant statistically (Figure 4.25b). The highest peak along the β curve suggests that the positive spatial association is optimal within 2900 m.

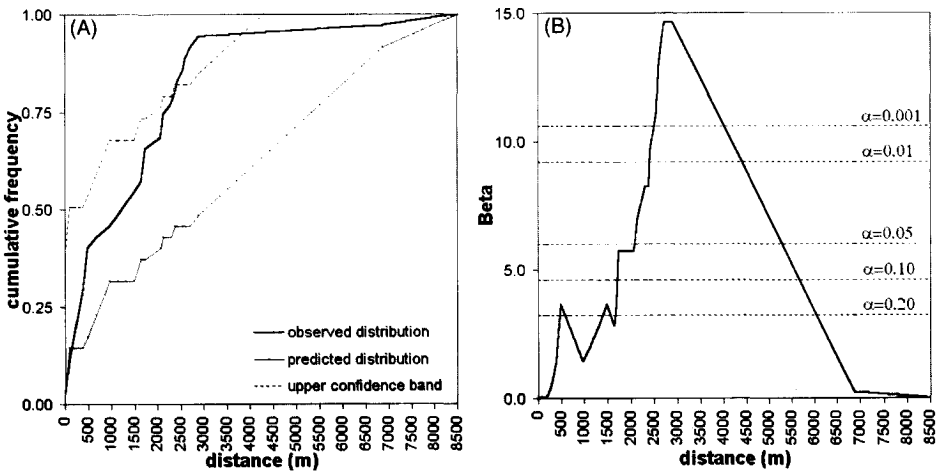

Figure 4.25. Batalay Intrusive centroids and nearest north-trending faults/fractures, Catanduanes Island: (a) distance distribution and (b) variation of β.

2. The variations in contrast C for cumulative distances from the north-trending faults/fractures with respect to the Batalay Intrusive centroids are shown in Table 4.46. The highest value of Studentised C is at 500 m; however, at this distance the W+ is highly significantly different from zero whilst the W- is not. The next highest value of Studentised C is at 2500 m. At the 2500 m, both the W+ and the W- are highly significantly different from zero. This implies that the positive spatial association is most optimal within 2500 m.

3. The distances between the Batalay Intrusive centroids and the north-trending faults/fractures at which the measured values of $r_{d_{jx}d_{jy}}$ are highest vary between 1500 and 2000 m (Table 4.47). The t-test indicates that these measured correlation coefficients are significantly different from zero at the 99.9% significance level. The spatial association is optimal within 1500 m. Within this distance, the spatial association is positive, i.e., $mcdioY_jmax_r$ is greater than $mcdooY_jmax_r$.

Table 4.46. Variation of weights and contrasts for cumulative distances from north-trending faults/fractures with respect to Batalay Intrusive centroids, Catanduanes Is.*

Distance buffer (m)	No. of pixels in D_P**	No. of gold/ copper occ. in D_P**	W+	s(W+)	W-	s(W-)	C	s(C)	C/s(C)
250	4548	6	0.963	0.409	-0.120	0.186	1.083	0.449	2.414
500	9670	14	1.056	0.267	-0.361	0.218	1.417	0.345	4.104
1000	17624	16	0.589	0.250	-0.318	0.229	0.907	0.339	2.672
1500	23779	19	0.461	0.230	-0.364	0.250	0.824	0.339	2.429
2000	29312	23	0.443	0.209	-0.522	0.289	0.965	0.356	2.708
2500	**34480**	**29**	**0.512**	**0.186**	**-1.077**	**0.408**	**1.590**	**0.449**	**3.544**
3000	39047	33	0.517	0.174	-2.036	0.707	2.553	0.728	3.506
4000	46251	33	0.347	0.174	-1.765	0.707	2.113	0.728	2.901
5000	51880	33	0.233	0.174	-1.487	0.707	1.720	0.728	2.361
6000	57633	33	0.127	0.174	-1.089	0.707	1.217	0.728	1.671
7000	62271	34	0.080	0.172	-1.283	1.000	1.363	1.015	1.343
8000	65682	34	0.026	0.172	-0.634	1.000	0.661	1.015	0.651
9000	67794	35	0.024	0.169					

*Table entries in bold pertain to optimal spatial association. **D_P = domain is present.

The Batalay Intrusives are positively spatially associated with the north-trending faults/fractures. The distance distribution method and the weights of evidence method indicate that the positive spatial association is optimal within 2900 and 2500 m, respectively. The distance correlation method indicates that the positive spatial association is optimal within 1500 m.

Table 4.47. Results of distance correlation calculations to quantify spatial association between Batalay Intrusive centroids and north-trending faults/fractures, Catanduanes Is.*

AP	Y_jmax_r (m)	$r_{d_{jx}d_{jy}}$ at Y_jmax_r	t-value for $r_{d_{jx}d_{jy}}$ at Y_jmax_r	$mcdioY_jmax_r$	$mcdooY_jmax_r$
Centre	2000	0.94427	16.478**		
North	2000	0.98129	29.276**		
NE	**1500**	**0.98088**	**28.951****	**0.97285**	**0.97027**
East	**1500**	**0.98886**	**38.164****	**0.98217**	**0.96997**
SE	**1500**	**0.99666**	**70.064****	**0.99323**	**0.98616**
South	2000	0.95071	17.612**		
SW	**1500**	**0.97168**	**23.624****	**0.95987**	**0.95518**
West	**1500**	**0.97809**	**26.987****	**0.97013**	**0.96760**
NW	**1500**	**0.98770**	**36.292****	**0.98199**	**0.97358**

*Table entries in bold pertain to optimal spatial association.
**Calculated t-values are significantly different from zero; critical t-value at α=0.001 and ν=35-2=33 degrees of freedom is 3.385 (Davis, 1973).

4.6.7 Batalay Intrusive centroids vs. northeast-trending faults/fractures

1. The curve for the observed cumulative frequency distribution of nearest distances between the Batalay Intrusive centroids and the northeast-trending faults/fractures is consistently above the predicted curve within 3500 m (Figure 4.26a). A positive spatial association is implied, which is significant statistically (Figure 4.26b). The highest peak along the β curve suggests that the positive spatial association is optimal within about 600 m.

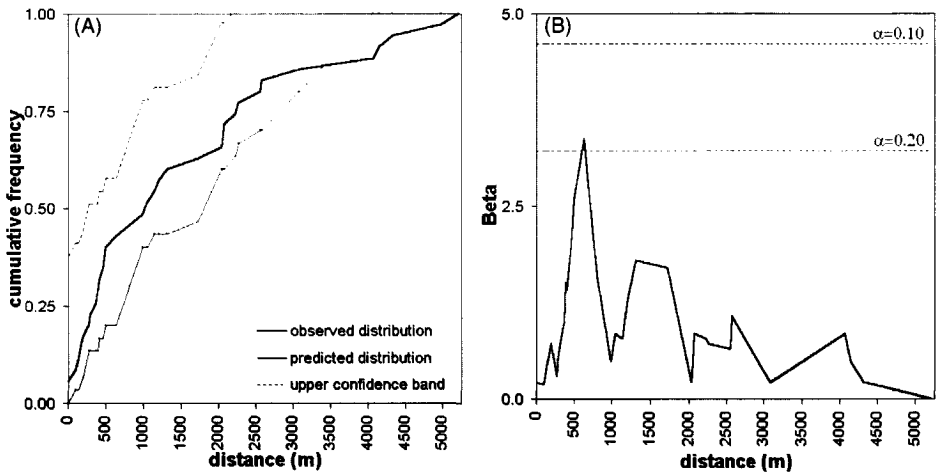

Figure 4.26. Batalay Intrusive centroids and nearest northeast-trending faults/fractures, Catanduanes Island: (a) distance distribution and (b) variation of β.

2. The variations in contrast C for cumulative distances from the north-trending faults/fractures with respect to the Batalay Intrusive centroids are shown in Table 4.48. The contrasts are significantly greater than zero, which indicate positive spatial association. The highest Studentised C indicates that the positive spatial association is optimal within 500 m.

3. The distances between the Batalay Intrusive centroids and the northeast-trending faults/fractures at which the measured values of $r_{d_{jx}d_{jy}}$ are highest vary between 500 and 2250 m (Table 4.49). The t-test indicates that these measured correlation coefficients are significantly different from zero at the 99.9% significance level. The spatial association is optimal within 1000 m. Within this distance, the spatial association is positive, i.e., $mcdioY_jmax_r$ is greater than $mcdooY_jmax_r$.

Table 4.48. Variation of weights and contrasts for cumulative distances from northeast-trending faults/fractures with respect to Batalay Intrusive centroids, Catanduanes Is.*

Distance buffer (m)	No. of pixels in D_P**	No. of gold/copper occ. in D_P**	W+	s(W+)	W-	s(W-)	C	s(C)	C/s(C)
250	5888	6	0.704	0.408	-0.099	0.186	0.804	0.449	1.791
500	**10826**	**12**	**0.788**	**0.289**	**-0.250**	**0.209**	**1.039**	**0.356**	**2.916**
1000	21702	17	0.441	0.243	-0.290	0.236	0.731	0.338	2.161
1500	29378	21	0.349	0.218	-0.366	0.267	0.716	0.345	2.073
2000	34834	22	0.225	0.213	-0.294	0.277	0.519	0.350	1.484
2500	39481	27	0.305	0.193	-0.635	0.354	0.940	0.403	2.335
3000	43589	29	0.278	0.186	-0.775	0.408	1.053	0.449	2.347
3500	47514	30	0.225	0.183	-0.793	0.447	1.018	0.483	2.107
4000	51260	30	0.149	0.183	-0.605	0.447	0.754	0.483	1.562
4500	54963	33	0.175	0.174	-1.294	0.707	1.468	0.728	2.016
5000	58375	34	0.144	0.172	-1.718	1.000	1.862	1.015	1.835
5500	61441	35	0.122	0.169					

*Table entries in bold pertain to optimal spatial association. **D_P = domain is present.

The Batalay Intrusives are positively spatially associated with the northeast-trending faults/fractures. The distance distribution method and the weights of evidence method indicate that the positive spatial association is optimal within 500 m. The distance correlation method indicates that the positive spatial association is optimal within 1000 m.

Table 4.49. Results of distance correlation calculations to quantify spatial association between Batalay Intrusive centroids and northeast-trending faults/fractures, Catanduanes Is.*

AP	Y_jmax_r (m)	$r_{d_{jx}d_{jy}}$ at Y_jmax_r	t-value for $r_{d_{jx}d_{jy}}$ at Y_jmax_r	$mcdioY_jmax_r$	$mcdooY_jmax_r$
Centre	500	0.99379	51.305**		
North	1250	0.97041	23.085**		
NE	2000	0.99230	46.029**		
East	**1000**	**0.99347**	**50.009****	**0.99260**	**0.99028**
SE	**1000**	**0.99316**	**48.850****	**0.99091**	**0.99001**
South	2250	0.96449	20.979**		
SW	**1000**	**0.99551**	**60.424****	**0.99461**	**0.99441**
West	**1000**	**0.99705**	**74.559****	**0.99592**	**0.99428**
NW	750	0.99323	49.099**		

*Table entries in bold pertain to optimal spatial association.
**Calculated t-values are significantly different from zero; critical t-value at α=0.001 and ν=35-2=33 degrees of freedom is 3.385 (Davis, 1973).

4.6.8 Batalay Intrusive centroids vs. northwest-trending faults/fractures

1. The curve for the observed cumulative frequency distribution of nearest distances between the Batalay Intrusive centroids and the northwest-trending faults/fractures is mostly just below the predicted curve (Figure 4.27a). A negative or lack of (i.e., random) spatial association is implied, which is not significant statistically (Figure 4.27b). The lowest and flat portion of the β curve suggests that a random spatial association is dominant within 5000 m.

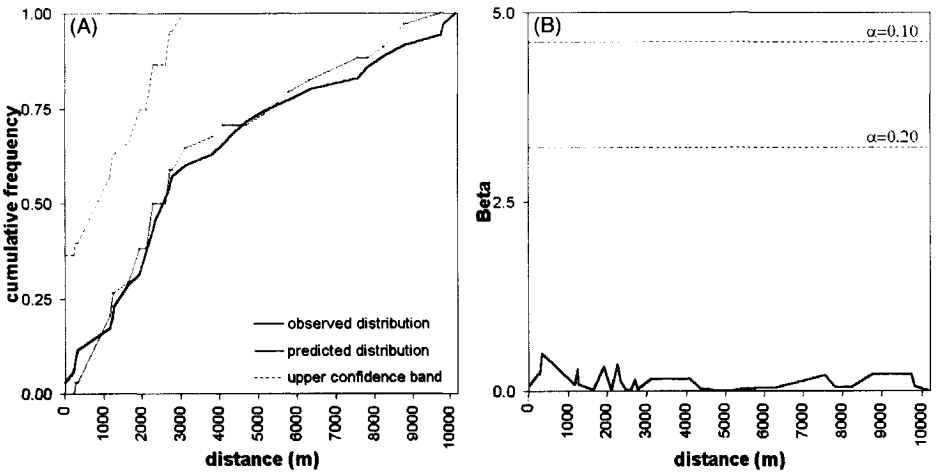

Figure 4.27. Batalay Intrusive centroids and nearest northwest-trending faults/fractures, Catanduanes Island: (a) distance distribution and (b) variation of β.

2. The contrasts C for cumulative distances from the north-trending faults/fractures with respect to the Batalay Intrusive centroids are mostly negative, which indicate negative spatial association (Table 4.50). The weights and the contrasts are, as indicated by their standard deviations, not significantly less than zero. This implies that the negative spatial association is not significant statistically. The most negative value of Studentised C indicates that the negative spatial association is optimal within 7000 m.

3. The distances between the Batalay Intrusive centroids and the northwest-trending faults/fractures at which the measured values of $r_{d_{ix}d_{iy}}$ are highest vary between 2000 and 4000 m (Table 4.51). The t-test indicates that the measured correlation coefficients are significantly different from zero at the 99.9% significance level. The spatial association is optimal within 3000 m, within which the spatial association is negative, i.e., $mcdioY_jmax_r$ is less than $mcdooY_jmax_r$.

Table 4.50. Variation of weights and contrasts for cumulative distances from northwest-trending faults/fractures with respect to Batalay Intrusive centroids, Catanduanes Is.*

Distance buffer (m)	No. of pixels in D_P*	No. of gold/ copper occ. in D_P*	W+	s(W+)	W-	s(W-)	C	s(C)	C/s(C)
500	7118	4	0.109	0.500	-0.013	0.180	0.122	0.531	0.229
1000	14136	4	-0.578	0.500	0.106	0.180	-0.684	0.531	-1.288
2000	28834	11	-0.279	0.302	0.160	0.204	-0.438	0.364	-1.204
3000	41213	20	-0.038	0.224	0.053	0.258	-0.091	0.342	-0.268
4000	48107	22	-0.098	0.213	0.190	0.277	-0.288	0.350	-0.823
5000	53486	25	-0.076	0.200	0.219	0.316	-0.295	0.374	-0.787
6000	57976	27	-0.079	0.192	0.327	0.354	-0.406	0.403	-1.009
7000	**61588**	**28**	**-0.103**	**0.189**	**0.573**	**0.378**	**-0.676**	**0.423**	**-1.599**
8000	64425	30	-0.079	0.183	0.686	0.447	-0.765	0.483	-1.584
9000	66315	32	-0.044	0.177	0.650	0.578	-0.694	0.604	-1.149
10000	67392	34	0.001	0.172	-0.023	1.000	0.024	1.015	0.024
11000	68176	35	0.018	0.169					

*D_P = domain is present

There is a lack of or negative spatial association between the Batalay Intrusives and the northwest-trending faults/fractures. The distance distribution method indicates that the lack of spatial association between the Batalay Intrusives and the northwest-trending faults/fractures is optimal within 5000 m. The weights of evidence method indicates that the negative spatial association is optimal within 7000 m. The distance correlation method indicates that the negative spatial association is optimal within 3000 m.

Table 4.51. Results of distance correlation calculations to quantify spatial association between Batalay Intrusive centroids and northwest-trending faults/fractures, Catanduanes Is.*

AP	Y_jmax_r (m)	$r_{d_{jx}d_{jy}}$ at Y_jmax_r	t-value for $r_{d_{jx}d_{jy}}$ at Y_jmax_r	$mcdioY_jmax_r$	$mcdooY_jmax_r$
Centre	2000	0.96235	20.340**		
North	**3000**	**0.83499**	**8.717****	**0.81052**	**0.82568**
NE	4000	0.92200	13.679**		
East	**3000**	**0.98316**	**30.903****	**0.97629**	**0.97746**
SE	**3000**	**0.98142**	**29.830****	**0.97315**	**0.97811**
South	**3000**	**0.91889**	**13.380****	**0.85445**	**0.89732**
SW	2000	0.97678	26.192**		
West	2000	0.98398	31.703**		
NW	2000	0.98739	35.832**		

*Table entries in bold pertain to optimal spatial association.

**Calculated t-values are significantly different from zero; critical t-value at α=0.001 and ν=35-2=33 degrees of freedom is 3.385 (Davis, 1973).

4.6.9 Discussion

The results of the quantitative characterisation of the gold-copper deposits with the different curvi-linear geological features are summarised in Table 4.52. The results of the distance distribution method and the weights of evidence method are generally similar. The results of the distance correlation method are similar to the results of (either of) the other two methods with respect to the optimal spatial association of the gold-copper deposits with the northeast-trending faults/fractures and the northwest-trending faults/fractures and spatial association between Batalay Intrusive centroids and northeast-trending faults/fractures. Where the results are different, the distances of optimal spatial association determined by the distance correlation method are within the ranges of distances of similar types of spatial associations as determined by the other two methods.

Table 4.52. Summary of results of quantitative characterisation of spatial associations of gold-copper deposits and Batalay Intrusives with curvi-linear geological features in Catanduanes Island.

Relation	Distance distribution Method			Weights of evidence Method			Distance correlation method		
	Spatial assn.	Dist. (m)	β	Spatial assn.	Dist. (m)	Studentised C	Spatial assn.	Dist. (m)	Mean $r_{d_{jx}d_{jy}}$
gcd-bic[1]	positive	2400	9.524	positive	1000	3.765	positive	3500	0.85920
gcd-nff[2]	positive	800	5.765	positive	750	2.455	positive	3000	0.99048
gcd-eff[3]	negative	11700	4.610	negative	11250	-2.578	negative	9000	0.96919
gcd-neff[4]	positive	1000	3.041*	positive	1000	2.677	positive	1000	0.99355
gcd-nwff[5]	negative	2000	5.421	negative	1500	-1.708*	negative	2500	0.99663
bic-nff[6]	positive	2900	14.628	positive	2500	3.544	positive	1500	0.98398
bic-neff[7]	positive	600	3.376	positive	500	2.916	positive	1000	0.99480
bic-nwff[8]	random	5000	0	negative	7000	-1.599*	negative	3000	0.92961

[1]gcd-bic = gold-copper deposits and Batalay Intrusive contacts
[2]gcd-nff = gold-copper deposits and north-trending faults/fractures
[3]gcd-eff = gold-copper deposits and east-trending faults/fractures
[4]gcd-neff = gold-copper deposits and northeast-trending faults/fractures
[5]gcd-nwff = gold-copper deposits and northwest-trending faults/fractures
[6]bic-nff = Batalay Intrusive centroids and north-trending faults/fractures
[7]bic-neff = Batalay Intrusive centroids and northeast-trending faults/fractures
[8]bic-nwff = Batalay Intrusive centroids and northwest-trending faults/fractures
*not significant statistically

The gold-copper deposits are positively spatially associated with the Batalay Intrusive contacts, the north-trending and the northeast-trending faults/fractures. The positive spatial association of the gold-copper deposits with the northeast-trending faults/fractures is strongest (mean distance ≈ 1000 m), with the north-trending faults/fractures it is intermediate (mean distance ≈ 1500 m), and with the Batalay Intrusive contacts it is weakest (mean distance ≈ 2300 m). The gold-

copper deposits are negatively spatially associated with the east-trending and the northwest-trending faults/fractures. The negative spatial association of the gold-copper deposits with the northwest-trending faults/fractures (mean distance ≈ 2000 m) is weaker than its negative spatial association with the east-trending faults/fractures (mean distance ≈ 10600 m).

The Batalay Intrusives are positively spatially associated with the north-trending and the northeast-trending faults/fractures but are randomly to negatively spatially associated with the northwest-trending faults/fractures. The positive spatial association of the Batalay Intrusives with the northeast-trending faults/fractures (mean distance ≈ 700 m) is stronger than their positive spatial association with the north-trending faults/fractures (mean distance ≈ 2300 m).

The results indicate that the east-trending and the northwest-trending faults/fractures are not important structural controls on the emplacement of the Batalay Intrusives and deposition of gold-copper vein-type mineralisation. Northeast-trending faults/fractures, rather than the north-trending faults/fractures, are the more important structural controls on the emplacement of the Batalay Intrusives and the mineral deposits. These structural controls are more important than heat source controls for the gold-copper vein-type mineralisation.

Based on the results of the quantitative characterisation of the spatial associations between the different geological features in Catanduanes Island, the following hypotheses can be postulated. The east-trending, northwest-trending and north-trending faults/fractures were pre-magmatic structural regimes. Later east-west compressive regimes that acted on the Philippine archipelago resulted in northeast-trending faults/fractures. Coeval with the formation of northeast-trending faults/fractures, magmatic intrusions were localised along these structures and near north-trending faults/fractures. The magmatic intrusions acted as heat sources for hydrothermal mineralisation. The younger northeast-trending faults/fractures acted as favourable channelways for the mineralising fluids.

4.7 GENERAL DISCUSSION

Two established methods (distance distribution method and weights of evidence method) and a new distance correlation method for quantitative characterisation of spatial associations between mineral deposits (represented as points) and geological features (represented as lines or points) are demonstrated in four study areas. These methods have their advantages and disadvantages with regard to the quantitative characterisation of spatial association between a set of points and a set of lines.

A major advantage of the distance distribution method is that it can be used to model spatial association between a set of points and a set of k-th nearest lines (Bonham-Carter, 1985). However, the examples shown here were only for the set of k=1 nearest lines (i.e., nearest neighbour lines) in order to make direct comparison with the results of the other two methods. The main disadvantage of the distance distribution method is in the creation of random points that must be confined to particular lithologic units known to host the mineral deposits studied whilst at the same time assuming a condition of CSR. It is believed that different 'optimum' sets of random points will provide different results. In all the analyses shown here, a single set of optimum random points that 'best' assumes a condition of CSR was used. Bonham-Carter et al. (1985) also used a single set of a very large number of random points to approach a reasonable estimate of the 'true' expected distance distribution. Here, the number of random points used is equal to the number of mineral deposit points to make a comparison between the distance distributions of two sets of points (observed and predicted), which have equal prior probability of occurrence per unit area. The adequacy of using a set of random points equal in number to the observed mineral deposit points is demonstrated by the very similar results between the distance distribution method and the weights of evidence method.

A strong advantage of the weights of evidence method is that it is a direct method (i.e., there is no need for random points) for evaluating spatial association between a set of points and a set of lines or a set of polygons. It is also worth pointing out at this stage that the weights of evidence is advantageous over the two methods because it leads to the next step of integrating spatial evidences for mineral potential mapping (see Chapter 6; Agterberg, 1989, 1992a; Bonham-Carter et al., 1988, 1989; Bonham-Carter and Agterberg, 1990; Bonham-Carter, 1991, 1994; Agterberg et al., 1993; Turner, 1997; Wilkinson et al., 1999) – the other two method do not give weights for integrated analysis. Its main disadvantage is in the case of a small number of points used in the analysis. It has been shown here that in such a case the highest Studentised C is a useful criterion for selecting the threshold distance within which the spatial association is optimal. However, it is shown later in Chapter 6 that in the case of a small number of points, the Studentised C alone is not useful in determining the threshold distance within which the spatial association is optimal to create binary predictor patterns for mineral potential mapping.

The new distance correlation was developed to avoid the limitations and/or disadvantages of the distance distribution method and the weights of evidence method. The main disadvantage of the distance correlation method is that several arbitrary points have to be used to characterise optimally the spatial association between a set of points and a set of lines (or another set of points). The problem with the several arbitrary points is not in choosing these points but in choosing which value of $Y_j max_r$ for the different arbitrary points is optimal. This was not a problem in the case when, among the different arbitrary points, there

is a particular Y_jmax_r with the highest frequency, which was considered optimal. In this case, the optimal Y_jmax_r distances determined by the distance correlation method are either similar to or within the optimal distances determined by the other two methods. The problem occurs when there are at least two different Y_jmax_r distances with equal frequencies for different arbitrary points (for example see Tables 4.2, 4.5, 4.15, 4.19, 4.34, 4.37, 4.37 and 4.51). As mentioned earlier (see p. 115, 2nd to the last paragraph), in cases of an equal frequency, a triple-tie or a quadruple-tie in frequencies, the higher or highest Y_jmax_r was considered optimal. The optimal Y_jmax_r distances that were chosen are usually similar, if not the same, as or within the distances at which certain spatial associations are optimal as determined by the other two methods. However, the results of the distance distribution method and the weights of evidence method were useful in selecting the optimal Y_jmax_r distances in the problematic cases. The results of the other two methods, which are very similar, were therefore useful in improving the efficacy of the distance correlation method.

The problematic case encountered with the distance correlation method illustrates the proposition of Bonham-Carter (1994) that the spatial association between mineral deposits and geological features can only be quantitatively explored but not finitely confirmed. The different yet invariably similar optimal distances within which the spatial associations between the mineral deposits and the different geological features were quantified by the three methods also illustrate the proposition of Bonham-Carter (1994). This implies that a single method can never be adequate to accurately characterise the spatial association between mineral deposits and geological features. It is therefore useful to employ not one but a number of methods to quantitatively characterise spatial associations between mineral deposits and geological features. The distance correlation method is an additional tool to the short list of methods.

The choice of the size of study area can be very critical to all the methods demonstrated here for evaluating spatial association between a set of points and a set of lines. The size of the study area was not a problem for the procedure adopted here for the distance distribution method in which the frequency of observed nearest distances was used (Bonham-Carter et al., 1985). However, in another distance distribution approach of Bonham-Carter (1985), line density (i.e., number of lines per unit area) was used as a variable, which influences estimates of the observed and predicted distance distribution functions. The size of study area is particularly critical to the weights of evidence method, which requires polygonal domains, as discussed in Chapter 6 and by Bonham-Carter (1994). The size of study area is also critical to the distance distribution method because the perpendicular line passing through the observed points and the nearest neighbour points on the lines (Figure 4.1) can extend beyond the limits of the study area, in which case the area is adjusted to properly analyse the correlation of distances from the arbitrary points.

4.8 CONCLUSIONS

Knowledge about the spatial association between mineral deposits and geological features is important in mineral exploration, but until recently was only qualitative. For the well-explored study areas, i.e., Benguet province and Baguio district, quantitative characterisation of spatial association between mineral deposits and geological features provides geoinformation that generally conforms to existing qualitative geoscientific knowledge pertinent to the genesis of the mineral deposits. For the less-explored study areas, i.e., Abra area and Catanduanes Island, the quantitative characterisation of spatial association between mineral deposits and geological features provides sound insights into the genesis of the mineral deposits. The results of the quantitative characterisation of the mineral deposits and geological features in the four study areas can therefore be useful for mineral potential mapping of these areas.

Two established methods (distance distribution method and weights of evidence method) and new distance correlation method were used in quantifying the spatial association between mineral deposits and geological features in four study areas. The distance correlation method, unlike the distance distribution method, has no assumption of the spatial distribution (e.g., Poisson distribution) of the mineral deposits. The distance correlation method, unlike the weights of evidence method, is effective even in the case of small number of points. The distance correlation method produced results that are invariably similar to the results of the two methods. It is therefore a satisfactory method.

The different yet similar results of the three quantitative methods demonstrate that qualitative approaches to characterise spatial association between mineral deposits and geological features can produce trivial results. Consequently, when qualitative knowledge alone is used in mineral exploration, the resulting mineral potential maps can also be trivial. The results of the quantitative characterisation of the spatial associations of the mineral deposits and geological features in the study areas based on the three methods will be used in the predictive mineral potential mapping techniques presented in the succeeding chapters.

Chapter 5

Geologically-Constrained Mineral Potential Mapping: Application of Deposit Exploration Models

"Even if there is only one possible unified theory, it is just a set of rules and equations. What is it that breathes fire into the equations and makes a universe for them to describe? The usual approach of science of constructing a mathematical model cannot answer the questions of why there should be a universe for the model to describe. Why does the universe go to all the bother of existing?"

Hawking, Stephen W. (1942-)

This Chapter demonstrates the application of geologic criteria provided by mineral deposit models, which are transformed into spatial geological evidence maps based on the quantitative characterisations in Chapter 4, in GIS-based geologically-constrained mineral potential mapping. Portions of this Chapter have been published as Application of Mineral Exploration Models and GIS to Generate Mineral Potential Maps as Input for Optimum Land-Use Planning in the Philippines (Carranza et al., 1999a)

5.1 INTRODUCTION

Every mineral deposit is unique. Similarities in characteristics of some mineral deposits, however, enable mineral deposits to be grouped into different classes. Each class of mineral deposit is represented by a generalised empirical model, known as a mineral deposit model. Mineral deposit models are conceptual models, usually described in words and diagrams that represent data and interpretations for a mineral deposit type (Barton, 1986; Sangster, 1986). Schematic diagrams of mineral deposit models are typically presented as cross-sections through the idealised systems. Mineral deposit models emphasize the general characteristics and the geologic, geochemical and geophysical environments of the different but similar mineral deposits. Mineral deposit models provide criteria for the recognition of favourable geologic terranes and 'ore guides' or 'clues to ore' within a particular favourable geologic terrane. These criteria can be referred to as the deposit exploration model. Deposit exploration models are important for providing the theoretical framework for GIS-based mineral potential mapping (Bonham-Carter, 1994). They are useful in guiding data selection and data modelling, in determining which features to enhance and extract as spatial evidence, and for deciding the relative importance of each of the spatial evidences in mapping mineral potential.

5.2 METHODOLOGY

Deposit exploration models for porphyry copper, epithermal gold and nickeliferous-laterite mineralisations were applied to the appropriate study areas to map potentially mineralised zones. Figure 5.1 shows the 3-step general methodology followed to undertake geologically-constrained mineral potential mapping based on deposit exploration models.

The first step involves (a) review of literature on mineral deposit models considered and (b) input of spatial data into the GIS. Concise descriptions of the mineral deposit models considered are given here. The spatial data inputs into the GIS have been described in Chapter 2 (for paper map data) and in Chapter 3 (for satellite imagery). The four types of spatial data layers indicated in Figure 5.1 are not necessarily used altogether to map potential of a particular type of mineral deposit. For example, structural and hydrothermal alteration data are not necessary for mapping nickeliferous-laterite potential (see below). This is the reason for the dashed arrows in the lower portion of the flowchart.

The second step involves procedures to (a) select and extract geological features that represent deposit exploration models and (b) create derivative maps to be used as spatial evidence of mineralisation. The quantification of spatial association between curvi-linear geological features and known mineral deposits is described Chapter 4, the results of which were used to select, extract and transform geological features based on the deposit exploration models into spatial geological evidence maps. Remote detection of hydrothermal alteration is described in Chapter 3. The extraction of topographic indicators for nickeliferous-laterite deposits is described in Chapter 2. The spatial evidence maps created are binary, that is, indicating presence (score = 1) or absence (score = 0) of favourable spatial evidences of mineralisation.

The third step involves (a) combining the spatial evidence maps to produce a geologically-constrained predictive mineral potential map and (b) validation of the predictive map. It is assumed that each of the spatial evidences has equal importance in delineating potentially mineralised zones. It was also assumed that mineral potential could be characterised by a 'linear' combination of a majority, if not all, of the spatial evidences. Each evidence map was thus given equal weights (i.e., 1) and the maps were 'added' together. Zones characterised by a combination of a majority of the input spatial evidences were considered to be favourable for mineral deposits. This simple scheme of mineral potential classification is a simulation of the 'light-table operation' of combining spatial information performed by mineral explorationists in the past. Finally, the validity of the geologically-constrained predictive mineral potential maps was assessed against the known mineral deposits. In addition, the reliability and/or adequacy of the geologically-constrained predictive mineral potential maps were determined. The geologically-constrained predictive mineral potential maps were considered reliable if the predicted favourable zones show spatial coincidence

with significant geochemical anomalies and/or with known mineralised zones. They were considered adequate if their success rates are similar to the success rates of the integrated geochemical-geological predictive mineral maps.

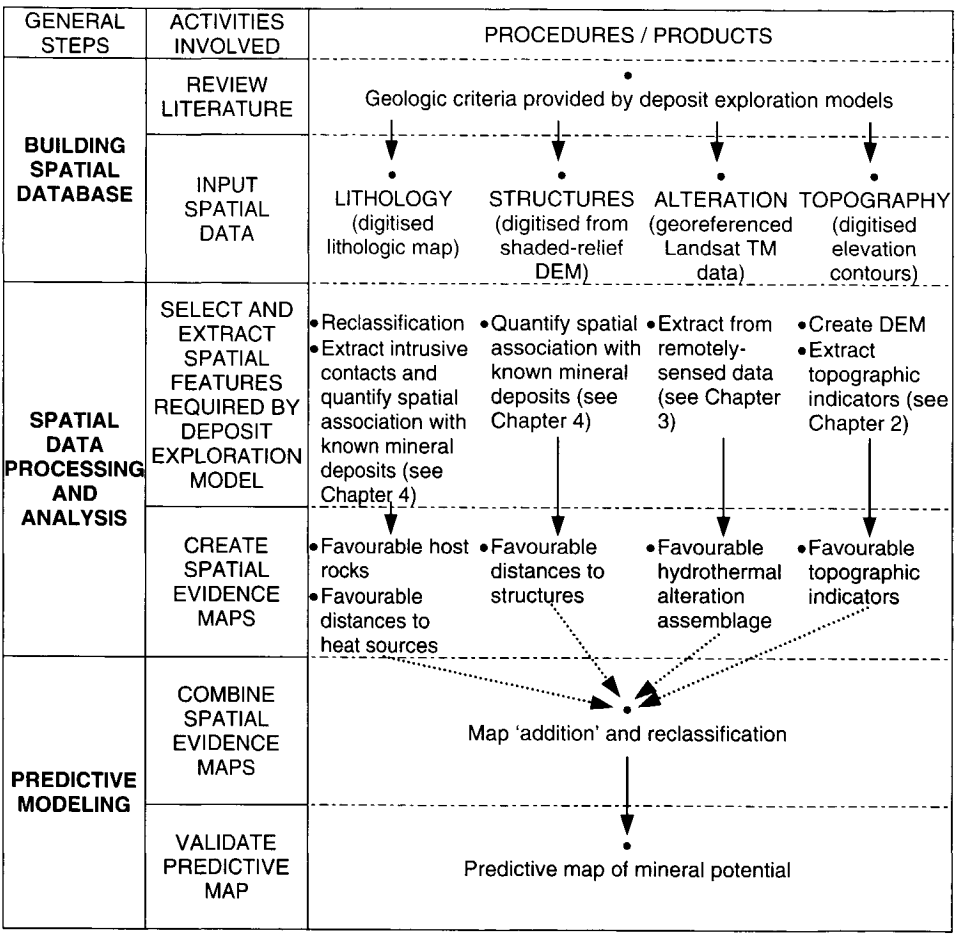

Figure 5.1. Flowchart of 3-step general methodology for geologically-constrained mapping of mineral potential based on deposit exploration models.

5.3 MAPPING PORPHYRY COPPER POTENTIAL

Geologic criteria provided by both generalised empirical models of porphyry copper deposits and studies of the general characteristics of Philippine porphyry copper deposits were applied to geologically-constrained mapping of porphyry copper mineral potential in the Benguet province and the Abra area.

5.3.1 General characteristics of porphyry copper deposits

Porphyry copper deposits are the products of large, intrusion-related hydrothermal systems (Titley and Beane, 1981; McMillan and Panteleyev, 1980, 1988; Pirajno, 1992; Sillitoe, 1992). They resulted from the emplacement at shallow depths (1-2 km) and the subsequent cooling of intrusive bodies that have a distinct porphyritic texture (hence, the name porphyry). The porphyry intrusions can be one of a variety of rocks, but quartz-bearing intermediate composition rocks, such as diorite, granodiorite, and tonalite are the most common. The porphyry plutons, commonly finger-like bodies, have small lateral extents (~0.5-2 km^2) but have large vertical dimensions. The porphyry plutons are emplaced in contact with a variety of wall rocks ranging from metamorphosed basement rocks through sedimentary and volcanic successions and to comagmatic volcanic rocks that may occur above them. Pre-existing rocks that are good hosts of porphyry copper mineralisation include plutonic rocks of intermediate composition, intermediate to mafic volcanic rocks, calcareous clastic rocks, and rocks of various compositions that are competent and closely-fractured.

Porphyry copper deposits generally occur at convergent plate margins and in rift-related tectonic settings with characteristic strike-slip fault systems (Bryner, 1969; Sillitoe, 1972, 1976; Field et al., 1974; Lowell, 1974; Laznicka, 1976; Hollister, 1974, 1978; Horton, 1978; Titley and Heidrick, 1978; Mitchell and Garson, 1981; Titley, 1981; Titley and Beane, 1981; Cox, 1982; Hutchison, 1983; Sillitoe and Gappe, 1984; Sawkins, 1989; Pirajno, 1992). At convergent margins, porphyry copper deposits form above subduction zones along continental boundaries and intra-oceanic island-arcs. Examples of the former are the Andean porphyries (Sillitoe, 1976, 1981, 1986), and of the latter are the Pacific island porphyries (Baldwin et al., 1978; Sillitoe and Gappe, 1984; Rogers and Mckee, 1990; Rush and Seegers, 1990). The Andean type porphyry copper deposits are usually molybdenum-rich whilst the island-arc type porphyry copper deposits are usually gold-rich. The origin and source of the metals such as Cu, Mo and Au has been debated by many authors and the problem has been considered in terms of Cu/Mo ratios or of the relative Cu-Au-Mo contents (Sillitoe, 1986; Pirajno, 1992). Hollister (1978) and Titley and Beane (1981) contend that the metals originated in the source region of the magmas, with subsequent assimilation of crustal materials and scavenging of metals from intruded rocks. They further purport that the Cu/Mo ratio decreases with

increasing thickness of the sialic crust and distance from the Benioff Zone. High Mo or low Cu/Mo ratios would therefore indicate a thick sialic crust as exemplified by the Andean porphyry copper deposits, in which the crustal sources of metals include sedimentary and volcanic rocks, pre-existing mineralised bodies and granitic rocks. In contrast, high Au or high Cu/Mo ratios indicate a thin and more simatic or mafic crust as exemplified by the Pacific Island porphyry copper deposits, in which the source of metals include the more mafic oceanic crust and the predominantly dioritic plutons.

Although the deposit-related porphyry plutons are usually small, their emplacement and subsequent migration of hydrothermal solutions produce large volumes, many cubic kilometres, of mineralised and altered rocks (Beane and Titley, 1981; Guilbert, 1986). The mineralisation-alteration is usually best developed in the form of a cylinder that may be closed at the top and characteristically centred on the deposit-related porphyry intrusion. The mineralisation is usually dominated by pyrite, together with molybdenite and chalcopyrite. Molybdenite mineralisation is usually present in the Andean porphyry copper deposits but is usually absent in the island-arc porphyry copper deposits (Pirajno, 1992). Accompanying the mineralisations are alteration assemblages, which are developed around the porphyry intrusions. There are two models of porphyry copper mineralisation-alteration: the Lowell-Guilbert model (Lowell and Guilbert, 1970; Guilbert and Lowell, 1974) and the diorite model (Hollister, 1975, 1978).

The Lowell-Guilbert model, also known as the quartz-monzonite model, relates to felsic rocks of granitic composition. The hydrothermal alteration zones form more or less concentric shells, which are centred on the deposit-related porphyry intrusion (Figure 5.2a). At the core of the hydrothermal alteration shells is the potassic zone, around which are distributed the phyllic zone, the argillic zone and the propylitic zone. The potassic zone contains the assemblage quartz + K-feldpsar + biotite + sericite + anhydrite + pyrite + chalcopyrite + bornite ± magnetite ± molybdenite. The 'ore shell' is typically contained within the outer limits of the potassic core. The phyllic zone, also known as quartz-sericite-pyrite (QSP) zone, surrounds and overlaps the potassic zone. It is characterised by the assemblage of quartz + sericite + pyrite ± chlorite ± rutile ± chalcopyrite. In the phyllic zone, pyrite can reach up to 30% by volume and form veinlets and granular disseminations. Chalcopyrite may be present in subordinate amounts. Contacts between the phyllic and argillic zones are gradational and indistinct. The argillic zone is characterised by the presence of clay minerals such as illite, kaolinite and montmorillonite. Pyrite, chalcopyrite and bornite are the main sulphide species associated with the argillic zone; pyrite, though present, is less common. The argillic zone grades outward to the propylitic zone, which is the largest of the alteration shells forming a wide halo in the country rocks around the porphyry intrusives. The main assemblage of the propylitic zone consists of chlorite + epidote + pyrite + calcite ± clay minerals. Pyrite is abundant and

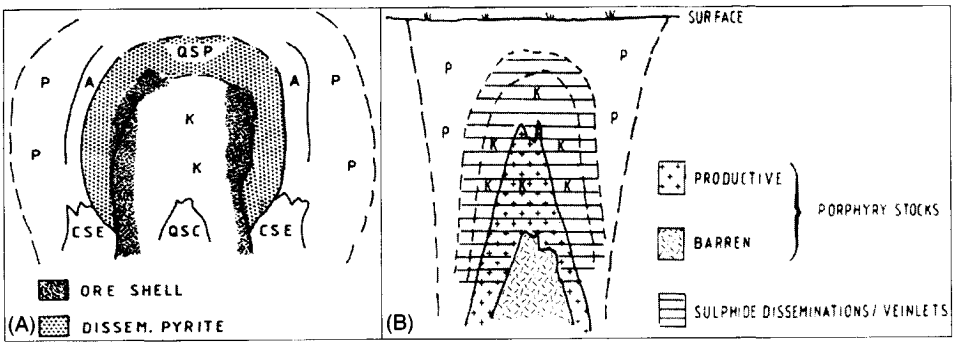

Figure 5.2. Schematic porphyry copper mineralisation-alteration patterns: (a) Lowell-Guilbert model related to quartz-monzonitic porphyry systems (Lowell and Guilbert, 1970; Guilbert and Lowell, 1974); (b) diorite model related to dioritic or syenitic porphyry systems (Hollister, 1975, 1978). K = potassic; QSP = quartz-sericite-pyrite (or phyllic); A = argillic; P = propylitic; CSE = chlorite-sericite-epidote; QSC = quartz-sericite-chlorite.

chalcopyrite is rare in the propylitic zone. Minor alteration zones in the model include quartz-sericite-chlorite (QSC) and chlorite-sericite-epidote (QSE) assemblages. The former is usually formed within the potassic zone whilst the latter is usually formed at the fringes of the potassic zone at the lower portions of the phyllic zone and grades outward into the propylitic zone and/or the argillic zone.

The diorite model typifies porphyry copper mineralisation-alteration associated with mafic intrusives of dioritic or syenitic composition, which are usually found in island-arcs built on oceanic or thin continental crust. The diorite model consists of two successive shells of potassic and propylitic zone (Figure 5.2b). The potassic zone is dominated by biotite and chlorite with little or no K-feldpsar. Propylitic alteration consists of an assemblage of chlorite + epidote + albite + carbonate, which is paragenetically younger than, and replaces, the potassic assemblages. Phyllic alteration, if present, is generally weakly developed. In diorite-type porphyry copper mineralisation-alteration, chalcopyrite disseminations are important and tend to accompany the potassic zone. The chalcopyrite to pyrite ratio is close to unity (Beane and Titley, 1981), whereas the chalcopyrite to bornite ratio is equal to or less than 2 (Hollister, 1978).

Whether the mineralisation-alteration is of the Lowell-Guilbert model or the diorite model, porphyry copper deposits comprise three broad types: (1) plutonic; (2) classic; and (3) volcanic (McMillan and Panteleyev, 1980; Pirajno, 1992; Figure 5.3). The plutonic type (Figure 5.3a) is characterised by a lack of obvious concentric mineral zoning and has broad, diffuse zones of weak mineralisation. The plutons are multiphase and form large batholithic complex of calc-alkaline chemistry. Alteration is fracture-controlled, pervasive and characterised by well-

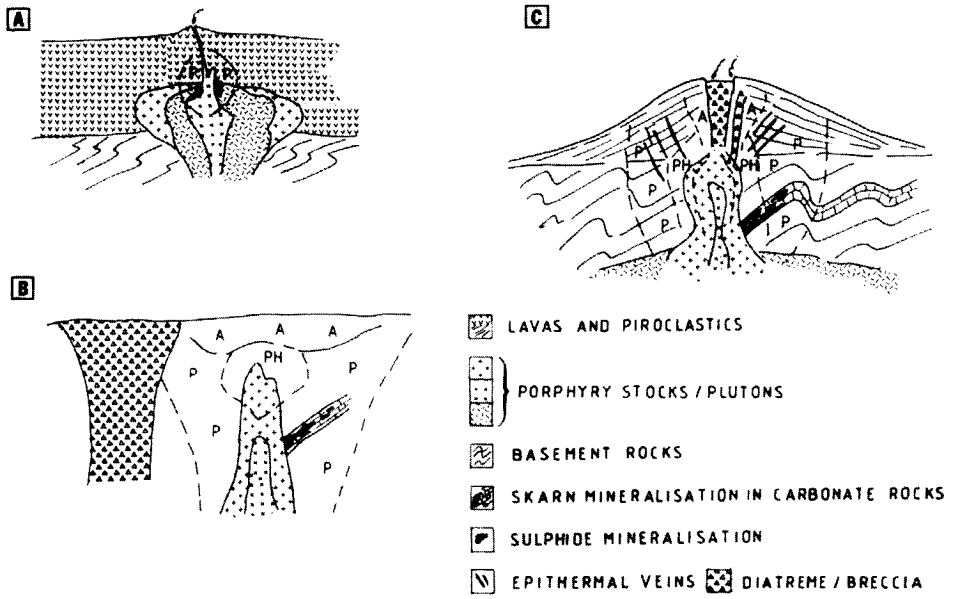

Figure 5.3. Schematic models of porphyry copper deposits: (a) plutonic type; (b) classic type; and (c) volcanic type. (From Pirajno, 1992). A = argillic; P = potassic; PH = phyllic.

developed phyllic and argillic types, whilst potassic alteration is localised. Mineralisation is typically associated with stockworks and sulphide zones progress outward from chalcopyrite to bornite to outlying pyrite-rich zones. The classic type (Figure 5.3b) consists of post-orogenic composite stocks with typical porphyritic textures and a complex array of plugs, diatremes, breccias and dykes. Potassic, phyllic and propylitic alterations are developed as shells around the porphyry intrusions. Mineralisation also occurs as shells – a weakly mineralised core in which pyrite is a dominant sulphide, surrounded by successive zones dominated by molybdenite, chalcopyrite and finally pyrite. The volcanic type (Figure 5.3c) represents near-surface expression of orogenic granitic rocks that have intruded a cogenetic volcanic pile. The vertical extent from the top of the volcano to upper portions of porphyry stock may be approximately 3-4 km (Sillitoe, 1973). McMillan and Panteleyev (1980) recognise calc-alkalic sub-types and alkalic sub-types. Calc-alkalic sub-types are represented by small plugs (0.2-1 km^2), sheets or dykes emplaced in a subvolcanic environment. The intrusive rocks have a small core of potassic alteration with phyllic and/or argillic alteration developed locally, whereas propylitic alteration is widespread. Mineralisation is predominantly Cu-Mo, forming lenses or irregularly shaped orebodies consisting of chalcopyrite, bornite and molybdenite. The alkalic sub-types are characterised by high-level plugs generally linked to underlying mesozonal batholiths. Potassic alteration is overprinted by propylitic, followed again by alkali metasomatism, which is mainly

sodic and/or potassic. The alkalic sub-type deposits are generally Cu-Au in breccias and/or highly fractured rocks. Mineral zoning consists of chalcopyrite + magnetite and bornite grading outwards to pyrite.

Porphyry copper deposits related to porphyry plutons emplaced in carbonate lithologies may or may not contain skarn mineralisation-alteration (Pirajno, 1992). The skarn or calc-silicate mineralisation-alteration is formed by contact metasomatic processes related to the igneous intrusions. The word 'skarn' was originally used by Swedish miners to indicate Fe-rich calc-silicate gangue material. The terminology, classification and characteristics of skarn-type mineralisation-alteration are discussed by Einaudi et al. (1981), Einaudi (1982a, 1982b) and Einaudi and Burt (1982) and are not further discussed here as they are minor elements of many Philippine porphyry copper deposits such as those in Benguet province and Abra area (Divis, 1983; Sillitoe and Gappe, 1984).

5.3.2 General characteristics of Philippine porphyry copper deposits

Among the tectonic settings in which porphyry copper deposits generally occur are island arcs. One such island arc is the Philippine Archipelago, where many porphyry intrusions are cut by many faults (Divis, 1983). Sillitoe and Gappe (1984) formulated a generalised schematic model for Philippine porphyry copper deposits (Figure 5.4). The deposits, which are of the classic type (see Figure 5.3b), are mostly centered on stocks of porphyry intrusions. The ore zones are associated spatially with sericite-clay-chlorite (SCC) alteration that grades downward into K-silicate alteration. Diatremes are present in the marginal parts of a number of Philippine porphyry copper systems but apparently are not genetically or spatially associated with the deposits.

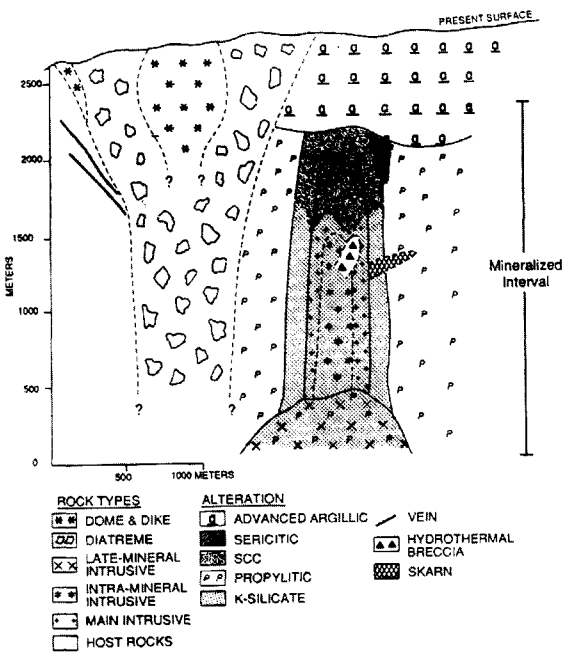

Figure 5.4. Schematic model of typical Philippine porphyry copper deposits. Essential features are bound by solid lines, optional features by dashed lines. (From Sillitoe and Gappe, 1984).

Porphyry copper deposits in the Philippines are localised near or along fault domains characterised by strike-slip movements (Bryner, 1968, 1969; Divis, 1983; Sillitoe and Gappe, 1984). Most deposits are associated with loci of fault intersections or branches and have formed with porphyry plutons near the axes of Tertiary (ge)anticlines. In addition to this qualitative spatial characterisation of the Philippine porphyry copper deposits, Sillitoe and Gappe (1984) identified four semi-quantitative spatial characteristics of porphyry copper deposits that provide, on a regional scale, an exploration model. First, more than 80 percent of the known porphyry copper mines and prospects are restricted to well-defined belts and clusters in magmatic arcs. Second, portions of regional strike-slip fault systems may reasonably be inferred to have localised more than 80 percent of all known deposits. Third, about 75 percent of the known deposits are located within 4 km of the margins of phaneritic-textured plutons, commonly of batholithic dimensions. Fourth, about 50 percent of the known deposits are located not more than 3 km away from each other.

5.3.3 Geologic criteria for porphyry copper potential mapping

Based on the general characteristics of porphyry copper deposits elsewhere and in the Philippines, the following were deduced as the geologic criteria for predictive mapping of favourable zones of porphyry copper potential.

1. Presence of and proximity to porphyry plutons (Sillitoe and Gappe, 1984; Pirajno, 1992; Sillitoe, 1992).
2. Presence of and proximity to intersections of strike-slip fault/fracture systems (Bryner, 1968, 1969; Sawkins, 1989).
3. Presence of pre-existing favourable host lithologies (McMillan and Panteleyev, 1988).
4. Presence of favourable hydrothermal alteration assemblages (Hollister, 1978; Sillitoe and Gappe, 1984).
5. Proximity to phaneritic-textured plutons, commonly of batholithic dimensions, which are probably pre-cursors of porphyry plutons (Sillitoe and Gappe, 1984).

These geologic criteria were applied to map favourable zones of porphyry copper potential in Benguet province and Abra area. The semi-quantitative spatial characterisation of the Philippine porphyry copper deposits by Sillitoe and Gappe (1984) are useful criteria but not necessarily applicable to either the Benguet province or the Abra area. These spatial characteristics pertain collectively to most, if not all, of the Philippine porphyry copper deposits and, as demonstrated in Chapter 4, the spatial association of the porphyry copper deposits to the different geological features in the Benguet province and Abra area are different. Hence, the quantified spatial associations between the porphyry copper deposits and the appropriate geological features in the Benguet province and Abra area were used to transform the appropriate geologic criteria

above into binary spatial geological evidence maps. These binary spatial geological evidence maps were integrated to map favourable zones of porphyry copper potential in these areas.

5.3.4 Porphyry copper potential mapping, Benguet province

The binary spatial geological evidence maps listed below were created, based on (a) the geologic criteria given above, (b) the geology and porphyry copper mineralisation of Benguet province (sub-section 2.2.1) and (c) the spatial associations between porphyry copper deposits and appropriate geological features in the province (section 4.3). These spatial geological evidences were considered appropriate for predictive mapping of favourable zones of porphyry copper potential in the province. The binary spatial geological evidence maps are shown in Figure 5.5 and explained below.

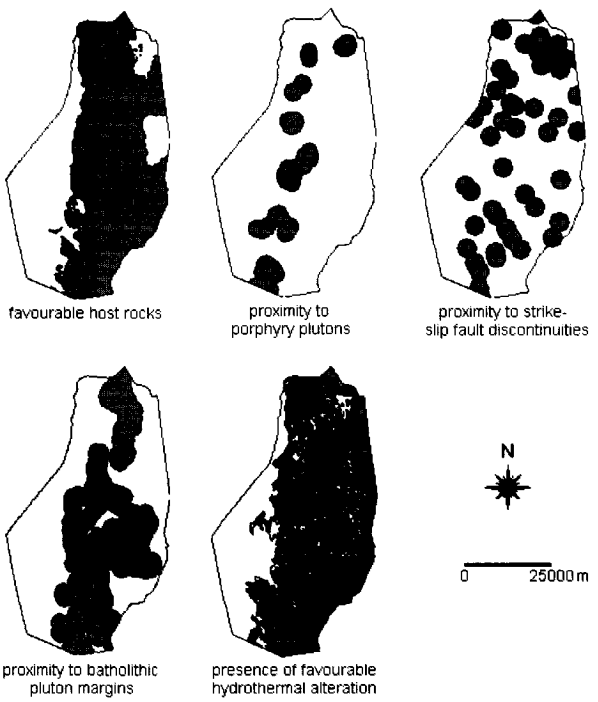

Figure 5.5. Spatial geological evidences of porphyry copper mineral potential, Benguet province.

1. Binary map of favourable host lithologies consisting of porphyry plutons, batholithic plutons and metavolcanic rocks (sub-section 2.2.1).
2. Binary map of presence of and proximity to within an average of 2100 m of porphyry plutons (section 4.3).
3. Binary map of presence and proximity to within an average of 2700 m of strike-slip fault discontinuities or strike-slip fault intersections/branches (section 4.3).
4. Binary map of proximity to within an average of 2250 m of batholithic pluton margins (section 4.3).
5. Binary map of presence of propylitic and sericite-clay-chlorite (or illitic) alteration zones (Sillitoe and Gappe, 1984; sub-section 3.3.6).

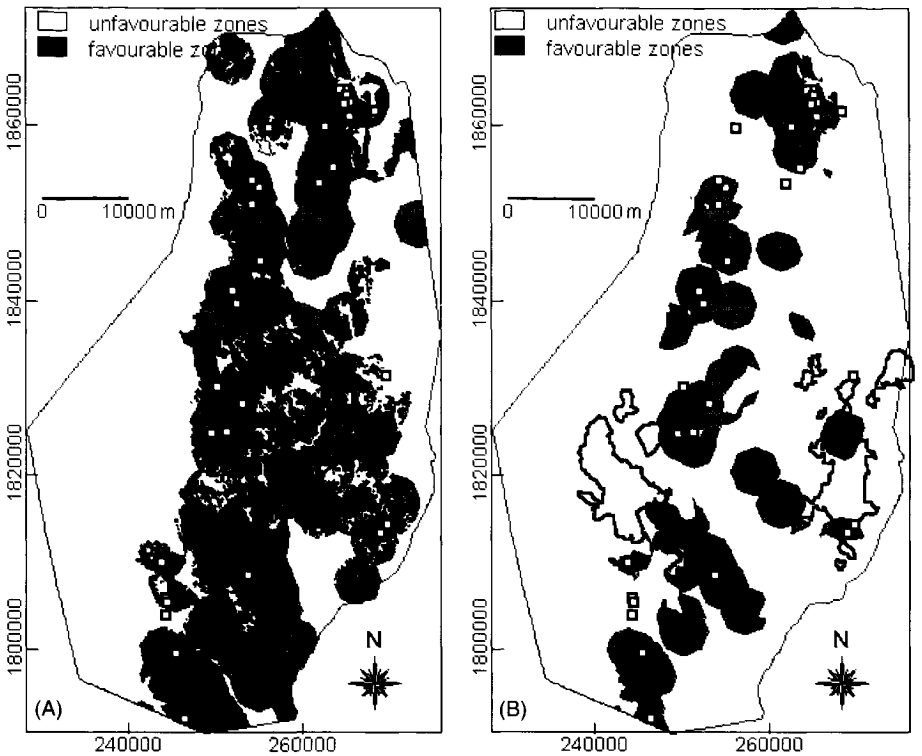

Figure 5.6. Predictive maps of porphyry copper potential, Benguet province: (a) inclusive of all spatial geological evidences in Figure 5.5; (b) exclusive of 'favourable hydrothermal alteration' evidence. Unfilled squares = porphyry copper deposits. Polygons in solid lines = catchment basins anomalous in Cu and Au.

Combining the spatial evidence maps resulted in a map with values ranging from zero to five. This was classified into a predictive map of favourable zones for porphyry copper potential. Zones with values ≥3 (i.e., combination of three to five spatial evidences) were considered to be favourable for porphyry copper deposits; zones with values <3 were considered not favourable.

The predictive map in Figure 5.6a predicts about 84% of the 31 known porphyry copper deposits in the province. The predictive map also indicates that almost half of Benguet province has favourability for porphyry copper deposits. The high prediction rate of the map is remarkable; however, the wide areal extent of the predicted favourable zones is unrealistic and is attributed to the incidence of extensive 'favourable alteration zones'. These zones were detected remotely but have low mapping accuracy (see sub-section 3.3.6).

The spatial evidence map of favourable alteration zones was considered to be of dubious value and removed from the analysis. In the resulting map, zones with values ≥3 (i.e., combination of three to four spatial evidences) were considered to be favourable for porphyry copper deposits; zones with values <3 were considered unfavourable (Figure 5.6b). The predictive map, exclusive of hydrothermal alteration evidence, indicates that about 22% of Benguet province has favourability for porphyry copper deposits. The delineated favourable zones predict correctly the location of 23 (or at least 74%) of the 31 known porphyry copper deposits. It is also interesting to note that two of the deposits not predicted correctly are just within 800 m (and their inclusion increases the success rate of the predictive map to 81%).

To assess further the reliability of the predictive map in Figure 5.6b, it is compared with the stream sediment geochemical anomalies (see sub-section 2.2.4). Portions of the predicted favourable zones spatially coincide with catchment basins that are anomalous for Cu and Au. Inspection of the DEM (Figure 2.7) and the anomalous catchment basins (see Figure 2.12) reveals that these overlap zones are headwater portions of the geochemically-anomalous catchment basins. These overlap zones probably represent the provenance of the geochemical anomalies. The predictive map in Figure 5.6b is reliable.

5.3.5 Porphyry copper potential mapping, Abra area

The binary spatial geological evidence maps listed below were created, based on (a) the geologic criteria given above, (b) the geology and porphyry copper mineralisation of Abra area (sub-section 2.4.1) and (c) the spatial association between the porphyry copper deposits and appropriate geological features in the area (section 4.5). These spatial geological evidences were considered appropriate to attempt predictive mapping of favourable zones of porphyry copper potential in the area. The binary

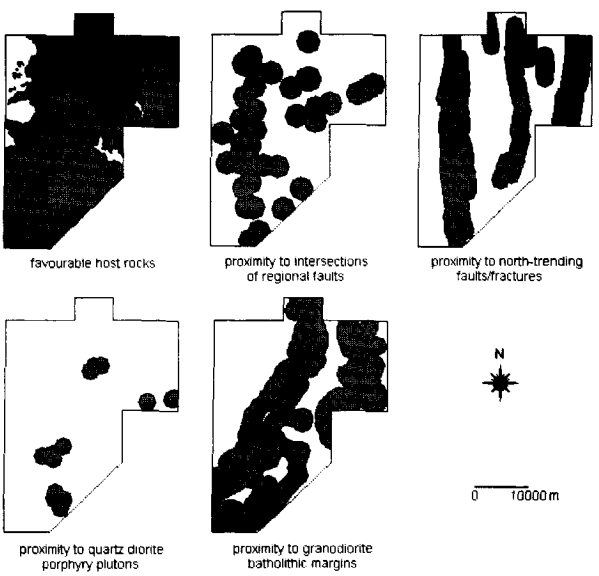

Figure 5.7. Spatial geological evidences of porphyry copper potential, Abra area.

spatial geological evidence maps are shown in Figure 5.7 and explained below.

1. Binary map of favourable host lithologies consisting of the quartz diorite porphyry plutons, the quartz diorite and granodiorite batholithic plutons and the Licuan Formation (sub-section 2.4.1).
2. Binary map of presence of and proximity to within 1500 m of north-trending faults/fractures (section 4.5).
3. Binary map of presence of and proximity to within 2000 m of intersections of regional faults (i.e., north-trending and northeast-trending faults/fractures; section 4.5).
4. Binary map of proximity to within 1500 m of granodiorite batholithic pluton margins (section 4.5).
5. Binary map of proximity to within 1500 m of mapped quartz diorite porphyry plutons (section 4.5).

Although presence/indication of hydrothermal alteration may be important, data to extract spatial evidence for this criterion are lacking. The result of 'adding' the binary evidences is a map with values ranging from zero to five. This was classified into a predictive map of favourable zones for porphyry copper mineralisation (Figure 5.8a). Zones with values ≥ 3 (i.e., combination of three to five spatial geological evidences) were considered to be favourable for porphyry copper deposits; zones with values <3 were considered unfavourable.

The integration of the five spatial geological evidences results in a predictive map shown in Figure 5.8a. It indicates that at least 44% of the area has favourability for porphyry copper deposits. It predicts correctly the location of nine (or 75%) of the 12 known porphyry copper deposits. The predictive map closely resembles the map of proximity to north-trending faults/fractures (Figure 5.7). This implies that the map of proximity to north-trending faults/fractures alone is sufficient to predict zones favourable for porphyry copper deposits in the area. This is inaccurate inasmuch as (deposit-related) porphyry plutons are not simply emplaced along faults but are emplaced at or near strike-slip fault discontinuities (or intersections) as indicated by Bryner (1968, 1969) and substantiated by the spatial association analyses in section 4.3.

The map of proximity to north-trending faults/fractures is thus removed from the analysis and the resulting predicted map is shown in Figure 5.8b. The predictive map, exclusive of the north-trending faults/fractures, indicates that 25% of the area is favourable for porphyry copper deposits. It correctly predicts the location of eight (or at least 66%) of the 12 known porphyry copper deposits. One of the known deposits falling in unfavourable zones is just 200 m beyond a favourable zone; their inclusion brings to nine the number of deposits within and near the favourable zones. Thus, based on the known deposits, the success rate of the prediction is at least 66% and reaches 75% with inclusion of deposits near to favourable zones.

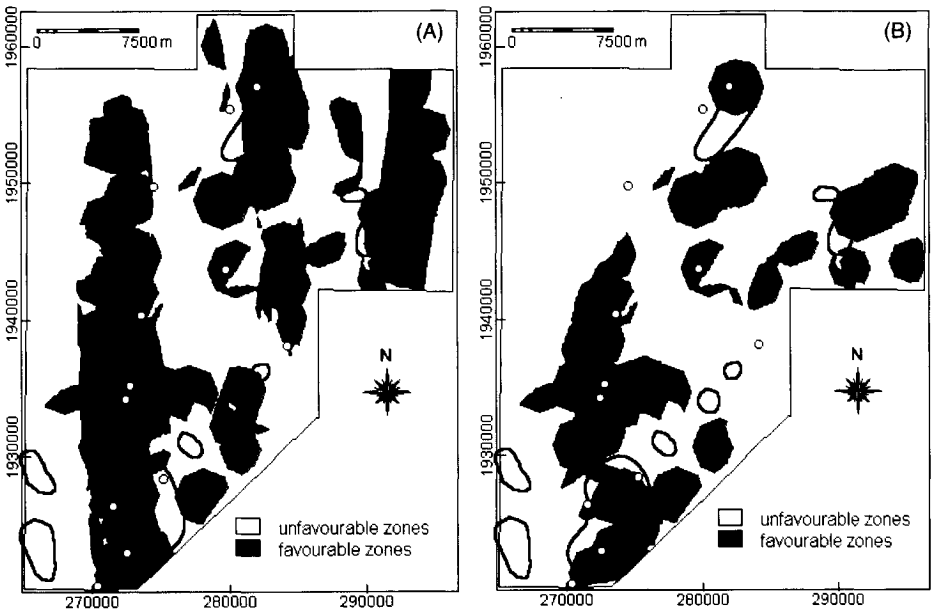

Figure 5.8. Predictive maps of porphyry copper potential, Abra area: (a) inclusive of all spatial geological evidences in Figure 5.7; (b) exclusive of the proximity to 'north-trending faults/fractures' evidence. Unfilled circles = porphyry copper deposits. Polygons in solid lines = known mineralised zones.

To determine the reliability of the predictive map in Figure 5.8b, it was compared with the known mineralised zones in the area (see Figure 2.18). The known mineralised zones occupy about 10% of the area. Of the 9623 pixels of known mineralised zones, 5891 are correctly predicted - a 61% success rate. The larger area of predicted favourable zones, compared to the area of known mineralised zones, suggests undiscovered mineralised zones. In Figure 2.18, the known mineralised zones have been observed mainly along major streams. The predictive map in Figure 5.8b is thus reliable and can be used to guide follow-up exploration work in the area.

To determine further the adequacy of the geologically-constrained predictive map in Figure 5.8b, it was compared with an integrated geological-geochemical predictive map. It was combined, by a logical Boolean OR operation, with a binary-transformed map of Figure 2.17a that indicates zones of background and anomalous stream sediment Cu contents, using 90 ppm Cu as threshold (Figure 5.9a). The integrated geochemical-geological predictive map is shown in Figure 5.9b. It resembles closely the geologically-constrained predictive map in Figure 5.8b. It contains 25137 'favourable' pixels. The geologically-constrained predictive map in Figure 5.8b contains 23471 'favourable' pixels. Integration of

the geochemical evidence thus results in only about a 7% increase in predicted favourable zones. The geological-geochemical predictive map predicts correctly nine of the 12 known porphyry copper deposits – a 75% success rate. It predicts correctly 6165 of the 9623 known mineralised zones - a 64% success rate. These success rates imply that integration of the geochemical evidence does not provide a significant increase to the success rates of geologically-constrained predictive favourable zones of porphyry copper deposits. Hence, the geologically-constrained predictive map in Figure 5.8b is adequate.

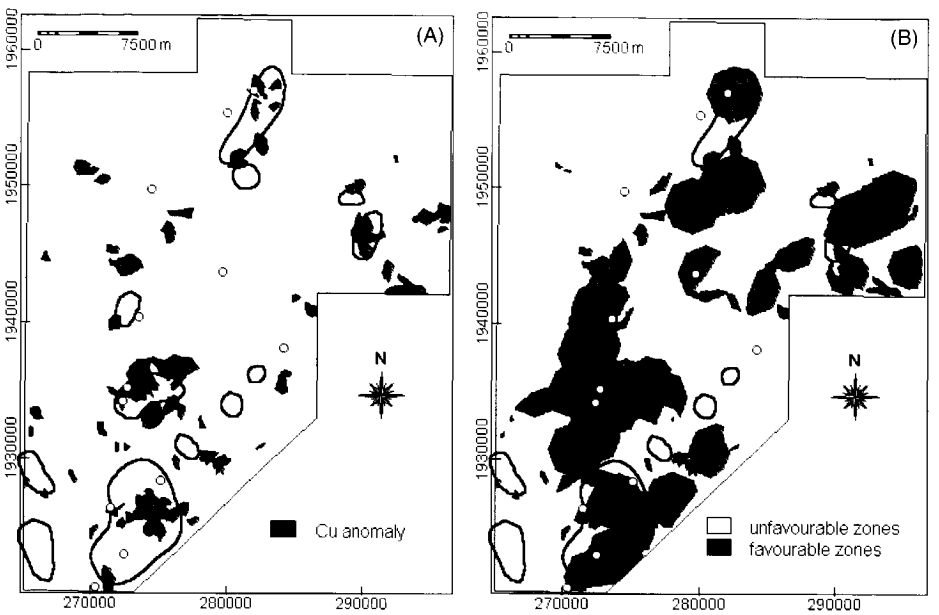

Figure 5.9. Abra area: (a) anomalous catchment basins with >90 ppm Cu; (b) integrated geochemical-geological predictive map of porphyry copper potential. Unfilled circles = porphyry copper deposits. Polygons in solid lines = known mineralised zones.

5.4 MAPPING EPITHERMAL GOLD POTENTIAL

Geologic criteria provided by both generalised empirical models of epithermal mineralisation and studies of the general characteristics of Philippine epithermal gold deposits were applied to geologically-constrained mapping of epithermal potential in Baguio district and in Catanduanes Island.

5.4.1 General characteristics of epithermal deposits

The term epithermal was applied by Lindgren (1922, 1933) to a type of hydrothermal deposit with mineralogy and texture then considered indicative of low temperature and shallow depth. As more and more data evolved, however, it has become evident that most epithermal deposits form within a temperature range of 180-300°C and at depths rarely exceeding 1.5 or at most 2 km (White and Hedenquist, 1990).

Epithermal deposits occur in a wide variety of types and geologic settings. Classification schemes have been based on plate tectonics (Sawkins, 1989), association with volcanic landforms (Sillitoe and Bonham, 1984), physical and mineralogical characteristics (Lindgren, 1933; Hayba et al., 1985), associated magma types and mineralogy (Bonham, 1986), and whether the deposits are volcanic-hosted (Hayba et al., 1985) or sediment-hosted (Bagby and Berger, 1985).

Two main types of epithermal deposits are recognised in terms of the vein mineralogy and in terms of wall rock alteration mineralogy. One type is known as quartz-adularia (Berger and Eimon, 1983), low sulphur (Bonham, 1986) or adularia-sericite (Heald et al., 1987), in which gold and silver are the only economic minerals. The other type is known as quartz-alunite (Ashley and Berger, 1985), high sulphur (Bonham, 1986) kaolinite-alunite (Berger and Henley, 1989), and commonly includes the copper mineral enargite in addition to gold. Global application of the two mineral assemblage classifications have met various difficulties, which include the absence of adularia in many island arc deposits, the widespread use of the term illite rather than sericite for clay-sized mica, and the variable sulphur content among many different deposits of the same class. These difficulties were overcome by Hedenquist (1987) and White and Hedenquist (1990) who proposed terms 'low-sulphidation' and 'high-sulphidation', which refer to the redox state of sulphur in the near-neutral pH and acid sulphate mineralising fluids, respectively. The 'low-sulphidation' and 'high-sulphidation' systems are essentially similar to the low sulphur and high sulphur systems of Bonham (1986) who described the characteristics and environments of these contrasting types of epithermal systems in North America. The essential features of the 'low-sulphidation' and 'high-sulphidation' epithermal systems are shown in Figure 5.10.

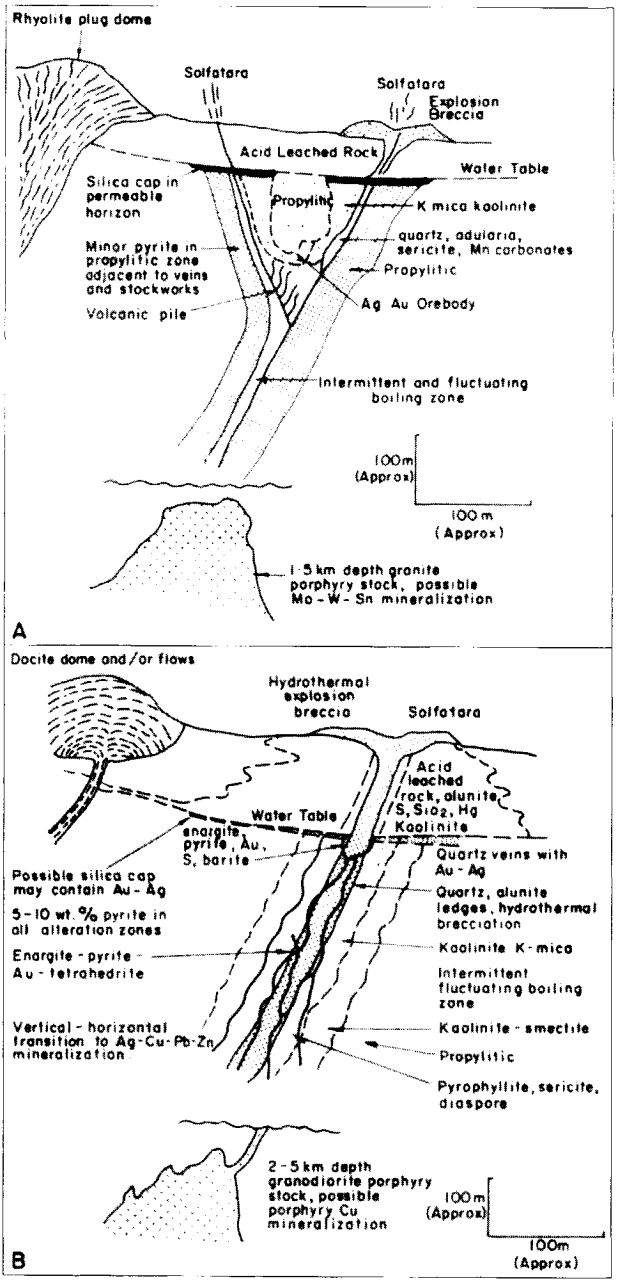

Figure 5.10. Schematic cross-sections of (a) low sulphur or 'low-sulphidation' and (b) high sulphur or 'high-sulphidation' epithermal systems, based largely on deposits in western U.S.A. (simplified from Bonham, 1986).

Igneous activity plays an important role in the formation of most epithermal deposits, if only in providing the heat necessary to generate a hydrothermal convection cell (White and Hedenquist, 1990). In most cases, epithermal deposits are spatially and temporally associated with subaerial volcanic rocks, and their related subvolcanic intrusions (Sillitoe and Bonham, 1984). Subaerial volcanism may occur in a variety of tectonic settings, but it occurs mainly along volcanic arcs in the convergent tectonic settings characteristic of oceanic-continental or oceanic-oceanic plate subduction (Le Pichon et al., 1973). Strong structural control is almost universally recognised for gold deposits (Henley, 1990). Fractures in the near surface cause permeability enhancement. Regional faults are also important (Mitchell and Balce, 1990), perhaps in guiding the emplacement of the magmatic heat source and influencing subsequent hydrothermal activity (Hedenquist, 1986; Sillitoe, 1993).

White and Hedenquist (1990) provided guidelines for regional- and project-scale exploration of epithermal deposits. For regional scale exploration, the igneous and tectonic environments logically form the basis for the initial area selection stage. Calc-alkaline to alkaline igneous provinces that have not been deeply eroded are the most prospective igneous environments. Convergent plate margins are the most favourable tectonic settings. For project-scale exploration, the hydrothermal alteration effects of epithermal systems can provide a broad target and assist in locating favourable areas. It must be remembered, however, that searching for alteration is an indirect approach to exploring for epithermal deposits. Studies of alteration mineralogy and zoning may provide valuable insights into the hydrology of the system, and indicate possible sites of deposits; however, only geochemistry offers a direct approach to locating epithermal mineralisation. The source of surficial geochemical anomalies detected is invariably the primary geochemical dispersion halo, which may or may not indicate the presence of an epithermal deposit (Clarke and Govett, 1990). At the project-scale, structural studies are useful. Typically, many structures are not mineralised, so it is necessary to distinguish the prospective structures by examining the correspondence between structures, geochemistry, mineral deposits and hydrothermal alteration (Hedenquist, 1986). In general, exploration techniques applied at project-scale should not be model specific (Hedenquist and White, 1990).

5.4.2 General characteristics of Philippine epithermal gold deposits

Most epithermal gold deposits in the Philippines are low-sulphidation types deposited along volcanic arcs during the mid-Miocene to mid-Pliocene (Mitchell and Balce, 1990; Mitchell and Leach, 1991). The geochemical nature of epithermal mineralisation in the country is described in UNDP (1987a). The deposits are largely in the form of veins or vein breccias and stockworks. A generalised schematic cross-section illustrating some features characteristic of many low-sulphidation systems in the Philippines is shown in Figure 5.11. There

is no direct evidence of genetic association between magmatism and the epithermal systems, but a causal relationship is implied by analogy with epithermal deposits elsewhere. Most epithermal systems are characterised by the presence of stratigraphic successions, basement anticlines and fractures favourable for focusing fluid flow at shallow depths following subaerial, predominantly andesitic, volcanism. There is no apparent relationship between the epithermal deposits and major fault systems, such as the Philippine Fault, but mineralisation is commonly situated on subsidiary faults or splays. In most of the epithermal gold districts, the stratigraphic succession comprises predominantly clastic andesitic or dacitic rocks lying unconformably on folded basement rocks. Andesitic clastic rocks host most of the deposits. Almost all deposits are associated with minor intrusions of andesitic porphyry plutons or less commonly dacitic porphyry plutons. Hydrothermal alteration associated with the deposits comprises local silicification, extensive and pervasive illitic assemblages, and propylitic alteration.

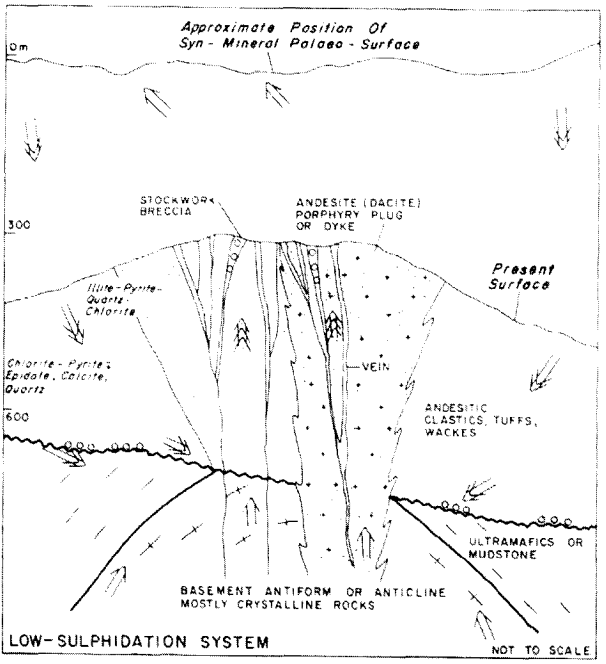

Figure 5.11. Generalised cross-section through low-sulphidation epithermal vein and vein-breccia deposits, Philippines (from Mitchell and Leach, 1991). Single arrows = ascending deep hydrothermal fluids; double arrows = descending meteoric water; triple arrows = mixed fluids.

Mitchell and Leach (1991) provide a summary of the geological features favourable for low-sulphidation epithermal gold mineralisation in the Philippines. On a regional scale, the epithermal gold deposits are very largely confined to areas where Neogene volcanic rocks intrude basement and overlying volcaniclastic rocks. The volcaniclastic cover rocks are largely calc-alkaline andesitic or dacitic clastics. The epithermal gold deposits do not occur preferentially along major regional strike-slip faults but along subsidiary faults or splays. On a district to prospect scale, most major deposits occur within a well-defined belt not more than 10 km wide extending along the length of the magmatic arc and situated near the axis of immediately pre-mineralisation

magmatic activity. Plutonic rocks of dioritic to granodioritic composition are of limited significance with regard to epithermal potential; in general it appears that the larger the pluton, the less likely it is to host a major deposit. Surficial geochemical characteristics over epithermal deposits are elevated values of Au, Ag, Sb and As.

5.4.3 Geologic criteria for epithermal gold potential mapping

Based on the general characteristics of epithermal gold deposits elsewhere and in the Philippines, the following were deduced as the geologic criteria for predictive mapping of favourable zones of epithermal gold potential.

1. Presence of favourable host lithologies, i.e., clastic rocks of andesitic to dacitic composition (Mitchell and Balce, 1990; Mitchell and Leach, 1991).
2. Presence of or proximity to subvolcanic (i.e., andesitic/dacitic) porphyry plutons (Sillitoe and Bonham, 1984; Mitchell and Leach, 1991).
3. Presence of or proximity to batholithic igneous bodies, which represent magmatic arcs (White and Hedenquist, 1990; Mitchell and Leach, 1991).
4. Presence of or proximity to faults/fractures, which are subsidiary to major faults (Hedenquist, 1986; Mitchell and leach, 1991).
5. Presence of illitic alteration (Bonham, 1986; Mitchell and Leach, 1991).

These geologic criteria were applied to map favourable zones of epithermal gold potential in Baguio district and Catanduanes Island. The quantified spatial associations of the epithermal gold deposits and the gold-copper deposits with the appropriate geological features, respectively, in Baguio district and in Catanduanes Island were used to transform the appropriate geologic criteria above into binary spatial geological evidence maps. These binary spatial geological evidence maps were integrated to map predictively favourable zones of epithermal gold potential in these areas.

5.4.4 Epithermal gold potential mapping, Baguio district

The binary spatial geological evidence maps listed below were created, based on (a) the geologic criteria given above, (b) the geology and epithermal gold mineralisation of Baguio district (sub-section 2.3.1) and (c) the spatial association between the epithermal gold deposits and appropriate geological features in the district (section 4.4). These spatial geological evidences were considered appropriate to attempt predictive mapping of favourable zones of epithermal gold potential in the district. The binary spatial geological evidence maps are shown in Figure 5.12 and explained below.

1. Binary map of favourable host lithologies consisting of the Cretaceous-Eocene Pugo Formation and Late to Early Eocene Zigzag Formation, which

are made up of andesitic clastic rocks (Balce et al., 1980; Mitchell and Leach, 1991; sub-section 2.3.1).

2. Binary map of presence of or proximity to within 2800 m of the Late Miocene to Pleistocene porphyry plutons (Mitchell and Leach, 1991; section 4.4).
3. Binary map of proximity to within 1000 m of Late Oligocene to Middle Miocene Agno Batholith, which may have acted as heat sources possibly for a first pulse of gold mineralisation in the district (Wolfe, 1988; section 4.4).
4. Binary map of presence of and proximity to within 400 m of northeast-trending faults/ fractures, which are conjugate shears of major northwest-trending faults/ fractures (Balce et al., 1980; Mitchell and Leach, 1991; section 4.4).
5. Binary map of presence of illitic alteration (UNDP, 1987a; sub-section 3.3.4).

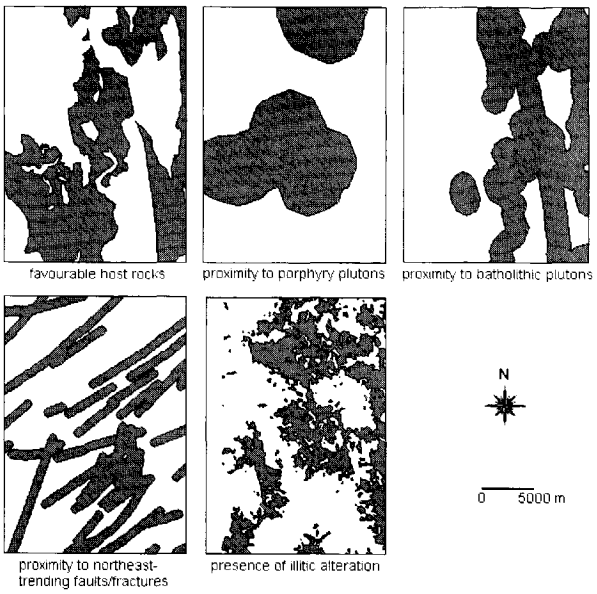

Figure 5.12. Spatial geological evidences of epithermal gold potential, Baguio district.

The result of 'adding' these binary evidence maps is a map with values ranging from zero to five. This was classified into a predictive map of favourable zones of epithermal gold potential. Zones with values ≥3 (i.e., combination of three to five spatial geological evidences) were considered favourable; zones with values <3 were considered not favourable.

The geologically-constrained predictive map, inclusive of all binary spatial evidences, is shown in Figure 5.13a. It indicates that about 33% of the district has favourability for epithermal gold deposits. It predicts correctly 15 (or about 79%) of the 19 known large-scale epithermal gold deposits and 48 (or at least 76%) of the 63 known small-scale deposits. Because the accuracy of the 'illitic alteration evidence' is suspect (Figure 3.15b; see sub-section 3.3.4), it was removed from the analysis and another predictive map exclusive of this evidence is created (Figure 5.13b). The favourable zones in this latter predictive map are a combination of three to four spatial evidences, the unfavourable

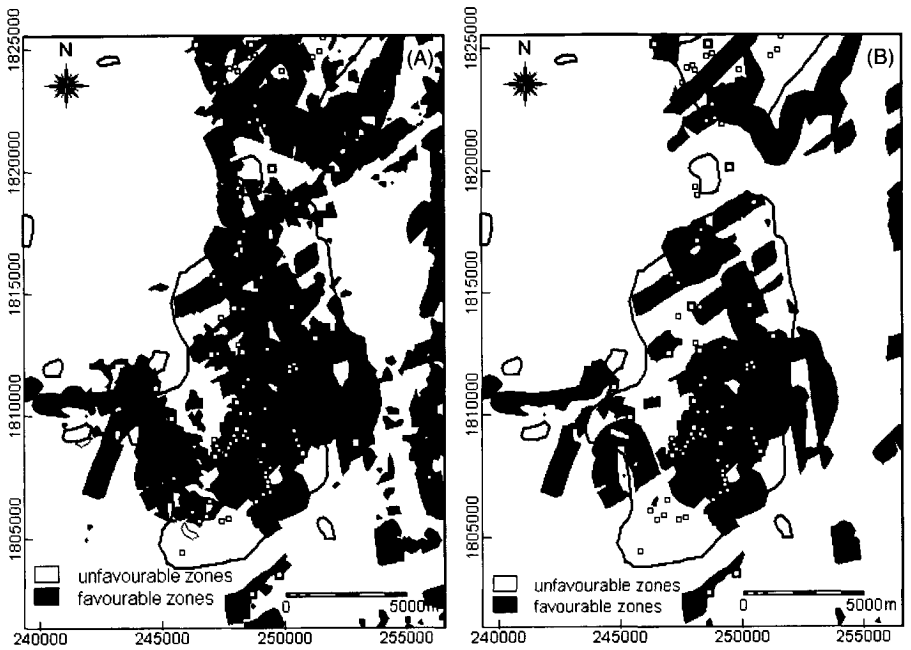

Figure 5.13. Predictive maps of epithermal gold potential, Baguio district: (a) inclusive of all spatial geological evidences in Figure 5.12; (b) exclusive of the 'illitic alteration' evidence. Large unfilled squares = large-scale gold deposits; small unfilled squares = small-scale gold deposits. Polygons in solid lines = Au geochemical anomaly.

zones of one to two spatial evidences. The predictive map in Figure 5.13b indicates that about 22% of the district has favourability for epithermal gold deposits. It predicts correctly 13 (or at least 68%) of the known large-scale deposits and 39 (or about 62%) of the known small-scale deposits.

The favourable zones in both predictive maps in Figure 5.13 show spatial coincidence with the stream sediment Au geochemical anomalies, which indicates that they are reliable. To determine which of the predictive maps in Figure 5.13 is more reliable, they were compared with the geoinformation from the stream sediment geochemical data (UNDP, 1987a, sub-section 2.3.3). The geochemical anomalies of Au, Ag, As and Sb cover an average of about 24% of the district and accurately reflect the locations of about 68% of the known large-scale deposits. Because geochemical anomalies represent materials dispersed from mineralised sources, one may deduce that lateral extents of geochemical anomalies are wider than lateral extents of 'geological anomalies' (i.e., intersections of spatial geological evidences). Hence, one may further deduce that 'geological anomalies' are reliable if they cover narrower lateral extents than the geochemical anomalies. The predictive map in Figure 5.13b is thus

considered more reliable than the predictive map in Figure 5.13a. The lateral extent of 'geological anomalies' in the predictive map in Figure 5.13b is narrower than the lateral extents of the geochemical anomalies; however, they have similar success rates. The lesser reliability of the predictive map in Figure 5.13a is due to the 'illitic alteration evidence', which is of dubious value.

To determine which of the predictive maps in Figure 5.13 is adequate, they were each integrated with binary-transformed maps of the geochemical anomalies (Figure 2.12). Integration of the predictive map in Figure 5.12a with the binary-transformed geochemical anomalies resulted in a map with values ranging from zero to nine. Integration of the predictive map in Figure 5.12b with the binary-transformed geochemical anomalies resulted in a map with values ranging from zero to eight. These integrated geochemical-geological predictive maps were each classified into a predictive map of zones favourable for epithermal gold deposits (Figure 5.14). The favourable zones in Figure 5.14 have values ≥5 (i.e., combination of at least five spatial evidences), whereas the unfavourable zones in either map have values <5.

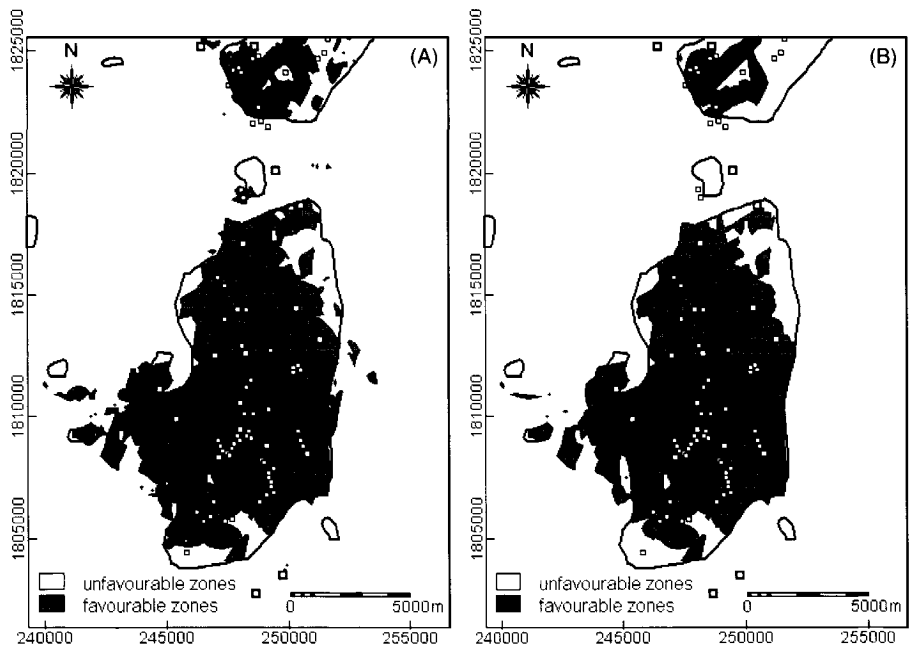

Figure 5.14. Integrated geochemical-geological predictive maps of epithermal gold potential, Baguio district: (a) inclusive of all spatial geological evidences in Figure 5.10; (b) exclusive of the 'illitic alteration' evidence. Large unfilled squares = large-scale gold deposits; small unfilled squares = small-scale gold deposits. Polygons in solid lines = Au geochemical anomaly.

The predictive maps in Figure 5.14 are apparently similar. The predictive map in Figure 5.14a indicates that about 22% of the district has favourability for potential for epithermal gold deposits. It correctly predicts 15 (or at least 79%) of the known large-scale deposits and 52 (or at least 82%) of the known small-scale deposits. The predictive map in Figure 5.14b indicates that about 20% of the district has favourability for epithermal gold deposits. It correctly predicts 13 (or at least 68%) of the known large-scale deposits and 50 (or at least 79%) of the known small-scale deposits. The success rates of the integrated geochemical-geological predictive maps are equal to the success rates of the geologically-constrained predictive maps with respect to the large-scale deposits. The success rates of the geologically-constrained predictive maps are lower than the success rates of the integrated geochemical-geological predictive maps with respect to the small-scale deposits. Hence, the geologically-constrained predictive maps in Figure 5.13 are adequate with respect to the large-scale gold deposits but are inadequate with respect to the small-scale deposits. The predictive map in Figure 5.13a has 6% lower success rate than the predictive map in Figure 5.14a with respect to the small-scale deposits. On the other hand, the predictive map in Figure 5.13b has 17% lower success rate than the predictive map in Figure 5.14b with respect to the small-scale deposits. Hence, the predictive map in Figure 5.13a is less inadequate (or more adequate) than the predictive map in Figure 5.13b. These findings indicate that although the geologically-constrained predictive maps are reliable, they are equally or less adequate than the integrated geochemical-geological predictive maps. Because the predictive map in Figure 5.13a is more adequate but less reliable than the predictive map in Figure 5.13b, it can be used with caution to guide further exploration work in the district.

5.4.5 Epithermal gold mineral potential mapping, Catanduanes Island

Because detailed genetic studies of the gold-copper deposits in the island are lacking, no particular deposit model has been developed yet for these deposits. As stated in Chapter 2, the absence of extensive and pervasive hydrothermal alteration (except for silicification and pyritisation adjacent to the veins and the presence of calcite in the veins) suggests that the deposits are replacement vein-type deposits. However, judging from the general geologic and geochemical characteristics of epithermal deposits in the Philippines (Mitchell and Leach, 1991; Mitchell and Balce, 1990; UNDP, 1987a), the gold-copper deposits in the island probably represent the deepest portions of the epithermal gold deposit model (Figure 5.11). The deepest portions are characterised by narrow veins with restricted envelopes of quartz-pyrite-illite alteration and geochemical enrichment in Cu (UNDP, 1987a). Hence, the gold-copper deposits in the island can be classified tentatively as epithermal.

The binary spatial geological evidence maps listed below were created, based on (a) the geologic criteria given above, (b) the geology and gold-copper

mineralisation of Catanduanes Island (sub-section 2.5.1) and (c) the spatial association between the gold-copper deposits and appropriate geological features in the district (section 4.6). These spatial geological evidences were considered appropriate to attempt to map predictively favourable zones of epithermal gold deposits in the island. The binary spatial geological evidence maps are shown in Figure 5.15 and explained below.

1. Binary map of favourable host lithologies consisting of the Catanduanes, Yop and Payo Formations, which contain clastic rocks of andesitic composition (Miranda and Vargas, 1967; Bureau of Mines and Geosciences, 1982).
2. Binary map of presence of and proximity to within an average of 2300 m of the porphyry Batalay Intrusives (section 4.6).
3. Binary map of presence of and proximity to within an average of 1500 m of north-trending faults/fractures (section 4.6).
4. Binary map of presence and proximity to within 1000 m of northeast-trending faults/fractures (section 4.6).

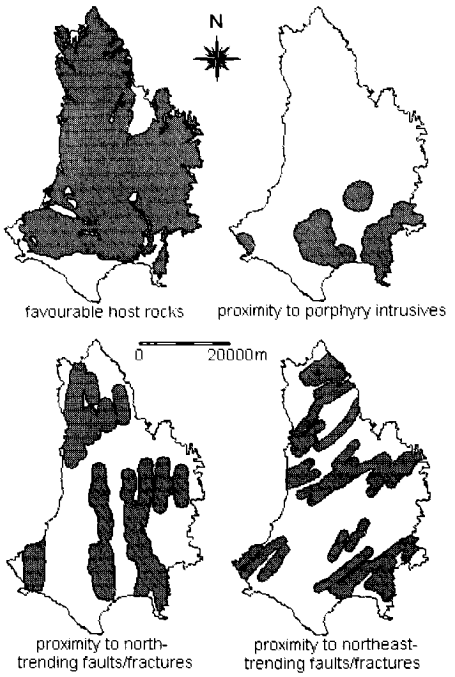

Figure 5.15. Spatial geological evidence maps for epithermal deposit potential, Catanduanes Island.

Combining the spatial evidence maps resulted in a map with values ranging from zero to four. This was classified into a predictive map of zones favourable for epithermal gold deposits. Zones with values ≥3 (i.e., combination of three to four spatial geological evidences) were considered favourable; zones with values <3 were considered unfavourable.

The geologically-constrained predictive map (Figure 5.16a) indicates that about 24% of the island has favourability for epithermal deposits. It predicts correctly ten (or about 59%) of the 17 known gold-copper deposits. It is interesting to note that three of the deposits not predicted correctly lie just within 825 m of a favourable zone. This means that 13 (or at least 76%) of the known deposits fall within and near the predicted favourable zones. The predicted favourable zones show high spatial coincidence with the geochemically-anomalous sample catchment basins (see sub-section 2.5.4; Figure 2.19). This indicates that the

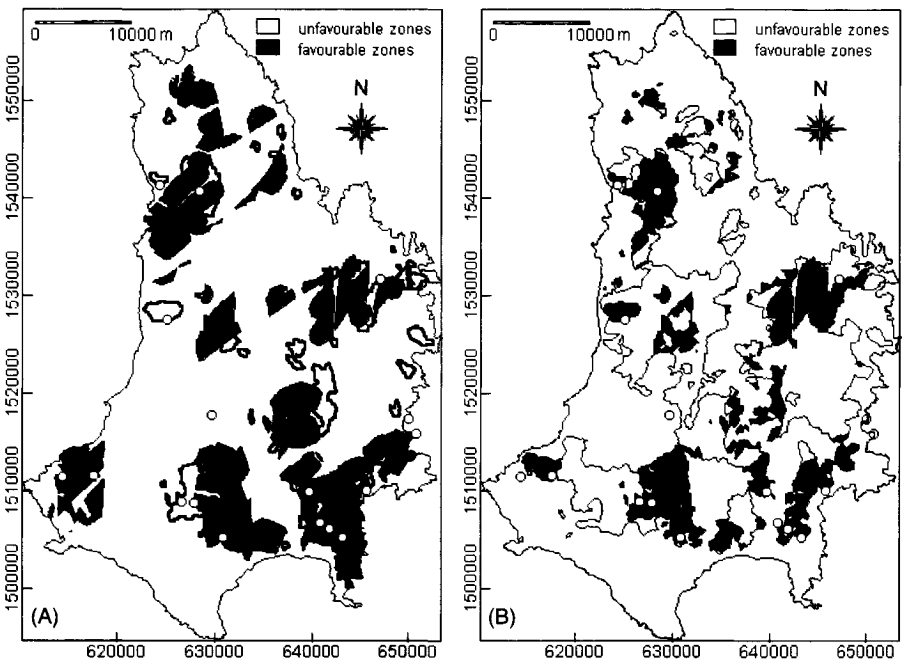

Figure 5.16. Predictive maps of epithermal deposit potential, Catanduanes Island: (a) geologically-constrained; (b) integrated geochemical-geological. Unfilled circles = known gold-copper deposits. Polygons in solid lines = catchment basins with anomalous geochemical signature (see sub-section 2.5.4).

predicted favourable zones are probably sources of the geochemical anomalies and that the predictive map is reliable.

Classification of the combined binary-transformed map of the geochemical anomalies and the binary spatial geological evidence maps results in the predictive map shown in Figure 5.16b. It indicates that about 15% of the island has favourability for epithermal deposits. It predicts correctly nine (or about 52%) of the 17 gold-copper deposits. The favourable zones in the geologically-constrained predictive map are 'dismembered' by the un-sampled areas and the integration of the geochemical evidence does not result in a significant increase in predicted favourable zones. Hence, the geologically-constrained predictive map in Figure 5.16a is adequate.

5.5 MAPPING NICKELIFEROUS-LATERITE POTENTIAL

Geologic criteria provided by a generalised empirical model of nickeliferous-laterite deposit and the general characteristics of Philippine nickeliferous-laterite deposits were applied to geologically-constrained predictive mapping of this type of deposit in the Isabela area.

5.5.1 General characteristics of nickeliferous-laterite deposits

The term laterite is usually credited to Buchanan (1807), who described naturally-hardening surficial materials that were used as bricks from Malabar, southern India. The term laterite is thus derived from the Latin word later, meaning brick. The literature on laterite is heavily encumbered by problems of its definition. McFarlane (1976) provides a summary definition of laterite as a highly weathered material rich in iron hydroxides, aluminum hydroxides or both, poor in humus, depleted in silica, containing limited amounts of primary minerals or silicate clays, and is either hard or subject to hardening upon exposure to alternate wetting and drying. Laterites can develop from most sedimentary, metamorphic and igneous rocks; however, they evolve mostly in regions with tropical to subtropical climate (Nahon and Tardy, 1992). Detailed description of laterite deposits and explanation of their evolution are given by, among others, McFarlane (1976) and Nahon and Tardy (1992), and are not further discussed here. When laterite consists purely of aluminum hydroxides, it is called bauxite (Bárdossy and Aleva, 1990). When laterite consists of appreciable amounts of Ni, it is called nickeliferous-laterite; Ni grades of economic interest range from 1% to more than 3% (Evans, 1987).

A general model of nickeliferous-laterite deposits by Golightly (1979, 1981) is adopted here. Those deposits of economic importance have developed on peridotitic bedrock. The nickel is provided by the leaching of forsteritic olivine, which contains about 0.3% nickel, and/or serpentine, which is derived from the hydrothermal alteration of olivine prior to weathering. Nickel is leached during deep tropical weathering of olivine- and serpentine-bearing peridotite to saprolite. Topography, which is a function of the geomorphic history of the land, plays an important role in the redistribution of nickel. As a generalisation, nickel enrichment occurs along the slopes immediately below the plateau edges (Figure 5.17a). The primary controlling feature is the low water table at the plateau edge, which forces meteoric groundwater circulation downward through the saprolite. A higher water table elsewhere on the plateau and in the lowlands inhibits nickel enrichment. Erosion can remove enriched saprolite from the convex brow of the plateau edges and the limiting slope for the formation of enriched saprolite to keep ahead of erosion is about 20°. Figure 5.17b shows a detailed profile through a nickeliferous-laterite deposit. The nickel occurs in both the laterite and the weathered zone of the peridotitic bedrock. In the latter,

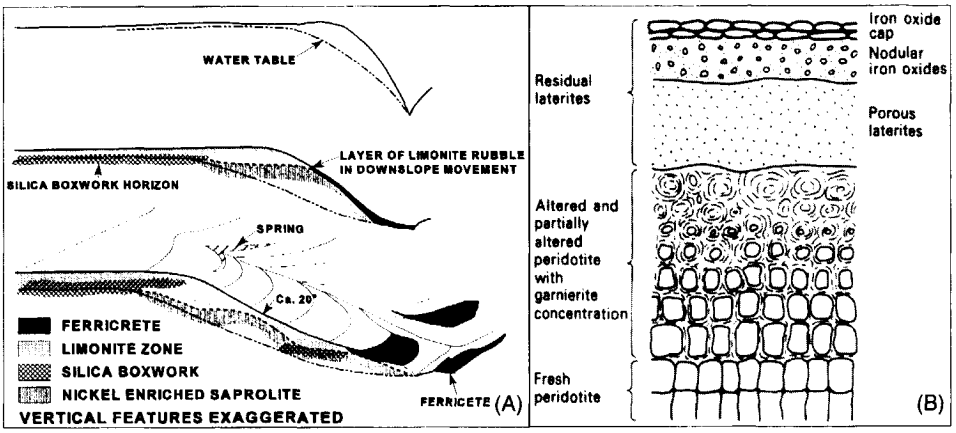

Figure 5.17. Nickeliferous-laterites: (a) idealised sequence of formation at edges of plateaus over peridotitic bedrock (from Golightly, 1979); (b) idealised profile (from Evans, 1987).

laterite forms distinct masses, veins, veinlets or pockets rich in garnierite (a Ni-bearing serpentine mineral), which occur around residual blocks of unweathered peridotitic rock and in fissures running down into the underlying rock.

5.5.2 General characteristics of Philippine nickeliferous-laterite deposits

The tropical climate in the Philippines resulted in the formation of nickeliferous-laterite deposits due to weathering of major ophiolitic bodies, which are predominantly of peridotitic composition (Bureau of Mines and Geosciences, 1986). The geographic distribution of nickeliferous-laterite deposits in the country follows the discontinuous belts of ophiolitic rocks, which are confined mainly along the eastern and western margins of the archipelago (see Figure 2.2). The nickeliferous-laterite deposits are composed mainly of garnierite and/or saprolite. The deposits contain average nickel contents ranging from less than 1% to about 3%. The deposits are relatively thin, averaging one to five meters, and are confined to relatively gentler slopes in the rather rugged topography of the ophiolitic terranes (Bureau of Mines and Geosciences, 1986). The development of thin lateritic profiles in the country is probably attributed to high erosion rates due to rapid uplift as a consequence of the tectonic setting of the archipelago (see sub-section 2.1.1). The most economic nickeliferous-laterite deposits in the country are found in Palawan Island and in Surigao in northeastern Mindanao (Lyday, 1998). In the Isabela area, there are reportedly substantial deposits of laterite along the Dinapique plateau ranging in thickness from 6 to 16 metres and grading more than 1% Ni (Mangaoang, 1997; http://www.stellarmetals.com/corpprofile.htm).

5.5.3 Geologic criteria for nickeliferous-laterite potential mapping

Based on the model of Golightly (1979, 1981) and the general characteristics of Philippine nickeliferous-laterite deposits, three geologic criteria were deduced for predictive mapping of favourable zones of nickeliferous-laterite. These geological criteria are: (1) presence of peridotitic rocks, (2) presence of plateau edges and (3) topographic slopes of ≤20°. These geologic criteria were applied to map favourable zones of nickeliferous-laterite potential in Isabela area.

5.5.4 Nickeliferous-laterite potential mapping, Isabela area

In the Isabela area, the Isabela Ultramafics is made up of peridotitic rocks (see Figure 2.20). The number of pixels represented by the peridotite terrane is 61,841 (a pixel size of 100x100 m was used in the analysis), which is equivalent to about 618 km^2. A binary map of the Isabela Ultramafics was created as evidence for the presence of peridotitic rocks. Zones of plateau edges and zones with slopes ≤20° in the area are shown in Figure 2.23. A binary map of each of these topographic features was created as evidences for presence of plateau edges and areas with slopes ≤20°, respectively.

Combining the binary-transformed maps of spatial geological evidences results in a map with values ranging from zero to three. This was classified into a predictive map of favourable zones for nickeliferous-laterite mineral potential (Figure 5.18a). In this map, the zones where all three spatial geological evidences are present were considered favourable; otherwise the zones were considered unfavourable. The geologically-constrained predictive map indicates that about 20% of the peridotite terrane has favourability for nickeliferous-laterite.

Ideally, the reliability of the geologically-constrained predictive map must be validated by comparing it with known deposits of nickeliferous-laterite. There is, however, only one area with reported nickeliferous-laterite because exploration has been curtailed due to land-use policy (Mangaoang, 1997). The 'nickel-area' where nickeliferous-laterite has been reported is indicated in Figure 5.18a; it contains 3302 pixels. The exploration company has not disclosed the distribution of nickeliferous-laterite in the 'nickel-area' and because access to the nickel-area is difficult no validation data have been obtained.

The geologically-constrained predictive map shows the 'nickel-area' to be mostly unfavourable for nickeliferous-laterite. It indicates that there are 279 'favourable' pixels within the 'nickel-area'. There are only small isolated favourable zones in the 'nickel-area'. A conspicuously larger favourable zone is indicated in the northern part of the 'nickel-area'.

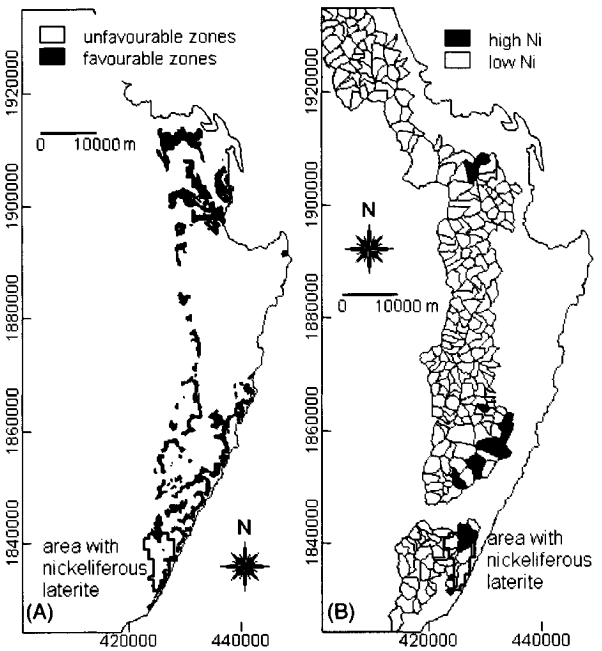

Figure 5.18. Isabela area: (a) geological-constrained predictive map of zones favourable for nickeliferous-laterite; (b) catchment basins with >2500 ppm Ni stream sediment contents.

To assess the reliability of the predictive map in Figure 5.18a, a binary map of catchment basins with stream sediment Ni contents above 2500 ppm, which is greater than the average abundance of Ni in ultramafic rocks (Levinson, 1974), was generated. The binary map of catchment basins with high Ni stream sediment contents is shown in Figure 5.18b. It indicates that the northern part of the 'nickel-area' has by high Ni stream sediment contents. It indicates that there are 642 'high Ni' pixels in the nickel-area. Crossing or overlaying the predictive map in Figure 5.18a with the binary map in Figure 5.18b indicates that 60 of the 642 'high Ni' pixels in the northern part of the 'nickel-area' has favourability for nickeliferous-laterite. The overlap between the 'high Ni' pixels and the favourable zones probably represents the source of the high Ni stream sediment contents in the 'nickel-area'. This implies that the predictive map in Figure 5.18a is reliable. However, the adequacy of the predictive map cannot be assessed because there are no known nickeliferous-laterite zones with which to compare an integrated geochemical-geological predictive map.

The section with known nickeliferous-laterite deposits is indicated to have less potential for this type of deposit than other portions of the ultramafic terrane. However, mineral exploration and development in the portions immediately north of the section with known nickeliferous-laterite deposits have been curtailed by land-use policy (Mangaoang, 1997). The prohibition of mineral resources development in the study area was imposed before the nickeliferous-laterite potential was mapped by the method presented here. It is not intended to contest this prohibition, but to stress the importance of mineral potential information to the land-use policy-making process.

5.6 CONCLUSIONS

The methodology devised and tested here for predictive mapping mineral potential through the application of deposit exploration models is sensitive to the type of spatial evidences that are used. This is to be expected, but unavoidable, because, the deposit exploration models are generalisations and thus are not specific to any particular area. The transformation of appropriate geologic features into spatial geological evidences of mineralisation is aided by the quantification of spatial association between the known mineral deposits and the geological features in the different test areas (Chapter 4).

The geologically-constrained predictive maps, based on the applications of deposit exploration models and the analyses of spatial associations between mineral deposits and geological features, are reliable and are either equally or less adequate than the integrated geochemical-geological predictive maps. For the Benguet province, the geologically-constrained predictive map of porphyry copper potential, exclusive of the hydrothermal alteration evidence because it is of dubious value, has a success rate of about 81%. The adequacy of the predictive map cannot, however, be assessed due to incomplete geochemical data in the data. For the Abra area, the geologically-constrained predictive map of porphyry copper potential, exclusive of the north-trending fault/fracture evidence because its inclusion produces a dubious predictive map, has a success rate of at least 60% to about 75%. The predictive map is equally adequate as the integrated geochemical-geological predictive map. For the Baguio district, the geologically-constrained predictive maps of epithermal gold potential, inclusive and exclusive of the hydrothermal alteration evidence, have success rates of at least 76% and at least 62%, respectively. Both predictive maps are reliable and are equally or less adequate than the integrated geochemical-geological predictive depending on which set of gold deposits they are compared with. For Catanduanes Island, the geologically-constrained predictive map of epithermal gold potential has a success rate of about 59% to about 76%. The predictive map is as reliable and adequate as the integrated geochemical-geological predictive map. For the Isabela area, the geologically-constrained predictive map of nickeliferous laterite potential is reliable when compared to catchment basins with stream sediment Ni contents greater than the average abundance of Ni in normal ultramafic rocks. Its reliability and adequacy have not been assessed because nickeliferous-laterite occurrence data are lacking.

Validation of the results of the geologically-constrained predictive maps based on the deposit exploration models is important to determine whether the methodology devised and tested is sound. To validate the geologically-constrained predictive maps, it is important to have information on any occurrence of the mineral deposit in question within the area of study. The geologically-constrained predictive maps for the appropriate deposits in Benguet province, Abra area, Benguet district and Catanduanes Island are valid. The

geologically-constrained predictive map for nickeliferous-laterite remains to be validated. Although the mineral potential maps resulting from this methodology are guidelines for exploration rather than facts, or subjective rather than based on statistical prediction, they provide a realistic basis for land-use policy making as demonstrated particularly by the results of mapping nickeliferous-laterite potential in Isabela area (Carranza and Hale, 1999a).

The validity of most of the geologically-constrained predictive maps based on the deposit exploration models demonstrates that the methodology devised and tested is an effective, rapid, and cheap methodology. A similar methodology for predictive mapping of potential for similar and other types of deposits can be applied to areas lacking mineral potential information other than basic geologic data (e.g., lithology, structure). The classification scheme can be modified according to the type and number of geologic criteria provided by a particular deposit exploration model.

In the methodology presented, the binary spatial geological evidences of mineralisation were combined by simple map addition without regard to whether they can be combined or not according to a statistical criterion. In the next chapter, Bayesian probability is applied to create and combine binary spatial geological evidences of mineralisation for predictive mapping of mineral potential. To combine the binary spatial geological evidences, the Bayesian probability model requires an assumption and testing of conditional independence between all pairs of binary evidences.

Chapter 6

Geologically-Constrained Probabilistic Mapping of Mineral Potential

> Probability Theory is the branch of Mathematics that studies the likelihood of occurrence of random events in order to predict the behavior of defined systems.
>
> American Heritage Dictionary

This Chapter demonstrates the application of the Bayesian probability model, which requires conditional independence between the input binary predictors patterns to map mineral potential. Portions of this Chapter have been published as Geologically Constrained Probabilistic Mapping of Gold Potential, Baguio District, Philippines (Carranza and Hale, 2000) and Where are Porphyry Copper Deposits Spatially Localized? A Case Study in Benguet Province, Philippines (Carranza and Hale, 2001h).

6.1 INTRODUCTION

Mineral deposits (of economic importance) are exceptional occurrences in nature. The statistical measure of the likelihood of an occurrence or event is probability (Davis, 1973; Grimmet and Welsh, 1983; Karr, 1993; McColl, 1995). The knowledge about past (or discovered) behaviour of a phenomenon can provide insights into its future (or undiscovered) behaviour. Thus, to predict the likelihood of an undiscovered mineral deposit, it is necessary to study the behaviour (genetic, temporal and spatial) of discovered mineral deposits.

The occurrence of mineral deposits is not random. Their occurrence depends on favourable geological processes or features. These favourable geological processes or features express themselves as geological, geophysical or geochemical anomalies. The presence of an anomaly can indicate the presence of a mineral deposit and vice versa. Mineral deposits and anomalies are thus related in some way, that is, indication(s) of the presence of one depends in part on the presence of the other. The joint probability of such occurrences is said to be conditional. However, the presence of an anomaly does not always mean the presence of a mineral deposit and vice versa. In this case, the probability of such occurrences is said to be unconditional. The relationship between conditional and unconditional probabilities is expressed in Bayes' theorem (Koch and Link, 1970; Davis, 1973; Hartigan, 1983; Bernardo and Smith, 1994; Lee, 1997). The application of Bayesian statistics to (geologically-constrained) mineral potential mapping is explained below.

6.2 BAYESIAN PROBABILITY MODEL

The following formulation of a Bayesian probability model (or weights of evidence model), as applied to mineral potential mapping, is drawn and synthesised from Agterberg (1989, 1992a), Bonham-Carter et al. (1988, 1989), Bonham-Carter and Agterberg (1990), Bonham-Carter (1991, 1994) and Agterberg et al., (1993). Weights of evidence modeling have been developed originally for medical diagnosis (Lusted, 1968; Aspinall and Hill, 1983; Spiegelhalter and Knill-Jones, 1984; Spiegelhalter, 1986). Weights of evidence modeling formulated for mineral potential mapping was first described by Agterberg (1989).

6.2.1 Conditional probability of mineral deposit: single binary pattern

If a study area is divided into unit cells (or pixels) with a fixed size, s, and a total area, t, then N{T}=t/s is the total number of unit cells in the study area. If there are a number of unit cells, N{D}, containing a mineral deposit D (Figure 6.1), equal to the number of mineral deposits if s is small enough (i.e., one mineral deposit per cell), then the prior probability of a mineral deposit is expressed by

$$P\{D\} = \frac{N\{D\}}{N\{T\}} . \qquad (6\text{-}1)$$

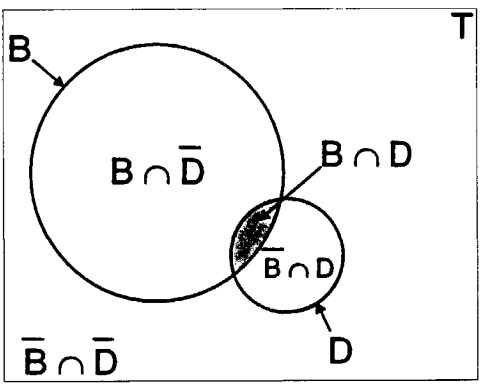

Figure 6.1. Venn diagram of schematic spatial overlap relationships between binary predictor pattern and binary deposit pattern. T, area; B, binary predictor present; $\overline{B}$, binary predictor absent; D, mineral deposit present; $\overline{D}$, mineral deposit absent.

Now suppose that a binary predictor pattern B (e.g., geological anomaly), occupying N{B} unit cells, occurs in the region and that a number of known mineral deposits occur preferentially within the pattern, i.e., N{D∩B}. Clearly, the probability of a mineral deposit occurring within the predictor pattern is greater than the prior probability. Conversely, the probability of a mineral deposit occurring outside the predictor pattern is lower than the prior probability. The probability of finding a mineral deposit given the presence of a predictor pattern can be expressed by the conditional probability

$$P\{D|B\} = \frac{P\{D \cap B\}}{P\{B\}} = P\{D\}\frac{P\{B|D\}}{P\{B\}}, \qquad (6\text{-}2)$$

where $P\{D \mid B\}$ is the conditional or posterior probability of a mineral deposit given the presence of the predictor pattern, $P\{B \mid D\}$ is the posterior probability of being in the predictor pattern B, given the presence of a mineral deposit D, and $P\{B\}$ is the prior probability of the predictor pattern. The probability of finding a mineral deposit given the absence of a predictor pattern can be expressed by the conditional probability

$$P\{D|\bar{B}\} = \frac{P\{D \cap \bar{B}\}}{P\{\bar{B}\}} = P\{D\}\frac{P\{\bar{B}|D\}}{P\{\bar{B}\}}, \tag{6-3}$$

where $P\{D|\bar{B}\}$ is the posterior probability of a mineral deposit given the absence of a predictor pattern, $P\{\bar{B}|D\}$ is the posterior probability of being outside the predictor B, given the presence of a mineral deposit D, and $P\{\bar{B}\}$ is the prior probability of the area outside the predictor pattern.

Equations 6-2 and 6-3 satisfy Bayes' theorem. The same model can be expressed in an odds formulation, where odds, O, are defined as $O = P/(1-P)$. Expressed as odds, Equations 6-2 and 6-3 respectively become

$$O\{D|B\} = O\{D\}\frac{P\{B|D\}}{P\{B|\bar{D}\}} \text{ and} \tag{6-4}$$

$$O\{D|\bar{B}\} = O\{D\}\frac{P\{\bar{B}|D\}}{P\{\bar{B}|\bar{D}\}}, \tag{6-5}$$

where $O\{D|B\}$ and $O\{D|\bar{B}\}$ are respectively the posterior odds of a mineral deposit given the presence and absence of a binary predictor pattern, and $O\{D\}$ is the prior odds of a mineral deposit. The terms $P\{B|D\} / P\{B|\bar{D}\}$ and $P\{\bar{B}|D\} / P\{\bar{B}|\bar{D}\}$ are known as the likelihood sufficiency ratio (LS) and likelihood necessity ratio (LN), respectively (Bonham-Carter, 1994).

The values of LS and LN as used in the Prospector, an expert system developed at the Stanford Research Institute in the 1970s for evaluating mineral prospects (Duda et al., 1978; McCammon, 1989a; Katz, 1991), are assigned by an expert. In weights of evidence modeling, the values of LS and LN are calculated using the mineral deposit data and by taking natural logarithms of both sides of Equations 6-4 and 6-5. The weights for the binary predictor pattern, or the $\log_e$ of LS and LN, are thus defined as

$$W^+ = \log_e \frac{P\{B|D\}}{P\{B|\bar{D}\}} \text{ and} \tag{6-6}$$

$$W^- = \log_e \frac{P\{\overline{B}|D\}}{P\{\overline{B}|\overline{D}\}}, \quad (6\text{-}7)$$

where W^+ and W^- are the positive weights and negative weights of evidence when a binary predictor pattern is present and absent, respectively. Hence, Equations 6-4 and 6-5 become

$$\log_e O\{D|B\} = \log_e O\{D\} + W^+ \text{ and} \quad (6\text{-}8)$$

$$\log_e O\{D|\overline{B}\} = \log_e O\{D\} + W^- . \quad (6\text{-}9)$$

The variances of the weights can be calculated by the following expressions (Bishop et al., 1975; Agterberg et al., 1990):

$$s^2(W^+) = \frac{1}{N\{B \cap D\}} + \frac{1}{N\{B \cap \overline{D}\}} \text{ and} \quad (6\text{-}10)$$

$$s^2(W^-) = \frac{1}{N\{\overline{B} \cap D\}} + \frac{1}{N\{\overline{B} \cap \overline{D}\}} . \quad (6\text{-}11)$$

The contrast, C, defined as

$$C = W^+ - W^- , \quad (6\text{-}12)$$

provides a useful measure of the spatial association between a binary predictor pattern and mineral deposit points (see also Chapter 4). For a positive spatial association, C is positive; C is negative in the case of negative association. The Studentised C, calculated as the ratio of C to its standard deviation, C/s(C), serves as a guide to the statistical significance of the spatial association (Bonham-Carter, 1994). The standard deviation of C, is calculated as:

$$s(C) = \sqrt{s^2(W^+) + s^2(W^-)} . \quad (6\text{-}13)$$

Bonham-Carter et al. (1989) and Bonham-Carter (1994) indicated that a Studentised C greater than 2 implies that C is statistically significant.

6.2.2 Conditional probability of mineral deposit: multiple binary patterns

Now suppose there are two binary predictor patterns, B_1 and B_2. From probability theory, it can be shown that the conditional probability of a mineral deposit given the presence of two predictor patterns is

$$P\{D|B_1 \cap B_2\} = \frac{P\{B_1 \cap B_2|D\}\ P\{D\}}{P\{B_1 \cap B_2|D\}\ P\{D\} + P\{B_1 \cap B_2|\overline{D}\}\ P\{\overline{D}\}}. \quad (6\text{-}14)$$

If B_1 and B_2 are conditionally independent of each other with respect to a set of points (as explained below), it means that the following relation is satisfied:

$$P\{B_1 \cap B_2|D\} = P\{B_1|D\}\ P\{B_2|D\}. \quad (6\text{-}15)$$

Equation 6-15 allows Equation 6-14 to be simplified, thus

$$P\{D|B_1 \cap B_2\} = P\{D\}\frac{P\{B_1|D\}}{P\{B_1\}}\frac{P\{B_2|D\}}{P\{B_2\}}. \quad (6\text{-}16)$$

Equation 6-16 is like Equation 6-2, except that multiplication factors for two binary predictor patterns are used to update the prior probability to give the posterior probability. Using the odds formulation, it can be shown that

$$\log_e O\{D|B_1 \cap B_2\} = \log_e O\{D\} + W_1^+ + W_2^+, \quad (6\text{-}17)$$

$$\log_e O\{D|B_1 \cap \overline{B}_2\} = \log_e O\{D\} + W_1^+ + W_2^-, \quad (6\text{-}18)$$

$$\log_e O\{D|\overline{B}_1 \cap B_2\} = \log_e O\{D\} + W_1^- + W_2^+, \text{ and} \quad (6\text{-}19)$$

$$\log_e O\{D|\overline{B}_1 \cap \overline{B}_2\} = \log_e O\{D\} + W_1^- + W_2^-. \quad (6\text{-}20)$$

Similarly, if more than two binary predictor patterns are used, they can be added provided they are also conditionally independent of one another with respect to the mineral deposit points. Thus, with B_j (j=1,2,...,n) binary predictor patterns, the $\log_e$ posterior odds are

$$\log_e O\{D|B_1^k \cap B_2^k \cap B_3^k ... B_n^k\} = \sum_{j=1}^{n} W_j^k + \log_e O\{D\}, \quad (6\text{-}21)$$

where the superscript k is positive (+) or negative (-) if the binary predictor pattern is present or absent, respectively. The posterior odds can then be converted to posterior probabilities, based on the relation P=O/(1+O), which represent mineral potential.

6.3 BAYESIAN PROBABILITY MODELING USING GIS

The weights of evidence modeling was applied to map mineral potential in Benguet province, Baguio district, Abra area and Catanduanes Island, where the locations of mineral deposits are known.

6.3.1 Data inputs

The appropriate geoexploration-datasets (i.e., lithologic units, faults/fractures, porphyry pluton contacts/centroids, batholithic pluton margins, locations of mineral deposits) captured or digitised in vector format (see Chapter 2) were rasterised. Binary predictor patterns of these datasets were created to calculate the weights. The mineral deposit datasets were split into two subsets. One subset of deposits was used to generate the probabilistic models (i.e., the 'model deposits'), whilst the other subset of deposits was used to validate the probabilistic mineral potential maps (i.e., the 'validation deposits'). A pixel size of 100x100 m was used in the probabilistic mapping of mineral potential. This pixel size was used to ensure that only one mineral deposit is present in any given pixel. The pixel size is also a realistic or a representative size of the mineralised zones in the study areas.

6.3.2 Generation of binary predictor patterns

Binary predictor patterns of geological features (i.e., lithologic units, curvi-linear features such as lithologic contacts and faults/fractures) were created to calculate the positive weights and negative weights of evidence. To generate binary predictor patterns of favourable host rocks, the lithologic maps were reclassified into two units – favourable and unfavourable units. Lithologic units that are known to host the mineral deposits were classified as 'favourable' units whilst those are not known to host mineral deposits were classified into 'unfavourable' units. The positive weights, W+, of the favourable units were calculated according to Equation 6-6. The negative weights, W-, of the unfavourable units were calculated according to Equation 6-7. To generate binary predictor patterns of curvi-linear geological features, different map operations were undertaken.

To generate binary predictor patterns of curvi-linear geological features, the optimum distance within which the spatial association between the mineral deposits and the geological features is most significant statistically was first determined. The optimum cutoff distance was determined by calculating the weights, according to Equations 6-6 and 6-7, for successive cumulative distances away from the geological features, and examining variations in contrast. The maximum C usually gives the cutoff distance at which the spatial association of the resulting binary pattern is optimal (Bonham-Carter et al., 1988,

1989). However, in cases of small numbers of deposits or small areas, such as the present cases, the uncertainty of the weights could be large so that C is meaningless. The maximum Studentised C, which indicates the most statistically significant C, was used to determine the cutoff distance (Bonham-Carter, 1994).

6.3.3 Combining binary predictor patterns

The binary predictor patterns, which are conditionally independent of each other with respect to the mineral deposit points, were combined to map mineral potential according to Equation 6-21. Conditional independence between the input binary predictor patterns was determined through a pairwise test (i.e., between two binary predictor patterns) and/or through an overall test (i.e., among all input binary predictor patterns. The conditional independence between or among the binary predictor patterns was tested prior to (by pairwise test) and/or after combining them (by an overall test).

6.3.4 Pairwise test of conditional independence

Equation 6-15 above defines the relationship if two binary predictor patterns, B_1 and B_2, are conditionally independent of each other with respect to a binary pattern of mineral deposit points. Algebraic manipulation will show that Equation 6-15 is equivalent to

$$N\{B_1 \cap B_2 \cap D\} = \frac{N\{B_1 \cap D\}\ N\{B_2 \cap D\}}{N\{D\}}. \qquad (6\text{-}22)$$

The connotation of pairwise conditional independence can be shown graphically by a Venn diagram as illustrated in Figure 6.2. The enlarged circle in the lower right portion of Figure 6.2 represents the spatial coincidence between two binary predictor patterns and their spatial coincidence with a binary pattern of a mineral deposit. In the enlarged circle, conditional independence implies that the number of pixels representing the spatial coincidence between the binary predictor patterns and the binary pattern of mineral deposit points (i.e., $N\{B_1 \cap B_2 \cap D\}$) equals the ratio of the product of the number of pixels representing spatial coincidence between B_1 and D (i.e., $N\{B_1 \cap D\}$) and the number of pixels representing spatial coincidence between B_2 and D (i.e., $N\{B_2 \cap D\}$) to the number of pixels or area of D (i.e., $N\{D\}$). The particular spatial relationship of conditional independence between the binary predictor patterns and the binary pattern of a mineral deposit depicted in the enlarged circle is depicted in Equation 6-22. Essentially, conditional independence is determined only if $N\{B_1 \cap B_2 \cap D\}$ is not equal to zero, i.e., if there is spatial coincidence between B_1 and B_2 and if their overlap coincides with D. If there is no spatial coincidence

between B_1 and B_2, then $N\{B_1 \cap B_2 \cap D\}$ is equal to zero and there is no conditional independence between B_1 and B_2. Certain binary predictor patterns, which have high spatial coincidence or spatial correlation (e.g., geochemical anomalies), will not be conditionally independent because the right-hand side of Equation 6-22 will be greater than the left-hand side. In such cases, one of the binary predictor patterns must either be discarded or possibly combined with the appropriate binary predictor pattern before the weights of evidence analysis, as discussed by Agterberg (1992b).

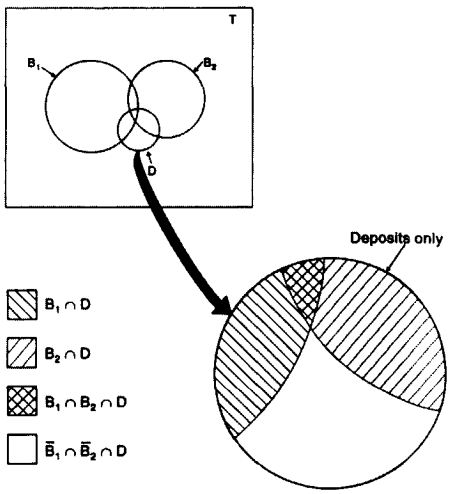

Figure 6.2. Venn diagram to illustrate the concept of conditional independence. Within the enlarged circle, the binary predictor patterns are conditionally independent with respect to binary pattern of mineral deposit if $N\{B_1 \cap D\}$ multiplied by $N\{B_2 \cap D\}$ and divided by $N\{D\}$ equals $N\{B_1 \cap B_2 \cap D\}$.

When there is spatial coincidence between two binary predictor patterns, B_1 and B_2, their conditional independence of each other with respect to a binary pattern of mineral deposit points is determined not only from the spatial relationships depicted in the enlarged circle in Figure 6.2, but also in other parts of the area where both B_1 and B_2 are absent or where either B_1 or B_2 are absent. Thus, two binary predictor patterns are conditionally independent of each other with respect to a binary pattern of mineral deposit points if the following spatial relationships are also satisfied:

$$N\{\bar{B}_1 \cap B_2 \cap D\} = \frac{N\{\bar{B}_1 \cap D\}\ N\{B_2 \cap D\}}{N\{D\}}, \tag{6-23}$$

$$N\{B_1 \cap \bar{B}_2 \cap D\} = \frac{N\{B_1 \cap D\}\ N\{\bar{B}_2 \cap D\}}{N\{D\}}, \text{ and} \tag{6-24}$$

$$N\{\bar{B}_1 \cap \bar{B}_2 \cap D\} = \frac{N\{\bar{B}_1 \cap D\}\ N\{\bar{B}_2 \cap D\}}{N\{D\}}. \tag{6-25}$$

The left-hand side of Equations 6-22 to 6-25 represents the observed number of deposits in the four overlap conditions between B_1 and B_2. The right-hand side of Equations 6-22 to 6-25 represents the predicted number of deposits in the four

overlap conditions between B_1 and B_2. The spatial relationships between the binary predictor patterns and the binary pattern of a mineral deposit lead to a contingency table calculation for testing the conditional independence of two binary predictor patterns (Table 6.1). The four cells in the table correspond to the four overlap conditions between B_1 and B_2 where mineral deposits are present. The conditional independence is tested by calculating χ^2 as follows:

$$\chi^2 = \sum_{i=1}^{4} \frac{(\text{observed}_i - \text{predicted}_i)^2}{\text{predicted}_i} . \tag{6-26}$$

Table 6.1. Contingency table for pairwise testing conditional independence based on pixels that contain a mineral deposit. Values are either calculated from the 'total' rows/columns using right-hand side of Equation 6-22 or determined by crossing/overlaying two binary predictor patterns and binary pattern of mineral deposit (i.e., left-hand side of Equation 6-22). There is one degree of freedom. (Adapted from Bonham-Carter, 1994).

	B_1 Present	B_1 Absent	Total
B_2 Present	$N\{B_1 \cap B_2 \cap D\}$	$N\{\bar{B}_1 \cap B_2 \cap D\}$	$N\{B_2 \cap D\}$
B_2 Absent	$N\{B_1 \cap \bar{B}_2 \cap D\}$	$N\{\bar{B}_2 \cap \bar{B}_2 \cap D\}$	$N\{\bar{B}_2 \cap D\}$
Total	$N\{B_1 \cap D\}$	$N\{\bar{B}_1 \cap D\}$	$N\{D\}$

Because the mineral deposits are considered as points, or unit cells, the resulting values of χ^2 are unaffected by the units of area measurement. The calculated values can be compared with critical values of χ^2 with one degree of freedom (Bonham-Carter, 1994). With a small predicted number of deposits, it is necessary to apply Yates correction (Walker and Lev, 1953; Bonham-Carter, 1994). The equation including the Yates correction is

$$\chi^2 = \sum_{i=1}^{4} \frac{(|\text{observed}_i - \text{predicted}_i| - 0.5)^2}{\text{predicted}_i} . \tag{6-27}$$

Where the absolute value of the difference between the observed and predicted number of deposits is less than 0.5, the correction is not made. Snedecor and Cochran (1967) state that when the predicted number of deposits is less than 5, the approximation of the χ^2 becomes poor. Nevertheless, Equations 6-26 and 6-27 are useful tests for pairwise conditional independence (Bonham-Carter, 1994).

Bonham-Carter et al. (1989) describe another statistical test to determine conditional independence between a pair of binary predictor patterns. The pairwise test involves calculation of observed and predicted numbers of pixels

with and without mineral deposits in eight unique overlap possibilities between the binary predictor patterns and the mineral deposit points (Table 6.2). For each of the eight unique overlap possibilities, the observed number of pixels, o, is measured directly by crossing or overlaying the three binary patterns (i.e., two binary predictor patterns and binary pattern of mineral deposit points).

Table 6.2. Eight unique overlap possibilities between two binary predictor patterns and binary pattern of mineral deposit points from which to determine conditional independence using the G^2 statistic (Adapted from Bonham-Carter et al., 1989).

	$B_1 \cap B_2$	$B_1 \cap \overline{B}_2$	$\overline{B}_1 \cap B_2$	$\overline{B}_1 \cap \overline{B}_2$
D	$N\{B_1 \cap B_2 \cap D\}$	$N\{B_1 \cap \overline{B}_2 \cap D\}$	$N\{\overline{B}_1 \cap B_2 \cap D\}$	$N\{\overline{B}_2 \cap \overline{B}_2 \cap D\}$
$\overline{D}$	$N\{B_1 \cap B_2 \cap \overline{D}\}$	$N\{B_1 \cap \overline{B}_2 \cap \overline{D}\}$	$N\{\overline{B}_1 \cap B_2 \cap \overline{D}\}$	$N\{\overline{B}_2 \cap \overline{B}_2 \cap \overline{D}\}$

The predicted number of pixels with or without deposits, e, where B_1 and B_2 are present for example, is calculated by

$$e = N\{B_1 \cap B_2\}\, P\{D|B_1 \cap B_2\}\, t \tag{6-28}$$

where $N\{B_1 \cap B_2\}$ is determined from overlap of B_1 and B_2, $P\{D|B_1 \cap B_2\}$ is calculated from the weights of evidence model and t is total area. The predicted numbers of pixels with or with without deposits in the seven other unique overlap possibilities between the two predictor patterns and the binary pattern of mineral deposits is calculated using a similar relationship to that in Equation 6-28. Then, the conditional independence is determined by calculating G^2, for i = 1,2,...,8 unique overlap possibilities, as follows

$$G^2 = -2\sum_{i=1}^{8} x_i \log_e \frac{e_i}{o_i}. \tag{6-29}$$

The calculated G^2 is distributed as χ^2 with 2 degrees of freedom (Bishop et al., 1975; Bonham-Carter et al., 1989). Where the predicted pixels, e, differ strongly from the observed pixels, o, the value of G^2 will be large and the hypothesis of conditional independence of B_1 and B_2 with respect to the points is rejected. For example, if more predicted deposits occur in the region where both binary predictor patterns are present than are observed, the pairwise test of conditional independence fails. To avoid the problem, one of the binary predictor patterns can be omitted from the analysis or possibly combined with an appropriate binary predictor pattern (Agterberg, 1992b).

Both the χ^2 and G^2 pairwise tests of conditional independence were applied to the four study areas and the results were, in most cases, similar. However, the

results of the χ^2 pairwise tests provided a practical advantage over the G^2 pairwise tests because of the small number of mineral deposits in the study areas. The results presented here are for the χ^2 pairwise tests, which include the Yates correction (Equation 6-27) for the appropriate cases (mostly in the Abra area and Catanduanes Island).

If any pair of binary predictor patterns shows some degree of conditional dependence, based on the critical χ^2 used, they can still be combined to map mineral potential according to Equation 6-21, but the statistical validity of the resulting posterior probability map must be examined by applying an overall test of conditional independence.

6.3.5 Overall test of conditional independence

To perform an overall test of conditional independence, the number of predicted mineral deposits $N\{D\}_{pred}$ is calculated (Bonham-Carter, 1994); thus

$$N\{D\}_{pred} = \sum_{k=1}^{m} P_k * N\{A\}_k \ , \qquad (6\text{-}30)$$

where $N\{A\}$ is the number of pixels with posterior probabilities P and $k = 1,2,\ldots,m$ pixels in the map. In practice, the number of predicted mineral deposits is usually larger than the observed number of mineral deposits. If the predicted number of occurrences is larger by 15% than the number of observed mineral deposits, then the assumption of conditional independence is seriously violated (Bonham-Carter, 1994). Problematic maps should then be removed from the analysis or combined prior to calculation of the weights (Agterberg, 1992b).

Bonham-Carter et al. (1989) and Bonham-Carter and Agterberg (1990) used a Kolmogorov-Smirnov statistic for an overall test of conditional independence through a goodness-of-fit between the number of observed mineral deposits and the number of predicted mineral deposits. The overall goodness-of-fit applies after the final posterior probability map has been calculated. As with pairwise testing of conditional independence, each unique overlap condition of the input binary predictor patterns is determined. The actual (or observed) number of pixels of mineral deposits occurring in each unique overlap condition is determined, and compared to the number of predicted mineral deposits in each of the unique overlap conditions. The cumulative proportion of actual (or observed) and predicted numbers of mineral deposits in each of the unique overlap conditions are then plotted against the calculated posterior probabilities of the unique overlap conditions. If the curve for the observed deposits stays within the upper and lower confidence bands of the curve for the predicted deposits, then the hypothesis of conditional independence is not rejected and

the assumptions of the probabilistic model is satisfied; otherwise, the assumption of conditional independence is violated.

The overall test of conditional independence using Equation 6-30 (Bonham-Carter, 1994) and the overall goodness-of-fit test using a Kolmogorov-Smirnov statistic were applied to the four study areas. The results of both tests were similar for the Benguet province and Baguio district where the number of deposits is relatively large. The Kolmogorov-Smirnov tests proved statistically rigorous for the Abra area and Catanduanes Island where the number of deposits is relatively small. The tests using Equation 6-30, however, were more favourable and are presented here.

6.3.6 Data integration and validation of results

The binary predictor patterns, buffered at distances with optimal spatial associations with respect to the mineral deposits, were assigned the weights and, after pairwise tests of conditional independence, were integrated according to Equation 6-21. Where a pair or pairs of input binary predictor patterns showed (some degree of) conditional dependence, based on the critical χ^2 value used, they were still used to create a posterior probability map, then an overall test of conditional independence was performed to test statistical validity of the posterior probability map. When a posterior probability map was considered statistically valid, based on the overall test of conditional independence, the calculated posterior probabilities were translated into mineral potential. The magnitude of the ratio of the posterior probability ($P_{posterior}$) to the prior probability (P_{prior}) was taken to represent mineral potential. Pixels with ratios less than one (i.e., $P_{posterior} < P_{prior}$) were classified as unfavourable (i.e., no mineral potential) whilst pixels with ratios greater than one were classified as favourable (i.e., with mineral potential). The classified probabilistic maps of mineral potential were validated against the set of mineral deposits not used to generate the probabilistic models. Results of geochemical exploration works were also used to validate the classified probabilistic maps.

6.4 APPLICATION TO BENGUET PROVINCE

The geological features that were used as predictors of porphyry copper potential in the province include strike-slip fault discontinuities, porphyry pluton centroids and batholithic pluton margins. A subset of 23 (or about 75%) of the 31 known porphyry copper deposits was used to generate the probabilistic model(s). The other subset of eight (or about 25%) of the 31 known porphyry copper deposits was used to validate the probabilistic model(s). The porphyry copper deposits that comprise the validation subset were chosen randomly; first, by labeling the deposits one to 31 and then, randomly generating eight numbers between zero and 32 with a random number generator.

6.4.1 Spatial association of porphyry copper deposits with geologic features

Variations of contrast for cumulative distances from the different geological features with respect to the porphyry copper deposits are shown in Table 6.3. For the strike-slip fault discontinuities, the most statistically significant contrast is for a distance of 3000 m, within which 20 deposits are present. For the batholithic pluton margins, the most statistically significant contrast is for a distance of 2250 m, within which 19 deposits are present. For the porphyry pluton centroids, the contrast is most significant statistically for a distance of 1000 m, within which 13 deposits are present.

Table 6.3. Variation of weights of evidence for cumulative distances from (a) strike-slip fault discontinuities, (b) batholithic pluton contacts and (c) porphyry pluton centroids with respect to the porphyry copper deposits, Benguet province.

B	Distance Buffer (m)	N{B}	N{B∩D}	W+	s(W+)	W-	s(W-)	C	s(C)	C/s(C)
strike-slip fault discontinuities	500	3475	1	1.18	1.00	-0.03	0.21	1.21	1.02	1.18
	1000	14135	2	0.47	0.71	-0.03	0.22	0.50	0.74	0.68
	1500	31048	9	1.19	0.33	-0.37	0.27	1.55	0.43	3.64
	2000	52362	11	0.86	0.30	-0.43	0.29	1.29	0.42	3.09
	2500	76758	15	0.79	0.26	-0.71	0.35	1.50	0.44	3.42
	3000	**100733**	**20**	**0.81**	**0.22**	**-1.55**	**0.58**	**2.35**	**0.62**	**3.80**
	3500	125127	21	0.64	0.22	-1.78	0.71	2.42	0.74	3.27
	4000	147844	21	0.47	0.22	-1.60	0.71	2.07	0.74	2.80
	4500	168041	22	0.39	0.21	-2.09	1.00	2.48	1.02	2.43
	5000	186137	23	0.33	0.21					
batholithic pluton margins	500	40871	6	0.50	0.41	-0.13	0.24	0.64	0.47	1.339
	1000	71950	7	0.09	0.38	-0.04	0.25	0.13	0.45	0.291
	1500	96140	13	0.42	0.28	-0.37	0.32	0.79	0.42	1.885
	2000	114561	17	0.52	0.24	-0.76	0.41	1.28	0.47	2.690
	2250	**122675**	**19**	**0.56**	**0.23**	**-1.11**	**0.50**	**1.67**	**0.55**	**3.032**
	2500	129745	19	0.50	0.23	-1.06	0.50	1.56	0.55	2.834
	3000	141746	19	0.41	0.23	-0.96	0.50	1.37	0.55	2.497
	3500	152738	21	0.44	0.22	-1.55	0.71	1.99	0.74	2.695
	4000	162238	22	0.43	0.21	-2.15	1.00	2.58	1.02	2.524
	4500	171347	23	0.42	0.21					
porphyry pluton centroids	500	9782	7	2.09	0.38	-0.32	0.25	2.41	0.45	5.324
	1000	**17783**	**13**	**2.11**	**0.28**	**-0.76**	**0.32**	**2.87**	**0.42**	**6.827**
	1500	26777	14	1.78	0.27	-0.83	0.33	2.60	0.43	6.095
	2000	36063	15	1.55	0.26	-0.91	0.35	2.45	0.44	5.602
	2500	46111	16	1.37	0.25	-0.99	0.38	2.36	0.45	5.206
	3000	56615	16	1.16	0.25	-0.94	0.38	2.10	0.45	4.642
	4000	80415	20	1.03	0.22	-1.67	0.58	2.70	0.62	4.358
	5000	103719	21	0.83	0.22	-1.93	0.71	2.76	0.74	3.728
	10000	185768	21	0.24	0.22	-1.18	0.71	1.43	0.74	1.930
	15000	231323	21	0.02	0.22	-0.22	0.71	0.25	0.74	0.337
	19000	253721	22	-0.02	0.21	0.65	1.00	-0.68	1.02	-0.660
	20000	256625	23	0.01	0.21					

Table entries in bold pertain to most statistically significant spatial association.

6.4.2 Spatial association of porphyry plutons with geologic features

The close spatial association of the porphyry copper deposits with the porphyry plutons makes the construction of a probabilistic porphyry pluton model appealing. Analysis of the spatial association of porphyry plutons with other geologic features was undertaken to construct the probabilistic model. Of the 23 digitised porphyry pluton centroids, 18 (or about 78%) were used for the spatial data analysis and the remainder was used to validate the probabilistic model.

Table 6.4 shows the variations in contrast for cumulative distances from different geological features with respect to porphyry pluton centroids. For the regional strike-slip fault discontinuities, the spatial association is most significant statistically for a distance of 2250 m, within which 12 of the 18 mapped porphyry plutons used for analysis are present. For the batholithic pluton margins, the most statistically significant contrast is for a distance of 2750 m, within which 16 porphyry plutons are present.

Table 6.4. Variation of weights of evidence for cumulative distances from (a) strike-slip fault discontinuities and (b) batholithic pluton contacts with respect to the porphyry pluton centroids, Benguet province.

B	Distance Buffer (m)	N{B}	N{B∩D}	W+	s(W+)	W-	s(W-)	C	s(C)	C/s(C)
strike-slip fault discontinuities	500	3475	1	1.42	1.00	-0.04	0.24	1.47	1.03	1.425
	1000	14135	3	1.12	0.58	-0.13	0.26	1.25	0.63	1.968
	1500	31048	5	0.84	0.45	-0.20	0.28	1.04	0.53	1.977
	2000	52362	10	1.01	0.32	-0.59	0.35	1.60	0.47	3.370
	2250	**64217**	**12**	**0.99**	**0.29**	**-0.81**	**0.41**	**1.81**	**0.50**	**3.611**
	2500	76758	13	0.89	0.28	-0.93	0.45	1.82	0.53	3.465
	2750	89286	15	0.88	0.26	-1.37	0.58	2.26	0.63	3.566
	3000	100733	15	0.76	0.26	-1.30	0.58	2.06	0.63	3.265
	3500	125127	16	0.61	0.25	-1.54	0.71	2.15	0.75	2.868
	4000	147844	17	0.51	0.24	-2.05	1.00	2.55	1.03	2.481
	4500	168041	17	0.38	0.24	-1.85	1.00	2.23	1.03	2.163
	5000	186137	17	0.28	0.24	-1.63	1.00	1.90	1.03	1.850
	5500	200738	18	0.26	0.24					
batholithic pluton margins	500	40871	4	0.34	0.50	-0.08	0.27	0.42	0.57	0.749
	1000	71950	5	0.00	0.45	0.00	0.28	0.00	0.53	0.006
	1500	96140	6	-0.11	0.41	0.06	0.29	-0.16	0.50	-0.325
	2000	114561	8	0.01	0.35	-0.01	0.32	0.01	0.47	0.027
	2500	129745	13	0.37	0.28	-0.59	0.45	0.96	0.53	1.817
	2750	**136313**	**16**	**0.53**	**0.25**	**-1.45**	**0.71**	**1.98**	**0.75**	**2.639**
	3000	141746	17	0.55	0.24	-2.10	1.00	2.65	1.03	2.574
	3250	147386	17	0.51	0.24	-2.05	1.00	2.56	1.03	2.488
	3500	152738	17	0.47	0.24	-2.00	1.00	2.48	1.03	2.406
	4000	162238	18	0.47	0.24					

Table entries in bold pertain to most statistically significant spatial association.

6.4.3 Probabilistic mapping of porphyry copper potential

A binary pattern of favourable host rocks was not used in the probabilistic modelling as all the known porphyry copper deposits are present within the areas underlain by the various rock units known to host them. Inclusion of such binary pattern would preclude potential of the other rock units to host porphyry copper deposits. The binary predictor patterns of the other geologic features, buffered at distances with optimal spatial association with the porphyry copper deposits based on the Studentised C (Table 6.3) were used as binary predictor patterns to map zones favourable for porphyry copper deposits (Figure 6.3).

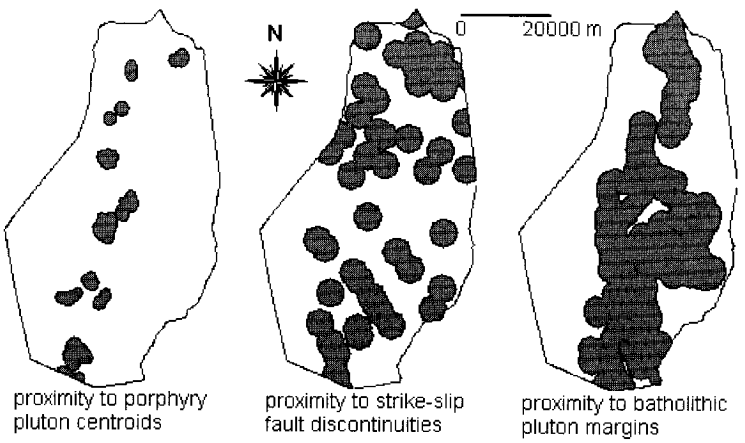

Figure 6.3. Binary predictor patterns of geological features, buffered at distances with optimal spatial associations (Table 6.3), indicating their presence (grey areas) with respect to the porphyry copper deposits, Benguet province.

Table 6.5 shows that the binary predictor patterns are conditionally independent of each other with respect to the porphyry copper deposits; hence, they are combined to create a probabilistic map of porphyry copper potential (Figure 6.4). The prior probability $P\{D\} = 23/259591 = 0.0000886$ and $\log_e O\{D\} = -9.3$.

Table 6.5. Calculated χ^2 values* for testing conditional independence between all pairs of binary maps with respect to porphyry copper deposits, Benguet province.

Binary predictor pattern	Batholithic pluton margins	Porphyry pluton centroids
Strike-slip fault discontinuities	**0.61**	**0.16**
Batholithic pluton margins		**0.67**

*With 1 degree of freedom and confidence level of 95%, critical χ^2 value is 3.84 (Davis, 1973). Values in bold indicate pairs for which the null hypothesis of conditional independence is not rejected at 95% confidence level.

The probabilistic map in Figure 6.4 indicates that about 24% of the province has potential for porphyry copper deposits. It predicts correctly 20 (or about 87%) of the 'model deposits' and predicts correctly five (or at least 62.5%) of the 'validation deposits'. Considering that only three spatial geological predictors were used to generate the probabilistic map, the 62.5% success rate assessed against the 'validation deposits' empirically validates the efficacy of the predictive map. It is of interest to note that two of the three 'validation deposits' not predicted correctly are within 1500 m of a favourable zone. In addition, the predictive map shows that portions of the predicted favourable zones spatially coincide with portions of geochemically-anomalous catchment basins. These overlap zones are headwater portions of the anomalous catchment basins (see Figures 2.12 and 2.17) and probably represent the source of the geochemical anomalies. The spatial coincidence between portions of the predicted favourable zones and portions of the geochemically-anomalous catchment basins further indicates the validity of the probabilistic map in Figure 6.4.

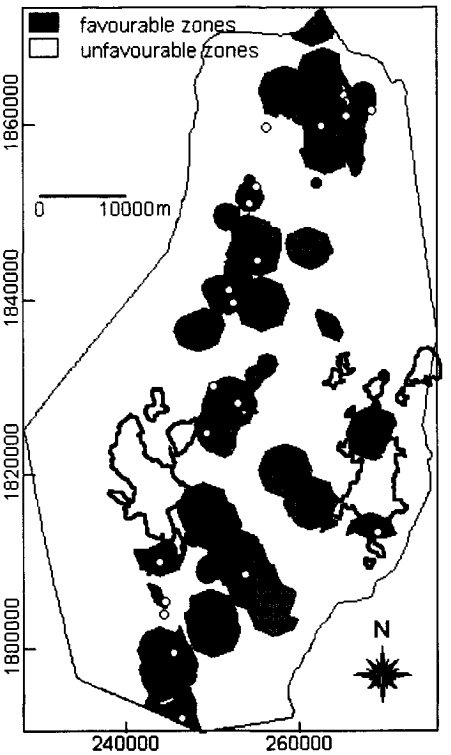

Figure 6.4. Probabilistic map of porphyry copper potential, Benguet province. Unfilled circles = 'model deposits'; filled circles = 'validation deposits'; polygons in solid lines = geochemically-anomalous catchment basins.

6.4.4 Probabilistic mapping of zones of porphyry pluton emplacement

The geologic features, buffered at distances with optimal spatial association with the porphyry pluton centroids based on the Studentised C (Table 6.4) were used as binary evidences to predict zones of porphyry pluton emplacement. Table 6.6 shows that the binary predictor patterns of porphyry pluton emplacement are conditionally independent of each other; they are combined to create a probabilistic map. The prior probability P{D} = 18/259591 = 0.0000693 and $\log_e$ O{D} = -9.6. The probabilistic map of porphyry pluton emplacement is shown in Figure 6.5.

Table 6.6. Calculated χ^2 values* for testing conditional independence between pair of binary maps with respect to porphyry pluton centroids, Benguet province.

Binary predictor pattern	Batholithic pluton margins
Strike-slip fault discontinuities	**0.28**

*With 1 degree of freedom and confidence level of 95%, critical χ^2 value is 3.84 (Davis, 1973). Values in bold indicate pairs for which the null hypothesis of conditional independence is not rejected at 95% confidence level.

The probabilistic map in Figure 6.5 indicates that about 15% of the area of the province is favourable for porphyry pluton emplacement. The probabilistic map predicts correctly only two (or 40%) of the five 'validation plutons'. The porphyry pluton model predicts correctly 11 (or at least 35%) of the 31 known porphyry copper deposits. These imply that the porphyry pluton model is not as good as the porphyry copper model in Figure 6.3 to guide further exploration work in the province. The smaller areal extents of favourable porphyry pluton zones and the wider areal extents of the zones favourable for porphyry copper deposits are reflecting the small areal extents of porphyry plutons and the wider areal extents of their hydrothermal effects. The probabilistic map also shows that portions of the predicted favourable zones are spatially coincident with portions of geochemically-anomalous catchment basins. The spatial coincidence between portions of the predicted favourable zones and portions of the geochemically-anomalous catchment basins are probably sources of the geochemical anomalies. This implies that the predicted favourable zones of porphyry pluton emplacement are (likely) geochemically-anomalous.

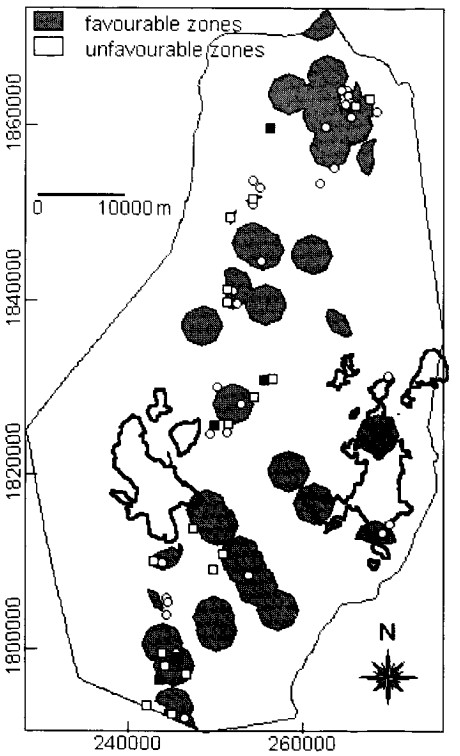

Figure 6.5. Probabilistic map of porphyry pluton emplacement, Benguet province. Unfilled squares = 'model plutons'; filled squares = 'validation plutons'; unfilled circles = porphyry copper deposits; polygons in solid lines = geochemically-anomalous catchment basins.

6.5 APPLICATION TO BAGUIO DISTRICT

The geological features that were used as predictors of epithermal gold potential in the district include lithologic units known to host the epithermal gold deposits, batholithic pluton margins, porphyry pluton contacts, northeast-trending faults/fractures and northwest-trending faults/fractures. The two sets of epithermal gold deposits (i.e., the 19 large-scale and 63 small-scale deposits) were each used to create probabilistic maps of epithermal gold potential. The probabilistic map based on the large-scale deposits was validated against the small-scale deposits. The probabilistic map based on the small-scale deposits was validated against the large-scale deposits.

6.5.1 Spatial association of gold deposits with geological features

The weights and contrast for the binary predictor pattern of favourable lithologic units were determined using the appropriate equations above. The weights and contrasts of the other binary predictor patterns with the most statistically significant contrast with the large-scale gold deposits are summarised in Table 6.7. The weights and contrasts of the different binary predictor patterns with most statistically significant contrast with respect to the small-scale gold deposits are summarised in Table 6.8. The similarities in relative magnitudes of the contrasts show that the spatial associations of the large-scale gold deposits with the different geological features are similar to the spatial associations of the small-scale occurrences with the different geological features. The spatial associations of both sets of gold deposits with the geological features are similar because their geneses are the same (Mitchell and Leach, 1991).

Table 6.7. Weights and contrasts of binary predictor patterns with highest Studentised C with respect to large-scale gold deposits, Baguio district.

Binary predictor pattern	Distance Buffer (m)	N{B}	N{B∩D}	W+	s(W+)	W-	s(W-)	C	s(C)	C/s(C)
Pugo & Zigzag Formations	-	18837	11	0.256	0.302	-0.271	0.354	0.527	0.465	1.134*
Batholithic pluton margins	1000	17907	15	0.617	0.258	-1.003	0.500	1.621	0.563	2.880
Porphyry pluton contacts	2750	14922	15	0.800	0.258	-1.120	0.500	1.920	0.563	3.411
NE-trending faults/fractures	400	14641	13	0.676	0.277	-0.725	0.408	1.401	0.494	2.837
NW-trending faults/fractures	1300	34666	12	-0.267	0.289	0.743	0.378	-1.010	0.476	-2.122

*not significant statistically.

Table 6.8. Weights and contrasts of binary predictor patterns with highest Studentised C with respect to small-scale gold deposits, Baguio district.

Binary Predictor pattern	Distance Buffer (m)	N{B}	N{B∩D}	W+	s(W+)	W-	s(W-)	C	s(C)	C/s(C)
Pugo & Zigzag Formations	-	18837	34	0.186	0.172	-0.182	0.186	0.368	0.253	1.455*
Batholithic pluton margins	750	14581	43	0.678	0.153	-0.722	0.224	1.401	0.271	5.171
Porphyry pluton contacts	1750	9366	44	1.146	0.151	-0.948	0.229	2.093	0.275	7.619
NE-trending faults/fractures	600	20928	50	0.467	0.142	-0.890	0.277	1.358	0.311	4.358
NW-trending faults/fractures	1400	35911	58	0.075	0.131	-0.609	0.447	0.684	0.466	1.466*

*not significant statistically.

It can be gleaned from Tables 6.7 and 6.8 that the spatial associations of the Pugo/Zigzag Formations and the northwest-trending faults/fractures with the gold deposits are not significantly positive (i.e., <2). The spatial association of the northwest-trending faults/fractures with the large-scale deposits is significantly negative. However, these geological features are observed to be spatially associated with some of the gold deposits in the district (see subsection 2.3.1). Probabilistic models of epithermal gold potential for the district, inclusive and exclusive of these geological features that are not significantly positively spatially associated with the gold deposits, were evaluated.

6.5.2 Probabilistic mapping of epithermal gold mineral potential

Binary predictor patterns of geologic features, buffered at distances with highest contrasts with the gold deposits (Figures 6.6 and 6.7), were tested pairwise for conditional independence. For the binary pattern of the northwest-trending faults/fractures, because of their negative spatial association with the large-scale occurrences, zones within 1300 m indicate their 'absence' and zones beyond 1300 m their 'presence'. Table 6.9 shows that all pairs of binary maps are conditionally independent of each other with respect to the large-scale gold deposits. Table 6.10 shows that all pairs of binary predictor patterns, except the pair batholithic pluton margins and porphyry pluton contacts, show conditional independence with respect to the small-scale gold deposits. This requires that the binary predictor patterns that exhibit conditional dependence of each other with respect to the small-scale deposits are not used together to predict gold potential based on the small-scale gold deposits.

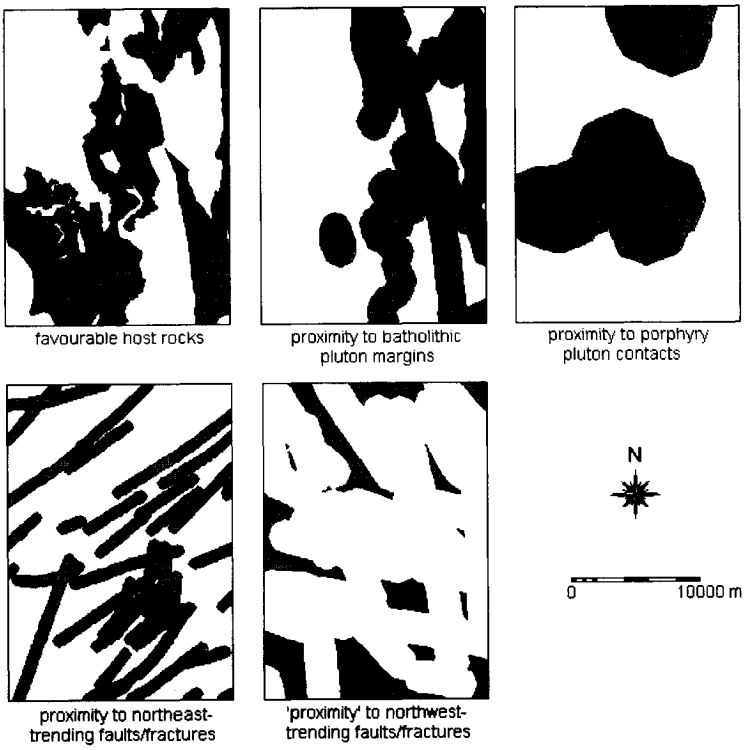

Figure 6.6. Binary predictor patterns of geological features, buffered at distances with optimal spatial associations (Table 6.7), indicating their presence (grey areas) with respect to large-scale gold deposits, Baguio district.

Table 6.9. Calculated χ^2 values* for testing conditional independence between all pairs of binary maps with respect to large-scale gold occurrences, Baguio district.

	Batholithic pluton margins	Porphyry pluton contacts	NE-trending faults/fractures	NW-trending faults/fractures
Pugo & Zigzag formations	**3.68**	**2.25**	**0.28**	**1.03**
Batholithic pluton margins		**1.35**	**0.80**	**0.31**
Porphyry pluton contacts			**0.10**	**0.31**
NE-trending faults/fractures				**1.53**

*With 1 degree of freedom and confidence level of 95%, critical χ^2 value is 3.84 (Davis, 1973). Values in bold indicate pairs for which the null hypothesis of conditional independence is not rejected at 95% confidence level.

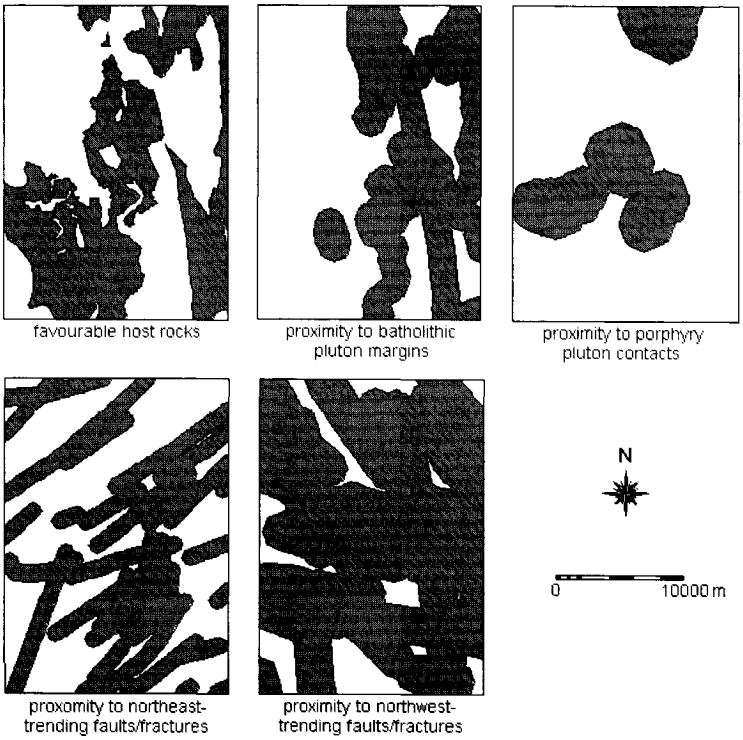

Figure 6.7. Binary predictor patterns of geological features, buffered at distances with optimal spatial associations (Table 6.8), indicating their presence (grey areas) with respect to small-scale gold deposits, Baguio district.

Table 6.10. Calculated χ^2 values* for testing conditional independence between all pairs of binary maps with respect to small-scale gold deposits, Baguio district.

	Batholithic pluton margins	Porphyry pluton contacts	NE-trending faults/fractures	NW-trending faults/fractures
Pugo & Zigzag formations	**3.03**	**2.29**	**1.59**	**2.52**
Batholithic pluton margins		8.58	**0.34**	**0.35**
Porphyry pluton contacts			**0.00**	**0.27**
NE-trending faults/fractures				**0.00**

*With 1 degree of freedom and confidence level of 95%, critical χ^2 value is 3.84 (Davis, 1973). Values in bold indicate pairs for which the null hypothesis of conditional independence is not rejected at 95% confidence level.

The weights in Tables 6.7 and 6.8 were assigned to the appropriate binary predictor patterns, which were combined to create the probabilistic maps. Pairs of binary predictor patterns showing conditional dependence were initially included in the analysis to evaluate the influence of using such binary predictor patterns. Based on the large-scale gold deposits, the prior probability P{D} = 19/42039 = 0.00045 and $\log_e$ O{D} = -7.7. Based on the small-scale gold deposits, the prior probability P{D} = 63/42039 = 0.0015 and $\log_e$ O{D} = -6.5. The probabilistic maps of epithermal gold potential are shown in Figure 6.8.

With the probabilistic map in Figure 6.8a, the number of predicted large-scale gold deposits is larger by 15.6% than the observed number of large-scale gold deposits. With the probabilistic map in Figure 6.8b, the number of predicted small-scale gold deposits is larger by 15.9% than the observed number of small-scale gold deposits. The results indicate that the assumption of conditional independence between the input binary predictor patterns with respect to the deposits is seriously violated (Bonham-Carter, 1994). For the probabilistic map in Figure 6.7a, the high predicted number of large-scale deposits is probably due to inclusion of binary predictor patterns whose spatial associations with the

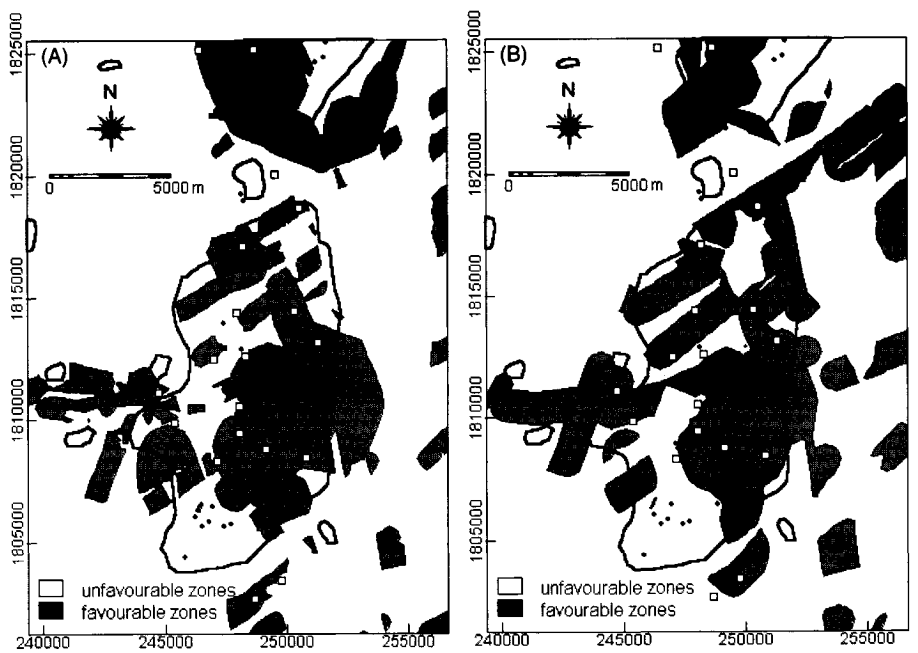

Figure 6.8. Probabilistic maps of epithermal gold potential, Baguio district, derived from all conditionally independent predictor patterns whose weights were calculated based on (a) large-scale gold deposits and (b) small-scale gold deposits. Unfilled squares = large-scale gold deposits; small dots = small-scale gold deposits; polygons in solid lines = outline of stream sediment Au anomaly (UNDP, 1987a).

occurrences are not statistically significant. For the probabilistic map in Figure 6.7b, the high number of predicted small-scale deposits is probably due in part to the conditional independence problem with one pair of binary predictor patterns and the inclusion of binary predictor patterns whose spatial associations with the occurrences are not significant statistically. These hypotheses are verified by removing first from the analysis those binary predictor patterns whose spatial associations with the deposits are not significant statistically; the resulting probabilistic maps are shown below.

The probabilistic maps in Figure 6.9 seem to show almost no differences from those shown in Figure 6.8. There are differences, however. With the probabilistic map in Figure 6.9a, the number of predicted large-scale gold deposits is larger by 15.1% than the observed number of large-scale deposits. With the probabilistic map in Figure 6.9b, the number of predicted small-scale gold deposits is larger by 14.2% than the observed number of small-scale deposits. Removal of the binary predictor patterns whose spatial associations with the gold deposits are not significant statistically thus reduces the seriousness of the

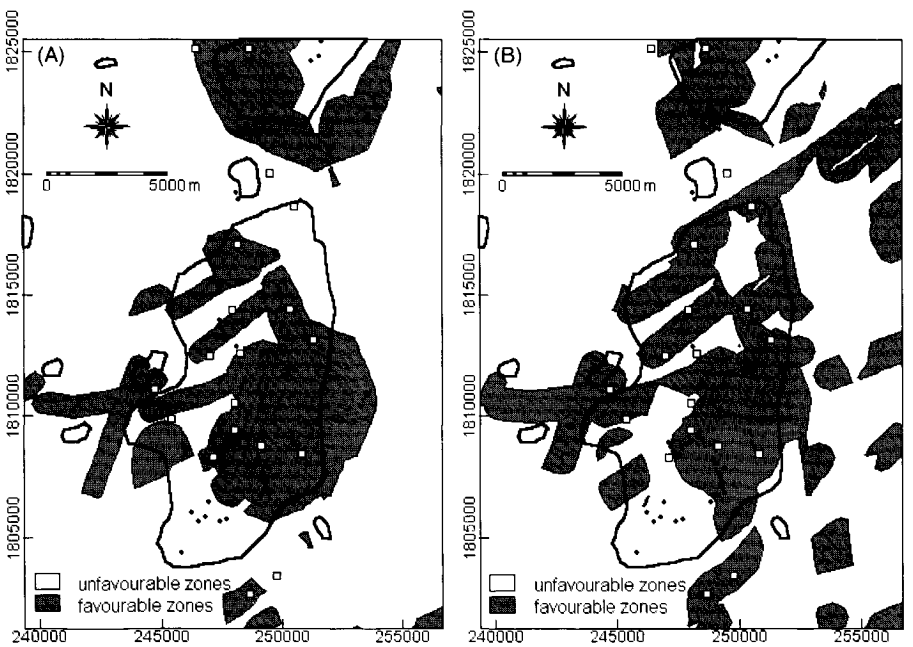

Figure 6.9. Probabilistic maps of epithermal gold potential, Baguio district, resulting from exclusion of binary predictor patterns with statistically non-significant spatial associations with (a) large-scale gold deposits and (b) small-scale gold deposits. Unfilled squares = large-scale gold deposits; small dots = small-scale gold deposits; polygons in solid lines = outline of stream sediment Au anomaly (UNDP, 1987a).

violation of conditional independence assumption based on an overall test. Figure 6.10 shows the differences in the $P_{posterior}/P_{prior}$ ratios prior to classification of the calculated posterior probabilities into the maps shown in Figures 6.8 and 6.9. The maps showing the differences in the $P_{posterior}/P_{prior}$ ratios illustrate mainly that binary predictor patterns of Pugo/Zigzag Formations and proximity to northwest-trending faults/fractures are not useful in the probabilistic mapping of epithermal gold potential in the district. Using the binary predictor patterns of the Pugo/Zigzag Formations and proximity to northwest-trending faults/fractures results mainly in minor increases in the posterior probabilities of many zones and the overestimation of posterior probabilities in some zones, which leads to overestimation of the number of predicted deposits.

With the probabilistic map in Figure 6.9a, the number of predicted large-scale gold deposits is still larger by 15.1% than the observed number of large-scale deposits. This implies that some conditional dependence is still present among the binary predictor patterns. Removal of any of the remaining binary predictor patterns, although correct statistically, is considered inappropriate geologically because these binary predictor patterns pertain to geological features that were responsible for epithermal gold deposition in the district (Wolfe, 1988; Mitchell

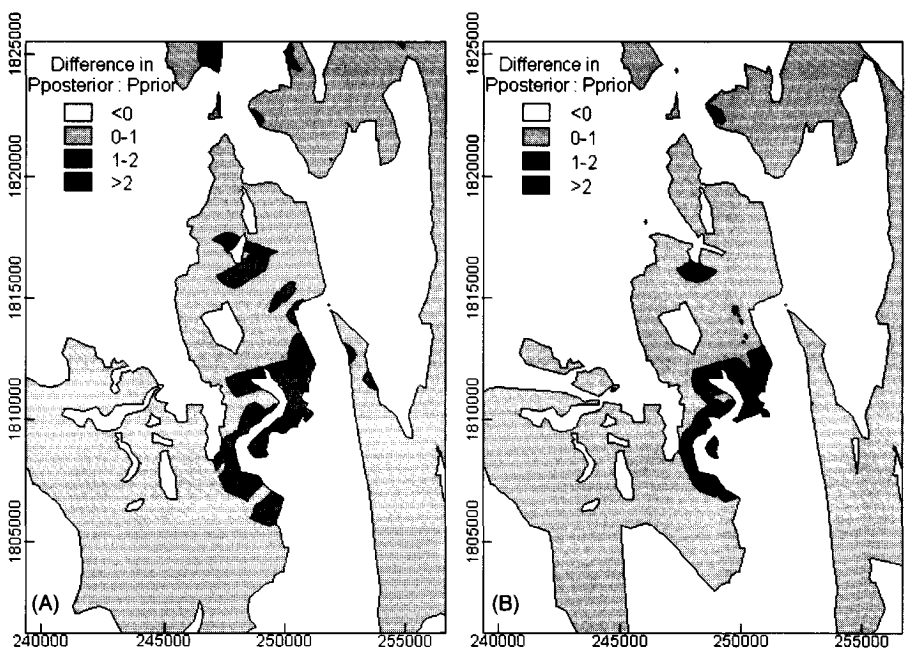

Figure 6.10. Baguio district: differences in $P_{posterior}/P_{prior}$ ratios of probabilistic maps using all binary predictor patterns and using only binary predictor patterns whose spatial associations are significant statistically based on (a) large-scale gold deposits and (b) small-scale gold deposits.

and Leach, 1991). If the problem of conditional dependence is ignored, the probabilistic map in Figure 6.8a may be considered for validation.

With the probabilistic map in Figure 6.9b, the number of predicted small-scale gold deposits is considered acceptable, despite the presence of conditional dependence between the binary predictor patterns of the batholithic pluton margins and the porphyry pluton contacts. Although it is incorrect statistically to use them together, it is appropriate geologically because both the batholithic plutons and the porphyry plutons have influenced different episodes of gold deposition in the district (Wolfe, 1988). As it is intended to map zones favourable for epithermal gold deposits, without regard to age of mineralisation, combining them is favoured over using them separately.

The results of the validation of the probabilistic maps in Figure 6.9 are given in Table 6.11. The probabilistic map based on the large-scale gold deposits (Figure 6.9a) has higher success rates yet lower percentages of predicted favourable zones than the probabilistic map based on the small-scale deposits. The probabilistic map in Figure 6.9a is considered better than the probabilistic map in Figure 6.9b. The predicted favourable zones in either of the probabilistic maps spatially coincide with about 60% of the zones geochemically-anomalous for stream sediment Au contents (UNDP, 1987a). Both probabilistic maps are considered valid.

Table 6.11. Inventory of epithermal gold deposits in the probabilistic maps in Figure 6.9 resulting from removal of binary predictor patterns whose spatial associations with the epithermal gold deposits are not significant statistically.

Epithermal gold potential	Probabilistic map based on large-scale gold occurrences (Figure 6.9a)					Probabilistic map based on small-scale gold occurrences (Figure 6.9b)				
	Area	'model large-scale gold deposits'		'validation small-scale gold deposits'		Area	'validation large-scale gold deposits		'model small-scale gold deposits'	
	% of district	No.	%	No.	%	% of district	No.	%	No.	%
Unfavourable	76	5	26	14	22	71	5	26	18	28
Favourable	24	14	74	49	78	29	14	74	45	72

6.6 APPLICATION TO ABRA AREA

The geological features that were used as predictors of porphyry copper potential in the area include porphyry pluton centroids, granodiorite batholithic margins, quartz-diorite batholithic margins, north-trending faults/fractures, northeast-trending faults/fractures, northwest-trending faults/fractures and intersections of regional faults (i.e., north-trending and northeast-trending faults/fractures). Dividing the 12 porphyry copper deposits in the area into two

sets - one to generate the probabilistic model and the other set to validate the model - was considered impractical as the former would be too small to generate a statistically sound model. The probabilistic modeling was thus generated using the 12 porphyry copper deposits. The known mineralised zones (see sub-section 2.4.1) and the delineated stream sediment Cu anomalies (see sub-section 2.4.4) were used to validate the model(s).

Binary predictor patterns of all the geological features, buffered at distances with the highest Studentised C, were used initially in the predictive mapping of porphyry copper potential. The predictive mapping then proceeded to remove, first those binary predictor patterns of geological features with non-significant negative contrasts and then those binary predictor patterns of geological features with non-significant positive contrasts. Then, only those binary predictor patterns of geological features with statistically significant positive contrasts were combined. Finally, binary predictor patterns with barely statistically significant positive contrasts but with higher 'predictive strength' (as explained below) were used in the predictive mapping of porphyry copper potential.

6.6.1 Spatial association of porphyry copper deposits with geological features

The weights of evidence of binary predictor patterns with highest Studentised C are summarised in Table 6.12 (see also Table 4.35). The intersection of regional faults and the porphyry pluton centroids are significantly positively associated with the porphyry copper deposits. The granodiorite batholithic margins and the

Table 6.12. Binary predictor patterns of geological features with highest Studentised C with respect to the porphyry copper deposits, Abra area.

Binary pattern	Distance Buffer (m)	N{B}	N{B∩D}	W+	s(W+)	W-	s(W-)	C	s(C)	C/s(C)
Intersections of regional faults	1000	12547	6	1.299	0.408	-0.547	0.408	1.846	0.577	3.196
Porphyry pluton centroids	1500	6658	3	1.240	0.577	-0.213	0.333	1.452	0.667	2.178
Granodiorite margins	1500	55421	10	-0.324	0.316	-0.869	0.707	1.193	0.775	1.540*
N-trending faults/fractures	1500	49849	9	0.325	0.333	-0.605	0.577	0.930	0.667	1.395*
Quartz-diorite margins	2500	33205	2	-0.773	0.707	0.266	0.316	-1.039	0.775	-1.341*
NW-trending faults/fractures	1500	24592	1	-1.166	1.000	0.224	0.302	-1.390	1.044	-1.331*
NE-trending faults/fractures	750	38487	2	-0.921	0.707	0.360	0.316	-1.281	0.775	-1.653*

*not significant statistically.

north-trending faults are not significantly positively spatially associated with the porphyry copper deposits. The quartz-diorite batholithic margins, the northwest-trending and the northeast-trending faults/fractures are not significantly negatively associated with the porphyry copper deposits. The geological implications of the spatial associations between the porphyry copper deposits and the geological features have been discussed in sub-section 4.5.8.

6.6.2 Probabilistic mapping of porphyry copper potential

Binary predictor patterns of geologic features, buffered at distances with the highest Studentised C, are shown in Figure 6.11. The binary maps in the upper row of Figure 6.11 have positive contrast whilst those in the lower row have negative contrast; the first two in the upper row have significant positive contrast. Table 6.13 shows that all pairs of binary maps, except the pair northwest-trending and northeast-trending faults/fractures, are conditionally independent with respect to the porphyry copper deposits. Because the binary pattern of

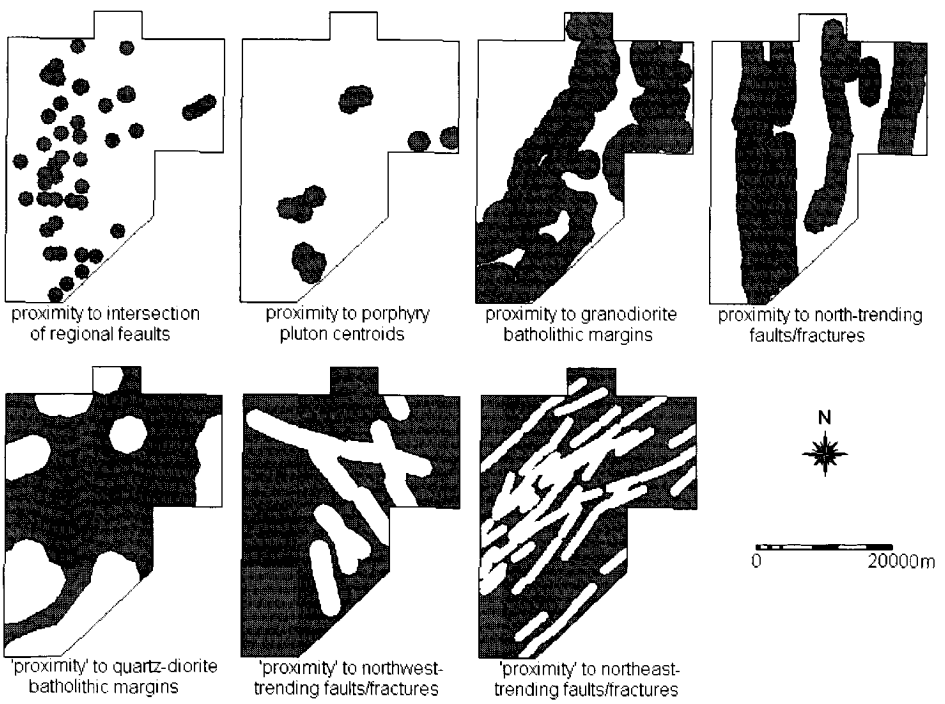

Figure 6.11. Binary predictor patterns of geological features indicating their presence (grey areas) with respect to the porphyry copper deposits, Abra area. The binary predictor patterns are arranged from binary pattern with highest positive Studentised C (top left) to binary pattern with most negative Studentised C (bottom right).

Table 6.13. Calculated χ^2 values* for testing conditional independence between all pairs of binary maps with respect to porphyry copper deposits, Abra area.

	Porphyry plutons centroids	Granodiorite margins	N-trending faults/ fractures	Quartz-diorite margins	NW-trending faults/ fractures	NE-trending faults/ fractures
Regional fault intersection	**0.44**	**0.00**	**0.44**	**2.40**	**1.09**	**0.00**
Porphyry pluton centroids		**0.80**	**1.33**	**0.80**	**0.36**	**0.80**
Granodiorite margins			**0.80**	**0.48**	**0.22**	**1.92**
N-trending faults/fractures				**0.80**	**3.27**	**0.80**
Quartz-diorite margins					**0.22**	**0.48**
NW-trending faults/fractures						5.45

*With 1 degree of freedom and confidence level of 95%, critical χ^2 value is 3.84 (Davis, 1973). Values in bold indicate pairs for which the null hypothesis of conditional independence is not rejected at 95% confidence level.

northwest-trending faults/fractures shows high χ^2 values with two other binary predictor patterns (i.e., intersections of regional faults and north-trending faults/fractures), it was not used in the analyses.

The prior probability P{D} = 12/91963 = 0.00013 and $\log_e$ O(D) = -8.9. The probabilistic maps based on different combinations of the binary predictor patterns are shown in Figure 6.12 and the percentage differences in the number of predicted deposits by each probabilistic map and the number of known deposits are summarised in Table 6.14.

There are three consequences of combining binary predictor patterns with different statistical significance. Using binary predictor patterns with non-significant positive contrast in combination with binary predictor patterns with significant contrast (i.e., Figures 6.12a and 6.12b) leads to overestimation of the predicted number of deposits (i.e., overestimation of posterior probabilities). Using binary predictor patterns with non-significant negative contrast in combination with binary predictor patterns with significant positive contrast (Figure 6.12c) leads to under-estimation of the predicted number of deposits

Table 6.14. Percentage differences in the predicted number of porphyry copper deposits based on probabilistic maps in Figure 6.11 and the known number of porphyry copper deposits, Abra area.

	Probabilistic map			
	Figure 6.11a	Figure 6.11b	Figure 6.11c	Figure 6.11d
% Difference between number of predicted and number of known deposits	25.3% larger	53.3% larger	2.5% smaller	15% larger

(i.e., under-estimation of posterior probabilities). Using only binary predictor patterns with significant positive contrasts (i.e., Figure 6.12d) leads to a number of predicted deposits that is larger, to an acceptable proportion, than the number of known deposits.

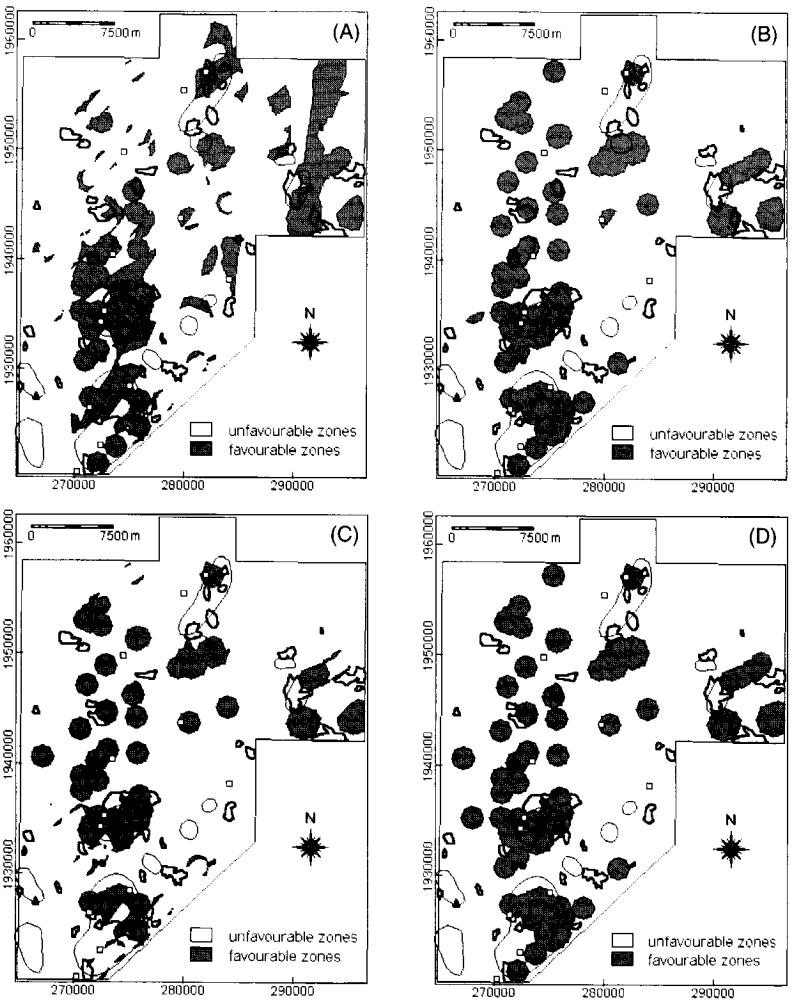

Figure 6.12. Probabilistic maps of porphyry copper potential in Abra area based on (a) all conditionally independent binary predictor patterns, (b) binary predictor patterns with significant positive and non-significant positive contrasts, (c) binary predictor patterns with significant positive and non-significant negative contrasts and (d) binary predictor patterns with significant positive contrasts. Unfilled squares = known porphyry copper deposits; polygons in thin lines = known mineralised zones; polygons in thick lines = stream sediment Cu anomalies.

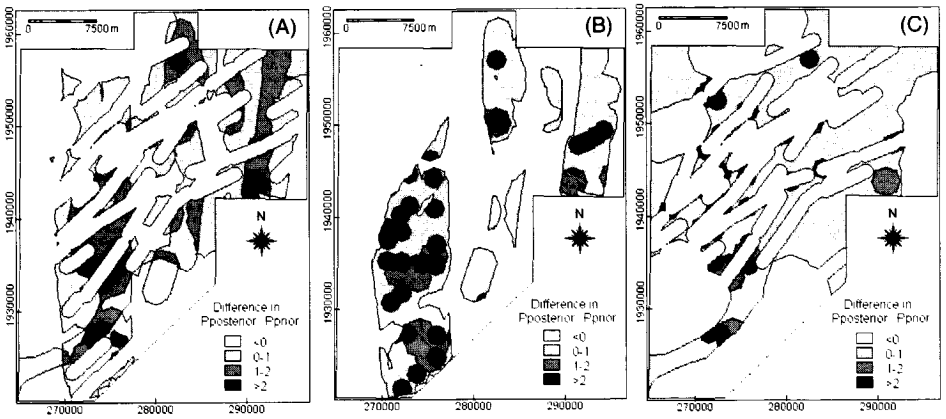

Figure 6.13. Abra area: differences in $P_{posterior}/P_{prior}$ ratios between classified probabilistic maps in (a) Figures 6.12a and 6.12d, (b) Figures 6.12b and 6.12d and (c) Figures 6.12c and 6.11d.

The probabilistic map in Figure 6.12a is visibly different from the probabilistic map in Figure 6.12d, although there are clear similarities between them. The probabilistic map in Figure 6.12b shows no marked visible differences with the probabilistic map in Figure 6.12d. The probabilistic map in Figure 6.12c shows very little visible differences with the probabilistic map in Figure 6.12d. There are, however, marked differences as shown in Figure 6.12, which illustrates the differences in the $P_{posterior}/P_{prior}$ ratios prior to classification of the posterior probabilities into the probabilistic maps in Figure 6.13. The 'difference' maps in Figure 6.13 indicate that analyses inclusive of binary predictor patterns with statistically non-significant contrasts can produce, at the post-classification stage, similar results to analyses exclusive of these binary predictor patterns. This means that an overall test of conditional independence must always be applied even if the pairwise tests show an apparent lack of serious conditional independence problems.

The probabilistic map in Figure 6.12d can be considered just valid statistically. It indicates that 18.5% of the area has potential for porphyry copper deposits. It predicts correctly 7 (or at least 58%) of the 12 known porphyry copper deposits. The probabilistic map predicts correctly only 46% of the known mineralised zones and 44% of the zones geochemically-anomalous for stream sediment Cu contents. The low success rates of the probabilistic map in Figure 6.12d suggest that it should be used with caution.

The probabilistic map in Figure 6.12d is derived from the combination of the binary predictor pattern of proximity to intersection of regional faults (i.e., north-trending and northeast-trending faults/fractures) and proximity to porphyry plutons centroids. Four possible reasons can be postulated for the poor success

rates of the probabilistic map in Figure 6.12d. First, the number of mineral deposits is small so that the calculated weights are non-significant statistically. Inspection of Tables 4.21, 4.23, 4.25, 4.27, 4.29, 4.31 and 4.33 shows that the weights for virtually all the cumulative distances from the geological features with respect to the deposits are not significantly different from zero. Second, the accuracy of the locations of the porphyry copper deposits is not definitive. Several of the porphyry copper deposits reported by earlier workers (Bureau of Mines, 1976) are not reflected in the mineralised zones reported by more recent workers (JICA, 1980) as shown in Figure 2.13. The accuracy of the map of mineralised zones (JICA, 1980), however, is also not definitive because it does not reflect the deposits mapped by Bureau of Mines (1976). The map of mineralised zones (JICA, 1980) was considered less accurate because it is an extrapolation of discontinuous mineralised outcrops that were probably observed mainly along the accessible drainage courses; hence, it was not used in the spatial modeling. Third, the map of structural features interpreted from shaded-relief images of DEM of the area is probably not detailed enough to quantify more accurately their spatial association with the porphyry copper deposits. More detailed structural mapping is probably required to characterise more accurately the spatial association between faults/fractures and the porphyry copper deposits in the area. Fourth, many of the known porphyry copper deposits are probably associated with non-outcropping porphyry plutons. The quantified spatial associations pertain only to mapped geological features.

Of the four postulated reasons for the low success rates of the probabilistic map in Figure 6.12d, the last three postulated reasons need further field verification to provide remedial spatial data inputs to probabilistic mapping of porphyry copper potential in the area. In relation to the first postulated reason, remedial measures for probabilistic mapping of porphyry copper potential can be devised by further inspection and analysis of the results of the weights of evidence calculations. Inspection and analysis of the weights of evidence calculations for the porphyry pluton centroids and the intersection of regional faults revealed that their binary predictor patterns of optimal spatial association with the porphyry copper deposits have low predictive strength. The predictive strength of a binary predictor pattern is here defined as the ratio of the number of deposits within a pattern indicating presence of a geological feature (i.e., $N\{B \cap D\}$) to the total number of deposits (i.e., $N\{D\}$) used in the analysis. If the ratio $N\{B \cap D\} : N\{D\}$ is greater than 50%, then the binary predictor pattern has high predictive strength. If the ratio $N\{B \cap D\} : N\{D\}$ is less than 50%, then the binary predictor pattern has low predictive strength.

From Table 6.10 it can be seen that the binary predictor patterns for the intersections of regional faults and porphyry pluton centroids, buffered at the distances at which the spatial contrast is most statistically significant, have low predictive strengths. In addition, although the contrast C is significant statistically, the negative weights are barely or not significantly different from zero. This implies that the binary predictor patterns were improperly buffered

based solely on the statistical significance of the contrast. Thus, additional criteria were considered to select properly the distance buffer for a binary pattern. These criteria are: (1) both the W+ and the W- must be significantly different from zero; and (2) the predictive strength of the binary pattern must be high. For the porphyry pluton centroids, these criteria are met only for a distance of 7000 m (Table 4.25), but the contrast is barely significant statistically. For the intersections of regional faults, these criteria are met for distances within 1500 to 2000 m (Table 4.33), within which distance range the contrasts are significant statistically. The criteria are also met for a distance of 2500 m, but the contrast is barely significant statistically. Experiments were made to test which probabilistic map would provide the best result based on the two criteria above. The results of the experiments are summarised in Table 6.15.

With an overall test of conditional independence, the result of combination 4 is not statistically valid. For combinations 1, 2 and 3, the problem of conditional independence is within acceptable levels. The probabilistic maps resulting from combinations 1, 2 and 3 are shown in Figure 6.14. The probabilistic maps do not resemble the probabilistic map in Figure 6.12d nor do they reflect the binary pattern of intersections of regional faults. The probabilistic map in Figure 6.14a has the lowest prediction rates and the lowest percentage of predicted favourable zones. It has similar prediction rates to the probabilistic map in Figure 6.12d. The probabilistic map in Figure 6.14b has intermediate prediction rates and percentages of predicted favourable zones. The probabilistic map in Figure 6.14c has highest prediction rates and highest percentage of predicted favourable zones. The probabilistic map in Figure 6.14c is considered optimal.

Table 6.15. Results of experiments using binary predictor patterns with statistically significant weights but with contrasts that are barely or not optimally statistically significant.

Spatial geoinformation characteristics	Combination 1[a] (Fig. 6.14a)	Combination 2[b] (Fig. 6.14b)	Combination 3[c] (Fig. 6.14c)	Combination 4[d]
% difference between number of predicted and known deposits	12.5% larger	13.3% larger	14.3% larger	15.5% larger
% area predicted as favourable zones	20%	25%	29%	37%
% of known deposits predicted correctly	58%	67%	75%	83%
% area of known mineralised zones predicted correctly	46%	53%	59%	67%
% area of Cu anomalies predicted correctly	41%	49%	57%	68%

[a]porphyry pluton centroids buffered at 7000 m and intersection of regional faults buffered at 1500 m
[b]porphyry pluton centroids buffered at 7000 m and intersection of regional faults buffered at 1750 m
[c]porphyry pluton centroids buffered at 7000 m and intersection of regional faults buffered at 2000 m
[d]porphyry pluton centroids buffered at 7000 m and intersection of regional faults buffered at 2500 m

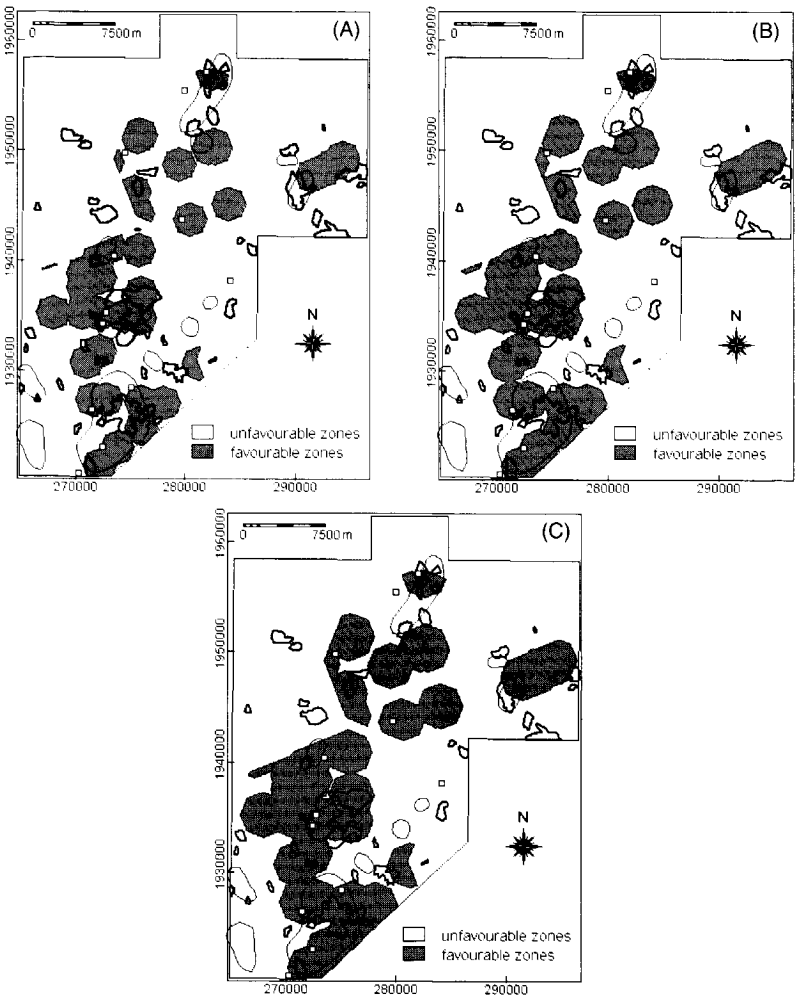

Figure 6.14. Probabilistic maps of porphyry copper potential in Abra area based on binary predictor patterns of porphyry pluton centroids buffered at 7000 m and binary predictor patterns of intersections of regional faults buffered at (a) 1500 m, (b) 1750 m and (c) 2000 m. Unfilled squares = known porphyry copper deposits; polygons in thin lines = known mineralised zones; polygons in thick lines = stream sediment Cu anomalies.

6.7 APPLICATION TO CATANDUANES ISLAND

The geological features that were used as predictors of gold-copper potential in the island include the Batalay Intrusive contacts, the northeast-trending faults/fractures, the north-trending faults/fractures, the northwest-trending faults/fractures and the east-trending faults/fractures. The number of gold-

copper deposits in the island was considered too small to be divided into a subset for building a probabilistic model and another subset for validating the model. The 17 gold-copper deposits were thus used to generate the probabilistic model(s) and the geochemically-anomalous catchment basins (see sub-section 2.5.4) were used to validate the model(s).

All binary predictor patterns, buffered at distances with highest positive or lowest negative Studentised C, which are conditionally independent of each other with respect to the gold-copper deposits, were used initially in the probabilistic modeling. Then, only those binary predictor patterns with highest positive contrasts and then only those binary predictor patterns with positive contrasts and high predictive strengths (as explained below) were used in the probabilistic modeling.

6.7.1 Spatial association of gold-copper deposits with geological features

The weights of evidence are summarised in Table 6.16. The Batalay Intrusive contacts, the northeast-trending faults/fractures and the north-trending faults/fractures are significantly positively spatially associated with the gold-copper deposits. The east-trending faults/fractures are significantly negatively spatially associated with the gold-copper deposits. The northwest-trending faults/fractures are not significantly negatively associated with the gold-copper deposits. The geological implications of the spatial associations between the gold-copper deposits have been discussed in the previous chapter (see sub-section 4.6.6).

Table 6.16. Binary predictor patterns of geological features with most positive or most negative Studentised C with respect to the gold-copper deposits, Catanduanes Island.

Binary pattern	Distance Buffer (m)	N{B}	N{B∩D}	W+	s(W+)	W-	s(W-)	C	s(C)	C/s(C)
Batalay Intrusive contacts	1000	10815	6	1.553	0.408	-0.358	0.302	1.911	0.508	3.765
NE-trending faults/fractures	1000	53005	12	0.657	0.289	-0.768	0.447	1.425	0.532	2.677
N-trending faults/fractures	750	30756	8	0.796	0.354	-0.397	0.333	1.193	0.486	2.455
NW-trending faults/fractures	1500	56260	3	-0.789	0.577	0.298	0.267	-1.087	0.636	-1.708*
E-trending faults/fractures	11250	90186	5	-0.750	0.447	0.627	0.289	-1.377	0.532	-2.587

*not significant statistically.

6.7.2 Probabilistic mapping of gold-copper potential

The binary predictor patterns, buffered at distances given in Table 6.16, are shown in Figures 6.15. It is indicated in Table 6.17 that all pairs of binary maps, except the pair Batalay Intrusive contacts and east-trending faults/fractures, are conditionally independent with respect to the gold-copper deposits. Because other pairs of binary predictor patterns with the Batalay Intrusive contacts have lower computed χ^2 values than the pairs of binary predictor patterns with the east-trending faults/fractures, the binary pattern of east-trending faults/fractures was not included in the probabilistic mapping of gold-copper potential.

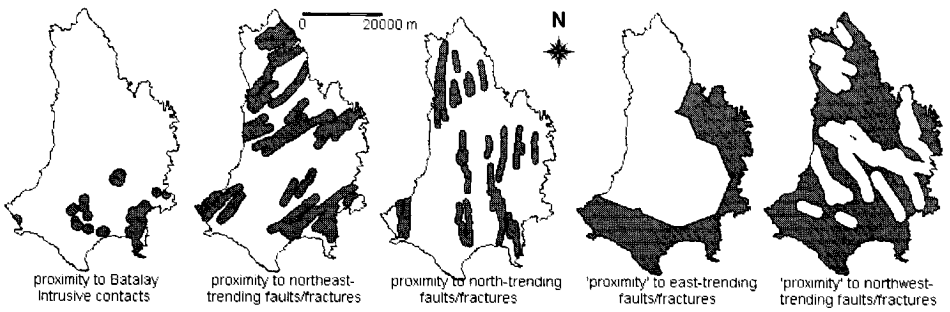

Figure 6.15. Binary predictor patterns of geological features buffered at distances with most positive/negative Studentised C to indicate their presence (grey areas) with respect to gold-copper deposits, Catanduanes Island.

The binary predictor patterns of the Batalay Intrusive contacts, the northeast-trending faults/fractures, the north-trending faults/fractures and the northwest-trending faults/fractures, buffered at the appropriate distances indicated in Table 6.16, were integrated to create a probabilistic map. The prior probability P{D} = 17/144811 = 0.00012 and the $\log_e$ O{D} = -9.05. The probabilistic map is shown

Table 6.17. Calculated χ^2 values* for testing conditional independence between all pairs of binary predictor patterns with highest Studentised C, Catanduanes Island.

	NE-trending faults/fractures	N-trending faults/fractures	NW-trending faults/fractures	E-trending faults/fractures
Batalay intrusive contacts	**0.07**	**0.03**	**0.01**	9.37
NE-trending faults/fractures		**2.08**	**0.03**	**0.38**
N-trending faults/fractures			**0.28**	**0.48**
NW-trending faults/fractures				**0.03**

*With 1 degree of freedom and confidence level of 95%, critical χ^2 value is 3.84 (Davis, 1983). Values in bold indicate pairs that show conditional independence at the 95% confidence level.

in Figure 6.16a.

The number of predicted gold-copper deposits based on the probabilistic map in Figure 6.16a is larger by 27.6% than the number of known gold-copper deposits. It is therefore not statistically valid. Inclusion of the binary pattern of the northwest-trending faults/fractures, which is not significantly negatively spatially associated with the gold-copper deposits, probably results in the overestimation of the posterior probabilities and the number of predicted gold-copper deposits.

The binary pattern of northwest-trending faults/fractures was removed from the analysis. Another probabilistic map was created using only the binary predictor patterns with optimal positive spatial association with the gold-copper deposits. This probabilistic map is shown in Figure 6.16b. The number of predicted gold-copper deposits based on the probabilistic map in Figure 6.16b is larger by 25.3% than the number of known gold-copper deposits. The probabilistic map is thus not valid statistically. The number of predicted gold-copper deposits is overestimated probably because the positive weights of the binary predictor patterns of Batalay Intrusive contacts and the north-trending faults/fractures are

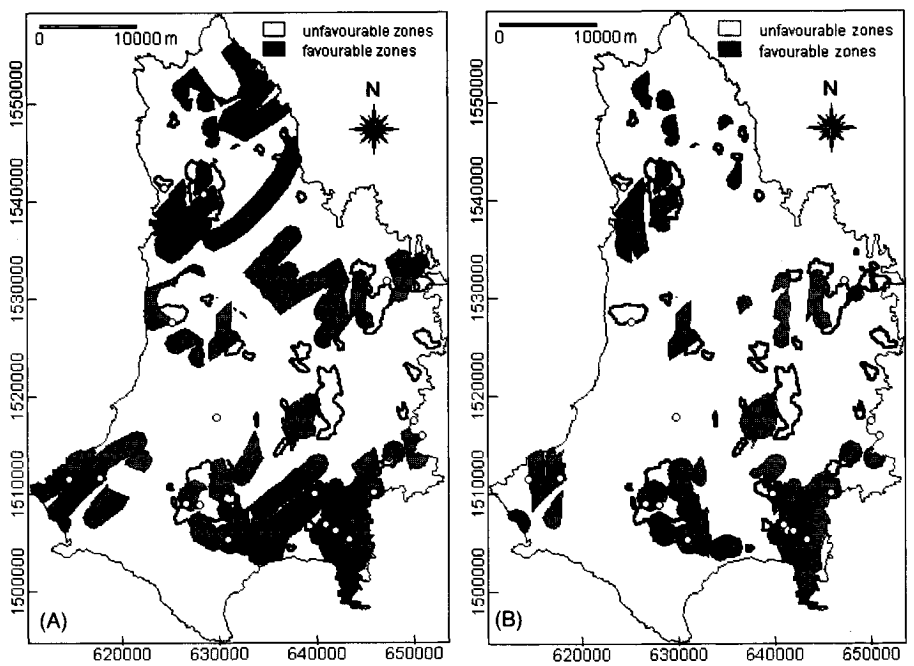

Figure 6.16. Probabilistic maps of gold-copper potential of Catanduanes Island, based on (a) all conditionally independent binary predictor patterns with most positive/negative Studentised C and (b) binary predictor patterns with highest positive Studentised C. Unfilled circles = gold-copper deposits; polygons in solid lines = geochemically-anomalous catchment basins.

significantly different from zero but the negative weights are not significantly different from zero.

A search was made for binary predictor patterns of the Batalay Intrusive contacts and the north-trending faults/fractures, in which (a) the positive and negative weights are both significantly different from zero, (b) the contrasts are statistically significant and (c) the predictive strengths are high. These criteria are met by a binary pattern of the Batalay Intrusive contacts buffered at 3000 m (see Table 4.36) and by a binary pattern of the north-trending faults/fractures buffered at 1000 m (see Table 4.38). These binary predictor patterns are shown in Figure 6.17. The results of the tests of conditional independence of the binary predictor patterns shown in Figure 6.17 and the binary pattern of the northeast-trending faults faults/fractures shown in Figure 6.15 are given in Table 6.18. The three binary predictor patterns are conditionally independent.

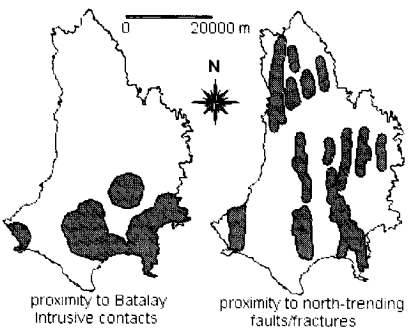

Figure 6.17. Binary predictor patterns of Batalay Intrusive contacts buffered at 3000 m (left) and north-trending faults/fractures buffered at 1000 m (right) indicating their presence (grey areas) with respect to gold-copper deposits, Catanduanes Island.

Table 6.18. Calculated χ^2 values* for testing conditional independence between all pairs of binary predictor patterns with statistically significant weights and high predictive strengths, Catanduanes Island.

	NE-trending faults/fractures (1000 m)	N-trending faults/fractures (1000 m)
Batalay intrusive contacts (3000 m)	**0.48**	**0.05**
NE-trending faults/fractures (1000 m)		**3.09**

*With 1 degree of freedom and confidence level of 95%, critical χ^2 value is 3.84 (Davis, 1973). Values in bold indicate pairs that show conditional independence at the 95% confidence level.

The binary predictor patterns shown in Figure 6.17 and the binary pattern of the northeast-trending faults/fractures shown in Figure 6.15 were combined to create another probabilistic map. This probabilistic map is shown in Figure 6.18. The number of predicted gold-copper deposits based on the probabilistic map is larger by 14.7% than the number of known gold-copper deposits. This means that the assumption of conditional independence between the input binary predictor patterns is not seriously violated. The probabilistic map is valid statistically. It indicates that 22% of the island has potential for gold-copper deposits. It predicts correctly about 60% of the known gold-copper deposits. The

predicted favourable zones coincide spatially with 42% of the geochemically-anomalous areas. The probabilistic map of gold-copper potential shown in Figure 6.18 can be used to guide further exploration work in the island.

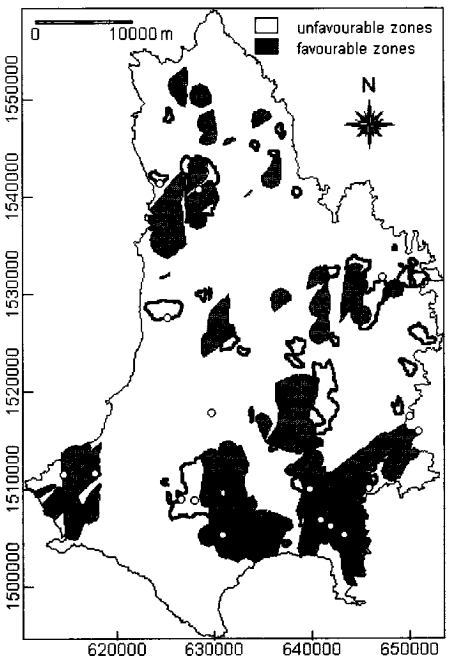

Figure 6.18. Probabilistic map of gold-copper potential based on binary predictor patterns with statistically significant weights, contrasts and high predictive strengths with respect to the gold-copper deposits, Catanduanes Island. Unfilled circles = known gold-copper deposits; polygons in solid lines = geochemically-anomalous catchment basins.

6.8 DISCUSSION

The approach of mineral potential mapping presented here using weights of evidence modeling involves the thresholding of multiclass maps of geological features (e.g., maps of distances to geological features) into binary maps that can be used as predictors of mineral potential. However, it is pointed out that weights of evidence modeling is not limited to using binary predictor patterns. An extension of the weights of evidence method to 'grey-scale' multi-class predictor patterns is discussed by Agterberg and Bonham-Carter (1990), who showed how individual weights (W+) can be derived based on cumulative distances, and by Bonham-Carter and Agterberg (1999), who explained how multi-class evidential themes can be created based on interpolation of point values. The 'grey-scale' approach was used by Goodacre et al. (1993) to spatially analyse

and spatially predict seismic epicentres in relation to drainage patterns and geophysical data. The results of the study of Goodacre et al. (1993) showed that the 'grey-scale' predictive model is very similar to the binary predictive model.

For the binary approach of weights of evidence modeling, Bonham-Carter et al. (1988, 1989), Agterberg et al. (1990) and Bonham-Carter (1991) have shown that the maximum value of the contrast, C, is helpful in deciding the suitable cutoff distance for thresholding multiclass maps into binary maps. However, as demonstrated by Bonham-Carter (1994) and by the examples shown here and in Chapter 4, the Studentised C is useful in determining the cutoff distance, within which the spatial associations between binary patterns of geological features and a binary pattern of mineral deposit points are optimal. The probable reason for the usefulness of the Studentised C over the maximum value of C in determining the cutoff distance is that the numbers of mineral deposits in the study areas are relatively small as compared to the numbers of mineral deposits in the study areas of Bonham-Carter et al. (1988, 1989), Agterberg et al. (1990) and Bonham-Carter (1991). The relatively small numbers of mineral deposits in the study areas results in large uncertainties in the weights so that the maximum values of C are usually statistically non-significant.

The highest Studentised C was more effective in Benguet province and in Baguio district than in Abra area and in Catanduanes Island in determining cutoff distance to convert the multiclass distance maps of geological features into binary predictor patterns. A probable reason for this finding is the differences in the number of mineral deposits in the four study areas. The number of mineral deposit points used was 23 in Benguet province, 19 and 63 in Baguio district, 12 in Abra area and 17 in Catanduanes Island. The results of the weights of evidence modeling show that most of the binary predictor patterns in Benguet province and in Baguio district have statistically significant spatial associations with the binary patterns of mineral deposit points. In contrast, the binary predictor patterns particularly in Abra area are mostly statistically non-significant. In addition, the binary predictor patterns in Benguet province and in Baguio district have high predictive strengths whilst the binary predictor patterns in Abra area and Catanduanes Island have mainly low predictive strengths. These imply that the Studentised C is useful where the number of deposits is greater than 18. The results of the study further imply that, where the number of deposit is less than 18, the statistical significance of the weights and the proportion of mineral deposits (i.e., predictive strength) must be considered in determining the optimum binary predictor pattern.

A probable reason why the Studentised C was more useful in Baguio (19 deposits) than in Abra area (17 deposits) is that weights of evidence modeling is sensitive to the area/size of the study region/district (Bonham-Carter, 1994). Note that the difference in the number of deposits in Baguio and Abra is small but the difference in their area is large (see Figure 2.4); Baguio is smaller than Abra. This implies that the choice of the area or size of the study region/district

can drastically influence weights of evidence modeling and must be considered in the interpretation, particularly in determining the optimum cutoff distance.

Pairwise testing of conditional independence between binary predictor patterns with respect to a binary pattern of mineral deposits invariably shows that not all binary predictor patterns can necessarily be combined to map mineral potential as in the simple 'map addition' method demonstrated in Chapter 4. In simple terms, the pairwise test for conditional independence means that redundant binary predictor patterns, i.e., those that predict the same sub-areas of mineral potential, must not be combined – a few 'prima facie' evidences is all that is necessary. A problem of the pairwise test of conditional independence is that it may reveal the statistical incorrectness of combining binary predictor patterns of distinct geological features that are known to be spatially and genetically associated with the mineral deposits. This problem of conditional independence can be avoided by combining spatial features, for example, univariate geochemical anomalies may be combined into a multivariate geochemical anomaly, prior to weights of evidence analysis (Bonham-Carter et al., 1988; Agterberg, 1992b). However, to circumvent the problem of conditional independence by combining two distinct geological features may be statistically correct, but it may also be geologically inappropriate. Sound geological judgment is thus needed to decide whether or not to combine conditionally dependent geological features. An alternative way to get around the problem of conditional independence in weights of evidence modeling is to perform logistic regression analysis (see Chapter 9; Agterberg, 1992a, 1992b; Agterberg et al., 1993) to determine statistically significant independent variables.

Whilst a pairwise test of conditional independence is important in determining which binary predictor patterns to combine to map mineral potential, an overall test of conditional independence is important in determining the statistical validity of the resulting posterior probability map. The results show that although the pairwise tests may show that the input binary predictor patterns are conditionally independent, the overall tests invariably show that there is serious violation of the assumption of conditional independence. The overall tests thus show that (a) binary patterns whose spatial associations with the known mineral deposits are not statistically significant must not be used in the analysis and (2) selection of cutoff distance to create binary predictor patterns must not be based solely on the most statistically significant contrast.

6.9 CONCLUSIONS

Weights of evidence modeling is useful for geologically-constrained probabilistic mapping of mineral potential for areas where a number of mineral deposits are known. The method, however, is sensitive to the number of deposits and the size of the study area. These two factors influence the statistical significance of the weights and the contrasts. The selection of cutoff distance to create the

binary predictors is critical to the statistical validity of the resulting mineral potential map and must be based not only on the Studentised C but also on the statistical significance of the weights and the predictive strength of the binary predictor pattern. Pairwise tests of conditional independence should serve only as a guide but not as a strict rule to dictate which binary predictor patterns must be combined. The statistical validity of the resulting probabilistic map is best indicated by an overall test of conditional independence.

The statistically valid probabilistic maps in the four study areas are reliable based on comparisons with the 'model deposits' and the 'validation deposits' and with the geochemically-anomalous areas. For Benguet province, the statistically valid probabilistic map has a prediction rate of at least 62% and indicates that about 24% of the province has potential for porphyry copper deposits. For Baguio district, the probabilistic maps, based on either the large-scale gold deposits or the small-scale deposits, have prediction rates of at least 72% and indicate that at least 24% of the district has potential for epithermal gold deposits. For Abra area, the most statistically valid probabilistic map has a prediction rate of at least 67% and indicates that about 37% of the area has potential for porphyry copper deposits. For Catanduanes Island, the statistically valid probabilistic map has a prediction rate of about 60% and indicates that about 22% of the island has potential for gold-copper deposits. The respective statistically valid probabilistic maps can be used to guide further exploration work in the study areas.

The weights of evidence modeling is a statistically rigorous method for combining binary representations of geological evidences to map mineral potential. An alternative method for combining geological evidences involves the application of the Dempster-Shafer theory (e.g., Moon, 1989), in which multiclass evidences are used without an assumption of conditional independence among the evidential maps. The application of the Dempster-Shafer theory to geologically-constrained mineral potential mapping is demonstrated in the next chapter.

Chapter 7

Evidential Belief for Mapping Mineral Potential

"A habit of basing convictions upon evidence,
and of giving to them only that degree of certainty
which the evidence warrants, would, if it became general,
cure most of the ills from which the world suffers."

Russell, Bertrand (1872-1970)
In G. Simmons, Calculus Gems:
Brief Lives and Memorable Mathematics
New York: McGraw Hill Inc., 1992.

This Chapter demonstrates the application of the theory of evidential belief to data-driven geologically-constrained mineral potential mapping. Portions of this Chapter have been submitted for publication as Geologically-Constrained Mapping of Gold Mineralization Potential Using Evidential Belief Functions, Baguio District, Philippines (Carranza and Hale, 2001a).

7.1 INTRODUCTION

The use of binary representation of geological evidences for mapping mineral potential as demonstrated in Chapters 5 and 6 is appealing due to its simplicity. The main weakness of the binary approach, however, is that the evidences of geological features represented in a given map layer are not truly binary; rather they have spatially varying degrees of certainty or are non-existent. Classifying mineral potential thus is likely to benefit from an approach capable of assigning varying degrees of certainty or belief to each piece of evidence in each set of bodies of evidence pertinent to the proposition that a mineral deposit exists.

The Dempster-Shafer theory of evidence provides a concept for assigning probabilities or degrees of belief to all subsets of bodies of evidence for a particular proposition (Shafer, 1976; Cohen, 1985). In the last three decades, the Dempster-Shafer theory of evidence has attracted considerable attention as a promising method of dealing with some of the basic problems arising in combination of evidence and data fusion. Zadeh (1986) provides a simplification of the Dempster-Shafer theory of evidence and demonstrates the capability of its rule of combination to integrate distinct probability distributions. Walley (1987) on the other hand, suggests that Dempster's rule of combination is not generally suitable for combining evidence from independent observations nor for combining prior beliefs with observational evidence. More recent applications of the Dempster-Shafer theory of evidence, however, prove its usefulness in

combining evidences from disparate sources (e.g., Lee et al., 1987; Kim and Swain, 1989). Chung and Fabbri (1993) describe the representation of geoscience information for data integration based on the belief function interpretation of the Dempster-Shafer theory of evidence. The management of uncertainty in integration of exploration data using the belief function is demonstrated by An et al., (1994b). The applicability of the evidential belief function and Dempster's rule of combination to knowledge-driven integration of multisource exploration data for mineral potential mapping is demonstrated by Moon (1989, 1990, Moon et al. (1991), An et al. (1992; 1994a) and Wright and Bonham-Carter (1996).

8.2 DEMPSTER-SHAFER EVIDENTIAL BELIEF FUNCTION

Dempster's work on the generalisation of Bayesian lower and upper probabilities provided the basis for the evidential belief function theory (Dempster, 1967, 1968). Shafer (1976) defined two functions, belief and plausibility, to represent the lower and upper probabilities, respectively, that a given body of evidence supports a particular proposition. The belief and plausibility functions can be interpreted as probabilities in the traditional probabilistic framework (Chung and Fabbri, 1993; An et al., 1994b). This interpretation is adopted here.

Suppose that a set of all geological possibilities, or a frame of discernment Θ (Shafer, 1976), for the mineral target propositions exists such that $\Theta = \{A_1, A_2, \ldots, A_n\}$. Then each proposition is defined completely by a subset of Θ that contains exactly those geological possibilities where the proposition is true. A function m: $2^{\Theta} \rightarrow [0,1]$ is called a basic probability assignment when

$$m(\phi) = 0 \tag{7-1}$$

and

$$\sum_{A \subset \Theta} m(A) = 1 , \tag{7-2}$$

where A is a subset of Θ. The function m is a measure of belief committed to each possibility (Walley, 1987). Equations 7-1 and 7-2 mean that no belief ought to be committed to an empty set $\varnothing$ and that total belief has a measure of one. The total belief committed to a proposition H is given by

$$Bel(H) = \sum_{A \subset H} m(A) . \tag{7-3}$$

The function Bel: $2^{\Theta} \rightarrow [0,1]$ is called the belief function over the frame of discernment Θ, if and only if it satisfies the following conditions:

$$Bel(\phi) = 0 , \tag{7-4}$$

$$Bel(\Theta) = 1 , \tag{7-5}$$

and for every positive integer n and every collection of possibilities $A_1, A_2, \ldots, A_n$ of a subset of Θ

$$Bel(A_1 \cup \ldots \cup A_n) \geq \sum_{I \subset \{1,\ldots,n\} \atop I \neq \phi} (-1)^{|I|+1} Bel(\cap_{i \in I} A_i) . \tag{7-6}$$

The plausibility function Pl: $2^{\Theta} \rightarrow [0,1]$ is defined using the belief function Bel as

$$Pl(H) = 1 - Bel(\overline{H}) = \sum_{A \subset \Theta} m(A) - \sum_{A \subset \overline{H}} m(A) = \sum_{A \cap H \neq \phi} m(A) \tag{7-7}$$

for every $H \subset \Theta$, where $\overline{H}$ is the negation of H. The belief and plausibility functions are in fact the lower and upper envelopes of a class of probability measures about H so that Bel (H) ≤ Pl (H), which can be viewed when comparing Equations 7-3 and 7-7. The degree of uncertainty about H is thus represented by the difference Pl (H) – Bel (H). When the degree of uncertainty equals zero, $Bel(H) + Bel(\overline{H}) = 1$, which is a Bayesian probability (An et al., 1994b).

Dempster's rule of combination is a generalised scheme of Bayesian inference to aggregate evidence provided by disparate sources. Now suppose that m_1 and m_2 are the basic probability assignments based on entirely distinct bodies of evidence D_1 and D_2. The belief functions Bel_1 and Bel_2 for the basic probability assignments m_1 and m_2, can be combined to generate a new belief function. For all $A_1, A_2, \ldots, A_n \in 2^{\Theta}$, Dempster's rule produces a new probability assignment defined by $m(\phi) = 0$ and

$$m(H) = (1 - k)^{-1} \sum_{\substack{i,j \\ A_i \cap B_j = H}} m_1(A_i)\, m_2(B_j) \tag{7-8}$$

$$\text{where, } k = \sum_{\substack{i,j \\ A_i \cap B_j = H}} m_1(A_i)\, m_2(B_j) < 1 \tag{7-9}$$

for all non-empty $H \subset \Theta$. Equation 7-9 is called the orthogonal sum of m_1 and m_2. The denominator (1-k) is a normalising factor to compensate for the measure of belief not committed to the empty set.

There are several points of interest regarding Dempster's rule (Kim and Swain, 1989). Firstly, it requires that the basic probability assignments to be combined be based on entirely distinct bodies of evidence. Combining entirely distinct bodies of evidence may be considered as a fusion of individual observations made by independent observers on the same experiment. The meaning of independence here is that one observation does not have an effect on any of the other observations, which is quite different from the conventional independence definitions in probability theory. Secondly, it is both commutative and associative. Therefore, different groupings or orderings of evidence combination do not affect the result. Finally, there is an additional piece of information provided by this rule. The constant k in Equation 7-9 is the amount of the total probability that is committed to disjoint (or contradictory) subsets of Θ. It represents a measure of conflict between two bodies of evidence. When k equals one, it means the two bodies of evidence are contradictory completely, and the orthogonal sum of their basic probability assignments does not exist.

7.3 APPLICATION OF EVIDENTIAL BELIEF FUNCTIONS USING GIS

The Dempster-Shafer evidential belief functions were applied by way of a data-driven approach to map mineral potential in Benguet province, Baguio district, Abra area and Catanduanes Island where mineral deposits are known. A knowledge-driven application of the Dempster-Shafer evidential belief functions was undertaken to map nickeliferous-laterite potential in Isabela area.

7.3.1 Data inputs

The appropriate geoexploration-datasets (i.e., lithologic units, hydrothermal alteration units, faults/fractures, porphyry pluton contacts/centroids, batholithic pluton margins, locations of mineral deposits, topographic geoinformation) were used in mapping mineral potential through the application of evidential belief functions. A pixel size of 100x100 m was used in the GIS-based raster analyses.

7.3.2 Belief function representation of geological map data

Suppose an area ψ with known mineral deposits and a set of geological features portrayed in a map

$X = \{D_1, D_2, \ldots, D_n\}$,

where D_i ($i = 1, 2, \ldots, n$) is a set of thematic evidence map data in ψ. Suppose also that all data sets are independent evidentially of each other. Given two

possibilities of a mineral deposit, T_i and $\bar{T}_i$, a complete set $2^{\Theta i}$, which corresponds to the propositions related to the mineral deposit based on D_i, may be defined as

$$2^{\Theta_i} = \{\phi, T_i, \bar{T}_i, \Theta_i\}$$

where

ϕ: an empty set,
T_i: belief that a mineral deposit exists based on D_i,
$\bar{T}_i$: disbelief that a mineral deposit exists based on D_i, and
Θ_i: { T_i, $\bar{T}_i$ } or the uncertainty that a mineral deposit exists based on D_i.

Probabilities may then be estimated to map a data set D_i from a data space into a probability space. The area can be divided into N_T pixels or square unit cells. Let N_D and $N_{\bar{D}}$ represent the number of pixels with and without a target mineral deposit, respectively. Let N_{Sij} represent the number of pixels with an attribute S_{ij} (j = 1,2,...,m lithologic or hydrothermal alteration units or proximity classes to curvi-linear geological features). Let N_{SijD} represent the number of pixels with the same attribute S_{ij} and a target mineral deposit. The basic probability assignment of T_i, or the degree of belief (or lower probability) that a mineral deposit exists, as defined by An et al. (1992), is

$$m_i(T_i) = \frac{N_{SijD}}{N_{Sij}}. \tag{7-10}$$

Let $N_{Sij\bar{D}}$ represent the number of pixels with the same attribute S_{ij}, in which no target mineral deposit exists. The basic probability assignment of $\bar{T}_i$, or the degree of disbelief that a mineral deposit exists, as defined by An et al. (1992) is

$$m_i(\bar{T}_i) = \frac{N_{Sij\bar{D}}}{N_{Sij}}. \tag{7-11}$$

The degree of uncertainty for the proposition and its negation is given by

$$m_i(\Theta_i) = 1 - \frac{N_{SijD}}{N_{Sij}} - \frac{N_{Sij\bar{D}}}{N_{Sij}}. \tag{7-12}$$

The plausibility (or higher probability) of the proposition is given by

$$Pl(T_i) = m_i(T_i) + m_i(\Theta_i) \text{ or } Pl(T_i) = 1 - m_i(\overline{T}_i). \quad (7\text{-}13)$$

For a data-driven approach, the direct application of Equations 7-10, 7-11 and 7-12 to the estimation of basic probability assignments of the different propositions encounters two problems. Firstly, because $N_{S_{ij}} = N_{S_{ij}D} + N_{S_{ij}\overline{D}}$, it means that $m_i(\Theta_i)$ in Equation 7-12 is equal to zero and uncertainty is not modeled. Secondly, Equations 7-10 and 7-11 represent the conditional probability that a target mineral deposit exists and does not exist, respectively, given the presence of attribute S_{ij}. The probability assignments according to Equations 7-10 and 7-11 thus represent the relationship of attribute S_{ij} with the target mineral deposit alone but do not represent the relationship of attribute S_{ij} with the other attributes in data set D_i. Chung and Fabbri (1993) aver that the relationships among the subsets of evidences within a set of evidence, aside from their spatial relationships to the prediction target, must be considered and represented in a favourability function (e.g., a belief function). The following modified equations were therefore developed for a data-driven approach to represent estimating basic probability assignments of the different propositions.

A weight $W_{S_{ij}D}$ for evidence or attribute S_{ij} for the proposition T_i was defined as

$$W_{S_{ij}D} = \frac{\dfrac{N_{S_{ij}D}}{N_{S_{ij}}}}{\dfrac{N_D - N_{S_{ij}D}}{N_T - N_{S_{ij}}}}. \quad (7\text{-}14)$$

The numerator represents the conditional probability that a target mineral deposit exists given the presence of attribute S_{ij}; it means simply that a target mineral deposit occurs in S_{ij}. The denominator represents the conditional probability that a target mineral deposit exists given the absence of attribute S_{ij}; it means simply that a target mineral deposit occurs outside S_{ij}. Thus, $W_{S_{ij}D}$ represents the weight or strength of attribute or evidence S_{ij} for the proposition T_i in relation to the target mineral deposit and in relation to the weight of the other subsets of evidences in data layer D_i.

A weight $W_{S_{ij}\overline{D}}$ for evidence or attribute S_{ij} for the proposition $\overline{T}_i$ was defined as

$$W_{S_{ij}\overline{D}} = \frac{\dfrac{N_{S_{ij}\overline{D}}}{N_{S_{ij}}}}{\dfrac{N_D - N_{S_{ij}\overline{D}}}{N_T - N_{S_{ij}}}} \quad (7\text{-}15)$$

The numerator represents the conditional probability that a target mineral deposit does not exist given the presence attribute S_{ij}; it means simply that a target mineral deposit does not occur in S_{ij}. The denominator represents the conditional probability that a target mineral deposit does not exist given the absence of attribute S_{ij}; it means simply that a target mineral deposit does not occur outside attribute S_{ij}. Thus, $W_{S_{ij}\bar{D}}$ represents the weight or strength of attribute or evidence S_{ij} for the proposition $\bar{T}_i$ in relation to the target mineral deposit and in relation to the weight of the other subsets of evidences in data layer D_i.

The following equations were then used, respectively, to represent estimates of probability assignments for T_i and $\bar{T}_i$

$$m_i(T_i) = \frac{W_{S_{ij}D}}{\sum_{j=1}^{m} W_{S_{ij}D}} \text{ and} \tag{7-16}$$

$$m_i(\bar{T}_i) = \frac{W_{S_{ij}\bar{D}}}{\sum_{j=1}^{m} W_{S_{ij}\bar{D}}}, \tag{7-17}$$

and the uncertainty was defined as

$$m_i(\Theta_i) = 1 - \frac{W_{S_{ij}D}}{\sum_{j=1}^{m} W_{S_{ij}D}} - \frac{W_{S_{ij}\bar{D}}}{\sum_{j=1}^{m} W_{S_{ij}\bar{D}}}. \tag{7-18}$$

If $N_{S_{ij}D} = 0$, it follows that $m_i(T_i) = 0$, then $m_i(\bar{T}_i)$ must be forced to zero (i.e., $N_{S_{ij}\bar{D}} = N_{S_{ij}}$) and the belief function is simply committed to $m_i(\Theta_i)$. The logical reason for this is that, if there is no belief that a mineral deposit exists, then there is also no disbelief for the proposition; there can only be uncertainty. If $N_{S_{ij}\bar{D}} = 0$ (i.e., $N_{S_{ij}D} = N_{S_{ij}}$), then the belief function Bel_i is defined by the following probability assignments:

$$m_i(T_i) = \frac{W_{S_{ij}D}}{\sum_{j=1}^{m} W_{S_{ij}D}};\ m_i(\bar{T}_i) = 0;\ m_i(\Theta_i) = 1 - \frac{W_{S_{ij}D}}{\sum_{j=1}^{m} W_{S_{ij}D}};\ \text{and}\ m_i(\phi) = 0.$$

7.3.3 Generation of belief functions

To generate belief functions for the propositions related to mineral deposits in any area, the lithologic map, the remotely-detected hydrothermal alteration map, and maps of proximity classes to curvi-linear geological features were 'crossed' (or overlain) with the map of mineral deposits. The 'crossing' operation yields $N_{S_{ij}D}$ and $N_{S_{ij}\bar{D}}$, which were used to estimate the basic probability assignments. As mineral deposits are invariably represented as individual points (i.e., N_D equals the number of known mineral deposits), $N_{S_{ij}D}$ could be very small compared to $N_{S_{ij}}$. Consequently, the probability assignment estimated by Equation 7-15 could be very small, or equal to zero. In reality, the mineral deposits have areal dimensions but these data are not available. The problem was resolved by buffering the mineral deposits to represent them as 'mineralised zones'. The optimum distance buffer that was used is derived from a point pattern analysis of the mineral deposit points and results in 'mineralised zone(s)' representing less than 1% of the study area and with zero probability for containing another mineral deposit. The optimum distance buffer is important so that (1) $N_{S_{ij}D}$ is not overestimated, (2) the probability assignments are not overestimated, and, more importantly, (3) the spatial associations between the spatial evidences and the mineral deposits are reflected by the probability assignments.

The belief functions for the lithologic and hydrothermal alteration evidences were generated with the application of Equations 7-16, 7-17 and 7-18. For the distance to curvi-linear geological features, optimum proximity classes had to be determined to generate belief functions that represent (1) the spatial association between the mineral deposits and the geological features and (2) the relative importance of the proximity classes. The quantified spatial associations in Chapters 4 and 6 serve as guides to determining the optimum proximity classes; however, the overall process was undertaken by trial-and-error. To determine the optimum proximity classes, a useful rule-of-thumb was developed: the values of $N_{S_{ij}}$ of the proximity classes need to increase progressively, though not necessarily monotonically, with increasing distance from a geological feature. The belief functions thus generated invariably portray the inverse relationship between the belief and disbelief propositions.

7.3.4 Integration of belief function maps

The probability assignments that define a belief function Bel_i can be combined with other belief functions. Consider two belief functions Bel_1 representing D_1 and Bel_2 representing D_2. The propositions for Bel_1 are A_1, A_2 and A_3, where A_1 is "the belief that a mineral deposit occurs based on D_1", $A_2 = \bar{A}_1$, and $A_3 = \{A1, A_2\}$. The corresponding probability assignments are $m_1(A_1)$, $m_1(A_2)$ and $m_1(A_3)$. Similarly,

Table 7.1. Possible combinations of two sets of propositions, A_1, A_2 and A_3 (for belief function Bel_1) and B_1, B_2 and B_3 (for belief function Bel_2), and the basic probability assignments of these combinations. (Adapted from An et al., 1992).

	A_1	A_2	A_3
B_1	$A_1 \cap B_1$ $m_1(A_1)m_2(B_1)$	$A_2 \cap B_1$ $m_1(A_2)m_2(B_1)$	$A_3 \cap B_1$ $m_1(A_3)m_2(B_1)$
B_2	$A_1 \cap B_2$ $m_1(A_1)m_2(B_2)$	$A_2 \cap B_2$ $m_1(A_2)m_2(B_2)$	$A_3 \cap B_2$ $m_1(A_3)m_2(B_2)$
B_3	$A_1 \cap B_3$ $m_1(A_1)m_2(B_3)$	$A_3 \cap B_3$ $m_1(A_2)m_2(B_3)$	$A_3 \cap B_3$ $m_1(A_3)m_2(B_3)$

the propositions for Bel_2 are B_1, B_2 and B_3, where B_1 is "the belief that a mineral deposit occurs based on D_2", $B_2 = \bar{B}_1$, and $B_3 = \{B_1, B_2\}$. The corresponding probability assignments are $m_2(B_1)$, $m_2(B_2)$ and $m_2(B_3)$. The possible combinations of propositions and their probability assignments are listed in Table 7.1.

The propositions of Bel that are being established by combining D_1 and D_2 are defined as $\{T, \bar{T}, \Theta\}$, where

T = degree of belief that a mineral deposit exists based on the data sets,
$\bar{T}$ = degree of disbelief that a mineral deposit exists based on the data sets, and
$\Theta = \{T_B, \bar{T}\}$, uncertainty of the proposition that a mineral deposit exists.

Based on Table 7.1 and using Dempster's rule of combination as depicted in Equation 7-8, the probability assignments of Bel are given by

$$m_i(T) = \frac{m_1(A_1)m_2(B_1) + m_2(B_1)m_1(A_3) + m_1(A_1)m_2(B_3)}{1 - m_1(A_1)m_2(B_2) - m_1(A_2)m_2(B_1)}, \tag{7-19}$$

$$m_i(\bar{T}) = \frac{m_1(A_2)m_2(B_2) + m_2(B_2)m_2(A_3) + m_2(A_2)m_2(B_3)}{1 - m_1(A_1)m_2(B_2) - m_1(A_2)m_2(B_1)}, \tag{7-20}$$

$$m_i(\Theta) = \frac{m_1(A_3)m_2(B_3)}{1 - m_1(A_1)m_2(B_2) - m_1(A_2)m_2(B_1)}, \text{ and} \tag{7-21}$$

$$Pl(T) = m_i(T) + m_i(\Theta) \text{ or } Pl(T) = 1 - m_i(\bar{T}). \tag{7-22}$$

The probability assignments are attributed to the respective units in a thematic evidence layer to create belief function (belief, disbelief and uncertainty) maps. Only two belief function maps were combined at one time (Dempster, 1967, 1968). The other belief function maps that represent D_3, . . ., D_n were combined one after another by repeated applications of Equations 7-19, 7-20 and 7-21.

The integrated new belief function maps, displayed as grey-scale maps, represent the degrees of belief, disbelief and uncertainty for the proposition for a mineral deposit based on all spatial evidence data sets used. The plausibility map was calculated according to Equation 7-13.

7.3.5 Generation and validation of mineral potential maps

To generate mineral potential maps, the belief maps (i.e., lower probability maps) were converted into binary favourability maps. To convert the belief maps into binary favourability maps of mineral potential, a search was made to find threshold probabilities in the belief maps to distinguish between zones that are geologically favourable and unfavourable for mineral deposits. It was found that the 80^{th} percentile probability was the most appropriate threshold to convert the belief maps into binary favourability maps. The favourability maps were validated against 'validation' mineral deposits and/or mineralised zones, which were not used in the predictive modeling of mineral potential. It is shown later that the threshold probabilities used to create the favourability maps result in prediction of at least 60% for most of the study areas. The geochemical anomalies were also used (a) to validate the predicted geologically-favourable zones in terms of their spatial coincidences (i.e., zones of geological sources of the geochemical anomalies) and (b) to determine superiority/inferiority of geologically-constrained predictive maps to integrated geochemical-geological predictive maps.

7.4 APPLICATION TO BENGUET PROVINCE

The geological features that were used as spatial evidences of porphyry copper potential in the province include lithologic units, hydrothermal alteration units, strike-slip fault discontinuities, porphyry pluton centroids and batholithic pluton margins. The predictive mapping of porphyry copper potential was based on the same subset of 23 'model' porphyry copper deposits used in the weights of evidence modeling (see Section 6.4). The subset of eight 'validation' porphyry copper deposits was used to validate the belief function predictive model(s).

7.4.1 Belief functions of spatial evidences of porphyry copper potential

Geoinformation about the spatial distribution of the known porphyry copper deposits that was used to generate the spatial association model is illustrated in Figure 7.1. There is zero probability of another porphyry copper deposit within about 600 m of a known porphyry copper deposit. The known porphyry copper deposits were buffered at 600 m to represent them as 'mineralised zones'. The porphyry copper 'mineralised zones', which occupy 0.9% of the province, were used to determine the variables needed to estimate the probability assignments for the different subsets of spatial evidences. The probability assignments of the

different subsets of spatial geological evidences of porphyry copper potential are given in Table 7.2.

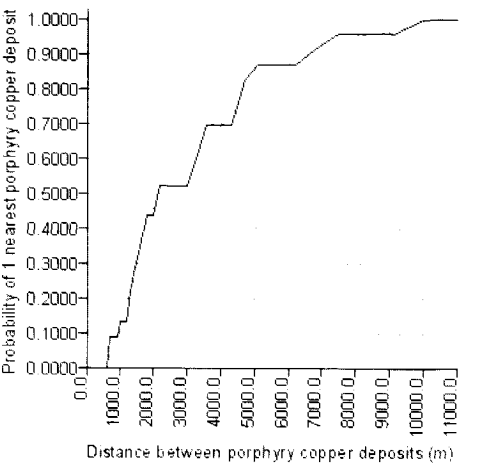

Figure 7.1. Distance and probability of a porphyry copper deposit nearby another porphyry copper deposit, Benguet province.

The probability assignments reflect the importance of the porphyry plutons for porphyry copper potential. The importance of the advanced argillic alteration over the illitic and propylitic alterations is indicated. The importance of the advanced argillic alteration may be a function of geologic map data representation as it is not consistent with conceptual porphyry copper exploration models (see Figure 5.2; Sillitoe and Gape, 1984). In particular, in the Mankayan mineral district (see Figures 3.17 and 3.18) the porphyry copper deposits, whose locations are their subsurface to surface projections, are buried beneath non-mineralised rocks that are hydrothermally altered to advanced argillic mineral assemblages. This implies therefore that alteration mineral assemblages that represent the upper levels of a hydrothermal system, which may not be mineralised, are important guides to locating hydrothermal deposits. The probability assignments of the proximity classes for the curvi-linear or point geological features reflect the quantified spatial association (see also sections 4.3 and 6.4). Proximity classes closer to the geological features generally have higher probability assignments for the proposition that a porphyry copper deposit exists based on a particular geological feature. Proximity classes farther from the geological features generally have higher probability assignments for the proposition that a porphyry copper deposit does not exist based on a particular geological feature.

7.4.2 Evidential belief mapping of porphyry copper potential

The belief function maps of evidences of porphyry copper mineralisation are combined to estimate new belief function maps that represent total belief from integrating all the evidential data layers for the following propositions:

T_C = "a porphyry copper deposit exists based on the data sets",

$\bar{T}_C$ = "a porphyry copper deposit does not exist based on the data sets", and

$\Theta_C = \{T_C, \bar{T}_C\}$, "uncertainty that a porphyry copper deposit exists".

Table 7.2. Basic probability assignments of spatial evidences of porphyry copper potential, Benguet province. (N_T = 259591; N_D = 2312).

	Data layer D_i	$N_{S_{ij}D}$	$N_{S_{ij}\bar{D}}$	$m_i(T_i)$	$m_i(\bar{T}_i)$	$m_i(\Theta_i)$
Lithologic units (Figure 2.5)	L. Miocene - Pleistocene porphyry plutons	298	2493	0.797	0.152	0.051
	L. Miocene - Pliocene clastics/volcanics	370	54578	0.042	0.170	0.788
	Miocene limestones;	4	6875	0.004	0.171	0.825
	Oligocene - M. Miocene batholithic plutons	202	41538	0.029	0.170	0.801
	Eocene - Miocene volcaniclastic rocks	318	31850	0.066	0.169	0.765
	Cretaceous - Paleogene metavolcanics	1120	119914	0.063	0.169	0.768
Hydrothermal alteration units (Figure 3.24)	Advanced argillic	707	34358	0.252	0.085	0.663
	Illitic	703	93060	0.069	0.086	0.845
	Propylitic	756	94321	0.075	0.086	0.839
	Unaltered	42	22850	0.017	0.086	0.897
	Water	1	874	0.011	0.086	0.903
	Clouds	103	5946	0.175	0.085	0.740
	Areas not classified	0	5870	0.000	0.000	1.000
Proximity to strike-slip fault discontinuities (km)	<1.50	801	30247	0.422	0.140	0.438
	1.50-2.25	593	32576	0.225	0.142	0.603
	2.25-2.95	514	34177	0.200	0.142	0.658
	2.95-3.70	193	35882	0.061	0.144	0.795
	3.70-4.60	129	36582	0.039	0.144	0.817
	4.60-5.90	82	37998	0.023	0.144	0.833
	>5.90	0	49817	0.000	0.000	1.000
Proximity to batholithic pluton margins (km)	<0.40	433	33879	0.186	0.142	0.672
	0.40-0.95	324	35252	0.126	0.143	0.731
	0.95-1.80	840	36590	0.416	0.141	0.446
	1.80-3.10	422	36780	0.164	0.142	0.694
	3.10-5.10	293	36522	0.108	0.143	0.749
	5.10-7.90	0	38941	0.000	0.000	1.000
	>7.90	0	39315	0.000	0.000	1.000
Proximity to porphyry pluton centroids (km)	<1.00	581	5895	0.335	0.042	0.623
	1.00-1.50	457	6206	0.239	0.043	0.718
	1.50-1.95	325	6571	0.153	0.044	0.803
	1.95-2.35	130	6922	0.054	0.045	0.901
	2.35-2.75	34	7535	0.013	0.046	0.941
	2.75-3.15	2	7644	0.001	0.046	0.953
	3.15-3.55	32	8446	0.011	0.046	0.943
	3.55-4.00	88	9677	0.026	0.046	0.928
	4.00-4.45	209	10072	0.061	0.045	0.894
	4.45-4.90	211	10688	0.058	0.045	0.897
	4.90-5.40	112	11083	0.029	0.046	0.925
	5.40-5.95	26	11784	0.006	0.046	0.948
	5.95-6.60	0	12500	0.000	0.000	1.000
	6.60-7.30	0	13167	0.000	0.000	1.000
	7.30-8.10	0	13980	0.000	0.000	1.000
	8.10-9.00	0	14615	0.000	0.000	1.000
	9.00-10.00	0	15016	0.000	0.000	1.000
	10.00-11.20	0	15844	0.000	0.000	1.000
	11.20-12.70	0	16349	0.000	0.000	1.000
	12.70-15.00	0	16550	0.000	0.000	1.000
	15.00-17.00	105	16883	0.015	0.046	0.939
	>17.00	0	19852	0.000	0.000	1.000

Belief function maps inclusive of the remotely-detected hydrothermal alteration evidence layer (Figure 7.2) and exclusive of the remotely-detected hydrothermal alteration evidence layer (Figure 7.3) were created to evaluate the importance of this evidence. The probability maps, inclusive and exclusive of the hydrothermal alteration evidence, are similar. Zones of high degrees of belief pertain mainly to areas underlain by and proximal to the porphyry plutons and areas that are proximal to the strike-slip fault discontinuities. Zones of high degrees of belief also pertain to areas about 1-2 km away from the batholithic pluton margins. Zones of low degrees of disbelief pertain to areas underlain by and/or proximal to the porphyry plutons, areas proximal to strike-slip fault discontinuities, and areas about 1-2 km away from the batholithic pluton margins. The zones of high degrees of belief and low degrees of disbelief have low degrees of uncertainty. The zones of very low degrees of disbelief pertain mainly to the western section, which is distal to the porphyry and batholithic plutons. The plausibility maps indicate zones of high degrees of belief and/or high degrees of uncertainty.

The belief maps in Figures 7.2a and 7.3a were classified into binary maps of favourable zones of porphyry copper potential by using threshold probabilities of 0.418 and 0.399 (i.e., 80^{th} percentile probabilities), respectively. The favourability maps are apparently similar (Figure 7.4). They show favourable zones that are circular and lenticular in shape. The 'model' and 'validation' porphyry copper deposits are spatially associated with circular favourable zones, which pertain to areas underlain by and/or proximal to the porphyry plutons and areas proximal to strike-slip fault discontinuities. The 'model' and 'validation' deposits are not preferentially spatially associated with the lenticular favourable zones, which pertain to areas that are 1-2 km away from the batholithic pluton margins. Both favourability maps indicate that portions of the geochemically-anomalous catchment basins are geologically-favourable. Both favourability maps predict the same percentage of favourable zones (Table 7.3). The favourability map inclusive of the hydrothermal alteration evidence predicts a slightly lower percentage of the 'model' deposits but predicts a much higher percentage of the 'validation' deposits. The lower percentage of 'model' deposits predicted by the favourability map in Figure 7.4a probably implies that some of the deposits are not characterised by favourable hydrothermal alteration at the surface. However, the favourability map inclusive of the hydrothermal alteration evidence is considered superior to the favourability map exclusive of this spatial evidence based on its higher prediction rate with respect to the 'validation' deposits.

Table 7.3. Spatial predictive geoinformation characteristics of classified favourability maps of porphyry copper potential, Benguet province, inclusive and exclusive of hydrothermal alteration evidence.

Spatial predictive characteristics	Figure 7.4a	Figure 7.4b
% predicted favourable zones	19.9	19.5
% 'model deposits' predicted correctly	86.9	91.3
% 'validation deposits' predicted correctly	62.5	37.5

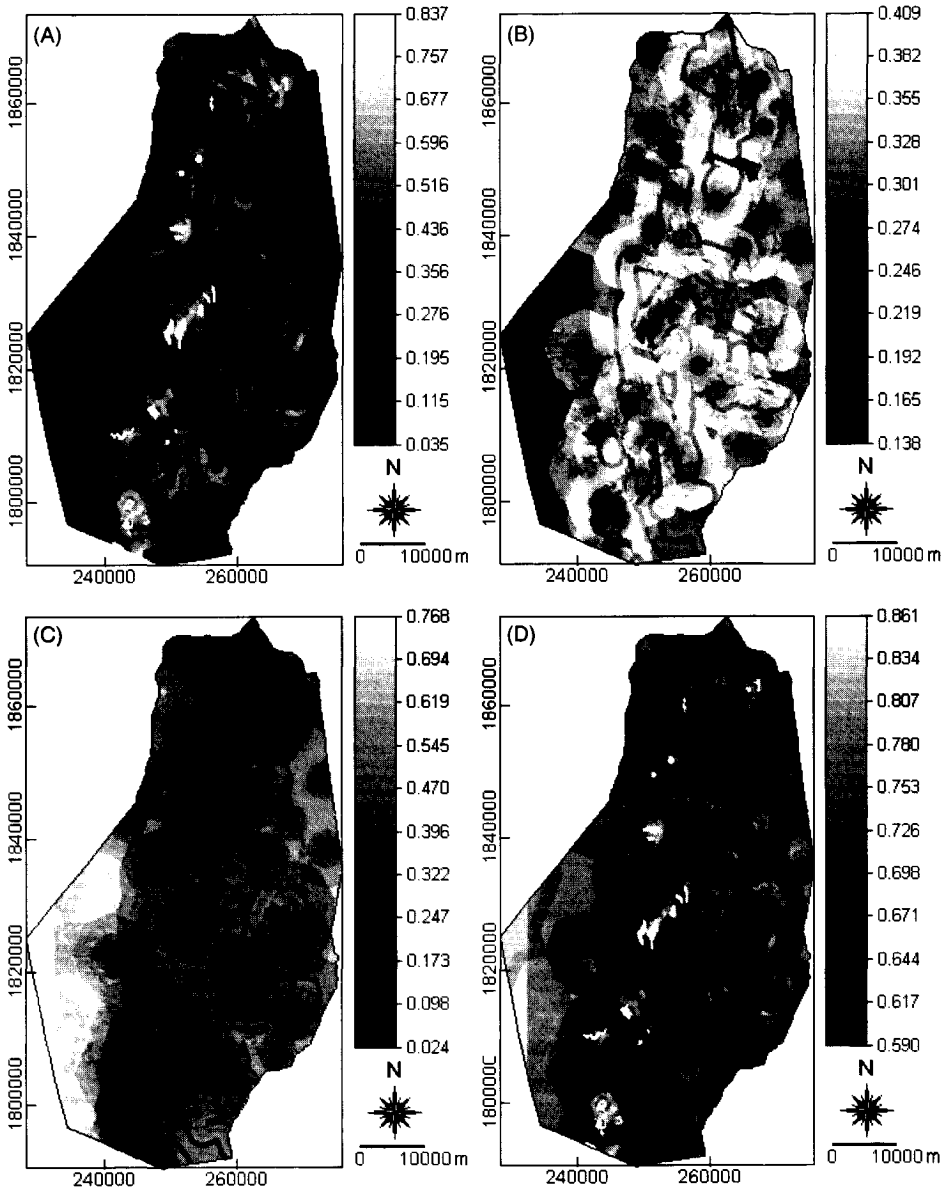

Figure 7.2. Probability maps of porphyry copper potential, Benguet province, inclusive of hydrothermal alteration evidence: (a) belief map; (b) disbelief map; (c) uncertainty map; and (d) plausibility map.

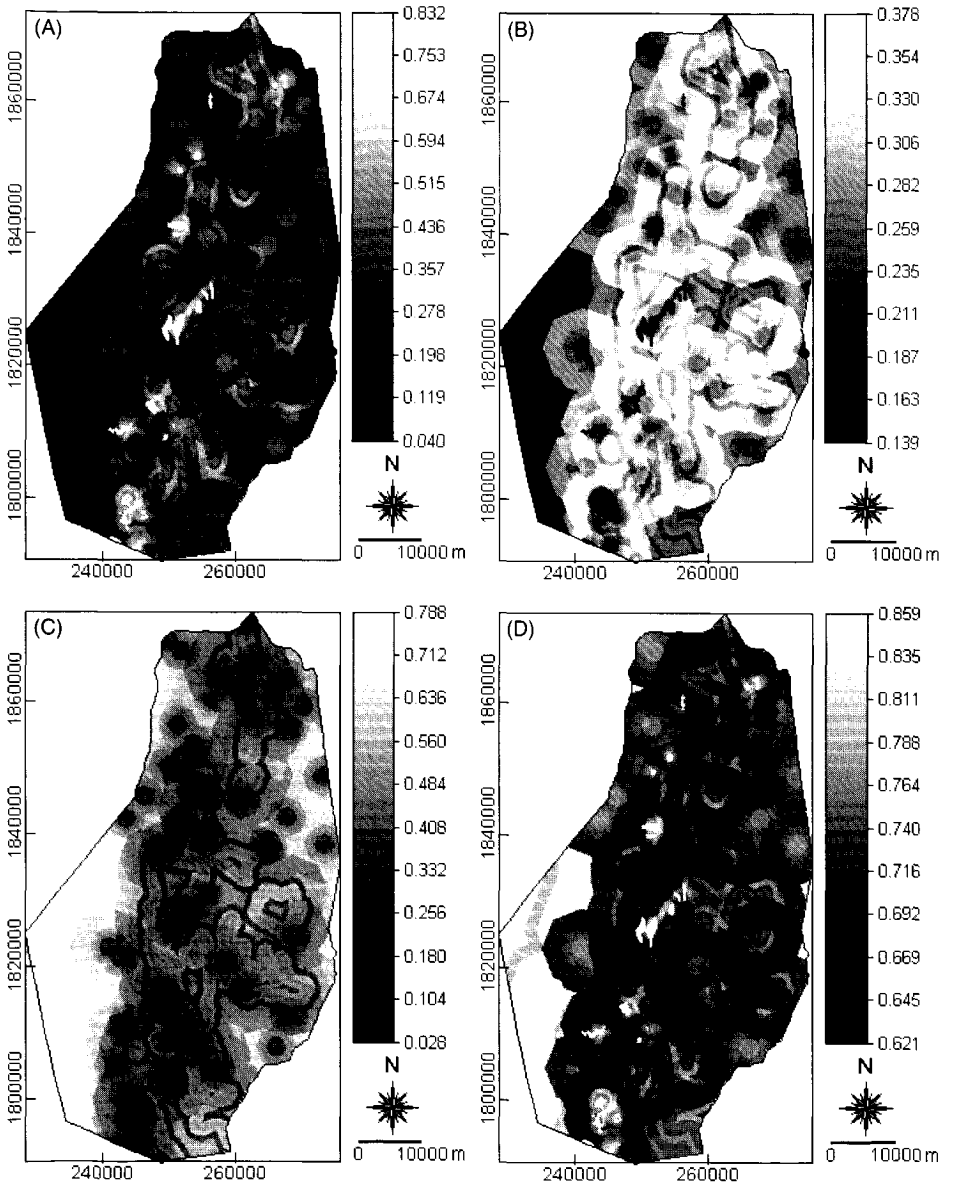

Figure 7.3. Probability maps of porphyry copper potential, Benguet province, exclusive of hydrothermal alteration evidence: (a) belief map; (b) disbelief map; (c) uncertainty map; and (d) plausibility map.

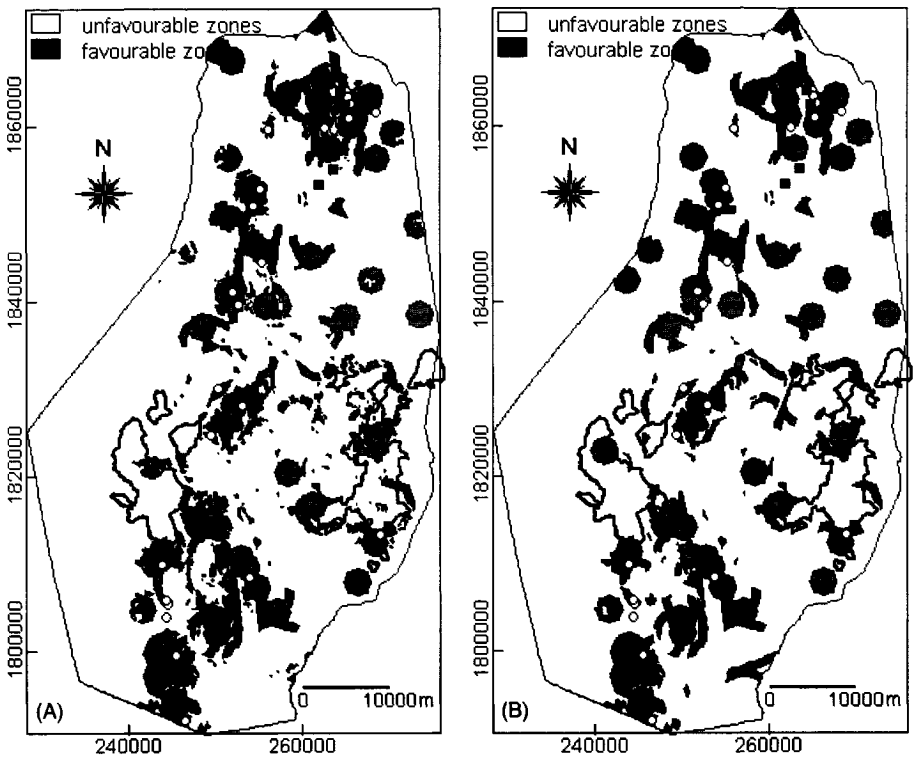

Figure 7.4. Favourability maps of porphyry copper potential, Benguet province: (a) inclusive of hydrothermal alteration evidence; (b) exclusive of hydrothermal alteration evidence. Unfilled circles = 'model' porphyry copper deposits'; filled squares = 'validation' porphyry copper deposits' polygons in solid lines = geochemically-anomalous catchment basins.

7.4.3 Discussion

Along the north-northeast trending belt of favourable zones of porphyry copper potential in the central portions of the province, there are several zones with circular shape where porphyry copper deposits have not been discovered. The favourability maps (i.e., classified belief function maps) clearly indicate that zones with potential for porphyry copper deposits are those that are underlain by or proximal to the porphyry plutons. The uncertainty maps indicate that the number of spatial evidence layers is sufficient to provide support for the proposition that a porphyry copper deposit exists. This implies that the geologically-constrained predictive mapping of porphyry copper potential using the data-driven belief function representation is adequate. The uncertainty maps and the plausibility maps indicate that it is only in the western section of the province where (a) there are insufficient evidential data layers to provide support

for the proposition or (b) the data layers used provide negative evidence for the proposition. Both of the two postulated factors that contribute to high degrees of uncertainty in the western section could be valid; however, the latter is favoured. The western section lies farther away from the imaginary axis of the north-northeast trending belt of favourable zones of porphyry copper potential thus delineated. These observations imply the exploration significance of the predictive belief function maps.

7.5 APPLICATION TO BAGUIO DISTRICT

The geological features that were used as spatial evidences of epithermal gold potential in the district include lithologic units, hydrothermal alteration units, batholithic pluton margins, porphyry pluton contacts, northeast-trending faults/fractures and northwest-trending faults/fractures. The predictive mapping of epithermal gold potential was based on the 19 large-scale gold 'mineralised zones'. The 63 known small-scale gold deposits were used to validate the predictive model(s). The stream sediment geochemical anomalies (UNDP 1987a; see Section 2.3.3) were also used to validate the predictive model(s).

7.5.1 Belief functions of spatial evidences of epithermal gold potential

Geoinformation about the spatial distribution of the large-scale gold deposits in the district is depicted in Figure 7.5. There is zero probability for another large-scale gold deposit within 1 km of any given large-scale gold deposit. However, the optimum distance buffer is 250 m as it results in large-scale gold 'mineralised zones' that occupy 0.95% of the district. The probability assignments, based on the large-scale gold 'mineralised zones', for the different subsets of spatial geological evidences of gold potential in the district are given in Table 7.4.

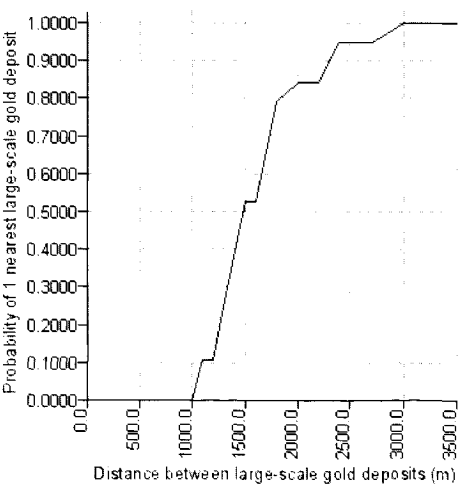

Figure 7.5. Distance and probability of a large-scale gold deposit nearby another large-scale gold deposit, Baguio district.

The probability assignments indicate the importance of the younger porphyry plutons over the older batholithic plutons for predicting epithermal gold potential. Among the hydrothermal alteration assemblages, illitic hydrothermal alteration is the most important geological indicator of epithermal

gold deposits. The unaltered zones are also important for predicting epithermal gold potential; however, this may not be valid because of the poor accuracy of the remotely sensed hydrothermal alteration map (see section 3.3.4). The probability assignments indicate the positive spatial association of the large-scale gold 'mineralised zones' with the northeast-trending faults/fractures, the batholithic pluton margins and the porphyry pluton contacts. The northwest-trending faults/fractures are a negative spatial evidence of epithermal gold potential (i.e., the probability assignments within 1 km are less than the probability assignments beyond 1 km of the northwest-trending faults/fractures).

7.5.2 Evidential belief mapping of epithermal gold potential

The belief functions of evidences of epithermal gold mineralisation are combined to estimate new belief functions that represent total belief from integrating all the evidential data layers for the following propositions:

T_G = "an epithermal gold deposit exists based on the data sets",
$\overline{T}_G$ = "an epithermal gold deposit does not exist based on the data sets", and
$\Theta_G = \{T_G, \overline{T}_G\}$, "there is uncertainty that an epithermal gold deposit exists".

Belief function maps inclusive of the remotely-detected hydrothermal alteration spatial evidence and exclusive of the remotely-detected hydrothermal alteration spatial evidence were generated to evaluate the importance of this spatial evidence. In addition, belief function maps inclusive of the northwest-trending fault/fracture spatial evidence and exclusive of the northwest-trending fault/fracture spatial evidence were generated to evaluate the contribution of negative spatial evidence in mapping mineral potential. The probability map inclusive of all spatial geological evidences is illustrated in Figures 7.6. The probability map exclusive of the northwest-trending fault/fracture spatial evidence is shown in Figure 7.7. The probability map exclusive of the hydrothermal spatial evidence is displayed in Figure 7.8. The probability map exclusive of the northwest-trending fault/fracture and the hydrothermal alteration spatial evidences is exhibited in Figure 7.9.

The different sets of probability maps are similar. The belief and disbelief maps indicate a north-south trending belt of high degrees of belief and low degrees of disbelief in the central section of the district. This belt extends westwards in the central section of the district. Another belt of high degrees of belief and low degrees of disbelief is in the easternmost sections of the district. These belts are sub-parallel in the central sections and converge to the northeast. The uncertainty maps indicate high degrees of uncertainty mainly in the western sections. The plausibility maps are similar to the belief maps except that the former maps also indicate the sections of high degrees of uncertainty.

Table 7.4. Basic probability assignments of spatial evidences of epithermal gold potential, Baguio district (N_T = 42039; N_D = 399).

Data layer D_i		$N_{S_{ij}D}$	$N_{S_{ij}\bar{D}}$	$m_i(T_i)$	$m_i(\bar{T}_i)$	$m_i(\Theta_i)$
Lithologic units (Figure 2.11)	L. Miocene Klondyke Formation	10	8061	0.015	0.169	0.816
	L. Miocene – Pleistocene Intrusives	18	762	0.340	0.165	0.495
	M. Miocene Kennon Formation	0	3297	0.000	0.000	1.000
	L. Oligocene – M. Miocene Agno Batholith	145	10753	0.221	0.166	0.613
	L. Eocene – E. Miocene Zigzag Formation	146	8120	0.320	0.165	0.515
	Cretaceous – Eocene Pugo Formation	80	10232	0.105	0.167	0.728
Hydrothermal alteration units (Figure 3.15b)	Advances argillic	34	7666	0.081	0.167	0.752
	Illitic	213	13900	0.443	0.165	0.392
	Propylitic	102	12852	0.151	0.167	0.682
	Unaltered	50	3289	0.325	0.167	0.510
	Water	0	102	0.000	0.000	1.000
	Area not classified	0	3893	0.000	0.000	1.000
Proximity to NE-trending faults/ fractures (m)	200	141	7679	0.409	0.198	0.393
	200-425	129	7946	0.343	0.198	0.459
	425-750	62	8247	0.128	0.201	0.671
	750-1200	46	8502	0.087	0.201	0.712
	>1200	21	9266	0.033	0.202	0.765
Proximity to NW-trending faults/ fractures (m)	<150	49	5921	0.168	0.200	0.632
	150-375	61	7131	0.174	0.200	0.626
	375-675	67	8343	0.161	0.200	0.639
	675-1075	70	9644	0.141	0.201	0.658
	>1075	152	10601	0.356	0.198	0.446
Proximity to batholithic pluton margins (m)	<400	168	8888	0.491	0.197	0.312
	400-1050	130	9305	0.310	0.199	0.491
	1050-2450	94	9695	0.188	0.200	0.612
	2450-6000	7	10070	0.011	0.202	0.787
	>6000	0	3682	0.000	0.000	1.000
Proximity to porphyry pluton contacts (m)	<700	122	3563	0.396	0.108	0.496
	700-1450	62	3732	0.160	0.110	0.730
	1450-2150	59	4062	0.138	0.111	0.751
	2150-2950	72	4336	0.162	0.110	0.728
	2950-3750	20	4507	0.038	0.112	0.850
	3750-4525	12	4760	0.021	0.112	0.867
	4250-5450	31	5084	0.053	0.112	0.835
	5450-6700	21	5494	0.032	0.112	0.856
	>6700	0	6102	0.000	0.000	1.000

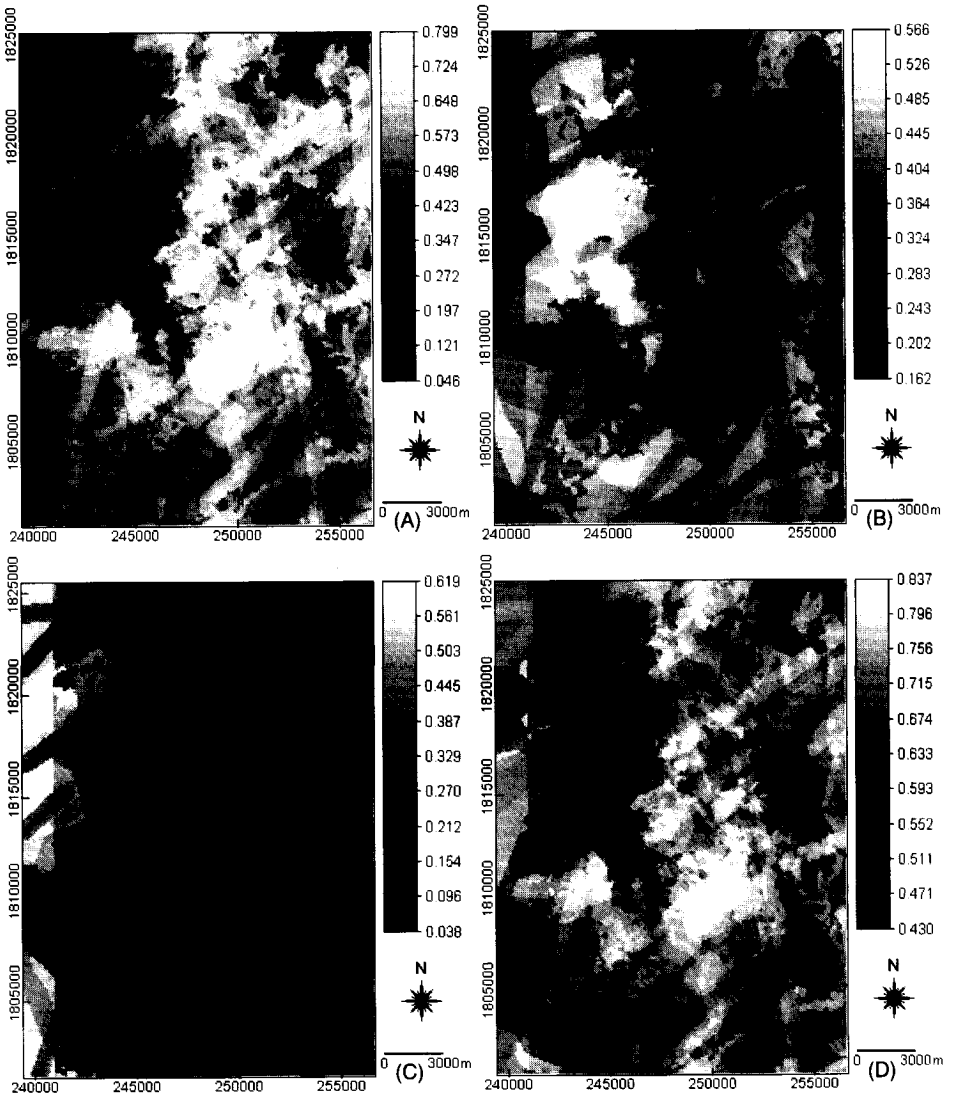

Figure 7.6. Probability maps of epithermal gold potential, Baguio district, inclusive of all spatial evidences: (a) belief map; (b) disbelief map; (c) uncertainty map; and (d) plausibility map.

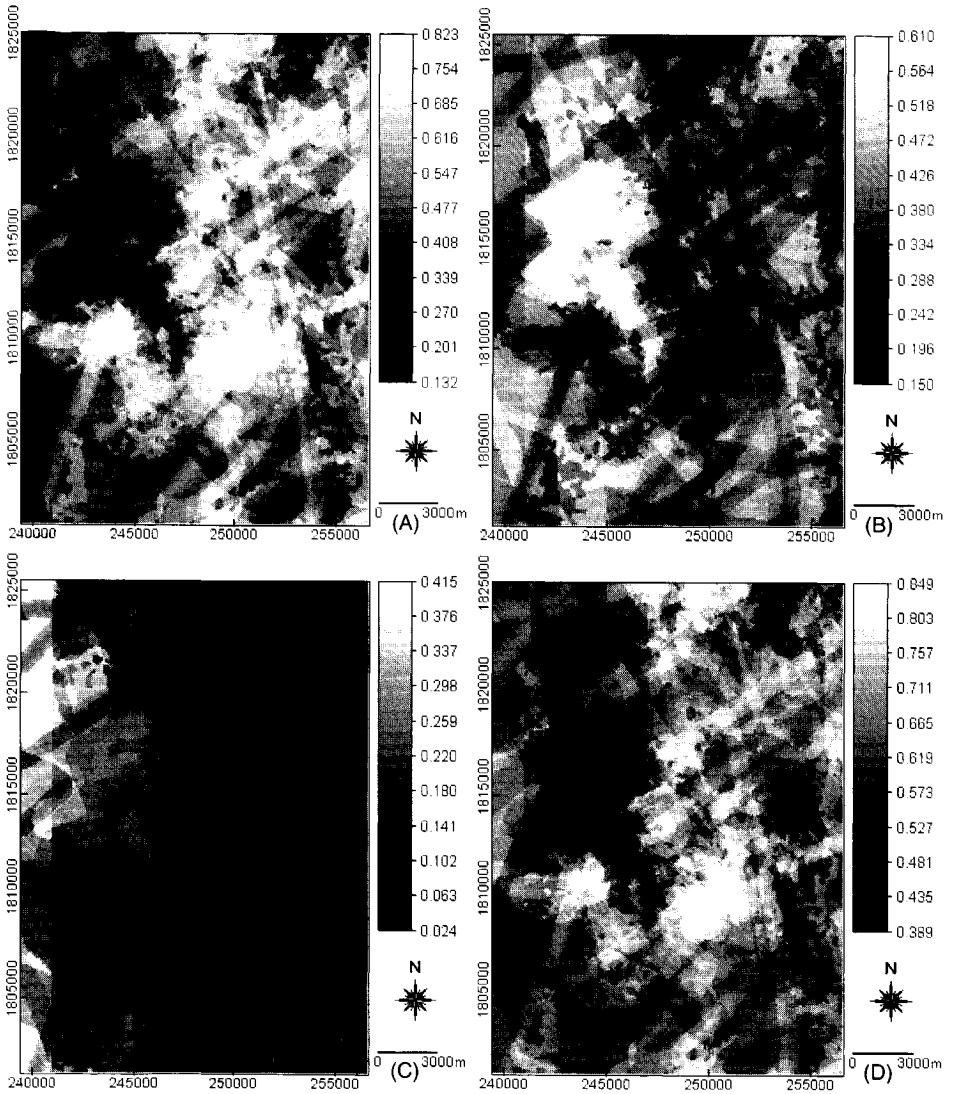

Figure 7.7. Probability maps of epithermal gold potential, Baguio district, exclusive of northwest-trending fault/fracture spatial evidence: (a) belief map; (b) disbelief map; (c) uncertainty map; and (d) plausibility map.

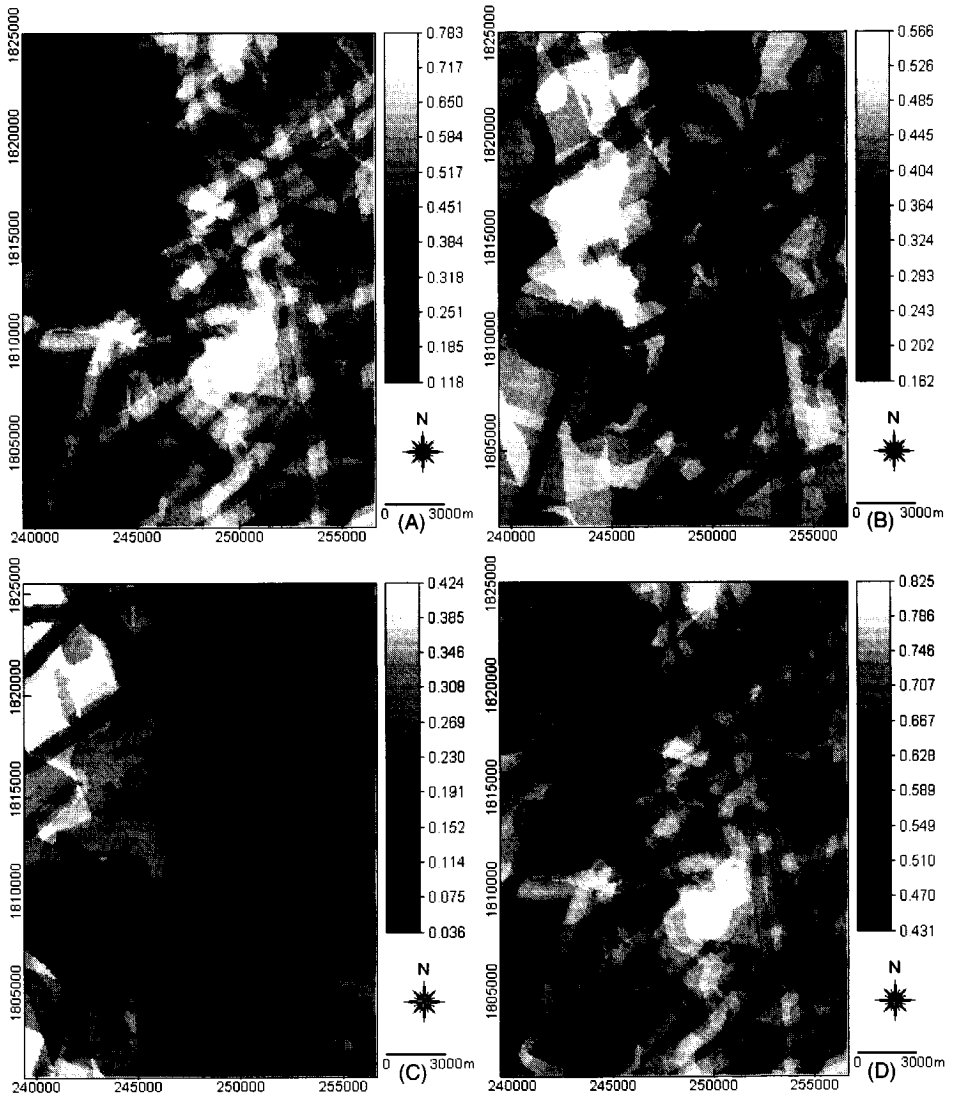

Figure 7.8. Probability maps of epithermal gold potential, Baguio district, exclusive of hydrothermal alteration spatial evidence: (a) belief map; (b) disbelief map; (c) uncertainty map; and (d) plausibility map.

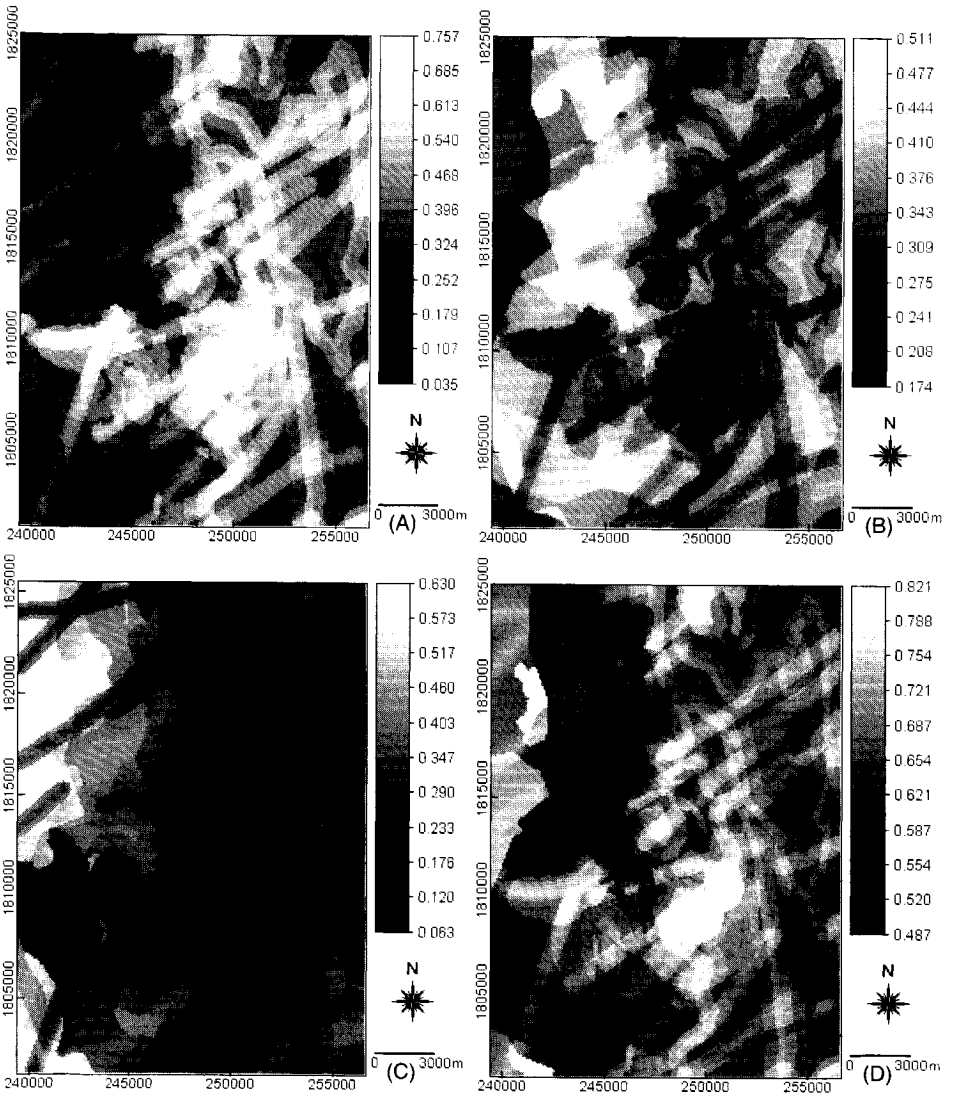

Figure 7.9. Probability maps of epithermal gold potential, Baguio district, exclusive of hydrothermal alteration and northwest-trending fault/fracture spatial evidences: (a) belief map; (b) disbelief map; (c) uncertainty map; and (d) plausibility map.

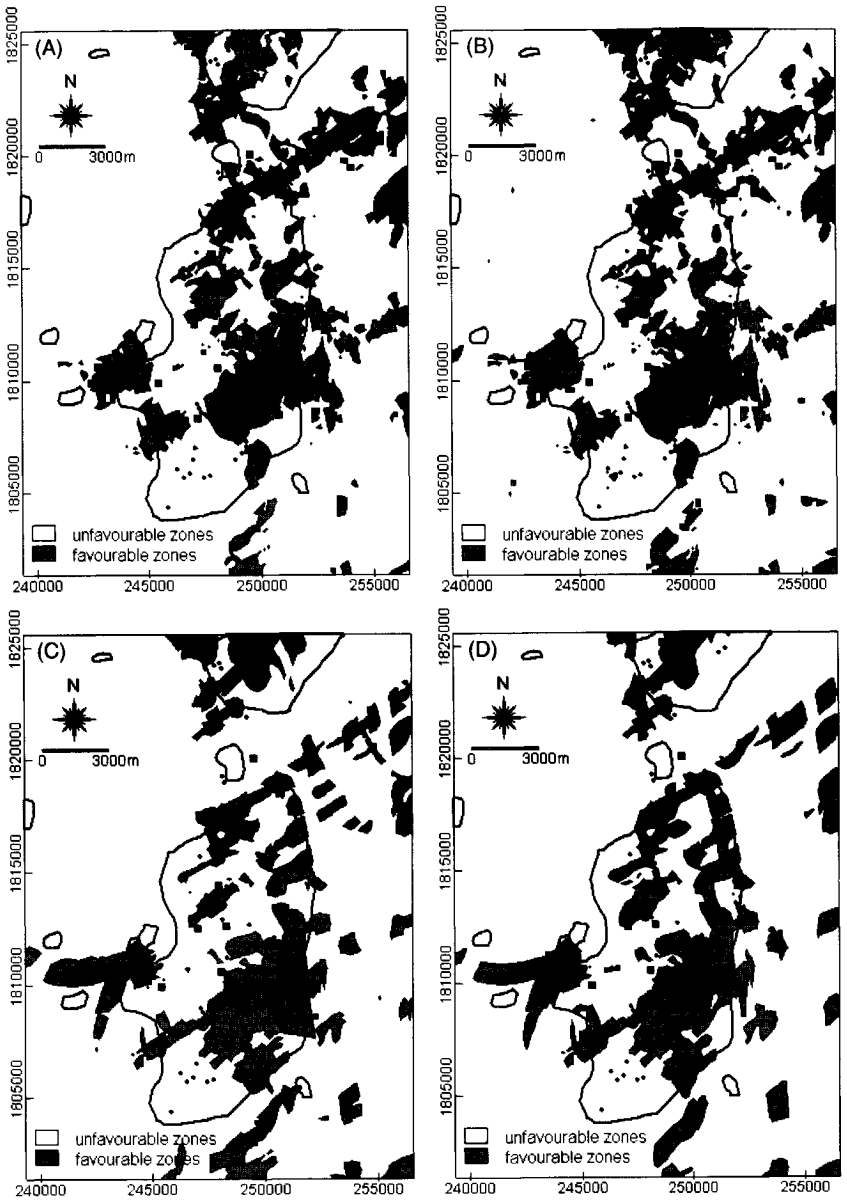

Figure 7.10. Favourability maps of epithermal gold potential, Baguio district: (a) inclusive of all spatial evidence layer; (b) exclusive of northwest-trending faults/fracture evidence; (c) exclusive of hydrothermal alteration evidence; and (d) exclusive of northwest-trending fault/fracture and hydrothermal alteration evidence layers. Filled squares = 'model large-scale gold deposits'; small dots = 'validation small-scale gold deposits; polygons in solid lines = stream sediment Au anomaly.

The differences between the four sets of probability maps, in terms of predicting zones of epithermal gold potential, can be determined by re-classifying the belief maps into binary maps that indicate favourable zones and unfavourable zones. For Figures 7.6a and 7.7a, threshold probabilities of 0.614 and 0.620 (i.e., 80^{th} percentile probabilities), respectively, were used to differentiate between favourable zones and unfavourable zones. For Figures 7.8a and 7.9a, threshold probabilities of 0.533 and 0.553 (i.e., 80^{th} percentile probabilities), respectively, were used to distinguish between favourable zones and unfavourable zones. The favourability maps are shown in Figure 7.10.

The favourability maps are similar. They depict the north-south trending belt of large-scale gold deposits. They also depict other favourable zones particularly in the southwest-central and northeast-central sections of the district. The spatial predictive geoinformation characteristics of the favourability maps are similar (Table 7.5). The favourability maps predict similar percentages of the 'model' large-scale gold deposits'. The favourability map in Figure 7.10a is superior to the other favourability maps; it has the highest prediction rate with respect to the 'validation' small-scale gold deposits. The favourability map in Figure 7.10b is the next superior; it has a higher prediction rate, with respect to the 'validation' small-scale gold deposits, as compared to the favourability maps in Figures 7.10c and 7.10d. The favourability map in Figure 7.10d is better than the favourability map in Figure 7.10c. The favourability maps have similar percentages of spatial coincidence with the stream sediment Au anomalies. The portions of the geologically-favourable zones that spatially coincide with the geochemically-anomalous are probably sources of the geochemical anomalies.

Table 7.5. Spatial predictive geoinformation characteristics of favourability maps after reclassification of belief maps, Baguio district.

Spatial geoinformation characteristics	Epithermal gold mineralisation favourability map			
	Figure 7.10a	Figure 7.10b	Figure 7.10c	Figure 7.10d
% predicted favourable zones	18.9	19.9	18.2	18.8
% 'model' large-scale gold deposits predicted correctly	68.4	68.4	68.4	68.4
% 'validation' small-scale gold deposits predicted correctly	60.3	58.7	55.6	57.1
% stream sediment Au anomaly zones predicted	40.0	41.1	42.1	40.8

7.5.3 Discussion

Combining all the spatial geological evidences is better than combining separately the hydrothermal alteration spatial evidence and the northwest-trending fault/fracture spatial evidence with the other spatial evidences. The hydrothermal alteration spatial evidence, however, provides a positive support to the proposition that a gold deposit exists when combined with the other spatial

evidences whilst the northwest-trending fault/fracture spatial evidence provides a negative support when combined with the other spatial evidences. The remotely-detected hydrothermal alteration evidence layer is useful despite its marginal accuracy (see section 3.3.4). It also follows that geological features that are negatively spatially associated with mineral deposits are not particularly important in mapping mineral potential.

The predicted geologically-favourable zones correctly delineate 13 (or at least 68%) of the 19 large-scale deposits. The geochemical anomalies correctly delineate 13 of the 19 large-scale deposits (see section 2.3.3). The geologically-constrained predictive maps are thus as adequately useful as the geochemical anomalies, with respect to the large-scale gold deposits. The predicted geologically-favourable zones, however, accurately delineate a higher proportion of the small-scale gold deposits than the geochemical anomalies (Figure 7.10; sub-section 2.3.3). This finding does not necessarily negate the usefulness of the geologically-constrained predictive maps for the following reason. The locations of the large-scale and small-scale gold deposits have been mapped on a project-scale whilst the geological features have been mapped on a district-scale. The geologically-constrained predictive maps are thus useful for delineating potentially mineralised zones on a district-scale rather than on a project-scale.

7.6 APPLICATION TO ABRA AREA

The geological features that were used as evidences of porphyry copper potential in the area include lithologic units, intersections of regional faults (i.e., north-trending and northeast-trending faults/fractures), porphyry pluton centroids, north-trending faults/fractures, and granodiorite batholithic margins. The stream sediment Cu anomalies (see sub-section 2.4.4) were also used as spatial evidence to determine whether an integrated geological-geochemical predictive modeling is better than a geologically-constrained predictive modeling. The estimation of the belief functions of the spatial evidences was based on the 'mineralised zones' of the 12 known porphyry copper deposits (Bureau of Mines, 1976). The validity of the predictive model(s) was assessed against the known mineralised zones (sub-section 2.4.1; JICA, 1980).

7.6.1 Belief functions of spatial evidences of porphyry copper potential

Geoinformation from the point pattern analysis of the porphyry copper deposits in the area is shown in Figure 7.11. There is zero probability for another porphyry copper deposit within 1 km of any given known porphyry copper deposit. However, the optimum distance buffer is 500 m because it yields porphyry copper 'mineralised zones' that occupy 0.95% of the area. The

probability assignments of the different subsets of spatial geological evidences, based on the 'mineralised zones', are given in Table 7.6.

The granodiorite batholithic plutons are relatively favourable host rocks among the different lithologic units. Proximity to the granodiorite batholithic plutons, however, is a negative evidence for mapping porphyry copper potential. The diorite porphyry plutons, despite their small sizes, are better predictors than the diorite batholithic plutons. The probability assignments of proximity classes to the porphyry plutons do not show a particular trend but are generally decreasing within 5 km, which indicates its positive spatial association with the porphyry copper 'mineralised zones' (see also subsections 4.5.8 and 6.6.1). The structural features are positive evidences of porphyry copper potential. Stream sediment catchment basins with >170 ppm Cu are positive evidences of favourable zones of porphyry copper potential.

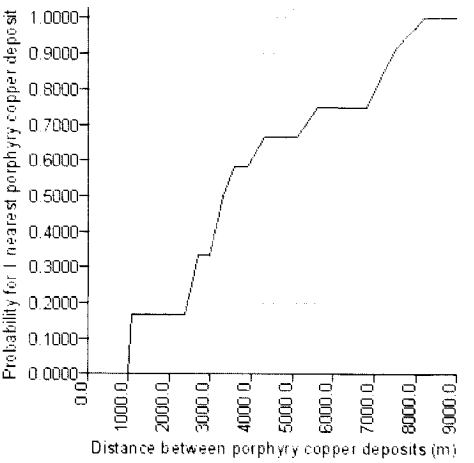

Figure 7.11. Distance and probability of a porphyry copper deposit nearby another porphyry copper deposit, Abra area.

7.6.2 Evidential belief mapping of porphyry copper potential

The belief functions of evidences of porphyry copper mineralisation are combined, inclusive and exclusive of the stream sediment geochemical evidence, to estimate new belief functions for the following propositions:

T_C = "a porphyry copper deposit exists based on the data sets",
$\bar{T}_C$ = "a porphyry copper deposit does not exist based on the data sets", and
$\Theta_C = \{T_C, \bar{T}_C\}$, "uncertainty that a porphyry copper deposit exists".

Belief function maps exclusive of the stream sediment geochemical evidence and inclusive of the stream sediment geochemical evidence were generated to evaluate the usefulness of geologically-constrained predictive maps. The probability maps exclusive of the stream sediment geochemical evidence and inclusive of the stream sediment geochemical evidence are very similar (Figure 7.12 and 7.13). Zones of high degrees of belief and low degrees of disbelief pertain mainly to the southwest quadrant of the area and to some portions in the northeast quadrant. These zones are characterised by low degrees of

uncertainty and high degrees of plausibility. Zones of high degrees of uncertainty are found in the northwest sections, which are underlain by rock units that are not associated with the known porphyry copper mineralisation in the area.

Table 7.6. Basic probability assignments of spatial evidences of porphyry copper potential, Abra area (N_T = 91963; N_D = 870).

	Data layer D_i	$N_{S_{ij}D}$	$N_{S_{ij}\bar{D}}$	$m_i(T_i)$	$m_i(\bar{T}_i)$	$m_i(\Theta_i)$
Lithologic units (Figure 2.13)	Alava Formation	0	487	0.000	0.000	1.000
	Tineg Formation	3	7465	0.007	0.168	0.825
	Licuan Formation	360	51958	0.092	0.167	0.741
	Quartz diorite porphyry pluton	4	308	0.234	0.166	0.600
	Quartz diorite batholithic pluton	67	5687	0.216	0.166	0.618
	Granodiorite batholithic pluton	436	25117	0.451	0.165	0.384
Proximity to intersections of regional faults (km)	<1.000	304	12243	0.413	0.140	0.447
	1.000-1.500	217	12412	0.254	0.142	0.604
	1.500-2.025	160	12792	0.167	0.142	0.691
	2.025-2.675	46	13098	0.041	0.144	0.815
	2.675-3.600	70	13210	0.063	0.144	0.793
	3.600-4.950	0	13479	0.000	0.000	1.000
	>4.950	73	13859	0.062	0.144	0.794
Proximity to porphyry pluton centroids (km)	<1.500	176	6482	0.241	0.082	0.677
	1.500-2.425	62	6743	0.071	0.083	0.846
	2.425-3.300	88	6900	0.102	0.083	0.815
	3.300-4.150	39	7174	0.041	0.084	0.875
	4.150-4.975	2	7459	0.002	0.084	0.914
	4.975-5.750	144	7619	0.160	0.083	0.757
	5.750-6.600	209	7847	0.245	0.082	0.673
	6.600-7.450	77	8063	0.074	0.083	0.843
	7.450-8.475	23	8263	0.021	0.084	0.895
	8.475-9.850	49	8502	0.043	0.084	0.873
	9.850-12.000	0	8632	0.000	0.000	1.000
	>12.000	0	7409	0.000	0.000	1.000
Proximity to north-trending faults/ fractures (km)	<0.55	259	20792	0.318	0.249	0.433
	0.55-1.25	342	21808	0.455	0.248	0.297
	1.25-2.40	144	23286	0.129	0.251	0.620
	>2.40	125	25207	0.098	0.252	0.650
Proximity to granodiorite batholithic margins (km)	<0.200	86	12442	0.107	0.167	0.726
	0.200-0.525	181	14489	0.213	0.166	0.621
	0.525-1.000	249	15448	0.294	0.165	0.541
	1.000-1.700	248	15840	0.289	0.165	0.546
	1.700-3.300	86	16042	0.079	0.168	0.753
	>3.300	23	16832	0.019	0.168	0.813
Stream sediment Cu contents (ppm)	No data	-	-	0.000	0.000	1.000
	<50	289	42258	0.051	0.203	0.746
	50-90	225	20137	0.108	0.202	0.690
	90-170	63	3698	0.162	0.201	0.637
	>170	98	1577	0.605	0.192	0.203

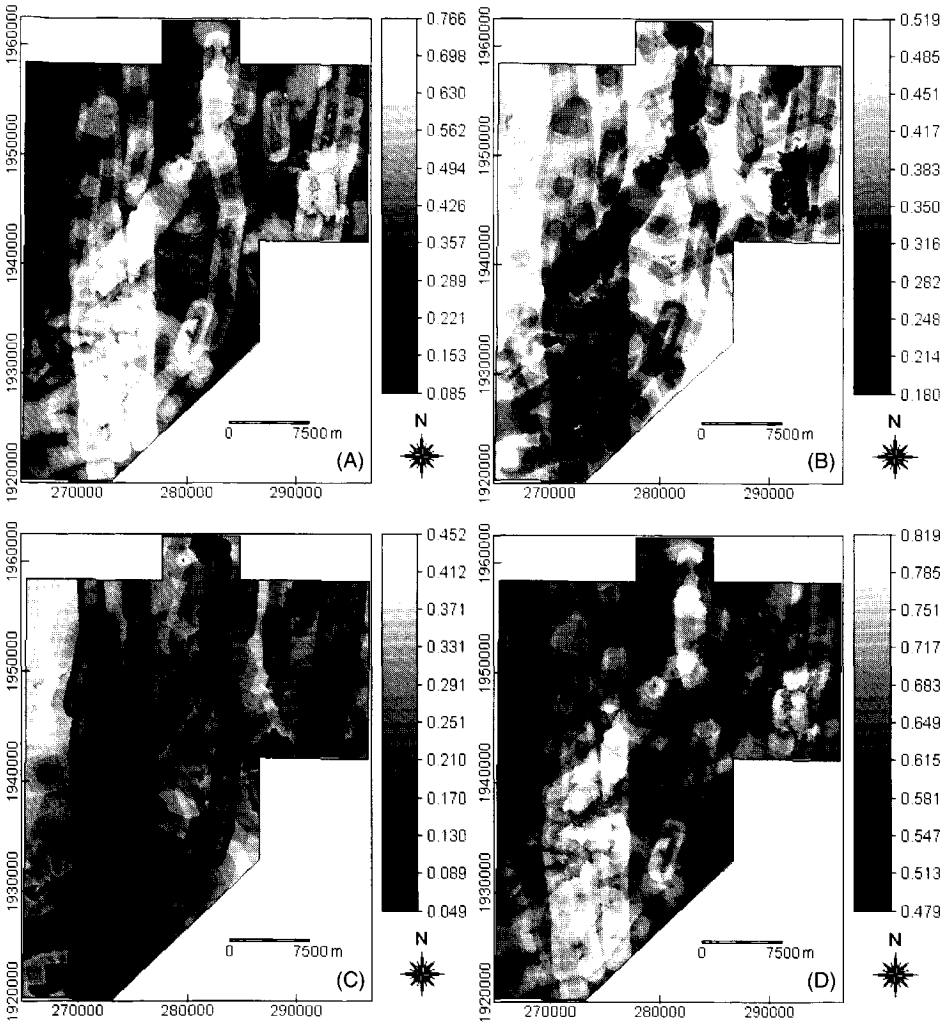

Figure 7.12. Probability maps of porphyry copper potential, Abra area, exclusive of the stream sediment geochemical evidence: (a) belief map; (b) disbelief map; (c) uncertainty map; and (d) plausibility map.

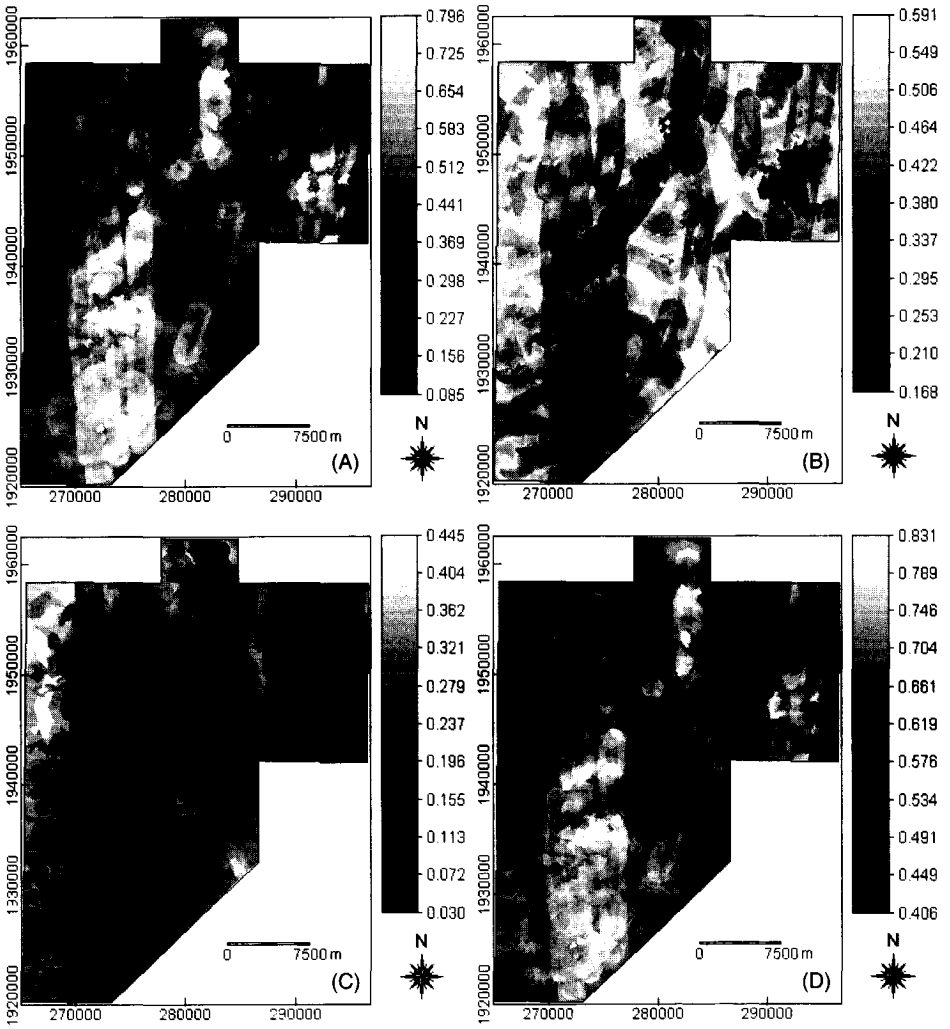

Figure 7.13. Probability maps of porphyry copper potential, Abra area, inclusive of the stream sediment geochemical evidence: (a) belief map; (b) disbelief map; (c) uncertainty map; and (d) plausibility map.

The probability maps exhibit clearly the strong support provided by the structural features for the proposition that porphyry copper deposits exist in the area. Circular or ring patterns of alternating low and high degrees of belief and disbelief are attributed to the proximity classes around porphyry plutons, which do not show a clear trend of probability assignments. Small circular areas of intermediate to high degrees of belief and low to intermediate degrees of disbelief are attributed to the intersection of regional faults. The strong support provided by the granodiorite body in the north-central section is exhibited clearly. The support provided by the stream sediment geochemical evidence (i.e., stream sediment sample catchment basins with >170 ppm Cu), is not readily discernible from Figure 7.13.

The belief maps are reclassified into binary maps of favourable zones of porphyry copper potential to determine the contribution of the stream sediment geochemical evidence and evaluate the usefulness of the geologically-constrained predictive maps. Threshold probabilities of 0.571 and 0.585 (i.e., 80^{th} percentile probabilities) were used to reclassify the belief maps in Figures 7.12a and 7.13a, respectively, into binary favourability maps (Figure 7.14). The spatial predictive geoinformation characteristics of the binary favourability maps are given in Table 7.7. Like the probability maps, the favourability maps are also very similar. Both favourability maps delineate similar potential areas of almost the same lateral extents. The predicted favourable zones delineate correctly similar percentages of the 'model' porphyry copper deposits. The geologically-constrained favourability map, however, predicts a slightly lower percentage of favourable zones (3.8%) than the integrated geochemical-geological favourability map. This implies that the stream sediment geochemical evidence adds little support to the proposition that porphyry copper deposits exist in the area. This implies further that the geologically-constrained evidential belief map is as useful as the integrated geochemical-geological evidential belief map.

Table 7.7. Spatial predictive geoinformation characteristics of reclassified belief maps inclusive and exclusive of stream sediment geochemical evidence, Abra area.

Spatial predictive characteristics	Favourability map	
	Figure 7.14a	Figure 7.14b
% predicted favourable zones	19.9	19.8
% 'model' deposits predicted correctly	58.3	58.3
% known mineralised zones predicted correctly	62.5	66.3

7.6.3 Discussion

Most favourable zones of porphyry copper potential are those where the north-, the northeast-trending fault/fractures, and the granodiorite batholithic plutons intersect. These favourable zones are where the small bodies of porphyry plutons have been mapped (see Figures 2.13 and 2.14). The interpretation is as

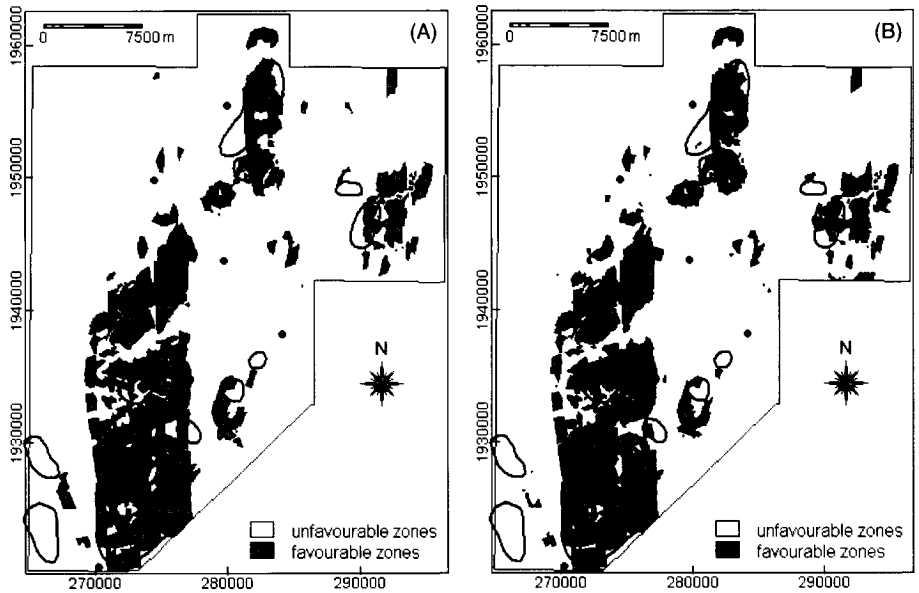

Figure 7.14. Favourability maps of porphyry copper potential, Abra area: (a) exclusive of stream sediment geochemical evidence; (b) inclusive of stream sediment geochemical evidence. Solid circles = 'model' porphyry copper deposits; polygons in solid lines = known mineralised zones.

follows. The intersections of the north- and northeast-trending faults/fractures are strike-slip fault discontinuities (see sub-section 4.3.1), which focussed later ascent of magma from the magma chamber associated with the pre-existing batholithic plutons and led to the emplacement of the porphyry plutons. The porphyry plutons are thus the most important geologic predictor of porphyry copper mineralisation. This may not be apparent, however, from the representation of the geological map data using belief functions because of the small sizes or limited occurrences (i.e., mapped outcrops) of porphyry plutons as compared to the intersections of the north- and the northeast-trending faults/fractures and granodiorite batholithic margins. The relatively low importance of the porphyry plutons as spatial evidence of porphyry copper potential is augmented by these other geological features.

7.7 APPLICATION CATANDUANES ISLAND

The geological features that were used as spatial evidences of gold-copper potential in the island include the lithologic units, Batalay Intrusive contacts, the northeast-trending faults/fractures and the north-trending faults/fractures. The stream sediment geochemical anomalies (see sub-section 2.5.4) were also used

as spatial evidence to determine whether an integrated geological-geochemical predictive modeling is better than a geologically-constrained predictive modeling. The gold-copper 'mineralised zones' were used to generate the belief functions for the predictive mapping of gold-copper potential in the island.

7.7.1 Belief functions of spatial evidences of gold-copper potential

Geoinformation about the spatial distribution of the gold-copper deposits is illustrated in Figure 7.15. There is zero probability for another gold-copper deposit within about 1200 m of a known gold-copper deposit. However, the optimum distance buffer is 525 m, which resulted in gold-copper 'mineralised zones', which occupy 0.98% of the total area of the island. The probability assignments of the different subsets of spatial evidences of gold-copper potential, based on the gold-copper 'mineralised zones', are given in Table 7.8

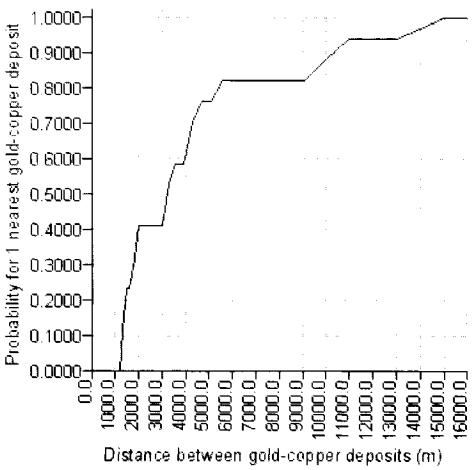

Figure 7.15. Distance and probability of a gold-copper deposit nearby another gold-copper deposit, Catanduanes Island.

Among the lithologic units, the Batalay Intrusives are the most important spatial evidence of gold-copper potential of the island. Proximity to within 1 km of the Batalay Intrusives is also an important spatial evidence of gold-copper potential. The north-trending faults/fractures and the northeast-trending fault/fractures are indicated to have similar strengths as spatial evidence of gold-copper potential. The anomalous stream sediment geochemical signature (i.e., >90th percentile PC3 scores; see sub-section 2.5.4) has the highest probability assignment.

7.7.2 Evidential belief mapping of gold-copper potential

The belief functions of evidences of gold-copper mineralisation are combined to estimate new belief functions that represent total belief from integrating all the evidential data layers for the following propositions:

T_{GC} = "a gold-copper deposit exists based on the data sets",

$\overline{T}_{GC}$ = "a gold-copper deposit does not exist based on the data sets", and

$\Theta_{GC} = \{T_{GC}, \overline{T}_{GC}\}$, "uncertainty that a gold-copper deposit exists".

Table 7.8. Basic probability assignments of spatial evidences of gold-copper potential, Catanduanes Island (N_T = 144811; N_D = 1432).

Data layer D_i		$N_{S_{ij}D}$	$N_{S_{ij}\bar{D}}$	$m_i(T_i)$	$m_i(\bar{T}_i)$	$m_i(\Theta_i)$
Lithologic units (Figure 2.17)	Alluvium	57	11564	0.035	0.127	0.838
	Viga Conglomerate	0	1507	0.000	0.000	1.000
	Sto. Domingo Formation	5	5527	0.006	0.127	0.867
	Batalay Intrusives	113	1546	0.541	0.118	0.341
	Payo Formation	329	55584	0.035	0.127	0.838
	Bonagbonag Limestone	31	1993	0.118	0.125	0.757
	Yop Formation	549	25156	0.211	0.124	0.665
	Catanduanes Formation	339	40511	0.058	0.126	0.816
Proximity to Batalay Intrusive contacts (km)	<0.400	243	4598	0.234	0.048	0.718
	0.400-0.900	228	4704	0.212	0.048	0.740
	0.900-1.375	134	5118	0.108	0.049	0.843
	1.375-1.950	33	5651	0.023	0.050	0.927
	1.950-2.550	75	5810	0.052	0.050	0.898
	2.550-3.150	30	6038	0.019	0.050	0.931
	3.150-3.800	29	6444	0.017	0.050	0.933
	3.800-4.550	98	6813	0.058	0.050	0.892
	4.550-5.500	103	7094	0.059	0.050	0.891
	5.500-6.550	94	7228	0.052	0.050	0.898
	6.550-7.725	0	7507	0.000	0.000	1.000
	7.725-9.300	0	7792	0.000	0.000	1.000
	9.300-11.300	0	7943	0.000	0.000	1.000
	11.300-13.550	0	8111	0.000	0.000	1.000
	13.550-16.025	139	8190	0.070	0.050	0.880
	16.025-18.550	39	8318	0.018	0.051	0.931
	18.550-21.500	0	8450	0.000	0.000	1.000
	21.500-26.300	89	8676	0.041	0.050	0.909
	26.300-32.500	89	9214	0.038	0.050	0.912
	>32.500	0	9689	0.000	0.000	1.000
Proximity to NE-trending faults/ fractures (km)	<0.500	467	26255	0.383	0.198	0.419
	0.500-1.025	417	26826	0.317	0.199	0.484
	1.025-1.900	224	28216	0.136	0.201	0.663
	1.900-3.500	56	29716	0.028	0.202	0.770
	>3.500	259	32375	0.136	0.201	0.663
Proximity to N-trending faults/fractures (km)	<0.375	394	14810	0.355	0.123	0.522
	0.375-0.750	275	15281	0.216	0.124	0.660
	0.750-1.175	131	16519	0.085	0.125	0.790
	1.175-1.725	86	17404	0.051	0.126	0.823
	1.725-2.475	190	18453	0.113	0.125	0.762
	2.475-3.475	170	19081	0.096	0.125	0.779
	3.475-5.000	66	19576	0.034	0.126	0.840
	>5.000	111	22264	0.050	0.126	0.824
Stream sediment geochemical signature (%le PC3 scores; Figure 2.19)	No data	-	-	0.000	0.000	1.000
	<50%le	140	30792	0.025	0.204	0.771
	50-75%le	139	11888	0.074	0.203	0.723
	75-90%le	150	6895	0.142	0.201	0.657
	>90%le	450	4972	0.735	0.187	0.078

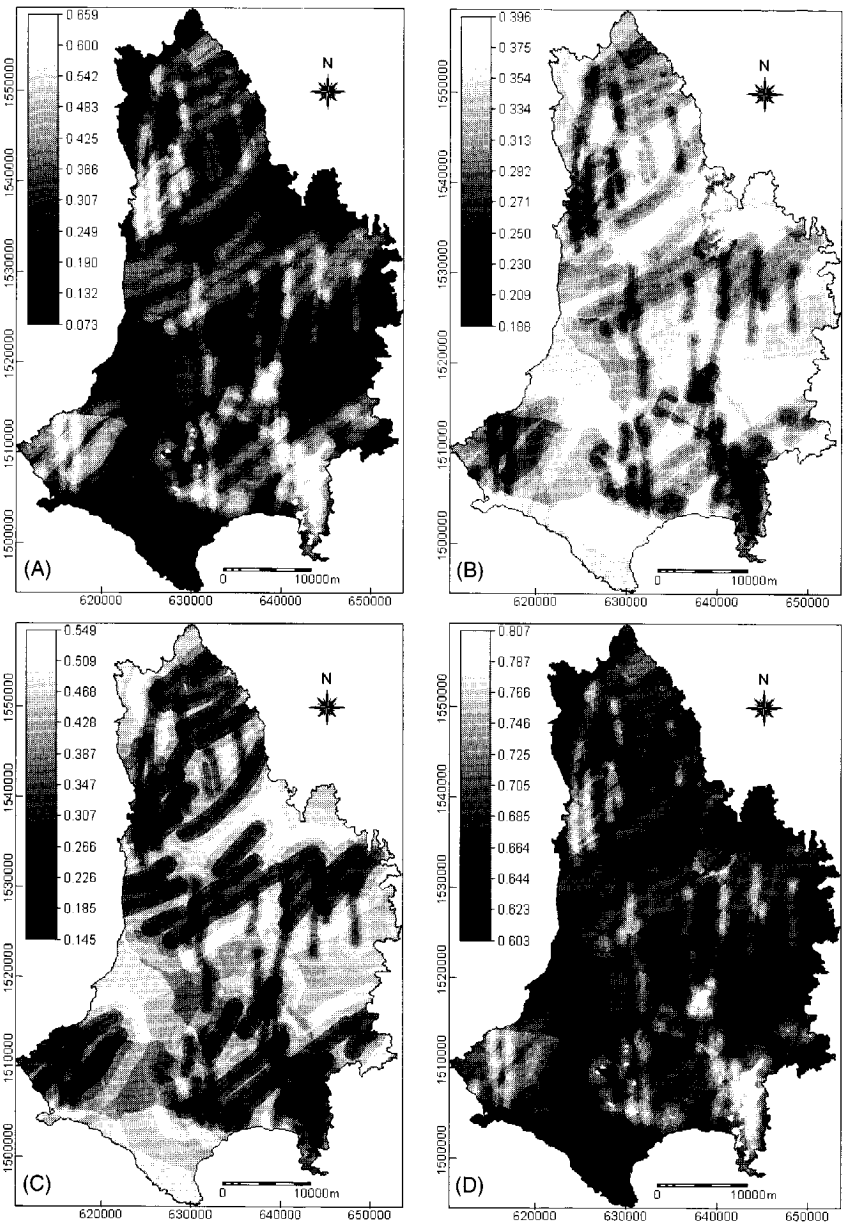

Figure 7.16. Probability maps of gold-copper potential, Catanduanes Island, exclusive of the stream sediment geochemical spatial evidence: (a) belief map; (b) disbelief map; (c) uncertainty map; and (d) plausibility map.

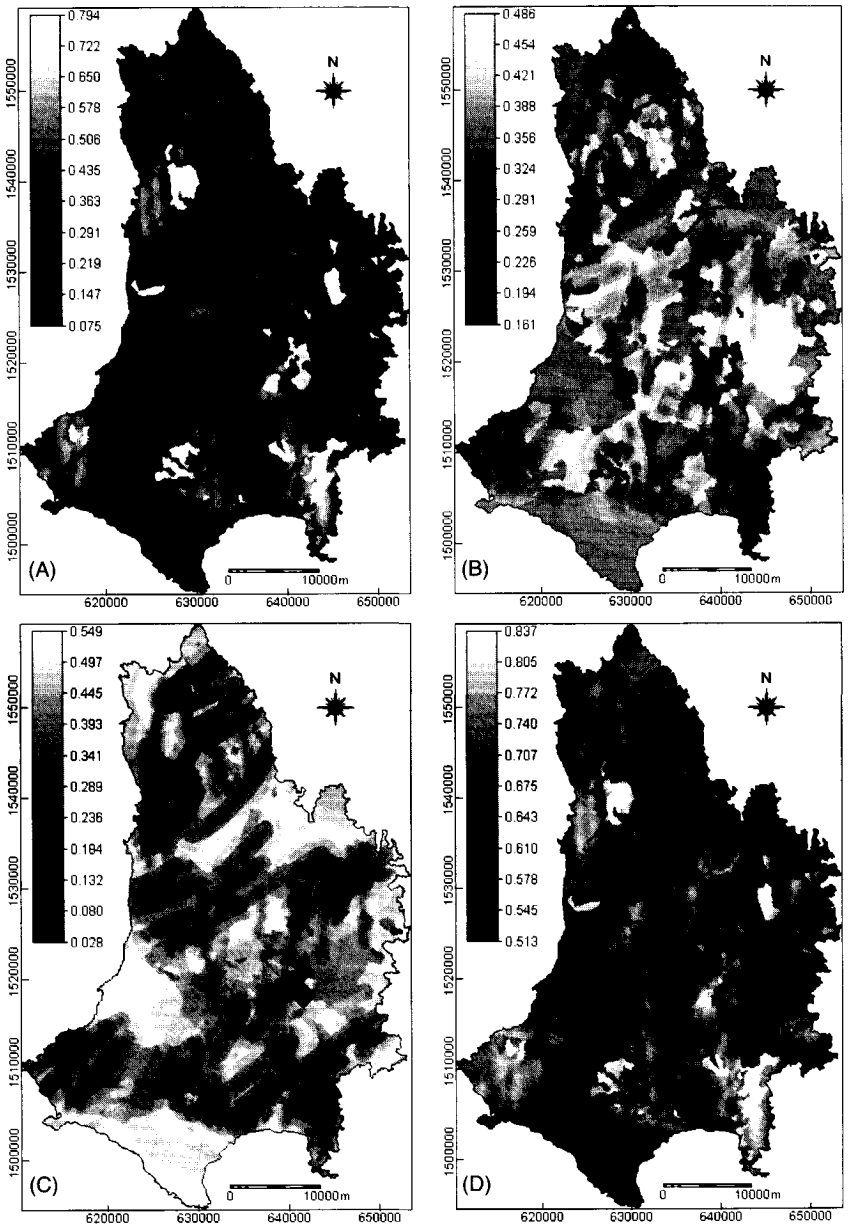

Figure 7.17. Probability maps of gold-copper potential, Catanduanes Island, inclusive of the stream sediment geochemical spatial evidence: (a) belief map; (b) disbelief map; (c) uncertainty map; and (d) plausibility map.

The probability maps exclusive of the stream sediment geochemical and inclusive of the stream sediment geochemical evidence are shown in Figures 7.16 and 7.17, respectively. The contributions of the belief functions of the stream sediment geochemical signature to the integrated geochemical-geological belief functions are visible clearly from the probability maps. Zones of high degrees of belief and low degrees of disbelief pertain to areas underlain by the Batalay Intrusives. Zones that are proximal to within 1 km of areas underlain by the Batalay Intrusives are characterised by intermediate degrees of belief and disbelief. Zones of high degrees of belief and low degrees of disbelief also pertain to areas that are proximal to the north-trending faults/fractures and northeast-trending faults/fractures. Zones of high degrees of belief and low degrees of disbelief, in addition to those depicted in the geologically-constrained probability maps, are those that are characterised by >90th percentile PC3 scores of the multi-element geochemical signature. The zones of high degrees of belief and low degrees of disbelief are characterised by low degrees of uncertainty. Zones underlain by and proximal to the Batalay Intrusives and the catchment basins with anomalous geochemical signature are characterised by particularly low degrees of uncertainty. Zones of high degrees of uncertainty are in the southern, western and northeastern sections where the geological evidences do not provide strong support for the proposition that gold-copper deposits exist. The catchment basins with <50th percentile PC3 scores of the multi-element geochemical signatures (see also Figure 2.19) have the lowest degrees of plausibility. Some of these zones are also indicated in the geologically-constrained plausibility map.

In order to evaluate the usefulness of the geologically-constrained predictive maps, the belief maps in Figures 7.16a and 7.17a were reclassified into binary favourability maps. The 80th percentile probabilities in the belief maps (i.e., 0.401 for both maps) were used to reclassify them into binary maps of favourability for gold-copper potential (Figure 7.18). The binary favourability maps are apparently similar. They predicted similar favourable zones with similar lateral extents. They predict correctly at least 70% (or at least 12) of the known gold-copper deposits, although the integrated geochemical-geological favourability map predicts about 6% (or 1) more deposit than the geologically-constrained favourability map (Table 7.9). This implies that the integrated geochemical-geological favourability map is slightly superior to the geologically-constrained favourability map. The integrated geochemical-geological favourability map, however, predicts only

Table 7.9. Spatial predictive geoinformation characteristics of reclassified belief maps exclusive and inclusive of stream sediment geochemical evidence, Catanduanes Island.

Spatial geoinformation characteristics	Favourability map	
	Figure 7.18a	Figure 7.18b
% predicted favourable zones	19.7	19.5
% known deposits predicted correctly	70.6	76.5
% geochemically-anomalous zones predicted correctly	36.5	64.2

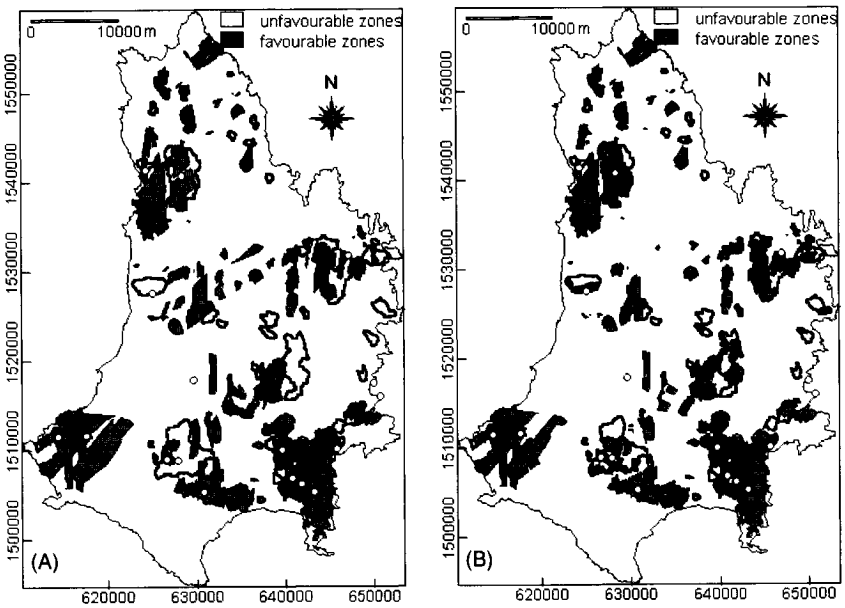

Figure 7.18. Favourability maps of gold-copper potential, Catanduanes Island: (a) exclusive of the stream sediment geochemical spatial evidence and (b) inclusive of the stream sediment geochemical evidence. Unfilled circles = 'model' gold-copper deposits; polygons in solid lines = geochemically-anomalous catchment basins.

about 64% of the geochemically-anomalous catchment basins. This finding implies that some of the geochemical anomalies are probably not significant or transported. The geologically-favourable zones that spatially coincide with the geochemical anomalies are probably the sources of significant geochemical anomalies. Notwithstanding the slight superiority of the integrated geochemical-geological favourability, the spatial coincidence of the geologically-favourable zones with the geochemical anomalies and the prediction rate of the geologically-constrained favourability map indicate its usefulness.

7.7.3 Discussion

The probability maps reflect the structural control of the vein-type gold-copper mineralisation in the island. The north-trending faults/fractures apparently controlled (passively) the emplacement of the Batalay Intrusives, which are the heat sources of the mineralisation (as can be deduced from the north-south trends of the intrusive bodies). The northeast-trending faults/fractures, which are interpreted to be coeval with the emplacement of the Batalay intrusives, represent the tectonic or seismic regime that brought about the magmatic intrusions. The geologically-constrained probability maps show that the Batalay

Intrusives are localised at the intersections of the north-trending faults/fractures and northeast-trending faults/fractures. Thus, zones where the Batalay Intrusives are absent (i.e., not mapped), but where the north-trending faults/fractures and the northeast-trending faults/fractures intersect, are probable heat flow zones. These inferred heat flow zones are where exploration for gold-copper deposits can be directed. The weak contribution of proximity to the Batalay Intrusives to the predictive mapping of gold-copper potential probably reflects either non-pervasive hydrothermal systems or non-reactive host rocks. This hypothesis is also based on field observations of narrow zones of silicification and pyritisation close to the mineralised veins (JICA-MMAJ, 1994). The narrow hydrothermal alteration zones around the mineralised veins suggest that the gold-copper deposits in the island could possibly represent the deepest portions of epithermal systems (see Figure 5.11; Mitchell and Leach, 1991).

7.8 APPLICATION TO ISABELA AREA

It has been demonstrated in Chapter 5 (see sub-section 5.5.4) that binary spatial evidences based on criteria provided by the nickeliferous-laterite deposit model (Golightly, 1979) are inadequate to classify accurately the nickeliferous-laterite potential of the area. The inadequacy of binary spatial evidences stems from the strict implementation of criteria provided by the conceptual deposit model, which are based on generalisations of characteristics of different but similar mineral deposits. Hence, these exploration criteria are imprecise or uncertain when applied to a particular area where the potential of a similar deposit is to be mapped. A knowledge-based application of the theory of evidential belief is therefore applied to map nickeliferous-laterite potential of the area.

Based on the conceptual nickeliferous-laterite model of Golightly (1979, 1981), the spatial evidences of nickeliferous-laterite mineralisation potential are (1) presence of peridotitic rocks, (2) topographic slopes of $\leq 20°$ and (3) presence of plateau edges. In Chapter 5, the mapping of nickeliferous-laterite potential is confined to the area underlain by the Isabela Ultramafics because of the binary representation of the lithologic criterion of the conceptual nickeliferous-laterite model. It follows that the model precludes the development of nickeliferous-laterite from other rock types. However, other non-peridotitic rocks could possibly contain forsteritic olivine and/or serpentine minerals, from which nickel is leached during lateritisation processes. Nahon and Tardy (1992) aver that laterite (though not necessarily nickeliferous) can develop from most sedimentary, metamorphic and igneous rocks. Hence, in the application of belief functions demonstrated here to map nickeliferous-laterite potential, all the lithologic units in the whole of map area in Figure 2.20 are considered.

7.8.1 Belief functions of spatial evidences of nickeliferous-laterite potential

The target proposition for the Isabela area is that "a pixel contains nickeliferous-laterite" in terms of its spatial attributes relevant to the criteria provided by the conceptual deposit model. Knowledge of the general mineralogical composition of different rock types was applied to assign subjective probabilities to the different lithologic units in the area (Figure 2.20) pertinent to the proposition, the negation of the proposition and the uncertainty of the proposition. Likewise, subjective probabilities are assigned to the different topographic indicators in the area in terms of the slope and landform criteria provided by the deposit model and the proposition, its negation and uncertainty. In assigning subjective probabilities to the topographic indicators, the scale of the topographic maps and the pixel size used were considered. Because of the inherent low accuracy of smaller scale maps and the smoothing effect caused by larger pixel sizes, variations in topographic conditions are necessarily present within certain generalised descriptors of the topography (e.g., slope class). Subjective probabilities were therefore assigned to the different slope classes to reflect variations in slopes within specific slope classes that make them more or less favourable in regard to formation of nickeliferous-laterite deposits. To assign subjective probabilities to ranges of topographic elevation where plateau edges probably occur, two general steps were followed as already described in Chapter 2. First, a DEM for each lithologic unit was extracted from the DEM of the map area. Second, graphical analysis of the histogram of pixels values (i.e., elevations) in the DEM of each lithologic unit was performed. (The histograms of the DEM for each lithologic unit are shown in Figure 8.29.) Subjective probabilities were assigned to elevation ranges depending on the interpretation of the of plateau edges within a particular elevation range. The subjective probability assignments for the different subsets of evidences of nickeliferous-laterite mineralisation are listed in Table 7.10.

7.8.2 Evidential belief mapping of nickeliferous-laterite potential

The belief functions of evidences of nickeliferous-laterite mineralisation are combined to estimate new belief functions that represent total belief from integrating all the evidential data layers for the following propositions:

T_{NL} = "a nickeliferous-laterite deposit exists based on the data sets",
$\overline{T}_{NL}$ = "a nickeliferous-laterite deposit does not exist based on the data sets", and
$\Theta_{NL} = \{T_{NL}, \overline{T}_{NL}\}$, "uncertainty that a nickeliferous-laterite deposit exists".

Table 7.10. Basic probability assignments of spatial evidences for nickeliferous-laterite potential, Isabela area.

	Data layer D_i	$m_i(T_i)$	$m_i(\bar{T}_i)$	$m_i(\Theta_i)$
Lithologic units (Figure 2.20)	Quaternary alluvium (QA)	0.00	0.00	1.00
	Miocene-Pliocene sedimentary rocks (MPSR)	0.05	0.15	0.80
	Oligocene dioritic intrusives (ODI)	0.10	0.13	0.77
	Oligocene sedimentary and volcanic rocks (OSVR)	0.10	0.13	0.77
	Cretaceous Rocks (CR)	0.25	0.10	0.65
	Cretaceous Isabela Ultramafics (CIU)	0.45	0.05	0.50
Elev. ranges of QA (m)	<100	0.05	0.08	0.87
	100-200	0.10	0.05	0.85
	>200	0.00	0.00	1.00
Elevation ranges of MPSR (m)	<100	0.10	0.05	0.85
	100-200	0.05	0.08	0.87
	200-300	0.10	0.05	0.85
	300-400	0.00	0.00	1.00
	400-500	0.00	0.00	1.00
	>500	0.00	0.00	1.00
Elevation ranges of ODI (m)	<100	0.10	0.05	0.85
	100-200	0.05	0.08	0.87
	200-300	0.05	0.08	0.87
	300-400	0.05	0.08	0.87
	400-500	0.10	0.05	0.85
	500-600	0.05	0.08	0.87
	600-700	0.05	0.08	0.87
	700-800	0.10	0.05	0.85
	800-900	0.00	0.00	1.00
	900-1000	0.00	0.00	1.00
	1000-1100	0.00	0.00	1.00
	1100-1200	0.00	0.00	1.00
	1200-1300	0.00	0.00	1.00
	1300-1400	0.00	0.00	1.00
	1400-1500	0.00	0.00	1.00
	1500-1600	0.00	0.00	1.00
	1600-1700	0.00	0.00	1.00
	1700-1800	0.00	0.00	1.00
	>1800	0.00	0.00	1.00
Elevation ranges of OSVR (m)	<100	0.10	0.05	0.85
	100-200	0.05	0.08	0.87
	200-300	0.10	0.05	0.85
	300-400	0.05	0.08	0.87
	400-500	0.10	0.05	0.85
	500-600	0.05	0.08	0.87
	600-700	0.05	0.08	0.87
	700-800	0.05	0.08	0.87
	800-900	0.10	0.05	0.85
	900-1000	0.10	0.05	0.85
	1000-1100	0.00	0.00	1.00
	1100-1200	0.00	0.00	1.00
	1200-1300	0.00	0.00	1.00
	1300-1400	0.00	0.00	1.00
	1400-1500	0.00	0.00	1.00

Table 7.10 continued.

Data layer D_i		$m_i(T_i)$	$m_i(\bar{T}_i)$	$m_i(\Theta_i)$
Elev. ranges of OSVR (m)	1500-1600	0.00	0.00	1.00
	1600-1700	0.00	0.00	1.00
	1700-1800	0.00	0.00	1.00
	>1800	0.00	0.00	1.00
Elevation ranges of CR (m)	<100	0.05	0.08	0.87
	100-200	0.05	0.08	0.87
	200-300	0.10	0.05	0.85
	300-400	0.05	0.08	0.87
	400-500	0.05	0.08	0.87
	500-600	0.10	0.05	0.85
	600-700	0.00	0.00	1.00
	700-800	0.00	0.00	1.00
	800-900	0.10	0.05	0.85
	900-1000	0.00	0.00	1.00
	>1000	0.00	0.00	1.00
Elevation ranges of CIU (m)	<100	0.05	0.08	0.87
	100-200	0.10	0.05	0.85
	200-300	0.05	0.08	0.87
	300-400	0.05	0.08	0.87
	400-500	0.05	0.08	0.87
	500-600	0.05	0.08	0.87
	600-700	0.05	0.08	0.87
	700-800	0.10	0.05	0.85
	800-900	0.00	0.00	1.00
	900-1000	0.00	0.00	1.00
	>1000	0.00	0.00	1.00
Slope classes	<10°	0.30	0.05	0.65
	10-20°	0.27	0.06	0.67
	20-30°	0.23	0.07	0.70
	30-40°	0.17	0.08	0.75
	>40°	0.05	0.15	0.80

The ultramafic terrane is characterised by very high degrees of belief, very low degrees of disbelief, very low degrees of low uncertainty and very high degrees of plausibility (Figure 7.19). The smaller bodies of basaltic rocks (Cretaceous Rocks) have intermediate degrees of belief, low degrees of disbelief, low degrees of uncertainty and intermediate degrees of plausibility. All other areas have low degrees of belief, intermediate to high degrees of disbelief and uncertainty and low to intermediate degrees of plausibility.

The belief map was reclassified into a favourability map of nickeliferous-laterite potential (Figure 7.20). A threshold probability of 0.365 (i.e., 80th percentile) was used to discriminate unfavourable zones (<0.365 probability) from favourable zones (≥0.365). The favourable zones were further classified, using the 90th percentile probability of 0.588, into low potential zones (<0.588 probability) and high potential zones (≥0.588 probability).

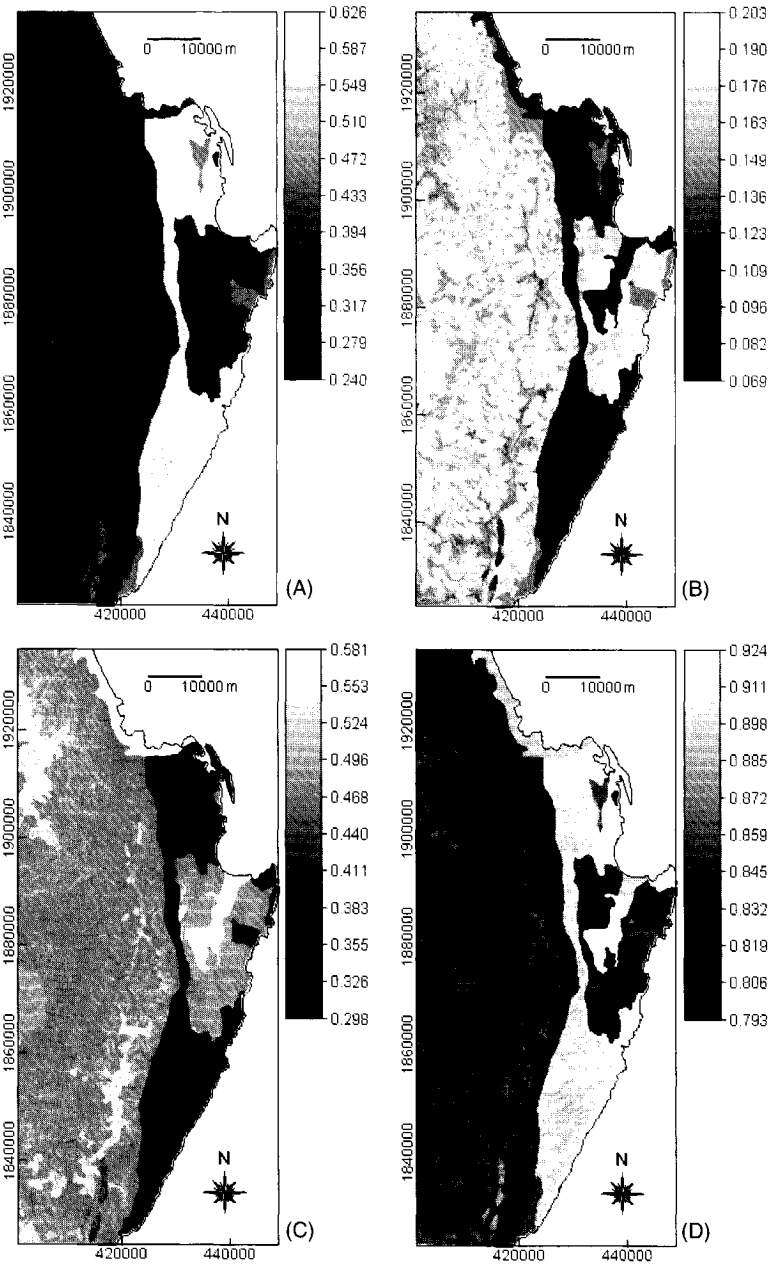

Figure 7.19. Probability maps of nickeliferous-laterite potential, Isabela area: (a) belief map; (b) disbelief map; (c) uncertainty map; and (d) plausibility map.

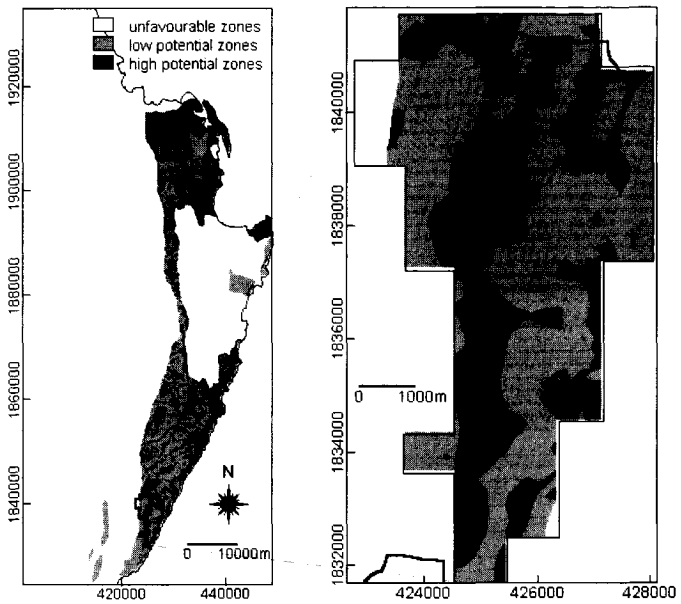

Figure 7.20. Favourability map of nickeliferous-laterite potential, Isabela area (left). Section with known nickeliferous-laterite deposits; solid lines represent catchment basins with stream sediment Ni contents >2500 ppm (right).

Favourable zones of nickeliferous-laterite potential pertain to the ultramafic terrane and to areas of basaltic rocks. About 62% of the ultramafic terrane has high potential and about 38% has low potential. Areas of basaltic rocks have low potential. About 45% of the section with known nickeliferous-laterite deposits has high potential, about 51% has low potential and about 4% is unfavourable. In the section with known nickeliferous-laterite deposits, about 67% of the catchment basins with stream sediment Ni contents >2500 ppm has high potential and about 33% has low potential.

7.8.3 Discussion

The evidential belief theory is useful for knowledge-based mapping of nickeliferous-laterite potential of the area. The lithology of the area is the most important spatial evidence. Whilst the ultramafic terrane is shown to have low to high potential, which fits the conceptual mineral deposit of Golightly (1979, 1991), areas underlain by basaltic rocks are also shown to have low potential. Hence, knowledge-based assignment of subjective probabilities of different rock units to map nickeliferous-laterite potential is important and provides a more realistic result than that based only on a binary representation of the lithologic

criterion provided by the conceptual nickeliferous-laterite model (see Section 5.5). Predictive mapping of nickeliferous-laterite potential within the whole area rather than within the ultramafic terrane alone leads to the recognition of other favourable zones, albeit of low potential, which are underlain by non-peridotitic rocks. Subjective assignment of probabilities to the topographic spatial evidences also enables the delineation of favourable zones of varying degrees of nickeliferous-laterite potential. The usefulness of the predictive maps was not fully assessed due to the lack of appropriate validation data. However, in the section with known nickeliferous-laterite deposits, the spatial coincidence between the predicted high potential zones and catchment basins with stream sediment Ni contents >2500 ppm indicates the validity of the favourability map.

There are less high potential zones in the section with known nickeliferous-laterite deposits than in some other sections of the ultramafic terrane (Figure 7.20). However, the nickeliferous-laterite potential of the portions of the ultramafic terrane immediately north of the section with known nickeliferous-laterite deposits is unknown because land-use regulations prohibit mineral resources development in these portions (Mangaoang, 1997). The ban on mineral resources development in the study area was enacted prior to the generation of the nickeliferous-laterite potential map in Figure 7.20. The ban on mineral resources development in the study area is not questioned but mineral potential maps such as in Figure 7.20 can be an important input to land-use decision-making.

7.9 DISCUSSION

The Dempster-Shafer theory of evidential belief is more commonly applied to knowledge-driven techniques to map mineral potential (Moon, 1989, 1990; An et al., 1992; Chung and Fabbri, 1993). The main reason for this is the insufficiency of target mineral deposits in areas for which mapping of mineral potential is undertaken. Here, a set of equations (Equations 7-14 to 7-18) were defined to represent estimates of probability assignments of spatial evidences allows a data-driven approach even in areas (i.e., Abra area and Catanduanes Island) where the number of known mineral deposits is considered too low to obtain statistically significant spatial association between the target deposits and the spatial geological evidences. The equations defined take into account not only the spatial relationship of a spatial evidence with the target mineral deposits but also the spatial relationships among the subsets of spatial evidences (Chung and Fabbri, 1993). Although Equations 7-16 to 7-18 do not strictly represent probabilities, the representation of estimates of probability assignments based on these equations not only adequately reflect the quantified spatial associations between the known mineral deposits and the geological features (see Chapters 4 and 6) but also reflect the spatial associations between the geochemical anomalies and the known mineral deposits.

Mineral deposits are invariably represented as points (or unit pixels) in predictive modelling of mineral potential using data-driven techniques such as weights of evidence modeling (Bonham-Carter et al., 1988, 1989; Agterberg et al., 1990; Bonham-Carter, 1991, 1994) and regression analyses (Chung and Agterberg, 1980, 1988; Agterberg, 1988). However, representation of mineral deposits as points in the data-driven application of evidential belief functions using the equations defined (i.e., Equations 7-14 to 7-18) was inadequate. Representation of the mineral deposits as 'mineralised zones' based on nearest neighbour point pattern analysis (Boots and Getis, 1988), due to the lack of appropriate data, proved adequate in the data-driven application of evidential belief functions using the equations defined.

Although the mineral potentials of the different study areas were deduced mainly from the belief maps, the usefulness of the disbelief, uncertainty and plausibility map is not unimportant. In particular, the uncertainty maps depict areas where the spatial evidences are insufficient/inefficient to provide support for the proposition that mineral deposits exist (An et al., 1992). On the other hand, the plausibility maps depict not only potentially mineralised areas (i.e., areas where the spatial evidences are sufficient/efficient to provide support for the proposition that mineral deposits exist) but also areas where more spatial evidences are required (i.e., areas where the spatial evidences are insufficient/inefficient to provide support for the proposition that mineral deposits exist). The disbelief map is complementary to the belief maps in depicting areas that are potentially mineralised and otherwise. Hence, the uncertainty and plausibility maps provide cautionary information and the disbelief maps provide complementary information when the favourability maps are used to guide further exploration work.

7.10 CONCLUSIONS

A data-driven application of the Dempster-Shafer evidential belief theory to geologically-constrained mapping of mineral potential is possible in areas where a number of representative mineral deposits are known. In Benguet province, where 23 known porphyry copper deposits were used in the predictive mapping of mineral potential, the optimum geologically-constrained favourability (i.e., inclusive of the remote-detected hydrothermal alteration evidence) predicts >86% of the 'model' deposits and >62% of the 'validation' deposits. In Baguio district, where 19 known large-scale epithermal gold deposits were used in the predictive modeling of mineral potential, the optimum geologically-constrained favourability maps (i.e., inclusive of the remotely-detected hydrothermal alteration evidence) predict >68% of the 'model' deposits and >58% of the 'validation' deposits. In Abra area, where 12 known porphyry copper deposits were used in the predictive modeling of mineral potential, the geologically-constrained favourability map predicts >58% of the 'model' deposits and >62% of the 'validation' porphyry copper mineralised zones. In Catanduanes Island,

where 17 known gold-copper deposits were used in the predictive modeling of mineral potential, the geologically-constrained favourability map predicts >70% of the 'model' deposits. The geologically-constrained favourability maps are as adequate as the geochemical anomaly maps and/or the integrated geochemical-geological predictive maps in delineating potentially mineralised zones on a district-scale to regional-scale.

A knowledge-driven application of the Dempster-Shafer evidential theory is the only appropriate approach for geologically-constrained mapping of mineral potential in areas where no mineral deposits are known. In Isabela area, the occurrence and distribution for nickeliferous-laterite is mainly unknown. In a small section of the area there is known nickeliferous-laterite but appropriate data for predictive modeling and validation of mineral potential are lacking. About 45% of the section with known nickeliferous-laterite deposits is indicated to have high potential for this type of deposit. The validity of the predictive nickeliferous-laterite potential map is not fully assessed, however, it shows that particular land areas that are protected from mineral resources development may contain important mineral deposits and therefore also shows that mineral potential classification is an important factor in land-use decision-making.

In the four examples presented here (i.e., in Benguet province, Baguio district, Abra area and Catanduanes Island), the generation of multi-class spatial evidences and the allocation of weights (i.e., probability assignments) to these multi-class spatial evidences are data-driven and the predictive maps are valid. In the Isabela area, however, the generation of multi-class spatial evidences and the allocation of weights (i.e., probability assignments) to these multi-class spatial evidences are knowledge-driven and there is indication that the predictive map is valid. These results imply that a knowledge-driven assignment of weights to multi-class spatial evidences generated through a data-driven approach could be a more efficient approach to mapping mineral potential. In the next chapter, knowledge is incorporated in the subjective assignments of weights to multi-class spatial predictors of mineral potential, which are generated based on the data-driven quantification of spatial associations between mineral deposits and geological features.

Chapter 8

Geologically-Constrained Fuzzy Mapping of Mineral Potential

"When useful fuzzy concepts are used in many concepts,
they have a host of varied meanings as recognized by human beings.
When Lotfi Zadeh's gifted mind turned to the concepts of this kind,
a great discovery was made that's not going to fade."

Klir, George J.

This Chapter demonstrates the application of the theory of fuzzy sets to generate and combine multi-class spatial evidences for geologically-constrained mineral potential mapping. Portions of this Chapter have been published as Geologically-Constrained Fuzzy Mapping of Gold Mineralization Potential, Baguio District, Philippines (Carranza and Hale, 2001b).

8.1 INTRODUCTION

Using binary predictor patterns for mapping mineral potential assumes a crisp boundary between favourable and unfavourable ground (e.g., Bonham-Carter et al., 1989; Carranza and Hale, 1999a, 2000). In most real cases, however, the boundary between grounds that are favourable and unfavourable for the occurrence of mineralisation is imprecise and thus fuzzy. Classifying mineral potential, therefore, requires a method capable of using imprecise concepts where a precise boundary membership or non-membership in a class of spatial evidence of mineral potential may be impossible or impractical. One such method is the application of the Dempster-Shafer evidential belief theory (Moon, 1989, 1990; Moon et al., 1991; An et al., 1992; Carranza and Hale, 2001a). An et al. (1994) show that representation of multi-class sets of spatial evidences of mineral potential using evidential belief functions can only be either data-driven or knowledge-driven (although in Chapter 5 an approach involving incorporation of knowledge to assign weights to multi-class spatial evidences derived through data-driven quantification of spatial associations between mineral deposits and geological features is demonstrated for mapping mineral potential). A partly knowledge-driven and partly data-driven approach to map mineral potential based on multi-class spatial evidences is feasible by the application of the theory of fuzzy sets (Zadeh, 1965).

There are a few of examples of partly knowledge-driven and partly data-driven applications of the theory of fuzzy sets to mineral potential mapping. Gettings and Bultman (1993) applied the possibility theory from fuzzy logic to the

quantification of favourableness of quartz-carbonate vein deposits in southeast Arizona. They defined conditions necessary for the formation of the deposits and represented each condition as a fuzzy set enumerated in a grid over the area. The intersection of the fuzzy sets measures the degree of simultaneous occurrence of the necessary conditions and provides a measure of the possibility of deposit occurrence. The example of Gettings and Bultman (1993) is based mainly on rock units and their genetic rather than spatial relationships to the known Ag-Pb vein-type deposits; the fuzzy membership functions of the different rock units were subjectively assigned. Cheng and Agterberg (1999) developed a weights of evidence approach based on fuzzy sets and fuzzy probabilities for mineral potential mapping. Instead of separating spatial evidences of mineralisation into binary or ternary form, they created fuzzy sets that contain genetic elements. They then defined fuzzy probabilities to construct a model for calculating the posterior probability of a unit area containing mineralisation based on the fuzzy evidence for a unit area. Since in weights of evidence modeling the requirement of conditional independence among the spatial evidences is not always satisfied (see Chapter 6), Knox-Robinson (2000) developed a new technique called vectorial fuzzy logic, based on fuzzy logic principles, for the integration of spatial data for enhanced mineral prospectivity mapping in the Kalgoorlie Terrane, Western Australia. The technique, based on vector mathematics, differs from existing methods of spatial data integration (e.g., Boolean logic, index-overlay, weights of evidence) in that it displays prospectivity as a continuous surface and allows a measure of confidence to be incorporated. The vectorial fuzzy logic technique of Knox-Robinson (2000) involves the subjective assignment of fuzzy prospectivity weights and fuzzy measures of confidence weights based on 80 deposits with known production of >500 kg gold. The method of Knox-Robinson (2000) is thus applicable to areas with well-known deposits (i.e., with production data) but is not readily applicable to the study areas in this work. The work presented is similar to the work of Wright and Bonham-Carter (1996) although here the subjective assignment of fuzzy membership values is based on quantified spatial associations between mineral deposits and geological variables (Carranza and Hale, 2001g).

8.2 FUZZY SETS

In classical set theory, the membership of an object in a set of objects is defined as complete (=1) or non-complete (=0). In fuzzy set theory, a fuzzy set is defined as a subset of objects whose membership in a set of objects is intermediate between complete membership and non-complete membership (Zadeh, 1965). Fuzzy sets are represented by means of membership functions. A membership function, $\mu_A(x)$, is a mapping of the fuzzy membership of x from the universe of discourse X into the unit interval [0,1], thus

$$\mu_A(x) : X \rightarrow [0,1] . \qquad (8\text{-}1)$$

The grade of membership is large (classically equal to 1) for objects that completely belong to the fuzzy set; it is small (classically equal to 0) for objects that do not completely belong to the fuzzy set. For a particular object or class of objects, the more completely it belongs to the fuzzy set, the closer its membership grade is to 1. Thus, individual objects or classes of objects represented in maps can be evaluated regarding their membership in a fuzzy set of geological objects, based on a subjective judgment. Grade of membership is usually represented by a membership function that need not be linear or even continuous; indeed, many fuzzy sets have extremely nonlinear membership functions (Zimmerman, 1991). The membership always relates to a certain proposition. In mineral exploration, the proposition is "favourable location for mineral deposit".

For the examples demonstrated here, one large set used is the set of distances from curvi-linear or point geological features. The subset is the distances, X, from a particular curvi-linear or point geological feature. Hence, employing the theory of fuzzy sets introduced by Zadeh (1965), the class "favourable distance", d, translates into a series of measures (x) such that:

$$d = \{(x,\ \mu_d(x)) | x \in X\} \tag{8-2}$$

where $\mu_d(x)$ defines a grade of membership of distance x in the class "favourable distance".

The other large sets used in this study are the sets of lithologic units and hydrothermal alteration units. The subset is the lithologic units or hydrothermal alteration units, Y, in the study area. Similarly, the class "favourable lithology" or "favourable hydrothermal alteration", l, translates into a series of measures (y) such that

$$l = \{y,\ \mu_l(y)) | y \in Y\}, \tag{8-3}$$

where $\mu_l(y)$ defines a grade of membership of lithologic formation or hydrothermal alteration y in the class "favourable lithology" or "favourable hydrothermal alteration".

As in classical set theory, set-theoretic operations can be defined or performed on fuzzy sets, including equality, containment, union and intersection, all of which have meanings analogous to their crisp set equivalents. Zadeh (1965, 1973, 1983) and Zimmerman (1991) discuss a variety of fuzzy operations. An et al. (1991) discuss five of the various fuzzy operators that are useful for combining mineral exploration datasets, namely the fuzzy AND, fuzzy OR, fuzzy algebraic product, fuzzy algebraic sum and fuzzy γ-operator.

The fuzzy AND operation is equivalent to a Boolean AND (logical intersection) operation on classical set values of 1 and 0. It is defined as

$$\mu_{\text{combination}} = \text{MIN}(\mu_A, \mu_B, \mu_C, \ldots), \tag{8-4}$$

where μ_A is the fuzzy membership value for map A at a particular location, μ_B is the fuzzy membership value for map B, and so on. The effect of this operation is that the output map is controlled by the smallest (minimum) fuzzy membership value occurring at each location. The fuzzy AND operation is appropriate where two or more pieces of evidence for a hypothesis must be present together for the hypothesis to be accepted.

The fuzzy OR is like the Boolean OR (logical union) whereby the output fuzzy membership values are controlled by the maximum values of any of the input maps, for any particular location. The fuzzy OR is defined as

$$\mu_{\text{combination}} = \text{MAX}(\mu_A, \mu_B, \mu_C, \ldots). \tag{8-5}$$

This operator can be, in some circumstances, reasonable for mineral potential mapping where favourable evidences for the occurrence of mineralisation are rare and the presence of any evidence may be sufficient to suggest favourability.

The fuzzy algebraic product is defined as

$$\mu_{\text{combination}} = \prod_{i=1}^{n} \mu_i, \tag{8-6}$$

where μ_i are the fuzzy membership values for the i-th (i=1,2,... n) maps that are to be combined. The combined fuzzy membership values tend to be very small with this operator, due to the effect of multiplying several numbers less than 1. The output is always smaller than, or equal to, the smallest contributing fuzzy membership value, and is thus 'decreasive'.

The fuzzy algebraic sum operator is complementary to the fuzzy algebraic product, and is defined as

$$\mu_{\text{combination}} = 1 - \prod_{i=1}^{n} (1 - \mu_i). \tag{8-7}$$

The result of this operation is always larger than, or equal to, the largest contributing fuzzy membership value. The effect is thus 'increasive'. Two or more pieces of evidence that both favour a hypothesis reinforce one another and

the combined evidence is more supportive than either piece of evidence taken individually.

The fuzzy "γ-operator" (Zimmerman and Zysno, 1980) is defined as

$$\mu_{\text{combination}} = \left(\prod_{i=1}^{n} \mu_i\right)^{1-\gamma} \left(1 - \prod_{i=1}^{n} (1-\mu_i)\right)^{\gamma} \quad . \tag{8-8}$$

This "γ-operator" is obviously a combination of the fuzzy algebraic product (Equation 8-6) and the fuzzy algebraic sum (Equation 8-7), where γ is a parameter in the range zero to one. When γ is equal to one, the combination is the same as the fuzzy algebraic sum; when γ is equal to zero, the combination equals the fuzzy algebraic product. The parameter indicates where the actual operator is located between the logical AND and OR.

Two or more fuzzy sets combined by any one of the fuzzy operators yield a fuzzy set. In the following examples, the appropriate fuzzy sets of favourable distances to curvi-linear or point geological features, fuzzy sets of favourable lithologic units and hydrothermal alteration units were combined to produce a fuzzy set (or map) of zones of mineral potential (i.e., "favourable locations of mineral deposits").

8.3 APPLICATION OF FUZZY SETS IN A GIS ENVIRONMENT

8.3.1 Data inputs

The appropriate geoexploration-datasets (i.e., lithologic units, hydrothermal alteration units, faults/fractures, porphyry pluton contacts/centroids, batholithic pluton margins, locations of mineral deposits, topographic geoinformation) in the different study areas were used in mapping mineral potential in the five study areas through the application of the theory of fuzzy sets. A pixel size of 100x100 m was used in the GIS-based raster analyses.

8.3.2 Generation of fuzzy sets

To generate the fuzzy sets of favourable distances to curvi-linear or point geological features, the results of the spatial association analyses in Chapter 4 were used. Based on the quantified spatial associations between the mineral deposits and the curvi-linear or point geological features, multiple distance classes were defined and fuzzy membership values were assigned to these classes based on subjective judgment. The results of the spatial association analyses in Chapter 4 invariably show three different distances, but of similar regional exploration significance, within which the mineral deposits and the

curvi-linear or point geological features are spatially associated. For description purposes, these three distances, arranged from shortest to longest, are called 'A', 'B' and 'C'. The longest distance over which there is no spatial association - between a mineral deposit and a curvi-linear or point geological feature is called 'D'. In the case of positive spatial association, the class for distance 'A' was given the highest fuzzy membership value of 0.9, the class for the distance interval 'B' minus 'A' was given a fuzzy membership value of 0.8 and the class for the distance interval 'C' minus 'B' was given a fuzzy membership value of 0.7. If all three distances are equal, then only a fuzzy membership value of 0.9 was assigned. If 'A' and 'B' are equal, a fuzzy membership value of 0.9 was assigned; the distance interval 'C' minus 'B' (or 'A') was given assigned a fuzzy membership value of 0.8. If 'B' and 'C' are equal, the distance interval 'B' (or 'C) minus 'A' was assigned a fuzzy membership value of 0.8. In the case of negative spatial association, the scheme of assigning fuzzy membership values to the distance classes was reversed accordingly. Whether the spatial association is positive or negative, the distance interval 'D' minus 'C' was divided subjectively into a number of classes, which were assigned gradually decreasing fuzzy membership values in the range of 0.4 to 0.1 from 'C' to 'D'. The class for distance beyond 'D' was assigned a fuzzy membership value of 0.1.

Fuzzy sets of favourable lithologic units and hydrothermal alteration units were generated by assigning subjective scores between 0 and 1 to the different map units depending on whether or not they are known to be genetically associated with the mineral deposits or not. Lithologic units known to be host rocks of the mineral deposits considered were assigned a fuzzy membership value of 0.9. Lithologic units that are potential host rocks according to conceptual mineral deposit models but are not known to host the mineral deposits considered were assigned a fuzzy membership value of 0.5. Lithologic units that are not potential host rocks and not known to host the mineral deposits considered were assigned a fuzzy membership value of 0.1. Similar subjective judgment is employed to assigning fuzzy membership values to remotely-detected hydrothermal alteration units. However, the accuracy of the hydrothermal alteration classification (see Chapter 3) was considered in the assignment of fuzzy membership values. The fuzzy membership values initially assigned to particular hydrothermal alteration units (i.e., by similar subjective assignment of fuzzy membership values to lithologic units) were multiplied by the average accuracy of the hydrothermal alteration classification map to derive the fuzzy membership values used in predictive mapping of mineral potential.

Fuzzy membership values of 0.0 and 1.0 were not assigned because it is never certain that a given class (distance interval to curvi-linear or point geological features, lithologic unit, hydrothermal alteration unit, etc.) is totally unfavourable or totally favourable for the occurrence of mineral deposits. Other conditions may be present within such classes to make them more or less favourable.

8.3.3 Integration of fuzzy sets

Fuzzy sets can be combined altogether using one fuzzy operator or a variety of different fuzzy operators. In the following examples, the fuzzy sets of geological evidences were combined in a number of steps that represent intermediate hypotheses regarding the mode of formation of the mineral deposits considered. Schematic inference networks depicting the intermediate hypotheses are drawn for predicting mineral potential using fuzzy logic as the 'inference engine'.

8.4 APPLICATION TO BENGUET PROVINCE

The spatial evidences used in the predictive mapping of porphyry copper potential in the province include lithologic units, hydrothermal alteration units, strike-slip fault discontinuities, porphyry pluton centroids and batholithic pluton margins. The predictive mapping of porphyry copper potential was based on the same subset of 23 'model' porphyry copper deposits used in the weights of evidence modeling (see Section 6.4). The subset of eight 'validation' porphyry copper deposits was used to validate the predictive model(s).

8.4.1 Fuzzy sets of evidences of porphyry copper potential

Summarised in Table 8.1 are the quantified spatial associations between the known porphyry copper deposits and the curvi-linear or point geological features in the province. The quantified spatial associations by the weights of evidence method are derived from Table 6.3 (sub-section 6.4.1). The quantified spatial associations by the distance distribution method and the distance correlation method are the same as those given in Section 4.3 (although separate extensive tables and graphs used for the subset of 'model' porphyry copper deposits are not shown here).

Table 8.1. Quantified spatial associations between 'model' subset of porphyry copper deposits and curvi-linear or point geological features, Benguet province.

Geological feature	Quantified spatial association (m)			Farthest distance between geological feature and porphyry copper deposit (m)
	By weights of evidence method	By distance distribution method	By distance correlation method	
Strike-slip fault discontinuities	3000 (+)	2800 (+)	2250 (+)	4627
Batholithic pluton margins	2250 (+)	1000 (-)	2000 (-)	4472
Porphyry pluton centroids	1000 (+)	1300 (+)	4000 (+)	19496

(+) = positive spatial association within distance; (-) = negative spatial association within distance.

Table 8.2. Distance and unit classes and fuzzy membership scores for the different curvi-linear or point geological features, lithologic formations and hydrothermal alteration units, Benguet province.

Strike-slip fault discontinuities		Batholithic pluton margins		Porphyry pluton centroids		Lithologic formations (Figure 2.5)		Hydrothermal alteration units (Figure 3.24)	
Distance class (km)	Fuzzy score	Distance class (km)	Fuzzy score	Distance class (km)	Fuzzy score	Unit* class	Fuzzy score	Unit** class	Fuzzy score
<2.25	0.9	<1	0.7	<1	0.9	LMPIP	0.9	AA	0.48
2.25-2.8	0.8	1-2	0.8	1-1.3	0.8	LMPCV	0.5	I	0.54
2.8-3	0.7	2-2.25	0.9	1.3-4	0.7	ML	0.1	P	0.54
3-4	0.3	2.25-3	0.4	4-7	0.3	OMMBI	0.9	U	0.01
4-4.65	0.2	3-3.75	0.3	7-10	0.2	EMVR	0.9	W	0.01
>4.65	0.1	3.75-4.5	0.2	10-19.5	0.1	CPM	0.9	C	0.01
		>4.5	0.1	>19.5	0.1				

*LMPIP = L. Miocene – Pleistocene Intrusive Porphyries; LMPCV = L. Miocene – Pliocene Clastics/Volcanics; ML = Miocene Limestones; OMMBI = Oligocene – M. Miocene Batholithic Intrusives; EMVR = Eocene – Miocene Volcaniclastic Rocks; CPM = Cretaceous-Paleogene Metavolcanics.

**AA = advance argillic; I = illitic; P = Propylitic; U = Unaltered; W = Water; C = Clouds.

The fuzzy membership values for the different sets of spatial evidences of porphyry copper potential are given in Table 8.2. The fuzzy sets of increasing distances within the range of optimal positive spatial association of the 'model' deposits with the strike-slip fault discontinuities and the porphyry pluton centroids were assigned decreasing fuzzy membership values of 0.9 to 0.7. The fuzzy sets of increasing distances within the range of optimal negative spatial association of the 'model' deposits with the batholithic pluton margins were assigned increasing fuzzy membership values of 0.7 to 0.9. The fuzzy sets of increasing distances beyond the range of optimal spatial associations of the 'model' deposits with the curvi-linear or point geological features were assigned decreasing fuzzy membership values in the range of 0.4 to 0.1. Those lithologic formations in the province that are genetically associated with the porphyry copper deposits were given the highest fuzzy membership value of 0.9. The Lower Miocene to Pliocene clastic/volcaniclastic rocks are potential host rocks but are not known to host porphyry copper deposits; they were given an intermediate fuzzy membership value of 0.5. The Miocene Limestones were given the lowest fuzzy membership value; they are not known to host porphyry copper deposits and have more potential for skarn deposits rather than porphyry copper deposits. Among the remotely-detected hydrothermal alteration units, the illitic and propylitic alterations are most important and a fuzzy membership value of 0.9 would have been assigned had the accuracy of their remote detection been better than 85%. The accuracy of their remote detection is on average 60% so that a fuzzy score of 0.54 (i.e., 0.9 x 0.6) was assigned to the illitic and propylitic alteration units. The advanced argillic alteration was assigned a fuzzy membership of 0.48 (i.e., 0.8 x 0.6) because of its lesser importance. The maps of fuzzy membership values are shown in Figure 8.1.

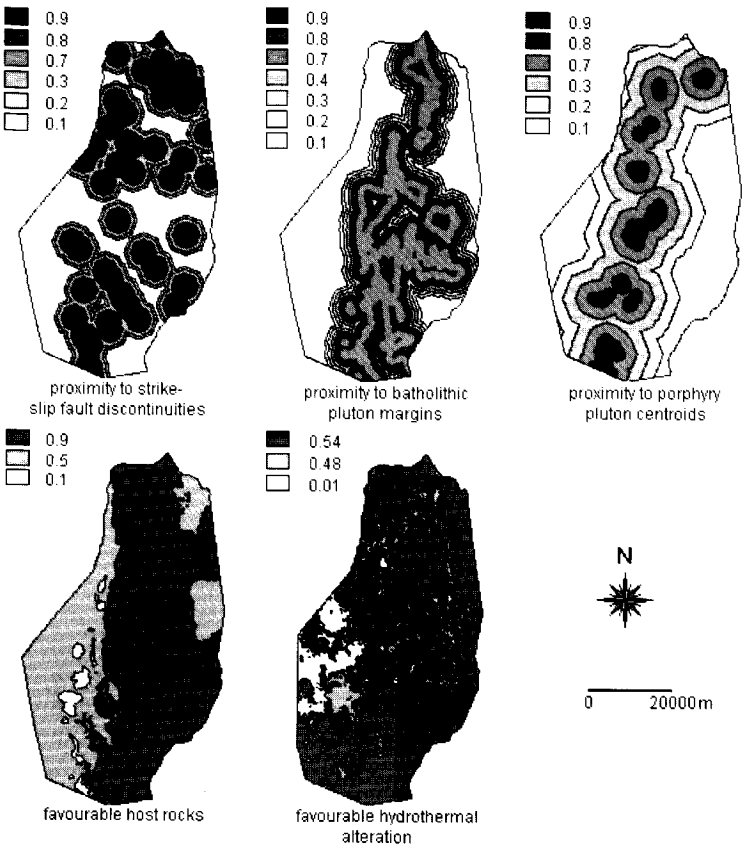

Figure 8.1. Maps of fuzzy membership values of sets of spatial evidences for predicting epithermal porphyry copper potential, Benguet province.

8.4.2 Integration of fuzzy sets of evidences of porphyry copper potential

The fuzzy sets are combined in a number of steps to represent intermediate hypotheses regarding the geological significance of the spatial evidences of porphyry copper potential. There are three hypotheses. First, the combined occurrences of the batholithic plutons, the porphyry plutons and the strike-slip fault discontinuities provide evidence for favourable zones of porphyry plutons emplacement. Second, the combined occurrences of favourable host rocks and hydrothermal alteration provide evidence for favourable zones of hydrothermal systems. Third, the combined occurrences of favourable zones of porphyry pluton emplacement and hydrothermal systems indicate zones of porphyry copper potential.

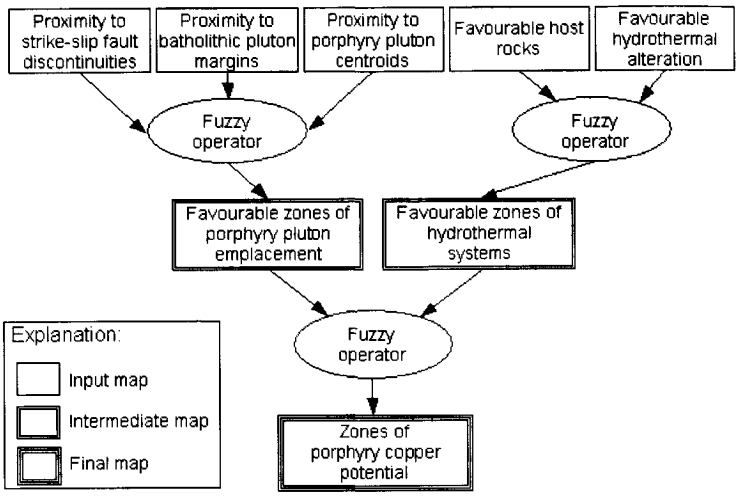

Figure 8.2. Schematic inference network for generating fuzzy predictive map of porphyry copper potential, Benguet province.

Figure 8.2 shows the inference network based on the three hypotheses to predict porphyry copper potential using fuzzy logic as the 'inference engine'. For the first hypothesis, the input maps of fuzzy scores for proximity to strike-slip fault discontinuities, batholithic pluton margins and porphyry pluton centroids were combined to derive an output map of evidence for favourable zones of porphyry pluton emplacement. For the second hypothesis, the input maps of fuzzy scores for favourable host rocks and hydrothermal alteration were combined to derive an output map of evidence of hydrothermal systems. For the third hypothesis, the intermediate output maps of favourable zones of porphyry pluton emplacement and of hydrothermal systems were combined to derive a map of zones of porphyry copper potential.

8.4.3 Fuzzy predictive mapping of porphyry copper potential

It is evident from Figure 8.2 that there are several possible combinations of fuzzy operations to integrate the fuzzy input maps in order to derive a final fuzzy membership map of favourable zones of porphyry copper potential. Several experiments were performed to produce a final fuzzy membership map that best predicts zones favourable for porphyry copper mineralisation. Prior to selecting the best predictive map, two criteria were used to select the best 'intermediate hypothesis' maps. First, the favourable zones depicted by the 'intermediate hypothesis' maps are characterised by a fuzzy score of ≥ 0.7. This criterion is based subjectively on visual inspection of the input fuzzy membership maps in Figure 8.1 and based on the expectation of fuzzy scores of 0.72 (i.e., 0.9 x 0.8).

Second, the favourable zones depicted by the 'intermediate hypothesis' maps contain at least 80% of the porphyry pluton centroids and the porphyry copper deposits used to generate the spatial association model. This criterion is formulated to give the 'intermediate hypothesis' maps a high predictive strength for delineating favourable zones of porphyry copper potential.

Three criteria were used to select the best predictive map of porphyry copper potential. The first criterion is that the favourable zones are characterised by a fuzzy score of ≥ 0.7. This criterion is based subjectively on visual inspection of the input fuzzy membership maps (Figure 8.1) and on the expectation of 0.72 (i.e., 0.9 x 0.8). The second criterion is that the favourable zones occupy at most 25% of the province. This criterion is based on point pattern analysis of the 'model' deposits (see Figure 7.1). Using a buffer distance of 3.6 km, which corresponds to a 70% probability that a porphyry copper deposit will be found nearby another porphyry copper deposit, results in 'mineralised zones' that occupy about 23% of the province (Figure 8.3). The third criterion is that the favourable zones predict at least 70% of the 'model' deposits and at least 60% of the 'validation' deposits. These prediction rates were considered adequate inasmuch as only geological evidences were used. The third criterion is based on (a) the 70% probability of a porphyry copper deposit within 3.6 km of another porphyry copper deposit and (b) the 62% prediction rate of the 'mineralised zones' based on the 'validation' copper deposits.

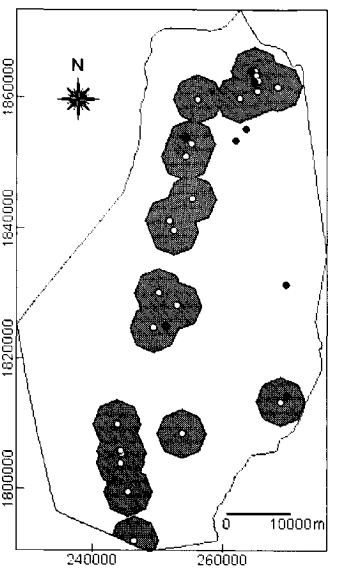

Figure 8.3. 'Mineralised zones' (grey areas) defined by 3.6 km buffer around 'model' deposits (unfilled circles), Benguet province. Filled circles = 'validation' deposits.

Of the several experimental combinations of fuzzy operations tested to produce a final predictive map, the predictive map resulting from the inference network shown in Figure 8.4 was considered optimal. The predictive map indicates that about 26% of the province has potential for porphyry copper deposits (Figure 8.5). It predicts correctly about 74% of the 'model' deposits and about 62% of the 'validation' deposits. The areas of overlap between the predicted favourable zones and the geochemically-anomalous catchment basins probably represent the sources of the geochemical anomalies because these areas are headwater portions of the geochemically-anomalous catchment basins.

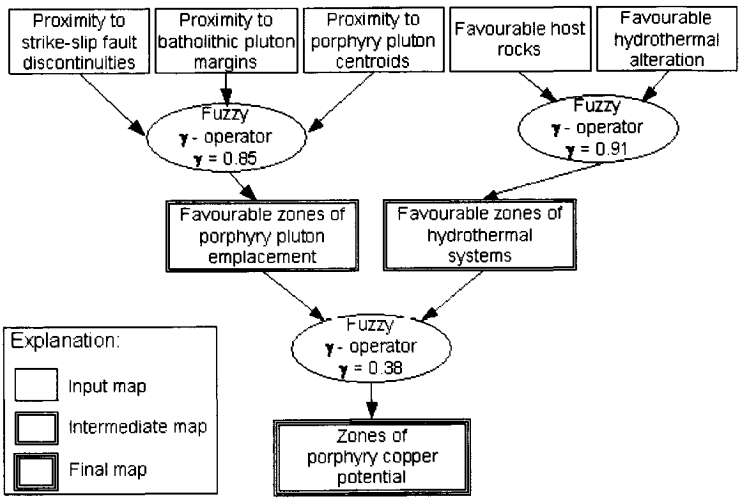

Figure 8.4. Inference network for producing predictive map of porphyry copper potential (Figure 8.5) inclusive of fuzzy set of hydrothermal alteration evidence, Benguet province.

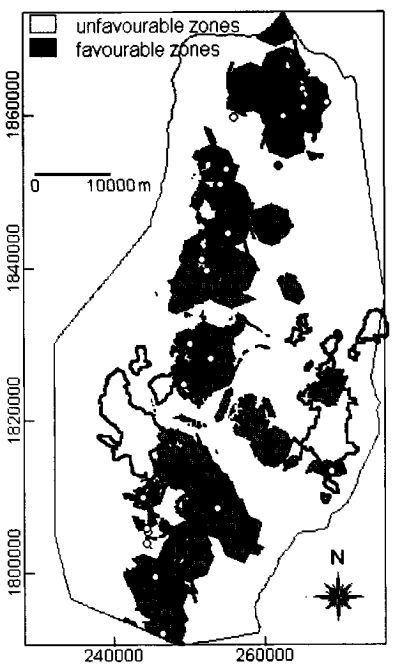

Figure 8.5. Predictive map of porphyry copper potential, Benguet province, inclusive of fuzzy set of hydrothermal alteration and based on inference network in Figure 8.4. Unfilled circles = 'model' deposits; filled circles = 'validation' deposits; polygons in solid lines = geochemically-anomalous catchment basins.

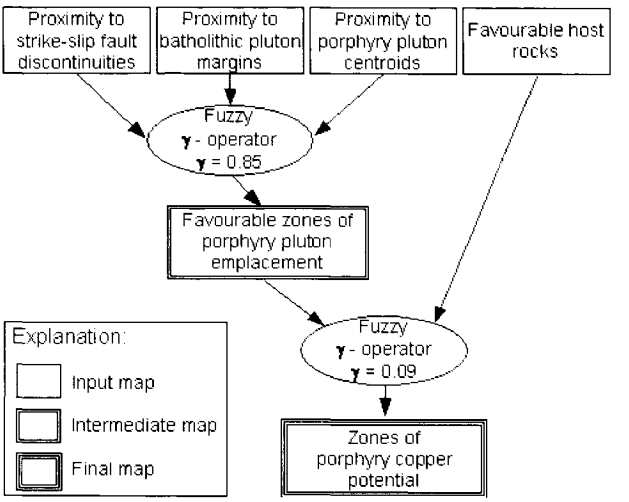

Figure 8.6. Inference network for producing predictive map of porphyry copper potential (Figure 8.7) exclusive of fuzzy set of hydrothermal alteration evidence, Benguet province.

Because of the poor accuracy of the map of remotely-detected hydrothermal alteration zones, its contribution to the predictive mapping of porphyry copper potential in the province was evaluated. The fuzzy set of favourable hydrothermal alteration was removed from the analysis. Again, several experimental combinations of fuzzy operations were tested to produce an optimal predictive map exclusive of the fuzzy set of hydrothermal alteration. The criteria mentioned above, were again applied to select the best fuzzy predictive map. The inference network in Figure 8.6 resulted in the best predictive map exclusive of the fuzzy set of hydrothermal alteration. The best predictive map exclusive of the fuzzy set of hydrothermal alteration indicates that about 26% of the province has potential for porphyry copper deposits (Figure 8.7). It predicts correctly about 57% of the 'model' deposits and about 62% of the 'validation' deposits. The predicted favourable zones show overlap areas with the geochemically-anomalous catchment basins similar to those mapped with inclusion of the fuzzy set of remotely-detected hydrothermal alteration.

8.4.4 Discussion

The subjective criteria applied to select the best 'intermediate hypotheses' and fuzzy predictive maps are guided by geological knowledge and experience in mineral exploration. These criteria were necessary to ensure that favourable zones are not over-predicted. Experience in mineral exploration shows that favourable grounds are quite rare. Indeed, it can be argued that a 25% area limit of favourable zones is quite high and a smaller area would mean higher

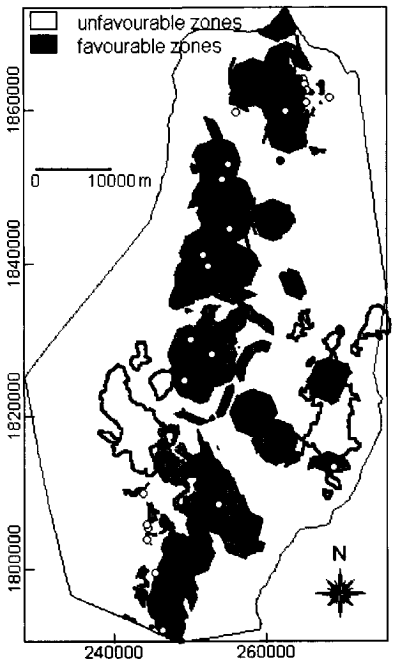

Figure 8.7. Predictive map of porphyry copper potential, Benguet province, exclusive of fuzzy set of hydrothermal alteration and based on inference network in Figure 8.6. Unfilled circles = 'model' deposits; filled circles = 'validation' deposits; polygons in solid lines = geochemically-anomalous catchment basins.

probability of finding a mineral deposit. However, the 25% area limit corresponds to at least 70% probability of finding a mineral deposit, which is here considered adequate. Similarly, the criteria of low prediction rates are based on the fact that few and only geological evidences are used to map favourable zones of porphyry copper potential.

Subjective as the criteria applied may be, the resulting inference network that produced the best fuzzy predictive map (Figure 8.5) is geologically sound. The fuzzy sets of proximity to strike-slip fault discontinuities, batholithic pluton margins and porphyry pluton centroids are best combined by using only the fuzzy γ-operator to produce an intermediate hypothesis map of favourable zones of porphyry pluton emplacement. The high γ of 0.85 implies a dominant effect of the fuzzy algebraic sum operator, which is appropriate for combining evidences that complement one another in support of a particular proposition. The batholithic plutons probably acted as effective buttresses to later ascent of porphyry plutons that were then localised at or near strike-slip fault discontinuities.

The fuzzy sets of favourable host rocks and hydrothermal alteration units are also best combined using the fuzzy γ-operator to produce an intermediate hypothesis map of favourable zones of hydrothermal systems. Again, the high γ of 0.91 implies a dominant effect of the fuzzy algebraic sum operator. The fuzzy sets of favourable host rocks and favourable hydrothermal units complement each other to delineate areas of favourable rock units that are hydrothermally-altered and areas of favourable rocks units that are not known to be mineralised but which have probably been affected by the hydrothermal systems. The intermediate hypothesis maps are also best combined using the fuzzy γ-operator. The low γ of 0.09 implies a dominant effect of the fuzzy algebraic product operator, which is appropriate where two or more pieces of evidences must be present together for a particular hypothesis to be supported. Indeed, the intermediate hypotheses or evidences of favourable zones of porphyry pluton emplacement and favourable zones of hydrothermal systems are together important to delineate zones that are favourable of porphyry copper deposits.

The fuzzy predictive map exclusive of the fuzzy set of hydrothermal alteration units is inferior to the predictive map inclusive of this fuzzy set. The former map has a poor prediction rate whilst the latter map has a good prediction rate based on the 'model' deposits. Thus, the map of remotely-detected hydrothermal alteration zones, albeit of marginal accuracy, proved useful in delineating zones of porphyry copper potential. It is particularly useful because in many areas of the province, such as in the Mankayan district, the porphyry copper deposits are buried beneath hydrothermally-altered rocks that do not host the mineralisation (Sillitoe and Angeles, 1985; Concepcion and Cinco, 1989).

8.5 APPLICATION TO BAGUIO DISTRICT

The spatial evidences used in the predictive modeling of epithermal gold potential are lithologic units, hydrothermal alteration units, batholithic pluton margins, porphyry pluton contacts, northeast-trending faults/fractures and northwest-trending faults/fractures. The quantified spatial associations of the 19 large-scale gold deposits with the curvi-linear or point geological features were used in generating the predictive model(s). The set of 63 small-scale gold deposits and the stream sediment geochemical anomalies (UNDP 1987a; see Section 2.3.3) were used to validate the predictive model(s).

8.5.1 Fuzzy sets of evidences of epithermal gold potential

Summarised in Table 8.3 are the quantified spatial associations between the 'model' large-scale gold deposits and the curvi-linear or point geological features in the district known to be associated genetically with the deposits. The quantified spatial associations are derived from Table 4.20 (see Section 4.4).

Table 8.3. Quantified spatial associations between model set of large-scale gold deposits and geological features, Baguio district.

Geological feature	Quantified spatial association (m)			Farthest distance between geological feature and gold deposit (m)
	By weights of evidence method	By distance distribution method	By distance correlation method	
NE-trending faults/fractures	400 (+)	400 (+)	400 (+)	1588
NW-trending faults/fractures	1300 (-)	1000 (-)	850 (-)	1800
Batholithic pluton margins	1000 (+)	400 (+)	950 (+)	2381
Porphyry pluton contacts	2750 (+)	2700 (+)	2800 (+)	5835

(+) = positive spatial association within distance; (-) = negative spatial association within distance.

The fuzzy membership values for the different sets of spatial evidences of epithermal gold potential are given in Table 8.4. The fuzzy sets of increasing distances within the range of optimal positive spatial associations of the 'model' deposits with the northeast-trending faults/fractures, the batholithic pluton margins and the porphyry pluton contacts were assigned decreasing fuzzy membership values in the range of 0.9 to 0.7. The fuzzy sets of increasing distances within the range of optimal negative spatial association of the 'model' deposits with the northwest-trending faults/fractures were assigned decreasing fuzzy membership values in the range of 0.6 to 0.9. The fuzzy sets of increasing distances beyond the range of optimal spatial associations of the 'model' deposits with the curvi-linear geological features were assigned decreasing fuzzy membership values in the range of 0.4 to 0.1.

Table 8.4. Distance and unit classes and fuzzy membership scores for the different curvi-linear geological features, lithologic units and hydrothermal alterations units , Baguio district.

NE-trending faults/fractures		NW-trending faults/fractures		Batholithic pluton margins		Porphyry pluton contacts		Lithologic formations (Figure 2.11)		Hydrothermal alteration units (Figure 3.15b)	
Distance class (km)	Fuzzy score	Distance class (km)	Fuzzy score	Distance class (km)	Fuzzy score	Distance class (km)	Fuzzy score	Unit class*	Fuzzy score	Unit class**	Fuzzy score
<0.4	0.9	<0.85	0.6	<0.4	0.9	<0.95	0.9	LMKF	0.5	AA	0.3
0.4-0.8	0.8	0.85-1.0	0.7	0.4-0.95	0.8	0.95-1.9	0.8	LMPI	0.8	I	0.54
0.8-1.2	0.3	1.0-1.3	0.8	0.95-1.0	0.7	1.9-2.8	0.7	MMKF	0.1	P	0.3
1.2-1.6	0.2	1.3-1.45	0.9	1.0-1.45	0.4	2.8-3.85	0.3	LOMMAB	0.8	U	0.01
>1.6	0.1	1.45-1.6	0.3	1.45-1.9	0.3	3.85-4.85	0.2	LEEMZF	0.9	W	0.01
		1.6-1.8	0.2	1.9-2.4	0.2	4.85-5.85	0.1	CEPF	0.9		
		>1.8	0.1	>2.4	0.1	>5.85	0.1				

*LMKF = L. Miocene Klondyke Fm; LMPI = L. Miocene – Pleistocene Intrusives; MMKF = M. Miocene Kennon Fm; LOMMAB = L. Oligocene – M. Miocene Agno Batholith; LEEMZF = L. Eocene – E. Miocene Zigzag Fm; CEPF = Cretaceous - Eocene Pugo Fm.

**AA = advance argillic; I = illitic; P = Propylitic; U = Unaltered; W = Water; C = Clouds.

For the lithologic formations, the Zigzag and Pugo Formations are both given the highest fuzzy membership value of 0.9 because they are known to host the gold deposits in the district. The batholithic and porphyry plutons are both given lower fuzzy membership values of 0.8 because they are thought to be the heat sources for the mineralisation although it is known that these rock units also host gold deposits. The Klondyke formation is assigned a fuzzy membership of 0.5 because it could probably host gold mineralisation as it is also intruded by the porphyry plutons but it has not been reported to contain gold deposits. The Kennon limestones are given the lowest membership value of 0.1 because they are intruded neither by the batholithic plutons nor by the porphyry plutons and are not known to host gold deposits. Among the remotely-detected hydrothermal alteration units, the illitic alterations are most important and a fuzzy membership value of 0.9 would have been assigned had the accuracy of the remote detection been better than 85% (see sub-section 3.3.4). The accuracy of the remote detection is on average 60% so that a fuzzy score of 0.54 (i.e., 0.9 x 0.6) was assigned to the illitic alteration units. The advanced argillic and propylitic alteration units are assigned fuzzy membership values of 0.3 (i.e., 0.5 x 0.6) because of their lesser importance. The maps of fuzzy membership values are shown in Figure 8.8.

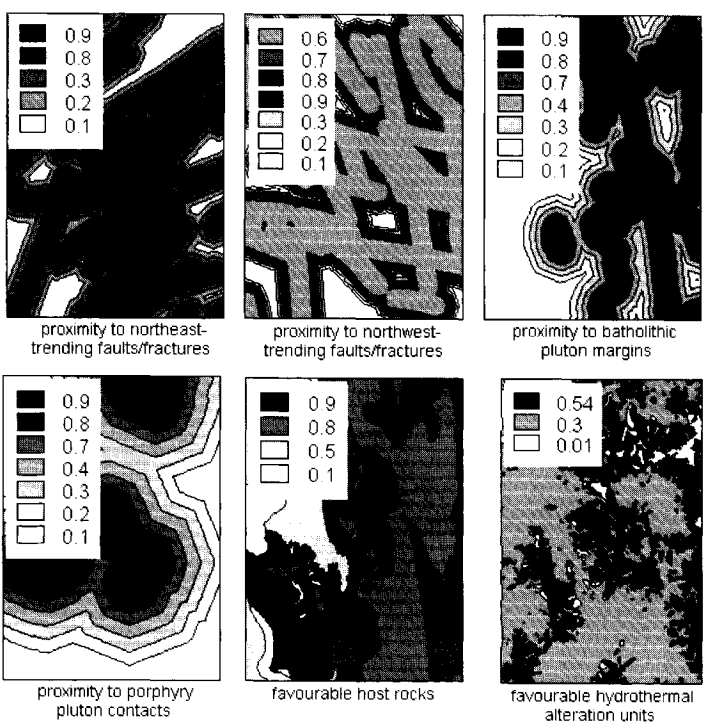

Figure 8.8. Maps of fuzzy membership values of sets of spatial evidences for predicting epithermal gold potential, Baguio district.

8.5.2 Integration of fuzzy sets of evidences of epithermal gold potential

The fuzzy sets of evidences of epithermal gold mineralisation were combined in a number of steps to represent intermediate hypotheses regarding the significance of the evidences for epithermal gold mineralisation. There are four intermediate hypotheses. First, the channelways for the mineralising solutions that brought about gold mineralisation in the district are the northeast-trending and/or the northwest-trending faults/fractures. Second, the heat sources for the epithermal gold mineralisation in the district are the batholithic plutons and/or the porphyry plutons. Third, the combination of favourable rock formations and favourable hydrothermal alterations provides evidence for favourable zones in the epithermal systems. Fourth, the combined occurrences of channelways for mineralising fluids, heat sources and favourable host rocks (that are later hydrothermally-altered) are essential for epithermal gold mineralisation.

Figure 8.9 shows the schematic inference network for predicting gold potential in the district. For the first hypothesis, the input maps of fuzzy scores of proximity to northeast-trending and northwest-trending faults/fractures were combined to derive a map of 'favourable fault/fracture zones'. For the second hypothesis, the input maps of fuzzy scores of proximity to the batholithic pluton margins and porphyry pluton contacts were combined to derive a map of 'favourable heat flow zones'. For the third hypothesis, the input maps of fuzzy scores of favourable lithologic formations and hydrothermal alterations were combined to derive a map of 'favourable zones of hydrothermal systems'. For the final hypothesis, the fuzzy maps of 'favourable fault/fracture zones', 'favourable heat flow zones' and 'favourable zones of hydrothermal systems' were combined to derive a final map of 'zones of epithermal gold potential'.

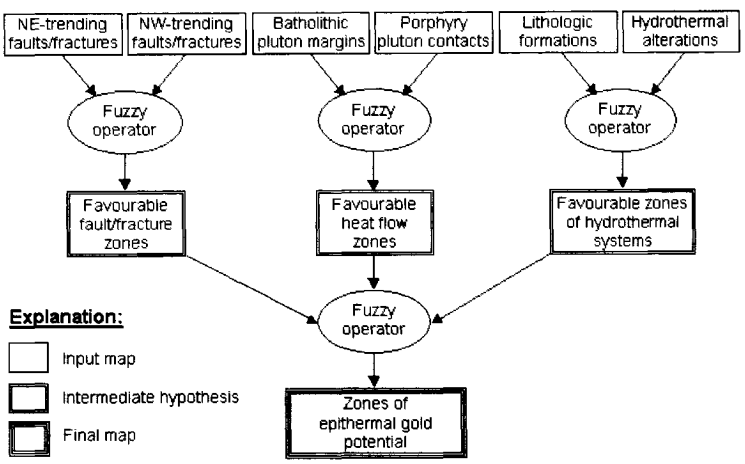

Figure 8.9. Schematic inference network for generating predictive map of epithermal gold potential, Baguio district.

8.5.3 Fuzzy predictive mapping of epithermal gold potential

From Figure 8.9, it is evident that several combinations are possible to derive an optimum final fuzzy membership map of 'zones of epithermal gold potential'. Several experiments were performed to produce an optimum predictive map. Three criteria were used to select the best predictive map. The first criterion is that the favourable zones are characterised by a fuzzy score of ≥ 0.7. This criterion is based on the expectation of fuzzy scores of 0.72 (i.e., 0.9 x 0.8). The second criterion is that the favourable zones occupy at most 24% of the district. This criterion is based on the geoinformation that the stream sediment geochemical anomalies cover an area of about 24% of the district (see Section 2.3.3; UNDP, 1987a). It is expected that surficial geochemical anomalies cover wider lateral extents than geological anomalies because the former represent dispersion of elements from the latter. The third criterion is that the favourable zones contain at least 68% of the 'model' large-scale gold deposits. This criterion is also based on the geoinformation that the stream sediment geochemical anomalies accurately reflect the location of about 68% of the large-scale deposits.

Of the various experimental combinations of fuzzy operations tested to produce a final map, the best predictive map is derived using the inference network shown in Figure 8.10a. The best predictive map is shown in Figure 8.11a. It delineates about 23% of the district as favourable for gold deposits, predicts at least 68% of the 'model' large-scale gold deposits and at least 77% of the 'validation' large-scale gold deposits (Table 8.5). There are three 'next best' predictive maps, which were derived using the inference networks shown in Figures 8.10b to 8.10d, and are shown in Figures 8.11b to 8.11d, respectively. The inference networks for deriving the best predictive maps and the 'next best' predictive maps are similar (as discussed below). Consequently, the predictive maps are similar. The 'next best' predictive maps have similar prediction rates to the best predictive but delineate more than 24% of the district as favourable for gold deposits.

Table 8.5. Spatial predictive characteristics of the predictive maps of gold potential, Baguio district, shown in Figure 8.11.

	Fuzzy predictive map			
	Figure 8.10a	Figure 8.10b	Figure 8.10c	Figure 8.10d
% predicted favourable zones	23.2	24.9	25.3	25.4
% 'model' deposits predicted	68.4	68.4	68.4	68.4
% 'validation' deposits predicted	77.8	77.8	77.8	76.2

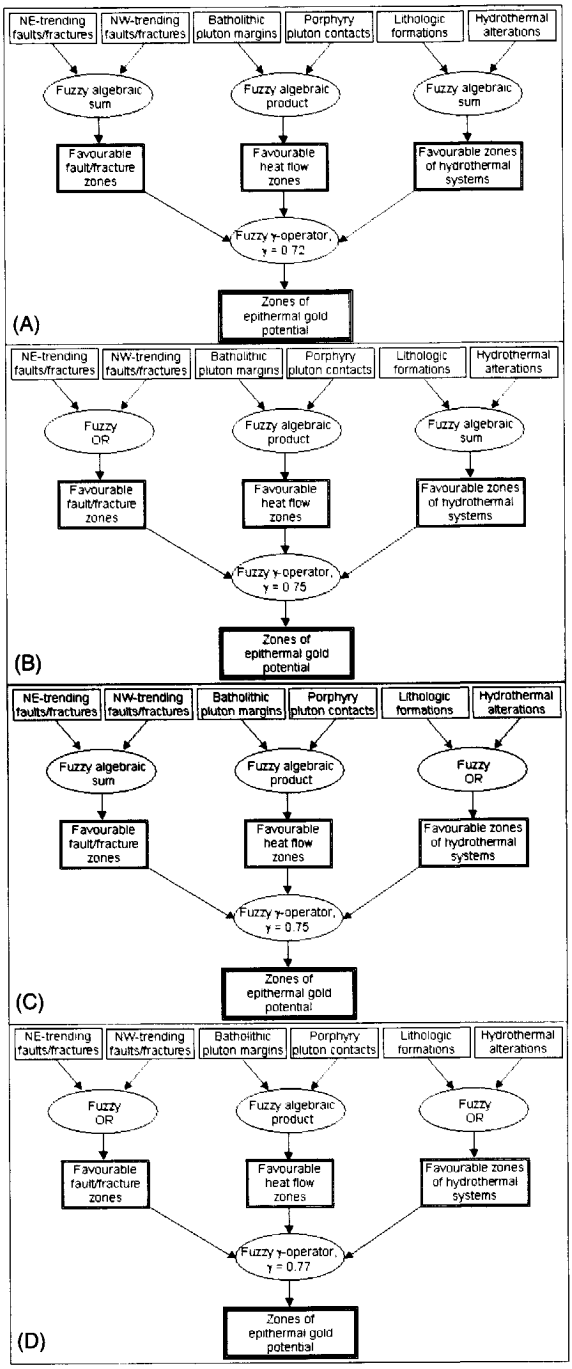

Figure 8.10. Inference networks used to predict gold potential of Baguio district: (a) resulting in Figure 8.11a; (b) resulting in Figure 8.11b; (c) resulting in Figure 8.11c and (d) resulting in Figure 8.11d.

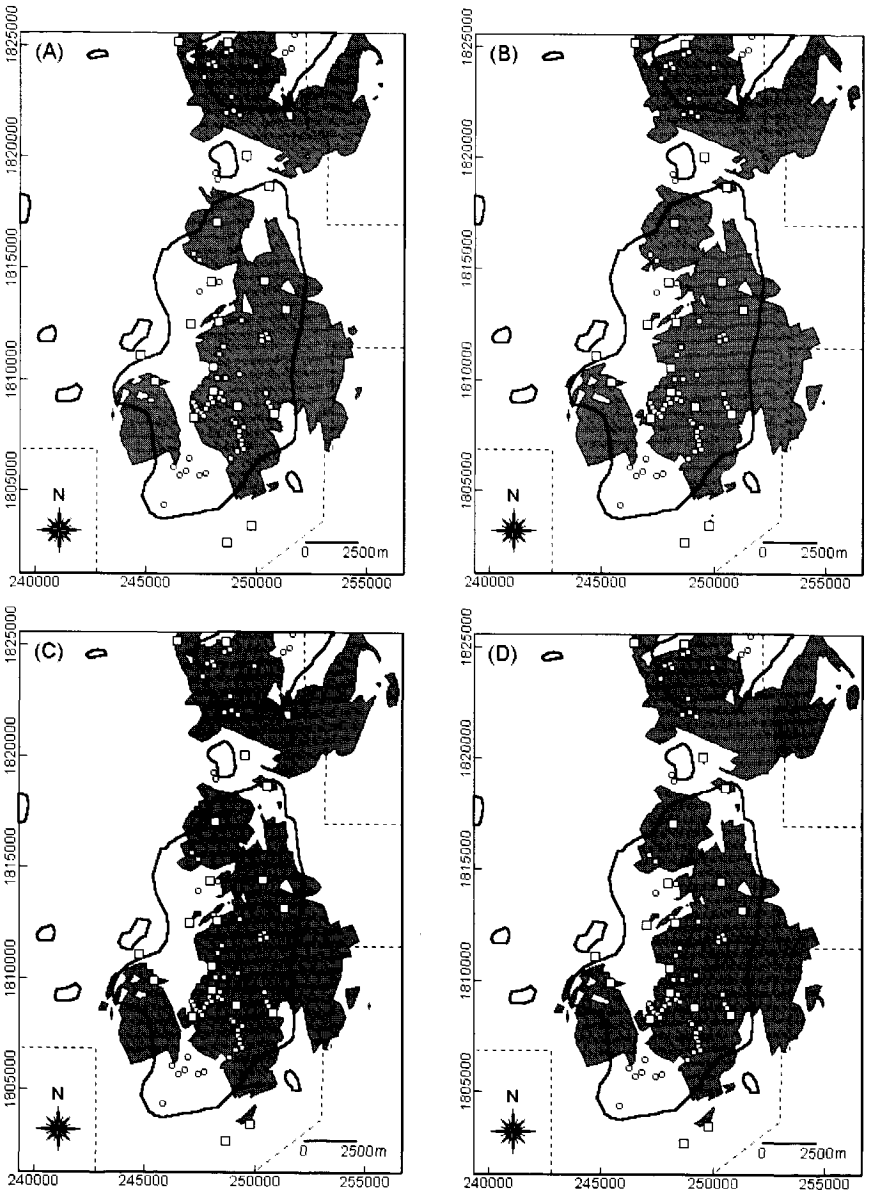

Figure 8.11. Predictive maps of gold potential, Baguio district, inclusive of hydrothermal alteration evidence: (a) result of inference network in Figure 8.10a; (b) result of inference network in Figure 8.10b; (c) result of inference network in Figure 8.10c; (d) result of inference network in Figure 8.10d. Grey-shaded areas = favourable zones; unfilled squares = 'model' large-scale gold deposits; small circles = 'validation' small-scale gold deposits; polygons in solid line = stream sediment Au anomaly; dashed line = boundary of geochemical survey (UNDP, 1987a).

Summarised in Table 8.6 are the percentages of the geochemically-anomalous zones delineated by the predictive maps. The predictive maps coincide with (or predict) about 50 to 60% of the zones that are anomalous for Au, Ag and Sb, and about 37 to 42% of the zones that are anomalous for As. The maps predict between 71 and 86% of the 'model' large-scale gold deposits delimited by the geochemical anomalies and between 75 and 92% of the 'validation' small-scale gold deposits delimited by the geochemical anomalies.

Table 8.6. Cross-table to compare predicted favourable zones (inclusive of hydrothermal alteration evidence) and geochemically-anomalous areas, Baguio district.

Fuzzy predictive map	Au geochemical anomaly (Fig. 2.13a)			Ag geochemical anomaly (Fig. 2.13b)			As geochemical anomaly (Fig. 2.13c)			Sb geochemical anomaly (fig. 2.13d)		
	% a.z.p.[1]	% m.d.p.[2]	% v.d.p.[3]	% a.z.p.[1]	% m.d.p.[2]	% v.d.p.[3]	% a.z.p.[1]	% m.d.p.[2]	% v.d.p.[3]	% a.z.p.[1]	% m.d.p.[2]	% v.d.p.[3]
Fig. 8.11a	54.5	78.6	78.9	50.0	71.4	77.6	37.8	76.9	80.8	50.1	81.8	91.9
Fig. 8.11b	58.3	78.6	78.9	53.5	71.4	77.6	41.0	76.9	80.8	52.5	72.7	91.9
Fig. 8.11c	59.4	85.7	78.9	54.8	71.4	77.6	41.6	76.9	80.8	52.5	81.8	91.6
Fig. 8.11d	59.2	78.6	77.2	54.5	71.4	75.9	41.5	76.9	78.4	52.4	72.7	89.2

[1]anomalous zones predicted; [2]'model' deposits predicted; [3]'validation' deposits predicted.

Summarised in Table 8.7 are the percentages of geochemically non-anomalous zones delineated by the predictive maps. The predictive maps delineate as favourable zones between 13 and 22% of the geochemically non-anomalous zones, depending on which element is considered. Between 20 and 63% of the 'model' large-scale gold deposits in geochemically non-anomalous zones are within the predicted geologically-favourable zones. Between 57 and 80% of the 'validation' small-scale gold deposits in geochemically non-anomalous zones are within the predicted geologically-favourable zones.

Table 8.7. Cross-table to compare predicted favourable zones (inclusive of hydrothermal alteration evidence) and geochemically non-anomalous areas, Baguio district.

Fuzzy predictive map	Au geochemical background (Fig. 2.13a)			Ag geochemical background (Fig. 2.13b)			As geochemical background (Fig. 2.13c)			Sb geochemical background (Fig. 2.13d)		
	% b.z.p.[1]	% m.d.p.[2]	% v.d.p.[3]	% b.z.p.[1]	% m.d.p.[2]	% v.d.p.[3]	% b.z.p.[1]	% m.d.p.[2]	% v.d.p.[3]	% b.z.p.[1]	% m.d.p.[2]	% v.d.p.[3]
Fig. 8.11a	13.0	40.0	66.7	13.8	60.0	80.0	16.8	50.0	68.7	19.6	50.0	57.7
Fig. 8.11b	14.0	40.0	66.7	14.8	60.0	80.0	17.8	50.0	68.7	21.1	62.5	57.7
Fig. 8.11c	14.2	20.0	66.7	14.9	60.0	80.0	18.2	50.0	68.7	21.7	50.0	57.7
Fig. 8.11d	14.3	40.0	66.7	15.0	60.0	80.0	18.2	50.0	68.7	27.7	62.5	57.7

[1]non-anomalous zones predicted; [2]'model' deposits predicted; [3]'validation' deposits predicted.

Because of the marginal accuracy of the remotely-detected hydrothermal alteration evidence, its contribution to the predictive mapping of epithermal gold potential in the district was evaluated. The fuzzy set of hydrothermal alteration was removed from the analysis. Similarly, several experimental combinations of

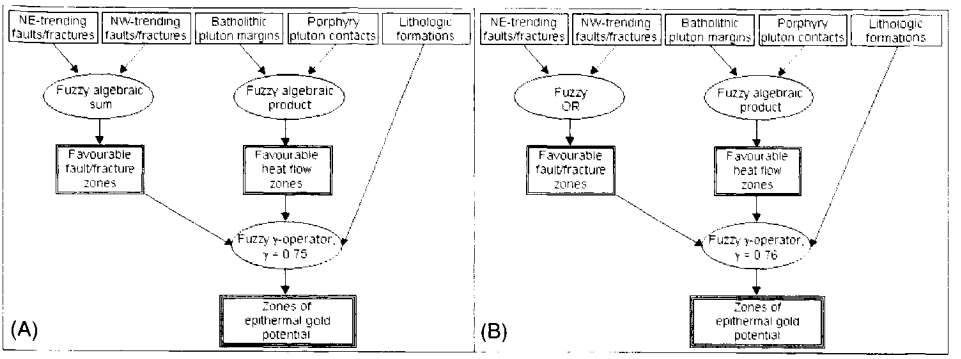

Figure 8.12. Inference networks used to predict gold potential of Baguio district exclusive of hydrothermal alteration evidence: (a) resulting in Figure 8.13a; (b) resulting in Figure 8.13b.

fuzzy operations were used to derive an optimum predictive map exclusive of the fuzzy set of hydrothermal alteration. The same criteria, mentioned above, were applied to select the best predictive map. There are two 'best' predictive maps, which were the products of similar inference networks shown in Figures 8.12a and 8.12b, and are illustrated in Figures 8.13a and 8.13b, respectively.

Both predictive maps, exclusive of the remotely-detected hydrothermal alteration evidence, delineate at least 25% of the district as favourable for epithermal gold deposits, predict at least 68% of the 'model' deposits and at least 76% of the 'validation' deposits. Specifically, the predictive maps in Figure 8.13a and 8.13b each have similar percentages of predicted favourable zones and the same prediction rates as the predictive maps in Figure 8.11c and 8.11d, respectively. The predictive maps exclusive of the remotely-detected hydrothermal alteration evidence show similar overlap zones between the geologically-favourable zones and the geochemically-anomalous areas and show similar geoinformation characteristics to the predictive maps inclusive of the remotely-detected hydrothermal alterations when compared with the stream sediment geochemical anomalies (Tables 8.8 and 8.9).

Table 8.8. Cross-table to compare predicted favourable zones (exclusive of hydrothermal alteration evidence) and geochemically-anomalous areas, Baguio district.

Fuzzy predictive map	Au geochemical anomaly (Fig. 2.13a)			Ag geochemical anomaly (Fig. 2.13b)			As geochemical anomaly (Fig. 2.13c)			Sb geochemical anomaly (fig. 2.13d)		
	% a.z.p.[1]	% m.d.p.[2]	% v.d.p.[3]	% a.z.p.[1]	% m.d.p.[2]	% v.d.p.[3]	% a.z.p.[1]	% m.d.p.[2]	% v.d.p.[3]	% a.z.p.[1]	% m.d.p.[2]	% v.d.p.[3]
Fig. 8.13a	59.2	85.7	78.9	54.8	76.9	91.8	41.5	76.9	80.8	52.5	81.8	91.9
Fig. 8.13b	59.2	78.6	77.2	54.5	76.9	91.8	41.5	76.9	78.7	52.3	72.7	89.2

[1]anomalous zones predicted; [2]'model' deposits predicted; [3]'validation' deposits predicted.

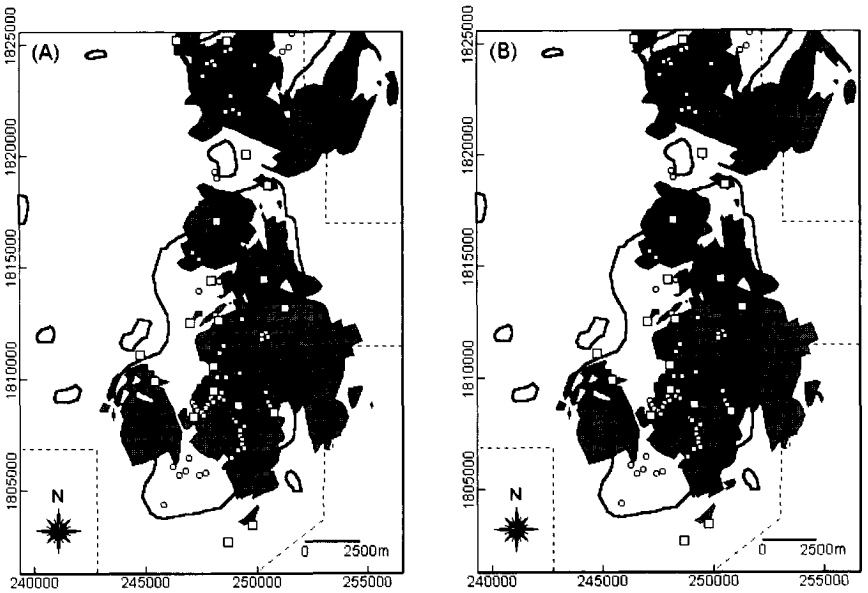

Figure 8.13. Predictive maps of gold potential, Baguio district, exclusive of hydrothermal alteration evidence: (a) result of inference network in Figure 8.12a; (b) result of inference network in Figure 8.12b. Grey-shaded areas = favourable zones; unfilled squares = 'model' large-scale gold deposits; small circles = 'validation' small-scale gold deposits; polygons in solid line = stream sediment Au anomaly; dashed line = boundary of geochemical survey (UNDP, 1987a).

The predictive maps, exclusive of the hydrothermal alteration evidence, delineate as geologically-favourable zones about 41 to 59% of the zones that are anomalous for As, Au, Ag and Sb (Table 8.8). The maps predict between 72 and 86% of the 'model' large-scale gold deposits delimited by the geochemical anomalies and between 77 and 92% of the 'validation' small-scale gold deposits delimited by the geochemical anomalies.

Table 8.9. Cross-table to compare predicted favourable zones (exclusive of hydrothermal alteration evidence) and geochemically non-anomalous areas, Baguio district..

Fuzzy predictive map	Au geochemical background (Fig. 2.13a)			Ag geochemical background (Fig. 2.13b)			As geochemical background (Fig. 2.13c)			Sb geochemical background (Fig. 2.13d)		
	% b.z.p.[1]	% m.d.p.[2]	% v.d.p.[3]	% b.z.p.[1]	% m.d.p.[2]	% v.d.p.[3]	% b.z.p.[1]	% m.d.p.[2]	% v.d.p.[3]	% b.z.p.[1]	% m.d.p.[2]	% v.d.p.[3]
Fig. 8.13a	14.2	20.0	66.7	14.8	66.7	92.6	18.1	50.0	68.7	21.6	50.0	57.7
Fig. 8.13b	14.3	40.0	66.7	15.0	66.7	93.3	18.1	50.0	68.7	21.6	62.5	57.7

[1]non-anomalous zones predicted; [2]'model' deposits predicted; [3]'validation' deposits predicted.

The predictive maps, exclusive of the hydrothermal alteration evidence, delineate as favourable zones between 14 and 22% of the geochemically non-anomalous zones, depending on which element is considered. The maps predict between 20 and 63% of the 'model' large-scale gold deposits in the geochemically non-anomalous areas and between 57 and 93% of the 'validation' small-scale gold deposits in the geochemically non-anomalous areas.

8.5.4 Discussion

The discriminant fuzzy score of 0.7 was chosen subjectively so that fewer areas are classified as favourable for gold potential, reflecting the fact that favourable ground is quite rare. Based on the results of previous geochemical exploration work in the district, two other criteria were applied to define geologically-unfavourable and geologically-favourable zones. First, the geologically-favourable zones should not be greater than the average area of the geochemical anomalies. Smaller areas generally mean higher probabilities for locating mineralisation. In addition, experience shows that significant geochemical anomalies have wider areal extent than the mineralised zones with which they are associated. Second, the geologically-favourable zones should predict a higher percentage of the known gold deposits.

The predictive maps show two zones favourable for gold deposits, one in the northern section and the other in the central section of the district. These two predicted geologically-favourable zones coincide spatially with the two main geochemically-anomalous areas (see Figure 2.12). The predictive maps not only demarcate a high percentage of the 'model' and 'validation' gold deposits but also demarcate a high percentage of the gold deposits delineated by the geochemical anomalies. These geoinformation characteristics demonstrate that the geologically-constrained fuzzy predictive mapping of gold potential is as useful or more useful than geochemical exploration techniques.

The inference networks (Figure 8.10) used to produce the best and 'next best' predictive maps inclusive of the remotely-detected hydrothermal alteration evidence (Figure 8.11) show a number of striking features. First, the fuzzy sets of igneous intrusive contact zones are best combined by using the fuzzy algebraic product operator. This operator is appropriate where two or more pieces of evidence for a hypothesis must be present together for the hypothesis to be supported. Indeed, both the Agno Batholith and the younger porphyry intrusives are together important for the epithermal gold mineralisation in the district (Fernandez and Damasco, 1979; Wolfe, 1988). Second, the fuzzy sets of fault/fracture zones are best combined by using either the fuzzy algebraic sum or the fuzzy OR operator. Likewise, the fuzzy sets of lithologic and hydrothermal alteration units are best combined by using either the fuzzy algebraic sum or the fuzzy OR operator. These operators are appropriate where two or more pieces of evidence complement one another, although the presence of any of the

evidence may be sufficient to suggest favourability. In the district, the northeast-trending faults are interpreted as conjugate shears with the northwest-trending faults/fractures (Balce et al., 1980). Hence, both sets of faults/fractures are complementary, although it is not necessary that both sets are present at a particular location for gold deposition to occur. The favourable lithologic and hydrothermal alteration units complement each other to delineate zones that represent portions of the epithermal systems that are genetically and spatially associated with the gold deposits. Third, the fuzzy sets of intermediate hypotheses are best combined by using the fuzzy γ-operator with very similar values of γ that range between 0.7 and 0.8. The values of γ used to produce the best and 'next best' predictive maps, inclusive of the remotely-detected hydrothermal alteration evidence, imply that the spatial evidences used complement one another and that they should not be taken individually. Indeed, all three intermediate evidences or factors used (i.e., heat sources, channelways and favourable portions of the epithermal systems) are important in mapping epithermal gold potential (White and Hedenquist, 1990; Mitchell and Leach, 1991; see also sub-sections 5.4.1 and 5.4.2).

The inference networks in Figures 8.12a and 8.12b (used to produce the best predictive maps exclusive of the remotely-detected hydrothermal alteration evidence in Figure 8.13a and 8.13b, respectively) are correspondingly similar to the inference networks in Figures 8.10c and 8.10d (used to produce the predictive maps inclusive of the remotely-detected hydrothermal alteration evidence in Figures 8.11c and 8.11d, respectively). Therefore, similar deductions made about the inference networks in Figures 8.10c and 8.10d can be made about the inference networks in Figures 8.12a and 8.12b, respectively, in regard to the implications of combining the structural, heat source and lithologic spatial evidences to map gold potential.

The predictive maps of gold potential exclusive of the fuzzy set of hydrothermal alteration units are inferior to the best predictive map inclusive of this fuzzy set. The predictive maps exclusive of the hydrothermal alteration evidence have more predicted favourable zones but with similar prediction rates based on the 'model' deposits and/or the 'validation' deposits as compared to the best predictive map inclusive of the hydrothermal alteration evidence. The results imply that, despite its marginal accuracy, the remotely-detected hydrothermal alteration evidence is useful in mapping epithermal gold potential in Baguio district. Hydrothermal alteration is a key to locating the main outflow zones of hydrothermal systems, which may lead to the recognition of mineral deposits (Lowell, 1991).

8.6 APPLICATION TO ABRA AREA

The spatial evidences used to map porphyry copper potential in the area include lithologic units, intersections of regional faults (i.e., north-trending and northeast-trending faults/fractures), porphyry pluton centroids, north-trending faults/fractures and granodiorite batholithic margins. The stream sediment Cu anomalies (see sub-section 2.4.4) were also used as a spatial evidence layer to determine whether integrated geochemical-geological predictive modeling is better than geologically-constrained predictive modeling. The quantified spatial associations of the 12 porphyry copper deposits with the curvi-linear or point geological features were used in the predictive modeling of porphyry copper potential. The known mineralised zones (sub-section 2.4.1; JICA, 1980) were used to validate the predictive model(s).

8.6.1 Fuzzy sets of evidences of porphyry copper potential

Summarised in Table 8.10 are the quantified spatial associations of the porphyry copper deposits with the curvi-linear or point geological features in the area. The quantified spatial associations are derived from Table 4.35 (see Section 4.5). It has been shown in Chapter 6 that curvi-linear or point geological features with negative spatial associations with the porphyry copper deposits are not important in predictive mapping of mineral potential. Hence, only those curvi-linear or point geological features with positive spatial associations with the porphyry copper deposits, as determined by the weights of evidence method, are considered here. These curvi-linear or point geological features, however, may have negative spatial associations with the copper deposits as determined by the distance distribution method and/or distance correlation method.

Table 8.10. Quantified spatial associations between copper deposits and curvi-linear or point geological features, Abra area.

Geological feature	Quantified spatial association* (m)			Farthest distance between geological feature and copper deposit (m)
	By weights of evidence method	By distance distribution method	By distance correlation method	
Intersection of regional faults	1000 (+)	1000 (+)	2000 (+)	6757
Porphyry pluton centroids	1500 (+)	5700 (-)	4000 (-)	8615
North-trending faults/fractures	1500 (+)	1250 (+)	1500 (+)	3735
Granodiorite batholithic margins	1500 (+)	800 (-)	1000 (-)	3323

* (+) = positive spatial association within distance; (-) = negative spatial association within distance.

Table 8.11. Distance and unit classes and fuzzy membership scores for the different curvi-linear or point geological features and lithologic units, Abra area.

Intersection of regional faults		Porphyry pluton centroids		North-trending faults/fractures		Granodiorite batholithic margins		Lithologic formations (Figure 2.13)		Cu geochemical anomaly (Figure 2.16a)	
Distance class (km)	Fuzzy score	Distance class (km)	Fuzzy score	Distance class (km)	Fuzzy score	Distance class (km)	Fuzzy score	Unit class	Fuzzy score	Conc. level (ppm)	Fuzzy score
<1.0	0.9	<1.5	0.9	<0.5	0.9	<0.8	0.7	AF	0.1	>170	0.9
1.0-2.0	0.8	1.5-4.0	0.4	0.5-1.0	0.8	0.8-1.0	0.8	TF	0.5	90-170	0.8
2.0-3.5	0.4	4.0-5.7	0.3	1.0-1.5	0.7	1.0-1.5	0.9	LF	0.9	50-90	0.2
3.5-5.0	0.3	5.7-8.7	0.2	1.5-2.5	0.3	1.5-2.5	0.3	QDP	0.9	<50	0.1
5.0-7.0	0.2	>8.7	0.1	2.5-4.0	0.2	2.5-3.5	0.2	QD	0.9		
>7.0	0.1			>4.0	0.1	>3.5	0.1	G	0.9		

AF = Alava Formation; TF = Tineg Formation; LF = Licuan Formation; QDP = Quartz diorite porphyry pluton; QD = Quartz diorite batholithic pluton; G = Granodiorite batholithic pluton.

The fuzzy membership values for the different sets of spatial evidences of porphyry copper potential are given in Table 8.11. The fuzzy sets of increasing distances within the range of optimal positive spatial association of the 'model' deposits with the intersection of regional faults were given decreasing fuzzy membership values in the range of 0.9 to 0.8. The fuzzy set of distance within the range of optimal positive spatial association of the 'model' deposits with the porphyry pluton centroids was given a fuzzy membership value of 0.9. The fuzzy sets of increasing distances within the range of optimal positive associations of the 'model' deposits with the north-trending faults/fractures were given decreasing fuzzy membership values of 0.9 to 0.7. The fuzzy sets of increasing distances within the range of optimal positive spatial association of the 'model' deposits with the granodiorite batholithic margins were given increasing fuzzy membership values of 0.7 to 0.9 because of the negative spatial association within the shorter distances (Table 8.9). The fuzzy sets of increasing distances beyond the range of optimal positive spatial associations of the 'model' deposits with the different curvi-linear or point geological features were given decreasing fuzzy membership values in the range of 0.4 to 0.1.

The lithologic units were given fuzzy membership values following the scheme in the Benguet example (see above). The porphyry plutons, batholithic plutons and the Licuan Formation were assigned fuzzy membership values of 0.9 because they are genetically and/or spatially associated with the porphyry copper deposits and/or the known mineralised zones (see Figure 2.13). The Tineg Formation consists of rocks that could act as host rocks to porphyry mineralisation (see sub-section 5.3.1) but are not known to contain mineralisation, so a fuzzy membership value of 0.5 is assigned to it. The Alava Formation was given a fuzzy membership value of 0.1 because it is younger than the plutonic rocks. For the stream sediment Cu geochemical data, concentration levels less than 90 ppm Cu were given low fuzzy membership

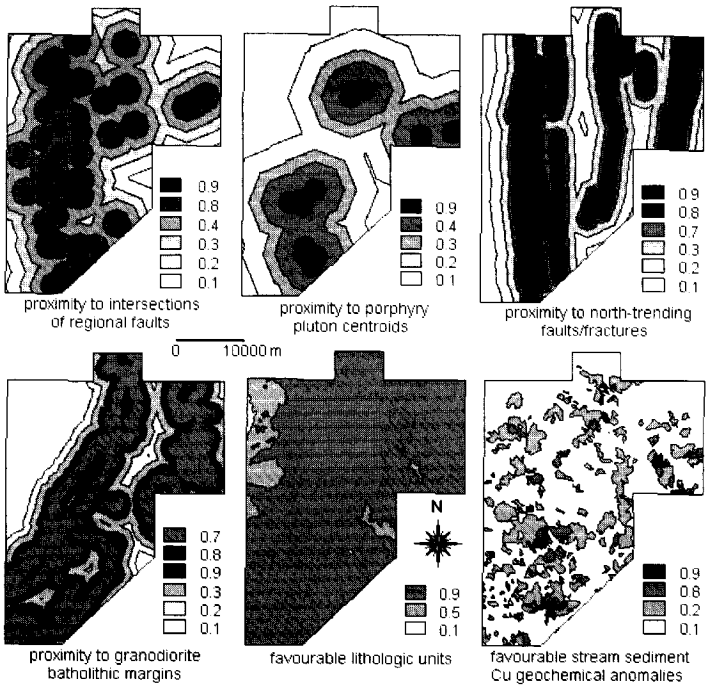

Figure 8.14. Maps of fuzzy membership values of sets of spatial evidences for predicting porphyry copper potential, Abra area.

values whilst concentration levels greater than 90 ppm Cu are given high fuzzy membership values. The fuzzy sets of spatial evidences of porphyry copper potential in the area are shown in Figure 8.14.

8.6.2 Integration of fuzzy sets of evidences of porphyry copper potential

The fuzzy sets of evidences of porphyry copper potential were combined in a number of steps to represent intermediate hypotheses regarding the significance of the evidences for the occurrence of porphyry copper mineralisation. There are two intermediate hypotheses. First, the combined occurrences of the faults structures and the plutonic rocks provide evidence for favourable zones of porphyry pluton emplacement. Second, the combined occurrences of favourable host rocks, favourable zones of porphyry pluton emplacement and favourable geochemical Cu anomalies are important for locating zones of porphyry copper potential. Figure 8.15 shows the schematic inference network for predicting porphyry copper potential in the area using fuzzy logic as the' inference engine'.

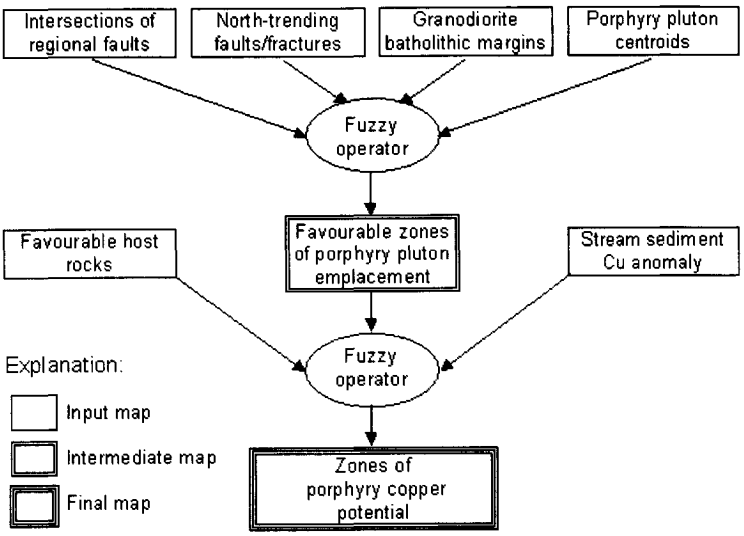

Figure 8.15. Schematic inference network for producing predictive map of porphyry copper potential, Abra area.

8.6.3 Fuzzy predictive mapping of porphyry copper potential

Two criteria were used to select the best fuzzy predictive map from the several possible combinations of fuzzy operations indicated in Figure 8.15. First, the predicted zones of favourable potential for porphyry copper mineralisation are characterised by fuzzy scores of ≥ 0.7. The first criterion is based on the expectation of fuzzy scores of 0.72 (i.e., 0.9 x 0.8). Second, the predicted favourable zones delineate a high percentage of the known mineralised zones but with an area of at most 25% of the total area. The second criterion is based on the spatial knowledge about the known porphyry copper deposits and the known mineralised zones. The known mineralised zones (JICA, 1980) contain only four of the 12 known copper deposits (Bureau of Mines, 1976) as shown in Figure 2.13. Of the eight other deposits, four are within 1 km of the known mineralised zones whilst the other four are beyond 1 km, the farthest being about 6.5 km

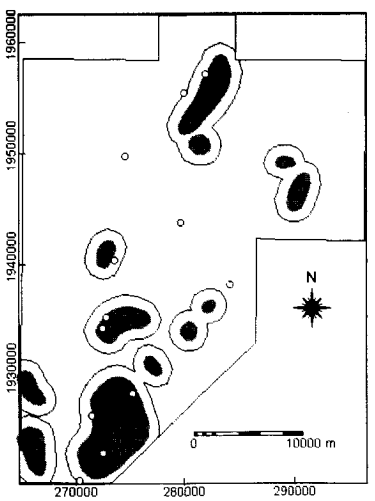

Figure 8.16. Mineralised zones (grey areas) and 1-km buffer zones, Abra area. Unfilled circles = known porphyry copper deposits.

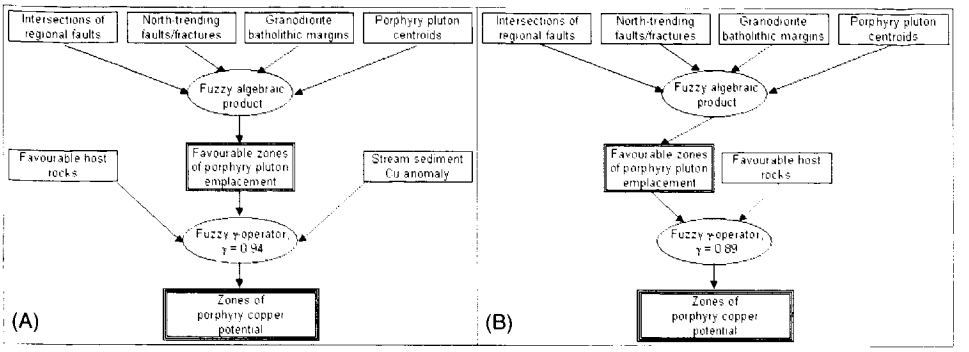

Figure 8.17. Inference networks used to predict gold potential of Abra area: (a) resulting in Figure 8.18a; (b) resulting in Figure 8.18b.

away. The known mineralised zones plus 1-km buffer zones around them form 'extended mineralised zones' that contain 8 (or 75%) of the known copper deposits and occupy 24.68% (say 25%) of the total area (Figure 8.16).

Predictive maps, inclusive and exclusive of the geochemical data, were created to determine the efficacy of geologically-constrained predictive mapping of porphyry copper potential. When the geochemical data were excluded from generating a predictive model, the catchment basins anomalous for Cu (i.e., >90 ppm; see Figure 5.9a) were also used to validate the predictive model(s). Shown in Figures 8.17a and 8.17b are the inference networks that resulted, respectively, in the best predictive map inclusive of the geochemical data (Figure 8.18a) and the best predictive map exclusive of the geochemical data (Figure 8.18b). The inference networks in Figures 8.17a and 8.17b are similar (as discussed below) and produced correspondingly similar predictive maps. The spatial geoinformation characteristics of the predictive maps in Figure 8.18 are summarised in Table 8.12.

The predictive map inclusive of the geochemical data (Figure 8.18a) delineates about 25% of the area as favourable for porphyry copper deposits whilst the predictive map exclusive of the geochemical data (Figure 8.18b) delineates about 23% of the area as favourable for porphyry copper deposits. The predictive map in Figure 8.18a correctly delineates 50% of the 'model' deposits whilst the predictive map in Figure 8.18b correctly delineates at least 58% of the 'model' deposits. The predictive map inclusive of the geochemical data has just

Table 8.12. Spatial geoinformation characteristics of fuzzy predictive maps, Abra area.

Fuzzy predictive map	% predicted favourable zones	% predicted 'model' deposits	% predicted mineralised zones	% predicted Cu anomalies
Figure 8.18a	24.9	50.0	68.2	-
Figure 8.18b	22.6	58.3	65.1	59.6

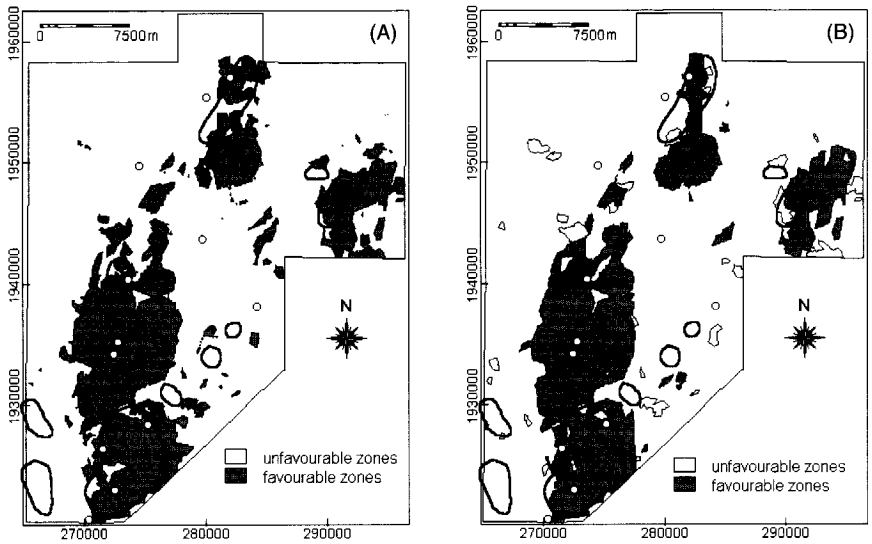

Figure 8.18. Predictive maps of porphyry copper potential, Abra area: (a) inclusive of geochemical data and result of inference network in Figure 8.17a; (b) exclusive of geochemical data and result of inference network in Figure 8.17b. Unfilled circles = 'model' deposits; polygons in thick lines = known mineralised zones; polygons in thin lines = catchment basins with stream sediment Cu contents >90 ppm.

3% higher prediction rate for the known mineralised zones than the predictive map exclusive of the geochemical data. The predictive map exclusive of the geochemical data demarcates about 60% of the Cu anomalies.

8.6.4 Discussion

The inference networks that resulted in the best predictive maps show a couple of similarities in terms of the fuzzy operators used to combine the spatial evidences. First, the fuzzy sets of intersections of regional faults, north-trending faults/fractures, batholithic margins and porphyry pluton centroids are best combined by using the fuzzy algebraic product operator. This fuzzy operator is appropriate where two or more pieces of evidence for a hypothesis must be present together for the hypothesis to be accepted. This implies that the four curvi-linear or point geological features are important for the emplacement of porphyry plutons. The north-trending faults/fractures controlled the intrusion of the batholithic plutons (Bureau of Mines and Geosciences, 1982). Later ascent of porphyry plutons, probably associated with the magma chamber of the batholithic plutons, were then localised at or near the intersection of regional faults (i.e., north-trending and northeast-trending faults/fractures). Second, the fuzzy sets of the intermediate hypothesis of zones of porphyry pluton

emplacement and the fuzzy sets of lithologic units are best combined, inclusive and exclusive of the fuzzy sets of Cu anomalies, by using the fuzzy γ-operator with values of γ of about 0.9. The high values of γ used to produce the best predictive maps imply that the spatial evidences complement each other and that these evidences should not be taken individually to support the proposition of zones of porphyry copper potential. Indeed, favourable rocks are required for the deposition of copper and other elements in mineralising fluids associated with porphyry pluton hydrothermal systems and surficial geochemical anomalies of Cu can indicate the locations of the porphyry copper deposits.

One of the two criteria applied for selecting the best fuzzy predictive maps is based on the known porphyry copper deposits (Bureau of Mines, 1976) and the known mineralised zones. Application of a criterion for selecting an optimum predictive map based only on point pattern analysis of the known porphyry copper deposits as in Benguet province (see subsection 8.4.3) was inadequate because the accuracy of the locations of the porphyry copper deposits reported by Bureau of Mines (1976) is not definitive. On the other hand, application of a criterion for selecting an optimum predictive map based only on the known mineralised zones was also inadequate because the accuracy of the map of mineralised zones (JICA, 1980) is also not definitive. Several of the known porphyry copper deposits are not reflected in the mineralised zones and vice versa. The map of mineralised zones (JICA, 1980), however, was considered less accurate because it is an extrapolation of discontinuous mineralised outcrops that were probably observed mainly along the accessible drainage courses. By extending the limits of the known mineralised zones to 1 km, the difference between the map of porphyry copper deposits (Bureau of Mines, 1976) and the map of mineralised zones (JICA, 1980) is reconciled, albeit not completely, as shown in Figure 8.16 (sub-section 8.6.3).

Based on the two criteria, the integrated geochemical-geological predictive map is considered inferior, albeit slightly, to the geologically-constrained predictive map. The former, as compared to the latter, delineates about 2% more favourable zones, has 8% lower prediction rate for the porphyry copper deposits and has about 3% higher prediction rate for the 'extended mineralised zones'. The slightly higher percentage of predicted favourable zones in Figure 8.18a is due to some of the Cu anomalies, which nonetheless result in a slight increase in prediction rate for the 'extended mineralised zones'. These imply that the geologically-constrained predictive map in Figure 8.18b is as useful as the integrated geochemical-geological predictive map in Figure 8.18a.

8.7 APPLICATION TO CATANDUANES ISLAND

The spatial evidences used in the predictive mapping of gold-copper potential in the island include the lithologic units, Batalay Intrusive contacts, the northeast-trending faults/fractures and the north-trending faults/fractures. The quantified spatial associations of the 17 gold-copper deposits with the curvi-linear geological features were used in the predictive modeling of gold-copper potential. The stream sediment geochemical data (see sub-section 2.5.4) were used to validate the predictive map(s) of gold-copper potential.

8.7.1 Fuzzy sets of evidences of gold-copper potential

Summarised in Table 8.13 are the quantified spatial associations between the gold-copper deposits and the curvi-linear geological features in the island. The quantified spatial associations are derived from Table 4.52 (see Section 4.6). It has been shown in Chapter 6 that curvi-linear geological features with negative spatial association with the gold-copper deposits are not important in predictive mapping of mineral potential. Hence, only those curvi-linear geological features with positive spatial associations with the gold-copper deposits were considered.

The fuzzy membership values for the different sets of spatial evidences of gold-copper potential are given in Table 8.14. The fuzzy sets of increasing distances within the range of optimal positive spatial associations of the gold-copper deposits with the curvi-linear geological features were given decreasing fuzzy membership values in the range of 0.9 to 0.7. The fuzzy sets of increasing distances beyond the range of optimal positive spatial associations of the gold-copper deposits with the curvi-linear geological features were given decreasing fuzzy membership values in the range of 0.4 to 0.1. The fuzzy sets of lithologic units that are known to host gold-copper deposits were given a fuzzy membership value of 0.9. The Batalay Intrusives were given a fuzzy membership value of 0.8 because they are thought to be the heat sources but

Table 8.13. Quantified spatial associations between gold-copper deposits and curvi-linear geological features, Catanduanes Island.

Geological feature	Quantified spatial association (m)			Farthest distance between geological feature and gold-copper deposits (m)
	By weights of evidence method	By distance distribution method	By distance correlation method	
Batalay Intrusive contacts	1000 (+)	2400 (+)	3500 (+)	27375
Northeast-trending faults/fractures	1000 (+)	1000 (+)	1000 (+)	5150
North-trending faults/fractures	750 (+)	800 (+)	3000 (+)	8673

(+) = positive spatial association within distance.

Table 8.14. Distance and unit classes and fuzzy membership scores for the different curvi-linear geological features and lithologic units, Catanduanes Island.

Batalay intrusive contacts		Northeast-trending faults/fractures		North-trending faults/fractures		Lithologic formations (Figure 2.17)	
Distance class (km)	Fuzzy score	Distance class (km)	Fuzzy score	Distance class (km)	Fuzzy score	Unit class*	Fuzzy score
<1.0	0.9	<0.5	0.9	<0.8	0.9	A	0.01
1.0-2.4	0.8	0.5-1.0	0.8	0.8-1.9	0.8	VC	0.01
2.4-3.0	0.7	1.0-1.5	0.4	1.9-3.0	0.7	SDF	0.01
3.0-8.0	0.4	1.5-2.5	0.3	3.0-6.0	0.3	BI	0.8
8.0-18.0	0.3	2.5-5.0	0.2	6.0-9.0	0.2	PF	0.9
18.0-28.0	0.2	>5.0	0.1	>9.0	0.1	BL	0.5
>28.0	0.1					YF	0.9
						CF	0.9

*A = Alluvium; VC = Viga Conglomerate; SDF = Sto. Domingo Formation; BI = Batalay Intrusives; PF = Payo Formation; BL = Bonagbonag Limestone; YF = Yop Formation; CF = Catanduanes Formation.

are also known to host some of the gold-copper deposits (see Table 2.8; subsection 2.5.1; Miranda and Vargas, 1967; MMAJ-JICA, 1994). The fuzzy sets of lithologic units that are not known to host gold-copper deposits but are older than the Batalay Intrusives were given a fuzzy membership value of 0.5. The fuzzy sets of lithologic units younger than the Batalay Intrusives were given a fuzzy score of 0.01. The maps of fuzzy membership values of the sets of spatial evidences of gold-copper potential are illustrated in Figure 8.19

8.7.2 Integration of fuzzy sets of evidences of gold-copper potential

The fuzzy sets of spatial evidences of gold-copper potential were combined in a number of steps to represent intermediate hypotheses regarding the significance of the evidences for the occurrence of gold-copper mineralisation. Because detailed genetic studies of the gold-copper mineralisation in the island are lacking, three sets of hypotheses were tested to contribute knowledge and/or substantiate existing concepts regarding their mode of emplacement. The three sets of hypotheses are illustrated in Figure 8.20.

In the first set of hypotheses (Figure 8.20a), the north-trending faults/fractures and the northeast-trending faults/fractures are favourable structural controls of gold-copper mineralisation. These favourable structural controls, together with the Batalay Intrusives, which act as heat sources, and the favourable host rocks are important evidences of favourable zones of gold-copper potential. In the second set of hypotheses (Figure 8.20b), the north-trending faults/fractures, the northeast-trending faults/fractures, and the Batalay Intrusives are evidences of favourable heat flow zones that controlled the gold-copper mineralisation. The presence of favourable heat flow zones and favourable host rocks are important evidences of zones of gold-copper potential. In the third set of hypotheses

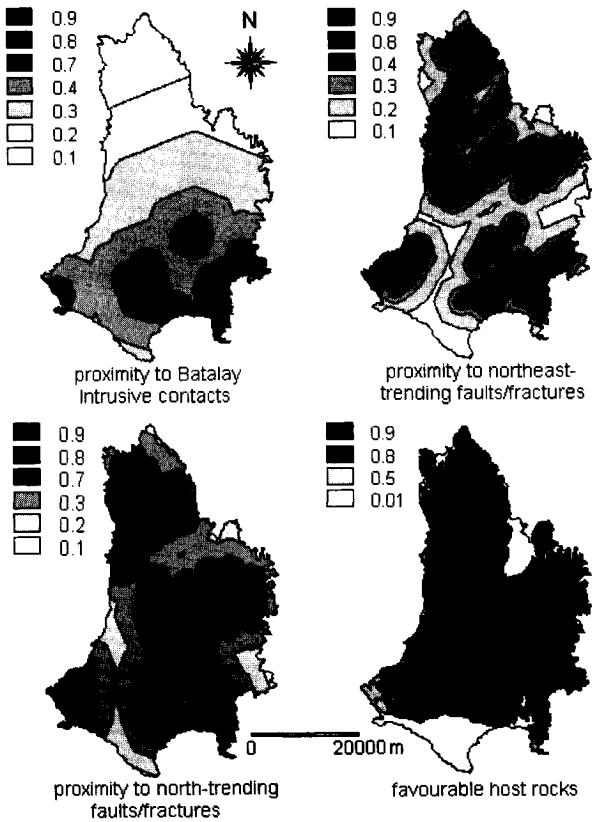

Figure 8.19. Maps of fuzzy membership values of spatial evidences for predicting gold-copper potential, Catanduanes Island.

(Figure 8.20c), the north-trending faults/fractures and the northeast-trending faults/fractures are favourable structural controls of gold-copper mineralisation. The combined occurrences of the Batalay Intrusives and the favourable host rocks suggest zones of hydrothermally-altered rocks that can be considered spatial indications of mineralisation. The presence of favourable structural zones and hydrothermally-altered zones are important evidences of zones of gold-copper potential. The best fuzzy predictive map(s) can reveal which of these hypotheses is the best hypothetical genetic model of the gold-copper mineralisation in the island.

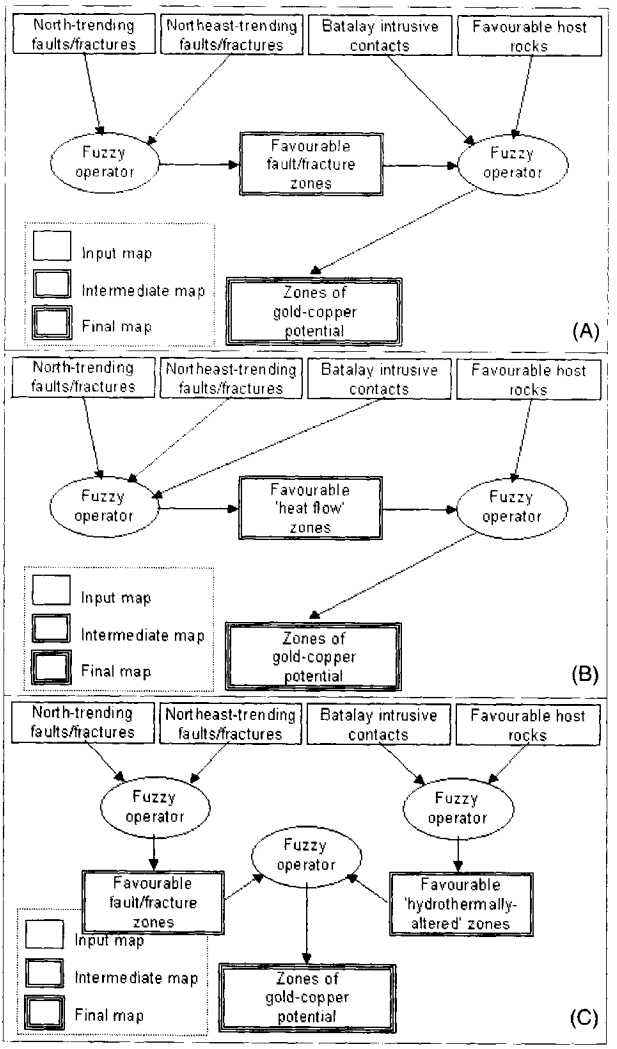

Figure 8.20. Schematic inference networks for producing predictive maps of gold-copper potential, Catanduanes Island

8.7.3 Fuzzy predictive mapping of gold-copper potential

Two criteria were used to select the best fuzzy predictive map(s) from the several possible combinations of fuzzy operations indicated in Figure 8.20. First, the predicted zones of gold-copper potential are characterised by fuzzy scores of ≥ 0.7. This criterion is based subjectively on the expectation of fuzzy scores of 0.72 (i.e., 0.9 x 0.8). Second, the predicted favourable zones do not exceed 20%

of the total area and predict ≥ 64.7% (or ≥ 11) of the known gold-copper deposits. This criterion is based on spatial knowledge about the known gold-copper deposits and the multi-element geochemical anomalies (i.e., >75th upper percentile PC3 scores; see subsection 2.5.4). Of the 17 known gold-copper deposits, seven are within the geochemically-anomalous catchment basins and four others are within just 500 m of a given geochemically-anomalous catchment basin. The geochemically-anomalous catchment basins and 500-m buffer zones around them occupy 19.5% of the island (Figure 8.21).

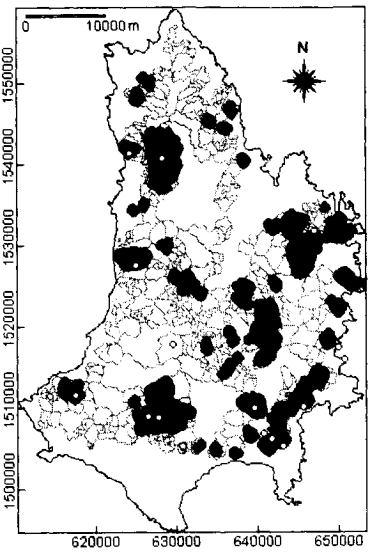

Figure 8.21. Geochemically-anomalous catchment basins buffered with 500-m zones (grey areas), Catanduanes Island. Unfilled circles = gold-copper deposits

The inference networks in Figure 8.22, which resulted in the best predictive maps, are similar but have different geological implications (as discussed below). The best predictive maps are shown in Figure 8.23. The spatial geoinformation characteristics of the best predictive maps are given in Table 8.15. Both predictive maps delineate different favourable zones with similar areas, which are less than the area of the buffered geochemically-anomalous catchment basins. Both predictive maps have similar prediction rates for the known gold-copper deposits and similar percentages of spatial coincidence with the geochemically-anomalous catchment basins. A main difference between the predictive maps, aside from the spatial distribution of their predicted favourable zones, pertains to the mean distances of the incorrectly predicted gold-copper deposits and geochemically-anomalous catchment basins to a given predicted favourable zone. In Figure 8.23a, the

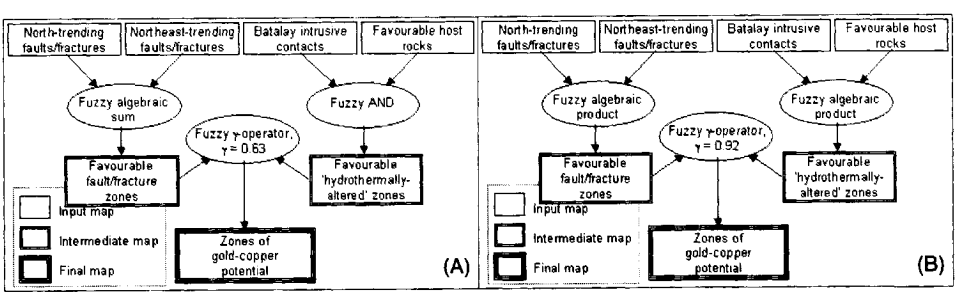

Figure 8.22. Inference networks used to predict gold-copper potential of Catanduanes Island: (a) resulting in Figure 8.23a; (b) resulting in Figure 8.23b.

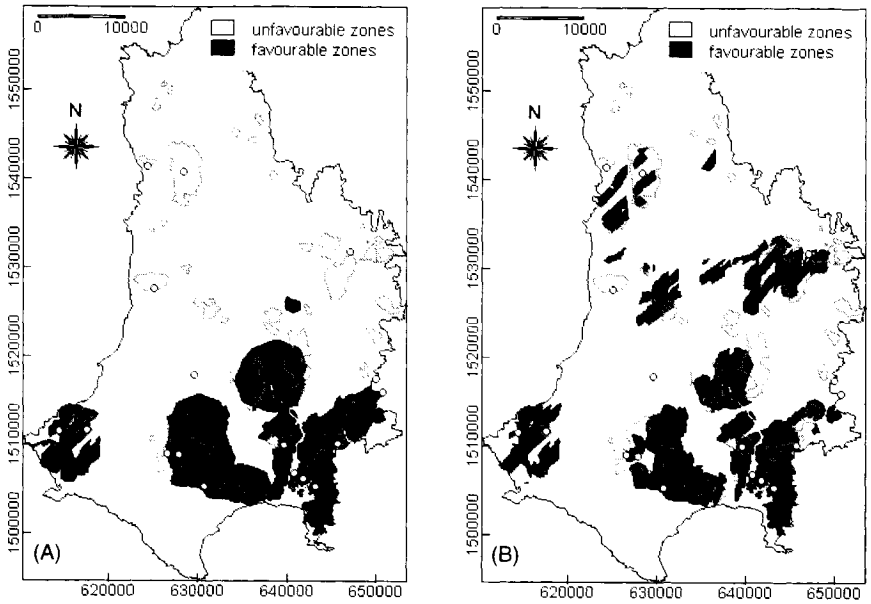

Figure 8.23. Geologically-constrained predictive maps of gold-copper potential, Catanduanes Island: (a) result of inference network in Figure 8.22a; (b) result of inference network in Figure 8.22b. Unfilled circles = gold-copper deposits; polygons in light-grey lines = geochemically-anomalous catchment basins.

gold-copper deposits and geochemically-anomalous catchment basins delineated incorrectly are distal to the predicted favourable zones. In Figure 8.23b, the gold-copper deposits and geochemically-anomalous catchment basins delineated incorrectly are proximal to the predicted favourable zones. The predictive map in Figure 8.23b is therefore considered the better of the two.

Because the predictive map in Figure 8.23b is considered superior to the predictive map in Figure 8.23a, its usefulness was tested against an integrated geochemical-geological predictive map. A fuzzy set of the quantified stream sediment geochemical signature that is indicative of the gold-copper deposits in the island (see sub-section 2.5.4; Figure 2.19) was generated (Figure 8.24a).

Table 8.15. Spatial geoinformation characteristics of predictive maps of gold-copper potential, Catanduanes Island.

Fuzzy predictive map	% predicted favourable zones	% predicted known deposits	% spatial overlap with geochemically-anomalous zones	Mean distance to favourable zones (m)	
				known deposits not delineated	geochemically-anomalous zones not delineated
Figure 8.23a	18.3	64.7	38.8	10,467	2,037
Figure 8.23b	18.5	64.7	39.4	2,130	196

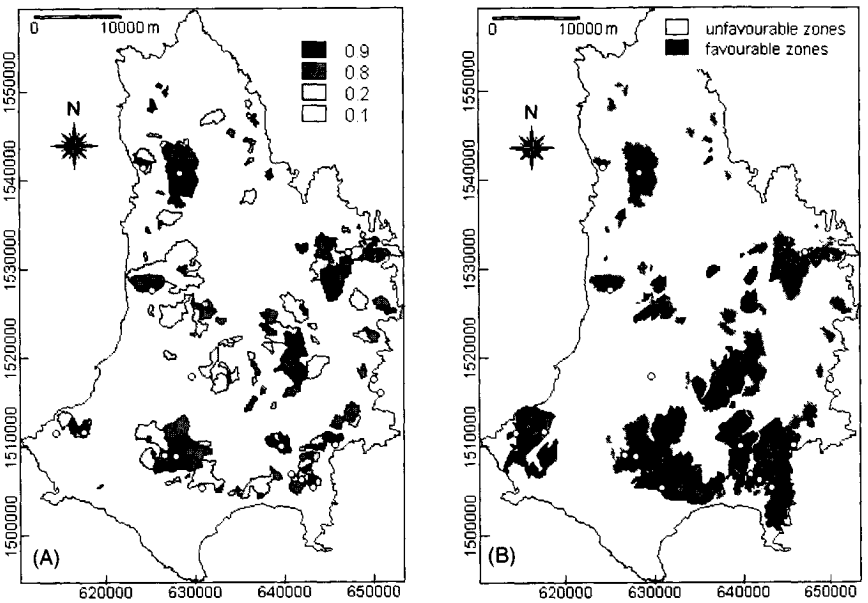

Figure 8.24. Catanduanes Island: (a) map of fuzzy membership values representing quantified stream sediment geochemical signature as evidence for predicting gold-copper potential; (b) integrated geochemical-geological predictive map of gold-copper potential. Unfilled circles = gold-copper deposits; polygons in light-grey lines = geochemically-anomalous catchment basins.

The map of fuzzy membership values of the quantified stream sediment geochemical signature was integrated with the map of fuzzy scores resulting from the inference network in Figure 8.22b prior to classification to the predictive map in Figure 8.23b. The two maps of fuzzy scores were integrated using the fuzzy γ-operator and the two criteria set above were applied to select the best output predictive map. The best integrated geochemical-geological predictive map shown in Figure 8.24b is the result of a γ-value of 0.96.

The integrated geochemical-geological predictive map delineates 19.2% of the island as favourable for gold-copper deposits. It predicts correctly 14 (or about 82%) of the 17 known gold-copper deposits. The mean distance of the gold-copper deposits not delineated by the predicted favourable zones is about 2400 m. Thus, the geologically-constrained predictive map in Figure 8.23b is inferior to the integrated geochemical-geological predictive map in Figure 8.24b. However, there are two additional spatial features worth noting to establish the usefulness of the former predictive map. First, the geochemically-anomalous catchment basins (i.e., with >75th percentile PC3 scores and fuzzy scores $\geq$0.8) delineate correctly only seven of the 17 known gold-copper deposits. Second,

the integration of the geochemical evidence provided only a prediction of three deposits in addition to the 11 deposits predicted by the geologically-constrained predictive map in Figure 8.23b. These two spatial features and the smaller mean distance of the unpredicted gold-copper deposits to the geologically-favourable zones imply that the best geologically-constrained predictive map in Figure 8.23b is also useful. It is useful in the sense that, in the absence of other exploration datasets such as the geochemical exploration data, it can serve as a reliable guide for follow-up exploration in the island.

8.7.4 Discussion

The best geologically-constrained predictive maps result from similar inference networks (Figure 8.22) that follow the third set of hypotheses, which postulate that the combined occurrences of favourable structural zones and favourable zones of hydrothermally-altered rocks are important indications of gold-copper potential. The difference between the inference networks in Figure 8.22 is the type of fuzzy operators used to derive the intermediate hypothesis maps. The type of fuzzy operators used largely controlled the output predictive map. For example, for the inference network in Figure 8.22a, the influence of the Batalay Intrusive fuzzy evidence (Figure 8.19) is reflected largely in Figure 8.23a. This is due to the use of the fuzzy AND operator and the fuzzy γ-operator with a low value of γ (i.e., towards the fuzzy algebraic product operator). These fuzzy operators are appropriate where two or more pieces of evidence for a hypothesis must be present for the hypothesis to be accepted. With these fuzzy operators, the output is controlled by the smallest fuzzy membership value at each pixel or location. For the inference network in Figure 8.22b, the use of a fuzzy γ-operator with a high value of γ (i.e., the fuzzy algebraic sum operator is highly dominant) results in a map that reflects the complementary contributions of each of the intermediate hypothetical evidences. Hence, in Figure 8.23b the influence of structural control is more pronounced in the central sections of the island where the Batalay Intrusives are not mapped. In the southern sections, where the Batalay Intrusives and the faults/fractures are present, a complementary contribution of each of the intermediate hypothetical evidences can be observed.

The predictive map in Figure 8.23b is superior to the predictive map in Figure 8.23a not only based on its spatial predictive geoinformation characteristics (Table 8.14) but also on the geological meaning of the spatial distributions of the predicted geologically-favourable zones. On the one hand, the predictive map in Figure 8.23a depicts only one geological meaning, i.e., gold-copper potential is indicated mainly by the presence of the Batalay Intrusives. This geological meaning is inadequate because the heat sources of mineralisation can be sub-outcropping (i.e., their presence is not indicated on the map) and therefore zones neither underlain by nor proximal to the Batalay Intrusives are indicated to

be unfavourable for gold-copper deposits. On the other hand, the predictive map in Figure 8.23b depicts two geological meanings. First, gold-copper potential is indicated by the presence of both intermediate hypothetical evidences (i.e., favourable fault/fracture zones and favourable hydrothermally-altered- zones). Second, the absence of either of the intermediate hypothetical evidences (derived from given map data) does not preclude gold-copper potential.

The latter geological meaning of the predictive map in Figure 8.23b is valid in the predicted geologically-favourable zones particularly in the east-central section of the island. Within these predicted geologically-favourable zones, detailed exploration revealed buried sub-economic gold-copper vein-type deposits, which were intersected by drillholes (JICA-MMAJ, 1996). These buried deposits are spatially associated with non-outcropping porphyry plutons, which were also intersected by drillholes. This suggests that other predicted geologically-favourable zones where the Batalay Intrusives have not been mapped but where north-trending and northeast-trending faults/fractures are present could possibly contain buried gold-copper mineralisation.

8.8 APPLICATION TO ISABELA AREA

The spatial evidences indicative of nickeliferous-laterite potential are (1) presence of peridotitic rocks, (2) topographic slopes of $\leq 20°$ and (3) presence of plateau edges (Golightly, 1979, 1981). Binary representation of the lithologic criterion necessarily implies that only the ultramafic terrane in Isabela areas has potential for this type of deposit (see Chapter 5). However, considering that laterite (though not necessarily nickeliferous) can develop from most type of rocks (Nahon and Tardy, 1992), the assignment of subjective weights to the different rocks units in the whole area based on knowledge of their forsteritic olivine and/or serpentine contents seems appropriate (see Chapter 7). In this Chapter, fuzzy predictive mapping of nickeliferous-laterite potential is also applied to the whole of the Isabela map area.

8.8.1 Fuzzy sets of spatial evidences of nickeliferous-laterite potential

Fuzzy membership values were assigned to the different lithologies to reflect subjective assumptions of their mineral compositions (Table 8.16). The Cretaceous Isabela Ultramafics were given a fuzzy score of 0.9. The basaltic Cretaceous Rocks were given a fuzzy score of 0.5. The Oligocene sedimentary/volcanic rocks and diorite intrusives were given a fuzzy score of 0.2. The Miocene-Pliocene sedimentary rocks were given a fuzzy score of 0.1 whilst the Quaternary alluvial deposits were given a fuzzy score of 0.01. The map of fuzzy scores of fuzzy sets of potential parent rocks of nickeliferous-laterite is shown in Figure 8.25a.

Table 8.16. Lithologic units, slope classes and fuzzy membership scores representing favourability for nickeliferous-laterite formation, Isabela area.

Lithologic units Figure 2.20)	Fuzzy score	Slope class	Fuzzy score
Quaternary alluvium (QA)	0.01	<10°	0.9
Miocene-Pliocene sedimentary rocks (MPSR)	0.1	10-20°	0.8
Oligocene dioritic intrusives (ODI)	0.2	20-30°	0.7
Oligocene sedimentary and volcanic rocks (OSVR)	0.2	30-40°	0.5
Cretaceous rocks (CR)	0.5	>40°	0.1
Cretaceous Isabela Ultramafics (CIU)	0.9		

Fuzzy membership values were assigned to the different slope classes to reflect variations in slopes within specific slope classes that make them more or less favourable in regard to formation of nickeliferous-laterite deposits. Variations in slopes are necessarily present in a particular slope class due to the inherent low accuracy of the small scale topographic maps used in the modeling. The more gentle slope class (<10°) and the less gentle slope class (10-20°) within the range of the maximum favourable slope required by the conceptual deposit model were assigned fuzzy scores of 0.9 and 0.8, respectively. The classes of increasing slopes greater than the maximum favourable slope required by the conceptual deposit model were assigned decreasing fuzzy membership values in the range of 0.7 to 0.1. The map of fuzzy scores of fuzzy sets of slopes favourable for nickeliferous-laterite formation is shown in Figure 8.25b.

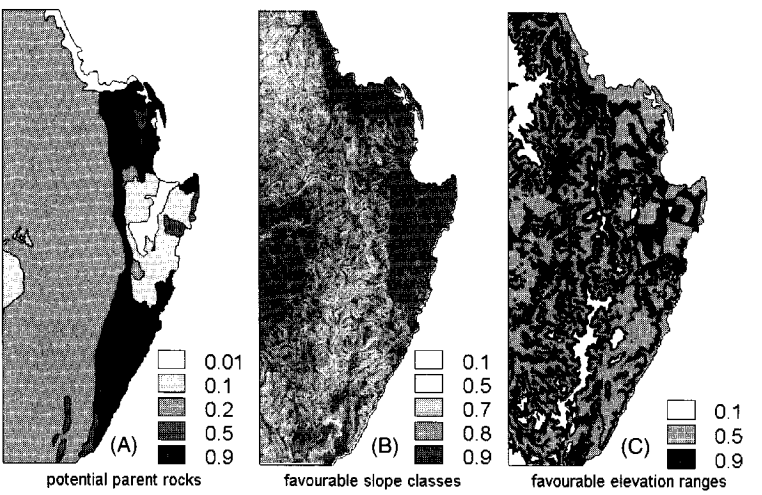

Figure 8.25. Maps of fuzzy membership values of spatial evidences of nickeliferous-laterite potential, Isabela area: (a) potential parent rocks; (b) favourable slopes; (c) favourable elevation ranges.

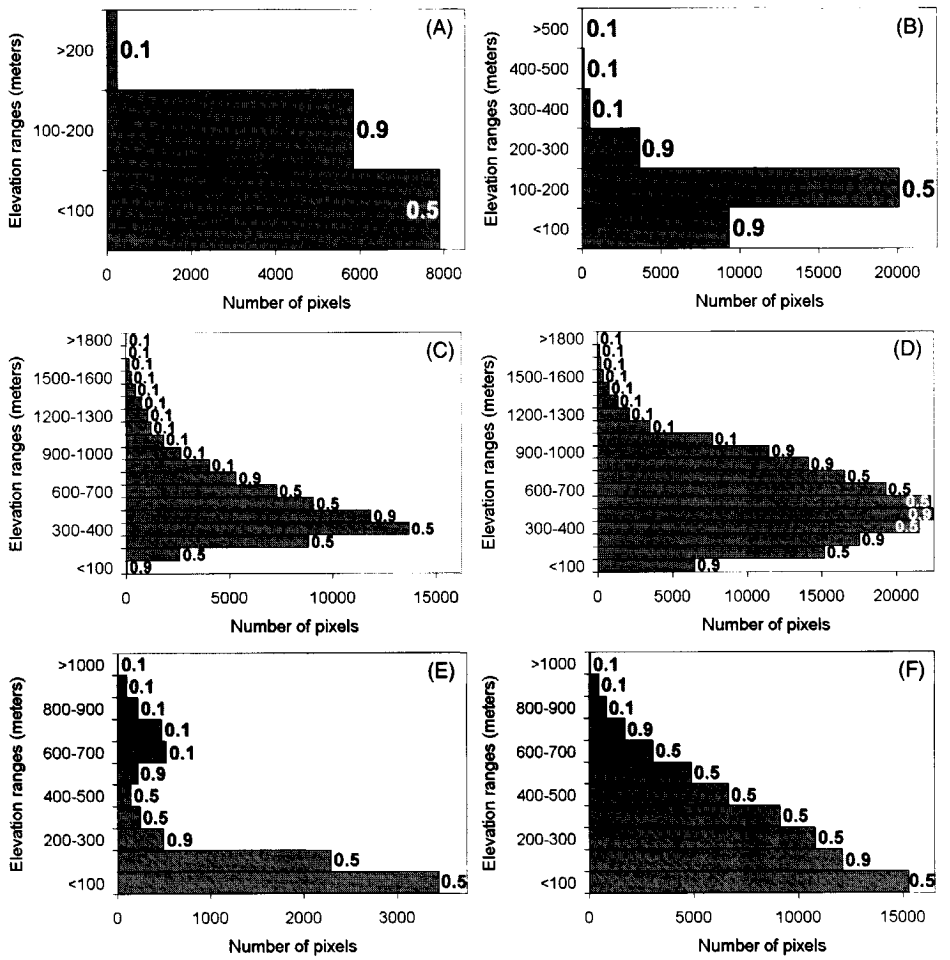

Figure 8.26. Isabela area: histograms of elevation ranges in DEM of different lithologic units and fuzzy membership values for likelihood of containing plateau edges: (a) Quaternary alluvium; (b) Miocene-Pliocene sedimentary rocks; (c) Oligocene diorite intrusives; (d) Oligocene sedimentary/volcanic rocks; (e) Cretaceous rocks; and (f) Cretaceous Isabela Ultramafics.

To generate a fuzzy set of favourable ranges of topographic elevations where plateau edges probably occur, two general steps were followed as already described in Chapter 2. First, a DEM for each lithologic unit was extracted from the DEM of the whole area. Second, graphical analysis was performed on the histogram of pixels values in the DEM (i.e., elevations) of each lithologic unit. Fuzzy scores of 0.1, 0.5 or 0.9 were assigned to elevation ranges depending on the interpretation of the probable occurrence of plateau edges within a particular

elevation range (Figure 8.26). A fuzzy score of 0.1 is assigned to elevation ranges that are not likely to contain plateau edges because either they form part of a plateau or they form part of a ridge. Elevation ranges that are interpreted as moderately likely to contain plateau edges were given a fuzzy score of 0.5. A fuzzy membership value of 0.9 is assigned to elevation ranges that are interpreted as highly likely to contain plateau edges. The fuzzy map of favourable elevation ranges is shown in Figure 8.25c.

8.8.2 Integration of fuzzy sets of evidences of nickeliferous-laterite potential

Because favourable slope classes and favourable elevation ranges are both topographic indicators that can occur independently of potential parent rocks, they were combined first to generate an intermediate fuzzy map of topographic indicators (Figure 8.27). The fuzzy γ-operator was used to combine the topographic evidences to derive a fuzzy map of topographic indicators. The intermediate fuzzy map of topographic indicators and the fuzzy evidence of potential parent rocks were then combined using the fuzzy γ-operator to derive a final fuzzy evidence of zones of nickeliferous-laterite potential. The fuzzy γ-operator was deemed appropriate, in the absence of other additional criteria, to create the intermediate fuzzy map of topographic indicators and the final fuzzy map of nickeliferous-laterite potential. A γ value of 0.5 was used so that the output fuzzy scores are not dominated by the smallest fuzzy score nor complemented by the largest fuzzy scores at each pixel.

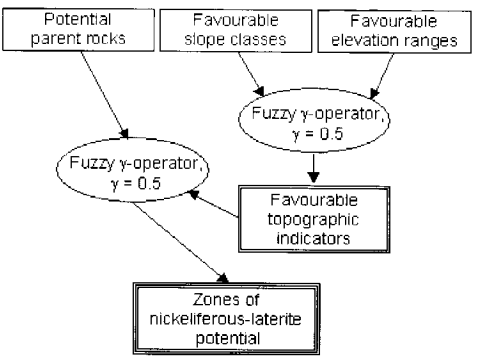

Figure 8.27. Schematic inference network for producing predictive map of nickeliferous-laterite potential, Isabela area.

8.8.3 Fuzzy predictive mapping of nickeliferous-laterite potential

Based on the resulting fuzzy map of membership values of zones of nickeliferous-laterite potential, the area is classified into favourable zones and unfavourable zones. The favourable zones are further classified into high potential zones and low potential zones. The high potential zones are characterised by fuzzy membership values >0.729 (0.9 x 0.9 x 0.9), i.e., all evidences are highly favourable. The low potential zones are characterised by fuzzy membership values of 0.729 to 0.405 (0.9 x 0.9 x 0.5), i.e., only two

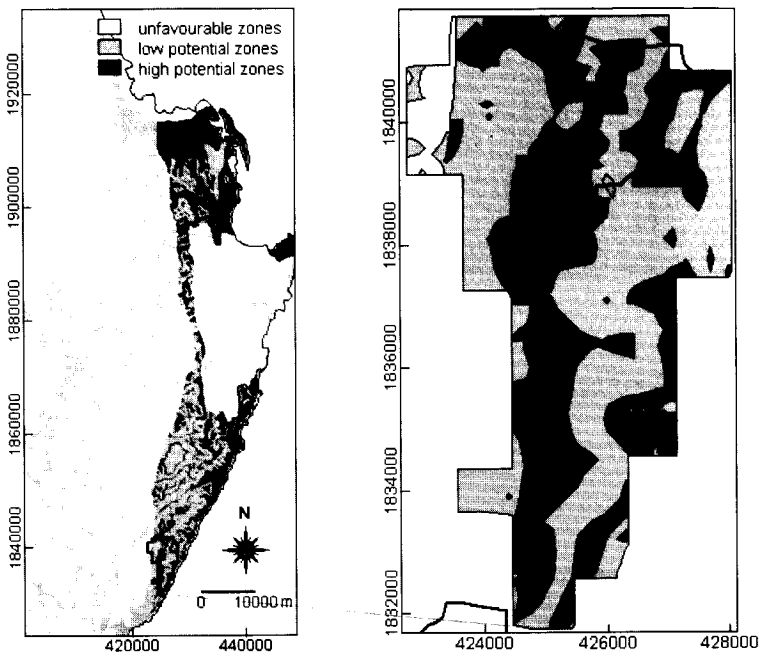

Figure 8.28. Predictive map of nickeliferous-laterite potential, Isabela area (left). Section with known nickeliferous-laterite deposits; solid lines represent catchment basins with stream sediment Ni contents >2500 ppm (right).

evidences are highly favourable). The unfavourable zones are characterised by fuzzy membership values of <0.405.

The classified fuzzy predictive map of nickeliferous-laterite potential (Figure 8.28) indicates that 72% of the area is unfavourable for nickeliferous-laterite, 18% has low potential and 11% has high potential. The favourable zones pertain mostly to the ultramafic terrane (see Figure 2.20). About 62% of the ultramafic terrane has high potential and 38% has low potential. The fuzzy predictive map indicates that about 45% of the section with known nickeliferous-laterite deposits has high potential, 53% has low potential and 2% is unfavourable. Within this section, zones that are unfavourable for nickeliferous-laterite are underlain by non-ultramafic rocks. The catchment basin with stream sediment Ni contents >2500 ppm has low or high potential for nickeliferous-laterite.

8.8.4 Discussion

The results indicate that using the fuzzy evidence map of favourable parent rock alone broadly delineates favourable zones of nickeliferous-laterite potential in

the area (see Figure 8.25a). Using the intermediate fuzzy evidence map of topographic indicators, however, allows further distinction between zones of low and high potential. The zones of low potential in the ultramafic terrane are due to lower favourability of topographic indicators. Predictive mapping of nickeliferous-laterite potential within the whole area instead of within the ultramafic alone allows the recognition of other favourable zones, although having low potential, which are underlain by non-ultramafic rocks. The zones of low potential in the non-ultramafic terrane, however, are mainly due to the presence of favourable topographic indicators. The areas underlain by the basaltic rocks are indicated to be either unfavourable or have low potential, which is different from the classification using the evidential belief functions in Chapter 7. The difference in the classification of the nickeliferous-laterite potential of the basaltic rock areas using the present method and the evidential belief mapping method probably lies in the different ways of combining the spatial evidences. It is interesting to note, however, that within the section with known nickeliferous-laterite deposits the predicted favourable zones are the same as the predicted favourable zones based on the evidential belief functions (see Figure 7.20). The validity of the predictive model of nickeliferous-laterite was not fully assessed due to the absence of appropriate validation data (i.e., locations of known nickeliferous-laterite deposits). However, the spatial coincidence of predicted high potential zones with catchment basins with stream sediment Ni contents >2500 ppm (i.e., above average abundance of Ni in ultramafic rocks; Levinson, 1974) goes some way of indicating the validity of the predictive model.

There are more zones of high potential in several other sections of the ultramafic terrane than in the section with known nickeliferous-laterite deposits (Figure 8.28). The other sections of the ultramafic terrane immediately north of the section with known nickeliferous-laterite deposits, however, is protected from mineral resources development and therefore the potential for this type of deposit is unknown (Mangaoang, 1997). The exclusion of particular sections in the study area to mineral resources development is not being challenged but the results demonstrate that mineral potential maps are important in land-use decision-making.

8.9 GENERAL DISCUSSION

Defining fuzzy membership functions of geological variables in regard to their importance as spatial evidences of mineral potential certainly requires knowledge about mineralisation. In some cases, conceptual or 'expert' knowledge of mineral deposits is applied in defining the fuzzy membership functions of spatial geological evidences of mineral potential (Gettings and Bultman, 1992; Bonham-Carter, 1994; Wright and Bonham-Carter, 1996). In other cases, both conceptual and factual knowledge of mineral deposits are applied to define the fuzzy membership functions of spatial geological evidences of mineral potential (Cheng and Agterberg, 1999; Knox-Robinson, 2000;

Carranza and Hale, 2001b). In contrast to the work of Cheng and Agterberg (1999) and Knox-Robinson (2000), the definition of fuzzy membership functions of spatial geological evidences presented in four examples here is applicable to areas where a number of representative mineral deposits are present but relatively little is known of each of these deposits. However, it is stressed that although the fuzzy membership is defined on the [0,1] interval, the fuzzy membership score of a particular spatial evidence does not represent probability of mineral deposit occurrence per unit area but rather a concept of favourability in a general and relative sense only.

Only one fuzzy score is required for a particular subclass or subset of evidence whilst three functions (belief, disbelief and uncertainty) are required in the application of the evidential belief theory (An et al., 1992). The single fuzzy score assigned nonetheless carries both a degree of confidence and a degree of uncertainty in a particular subclass or subset of evidence. Representation of spatial geological evidences of mineral potential as fuzzy membership functions is thus more versatile than evidential belief functions. Both fuzzy logic and evidential reasoning methods, however, are related in representing multiclass spatial evidences of particular hypotheses (Palacharla and Nelson, 1994).

Combining multiple sets of spatial evidences of mineral potential by way of a fuzzy logic approach can be less straightforward than by simple overlay techniques (see Chapter 5), weights of evidence modeling (see Chapter 6; Agterberg, 1989, 1992a; Bonham-Carter et al., 1988, 1989; Bonham-Carter and Agterberg, 1990; Bonham-Carter, 1991, 1994; Agterberg et al., 1993) or by Dempster's rule of combination of evidences (see Chapter 7; Moon, 1989; 1990; An et al., 1992; Chung and Moon, 1991; Chung and Fabbri, 1993). However, combining spatial evidences to map mineral potential by using fuzzy logic as an inference engine allows representation and evaluation of intermediate hypotheses regarding the significance of the spatial evidences. The method of combining spatial evidences of mineral potential presented here is a simplified scheme of applying inference networks compared to the more complex scheme of inference networks in expert systems (Duda et al., 1978; McCammon, 1989b; Katz, 1991; Reddy et al., 1992).

The several experimental combinations of spatial evidences in the four study areas invariably showed the usefulness of the fuzzy γ-operator. Based on the value of γ, it can be determined whether a particular mineral potential map is the result of complementary contributions of the input spatial evidences or the result of dominance of one or more of the input spatial evidences. The usefulness of the fuzzy γ-operator for combining spatial fuzzy sets of evidences in mineral exploration has also been demonstrated by An et al. (1991), Bonham-Carter (1994) and D'Ercole and Knox-Robinson (1997). The application of the fuzzy AND, fuzzy OR, fuzzy algebraic sum and fuzzy algebraic product has shown be useful mostly in combining initial input spatial evidences to support intermediate

hypotheses but not to support the final mineral potential hypothesis. This finding is also in accordance to the findings of Knox-Robinson (2000) who avers that these fuzzy operators are not particularly suitable for use in mineral prospectivity mapping. Moreover, the geological significance of output fuzzy maps resulting from any of the fuzzy operators used must be clarified and understood in order for these fuzzy maps to be useful.

8.10 CONCLUSIONS

The application of the theory of fuzzy sets to mineral potential mapping provides a quantitative yet subjective technique for predicting mineral potential where a number of mineral deposits are known. The design of the fuzzy inference network to combine the spatial geological evidences for mapping mineral potential must be guided by knowledge of the mode of formation of the mineralisation considered. Other spatial geoinformation (or knowledge) pertaining to the known mineral deposits is needed to guide in the selection and/or validation of the best fuzzy predictive map(s).

For Benguet province, the optimal geologically-constrained predictive map of porphyry copper potential includes the remotely-detected hydrothermal alteration evidence. The predicted favourable zones comprise about 26% of the province, delineate about 74% of the 'model' deposits and about 62% of the 'validation' deposits and show spatial coincidence with significant geochemical anomalies. For Baguio district, the best geologically-constrained predictive map of epithermal gold potential includes the remotely-detected hydrothermal alteration evidence. The predicted favourable zones comprise about 23% of the district, demarcate at least 68% of the 'model' deposits and at least 77% of the 'validation deposits and show good spatial coincidence with significant geochemical anomalies. For Abra area, the optimal geologically-constrained predictive map delineates about 23% of the area as favourable for porphyry deposits, accurately reflects at least 58% of the 'model' deposits and at least 65% of the 'validation' deposits and shows good spatial coincidence between the predicted favourable zones and the significant Cu anomalies. The optimal geologically-constrained predictive map is as useful as the optimal integrated geochemical-geological predictive map. For Catanduanes Island, the best geologically-constrained predictive map demarcates about 18% of the island as favourable for gold-copper deposits, accurately delineates about 65% of the 'model' deposits and shows good spatial coincidence between the predicted favourable zones and the geochemically-anomalous catchment basins. The optimal geologically-constrained predictive map is inferior to the integrated geochemical-geological predictive map but is nonetheless useful inasmuch as only geological map data are used and yet it is valid and predicts similar favourable zones. For Isabela area, the predictive map of nickeliferous-laterite potential demarcates mostly the ultramafic terrane as favourable for this type of deposit. It indicates that about 45% of the section with known nickeliferous-

laterite has high potential; however, only geochemical data are available to indicate the validity of the predictive map.

The examples here demonstrate the application of the theory of fuzzy sets in the generation of geologically-constrained predictive maps of mineral potential that can be useful to guide further exploration in the search for undiscovered mineral deposits in the respective study areas and as inputs to land-use policy-making. Whilst the application of the theory of fuzzy sets explicitly considers whether particular sets of geological objects have grades of membership intermediate between completely and not completely favourable evidence of miner potential, it does not explicitly consider whether mineral deposits have grades of membership intermediate between complete and incomplete dependence on the geological variables. In the next chapter, the dependence or independence of mineral deposits on geological variables is considered by way of a logistic regression approach.

Chapter 9

Logistic Regression for Mineral Potential Mapping

"What could be cuter than to feed a computer
With wrong information but naïve expectation
To obtain with precision a Napoleonic decision?"

Maj. de Seversky, Alexander P.
In: J.C. Davis (1973), Statistics & Data Analysis in Geology,
John Wiley & Sons, Inc., New York, 550 pp.

This Chapter demonstrates the application of logistic regression technique to geologically-constrained mineral potential mapping. Portions of this Chapter have been submitted for publication as Logistic Regression for Geologically-Constrained Mapping of Gold Mineralization Potential, Baguio District, Philippines (Carranza and Hale, 2001c).

9.1 INTRODUCTION

Mineral deposit formation clearly depends on a number of favourable geological processes (Park and MacDiarmid, 1975; Evans, 1987, 1993; Pirajno, 1992). The detailed study of the way in which a dependent variable (e.g., mineral deposits) is controlled by one or more independent variables (e.g., faults/fractures, plutonic rocks) is regression (Kendall and Buckland, 1982). In the past 20 years or so, a number of quantitative studies using regression models have been conducted to map mineral potential based on geological map data (Chung and Agterberg, 1980, 1988; Agterberg, 1988). Of the various regression models applied to mineral exploration, logistic regression is favoured due to its many advantages over the linear and other regression models as demonstrated by Agterberg (1974), Chung (1978), Chung and Agterberg (1980), Bonham-Carter and Chung (1983), Wrigley and Dunn (1986), Reddy et al. (1990), Harris and Pan (1991), Reddy et al. (1991), Reddy et al. (1992).

One particular advantage of the logistic regression model over linear and other regression models is its ability to constrain the probability estimates within the unit interval of zero and one (see below). In addition, logistic regression is most appropriate for studying relationships involving a dichotomous dependent or response variable, which can be represented only by a value of one or zero (i.e., present or absent, etc.), and a number of independent or predictor variables, which can be a mixture of dichotomous, nominal and/or ratio variables (Rock, 1988). The independent variables in logistic regression can take any form. That is, logistic regression makes no assumption about the distribution of the independent variables. They do not have to be normally distributed, linearly

related or of equal variance within each group. The relationship between the predictor and response variables is not a linear function in logistic regression. An obvious application of the logistic model is therefore to mineral potential mapping, where the target mineral deposit is usually represented as present or absent and the probability of its occurrence (lying within the unit interval 0 and 1) is determined by numerous interlocking variables of the geological environment. The distribution of the geological variables is usually imprecise and the relationships among the different geological variables and their relationships to mineral deposits are, in general, complex. Thus, to ask whether the occurrence (presence or absence) of mineral deposits can be predicted quantitatively from a collage of geological variables is to demand logistic regression (Rock, 1988).

Agterberg (1974), Chung (1978), Chung and Agterberg (1980) and Wrigley and Dunn (1986) performed logistic regression analyses using equal-area cells (i.e., pixels). On the other hand, Agterberg (1992a, 1992b) and Agterberg et al. (1993) described an algorithm for weighted logistic regression analysis using irregular polygons, which are weighted according to their areas (i.e., number of unit cells). The irregular polygons are unique overlap conditions of the input binary independent geological variables. Agterberg et al. (1993) extended their analyses to multi-class independent geological variables (i.e., proximity to geological variables) but found that the results of using either binary independent geological variables or multi-class independent geological variables have small differences. Agterberg (1992a, 1992b) and Agterberg et al. (1993) have shown that weighted logistic regression produces results similar to weights of evidence modeling, but the former has the advantage over the latter because it has no assumption of conditional independence between the predictor geological variables. Although Agterberg (1992a, 1992b) and Agterberg et al. (1993) have not shown the advantage of their weighted logistic regression over the logistic regression using equal-area cells, it is believed that the different applications would give similar results especially if the pixel size used is the same (Bonham-Carter, pers. comm.)

In this work, logistic regression using equal-area cells, instead of the weighted logistic regression, was applied to determine whether the results are better than the results of the other methods demonstrated in Chapters 5 to 8. Chung and Agterberg (1980, 1988) and Agterberg (1988) used rock types as independent geological variables and mineral deposits as dependent variables. Here, lithologic units, hydrothermal alteration units and proximity to curvi-linear or point geological features were used as independent geological variables.

9.2 LOGISTIC REGRESSION MODEL

The following formulation of the logistic regression model is drawn mainly from Chung and Agterberg (1980). Suppose that a study area is divided into equal-area cells or pixels and that p geological features, x_{ij} (j = 1, 2, . . ., p), are coded

for every i-th cell. To map zones of mineral potential, two types of mineral deposit data, (1) number of mineral deposits and (2) presence or absence of mineral deposits in a cell, can be considered as dependent variables in regression models and related to the p geological variables. Let Y_i be a binary random variable representing presence (=1) or absence (=0) of mineral deposits with the probability θ_i that at least one mineral deposit is present in the i-th cell. The probability θ_i can be expressed as a function of the p geological variables, thus

$$\theta_i = g(x_{i1}, x_{i2}, ..., x_{ip}) . \quad (9\text{-}1)$$

The most commonly used form of g is the linear function, in which the probability θ_i in cell i is assumed to be a linear function of the p geological variables such that

$$\theta_i = X_i' b \quad (9\text{-}2)$$

for all i = 1, 2, . . ., n cells, where $X_i' = (1, x_{i1}, x_{i2}, ..., x_{ip})$ is the (p+1) dimensional vector for constant 1 and the p geological variables in cell i, and b is the corresponding vector of (p+1) unknown regression coefficients to be estimated. Ordinary least squares is often used to estimate b

$$\hat{b} = (X_i' X)^{-1} X_i' y \quad (9\text{-}3)$$

and model

$$Y_i = \theta + r = Xb + r \quad (9\text{-}4)$$

where y is an n-dimensional column vector with the i-th element y_i representing the observed binary values of random variable Y_i; X is the nx(p+1) matrix of the values X_i; and r is the n-dimensional column vector of the residuals r_i. The ordinary least squares estimate

$$\hat{\theta} = X_i' \hat{b} \quad (9\text{-}5)$$

can then be used to estimate θ_i for all i = 1, 2, . . ., n. Among the limitations of the ordinary least squares estimates is that $\hat{\theta}$ may fall outside the interval between 0 and 1, which is contradictory with the definition of probability θ_i (Cox and Snell, 1989).

In order to constrain the estimate of θ_i within the unit interval [0,1], Cox and Snell (1989) advocate using a logistic model as an alternative to the linear model in Equation 9-2. To represent the probability, θ_i, in Equation 9-1 of a mineral

deposit in the i-th cell in terms of p geological variables in order that estimates of $\hat{\theta}$ lie within the unit interval [0,1], the logistic form is postulated thus

$$\theta_i = e^{X_i'b} / (1 + e^{X_i'b}) \text{ or} \tag{9-6}$$

$$\text{log it}(\theta_i) = \log_e\left(\frac{\theta_i}{1-\theta_i}\right) = X_i'b \tag{9-7}$$

where $X_i'b$ is the same as in Equation 9-2. Cox and Snell (1989) suggest the use of the maximum likelihood method to estimate b. Let $Y_1, Y_2, \ldots, Y_n$ be independent binary random variables. Let Y_i have the probability of 1, i.e., θ_i in Equation 9-6 equals 1 for all i = 1, 2, . . ., n. Without loss of generality, it can be assumed that the first values of my_i are equal to 1 and the last values of $(n\text{-}m)y_i$ are equal to zero, and since Prob $(Y_i = 1) = \theta_i$ and Prob $(Y_i = 0) = 1\text{-}\theta_i$, the likelihood function (Chung and Agterberg, 1980) is

$$\prod_{i=1}^{m} \theta_i \prod_{j=m+1}^{n} (1-\theta_i) . \tag{9-8}$$

By substituting θ_i in Equation 9-6 for θ_i in Equation 9-8 and taking the logarithm, the log-likelihood L(b) is obtained as

$$L(b) = \sum_{i=1}^{m} X_i'b - \sum_{i=1}^{n} \log_e(1 + e^{X_i'b}) . \tag{9-9}$$

Thus, the maximum likelihood estimate $\hat{b}$ of b in Equation 9-6 is obtained by solving the following system of (p+1) equations

$$\sum_{i=1}^{m} x_{is} - \sum_{j=1}^{n} \frac{x_{js} e^{X_j'\hat{b}}}{1 + e^{X_j'\hat{b}}} = 0 \tag{9-10}$$

for all elements s = 0, 1, 2, . . . , p. The system of nonlinear equations in Equation 9-9 can be solved by the scoring method (Rao, 1973).

The Wald statistic is used to test the null hypothesis in logistic regression that a particular coefficient is zero (Menard, 1995). It is the ratio of the unstandardised coefficient to its asymptotic standard error. The Wald statistic tests the significance of the coefficient associated with a given independent variable. Computationally, the Wald statistic = b^2/ASE_b^2, where ASE_b^2 is the asymptotic standard error of the logistic regression coefficient.

9.3 APPLICATION OF LOGISTIC REGRESSION MODEL USING GIS

9.3.1 Data inputs

The appropriate geological features (lithologic units, hydrothermal alteration units, faults/fractures, porphyry pluton contacts/centroids, batholithic pluton margins, topographic geoinformation) were used as independent or predictor variables whilst the locations of mineral deposits were used as dependent variables in the logistic regression modeling of mineral potential in Benguet province, Baguio district, Abra area and Catanduanes Island.

9.3.2 Data representation for logistic regression modeling

Analyses of spatial associations between mineral deposits and geological features (Chapters 4 and 6) suggest that, in addition to lithologic units and hydrothermal alterations units, proximity to curvi-linear or point geological features can be used as predictor variables for mapping mineral potential. These variables were quantified systematically as follows. A study area was first converted into an equal-area grid by rasterising the input vector maps (i.e., polygon maps of lithologic units, hydrothermal alteration units, segment maps of curvi-linear or point geological features and point maps of mineral deposits) using a 100x100 m pixel size. Rasterisation was all that is needed for the lithologic and hydrothermal alteration maps, whilst further map operations were performed for the curvi-linear or point geological features and the mineral deposits. Raster maps portraying distances from the curvi-linear or point geological features were first generated. The distance maps were then categorised into proximity classes based on the quantified spatial associations between the mineral deposits and the curvi-linear or point geological features. The optimum proximity classes determined in Chapter 7 were used in this Chapter. For the mineral deposits, a pixel size of 100x100 m resulted in a number of pixels of mineral deposits that is equal to the number of known mineral deposits. The number of mineral deposits in the different study areas is invariably low compared to the total number of 100x100 m pixels. This tends to undermine reliable logistic regression modeling of mineral potential. The problem was resolved by buffering the mineral deposits to represent them as 'mineralised zones' (see Chapter 7), which approximate the likely actual areal dimensions of the deposits

A study area was then divided into equal-area cells by rasterising a polygon map, which represents the boundary of that particular study area, using a 1000x1000 m pixel size. For each of the 1x1 km cells, a unique identifier was assigned through the following steps. First, the 1x1 km cells were vectorised into points (i.e., each cell is represented by its centre point), which results in a point map. Second, the label of each point, which was originally the same as the label of the polygon of the study area, was revised and a unique label was assigned

to each point. From the point map, a table file was generated, which contains the easting and northing coordinates and labels of each point, and in which other spatial attributes of each 1x1 km cell were stored.

For each 1x1 km cell, spatial attributes representing the occurrences of particular geological features and 'mineralised pixels' were systematically quantified by determining the number of 100x100 m pixels that represent these features through the following steps. First, the 1x1 km raster cells were re-sampled or georeferenced to the 100x100 m pixel grid that was used to rasterise the input vector maps. This step ensured that the pixels in the 1x1 km cells have a one-to-one correspondence with the pixels in the raster maps of the geological features. Second, the re-sampled map of 1x1 km cells is 'crossed' or overlain with each of the raster maps of geological features and 'mineralised zones'. This step resulted in a cross-table that provides, for each of the 1x1 km cells, the number of 100x100 m pixels of lithologic units, hydrothermal alteration units, proximity classes of curvi-linear and point geological features, and 'mineralised zones'.

9.3.3 Logistic regression modeling

The number of occurrences (i.e., number of 100x100 m pixels) of lithologic units, hydrothermal alteration units and proximity classes of curvi-linear and point geological features in the 1x1 km cells were used as independent variables in logistic regression to predict the probability of presence or absence of a mineral deposit, but not the number of mineral deposits. Hence, as dependent variables, the observed presence or absence of 'mineralised zones' was represented simply by assigning a probability of 1 to cells that contain a 'mineralised pixel', otherwise a probability of zero was assigned.

In order for the results of the logistic regression to be geological and spatially meaningful, only those geological variables with the following characteristics were used as independent variables. First, only those lithologic units and/or hydrothermal alteration units that are known to be genetically associated with the mineral deposits were considered. Second, only those proximity classes of curvi-linear or point geological features that are positively spatially associated with the mineral deposits (see Chapters 4 and 6) and those that have good probability assignments (see Chapter 7) were considered. In order to determine whether all independent variables (with the two characteristics defined above) or only statistically significant predictor variables (with the two characteristics defined above) are useful as predictors of mineral potential, two sets of logistic regression experiments were performed. First, all independent variables were forced into the logistic regression (i.e., the most significant independent variables were not searched according to a statistical criterion but all independent variables were included in the final logistic regression model). The first set of experiments is hereafter referred to as the forced regression

modeling. Second, a backward stepwise logistic regression was performed, which is hereafter referred to as the backward regression modeling. In backward regression modeling, analysis begins with a model inclusive of all independent variables (i.e., model of first set of regression experiments) and, through iterative steps, proceeds to eliminate those predictor variables that do not contribute significantly to the regression (Menard, 1995). The backward regression modeling terminates when no more independent variables can be eliminated from the model according to a statistical criterion. In all the experiments that were performed for backward regression modeling, a 90% significance level was used as the statistical criterion to retain an independent variable in the final logistic regression model. The results of forced regression modeling and the backward regression modeling were then compared and validated as described below.

9.3.4 Presentation and validation of mineral potential maps

The maps of predicted probabilities of presence or absence of mineral deposits based on the forced regression modeling and the backward regression modeling were converted into binary favourability maps. To convert the maps of predicted probabilities into binary favourability maps, a search was made for a suitable threshold predicted probability to distinguish between favourable zones and unfavourable zones. It was found that the 80^{th} percentile probability (see also Chapter 7) was suitable to convert the maps of predicted probabilities into favourability maps. The favourability maps were then validated against 'model' and 'validation' mineral deposits and/or mineralised zones. It is demonstrated later that the 80^{th} percentile probabilities used to generate the binary favourability maps for each of the different study areas result in prediction rates of at least 65% for most of the 'model' and/or 'validation' deposits.

The reliability of the logistic regression models was tested by comparing the predicted number of favourable cells with 'mineralised zones' with the observed number of favourable of cells with 'mineralised zones'. The predicted number of cells with 'mineralised zones' was obtained as the product of the estimated probabilities and the area of the 1x1 km cells in the predicted favourable zones. The corresponding observed number of cells with 'mineralised zones' was obtained as the number of 1x1 km cells in the predicted favourable zones that contain a 'mineralised zone'. A logistic regression model was considered reliable if the predicted number of cells with 'mineralised zones' in the favourable zones is closely similar to or the same as the observed number of cells of 'mineralised zones' in the favourable zones (Agterberg et al., 1993).

The usefulness of the favourability maps based on the forced regression modeling and the backward regression modeling was determined by comparing their corresponding prediction rates for the 'model' and/or 'validation' deposits. The geochemical anomalies were also used (a) to validate the predictive maps

in terms of spatial overlap between the predicted geologically-favourable zones and the geochemical anomalies and (b) to judge whether the geologically-constrained predictive maps are superior/inferior to the integrated geochemical-geological predictive maps.

9.4 APPLICATION TO BENGUET PROVINCE

The geological features that were used in the logistic regression modeling include lithologic units, hydrothermal alteration units, strike-slip fault discontinuities, porphyry pluton centroids, batholithic pluton margins and mineral deposits. The predictive mapping of porphyry copper potential was based on the same subset of 23 'model' porphyry copper deposits used in the weights of evidence modeling (see Section 6.4). The subset of eight 'validation' porphyry copper deposits was used to validate the predictive model(s).

9.4.1 Variables in logistic regression modeling

Among the lithologic units (Figure 2.5), the Miocene Limestones were not used as an independent variable because they are not genetically and spatially associated with the porphyry copper deposits (Sillitoe and Gappe, 1984). Among the remotely-detected hydrothermal alteration units (Figure 3.24), only the argillic alteration unit was used as an independent variable because the illitic and propylitic alteration units are poor spatial predictors (see Table 7.2). Of the different proximity classes of curvi-linear or point geological features, only the first three classes (i.e., nearest proximity classes; see Table 7.2) were used as independent variables because they represent the ranges of optimal positive spatial associations with the porphyry copper deposits. The 'mineralised zones' of the 23 'model' deposits used in Chapter 7 (subsection 7.4.1) were used here to determine the dependent variable. Shown in Figure 9.1 are the 1x1 km cells and the 'mineralised zones' of the 'model' deposits, which occur in 85 of the 2547 1x1 km cells. In Table 9.1, the quantified independent and dependent variables are exemplified for 10 of the 2547 cells.

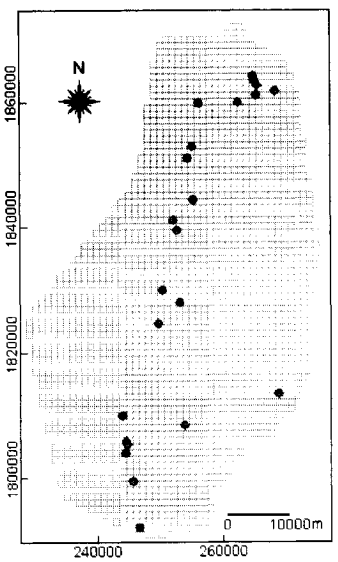

Figure 9.1. Porphyry copper 'mineralised zones' and 1x1 km cells, Benguet province.

Table 9.1. Data for independent and dependent variables used in logistic regression as exemplified for 10 of the 2547 1x1 km cells, Benguet province. Values of independent variables are numbers of 100x100 m pixels in 1x1 km cells. Values of dependent variable (OP) are probabilities that a 1x1 km cell contains at least a 100x100 m 'mineralised pixel'.

Cell ID	Independent variables															OP**
	IP	CV	BI	VR	M	AA	SS1	SS2	SS3	BP1	BP2	BP3	PP1	PP2	PP3	
b0001	0	0	3	0	94	0	99	0	0	35	58	6	0	0	0	0
b0002	0	0	0	0	99	0	56	42	0	0	1	80	0	0	0	0
b0003	0	0	70	0	24	0	52	45	0	93	4	0	0	0	0	0
b0004	0	0	18	0	82	0	64	36	0	67	33	0	0	0	0	0
b0005	0	0	0	0	100	0	10	78	12	0	19	81	0	0	0	0
b0006	0	0	0	0	76	0	0	1	57	0	0	5	0	0	0	0
b0007	0	0	0	0	96	6	65	34	0	0	0	0	0	0	0	0
b0008	0	0	0	0	100	0	1	74	25	0	0	0	0	0	0	0
b0009	0	0	0	0	100	8	0	8	74	0	0	0	0	0	0	0
b0010	0	0	0	0	100	54	0	0	28	0	0	0	0	0	0	0

IP = L. Miocene – Pleistocene Intrusive Porphyries; CV = L. Miocene – Pliocene Clastics/volcanics; BI = Oligocene – M. Miocene Batholithic Intrusives; VR = Eocene – Miocene Volcaniclastic rocks; M = Cretaceous – Paleogene Metavolcanics. AA = advanced argillic alteration; SS = strike-slip fault discontinuities; SS1 = <1.50 km; SS2 = 1.50-2.25 km; SS3 = 2.25-2.95 km; BP = batholithic pluton margins; BP1 = <0.40 km; BP2 = 0.4-0.95 km; BP3 = 0.95-1.80 km; PP = porphyry pluton contacts; PP1 = <1.00 km; PP2 = 1.00-1.50 km; PP3 = 1.50-1.95 km.

** OP = porphyry copper occurrence probability.

9.4.2 Predictors of porphyry copper potential

The results of the forced regression modeling and the backward regression modeling are shown in Tables 9.2 and 9.3, respectively. Among the independent variables, the advanced argillic alteration units, the proximity classes of strike-slip fault discontinuities (<1.5 km, 1.5-2.25 km, 2.25-2.95 km), the proximity class of batholithic pluton margins (0.95-1.80 km) and the proximity classes of porphyry pluton centroids (<1.00 km, 1.00-1.50 km, 1.50-1.95 km) are significant predictors of porphyry copper potential. The lithologic units are not significant predictors of porphyry copper potential. Zones proximal to the batholithic pluton margins (i.e., <0.95 km) are also not significant predictors.

9.4.3 Predictive mapping of porphyry copper potential

Based on the two sets of regression experiments, the regression coefficients, b, in Tables 9.2 and 9.3 were used to estimate the probabilities of porphyry copper occurrence using Equation 9-6 above. A threshold probability of 0.035 (80^{th} percentile) was used to distinguish between favourable zones and unfavourable zones based on the probability estimates resulting from the forced regression modeling. A threshold probability of 0.032 (80^{th} percentile) was used to map favourable zones and unfavourable zones based on the probability estimates resulting from the backward regression modeling.

Table 9.2. Logistic regression coefficients and their corresponding statistical indicators of significance obtained by forced regression modeling, Benguet province. Rows in bold pertain to statistically significant predictors at 90% significance level.

Independent variable*	b	Asymptotic standard error	Wald-statistic	Significance level (α)
IP	0.0236	0.0256	0.8529	0.3557
CV	0.0305	0.0230	1.7590	0.1848
BI	0.0304	0.0228	1.7819	0.1819
VR	0.0273	0.0234	1.3630	0.2430
M	0.0311	0.0224	1.9153	0.1664
AA	**0.0080**	**0.0046**	**2.9594**	**0.0854**
SS1	**0.0193**	**0.0040**	**23.2702**	**0.0000**
SS2	**0.0190**	**0.0043**	**19.6946**	**0.0000**
SS3	**0.0142**	**0.0055**	**6.7399**	**0.0094**
BP1	0.0030	0.0051	0.3502	0.5540
BP2	0.0043	0.0052	0.6798	0.4097
BP3	**0.0134**	**0.0042**	**9.9805**	**0.0016**
PP1	**0.0332**	**0.0068**	**23.7785**	**0.0000**
PP2	**0.0150**	**0.0078**	**4.2027**	**0.0404**
PP3	**0.0381**	**0.0084**	**20.5098**	**0.0000**
Constant	-8.6175	2.2606	14.5315	0.0001

*See Table 9.1 for explanation of codes for variables.

The spatial distributions of the predicted zones of porphyry copper potential based on the forced regression modeling (Figure 9.2a) and based on the backward regression modeling (Figure 9.2b) are similar. In Figure 9.2a, the observed number of cells with 'mineralised zones' in the predicted favourable zones is 71 whilst the predicted number of favourable cells with 'mineralised zones' is 64.9 (say 65), or an underestimation by 8%. In Figure 9.2b, the observed number of cells with 'mineralised zones' in the predicted favourable zones is 68 whilst the predicted number of cells with 'mineralised zones' is 63.6 (say 64), or an underestimation by about 6%. Hence, the predictive map in Figure 9.2b is more reliable than the predictive map in Figure 9.2a.

Table 9.3. Logistic regression coefficients and their corresponding statistical indicators of significance obtained by backward regression modeling, Benguet province.

Independent variable*	b	Asymptotic standard error	Wald-statistic	Significance level (α)
AA	0.0080	0.0045	3.1397	0.0764
SS1	0.0193	0.0039	23.7995	0.0000
SS2	0.0194	0.0043	20.6000	0.0000
SS3	0.0142	0.0055	6.7097	0.0096
BP3	0.0127	0.0038	11.4113	0.0007
PP1	0.0301	0.0043	48.4870	0.0000
PP2	0.0184	0.0072	4.6107	0.0318
PP3	0.0357	0.0081	19.2333	0.0000
Constant	-5.4830	0.3191	295.2051	0.0000

*See Table 9.1 for explanation of codes for variables.

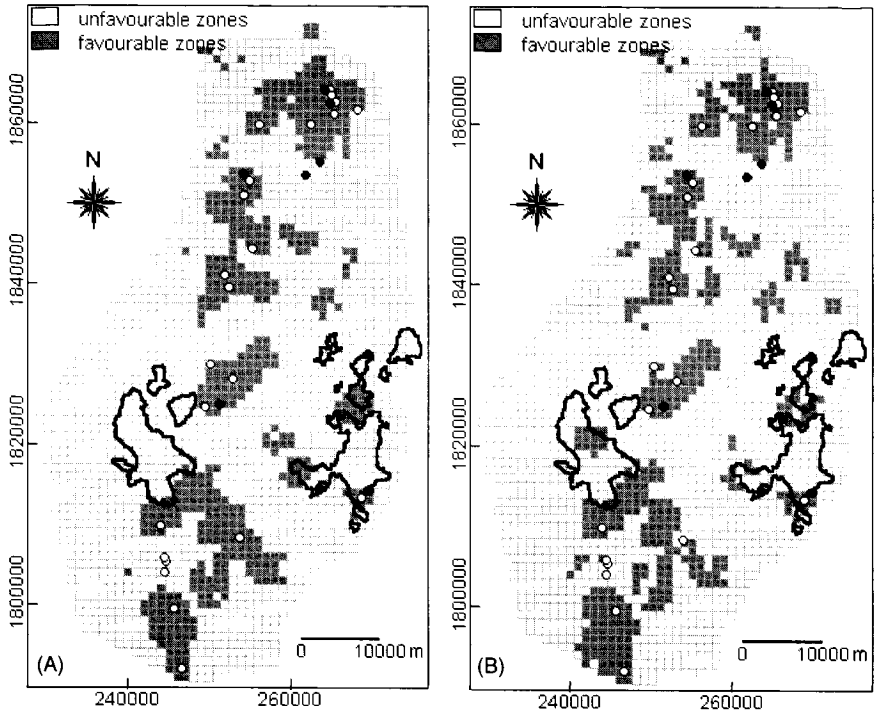

Figure 9.2. Predictive maps of porphyry copper potential, Benguet province, based on (a) forced regression modeling and (b) backward regression modeling. Unfilled circles = 'model' deposits; filled circles = 'validation' deposits; polygons in solid lines = geochemically-anomalous catchment basins.

Both of the predictive maps in Figure 9.2 delineate about 20% of the province as favourable for porphyry copper deposits and have the same prediction rates of 62.5% for the 'validation' deposits (Tables 9.4). However, the predictive map based on the backward regression modeling (Figure 9.2b) has a higher prediction rate for the 'model' deposits and is therefore superior to the predictive map in Figure 9.2a. The predicted favourable zones in either of the predictive maps in Figure 9.2 show spatial overlap with the geochemically-anomalous catchment basins. These zones of overlap are probably the sources of the geochemical anomalies.

Table 9.4. Spatial geoinformation characteristics of predictive maps of porphyry copper potential based on logistic regression modeling, Benguet province.

Predictive map	% predicted favourable zones	% predicted 'model' deposits	% predicted 'validation' deposits
Figure 9.2a	19.9	78.3	62.5
Figure 9.2b	19.9	82.6	62.5

9.4.4 Discussion

The relative importance of the different geological variables as spatial predictors of porphyry copper potential is reflected by the statistical significance levels of the logistic regression coefficients. For example, the proximity classes within 2.95 km of strike-slip fault discontinuities and the proximity classes within 1.95 km of porphyry pluton centroids are more statistically significant than the proximity class 0.95-1.80 km of batholithic pluton margins. Indeed, porphyry copper deposits in the province are genetically and spatially associated with the porphyry plutons localised at or near discontinuities of strike-slip faults that tend not to cut the batholithic plutons, which are nonetheless precursors of the porphyry plutons. The advanced argillic alteration units are less statistically significant spatial predictors than the porphyry plutons, strike-slip discontinuities and batholithic plutons. The advanced argillic alteration units represent the upper levels of the porphyry hydrothermal systems; however, some of these alteration units are associated with younger epithermal systems and overprinted on the older porphyry systems (UNDP, 1987b). Hence, advanced argillic alterations are important but indirect spatial guides to porphyry copper deposits. The different lithologic units are not statistically significant spatial predictors of porphyry copper potential, reflecting that various types of lithologies can be potential hosts of porphyry copper mineralisation. The lack of statistical significance of the porphyry plutons as spatial predictors is attributed to the fact that mapped porphyry plutons represent very narrow areas as compared to the wide lateral extents of the other lithologic units. It is known, however, that some of the porphyry copper deposits are associated with non-outcropping porphyry plutons (Sillitoe and Gappe, 1984; Sillitoe and Angeles, 1985). Nonetheless, the low importance of the porphyry plutons as spatial predictors of porphyry copper potential is augmented by the high importance of proximity to these plutons and proximity to strike-slip fault discontinuities where they are emplaced (see subsection 4.3.1).

9.5 APPLICATION TO BAGUIO DISTRICT

The geological features used in the logistic regression modeling include lithologic units, hydrothermal alteration units, batholithic pluton margins, porphyry pluton contacts, northeast-trending faults/fractures, northwest-trending faults/fractures and the 19 large-scale gold deposits. The 63 small-scale gold deposits and the stream sediment geochemical anomalies (see section 2.3.3; UNDP 1987a) were used to validate the predictive model(s).

9.5.1 Variables in logistic regression modeling

Of the lithologic units (Figure 2.11), the Kennon Formation was not used as an independent variable as it is not genetically/spatially associated with the gold

deposits (Mitchell and Leach, 1991; Cooke and Bloom, 1996). Among the remotely-detected hydrothermal alteration units (Figure 3.15b), only illitic alteration was used as an independent variable because they are known to be genetically/spatially associated with the gold deposits (UNDP, 1987b). Of the different proximity classes of curvi-linear geological features, the first four proximity classes of the porphyry pluton contacts and the first two proximity classes of the northeast-trending faults/fractures and the batholithic pluton margins were used as independent variables as these proximity classes represent the ranges of optimal positive spatial associations with the gold deposits (see sub-sections 4.4.5 and 6.5.1). The 'mineralised zones' of 19 known large-scale gold deposits (see Chapter 7; sub-section 7.5.1), which occur in 35 of the 408 cells, were used as the dependent variable (Figure 9.3). In Table 9.5, the quantified predictor and dependent variables are exemplified for 10 of the 408 1x1 km cells.

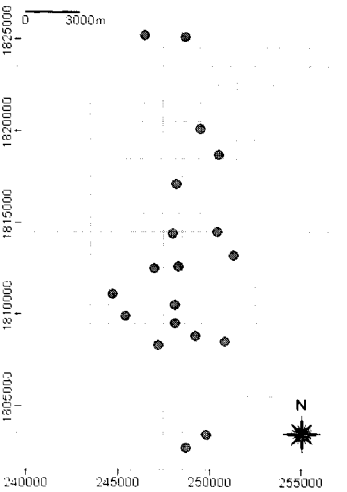

Figure 9.3. Large-scale gold 'mineralised zones' and 1x1 km cells, Baguio district.

Table 9.5. Data for independent and dependent variables used in logistic regression as exemplified for 10 of the 408 1x1 km cells, Baguio district. Values of independent variables are numbers of 100x100 m pixels in 1x1 km cells. Values of dependent variable (OP) are probabilities that a 1x1 km cell contains at least a 100x100 m 'mineralised pixel'.

Cell ID	Independent variables														OP**
	KF	I	AB	ZF	PF	IA	NE1	NE2	BP1	BP2	PP1	PP2	PP3	PP4	
b001	100	0	0	0	0	0	0	10	0	0	0	0	0	0	0
b002	100	0	0	0	0	12	0	13	0	0	0	0	0	0	0
b003	100	0	0	0	0	0	18	29	0	0	0	0	0	0	0
b004	100	0	0	0	0	0	56	42	0	0	0	0	0	0	0
b005	100	0	0	0	0	0	47	25	0	0	0	0	0	0	0
b006	11	0	0	32	0	0	51	34	0	0	0	0	0	0	0
b007	0	0	0	100	0	11	40	20	0	10	0	0	0	30	1
b008	5	0	1	94	0	72	10	15	50	50	0	0	49	51	1
b009	0	0	100	0	0	66	0	0	40	60	0	75	25	0	0
b010	0	23	77	0	0	33	10	35	67	33	99	1	0	0	1

*KF = L. Miocene Klondyke Formation; I = L. Miocene – Pleistocene Intrusives; AB = L. Oligocene – M. Miocene Agno Batholith; ZF = L. Eocene – E. Eocene Zigzag Formation; PF = Cretaceous-Eocene Pugo Formation; IA = illitic alteration; NE = northeast-trending faults/fractures; NE1 = <200 m; NE2 = 200-425 m; BP = batholithic plutons; BP1 = <400 m; BP2 = 400-1025 m; PP = porphyry pluton contacts; PP1 = <700 m; PP2 = 700-1450 m; PP3 = 1450-2150 m; PP4 = 2150-2950 m.

**OP = gold occurrence probability.

9.5.2 Predictors of epithermal gold potential

The illitic alteration units and proximity classes (<700 m and 700-1450 m) of the porphyry pluton contacts are significant predictors of gold potential based on the forced regression modeling (Table 9.6). The backward regression modeling also shows that the Zigzag Formation and proximity classes of northeast-trending faults/fractures (200-425 m) and batholithic pluton margins (400-1025 m) are significant predictors of gold potential (Table 9.7).

Table 9.6. Logistic regression coefficients and their corresponding statistical indicators of significance obtained by forced regression modeling, Baguio district. Rows in bold pertain to statistically significant predictors at 90% significance level.

Independent variable*	b	Asymptotic standard error	Wald-statistic	Significance level (α)
KF	0.0743	0.0849	0.7662	0.3814
I	0.0776	0.0865	0.8053	0.3695
AB	0.0819	0.0846	0.9383	0.3327
ZF	0.0892	0.0853	1.0930	0.2958
PF	0.0781	0.0841	0.8626	0.3530
IA	**0.0111**	**0.0063**	**3.1026**	**0.0782**
NE1	0.0003	0.0111	0.0009	0.9766
NE2	0.0229	0.0158	2.1105	0.1463
BP1	0.0033	0.0064	0.2645	0.6070
BP2	0.0106	0.0081	0.7268	0.1888
PP1	**0.0211**	**0.0094**	**5.0690**	**0.0244**
PP2	0.0081	0.0093	0.7536	0.3853
PP3	**0.0237**	**0.0073**	**9.1840**	**0.0024**
PP4	0.0075	0.0089	0.7213	0.3957
Constant	-12.7357	8.4045	2.2973	0.1296

*See Table 9.5 for explanation of codes for variables.

The lithologic units are generally less significant than the proximity classes of curvi-linear geological features as predictors of gold potential. Zones within 200 m of the northeast-trending faults/fractures and within 400 m of the batholithic pluton margins are not significant spatial predictors.

Table 9.7. Logistic regression coefficients and their corresponding statistical indicators of significance obtained by backward regression modeling, Baguio district.

Independent variable*	b	Asymptotic standard error	Wald-statistic	Significance level (α)
ZF	0.0098	0.0051	3.7031	0.0543
IA	0.0130	0.0058	5.0322	0.0249
NE2	0.0287	0.0120	5.6787	0.0172
BP2	0.0144	0.0071	4.0546	0.0442
PP1	0.0202	0.0060	11.3296	0.0008
PP3	0.0249	0.0073	11.5139	0.0007
Constant	-4.8978	0.5889	69.1605	0.0000

*See Table 9.5 for explanation of codes for variables.

9.5.3 Predictive mapping of epithermal gold potential

The regression coefficients in Tables 9.6 and 9.7 were applied to estimate the probabilities of epithermal gold occurrence using Equation 9-6 above. The probability estimates based on the forced regression modeling were classified using a threshold probability of 0.138 (80^{th} percentile) to differentiate between favourable zones and unfavourable zones. A threshold probability of 0.133 (80^{th} percentile) was used to classify the probability estimates based on the backward regression modeling to discriminate unfavourable zones from favourable zones. The predictive maps are shown in Figure 9.4.

In Figure 9.4a, the observed number of cells with 'mineralised zones' in the predicted favourable zones is 22 whilst the predicted number of cells with 'mineralised zones' in the favourable zones is 21.9 (say 22). In Figure 9.2b, the observed number of cells with 'mineralised zones' in the predicted favourable zones is 20 whilst the predicted number of cells with 'mineralised zones' in the favourable zones is 20.4 (say 20). Hence, both predictive maps are reliable.

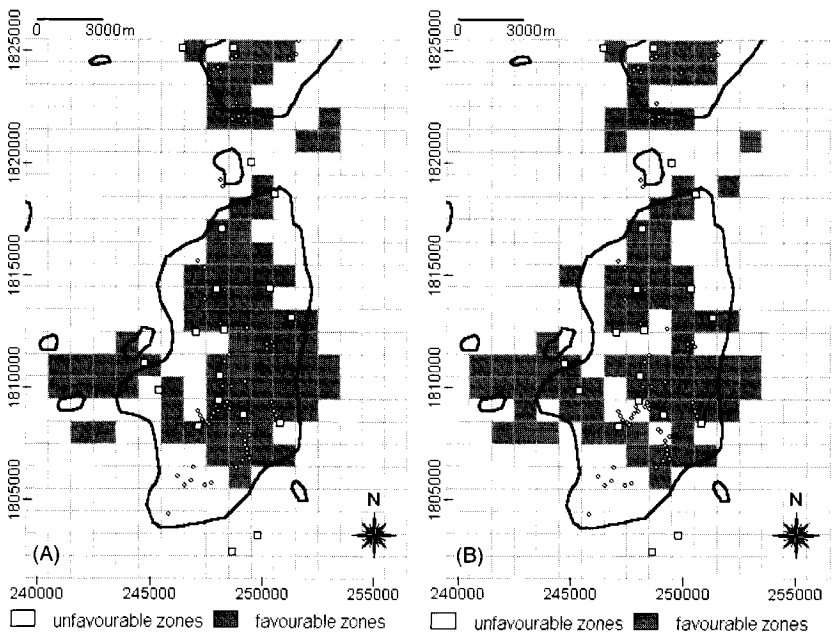

Figure 9.4. Predictive maps of epithermal gold potential, Baguio district, based on (a) forced regression modeling and (b) backward regression modeling. Unfilled squares = 'model' deposits; small circles = 'validation' deposits; polygons in solid lines = stream sediment Au anomaly (UNDP, 1987a).

Table 9.8. Spatial geoinformation characteristics of predictive maps of epithermal gold potential based on logistic regression modeling, Baguio district.

Predictive map	% predicted favourable zones	% predicted 'model' deposits	% predicted 'validation' deposits
Figure 9.4a	20.3	78.9	76.2
Figure 9.4b	20.1	73.4	60.3

Both of the predictive maps in Figure 9.4 indicate that about 20% of the district has potential for epithermal gold deposits (Table 9.8). However, the predictive map in Figure 9.4a has more than a 5% prediction rate for the 'model' deposits and more than a 6% prediction rate for the 'validation deposits. The predictive map in Figure 9.4a is therefore superior to the predictive map in Figure 9.4b.

The predicted favourable zones in Figures 9.4a and 9.4b spatially coincide with about 56.9% and 52.9%, respectively, of the stream sediment Au anomaly. Both predictive maps show, at the centre of the district, a large favourable zone that coincides with the largest geochemical anomaly. The geologically-favourable zone at the centre extends westwards where it coincides with small geochemical anomalies. In the northern section is another predicted favourable zone, which also coincides with a geochemical anomaly. The predicted favourable zones have a higher prediction rate for the 'model' large-scale deposits than the geochemical anomalies (see section 2.3.3). Yet, it is clear from Figure 9.4 that the geochemical anomalies have a higher prediction rate for the 'validation' small-scale deposits than the geologically-favourable zones. This observation does not undermine the usefulness of the geologically-constrained predictive map because the geological features used in the predictive modeling have been mapped on a district-scale whilst the locations of the gold deposits have been mapped on a project-scale. Hence, the predictive maps in Figure 9.4 are useful on a district-scale rather than on a project-scale.

9.5.4 Discussion

The results indicate that (proximity to) the porphyry plutons are the most important control on gold mineralisation in the district. This has been postulated on the basis of field observations by Cooke and Bloom (1990) and Cooke et al. (1996). Also, the gold deposits occur within 700 m and between 1500 and 2000 m of the porphyry plutons. Further field observations are needed to clarify this finding. The results also indicate that gold-bearing quartz veins occur farther from the main traces of major northeast-trending fractures/fractures. Livingston (1939) observed that the deposits occur along shears subsidiary to these northeast-trending faults/fractures. The predictive maps in Figure 9.4 suggest other cells in the district where undiscovered deposits are probably present. In particular, the westward extension of the main geologically-favourable and geochemically-favourable zone in the central portion is prospective.

9.6 APPLICATION TO ABRA AREA

The geological features used in the logistic regression modeling include lithologic units, batholithic margins, porphyry pluton centroids, intersections of regional faults (i.e., north-trending and northeast-trending faults/fractures), north-trending faults/fractures and the 12 porphyry copper deposits. The geochemical data were also used in the logistic regression modeling. The known mineralised zones sub-section 2.4.1; JICA, 1980 were used to validate the predictive model(s). The stream sediment geochemical anomalies were also used to validate the predictive model(s).

9.6.1 Variables in logistic regression modeling

Of the lithologic units (Figure 2.13), only the plutonic rocks were used as independent variables because they represent the hydrothermal activity with which the known porphyry copper deposits are associated. The following proximal classes of curvi-linear or point geological features were used as independent variables: (a) the first three proximity classes of intersections of regional faults; (b) the first proximity class of porphyry pluton centroids; (c) the first two proximity classes of north-south trending faults/fractures; and (d) the first four proximity classes of granodiorite batholithic margins. These proximity classes of curvi-linear or point geological features represent the ranges of their optimal positive spatial associations with the porphyry copper deposits and they have high probability assignments (see Table 7.7). The geochemically-anomalous catchment basins (i.e., with Cu contents >170 ppm) were also used as independent variables because they show spatial association with the porphyry copper deposits (Figure 2.16a). The 'mineralised zones' of the 12 known porphyry copper deposits used in Chapter 7 (see sub-section 7.6.1) were used here as the dependent variable (Figure 9.5). The 'mineralised zones' occur in 39 of the 894 1x1 km cells. In Table 9.9, the quantified data representing the independent and dependent variables are exemplified for 10 of the 894 1x1 km cells.

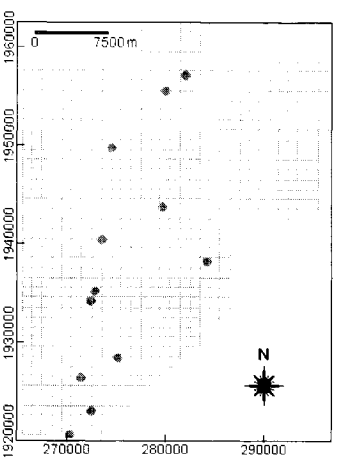

Figure 9.5. Porphyry copper 'mineralised zones' and 1x1 km cells, Abra area.

Table 9.9. Data for independent and dependent variables used in logistic regression as exemplified for 10 of the 894 1x1 km cells, Abra area. Values of independent variables are numbers of 100x100 m pixels in 1x1 km cells. Values of dependent variable (OP) are probabilities that a 1x1 km cell contains at least a 100x100 m 'mineralised pixel'.

Cell ID	Independent variables														OP**
	QDP	QD	G	FI1	FI2	FI3	PP1	NS1	NS2	GR1	GR2	GR3	GR4	STS	
b0001	0	0	0	0	0	0	0	0	0	0	0	0	0	0	0
b0002	0	0	0	0	0	0	0	0	0	0	0	16	57	0	0
b0003	0	0	9	0	0	0	0	0	0	32	25	23	0	0	0
b0004	0	0	80	0	0	0	0	0	0	8	24	44	4	0	0
b0005	0	0	80	0	0	0	0	0	0	0	0	26	54	0	0
b0006	0	0	70	0	0	0	0	0	0	26	37	17	0	0	0
b0007	0	0	18	0	0	0	0	0	0	34	38	8	0	0	0
b0008	0	0	0	0	0	0	0	0	0	0	0	0	34	0	0
b0009	0	7	0	0	0	0	0	0	0	0	4	47	49	0	0
b0010	0	19	13	0	0	0	0	0	0	35	49	16	0	0	0

* QDP = Quartz diorite porphyry pluton; QD = Quartz diorite batholithic pluton; G = Granodiorite batholithic pluton; FI = intersection of regional faults; FI1 = <1 km; FI2 = 1-1.5 km; FI3 = 1.5-2.025 km; PP = porphyry pluton centroids; PP1 = <1.5 km; NS = north-south trending faults/fractures; NS1 = <0.55 km; NS2 = 0.55-1.25 km; GR = granodiorite batholithic margins; GR1 = <0.2 km; GR2 = 0.2-0.525 km; GR3 = 0.525-1 km; GR4 = 1-1.7 km; STS = geochemically-anomalous catchment basins with stream sediment Cu contents >170 ppm.

** OP = porphyry copper occurrence probability.

9.6.2 Predictors of porphyry copper potential

The forced regression modeling shows that the proximity classes within 2 km of the intersections of regional faults and the proximity classes (0.2-0.525 km, 1-1.7 km) of granodiorite batholithic margins are significant predictors of porphyry copper potential (Table 9.10). The geochemically-anomalous catchment basins are also significant predictors. However, inclusive and exclusive of this geochemical predictor, the regression coefficients and significance levels of the geological variables are stable, which implies that the estimated probabilities are not significantly affected by excluding the geochemical predictor. Indeed, although the geochemically-anomalous catchment basins are shown to be significant predictors in the forced regression modeling, they are eliminated in the backward regression modeling (Table 9.11). In addition to the proximity classes of granodiorite batholithic plutons found to be significant predictors by the forced regression modeling, the proximity class within 200 m of the granodiorite batholithic plutons is also a significant predictor. The forced regression modeling and backward regression modeling show that, among the proximity classes of curvi-linear or point geological features, the proximity class within 1 km of the intersections of regional faults is the most statistically significant predictor or porphyry copper potential. Among the lithologic units, the granodiorite batholithic plutons are the most statistically significant predictor.

Table 9.10. Logistic regression coefficients and their corresponding statistical indicators of significance obtained by forced regression modeling, Abra area. Rows in bold pertain to statistically significant predictors, at 90% significance level, inclusive and exclusive of the stream sediment geochemical predictor.*

Independent variable**	b	Asymptotic standard error	Wald-statistic	Significance level (α)
QDP	0.0249 (0.0240)	0.0353 (0.0344)	0.4951 (0.4863)	0.4817 (0.4856)
QD	0.0010 (0.0004)	0.0082 (0.0084)	0.0147 (0.0020)	0.9036 (0.9641)
G	0.0070 (0.0074)	0.0044 (0.0044)	2.4551 (2.8313)	0.1171 (0.0924)
FI1	**0.0210 (0.0207)**	**0.0065 (0.0065)**	**10.3044 (10.0655)**	**0.0013 (0.0015)**
FI2	**0.0135 (0.0138)**	**0.0080 (0.0080)**	**2.8507 (3.0222)**	**0.0913 (0.0821)**
FI3	**0.0179 (0.0191)**	**0.0094 (0.0093)**	**3.6172 (4.1701)**	**0.0572 (0.0411)**
PP1	-0.0076 (-0.0043)	0.0074 (0.0068)	1.0451 (0.4047)	0.3066 (0.5241)
NS1	0.0030 (0.0035)	0.0056 (0.0055)	0.2938 (0.3996)	0.5878 (0.5273)
NS2	0.0059 (0.0065)	0.0068 (0.0067)	0.7488 (0.8353)	0.3869 (0.3601)
GR1	-0.0217 (-0.0223)	0.0148 (0.0149)	2.3427 (2.2387)	0.1259 (0.1346)
GR2	**0.0310 (0.0333)**	**0.0153 (0.0153)**	**4.1175 (4.7455)**	**0.0424 (0.0294)**
GR3	0.0022 (0.0016)	0.0098 (0.0099)	0.0520 (0.0268)	0.8196 (0.8699)
GR4	**0.0156 (0.0156)**	**0.0081 (0.0081)**	**3.7112 (3.7061)**	**0.0540 (0.0542)**
STS	**0.0201**	**0.0115**	**3.0485**	**0.0808**
Constant	-5.3383 (-5.3847)	0.5989 (0.5992)	79.4484 (80.7596)	0.0000 (0.0000)

*Values in parentheses are results exclusive of STS.
**See Table 9.9 for explanation of codes for variables.

9.5.3 Predictive mapping of porphyry copper potential

Probabilities of porphyry copper occurrence were estimated by using the regression coefficients (Tables 9.10 and 9.11) in Equation 9-6 above. A threshold probability of 0.063 (80^{th} percentile) was used to classify the probability estimates based on the forced regression modeling to distinguish between favourable zones and unfavourable zones. A threshold probability of 0.066 (80^{th} percentile) was used to classify the probability estimates based on the backward regression modeling to define favourable zones and unfavourable zones. The predictive maps of porphyry copper potential are shown in Figure 9.6.

Table 9.11. Logistic regression coefficients and their corresponding statistical indicators of significance obtained by backward regression modeling, Abra area.

Independent variable*	b	Asymptotic standard error	Wald-statistic	Significance level (α)
G	0.0075	0.0040	3.6347	0.0566
FI1	0.0220	0.0059	13.8300	0.0002
FI2	0.0156	0.0075	4.3695	0.0366
FI3	0.0202	0.0092	4.8040	0.0284
GR1	-0.0245	0.0124	3.8979	0.0483
GR2	0.0350	0.0134	6.8533	0.0088
GR4	0.0158	0.0079	3.9870	0.0459
Constant	-5.1824	0.5340	94.1928	0.0000

*See Table 9.9 for explanation of codes for variables.

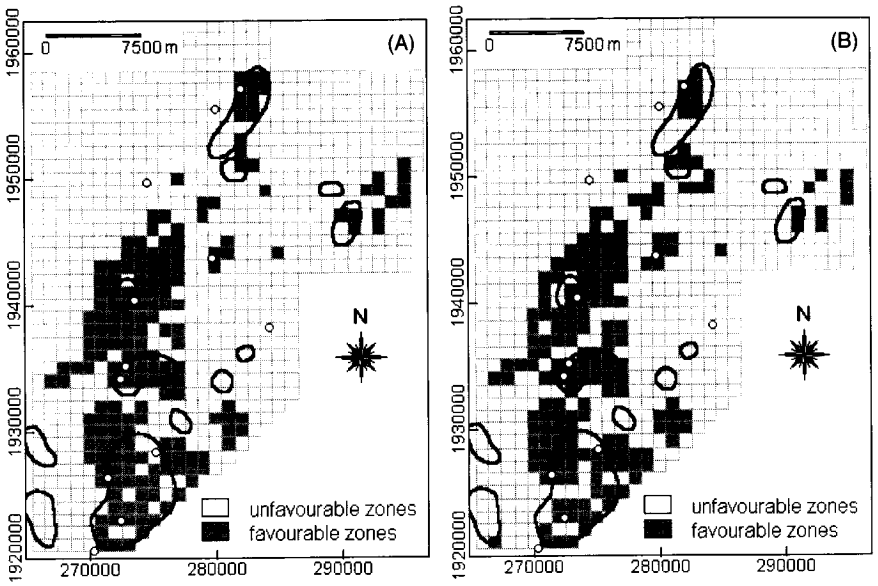

Figure 9.6. Predictive maps of porphyry copper potential, Baguio district, based on (a) forced regression modeling and (b) backward regression modeling. Unfilled circles = 'model' deposits; polygons in solid lines = known mineralised zones (JICA, 1980).

In both Figures 9.6a and 9.6b, the observed number of favourable cells with 'mineralised zones' is 23. In Figure 9.6a, the predicted number of cells with 'mineralised zones' in the favourable zones is 24.4 (say 24) whilst in Figure 9.6b, the predicted number of cells with 'mineralised zones in the favourable zones is 23.7 (say 24). Both predictive maps in Figure 9.6 were considered reliable although, based on the precise predicted numbers of cells with 'mineralised zones, the predictive map in Figure 9.6b is more reliable, albeit slightly, than the predictive map in Figure 9.6a. The spatial geoinformation characteristics of the predictive maps are given in Table 9.12.

Table 9.12. Spatial geoinformation characteristics of predictive maps of porphyry copper potential based on logistic regression modeling, Abra area.

Predictive map	% predicted favourable zones	% predicted 'model' deposits	% predicted 'validation' mineralised zones
Figure 9.6a	19.3	66.7	54.0
Figure 9.6b	19.8	66.7	52.9

The predictive maps indicate similar percentages (19.3 and 19.8%) of the area to have potential for porphyry copper deposits (Table 9.12). Both predictive maps have the same prediction of 66.7% for the 'model' deposits. However, the

predictive map in Figure 9.6a has about 1% higher prediction rate for the 'validation' mineralised zones. These indicate that the geologically-constrained predictive map in Figure 9.6b (i.e., exclusive of the geochemical predictor; see Table 9.11) is as useful as the integrated geochemical-geological predictive map in Figure 9.6a (see Table 9.10).

9.6.4 Discussion

The granodiorite batholithic plutons are, among the different suites of plutonic rocks, the most important spatial (and probably genetic) controls of porphyry copper mineralisation in the area. This is consistent with field observations (JICA, 1980; Table 2.4). The intersections of regional faults are the most statistically significant structural controls of porphyry copper potential in the area. Intersections of regional faults (or strike-slip fault discontinuities) are considered theoretically to be favourable zones of porphyry pluton emplacement (see Chapter 4). However, the porphyry plutons themselves are not statistically significant predictors of porphyry copper potential. The interpretation of these findings is as follows. Ascent of magma from the magma chamber associated with pre-existing granodioritic batholithic plutons was controlled by intersections of north-trending and northeast-trending faults/fractures near the batholithic plutons and led to the emplacement of porphyry plutons. Although genetically associated with the porphyry copper mineralisation, the porphyry plutons occupy small areas and some are sub-outcropping (Sillitoe and Gappe, 1984), which make them poor spatial predictors.

9.7 APPLICATION TO CATANDUANES ISLAND

The geological features used in the logistic regression modeling of gold-copper potential are lithologic units, intrusive contacts, faults/fractures and mineral deposits. The stream sediment geochemical data (see sub-section 2.5.4) were also used in the logistic regression modeling and in the validation of the predictive models(s) of gold-copper potential.

9.7.1 Variables in logistic regression modeling

Among the lithologic units, the Batalay Intrusives and the Yop Formation were used as independent variables. The Batalay Intrusives are known to be genetically associated with the gold-copper deposits whilst the Yop Formation are known to host the more important gold-copper deposits in the island (Table 2.8; Miranda and Vargas, 1967; JICA-MMAJ, 1994). The first three proximity classes within about 1.4 km of the Batalay Intrusive contacts and the first two proximity classes within about 1 km of the northeast-trending faults/fractures and within about 800 m of the north-south trending faults/fractures were also

considered as independent variables. These proximity classes represent the distances within which the positive spatial associations of the gold-copper deposits with the Batalay Intrusive contacts, the northeast-trending faults/fractures and the north-south trending faults/fractures are optimal (see sub-section 4.6.9). Stream sediment catchment basins with highly anomalous geochemical signatures (i.e. >90th percentile PC3 scores) were also used as independent variables because they show good spatial coincidence with the gold-copper deposits (see Figure 2.19). The 'mineralised zones' of the 17 known gold-copper deposits used in Chapter 7 (see sub-section 7.7.1) were used here as the dependent variable. The 'mineralised zones' occur in 53 of the 1415 1x1 km cells (Figure 9.7). In Table 9.13, the quantitative representations of the independent and dependent variables are exemplified for 10 of the 1415 1x1 km cells.

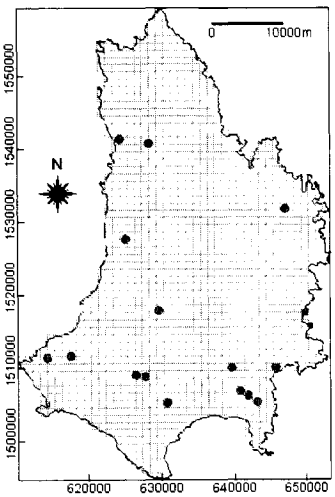

Figure 9.7. Gold-copper 'mineralised zones' and 1x1 km cells, Catanduanes Island.

Table 9.13. Data for independent and dependent variables used in logistic regression as exemplified for 10 of the 1415 1x1 km cells, Catanduanes Island. Values of independent variables are numbers of 100x100 m pixels in 1x1 km cells. Values of dependent variable (OP) are probabilities that a 1x1 km cell contains at least a 100x100 m 'mineralised pixel'.

Cell ID	Independent variables										OP**
	BI	YF	BIC1	BIC2	BIC3	NE1	NE2	NS1	NS2	STS	
b0001	0	42	0	0	0	0	0	0	0	0	0
b0002	0	100	0	0	0	0	0	0	0	0	0
b0003	0	100	0	0	0	0	0	0	0	0	0
b0004	0	100	0	0	0	0	0	0	0	0	0
b0005	0	69	0	0	0	0	0	0	0	0	0
b0006	0	100	0	0	0	0	0	0	0	0	0
b0007	0	100	0	0	0	0	0	0	0	0	0
b0008	0	100	0	0	0	0	39	0	0	0	0
b0009	0	47	0	0	0	26	27	0	0	0	0
b0010	0	0	0	0	0	0	0	0	0	0	0

BI = Batalay Intrusives; YF = Yop Formation; BIC = Batalay Intrusive contacts; BIC1 = <0.4 km; BIC2 = 0.4-0.9 km; BIC3 = 0.9-1.375 km; NE = northeast-trending faults/fractures; NE1 = <0.5 km; NE2 = 0.5-1.025 km; NS = north-south trending faults/fractures; NS1 = <0.375 km; NS2 = 0.375-0.75 km; STS = stream sediment catchment basins with >90th percentile PC3 scores (see Figure 2.19).

** OP = gold-copper occurrence probability.

9.7.2 Predictors of gold-copper potential

The forced regression modeling and the backward regression modeling show that the Yop Formation and the first proximity classes of the Batalay Intrusive contacts (<0.4 km), the northeast-trending faults fractures (<0.5 km) and the north-south trending faults/fractures (<0.375 km) are the most significant predictors of gold-copper potential (Tables 9.14 and 9.15). The stream sediment geochemical signature is also a significant predictor of gold-copper potential.

Table 9.14. Logistic regression coefficients and their corresponding statistical indicators of significance obtained by forced regression modeling, Catanduanes Island. Rows in bold pertain to statistically significant predictors, at 90% significance level, inclusive and exclusive of the stream sediment geochemical predictor.*

Independent variable**	b	Asymptotic standard error	Wald-statistic	Significance level (α)
BI	-0.0021 (-0.0017)	0.0119 (0. 106)	0.0306 (0.0259)	0.8612 (0.8722)
YF	**0.0193 (0.0180)**	**0.0038 (0.0036)**	**25.9775 (24.8436)**	**0.0000 (0.0000)**
BIC1	**0.0176 (0.0191)**	**0.0049 (0.0046)**	**12.8956 (16.8905)**	**0.0003 (0.0000)**
BIC2	0.0081 (0.0084)	0.0054 (0.0050)	2.2665 (2.7803)	0.1322 (0.0954)
BIC3	-0.0158 (-0.0142)	0.0122 (0.0120)	1.6895 (1.4065)	0.1937 (0.2356)
NE1	**0.0148 (0.0143)**	**0.0045 (0.0042)**	**10.3913 (11.7221)**	**0.0013 (0.0006)**
NE2	0.0063 (0.0079)	0.0066 (0.0061)	0.9325 (1.6727)	0.3342 (0.1959)
NS1	**0.0087 (0.0101)**	**0.0040 (0.0038)**	**4.6804 (7.2076)**	**0.0304 (0.0073)**
NS2	0.0006 (0.0017)	0.0050 (0.0052)	0.0117 (0.1032)	0.9139 (0.7480)
STS	**0.0371**	**0.0052**	**50.3546**	**0.0002**
Constant	-5.3986 (-5.0546)	0.4458 (0.3990)	146.6797 (160.5008)	0.0000 (0.0000)

*Values in parentheses are results exclusive of STS. **Codes are explained in Table 9.13.

The apparent differences in the regression coefficients and their significance levels (Tables 9.14 and 9.15) imply that estimates of probabilities of gold-copper occurrence, inclusive and exclusive of the geochemical predictor, will differ significantly. Predictive maps inclusive and exclusive of the geochemical predictor were therefore generated to evaluate properly the efficacy of geologically-constrained predictive mapping.

Table 9.15. Logistic regression coefficients and their corresponding statistical indicators of significance obtained by backward regression modeling, Catanduanes Island.*

Independent variable**	b	Asymptotic standard error	Wald-statistic	Significance level (α)
YF	0.0188 (0.0169)	0.0037 (0.0035)	25.6409 (23.2207	0.0000 (0.0000)
BIC1	0.0177 (0.0192)	0.0040 (0.0039)	19.2119 (24.1649)	0.0000 (0.0000)
NE1	0.0140 (0.0140)	0.0043 (0.0040)	10.4512 (12.1720)	0.0012 (0.0005)
NS1	0.0096 (0.0109)	0.0038 (0.0034)	7.2771 (10.6292)	0.0070 (0.0011)
STS	0.0373	0.0052	51.9428	0.0000
Constant	-5.1235 (-4.7838)	0.3410 (0.2973)	233.7910 (258.8993)	0.0000 (0.0000)

*Values in parentheses are results exclusive of STS. **Codes are explained in Table 9.13.

9.7.3 Predictive mapping of gold-copper potential

Probabilities of gold-copper occurrence were estimated based on Equation 9-6 above using the regression coefficients in Tables 9.14 and 9.15. A predictive map based on the forced regression modeling and exclusive of the geochemical predictors was created by classifying the probability estimates with a threshold probability of 0.047 (80th percentile) to define favourable zones and unfavourable zones. A predictive map based on the backward regression modeling and exclusive of the geochemical predictor was generated by classifying the probability estimates with a threshold probability of 0.043 (80th percentile) to differentiate between favourable zones and unfavourable zones. The predictive maps exclusive of the geochemical predictor are shown in Figure 9.8.

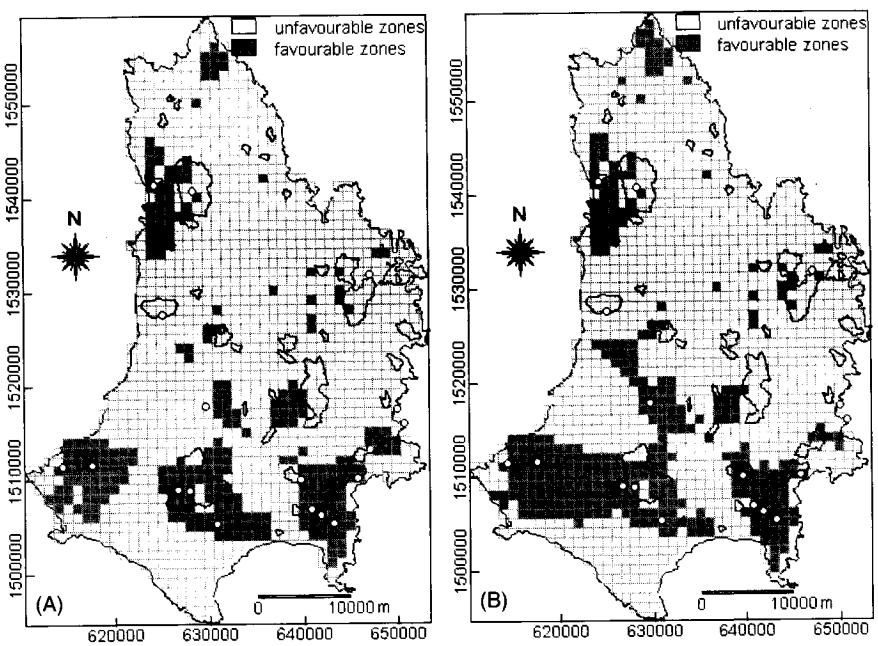

Figure 9.8. Predictive maps of gold-copper potential, Catanduanes Island, exclusive of geochemical predictor and based on (a) forced regression modeling and (b) backward regression modeling. Unfilled circles = 'model' deposits; irregular polygons in thin lines = geochemically-anomalous catchment basins.

In Figure 9.8a, the observed number of favourable cells with 'mineralised zones' is 34 whilst the predicted number of cells with 'mineralised zones' in the favourable zones is 35.4 (say 35), or an overestimation by about 3%. In Figure 9.8b, the observed number of favourable cells with 'mineralised zones' is 38

whilst the predicted number of cells with 'mineralised zones' in the favourable zones is 36.6 (say 37), or an underestimation by about 3%. Hence, both predictive maps can be considered equally reliable with respect to each other. Both predictive maps have similar spatial geoinformation characteristics with respect to the 'model' deposits and spatial overlap with the geochemically-anomalous catchment basins (Table 9.16). The predictive map in Figure 9.6b, however, has about 4% more predicted favourable zones than the predictive map in Figure 9.6a. They are compared with predictive maps inclusive of the geochemical predictor.

Table 9.16. Spatial geoinformation characteristics of predictive maps of gold-copper potential based on logistic regression modeling exclusive of geochemical predictor, Catanduanes Island.

Predictive map	% predicted favourable zones	% predicted 'model' deposits	% of geochemically-anomalous catchment basins classified as geologically-favourable
Figure 9.8a	20.1	70.6	40.0
Figure 9.8b	24.2	70.6	40.0

A predictive map based on the forced regression modeling and inclusive of the geochemical predictors was generated by classifying the probability estimates with a threshold probability of 0.038 (80^{th} percentile) to distinguish between favourable zones and unfavourable zones. A predictive map based on the backward regression modeling and inclusive of the geochemical predictor was generated by classifying the probability estimates with a threshold probability of 0.034 (80^{th} percentile) to discriminate unfavourable zones from unfavourable zones. The predictive maps inclusive of the geochemical predictor are shown in Figure 9.9 and their spatial geoinformation characteristics are given in Table 9.17.

Table 9.17. Spatial geoinformation characteristics of predictive maps of gold-copper potential based on logistic regression modeling inclusive of geochemical predictor, Catanduanes Island.

Predictive map	% predicted favourable zones	% predicted 'model' deposits	% of geochemically-anomalous catchment basins classified as geologically-favourable
Figure 9.9a	19.1	70.6	55.4
Figure 9.9b	18.1	76.5	54.6

In Figure 9.9a, the observed number of favourable cells with 'mineralised zones' is 38 whilst the predicted number of cells with 'mineralised zones' in the favourable zones is 39.8 (say 40), or an overestimation by about 5%. In Figure 9.8b, the observed number of favourable cells with 'mineralised zones' is 37 whilst the predicted number of cells with 'mineralised zones' in the favourable

zones is 38.4 (say 38), or an underestimation by about 3%. The predictive map in Figure 9.9b is therefore more reliable than the predictive map in Figure 9.9a. The predictive map in 9.9a is also less reliable than the predictive maps in Figure 9.8

The predictive map in Figure 9.9b, as compared to the predictive map in Figure 9.9a, has 1% less predicted favourable zones, has about a 6% higher prediction rate for the 'model' deposits and has about a 1% less spatial overlap between the predicted favourable zones and the geochemically-anomalous catchment basins (Table 9.17). The predictive map in Figure 9.9b is therefore considered superior to the predictive map in Figure 9.9a. The lower percentage of spatial coincidence of the predicted favourable zones in Figure 9.9b with the geochemically-anomalous catchment basins implies that some of the geochemical anomalies are non-significant.

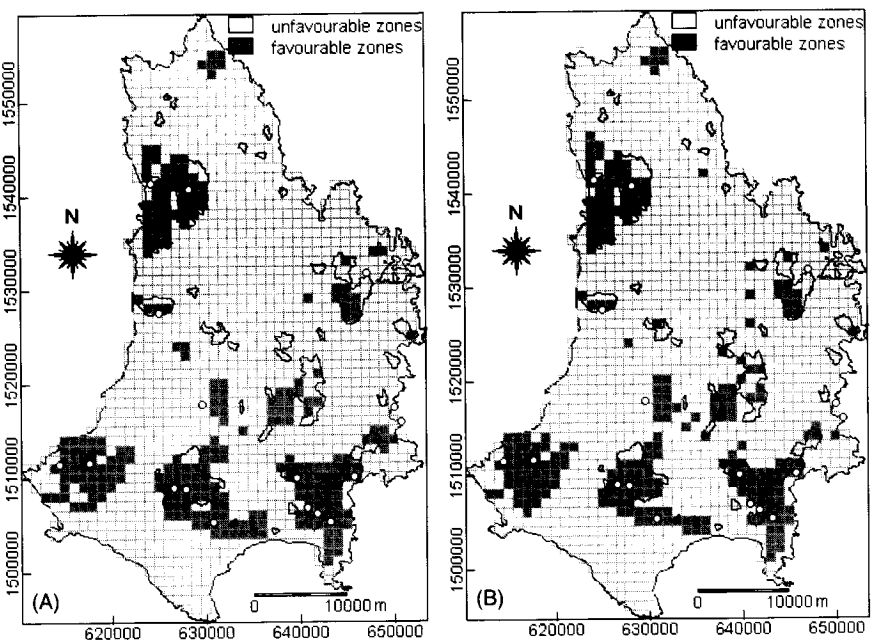

Figure 9.9. Predictive maps of gold-copper potential, Catanduanes Island, inclusive of geochemical predictor and based on (a) forced regression modeling and (b) backward regression modeling. Unfilled circles = 'model' deposits; irregular polygons in thin lines = geochemically-anomalous catchment basins.

The integrated geochemical-geological predictive map in Figure 9.9b is also superior to either of the geologically-constrained predictive maps in Figure 9.8. These three predictive maps have similar small differences of about 3% between

the predicted number of cells with 'mineralised zones' in the favourable zones and the observed number of favourable cells with 'mineralised zones'. However, despite its 2-6% lower percentage of predicted favourable zones, the predictive map in Figure 9.9b has about a 6% higher prediction rate for the 'model' deposits' than the predictive maps in Figure 9.8. Following a similar logic, the geologically-constrained predictive map in Figure 9.8a is considered next superior in view of its 4% less predicted favourable zones but the same prediction rate for the 'model' deposits as compared to the predictive map in Figure 9.8b.

9.7.4 Discussion

The gold-copper mineralisation is, according to Miranda and Vargas (1967) and JICA-MMAJ (1994), associated genetically with the Batalay Intrusives. Although the Batalay Intrusives, because of their small areal extents, are not significant predictors, the first proximity class (within 0.4 km) of the Batalay Intrusive contacts is the most significant predictor among the curvi-linear geological features. The first proximity classes (within 0.375 km) of the north-south trending faults/fractures and (within 0.5 km) of the northeast-trending faults/fractures are also significant predictors. This also reflects the fact that the gold-copper deposits are confined to narrow zones close to the structural features, which is characteristic of vein-type mineralisation.

The lower to similar percentages of predicted favourable zones and higher to similar prediction rates for the 'model' deposits, which characterise the predictive maps in Figure 9.9 as compared to the characteristics of the predictive maps in Figure 9.8, reflect the advantage of integrated geochemical-geological predictive mapping over geologically-constrained predictive mapping of mineral potential. The advantage of the former is that the degree of favourability for mineral potential is enhanced. This is to be expected, of course, due to additional evidence. However, if the main exploration objective is to distinguish between favourable and unfavourable grounds, then a geologically-constrained predictive mapping of the gold-copper potential using logistic regression is adequate in terms of data acquisition and is more economical.

9.8 DISCUSSION

Although the results as presented here are based on those curvi-linear or point geological features, aside from the other geological variables, that are positively spatially associated with the mineral deposits, regression experiments were also performed using those curvi-linear or point geological features that are negatively spatially associated with the mineral deposits. The results of the regression experiments using the latter type of geological features, however, proved not useful, both in statistical and practical aspects, and therefore were

not presented here. This goes to show that determining the spatial relationships between the different geological features and the mineral deposits is necessary before they can be used in predictive mapping of mineral potential. This finding is analogous to what Chung and Fabbri (1993) advocate in the integration of geoscience data for mineral resource assessment or similar applications. Using spatial data layers representing geological variables that are not positively spatially associated with the response variable can lead to statistically non-valid and practically erroneous results.

The results of the forced regression modeling and the results of the backward regression modeling are similar. In the forced regression modeling, statistically significant and statistically non-significant predictors are included in the predictive models whilst in the backward regression modeling only statistically significant predictors are included in the predictive models. The similar results of the forced regression modeling and the backward regression modeling are probably due to the fact that the predictors used are those that are genetically associated with the response variable and those that are positively spatially associated with the response variable. The results of the forced regression modeling, however, do not undermine the importance of testing the statistical significance of the predictors but further underscore the importance of quantifying the spatial associations between the different geological variables and the mineral deposits prior to predictive modeling of mineral potential. Most of the results of the backward regression modeling show that using statistically significant predictors result in statistically more valid predictive models.

The statistical validity (i.e., goodness-of-fit) of the regression models were indicated mainly by comparing the predicted number of cells with 'mineralised zones' with the observed number of cells with 'mineralised zones'. The goodness-of-fit of regression models is invariably evaluated by means of χ^2-tests and/or Kolmogorov-Smirnov tests on the predicted and observed number of the response variable on every unit cell or unique conditions polygon (Agterberg, 1992a, 1992b; Agterberg et al., 1993). These tests were performed on the regression models but the results of such tests indicate that the models are not satisfactory. The reason for the statistical non-validity of the regression models based on either χ^2-tests or Kolmogorov-Smirnov tests is that for small unit cell sizes the χ^2-statistics or Kolmogorov-Smirnov statistics are large (Agterberg et al., 1993). However, for the study areas, using large pixel sizes resulted in statistically non-satisfactory results due to misrepresentation of several of the geological variables particularly those smaller geological features such as the mineral deposits and the porphyry plutons. The 100x100 m pixel size was found to be the most suitable pixel size and using the 'mineralised zones' instead of a unit pixel to represent the response variable alleviated the problem.

It has been indicated in the discussion in Chapter 6 (section 6.8) that logistic regression can be used to check the results of conditional independence tests in

weights of evidence modeling. This is illustrated by the results in the Baguio district where the backward regression model shows that proximity to batholithic plutons and to porphyry plutons are statistically significant independent variables for spatial prediction of epithermal gold potential (Table 9.7). Logistic regression and weights of evidence modeling are therefore complementary methods – weights of the evidence is important for determining bivariate associations between mineral deposits and geological predictor variables and for generalising univariate spatial predictors whilst logistic regression is important for checking results of conditional independence and determining multivariate associations between mineral deposits and geological predictor variables.

9.9 CONCLUSIONS

Logistic regression is a feasible method for integrating geological variables for predictive mapping of mineral potential for areas where there are a number of representative mineral deposits, which is usually represented as a dichotomous response variable. Analysis of spatial association between the predictor and response variables is an important prerequisite step to the application of logistic regression. The results of the regression modeling show that, although statistical testing of the predictive models is important in evaluating their validity, the proper representation of the geological variables is also important in deriving geologically meaningful predictive models.

For Benguet province, the optimum predictive map, which is based on the backward regression modeling, delineates about 20% of the province as prospective for porphyry copper deposits, accurately reflects at least 82% of the 'model' deposits and at least 62% of the 'validation' deposits. For Baguio district, the best predictive map, which is based on the forced regression modeling, outlines about 20% of the district as likely to contain epithermal gold deposits and has prediction rates of about 79% for the 'model' deposits and at least 76% for the 'validation' deposits. For Abra area, the statistically more reliable predictive map, which is based on the backward regression modeling and exclusive of the geochemical predictor, demarcates about 20% of the area as favourable for porphyry copper deposits and correctly delineates about 67% of the 'model' deposits and 54% of the 'validation' mineralised zones. For Catanduanes Island, the best predictive map, which is based on the backward regression modeling and inclusive of the geochemical predictor, defines about 18% of the island as having potential for gold-copper deposits and has a prediction rate of at least 76% for the 'model' deposits. The next best predictive map, which is based on the forced regression modeling and exclusive of the geochemical predictor, delimits about 20% of the island as prospective for gold-copper deposits, has a prediction rate of about 71% for the 'model ' deposits and the predicted geologically-favourable zones spatially coincide with 40% of the geochemical anomalies. The results demonstrate that the geologically-

constrained predictive maps can be as useful as the integrated geochemical-geochemical predictive maps.

The logistic regression modeling presented here, like weights of evidence modeling and the applications of evidential belief theory and the theory of fuzzy sets presented in the preceding chapters, is based upon the quantitative analysis of spatial associations of the geological variables with the known mineral deposits. In the next chapter, a predictive modeling technique is demonstrated for cases in which mineral deposit data are lacking.

Chapter 10

Wildcat Mapping of Mineral Potential

"When I am working on a problem I never think about beauty.
I only think about how to solve the problem. But when I have finished,
if the solution is not beautiful, I know it is wrong. "

Fuller, Buckminster (1895-1983)

This Chapter demonstrates a methodology for mapping favourable zones of mineral potential based on only geological map data. Portions of this Chapter have been submitted for publication as Wildcat Mapping of Gold Potential, Baguio District, Philippines (Carranza and Hale, 2001i).

10.1 INTRODUCTION

For areas where a number of representative mineral deposits are known, the procedure for quantitative predictive mapping of mineral potential is that predictive models are first generated based on analyses of spatial associations between known mineral deposits and geological features. This first step is generally called 'training of the data'; the known mineral deposits are called 'training points'. Training of the data to quantify spatial associations between mineral deposits and geological features can be performed by way of a bivariate analysis (i.e., between mineral deposits and a particular geological feature) or by way of a multivariate analysis (i.e., between mineral deposits and a number of geological features). Bivariate analyses of spatial associations between mineral deposits and a particular geological feature include weights of evidence modeling (Agterberg, 1989, 1992a; Bonham-Carter et al., 1988, 1989; Watson and Rencz, 1989; Agterberg et al., 1990; Bonham-Carter and Agterberg, 1990; Bonham-Carter, 1991,1994; Agterberg et al., 1993; Turner, 1997; Carranza and Hale, 1999b, 1999d, 1999e, 2000, 2001g), distance distribution method (Huntington and Green, 1978; Simpson et al., 1980; Bonham-Carter et al., 1985; Bonham-Carter, 1985; Carranza and Hale, 2001g) and distance correlation method (see Chapter 4; Carranza and Hale, 2001g). Multivariate analyses of spatial association between mineral deposits and a number of geological features include regression analysis (Agterberg, 1974, 1992a, 1992b; Chung, 1978; Chung and Agterberg, 1980; Wrigley and Dunn, 1986; Rock, 1988; Reddy et al., 1990; Reddy et al., 1991; Agterberg et al., 1993; Carranza and Hale, 2001c), characteristic analysis (Botbol, 1971; Botbol et al., 1978; Harris, 1984; McCammon et al., 1983a, 1983b, 1984; Pan and Harris, 1992a), canonical correlation analysis (Seber, 1984; Davis, 1986; Johnson and Wichern, 1998) and favourability analysis (Pan and Harris, 1992b, 2000; Pan, 1993a, 1993b,

Pan, 1993c; Chung and Fabbri, 1993; Pan and Portefield, 1995). The quantified spatial association models are then applied to predict zones that have similar spatial associations with the predictor geological variables but where mineralisation is unknown.

In practice, it is often difficult to generate a spatial association model, especially at the early stages of mineral exploration. The difficulty arises when only a geological map is available for a given exploration area in which few or no mineral deposits are known. Hence, the problem of quantitative predictive mapping of mineral potential without 'training of the data' arises. The problem is comprised of two basic questions: (1) how to represent geological map data for predictive modeling without 'training points' and (2) how to predict sub-areas with mineral potential. To solve the problem and answer the two questions, a 'wildcat' methodology of predictive mapping of favourable zones of mineral potential based on only geological map data has to be devised. The term 'wildcat' is used, being a mineral exploration term for blindly pursuing mineralisation (Whitten and Brooks, 1972), invariably based on limited geological information.

10.2 WILDCAT MODEL OF MINERAL POTENTIAL

The wildcat model of mineral potential is built upon the general qualitative characteristics of the geological environment of the type of mineral deposit sought. It is also based upon the assumption that the favourability for the occurrence of the type of mineral deposit sought can be characterised by a quantitative function of a linear combination of indicative geological variables.

A mineral deposit occurs in a particular environment that has distinct or anomalous geological characteristics compared to other environments. According to mineral deposit models, anomalous environments are characterised by a set of special geological features (Barton, 1986; Sangster, 1986; Bonham-Carter, 1994). The anomalous geological environments of the hydrothermal mineral deposits studied here can be characterised by presence of or proximity to plutonic rocks, hydrothermal alterations and faults/fractures. Plutonic rocks provide heat whilst faults/fractures allow favourable circulation or transmission of heat, which can cause changes in the geochemical and geophysical conditions of the environment and can lead to hydrothermal mineralisation/alteration. The anomalous geological environments of hydrothermal mineral deposits can also be characterised by surficial geochemical anomalies. Inasmuch as mineral deposits are not necessarily present in every geological environment characterised by the presence of or proximity to igneous intrusions, hydrothermal alterations, faults/fractures and/or surficial geochemical anomalies, these geological features can only be considered as indicative geological variables of mineral potential.

It has been shown in the preceding Chapters that presence of and/or proximity to certain geological features (e.g., plutonic rocks, hydrothermal alterations, faults/fractures, surficial geochemical anomalies) characterises the favourability of a particular zone for mineral potential. The presence of or proximity to indicative geological variables can therefore be used in quantitative mapping of mineral potential. Quantitatively, the potential for hydrothermal mineral deposit occurrence can be represented by a favourability function, Y, of a number of indicative geological variables X_i (i = 1, 2, . . ., n), thus

$$Y = f(X_1, \cdots, X_n). \tag{10-1}$$

Let the working area be divided into equal-size cells or pixels. Suppose that there are n numbers of X_i (i = 1, 2, . . ., n) indicative geological variables in the pixels. The favourability function Y is defined as a linear combination of X_i, thus

$$Y = a_1 X_1 + a_2 X_2 + \cdots + a_n X_n, \tag{10-2}$$

where a_i (i = 1, 2, . . ., n) are the weights to be determined. In the preceding Chapters, the favourability function Y has been estimated by binary scoring (Chapter 5), weights of evidence (Chapter 6), belief function (Chapter 7), fuzzy membership function (Chapter 8) and regression (Chapter 9) based on the spatial association models. For areas without training data, Luo (1990) proposed a method for estimating Y by constrained least squares analysis. The criterion of Luo's approach (1990) is to minimise variance $\mathrm{var}(Y) = E[Y - \mu_Y]^2$ with constraint $\sum_{i=1}^{n} a_i \mu_i = \mu_Y$, where $\mu_Y = E(Y)$, $\mu_i = E(X_i)$; E denotes expectation. The estimate for Equation 10-1 is given by

$$\hat{Y} = X C_{XX}^{-1} \mu \tag{10-3}$$

where $\mu = (\mu_1, \cdots \mu_n)^T$ and C is the covariance matrix of the multivariate dataset T. The method of Luo (1990) is essentially a principal components method where $C_{XX}^{-1}\mu$ is the unit eigenvector associated with the largest eigenvalue of the similarity matrix of $X = (X_1, x_2, . . ., X_n)$. The favourability function Y estimated by the principal components method is useful to characterise a typical linear combination with minimised variance of the favourability function and is necessarily meaningful particularly if the predictor variables are pre-selected (Pan and Harris, 1992b). In order to avoid singularity of the matrix C, the chosen predictor variables X_i should not be linearly dependent (Luo, 1990). In Chapter 6, it has been shown that binary representations of most of the geological features in the different study areas are not conditionally dependent on each other with respect to the mineral deposit points. For this reason, it is assumed that the indicative geological variables used here are not linearly dependent on each other and can be used in the wildcat modeling of mineral potential.

10.3 WILDCAT MODELING OF MINERAL POTENTIAL USING GIS

The wildcat modeling of mineral potential was applied to Benguet province, Baguio district, Abra area and Catanduanes Island.

10.3.1 Data inputs

The indicative geological variables used in the wildcat modeling of mineral potential include curvi-linear or point geological features (i.e., batholithic pluton margins, porphyry pluton contacts/centroids, faults/fractures, intersections of faults/fractures or strike-slip fault discontinuities), hydrothermal alterations and/or geochemical anomalies. The curvi-linear or point geological features, captured in vector format (see Chapter 2), were rasterised. Distance maps were generated for each of the raster maps of curvi-linear or point geological features. The hydrothermal alterations were remotely-detected from Landsat TM imagery (see sub-sections 3.3.4 and 3.3.6). The geochemical anomalies were interpreted from stream sediment geochemical data (see sub-sections 2.4.4 and 2.5.4). A pixel size of 100x100 m was used in the GIS-based raster analyses.

10.3.2 Representation of indicative geological variables

The distance maps of indicative curvi-linear or point geological variables were categorised into equal-interval proximity classes without regard to the spatial association between the known mineral deposits and the indicative geological variables. Since proximity to indicative geological features characterises the favourability of a certain zone for mineral potential, the degree of favourability of a proximity class is represented by the inverse of the distance. Thus, proximal classes have higher degrees of favourability than distal classes. The degree of favourability of a proximity class was equated to the inverse of its mid-distance; for example, a proximity class of 0-1000 m was assigned a degree of favourability of 1/500. In pixel-based raster calculations of distances, however, the calculated distance between a point and a geological feature within a given 100x100 m pixel is 0 m, but actually the maximum distance could be 141 m (i.e., $\sqrt{100^2+100^2}$). To accommodate this fractal nature of dimensions in pixel-based calculations, and for simplicity, the degree of favourability is equal to the inverse of the mid-distance multiplied by 100 (instead of 141). Raster maps of degrees of favourability of proximity classes of an indicative geological variable were then generated. The degrees of favourability are equal for the same proximity classes of the different indicative curvi-linear or point geological variables.

Due to the absence of control data (i.e., it is assumed that mineral deposits in the study areas are not known), the indicative hydrothermal alteration variables and the indicative geochemical variables were quantitatively represented in a

subjective way such that they have importance equal to the indicative curvi-linear or point geological variables. The fuzzy weights assigned to the particular hydrothermal alteration units and the geochemical anomalies in the corresponding study areas (see Chapter 8) can be used. However, using the fuzzy weights of the hydrothermal alteration units and the geochemical anomalies, are higher than the quantified degrees of favourability of the proximity classes of the indicative curvi-linear or point geological variables, can undermine the importance of the curvi-linear or point geological variables in the predictive modeling of mineral potential. The degrees of favourability of the hydrothermal alteration units and the geochemical anomalies were thus 'equalised' to the degrees of favourability of the proximity classes of curvi-linear or point geological variables in the following way. For a particular area, the degree of favourability of hydrothermal alteration unit(s) and/or geochemical anomaly(ies) considered most indicative of the mineral deposit sought is equated to the degree of favourability of the first proximity classes (i.e., nearest proximity classes) of curvi-linear or point geological variables. For the hydrothermal alteration units and/or geochemical anomalies considered less indicative, the degree of favourability assigned is equal to one-half the degree of favourability assigned to the hydrothermal alteration unit(s) and/or geochemical anomaly(ies) considered to rank next.

10.3.3 Generation and validation of wildcat favourability maps

The raster maps of degrees of favourability of indicative geological variables were integrated by principal components (PC) analysis. Interpretation of a particular PC as a favourability function representing mineral potential is based on the knowledge of the geological history of a particular study area and on the knowledge of geological processes that bring about mineralisation. Score maps of the PC interpreted as the favourability function representing mineral potential were then generated by calculating Y in Equation 10-2 using the PC loadings as the weights a_i and the degrees of favourability of a particular indicative geological variable as X_i. The PC score maps were then converted into binary wildcat favourability maps using the 75th percentile PC score as a threshold to discriminate unfavourable from favourable zones. The wildcat favourability maps were validated against the known mineral deposits, known mineralised zones and/or geochemical anomalies.

10.4 APPLICATION TO BENGUET PROVINCE

The type of mineral deposit sought in the province is porphyry copper. The indicative geological variables used in the wildcat modeling of porphyry copper potential were curvi-linear or point geological features (batholithic pluton margins, porphyry pluton centroids and strike-slip fault discontinuities) and remotely-detected hydrothermal alteration units.

10.4.1 Degrees of favourability of indicative geological variables

The distances to indicative curvi-linear or point geological variables were categorised into 1-km interval proximity classes (Table 10.1). The first proximity classes (<1 km) of the curvi-linear or point geological variables have quantified degrees of favourability of 0.2. The proximity classes less than 1 km from the curvi-linear or point geological variables have degrees of favourability less than 0.1.

Of the hydrothermal alteration units, the illitic alteration and propylitic alteration were considered of equal importance in indicating porphyry copper potential (see sub-sections 5.3.1 and 5.3.2) and were assigned a favourability score of 0.2 (i.e., favourability scores of first proximity classes of curvi-linear or point geological variables). A favourability score of 0.1 was assigned to the advanced argillic alteration units because of its lower importance in indicating porphyry copper potential (Sillitoe and Gappe, 1984; Pirajno, 1992).

Table 10.1. Favourability scores of indicative geological variables for predicting porphyry copper potential, Benguet province.

Batholithic pluton margins		Porphyry pluton centroids		Strike-slip fault discontinuities		Hydrothermal alteration	
Proximity classes (km)	Score	Proximity classes (km)	Score	Proximity classes (km)	Score	Assem-blage*	Score
<1	0.200	<1	0.200	<1	0.200	AA	0.100
1-2	0.067	1-2	0.067	1-2	0.067	I	0.200
2-3	0.040	2-3	0.040	2-3	0.040	P	0.200
3-4	0.029	3-4	0.029	3-4	0.029		
4-5	0.022	4-5	0.022	4-5	0.022		
5-6	0.018	5-6	0.018	5-6	0.018		
6-7	0.015	6-7	0.015	6-7	0.015		
7-8	0.013	7-8	0.013	7-8	0.013		
8-9	0.012	8-9	0.012	8-9	0.012		
9-10	0.011	9-10	0.011	9-10	0.011		
10-11	0.010	10-11	0.010	10-11	0.010		
11-12	0.009	11-12	0.009	11-12	0.009		
12-13	0.008	12-13	0.008	12-13	0.008		
13-14	0.007	13-14	0.007	13-14	0.007		
14-15	0.007	14-15	0.007				
15-16	0.006	15-16	0.006				
16-17	0.006	16-17	0.006				
17-18	0.006	17-18	0.006				
18-19	0.005	18-19	0.005				
19-20	0.005						
20-21	0.005						
21-22	0.005						
>22	0.004						

*AA = advanced argillic; I = illitic; P = propylitic

10.4.2 Favourability function for porphyry copper potential

Principal components analyses of the indicative geological variables inclusive of the hydrothermal alteration variable and exclusive of the hydrothermal alteration variable were performed to evaluate the usefulness of the remotely-detected hydrothermal alteration units in wildcat predictive mapping of porphyry copper potential. The results of the principal components analysis inclusive of the hydrothermal alteration variable are given in Table 10.2. The results of the principal components analysis exclusive of the hydrothermal alteration variable are given in Table 10.3.

Table 10.2. Principal components analysis of favourability scores of indicative geological variables, inclusive of hydrothermal alteration variable, for predicting porphyry copper potential, Benguet province.

	PC1	PC2	PC3	PC4
Batholithic pluton margins	0.917	0.374	-0.135	-0.043
Porphyry pluton centroids	0.096	0.040	0.898	-0.428
Strike-slip fault discontinuities	0.105	-0.001	0.419	0.902
Hydrothermal alteration	0.374	-0.927	-0.016	-0.037
Explained variance (%)	43.41	30.13	15.70	10.76
Cum. Variance (%)	43.41	73.54	89.24	100.00

In the principal components analysis of the favourability scores of the indicative geological variables, inclusive of the hydrothermal alteration variable, PC3 is interpreted as the favourability function representing porphyry copper potential (Table 10.2). It reflects the association between porphyry plutons and strike-slip fault discontinuities, which are considered important for porphyry copper mineralisation. The PC1 reflects mainly the batholithic plutons and hydrothermal alterations. The PC2 reflects an antipathetic association between the batholithic plutons and hydrothermal alteration. The PC4 reflects mainly the strike-slip fault discontinuities. These three PCs are not good indicators of porphyry copper mineralisation as compared to PC3.

In the principal components of the favourability scores of the indicative geological variables, exclusive of the hydrothermal alteration variable, PC2 is interpreted as the favourability function representing porphyry copper potential

Table 10.3. Principal components analysis of favourability scores of indicative geological variables, exclusive of hydrothermal alteration variable, for predicting porphyry copper potential, Benguet province.

	PC1	PC2	PC3
Batholithic pluton margins	0.993	0.110	-0.031
Porphyry pluton centroids	0.058	-0.249	0.967
Strike-slip fault discontinuities	0.099	-0.962	-0.254
Explained variance (%)	69.02	20.09	10.89
Cum. Variance (%)	69.02	89.11	1000

(Table 10.3). It reflects the association between porphyry plutons and strike-slip fault discontinuities, which are considered important for porphyry copper mineralisation. The PC1 reflects mainly the batholithic plutons. The PC3 reflects mainly the porphyry plutons. These two PCs are not good indicators of porphyry copper mineralisation as compared to PC2.

10.4.3 Wildcat mapping of favourability for porphyry copper potential

A score map of PC3, based on the PC analysis inclusive of the hydrothermal alteration variable, was generated. The PC3 scores were classified using a threshold PC3 score of 0.045 (75^{th} percentile) to define favourable zones and unfavourable zones. The favourability map of porphyry copper potential, inclusive of the hydrothermal alteration variable, is shown in Figure 10.1a. A

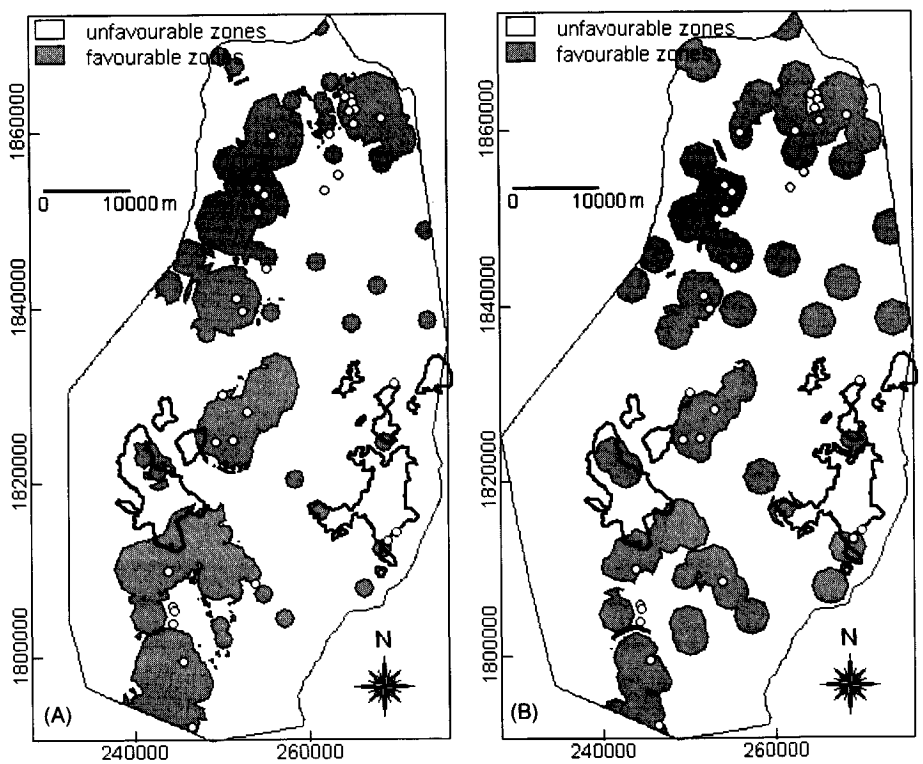

Figure 10.1. Wildcat favourability map of porphyry copper potential, Benguet province: (a) inclusive of hydrothermal alteration variable; (b) exclusive of hydrothermal alteration variable. Unfilled circles = known porphyry copper deposits; polygons in solid lines = geochemically-anomalous catchment basins.

score map of PC2, based on the PC analysis exclusive of the hydrothermal alteration variable, was generated. Because of the negative signs of the PC2 loadings for the porphyry plutons and the strike-slip fault discontinuities (Table 10.3), PC2 is negated (i.e., multiplied by −1) to represent favourability for porphyry copper potential as positive PC scores. The negated PC2 scores were then classified using a threshold PC2 score of 0.036 (75^{th} percentile) to distinguish between favourable zones and unfavourable zones. The favourability map of porphyry copper potential, exclusive of the hydrothermal alteration evidence, is shown in Figure 10.1b.

The wildcat favourability maps depict favourable zones that are spatially associated with the known porphyry copper deposits (Figure 10.1). Some portions of the geochemically-anomalous catchment basins overlap with some of the geologically-favourable zones, which are probably sources of the geochemical anomalies. The favourability maps predict about 25% of the province as favourable for porphyry copper deposits (Table 10.4). The favourability map in Figure 10.1b, as compared to the favourability map in Figure 10.1a, has a 3% higher prediction rate for the known porphyry copper deposits. The favourability map exclusive of the hydrothermal alteration variable is therefore superior to the favourability map inclusive of the hydrothermal alteration.

Table 10.4. Spatial geoinformation characteristics of wildcat favourability maps of porphyry copper potential, Benguet province.

	Figure 10.1a	Figure 10.1b
% predicted favourable zones	25.1	25.5
% predicted known porphyry copper deposits	67.7	70.9

10.4.4 Discussion

The favourability map inclusive of the hydrothermal alteration variable is indicated to be inferior, albeit slightly, to the favourability map exclusive of the hydrothermal alteration variable. However, further spatial analyses of the favourability maps indicate the usefulness of the remotely-detected hydrothermal alteration units. The smaller circular favourable zones in Figure 10.1a are those zones that are proximal to strike-slip fault discontinuities where porphyry plutons and favourable hydrothermal alteration are absent. The larger circular favourable zones in Figure 10.1a are those zones that are proximal to the porphyry plutons and the strike-slip fault discontinuities where favourable hydrothermal alteration is present. In Figure 10.1b, the circular favourable zones, which have similar sizes, are those that are proximal either to both the porphyry plutons and the strike-slip fault discontinuities or to the strike-slip fault discontinuities only. These findings suggest that the hydrothermal alteration variable is useful in reducing the favourability of zones proximal to only the strike-slip fault discontinuities.

10.5 APPLICATION TO BAGUIO DISTRICT

The type of mineral deposit sought in the district is epithermal gold. The indicative geological variables used in the wildcat modeling of epithermal gold potential were curvi-linear or point geological features (batholithic pluton margins, porphyry pluton contacts, northeast-trending faults/fractures, northwest-trending faults/fractures) and remotely-detected hydrothermal alteration units.

10.5.1 Degrees of favourability of indicative geological variables

The distances to indicative curvi-linear or point geological variables were categorised into 500-m interval proximity classes (Table 10.5). The first proximity classes (<500 m) of the curvi-linear or point geological variables have quantified degrees of favourability of 0.4. The second proximity classes (500-1000 m) of the curvi-linear or point geological variables have quantified degrees of favourability of 0.133. The favourability scores of distance classes less than 1 km from the curvi-linear geological variables are less than 0.1.

Table 10.5. Favourability scores of indicative geological variables for predicting epithermal gold potential, Baguio district.

Batholithic pluton margins		Porphyry pluton contacts		Northeast-trending faults/fractures		Northwest-trending faults/fractures		Hydrothermal alteration	
Proximity class (km)	Score	Proximity class (km)	Score	Proximity class (km)	Score	Proximity class (km)	Score	Assem-blage*	Score
<0.5	0.400	<0.5	0.400	<0.5	0.400	<0.5	0.400	AA	0.200
0.5-1.0	0.133	0.5-1.0	0.133	0.5-1.0	0.133	0.5-1.0	0.133	I	0.400
1.0-1.5	0.080	1.0-1.5	0.080	1.0-1.5	0.080	1.0-1.5	0.080	P	0.200
1.5-2.0	0.057	1.5-2.0	0.057	1.5-2.0	0.057	1.5-2.0	0.057		
2.0-2.5	0.044	2.0-2.5	0.044	2.0-2.5	0.044	2.0-2.5	0.044		
2.5-3.0	0.036	2.5-3.0	0.036	2.5-3.0	0.036	2.5-3.0	0.036		
3.0-3.5	0.031	3.0-3.5	0.031	3.0-3.5	0.031	3.0-3.5	0.031		
3.5-4.0	0.027	3.5-4.0	0.027						
4.0-4.5	0.023	4.0-4.5	0.023						
4.5-5.0	0.021	4.5-5.0	0.021						
5.0-5.5	0.019	5.0-5.5	0.019						
5.5-6.0	0.017	5.5-6.0	0.017						
6.0-6.5	0.016	6.0-6.5	0.016						
6.5-7.0	0.015	6.5-7.0	0.015						
7.0-7.5	0.014	7.0-7.5	0.014						
7.5-8.0	0.013	7.5-8.0	0.013						
8.0-8.5	0.012	8.0-8.5	0.012						
8.5-9.0	0.011	8.5-9.0	0.011						
		9.0-9.5	0.011						
		9.5-10.0	0.010						
		>10.0	0.010						

*AA = advanced argillic; I = illitic; P = propylitic

Of the hydrothermal alteration units, the illitic alteration was considered most important in indicating epithermal gold potential (see sub-sections 5.4.1 and 5.4.2) and was assigned a favourability score of 0.4 (i.e., favourability scores of first proximity classes of curvi-linear or point geological variables). A favourability score of 0.2 was assigned to the advanced argillic alteration units and propylitic alteration units because of their lower importance in indicating epithermal gold potential (Mitchell and Leach, 1991).

10.5.2 Favourability function for epithermal gold potential

Two sets of principal components analyses were performed to map epithermal gold potential and to evaluate the importance of the remotely-detected hydrothermal alteration variable. The first set of principal components analysis is inclusive of the hydrothermal alteration variable and the results are given in Table 10.6. The second set of principal components analysis is exclusive of the hydrothermal alteration variable and the results are given in Table 10.7.

The PC1 of the PC analysis inclusive of the hydrothermal alteration variable is interpreted as the favourability function representing epithermal gold potential (Table 10.6). It reflects an association of the heat sources, structural controls by northeast-trending faults/fractures and hydrothermal effects of mineralisation. The PC2 reflects mostly the northwest-trending faults/fractures. The PC3 reflects mostly the northeast-trending faults/fractures and the northwest-trending faults/fractures. The PC4 reflects an association similar to PC1; however, it reflects strongly hydrothermal alteration that is antipathetic to a possible heat source of mineralisation (i.e., batholithic plutons). The PC5 reflects association between northeast-trending faults/fractures and hydrothermal alteration, which is antipathetic to possible heat sources of mineralisation. The other four PCs are therefore poor indicators of favourability for epithermal gold potential as compared to PC1.

Table 10.6. Principal components analysis of favourability scores of indicative geological variables, inclusive of hydrothermal alteration variable, for predicting epithermal gold potential, Baguio district.

	PC1	PC2	PC3	PC4	PC5
Batholithic pluton margins	0.769	0.156	-0.420	-0.401	-0.055
Porphyry plutons	0.083	-0.031	0.035	0.237	-0.967
Northeast-trending faults/fractures	0.572	-0.100	0.800	0.107	0.108
Northwest-trending faults/fractures	-0.069	0.982	0.167	0.056	-0.018
Hydrothermal alteration	0.264	0.029	-0.333	0.877	0.225
Variance explained (%)	29.49	23.54	23.20	15.27	8.50
Cum. variance (%)	29.49	53.03	76.23	91.50	100.00

Table 10.7. Principal components analysis of favourability scores of indicative geological variables, inclusive of hydrothermal alteration variable, for predicting epithermal gold potential, Baguio district.

	PC1	PC2	PC3	PC4
Batholithic pluton margins	0.745	-0.013	-0.666	-0.030
Porphyry plutons	0.020	0.121	-0.024	0.992
Northeast-trending faults/fractures	0.367	0.834	0.399	-0.100
Northwest-trending faults/fractures	0.557	-0.537	0.630	0.070
Variance explained (%)	36.50	29.99	22.33	11.19
Cum. variance (%)	36.50	66.49	88.82	100.01

The PC1 of the PC analysis exclusive of the hydrothermal alteration variable is considered as the favourability function representing epithermal gold potential (Table 10.7). It reflects an association between the heat sources and structural controls on gold mineralisation. The PC2 also reflects association between a heat source control and a structural control, which is antipathetic to a similar association. It could also represent a favourability function of epithermal gold mineralisation, however, it reflects more strongly the presence of northeast-trending faults/fractures. The PC3 reflects an antipathetic relation between plutonic rocks and faults/fractures. The PC4 reflects the porphyry plutons. These last three PCs are therefore not good indicators of favourability for epithermal gold potential as compared to PC1.

10.5.3 Wildcat mapping of favourability for epithermal gold potential

A score map of PC1, based on the PC analysis inclusive of the hydrothermal alteration variable, was generated. The PC1 scores were classified using a threshold PC1 score of 0.404 (75^{th} percentile) to define favourable zones and unfavourable zones. The favourability map of epithermal gold potential, inclusive of the hydrothermal alteration variable, is shown in Figure 10.2a. A score map of PC1, based on the PC analysis exclusive of the hydrothermal alteration variable was generated. The PC1 scores were classified using a threshold PC1 score of 0.428 (75^{th} percentile) to delimit favourable zones from unfavourable zones. The favourability map of epithermal gold potential, exclusive of the hydrothermal alteration variable, is shown in Figure 10.2b. The spatial geoinformation characteristics of the wildcat favourability maps are given in Table 10.8.

Table 10.8. Spatial geoinformation characteristics of wildcat favourability maps of epithermal gold potential, Baguio district.

	Figure 10.2a	Figure 10.2b
% predicted favourable zones	22.9	25.0
% predicted known large-scale gold deposits	57.9	57.9
% predicted known small-scale gold deposits	63.5	68.2

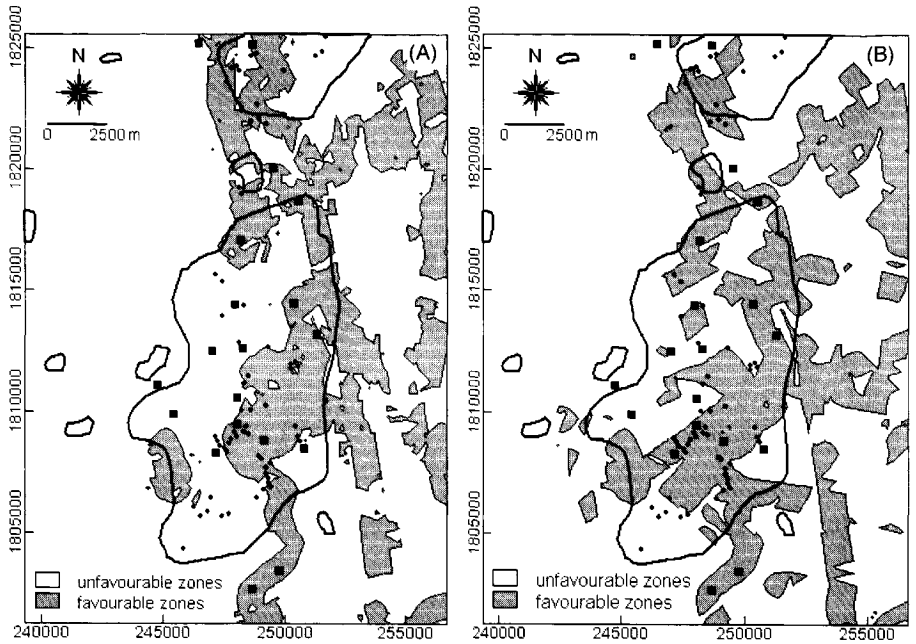

Figure 10.2. Wildcat favourability map of epithermal gold potential, Baguio district: (a) inclusive of hydrothermal alteration variable; (b) exclusive of hydrothermal alteration variable. Filled squares = large-scale gold deposits; small dots = small-scale gold deposits; polygons in solid lines = stream sediment Au anomaly (UNDP, 1987a).

The wildcat favourability map exclusive of the hydrothermal alteration variable (Figure 10.2b), as compared to the wildcat favourability map inclusive of the hydrothermal alteration variable (Figure 10.2a), delineates about 3% more favourable zones, has about 5% higher prediction for the known small-scale gold deposits and the same prediction rate of 58% for the known large-scale gold deposits. The wildcat favourability map in Figure 10.2b is therefore considered superior to the wildcat favourability map in Figure 10.2a.

10.5.4 Discussion

Among the indicative geological variables, the batholithic pluton margins are the strongest contributor to the wildcat model whilst the porphyry plutons are the poorest contributor (Tables 10.6 and 10.7). This is because the former covers a larger percentage of the district (Figure 2.11) than the latter. The wildcat favourability map also shows a stronger influence of the northeast-trending faults/fractures than of the northwest-trending faults/fractures despite the latter having higher loadings on PC1. The reason for this is that there are more

northwest-trending faults/fractures that are distal to the batholithic plutons than the northeast-trending faults/fractures (Figure 2.11).

The favourability map exclusive of the hydrothermal alteration variable (Figure 10.2b is superior to the favourability inclusive of the hydrothermal alteration variable (Figure 10.2a) because the former demarcates favourable zones with larger lateral extents than the latter. However, inclusion of the hydrothermal alteration variable reduces the importance of some of the favourable zones delineated by the favourability map exclusive of this indicative geological variable. Nonetheless, the favourability map inclusive of the hydrothermal alteration variable is also considered useful based on its prediction rate of at least 63% for the small-scale gold deposits.

10.6 APPLICATION TO ABRA AREA

The type of mineral deposit sought in the area is porphyry copper. The indicative geological variables used in the wildcat modeling of porphyry copper potential were curvi-linear or point geological features (batholithic pluton margins, porphyry pluton centroids, faults/fractures, intersections of regional faults/fractures) and stream sediment geochemical anomalies. The intersections of regional faults/fractures are between the north-trending and northeast-trending faults/fractures.

10.6.1 Degrees of favourability of indicative geological variables

The distances to indicative curvi-linear or point geological variables were categorised into 1-km interval proximity classes (Table 10.9). The first proximity classes (<1 km) of the curvi-linear or point geological variables have degrees of favourability of 0.2. The degrees of favourability for distance classes less than 1 km from the curvi-linear or point geological variables are less than 0.1.

Highly anomalous stream sediment Cu contents (i.e., >170 ppm; see sub-section 2.4.4) were assigned a degree of favourability of 0.2 (i.e., equal to degree of favourability of the first proximity classes of curvi-linear or point geological variables). Slightly anomalous stream sediment Cu contents (90-170 ppm) were assigned a degree of favourability of 0.1. High background stream sediment Cu contents (50-90 ppm) were given a degree of favourability of 0.05. Low background stream sediment Cu contents (<50 ppm) were given a degree of favourability of 0.025.

Table 10.9. Favourability scores of indicative geological variables for predicting porphyry copper potential, Abra area.

Curvi-linear or point geological variables								Stream sediment geochemical variable	
Dist. class (km)	Grano-diorite batho-lithic margins	Porphyry pluton centroids	Quartz diorite batholithic margins	NE-trending faults/ fractures	NW-trending faults/ fractures	North-trending faults/ fractures	Inter-sections of regional faults	Cu conc. (ppm)	Score
<1	0.200	0.200	0.200	0.200	0.200	0.200	0.200	>170	0.200
1-2	0.067	0.067	0.067	0.067	0.067	0.067	0.067	90-170	0.100
2-3	0.040	0.040	0.040	0.040	0.040	0.040	0.040	50-90	0.050
3-4	0.029	0.029	0.029	0.029	0.029	0.029	0.029	<50	0.025
4-5	0.022	0.022	0.022	0.022	0.022	0.022	0.022		
5-6	0.018	0.018	0.018	0.018	0.018	0.018	0.018		
6-7	0.015	0.015	0.015	0.015	0.015	0.015	0.015		
7-8	0.013	0.013	0.013	0.013	0.013	NA	0.013		
8-9	0.012	0.012	0.012	NA	0.012	NA	0.012		
9-10	0.011	0.011	0.011	NA	0.011	NA	0.011		
10-11	0.010	0.010	0.010	NA	0.010	NA	NA		
11-12	0.009	0.009	NA	NA	0.009	NA	NA		
12-13	0.008	0.008	NA	NA	0.008	NA	NA		
13-14	0.007	0.007	NA	NA	0.007	NA	NA		
14-15	0.007	0.007	NA	NA	0.007	NA	NA		
15-16	NA	0.006	NA	NA	0.006	NA	NA		
16-17	NA	0.006	NA	NA	NA	NA	NA		
17-18	NA	0.006	NA	NA	NA	NA	NA		
>18	NA	0.005	NA	NA	NA	NA	NA		

NA = proximity class is not applicable.

10.6.2 Favourability function for porphyry copper potential

Two sets of principal components analyses were performed to evaluate whether geologically-constrained wildcat mapping of porphyry copper potential is superior/inferior to integrated geochemical-geological wildcat mapping of porphyry copper potential. The first set of principal components analysis is inclusive of the indicative geochemical variable and the results are given in Table 10.10. The second set of principal components analysis is exclusive of the indicative geochemical variable and the results are given in Table 10.11.

Of the eight principal components of the favourability scores of the indicative geological variables, inclusive of the geochemical variable, PC1 is interpreted as the favourability function representing porphyry copper potential (Table 10.10). It shows an association between the heat source controls, structural controls and surficial geochemical indications on porphyry copper mineralisation. The PC2 reflects a relation between plutonic rocks that is antipathetic to a relation between the structural features. The PC3 reflects mainly the northeast-trending faults/fractures. The PC4 represents the northwest-trending faults/fractures. The PC5 reflects the structural control on emplacement of the quartz diorite batholithic plutons by north-trending faults/fractures (see sub-section 4.5.8). The PC6 represent mainly an association between faults/fractures that is antipathetic

to intersections of regional faults/fractures. The PC7 represents the porphyry plutons. The PC8 represents the indicative geochemical variable. The other PCs are therefore not good indications of porphyry copper potential as compared to PC1.

Table 10.10. Principal components analysis of favourability scores of indicative geological variables, inclusive of indicative geochemical variable, for predicting porphyry copper potential, Abra area.

	PC1	PC2	PC3	PC4	PC5	PC6	PC7	PC8
Granodiorite batholithic margins	0.586	-0.641	-0.174	-0.346	-0.220	0.058	-0.210	0.018
Porphyry plutons	0.228	-0.087	-0.076	-0.065	0.128	-0.322	0.812	-0.388
Quartz diorite batholithic margins	0.089	-0.438	0.260	0.436	0.706	0.203	-0.024	0.040
Northeast-trending faults fractures	0.382	0.263	0.793	-0.166	-0.157	0.298	0.127	0.004
Northwest-trending faults/fractures	0.541	0.450	-0.479	0.333	0.070	0.398	0.020	-0.010
North-trending faults/fractures	-0.044	0.218	-0.142	-0.737	0.597	0.158	-0.030	0.079
Intersections of regional faults	0.385	0.264	0.130	0.069	0.226	-0.744	-0.396	-0.008
Cu geochemical anomaly	0.092	-0.017	-0.035	0.029	-0.020	-0.163	0.348	0.917
Explained variance (%)	25.15	19.33	16.51	15.89	9.33	6.37	5.02	2.40
Cum. Variance (%)	25.15	44.48	60.99	76.88	86.21	92.58	97.6	100.0

The PC1 of the PC analysis exclusive of the geochemical variables is considered as the favourability function representing porphyry copper potential (Table 10.11). It shows an association between the heat source controls and structural controls on porphyry copper mineralisation. The PC2 shows an antipathetic relation between plutonic rocks and structural features. The PC3 reflects mainly the northeast-trending faults/fractures. The PC4 represents an association between quartz diorite batholithic plutons and north-trending faults/fractures. The PC6 reflects mainly the intersections of regional faults. The PC7 reflects an association between batholithic plutons and structures, which is antipathetic to the porphyry plutons. The other PCs are therefore interpreted as poor indications of porphyry copper potential as compared to PC1.

Table 10.11. Principal components analysis of favourability scores of indicative geological variables, exclusive of indicative geochemical variable, for predicting porphyry copper potential, Abra area.

	PC1	PC2	PC3	PC4	PC5	PC6	PC7
Granodiorite batholithic margins	0.586	0.645	-0.190	-0.335	-0.222	-0.027	0.203
Porphyry plutons	0.224	0.087	-0.077	-0.064	0.132	0.249	-0.924
Quartz diorite batholithic margins	0.088	0.440	0.267	0.432	0.705	-0.202	0.056
Northeast-trending faults fractures	0.390	-0.257	0.786	-0.183	-0.157	-0.312	-0.089
Northwest-trending faults/fractures	-0.040	-0.217	-0.159	-0.753	0.597	-0.163	0.075
North-trending faults/fractures	0.543	-0.449	-0.475	0.348	0.066	-0.390	0.009
Intersections of regional faults	0.387	-0.261	0.129	0.067	0.226	0.788	0.298
Explained variance (%)	25.75	19.93	17.02	16.38	9.62	6.48	4.82
Cum. Variance (%)	25.75	45.68	62.70	79.08	88.70	95.18	100.00

10.6.3 Wildcat mapping of favourability for porphyry copper potential

A score map of PC1, based on the PC analysis inclusive of the indicative geochemical variable, was created. The PC1 scores were classified using a threshold PC1 score of 0.271 (75th percentile) to distinguish between favourable zones and unfavourable zones. The favourability map of porphyry copper potential, inclusive of the indicative geochemical variable, is shown in Figure 10.3a. A score map of PC1, based on the PC analysis exclusive of the indicative geochemical variable was generated. The PC1 scores were classified using a threshold PC1 score of 0.272 (75th percentile) to define unfavourable zones and favourable zones. The favourability map of porphyry copper potential, exclusive of the indicative geochemical variable, is shown in Figure 10.3b.

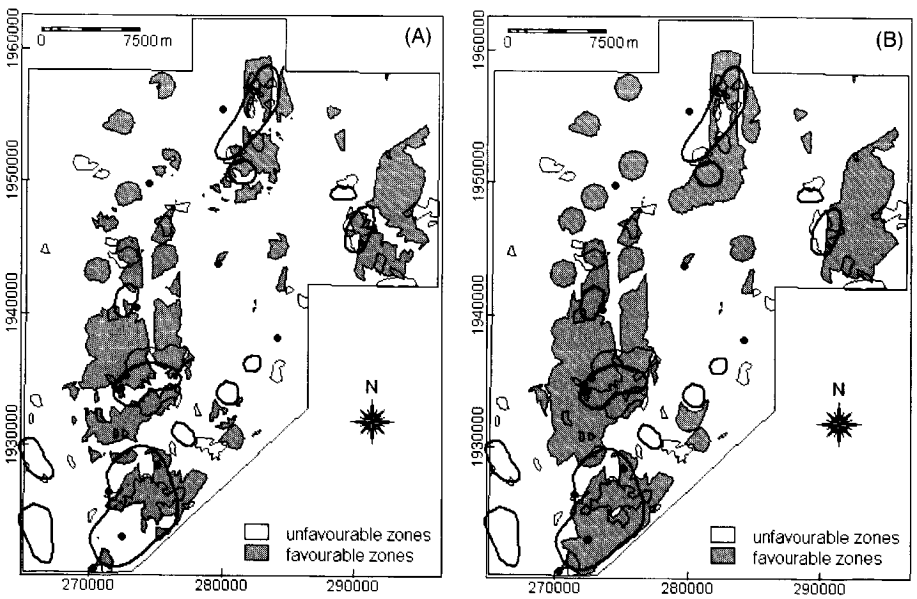

Figure 10.3. Wildcat favourability map of porphyry copper potential, Abra area: (a) inclusive of indicative geochemical variable; (b) exclusive of indicative geochemical variable. Filled circles = porphyry copper deposits; polygons in solid lines = known mineralised zones; polygons in thin lines = geochemically-anomalous catchment basins.

The spatial geoinformation characteristics of the wildcat favourability maps are given in Table 10.12. The wildcat favourability map exclusive of the indicative geochemical variable (Figure 10.3b), as compared to the wildcat favourability map inclusive of the indicative geochemical variable (Figure 10.3a), delimits at least 6% more favourable zones, has at least an 8% higher prediction rate for the known porphyry copper deposits and has at least a 23% higher prediction

Table 10.12. Spatial geoinformation characteristics of wildcat favourability maps of porphyry copper potential, Abra area.

	Figure 10.3a	Figure 10.3b
% predicted favourable zones	18.6	24.9
% predicted known porphyry copper deposits	58.3	66.7
% predicted known mineralised zones	34.7	58.2
% geochemical anomaly delineated	60.8	60.8

rate for the known mineralised zones. The favourable zones delineated in Figures 10.3a and 10.3b coincide with the same percentage (60.8%) of the area of the stream sediment geochemical anomalies. These observations indicate that the geologically-constrained wildcat favourability map is superior to the integrated geochemical-geological wildcat favourability map.

10.6.4 Discussion

The favourability function inclusive of the indicative geochemical variable and the favourability function exclusive of the indicative geochemical variable show that the quartz diorite batholithic margins and the northwest-trending faults/fracture are not important predictors of porphyry copper mineralisation in the area (Tables 10.10 and 10.11). These observations conform to geological knowledge of porphyry copper mineralisation in the area. The porphyry plutons are a weaker indicator than the granodiorite batholithic plutons. This is due to the smaller areas occupied by the porphyry plutons than the granodiorite batholithic plutons. Strong structural control on the porphyry copper mineralisation is indicated by the results. The north-trending faults/fractures are related to the intrusion of the granodiorite batholithic plutons, which are precursors of the porphyry plutons. The younger northeast-trending faults controlled the emplacement of porphyry plutons, which were emplaced at or near the intersections of north-trending and northeast-trending faults/fractures.

The wildcat favourability maps inclusive of the indicative geochemical variable and exclusive of the indicative geochemical variable depict similar areas of porphyry copper potential (Figure 10.3). The main difference between the two favourability maps is that in Figure 10.3a, the areas not represented by the geochemical data were not considered in wildcat mapping of porphyry copper potential (see Figure 2.16). Consequently, inclusion of the indicative geochemical variable does not result in an increase in the prediction rates for the known deposits and mineralised zones but rather results in the 'dismembering' of the delineated geologically-favourable zones. Nonetheless, the geochemical variable is useful in validating the reliability of the geologically-constrained favourability map and in providing greater certainty to the delineated geologically-favourable zones that overlap with the geochemical anomalies.

10.7 APPLICATION TO CATANDUANES ISLAND

Hydrothermal mineral deposits associated with the Batalay Intrusives are sought in the island. The indicative geological variables used in the wildcat modeling of hydrothermal mineral potential were curvi-linear or point geological features (intrusive contacts, faults/fractures) and multi-element stream sediment geochemical signatures.

10.7.1 Degrees of favourability of indicative geological variables

The distances to indicative curvi-linear geological variables were categorised into 1-km interval proximity classes (Table 10.13). A favourability score of 0.2 was assigned for the first proximity classes (<1 km) of the indicative curvi-linear geological variables. The degrees of favourability for distance classes beyond 1 km of the curvi-linear geological variables are less than 0.1.

Table 10.13. Favourability scores of indicative geological variables for predicting potential for hydrothermal mineral deposits, Catanduanes Island.

Indicative curvi-linear geological variables					Indicative stream sediment geochemical signature	
Proximity class (km)	NE-trending faults/fractures	N-trending faults/fractures	NW-trending faults/fractures	Batalay intrusive contacts	PC3 percentile	Score
<1	0.200	0.200	0.200	0.200	>90th	0.200
1-2	0.067	0.067	0.067	0.067	75-90th	0.100
2-3	0.040	0.040	0.040	0.040	50-75th	0.050
3-4	0.029	0.029	0.029	0.029	<50th	0.025
4-5	0.022	0.022	0.022	0.022		
5-6	0.018	0.018	0.018	0.018		
6-7	0.015	0.015	0.015	0.015		
7-8	0.013	0.013	0.013	0.013		
8-9	0.012	0.012	0.012	0.012		
9-10	0.011	0.011	0.011	0.011		
10-11	0.010	0.010	0.010	0.010		
11-12	NA	NA	0.009	0.009		
12-13	NA	NA	0.008	0.008		
13-14	NA	NA	0.007	0.007		
14-15	NA	NA	NA	0.007		
15-16	NA	NA	NA	0.006		
16-17	NA	NA	NA	0.006		
17-18	NA	NA	NA	0.006		
18-19	NA	NA	NA	0.005		
19-20	NA	NA	NA	0.005		
>20	NA	NA	NA	0.005		

NA = proximity class is not applicable.

Catchment basins characterised by >90th percentile PC3 scores of the quantified stream sediment geochemical signature (see sub-section 2.5.4) were assigned a degree of favourability of 0.2 (i.e., equal to degree of favourability of the first proximity classes of curvi-linear or point geological variables). Catchment basins characterised by 75-90th percentile PC3 scores of the quantified stream sediment geochemical signature were assigned a degree of favourability of 0.1. Catchment basins characterised by 50-75th percentile PC3 scores of the quantified stream sediment geochemical signature were assigned a degree of favourability of 0.05. Catchment basins characterised by <50th percentile PC3 scores of the quantified stream sediment geochemical signature were assigned a degree of favourability of 0.025.

10.7.2 Favourability function for hydrothermal deposit potential

Two sets of principal components analyses were performed to evaluate whether geologically-constrained wildcat mapping of potential for hydrothermal mineral deposits is superior or inferior to integrated geochemical-geological wildcat mapping of potential for hydrothermal mineral deposits. The first set of principal components analysis is inclusive of the multi-element geochemical signature (Table 10.14). The second set is exclusive of the multi-element geochemical signature (Table 10.15).

Table 10.14. Principal components analysis of favourability scores of indicative geological variables inclusive of the indicative geochemical variable, Catanduanes Island.

	PC1	PC2	PC3	PC4	PC5
Northeast-trending faults/fractures	0.706	-0.463	-0.535	0.022	0.027
North-trending faults/fractures	0.660	0.321	0.582	-0.344	0.065
Northwest-trending faults/fractures	0.140	0.824	-0.528	0.127	-0.085
Batalay Intrusive contacts	0.162	-0.042	0.230	0.506	-0.815
Multi-element geochemical signature	0.144	0.048	0.209	0.781	0.569
Explained variance (%)	32.30	26.56	18.54	13.09	9.51
Cum. Variance (%)	32.30	58.86	77.40	90.49	100.00

The PC1 of the five principal components, inclusive of the indicative geochemical variable (Table 10.14), is interpreted as the favourability function representing potential for hydrothermal mineral deposits. It reflects a positive association among the indicative geological variables. The PC2 reflects mainly the north-trending and northwest-trending faults/fractures. The PC3 could also be interpreted as a favourability function representing mineral potential; however, it precludes structural controls on mineralisation by northeast-trending and northwest-trending faults/fractures. The PC4 reflects geochemical anomalies related mainly to the Batalay Intrusives but not to faults/fractures. The PC5 reflects geochemical anomalies not related to the Batalay Intrusives nor to

the faults/fractures. These last fours PCs are poorer indicators of potential for hydrothermal mineral deposits than PC1.

The PC1 of the PC analysis exclusive of the indicative geochemical variable is interpreted as the favourability function representing potential for hydrothermal mineral deposits (Table 10.15). It shows a positive relationship between the heat source and structural controls on mineralisation. The PC2 reflects an association between north-trending and northwest-trending faults/fractures. The PC3 can also be regarded as a favourability function representing potential for hydrothermal mineral deposits; however, it rules out structural controls of mineralisation by northeast-trending and northwest-trending faults/fractures. The PC4 reflects mainly the Batalay Intrusives. The last three PCs are poor indicators of potential for hydrothermal mineral deposits as compared to PC1.

Table 10.15. Principal components analysis of favourability scores of indicative geological variables exclusive of the indicative geochemical variable, Catanduanes Island.

	PC1	PC2	PC3	PC4
Northeast-trending faults/fractures	0.729	-0.441	-0.523	-0.029
North-trending faults/fractures	0.654	0.334	0.643	-0.216
Northwest-trending faults/fractures	0.132	0.832	-0.525	0.124
Batalay Intrusives	0.151	-0.045	0.195	0.968
Explained variance (%)	36.49	30.35	20.89	12.28
Cum. Variance (%)	36.49	66.84	87.73	100.01

10.7.3 Wildcat mapping of favourability for hydrothermal deposit potential

A score map of PC1, based on the PC analysis inclusive of the geochemical variable, was generated. The PC1 scores were classified using a threshold PC1 score of 0.197 (75^{th} percentile) to map favourable zones and unfavourable zones. The favourability map of hydrothermal deposit potential, inclusive of the geochemical variable, is shown in Figure 10.4a. A score map of PC1, based on the PC analysis exclusive of the geochemical, variable was created. The PC1 scores were classified using a threshold PC1 score of 0.217 (75^{th} percentile) to demarcate favourable zones from unfavourable zones. The favourability map of hydrothermal deposit potential, exclusive of the geochemical variable, is shown in Figure 10.4b. The spatial geoinformation characteristics of the wildcat favourability maps are given in Table 10.16.

Table 10.16. Spatial geoinformation characteristics of wildcat favourability maps of hydrothermal deposit potential, Catanduanes Island.

	Figure 10.4a	Figure 10.4b
% predicted favourable zones	9.5	25.1
% predicted known gold- copper deposits	47.1	58.8
% geochemical anomaly delineated	46.9	46.7

The wildcat favourability map exclusive of the geochemical variable (Figure 10.4b), as compared to the wildcat favourability map inclusive of the geochemical variable (Figure 10.4a), delineates at least 15% more favourable zones, has about 12% higher prediction rate for the known gold-copper deposits. The favourable zones delineated by both favourability maps spatially coincide with similar percentages of about 47% of the area of the geochemically-anomalous catchment basins. Based mainly on the prediction rate for the known gold-copper deposits, the wildcat favourability map exclusive of the geochemical variable is superior to the wildcat favourability map inclusive of the geochemical variable.

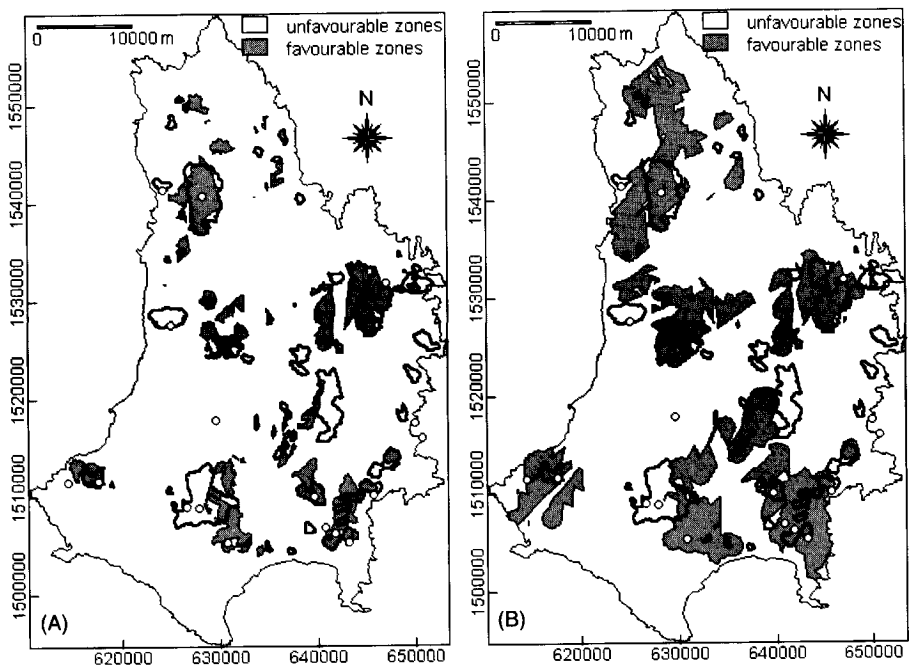

Figure 10.4. Wildcat favourability map of hydrothermal deposit potential, Catanduanes Island: (a) inclusive of indicative geochemical variable; (b) exclusive of indicative geochemical variable. Unfilled circles = gold-copper deposits; polygons in solid lines = geochemically-anomalous catchment basins.

10.7.4 Discussion

The results indicate strong structural control on hydrothermal mineralisation by the north-trending faults/fractures and the northeast-trending faults/fractures. These structures could have controlled the emplacement of the Batalay Intrusives, which are believed to be the heat sources of the known gold-copper

mineralisation in the island (Miranda and Vargas, 1967; JICA-MMAJ, 194, 1996). The small magnitude of the loading for the Batalay Intrusives on PC1 is due to the small areas that this indicative geological variable occupies. The wildcat favourability map indicates that zones where the Batalay Intrusives are absent (i.e., not mapped and probably sub-outcropping) but where the north-trending and northeast-trending faults/fractures are present are probable heat flow zones.

The wildcat favourability map inclusive of the geochemical variable (Figure 10.4a) delineates favourable zones that represent intersections of geologically-anomalous and geochemically-anomalous areas, which are also delineated by the wildcat favourability map exclusive of the geochemical variable (Figure 10.4b). The favourable zones that represent intersections of geologically-anomalous and geochemically-anomalous areas are therefore prospective for hydrothermal mineral deposits. However, as the absence of a geochemical anomaly does not necessarily mean the absence of mineralisation, the geologically-favourable zones delineated by the wildcat favourability map in Figure 10.4b are also prospective based on the high prediction rate for the known gold-copper deposits. Although the wildcat favourability map inclusive of the geochemical variable is inferior to the wildcat favourability map exclusive of the geochemical variable, the geochemical variable is useful in validating the reliability of the delineated geologically-favourable zones.

10.8 APPLICATION TO ISABELA AREA

The geological variables that are indicative of nickeliferous-laterite are (a) presence of peridotitic rocks, (b) topographic slopes of not more than 20 degrees and (c) presence of plateau edges (Golightly, 1979, 1981). A binary presentation of the indicative lithologic variable precludes the potential of other rocks units as parent rocks of nickeliferous-laterite. However, in view of the fact that laterite deposits, although not necessarily nickeliferous, can develop from most types of rocks (Nahon and Tardy, 1992), the other lithologic units in the area need to be considered for a more realistic modeling of nickeliferous-laterite potential. Hence, the application of the wildcat method to map nickeliferous-laterite potential is applied to the whole of the Isabela area as in the application of the theory of evidential belief (see Chapter 7) and the application of the theory of fuzzy sets (see Chapter 8). In addition, it is hypothesised that not only the presence of plateau edges, but also proximity to these indicative topographic features, is important for the formation of nickeliferous-laterite. As illustrated in Figure 5.17, nickel-enriched saprolite occurs not only at the edges of plateaus but also at some distances upslope and downslope of the plateau edges. Proximity to plateau edges is therefore represented and quantified in a similar fashion to the representation and quantification of indicative curvi-linear or point geological variables for mapping potential for hydrothermal mineral deposits in the other study areas. Also, a similar scheme of assigning degrees of favourability for the polygonal indicative geological variables for mapping

hydrothermal deposit potential in the other study areas is followed for the indicative lithologic and slope variables for mapping nickeliferous-laterite potential.

10.8.1 Degrees of favourability of indicative geological variables

The distances to plateau edges were categorised into 250-m interval proximity classes (Table 10.17). A favourability score of 0.8 was quantified for the first proximity class (<0.25 km) of the distances to plateau edges. The quantified degree of favourability for the second proximity class of distance to plateau edges is 0.267. The quantified degree of favourability for the third proximity class of distance to plateau edges is 0.160. The quantified degree of favourability for the fourth proximity class of distance to plateau edges is 0.114. The degrees of favourability of proximity classes for distances beyond 1.25 km of the plateau edges are less than 0.1.

Table 10.17. Favourability scores of indicative geological variables for predicting potential for nickeliferous-laterite, Isabela area.

Plateau edges		Lithologic formations		Slopes	
Proximity classes (km)	Score	Name	Score	Ranges	Score
<0.25	0.800	Quaternary alluvium	0.050	<10°	0.800
0.25-0.50	0.267	Miocene-Pliocene sedimentary rocks	0.100	10-20°	0.400
0.50-1.00	0.160	Oligocene dioritic intrusives	0.200	20-30°	0.200
1.00-1.25	0.114	Oligocene sedimentary and volcanic rocks	0.200	30-40°	0.100
1.25-1.50	0.089	Cretaceous rocks	0.400	>40°	0.050
1.50-1.75	0.073	Cretaceous Isabela Ultramafics	0.800		
1.75-2.00	0.062				
2.00-2.25	0.053				
2.25-2.50	0.047				
2.50-2.75	0.042				
2.75-3.00	0.038				
3.00-3.25	0.035				
3.25-3.50	0.032				
3.50-3.75	0.030				
3.75-4.00	0.028				
4.00-4.25	0.026				
4.25-4.50	0.024				
4.50-4.75	0.023				
4.75-5.00	0.022				
5.00-5.25	0.021				
5.25-5.50	0.020				
>5.50	0.019				

10.8.2 Favourability function for nickeliferous-laterite potential

A principal components analysis was performed on the favourability scores of the geological variables indicative of nickeliferous-laterite deposits. The results of the PC analysis are given in Table 10.18.

Table 10.18. Principal components analysis of favourability scores of indicative geological variables for predicting nickeliferous-laterite potential, Isabela area.

	PC1	PC2	PC3
Lithologic units	0.281	0.403	0.871
Proximity to plateau edges	-0.936	-0.084	0.341
Slope ranges	0.210	-0.912	0.354
Explained variance (%)	48.38	27.48	24.14
Cum. Variance (%)	48.38	75.86	100.00

The PC3 of the favourability scores of the indicative geological variables is interpreted as the favourability function representing nickeliferous-laterite potential. It shows a positive association between the indicative geological variables, in which the dominant contributor to the favourability for nickeliferous-laterite potential is the lithologic variable whilst the slope and geomorphologic variables make similar contributions to the favourability for nickeliferous-laterite potential. The PC1 reflects areas of different lithologic units with similar slopes. The PC2 reflects areas of the same lithologic units with different slopes. Neither PC1 nor PC2 are indicators of favourability for nickeliferous-laterite potential as compared to PC3.

10.8.3 Wildcat mapping of favourability for nickeliferous-laterite potential

A score map of PC3 was generated. The PC3 scores were classified using a threshold PC3 score of 0.727 (75^{th} percentile) to discriminate unfavourable zones from favourable zones. The favourable zones were further classified into low potential zones and high potential by using a PC3 score of 1.010 (90^{th} percentile). The wildcat favourability map of nickeliferous-laterite potential is shown in Figure 10.5.

The wildcat favourability map indicates that 67% of the area is unfavourable for the occurrence of nickeliferous-laterite, 23% has low potential and 10% has high potential for nickeliferous-laterite. The low and high potential zones pertain mostly to the ultramafic terrane (see Figure 2.20). About 38% of the ultramafic terrane has low potential for nickeliferous-laterite and about 58% of the ultramafic terrane has high potential for nickeliferous-laterite. The wildcat favourability map indicates that about 39% of the section with known nickeliferous-laterite deposits has high potential, about 57% has low potential and about 4% is unfavourable. Within this section, zones underlain by non-

ultramafic rocks are unfavourable for nickeliferous-laterite. Zones of low to high potential characterise the catchment basins with stream sediment Ni contents >2500 ppm.

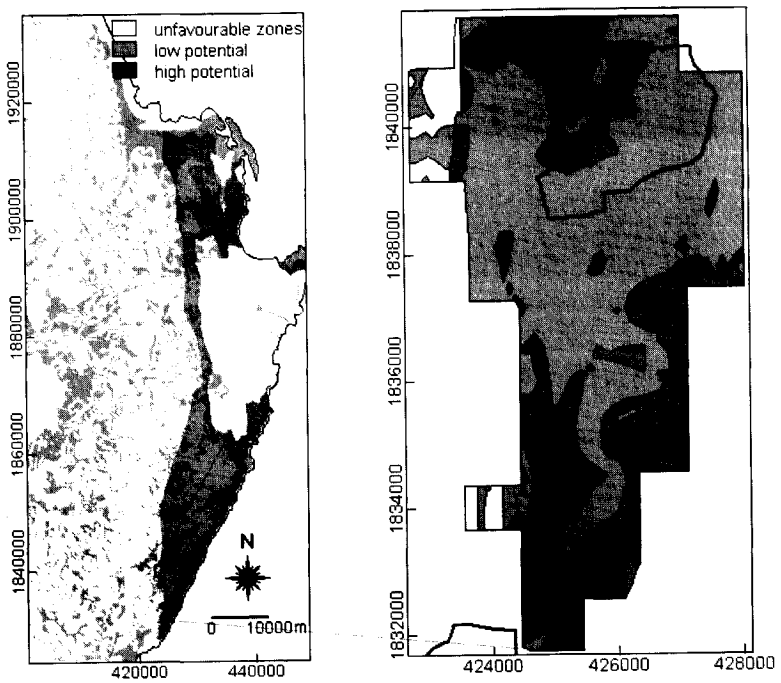

Figure 10.5. Wildcat favourability map of nickeliferous-laterite potential, Isabela area (left). Section with known nickeliferous-laterite deposits; solid lines represent catchment basins with stream sediment Ni contents >2500 ppm (right).

10.8.4 Discussion

Representation of the plateau edges as proximity classes of distances to these indicative topographic features allows a more realistic mapping of nickeliferous-laterite potential than a binary representation of these topographic features (see sub-section 5.5.4). Consideration of the possibility that laterite can form from non-peridotitic rocks and therefore wildcat mapping within the whole area instead of only within the ultramafic terrane allows the recognition of low potential zones underlain by non-ultramafic rocks such as the zones underlain by the basaltic rocks in the southern portion of the area. The wildcat favourability map of nickeliferous-laterite potential is similar to the predictive maps resulting from the applications of the theory of evidential belief (see Figure 7.20) and the theory of fuzz sets (see Figure 8.28) but with different spatial geoinformation

characteristics. The validity of the wildcat favourability map was not fully assessed due to the lack of appropriate validation data (i.e., locations and areal extents of known nickeliferous-laterite deposits. An indication of its validity, however, is shown by the spatial coincidence of the predicted low and high potential zones in the section with known nickeliferous-laterite deposits with the catchment basin containing stream sediment with more than 2500 ppm Ni contents.

There are less high potential zones in the section with known nickeliferous-laterite deposits than in other sections of the ultramafic terrane (Figure 10.5). There are, however, no known nickeliferous-laterite deposits in the sections of the ultramafic terrane immediately north of the section with known nickeliferous-laterite because of the prohibition of mineral resource development in these sections (Mangaoang, 1997). The protection of particular sections in the area from mineral resource development, which was imposed before the nickeliferous-laterite potential map in Figure 10.5 was generated, is not being disputed; however, the results demonstrate that mineral potential maps are important inputs to optimum land-use planning.

10.9 DISCUSSION

Quantitative mapping of mineral potential without training data or control data is an important problem, which is comprised of two questions that need to be addressed. The first question of the problem is: how to represent geological map data for predictive modeling without training points (i.e., locations of mineral deposits). The representation of the indicative curvi-linear or point geological variables demonstrated here is based on the results of modeling of the spatial associations between mineral deposits and curvi-linear or point geological features (see Chapter 4), which show that mineral deposits are not located directly on particular geological features but rather at some range of proximity to the geological features. The results of modeling the spatial associations between the mineral deposits and curvi-linear or point geological features were, however, not used in the quantitative representation of the indicative geological variables. Instead, it was assumed that the degree of favourability of particular indicative geological variables could be represented as the inverse of distances to these indicative geological features. The non-linear decrease in the degrees of favourability with increasing distance from the curvi-linear or point geological features is a realistic representation of the controls on mineralisation by these indicative geological variables. This method of representing the indicative geological variables, particularly the plutonic rocks, simulates the non-linear flow of heat from geological objects (Rybach, 1985).

In the work of Luo (1990), who reported a statistical mineral prediction technique without defining a training area, granite veins were represented as proportions of cells (or pixels) covered by the granite veins and represented faults as total

length of faults of particular strike directions. Representation of geological objects as proportions in unit cells, however, is sensitive to the cell size (see Chapter 9; Agterberg et al., 1993). In this work, the fractal nature of distance measurements in pixel-based raster calculations was considered (see sub-section 10.3.2). Luo's (1990) representation of faults as total length is also inadequate because the length of faults is considered less important than the presence of (or proximity to) the faults in controlling mineralisation.

The second question which comprises the problem of quantitative mapping of mineral potential without training or control data is: how to predict sub-areas with mineral potential. With the assumption that the mineral deposit sought can be characterised by a quantitative function of a linear combination of indicative geological variables, principal components analysis was applied to combine the indicative geological variables. The principal components method is useful to characterise a typical linear combination with minimised variance of the favourability function and is necessarily meaningful particularly if the predictor variables are pre-selected (Pan and Harris, 1992b). In addition, Luo (1990) advocates that the variables input to principal components should not be linearly dependent. In the characteristic analysis of McCammon et al. (1983a), which is also a principal components method for estimating mineral potential in areas with training or control data, pre-selection of input variables is possible. In this work, the input variables in the principal components analysis were not pre-selected as it is assumed that the mineral deposits in the study areas are unknown and therefore knowledge is insufficient to pre-select the input variables in the analysis. The assumption of non-linear dependence among the input indicative geological variables, which is based of the results on the pairwise conditional independence tests (see Chapter 6), is probably valid because the resulting principal components in the different study areas are geologically meaningful.

10.10 CONCLUSIONS

The methodology presented here is built on the belief that there should be a simple and meaningful way to quantitatively represent and integrate geological map information for wildcat mapping of mineral potential. Conceptual information about how and where mineral deposits occur is an important input for such wildcat mapping of mineral potential. Proximity to indicative geological variables is demonstrated to be an important predictor of zones that are favourable for mineral deposits. Principal components analysis is shown to be a quantitative method for integrating systematically quantified indicative geological variables, in which the favourability function representing mineral potential is assumed as a linear combination of these indicative geological variables.

For Benguet province, the wildcat favourability maps, inclusive and exclusive of the remotely-detected hydrothermal alteration data, delineate about 25% of the

province as favourable for porphyry copper deposits and reflect accurately at least 67% of the known porphyry copper deposits. For Baguio district, the wildcat favourability maps, inclusive and exclusive of the remotely-detected hydrothermal alteration data, delimit 22-25% of the district as favourable for epithermal gold deposits and delineate correctly about 58% of the known large-scale gold deposits and at least 63% of the known small-scale deposits. For Abra area, the geologically-constrained wildcat favourability maps demarcates about 25% of the area as having potential for porphyry copper deposits and maps correctly at least 66% of the known porphyry copper deposits and at least 58% of the known mineralised zones. For Catanduanes Island, the geologically-constrained wildcat favourability map outlines about 25% of the island as prospective for hydrothermal mineral deposits and has a prediction rate of about 59% of the known gold-copper deposits. For Isabela area, the wildcat favourability map delineates mostly the ultramafic terrane as favourable for nickeliferous-laterite deposits. It indicates that about 36% of the section with known nickeliferous-laterite deposits has high potential; however, the validity of the wildcat favourability map was not fully evaluated.

The geologically-constrained wildcat favourability maps of mineral potential are as useful or superior to the integrated geochemical-geological wildcat favourability maps of mineral potential. The wildcat modeling of mineral potential presented here can therefore be used to map mineral potential in areas where geological map data are available but where mineral deposit data are lacking to ensure that prospective areas are not closed to exploration and to guide further exploration work. In the next chapter, the results of the wildcat mapping of mineral potential are compared and contrasted with the results of the predictive mapping of mineral potential presented in the preceding chapters, which are based on training or control data.

Chapter 11

Conclusions

"The most important fundamental laws and facts
of physical science have all been discovered,
and these are now so firmly established that
the possibility of their being supplemented
in consequence of new discoveries
is exceedingly remote."

Michelson, Abraham Albert (1852-1931)
In P. Coveney and R. Highfield, The Arrow of Time,
Flamingo, London 1991, p 67.

This Chapter first reviews the rationale and objectives of the research. It then reviews and evaluates the methods developed for remote detection of indications of mineralisation in heavily-vegetated terranes; reviews and evaluates the methods used and developed for quantifying spatial associations between mineral deposits and geological features; discusses and compares the methods developed for geologically-constrained predictive mapping of mineral potential; compares the mineral potential maps; and reviews the results of the geologically-constrained predictive mapping of mineral potential of the different study areas. Finally, it provides suggestions about which method to apply to map potential in different situations of mineral deposit data availability for areas with geological settings and mineral deposits similar to the study areas and provides recommendations for further research.

11.1 INTRODUCTION

The rationale for this research is based on two principles:

- The geology of a particular area is the single most important indicator of its mineral potential.
- The geoexploration data available, in many countries, are more in the form of geologic maps.

Cognisant of these principles, it is hypothesised that there should be ways to classify or map mineral potential when the geology is known but systematic and comprehensive geoexploration data are lacking.

The major objective of this research is to test this hypothesis by the development of methods of geologically-constrained predictive mapping of mineral potential for areas in countries where the geology is known but systematic and comprehensive geoexploration data are lacking.

One such country where the geology is known but systematic and comprehensive geoexploration data are lacking is the Philippines. This lack of geoexploration data and nationwide comprehensive mineral potential assessment and classification have, in the Philippines, brought about conflicts and competing demands between land-uses that permit mineral resources development and those that promote protection of ecosystems.

Development of methods for geologically-constrained predictive mapping of mineral potential can help public service organisations:

- to define prospective land;
- to weigh mineral potential vis-à-vis exigent demands for land-use other than mineral resource development; and
- to foster exploration investment through non-closure of areas likely to contain mineral deposits.

Two limitations were taken into account for achieving the major research objective.

- Many geological maps do not portray sufficient information about indications of mineralisation (e.g., hydrothermal alteration), which can be used as inputs to geologically-constrained predictive mapping of mineral potential.
- A qualitative knowledge of the spatial associations between the known mineral deposits and geological features, which can be deduced from the geological maps, is deemed inadequate in geologically-constrained predictive mapping of mineral potential.

In respect of the first limitation and the fact that remote sensing can provide additional information useful to mineral potential mapping (although for many areas vegetation can be a nuisance to remote detection of valuable information), the research also aimed to develop a methodology for remote detection of indications of mineralisation in heavily-vegetated terranes to augment available geological data as inputs to geologically-constrained predictive mineral potential mapping (Chapter 3).

In respect of the second limitation and the fact that spatial associations between mineral deposits and geological features can vary from place to place, the research also aimed to develop a methodology for quantifying spatial associations association between mineral deposits and geological features as inputs to geologically-constrained predictive mapping of mineral potential (Chapter 4).

11.2 METHODS FOR REMOTE DETECTION OF INDICATIONS OF MINERALISATION USING LANDSAT TM DATA

One indication of mineralisation is hydrothermal alteration. Remote detection of hydrothermally-altered rocks can be difficult in the presence of dense as the spectral response of the underlying ground is obstructed by and complicated by the spectral response of vegetation.

- Applications of existing methods, the Crósta technique and the software defoliant technique, which reduce the spectral effects of vegetation, proved inadequate in the remote mapping of limonitic and clay alterations in the Baguio district.
- Applications of the Crósta technique and the software defoliant technique were not only inadequate but also inappropriate because the target materials of these techniques are not characteristic of the hydrothermal alterations in the Baguio district.
- Published reflectance spectra of minerals characteristic of the hydrothermal alteration in the Baguio district suggest that different techniques are needed to map at least the known hydrothermal alterations there.
- Hence, a new technique of remote detection of mineralisation-related hydrothermal alteration is developed – a mineral imaging method using Landsat TM data.

In the mineral imaging method the use of two appropriate Landsat TM band ratio images in principal components analysis allows the removal of the effects of vegetation from the Landsat TM data and the creation of separate mineral images that portray relative abundance of each of the predominant alteration minerals.

- A supervised classification of only the mineral images to map hydrothermal alteration units in the Baguio district produced poor and unacceptable results.
- Inclusion of a DEM image in the classification, however, yielded maps with better accuracy that agree with reference data.
- For Baguio district, the accuracy of remote detection of hydrothermal alterations by the mineral imaging method reaches 82%.
- For Mankayan district, the accuracy of remote detection of hydrothermal alterations by the mineral imaging method is 69%.
- For Benguet province, the accuracy of remote detection of hydrothermal alterations by the mineral imaging method reaches 73%.

The results of the mineral imaging method are statistically different and better than the results of supervised classification of only Landsat TM spectral bands.

Vegetation cover, which obstructs the spectral response of mineralised zones and/or geochemically-enriched zones, can be geochemically-stressed. Vegetation stress is thus another indication of mineralisation.

- Analyses of Landsat TM data indicate that, for the Catanduanes area, vegetation in and near gold-copper deposits and Zn-enriched catchment basins is geochemically-stressed.
- There is a blue-shift in the red-edge vegetation spectra in geochemically-enriched and mineralised zones.
- The results of the analyses indicate that a broad band spectral scanner like the Landsat TM can detect changes in the red-edge position of vegetation spectra caused by a geochemically-enriched substrate.
- Vegetation in geochemically-enriched and/or mineralised zones has different spectral characteristics to vegetation in geochemically-background and/or non-mineralised zones based on the NDVI image and band ratio images with band 3 as denominator.
- Supervised classification of an NDVI image and band ratio images (with band 3 as denominator and bands 1, 2, 5 and 7 as numerators) reveals a dense neighbourhood of geochemically-stressed vegetation in Catanduanes. The accuracy of the classification is 52-54%.

Intrusive margins/contacts and faults/fractures can indicate the presence of mineralisation. Spatial data for such curvi-linear geological features, although amenable to remote detection, were not remotely-detected but digitally-captured from paper maps and/or interpreted from hill-shaded relief images of DEMs.

11.3 METHODS FOR QUANTIFYING SPATIAL ASSOCIATION OF MINERAL DEPOSITS AND CURVI-LINEAR OR POINT GEOLOGICAL FEATURES

To quantify spatial associations between the mineral deposits and curvi-linear or point geological features, two established methods (distance distribution method and weights of evidence method) were used and a new distance correlation method was developed (Chapter 4).

The distance distribution method is a point pattern analytical technique that is useful to determine spatial association between points and nearest neighbour points on linear features.

- The most important limitation of the distance distribution method is that it assumes mineral deposits to have a Poisson distribution; however, mineral deposits that are related to a certain magmatic regime, as in the study areas, are not essentially independent and do not necessarily have a Poisson distribution.
- Another limitation of the distance distribution method is that searching for the optimum random points, whose frequency distribution function of nearest distances to linear features is compared with the frequency distribution of

nearest distances between mineral deposits and linear features, is not easy and that different sets of 'optimum' random points can produce different results.

The weights of evidence method is useful to analyse spatial associations between mineral deposits and polygonal geological features (e.g., lithologic units) and binary patterns of curvi-linear or point geological features. It avoids the limitations of the distance distribution method.

- The main limitation of the weights of evidence method is that there should be a fairly larger number of mineral deposit points; otherwise the quantified spatial association can be statistically non-significant.

The new distance correlation is an innovative point pattern analysis.

- Unlike the distance correlation method, it has no assumption of the probability distribution of the mineral deposit points.
- Unlike the weights of evidence method, it is effective even in the case of small number of points.
- The main disadvantage of the new distance correlation method is that several arbitrary points are needed to characterise optimally the spatial association of a set of points with a set of lines (or another set of points).

The results of the distance correlation method are mostly similar to the results of the distance distribution method and the weights of evidence method when the number of mineral deposits is ≥ 17 as in Benguet province (see (Table 4.11), in Baguio district (see Table 4.20) and in Catanduanes Island (see Table 4.52). The results of the three methods are mostly statistically significant when the number of mineral deposits is ≥ 17. The results of the distance correlation method are mostly different but statistically significant as compared to the mostly non-significant results of the distance distribution method and the weights of evidence method when the number of mineral deposits is 12 as in Abra area (see Table 4.35).

- The distance correlation method is therefore a satisfactory method.
- The distance correlation method is considered useful in situations where few mineral deposits are known and therefore where the probability distribution of the mineral deposits is inadequately known.
- The distance correlation method is considered useful to quantify spatial associations between known mineral deposits and curvi-linear or point geological features in areas where systematic and comprehensive geoexploration data are insufficient to classify mineral potential.

11.4 METHODS FOR GEOLOGICALLY-CONSTRAINED PREDICTIVE MINERAL POTENTIAL MAPPING

11.4.1 General overview

The fundamental question underlying the research objective of developing methods for geologically-constrained predictive mineral potential mapping is this.

> For an area with a certain geologic setting (with or without a number of known mineral deposits of a certain type), where systematic and comprehensive geoexploration data are lacking except geologic maps (and satellite imagery), which method or methods are applicable to define potentially-mineralised areas (i.e., those areas that warrant further detailed exploration)?

To answer the fundamental question, five study areas were selected in the Philippines to develop, apply and validate methods for geologically-constrained predictive mapping of mineral potential.

Benguet province covers 2,596 km^2 and contains porphyry copper deposits that are related to an early mid-Miocene to late-Miocene magmatic arc (Figure 2.4). The geoexploration data used to map areas with potential for porphyry copper deposits included locations of 31 known porphyry copper deposits derived from various geological maps/reports (Table 2.4), lithological data extracted from various geological maps (sub-section 2.2.2), structural data extracted from shaded-relief images of a DEM (sub-section 2.2.3) and hydrothermal alteration data extracted from Landsat TM data (sub-section 3.3.8).

Baguio district measures about 420 km^2 and contains epithermal gold deposits that are related an early mid-Miocene to late-Miocene magmatic arc (Figure 2.4). The geoexploration data used to map areas with potential for epithermal gold deposits included locations of known epithermal gold deposits (19 large-scale and 63 small-scale deposits), lithological data and structural data derived from various published/unpublished geological maps/reports (sub-section 2.3.2) and hydrothermal alteration data derived from Landsat TM data (sub-section 3.3.6).

Abra area covers 920 km^2 and contains porphyry copper deposits that are related to an early mid-Miocene to late-Miocene magmatic arc (Figure 2.4). The geoexploration data used to map areas with potential for porphyry copper deposits included locations of 12 known porphyry copper deposits from the 1:250,000 scale geological map (sub-section 2.4.2; Bureau of Mines, 1976), lithological data derived from 1:50,000 scale geologic maps (sub-section 2.4.2; JICA, 1980) and structural data derived from shaded-relief images of a DEM (sub-section 2.4.3).

Catanduanes Island measures 1,448 km^2 and contains gold-copper vein deposits that are related to a late Eocene to Oligocene magmatic arc, whose tectonic affinity is still under debate (Mitchell and Leach, 1991). The

geoexploration data used to map areas with potential for gold-copper vein deposits included locations of 17 known gold-copper vein deposits, lithological data derived from the 1:100,000 scale geological map (sub-section 2.5.2) and structural data derived from shaded-relief images of a DEM (subsection 2.5.3).

Isabela area occupies 3,676 km^2 and reportedly contains nickeliferous-laterite deposits that are associated with ophiolitic ultramafic rocks (Figures 2.2 and 2.4). However, the locations of reported nickeliferous-laterite deposits in the area are unknown. The geoexploration data used to map areas with potential for nickeliferous-laterite deposits included lithological data derived from 1:250,000 scale geological maps (section 2.6.2) and topographic data derived from 1:250,000 scale topographic maps (section 2.6.3).

To provide the theoretical framework for the GIS-based geologically-constrained mineral potential mapping in the different study areas, conceptual deposit exploration models were defined based upon:

- knowledge of the local geological setting (Chapter 2);
- quantified spatial associations between mineral deposits and geological features (Chapter 4); and
- knowledge of the general characteristics of the type of mineral deposit sought (Chapter 5).

The conceptual deposit exploration models provide useful guides for determining which geological features to enhance and extract as spatial evidences and for weighting and combining the spatial evidences based on the different methods for mapping mineral potential.

The different methods developed for GIS-based geologically-constrained predictive mapping of mineral potential involve operations for the application of:

- simple map algebra (Chapter 5);
- weights of evidence modeling (Chapter 6);
- the theory of evidential belief (Chapter 7);
- the theory of fuzzy sets (Chapter 8);
- logistic regression (Chapter 9); and
- principal components analysis for wildcat mapping (Chapter 10).

The operations for the application of simple map algebra and weights of evidence modeling involve binary representation and weighting of geological evidences/indicators of mineralisation. The operations for the application of the Dempster-Shafer theory of evidential belief, the theory of fuzzy sets, logistic regression and wildcat mapping involve multi-class representation and weighting of geological evidences/indicators of mineralisation. The decision to test/apply particular methods in/to the different study areas was based mainly on the conceptual aspects of each method and whether training data (i.e., 'model' deposits) are available.

11.4.2 Methods involving binary evidences

The application of simple map algebra involves the assignment of favourability scores (favourable = 1; unfavourable = 0) first to convert geological features into binary predictor patterns based on the criteria provided by conceptual deposit models and then to combine these predictor patterns by simple map addition to map mineral potential (Chapter 5). The method is essentially knowledge-driven. It is applicable to areas where mineral deposits are unknown. In areas where mineral deposits are known, however, analyses of spatial associations of mineral deposits and curvi-linear or point geological features are useful in the binary representation of geological evidence of mineralisation based on criteria provided by conceptual deposit models. In this case, the application of simple map algebra is a combined data-driven and knowledge-driven method. This simple scheme of mineral potential classification simulates the 'light-table operation' of stacking maps on top of each other to find sub-areas of mineral potential characterised by the intersections of the spatial evidences. Statistical testing of validity of results is not required in the simple map algebra method.

- A weakness of the simple map addition of binary evidences of mineral potential is the assumption that the different spatial evidences have equal importance in delineating potentially mineralised zones.

Weights of evidence modeling involves calculation of weights and contrasts of binary patterns of multi-class maps of geological features (e.g., distance to curvi-linear geological features) to determine cutoff distance to convert multi-class maps into binary predictor patterns as evidence layers for mapping mineral potential. It is a data-driven method and applicable only to areas where mineral deposits are known (Chapter 6). The binary predictor patterns of geological evidences of mineralisation are combined with the assumption of, and therefore a test for, conditional independence among the binary predictor patterns with respect to the mineral deposits. Pairwise testing of conditional independence prior to combining the binary predictor patterns can lead to rejection and exclusion of some binary predictor patterns of geological evidences of mineralisation in the analysis. Overall testing of conditional independence after combining the binary predictor patterns of geological evidence of mineralisation may or may not necessitate further re-inspection of pairwise conditional independence. A disadvantage of the weights of evidence method is that it is sensitive to the number of deposits and size of the area in generating the binary predictor patterns. The selection of cutoff distance to create a binary predictor pattern is critical to the statistical validity of the output mineral potential map.

- The highest Studentised C (i.e., statistically significant contrast) was more effective in Benguet province (number of deposits used in modeling = 23) and in Baguio district (number of deposits used in modeling = 19) than in Abra area (number of deposits used in modeling = 12) and in Catanduanes Island (number of deposits used in modeling = 17) in determining the cutoff

distance to convert the multi-class distance maps of geological curvi-linear or point features into binary predictor patterns.

- Where the number of mineral deposits is 17 or less (i.e., in Abra area and Catanduanes Island), the statistical significance of the weights of the binary patterns and the proportion of mineral deposits (here defined as the predictive strength) in the binary patterns must be considered in determining an optimum binary predictor pattern. Binary patterns with statistically significant weights and predictive strength of >50% are optimum binary predictor patterns.

Representation of geological evidences as binary predictor patterns and integration of these binary predictor patterns to map mineral potential, either by simple map algebra or the weights of evidence method, is appealing due to its simplicity. However, the weaknesses of the binary approach are that:

- evidences of presence or absence of geological features important to mineralisation are not really binary but have spatially varying degrees of certainty or are non-existent.; and
- degrees of uncertainty for particular geological features as evidence of mineralisation are not incorporated in the weights.

Alternative methods to the binary approaches of mapping mineral potential are discussed below.

11.4.3 Methods involving multi-class evidences

The application of the Dempster-Shafer theory of evidential belief involves the assignment of basic probabilities to each class of evidence in a layer of multi-class evidence with respect to the mineral deposits. These basic probabilities are the degree of belief, the degree of disbelief, the degree of uncertainty and the degree of plausibility. The method is applicable in areas where mineral deposits are either known (knowledge-driven and data-driven) or unknown (knowledge-driven). However, in the examples found in the literature about the application of the Dempster-Shafer theory of evidential belief to mineral potential mapping, the four basic probability assignments are invariably assigned by an expert (i.e., knowledge-driven) rather than calculated from the geological and mineral deposit data (i.e., data-driven).

- Previously-defined equations for calculating the basic probability assignments of the multi-class geological evidences of mineralisation in the different study areas proved inadequate for a data-driven application of the evidential belief functions. The previously defined equations for calculating the basic probability assignments take into account only the spatial relationship of a class of evidence with the mineral deposits but do not take into account the spatial relationship of a class of evidence with other classes of evidence within a layer of multi-class evidence.

- Equations for calculating representative estimates of basic probability assignments were defined by taking into consideration the spatial relationship of a class of evidence with the mineral deposits and the spatial relationship of a class of evidence with other classes of evidence within a layer of multi-class evidence. The equations defined for calculating representative estimates of the basic probability assignments allow adequate data-driven applications of the theory of evidential belief. The degrees of belief and degrees of disbelief, estimated using the defined equations, accurately reflect the spatial associations between the mineral deposits and the curvi-linear or point geological features quantified by the three methods described above.
- The management of uncertainty by the calculation of degrees of uncertainty of multi-class spatial evidences and the creation of an uncertainty map is an advantage of the application of the Dempster-Shafer theory of evidential belief. However, the calculation of four weights and creation of four maps (i.e., belief map, disbelief map, uncertainty map and plausibility map) can also be a disadvantage.

Where mineral deposits are unknown, only a knowledge-driven application of the evidential theory of belief is possible. Statistical evaluation of the validity of the results in either a data-driven application or a knowledge-driven application of the theory of evidential belief is not required. However, the validity of the results must be carefully scrutinised against their geological significance in terms of mineralisation.

The application of the theory of fuzzy sets involves the assignment of only one weight (a fuzzy membership score) to a sub-set of spatial evidence within a fuzzy set or layer of geological evidence. The method is essentially knowledge-driven. It can be applied in areas where mineral deposits are unknown. However, in areas where mineral deposits are known, the subjective assignment of weights can be guided by a quantitative knowledge of the spatial associations between the mineral deposits and the geological features. In this case, the application of the theory of fuzzy sets is both data-driven and knowledge-driven. Knowledge about the accuracy of input maps can be considered in the assignment of fuzzy membership scores. Uncertainty in the geological evidences can therefore be incorporated in the assignment of fuzzy weights. Statistical validation of the results is not required; only logic is applied to determine the geological significance of the results. The incorporation of knowledge in the integration of spatial evidences is a major advantage of the application of the theory of fuzzy sets over the other methods. Combining multiple spatial evidences to map mineral potential using fuzzy logic as an inference engine allows representation and evaluation of intermediate hypotheses regarding the significance of the spatial evidences pertinent to mineralisation. For areas where mineral deposits are unknown, the several possible combinations of the fuzzy spatial evidence layers through a number of different fuzzy logic operators can be a disadvantage over a knowledge-driven

application of the evidential theory of belief. Another weakness of the application of fuzzy sets, like the application of the theory of evidential belief, is the subjective assignment of weights, which can be prone to bias.

Logistic regression involves the analysis of the relationship of a dichotomous variable (e.g., mineral deposits) to a number of independent variables (e.g., geological features). Logistic regression is a data-driven method, which is feasible for integrating geological variables for predictive mapping of mineral potential only for areas with known mineral deposits, which are used as the dependent variables. It was therefore applied only to Benguet, Baguio, Abra and Catanduanes. The generation and weighting of binary evidences of mineralisation were based on the quantified spatial associations between a subset of 'model' deposits and curvi-linear or point geological features and the predictive models were validated against a subset of 'validation' deposits.

- Analysis of spatial associations between mineral deposits and geological features is an important prerequisite to the useful application of logistic regression. Logistic regression modeling using independent curvi-linear or point geological features that are positively spatially associated with the mineral deposits provides statistically-valid results. Logistic regression modeling using independent curvi-linear or point geological features that are negatively spatially associated with the mineral deposits provides statistically-erroneous results.
- A disadvantage of logistic regression modeling is that the statistical validity of the predictive models is sensitive to pixel/cell size. The 100x100 m pixel size, which is used in the quantitative spatial association modeling to ensure that only one mineral deposit occurs in a pixel, was found to be the most suitable in the logistic regression experiments. The sensitivity to pixel size of predictive models by the other methods was not evaluated but is likely similar to that found for the logistic regression modeling.

A wildcat method for geologically-constrained predictive mapping of mineral potential is developed for areas where no mineral deposits are known. The wildcat method for mapping mineral potential employs principal components analysis, which involves the quantification of a linear multivariate association of indicative geological variables that can characterise a particular geological environment, which in this case is a mineralised geological environment.

- Representation of geological features as proximity classes and representation of the degree of favourability of geological features as the inverse of the mid-distance of the proximity classes allow the application of principal components analysis to wildcat geologically-constrained predictive mapping of mineral potential in areas where mineral deposits are unknown.

Statistical testing of the results is not required but the geological significance of the principal component interpreted as the favourability function representing mineral potential must be carefully scrutinised.

Representation of geological evidences as multi-class predictor patterns and integration of these multi-class predictor patterns to map mineral potential can be complicated. However, representation of geological evidences as multi-class predictor patterns is realistic. It allows representation and quantification of the spatially-varying degrees of favourability and certainty of a class of evidence in a multi-class layer of evidence as a predictor of mineral potential.

11.4.4 Methods applied to different study areas

All the different methods were applied to areas where mineral deposits are known (i.e., Benguet, Baguio, Abra and Catanduanes). In the application of simple map algebra, weights of evidence modeling, the theory of evidential belief, the theory of fuzzy sets and logistic regression, the whole set or a subset of the known mineral deposits was used in quantifying spatial associations between mineral deposits and geological features, which were the bases for weighting the spatial evidences in the predictive modeling of mineral potential. When the whole set of known mineral deposits was used in the predictive modeling, as in the case of a small number of mineral deposits, another mineralisation-related geoinformation was used to validate the predictive models. When a subset of the known mineral deposits was used in the predictive modeling, the remaining subset was used to validate the predictive models.

- For Benguet province, 23 'model' deposits (chosen randomly) out of the 31 known porphyry copper deposits were used to generate the predictive models of porphyry copper potential whilst the remaining eight deposits were used to validate the predictive models.
- For Baguio district, the 19 large-scale gold deposits were used to generate the predictive models of epithermal gold potential whilst the 63 small-scale gold deposits and stream sediment geochemical anomalies were used to validate the predictive models.
- For Abra area, the 12 porphyry copper deposits were used to generate the predictive models of porphyry copper potential whilst known mineralised zones and stream sediment Cu anomalies (JICA, 1980) were used to validate the predictive models.
- For Catanduanes Island, the 17 gold-copper deposits were used to generate the predictive models of gold-copper vein deposit potential whilst multi-element stream sediment geochemical anomalies (sub-section 2.5.4) were used to validate the predictive models.

The different numbers of mineral deposits in the different study areas allow the establishment of empirical guidelines for considering which method or methods to apply to an area with a given number of mineral deposits.

In the application of wildcat mapping to Benguet, Baguio, Abra and Catanduanes, the known mineral deposits were not used in generating but in validating the predictive mineral potential models. The validation of the wildcat predictive models with known mineral deposits determines the usefulness of the method to areas with geological settings similar to the study areas but with unknown mineral deposits.

Simple map algebra, the theory of evidential belief, the theory of fuzzy sets and wildcat mapping were applied to Isabela area (i.e., locations of mineral deposits are unknown). The generation, weighting and combining of spatial indicators of nickeliferous-laterite mineralisation were based subjectively upon the criteria provided by the deposit exploration model. In this case, only a subjective validation of the predictive model was possible using stream sediment Ni anomalies and the location of an area reportedly endowed with nickeliferous-laterite.

11.5 COMPARISON OF MINERAL POTENTIAL MAPS

The different final mineral potential maps made using by the different methods show both broad similarities and differences. In general, the favourable zones predicted by the different methods delineate similar areas with known mineral deposits. However, there are some areas where the mineral potential maps differ. A measure of similarity and dissimilarity of the delineated favourable zones between a pair of binary predictive maps by different methods was determined by calculating Jaccard's similarity coefficient (Bonham-Carter, 1994), which is defined as

$$C_J = \frac{O_{F_1F_2}}{O_{F_1U_2} + O_{U_1F_2} + O_{F_1F_2}} \qquad (11\text{-}1)$$

where $O_{F_1F_2}$ is the number of pixels of the 'positive overlap' of predicted favourable zones, $O_{F_1U_2}$ and $O_{U_1F_2}$ are number of pixels of mismatch (i.e., overlap of favourable zones in one map with unfavourable zones in the other map). Note that the 'negative overlap' of unfavourable zones is not considered, so the comparison is about the predicted favourable zones only. Jaccard's similarity coefficient ranges between zero (complete dissimilarity) and one (complete similarity). A coefficient of at least 0.66 is here considered to represent good similarity, a coefficient of 0.33-0.66 is considered to represent fair similarity and a coefficient below 0.33 is considered to represent poor similarity. The objective of determining the degree of similarity/dissimilarity between the different mineral potentials is to determine which methods would provide similar/dissimilar results and provide probable explanations for the similarities/dissimilarities.

11.5.1 Porphyry copper potential maps of Benguet province

Exclusive of the remotely-sensed hydrothermal alteration evidence. The final binary predictive maps resulting from simple map algebra, weights of evidence and application of fuzzy sets have good similarity (Table 11.1). The final binary predictive maps resulting from application of evidential belief and wildcat mapping have fair similarity with each other and with the binary predictive maps by the other methods.

Table 11.1. Jaccard's similarity coefficients of pairs of predictive maps of porphyry copper potential, exclusive of hydrothermal alteration evidence, Benguet province.

	Weights of evidence (Fig. 6.4)	Evidential belief (Fig. 7.4b)	Fuzzy sets (Fig. 8.7)	Wildcat mapping (Fig. 10.1b)
Simple map algebra (Fig. 5.6b)	0.75	0.42	0.71	0.43
Weights of evidence (Fig. 6.4)		0.47	0.66	0.46
Evidential belief (Fig. 7.4b)			0.36	0.53
Fuzzy sets (Fig. 8.7)				0.37

Inclusive of the remotely-sensed hydrothermal alteration evidence. The final binary predictive maps resulting from the application of evidential belief, the application of fuzzy sets and logistic regression have fair similarity with each other (Table 11.2). The final predictive maps resulting from simple map algebra and wildcat mapping have fair to poor similarity with the final predictive maps by the other methods.

Table 11.2. Jaccard's similarity coefficients of pairs of predictive maps of porphyry copper potential, inclusive of hydrothermal alteration evidence, Benguet province.

	Evidential belief (Fig. 7.4a)	Fuzzy sets (Fig. 8.5)	Logistic regression (Fig. 9.2b)	Wildcat mapping (Fig. 10.1a)
Simple map algebra (Fig. 5.6a)	0.31	0.48	0.31	0.27
Evidential belief (Fig. 7.4a)		0.44	0.49	0.36
Fuzzy sets (Fig. 8.5)			0.46	0.32
Logistic regression (Fig. 9.2b)				0.43

11.5.2 Epithermal gold potential maps of Baguio district

Exclusive of the remotely-sensed hydrothermal alteration evidence. The final binary predictive maps resulting from simple map algebra, weights of evidence and application of fuzzy sets have good similarity (Table 11.3). The final predictive map based on evidential belief have marginally good to poor similarity with the final predictive maps based on simple map algebra, weights of evidence and application of fuzzy sets. The final predictive map based on wildcat mapping has poor similarity with the other final predictive maps by the other methods.

Table 11.3. Jaccard's similarity coefficients of pairs of predictive maps of epithermal gold potential, exclusive of hydrothermal alteration evidence, Baguio district.

	Weights of evidence (Fig. 6.9a)	Evidential belief (Fig. 7.10c)	Fuzzy sets (Fig. 8.13a)	Wildcat mapping (Fig. 10.2b)
Simple map algebra (Fig. 5.13b)	0.805	0.425	0.591	0.351
Weights of evidence ((Fig. 6.9a)		0.430	0.648	0.373
Evidential belief (Fig. 7.10c)			0.360	0.382
Fuzzy sets (Fig. 8.13a)				0.393

Inclusive of the remotely-sensed hydrothermal alteration evidence. The pair of final predictive maps based on simple map algebra and application of fuzzy sets and the pair of final predictive maps based on logistic regression and wildcat mapping have good similarity. All the other pairs of final predictive maps have poor similarity.

Table 11.4. Jaccard's similarity coefficients of pairs of predictive maps of epithermal gold potential, inclusive of hydrothermal alteration evidence, Baguio district.

	Evidential belief (Fig. 7.10a)	Fuzzy sets (Fig. 8.11a)	Logistic regression (Fig. 9.4a)	Wildcat mapping (Fig. 10.2a)
Simple map algebra (Fig. 5.13a)	0.446	0.549	0.450	0.429
Evidential belief (Fig. 7.10a)		0.401	0.399	0.536
Fuzzy sets (Fig. 8.11a)			0.453	0.419
Logistic regression (Fig. 9.4a)				0.269

11.5.3 Porphyry copper potential maps of Abra area

Geologically-constrained predictive maps. The final predictive maps based on the different methods have fair similarity with each other (Table 11.5).

Table 11.5. Jaccard's similarity coefficients of pairs of geologically-constrained predictive maps of porphyry copper potential, Abra area.

	Weights of evidence (Fig. 6.14c)	Evidential belief (Fig. 7.14a)	Fuzzy sets (Fig. 8.18b)	Logistic regression (Fig. 9.6b)	Wildcat mapping (Fig. 10.3b)
Simple map algebra (Fig. 5.8b)	0.59	0.40	0.60	0.48	0.48
Weights of evidence (Fig. 6.14c)		0.43	0.56	0.52	0.46
Evidential belief (Fig. 7.14a)			0.54	0.46	0.45
Fuzzy sets (Fig. 8.18b)				0.50	0.56
Logistic regression (Fig. 9.6b)					0.38

Integrated geological-geochemical predictive maps. The pair of final predictive maps based on simple map and logistic regression and the pair of final predictive maps based on the application of fuzzy sets and logistic regression have good similarity (Table 11.6). The other pairs of final predictive maps based on the different methods have fair similarity.

Table 11.6. Jaccard's similarity coefficients of pairs of integrated geological-geochemical predictive maps of porphyry copper potential, Abra area.

	Evidential belief (Fig. 7.14b)	Fuzzy sets (Fig. 8.18a)	Logistic regression (Fig. 9.6a)	Wildcat mapping (Fig. 10.3a)
Simple map algebra (Fig. 5.9b)	0.41	0.61	0.72	0.38
Evidential belief ((Fig. 7.14b)		0.51	0.62	0.34
Fuzzy sets (Fig. 8.18a)			0.69	0.43
Logistic regression (Fig. 9.6a)				0.49

11.5.4 Gold-copper vein deposit potential maps of Catanduanes Island

Geologically-constrained predictive maps. The pair final predictive maps based on simple map algebra and weights of evidence has good similarity (Table 11.7). The other pairs of final predictive maps based on the different methods have fair similarity.

Table 11.7. Jaccard's similarity coefficients of pairs of geologically-constrained predictive maps gold-copper vein deposit potential, Catanduanes Island.

	Weights of evidence (Fig. 6.18)	Evidential belief (Fig. 7.18a)	Fuzzy sets (Fig. 8.23b)	Logistic regression (Fig. 9.8a)	Wildcat mapping (Fig. 10.4b)
Simple map algebra (Fig. 5.16a)	0.72	0.48	0.61	0.58	0.63
Weights of evidence (Fig. 6.18)		0.53	0.61	0.59	0.61
Evidential belief (Fig. 7.18a)			0.48	0.65	0.51
Fuzzy sets (Fig. 8.23b)				0.55	0.52
Logistic regression (Fig. 9.8a)					0.57

Integrated geological-geochemical predictive maps. The pair of final predictive map based on simple map algebra and the application of fuzzy sets has good similarity (Table 11.8). The final predictive maps based on simple map algebra the application of evidential belief, the application of fuzzy sets and logistic regression have fair similarity with each other. The final predictive map based on wildcat mapping have fair to poor similarity with the final predictive maps based on the other methods.

Table 11.8. Jaccard's similarity coefficients of pairs of integrated geological-geochemical predictive maps of gold-copper vein deposit potential, Catanduanes Island.

	Evidential belief (Fig. 7.18b)	Fuzzy sets (Fig. 8.24b)	Logistic regression (Fig. 9.9b)	Wildcat mapping (Fig. 10.4b)
Simple map algebra (Fig. 5.16b)	0.47	0.67	0.39	0.56
Evidential belief ((Fig. 7.18b)		0.48	0.52	0.28
Fuzzy sets (Fig. 8.24b)			0.39	0.34
Logistic regression (Fig. 9.9b)				0.24

11.5.5 Nickeliferous-laterite potential maps of Isabela area

The final predictive map based on the application of fuzzy sets has good similarity with the final predictive maps based on wildcat mapping and fair similarity with the final predictive map based on the application of evidential belief (Table 11.9). The pair or final predictive maps based on the application of evidential belief and wildcat mapping have fair similarity. The final predictive map based on simple map algebra has poor similarity with the final predictive maps based on the other methods.

Table 11.9. Jaccard's similarity coefficients of pairs of predictive maps of nickeliferous-laterite potential, Isabela area.

	Evidential belief (Fig. 7.20)	Fuzzy sets (Fig. 8.28)	Wildcat mapping (Fig. 10.5)
Simple map algebra (Fig. 5.18a)	0.18	0.12	0.10
Evidential belief (Fig. 7.20)		0.64	0.39
Fuzzy sets (Fig. 8.28)			0.67

11.5.6 Summary of comparison of mineral potential maps

There is good to fair similarity in most of the final predictive mineral potential maps based on simple map algebra, weights of evidence, application of fuzzy sets and logistic regression. This is presumably because the input binary predictor maps used in the simple map algebra approach and the input multi-class predictor maps used in the application of fuzzy sets and logistic regression were generated based on the spatial associations between the mineral deposits and the geological features as quantified by the weights of evidence, distance distribution and distance correlation methods. The good similarity between most of the final predictive maps based on simple map algebra, weights of evidence, application of fuzzy sets and logistic regression illustrate that both qualitative and quantitative knowledge of spatial association between mineral deposits and geological features are important for mineral potential mapping.

In general, the dissimilarity between the different predictive mineral potential maps made using the different methods is probably due to the difference in thresholding of the integrated maps into the binary favourability maps. The dissimilarity of the final predictive mineral potential maps based on the data-driven application of evidential belief with many of the final predictive maps made by the other methods is presumably due the difference in the generation of input maps. The dissimilarity of the final predictive mineral potential maps based on wildcat mapping with many of the final predictive maps by the other methods is probably due to the representation and weighting of the multi-class predictor patterns. This illustrates that qualitative knowledge alone of geological indicators of particular mineral deposits can be insufficient for mineral potential mapping.

11.6 MINERAL PROSPECTIVITY OF THE STUDY AREAS AND PERFORMANCE OF PREDICTIVE METHODS

Mineral potential estimates of the different study areas are summarised according to the different methods for geologically-constrained predictive mapping of mineral potential. Conclusions are then drawn about the usefulness

of the remotely-detected hydrothermal alterations, the superiority or otherwise of geologically-constrained predictive maps compared to integrated geochemical-geological predictive maps and the performance of the different methods in the different study areas based on the prediction rates of the predictive models.

11.6.1 Porphyry copper potential of Benguet province

Table 11.10 shows the geoinformation characteristics of the different predictive maps of the porphyry copper potential of Benguet province based on the different methods of predictive mapping of mineral potential.

Table 11.10. Spatial geoinformation characteristics of predictive maps of porphyry copper potential based on different methods of predictive mapping of mineral potential, Benguet province.

Method	Simple map algebra		Weights of evidence	Evidential belief		Fuzzy sets		Logistic regression		Wildcat mapping	
Predictive map	Fig. 5.6a[1]	Fig. 5.6b[2]	Fig. 6.4[2]	Fig. 7.4a[1]	Fig. 7.4b[2]	Fig. 8.5[1]	Fig. 8.7[2]	Fig. 9.2a[1]	Fig. 9.2b[1]	Fig. 10.1a[1]	Fig. 10.1b[2]
% predicted favourable zones	49	22	24	20	19	26	26	20	20	25	25
% predicted 'model' deposits	84	74	87	87	91	74	52	79	83	-	-
% predicted 'validation' deposits	-	-	62	62	37	62	62	62	62	68	71

[1]inclusive of hydrothermal alteration evidence; [2]exclusive of hydrothermal alteration evidence.

- On average, about 25% of Benguet province has potential for porphyry copper deposits. On average, the geologically-constrained predictive maps have prediction rates of about 79% for the 'model' deposits. On average, the geologically-constrained predictive maps have prediction rates of about 61% for the 'validation' deposits.
- The usefulness of the remotely-detected hydrothermal alteration evidence is indicated by the geologically-constrained predictive maps inclusive of this spatial evidence (Figure 7.4a, 8.3a, 9.2a, 9.2b and 10.1a), which have more than an 80% prediction rate for the 'model' deposits and about 63% for the 'validation' deposits based on the applications of the theory of evidential belief, the theory of fuzzy sets, logistic regression modeling and the wildcat mapping method. However, based on the application of theory of evidential belief and the wildcat mapping method, the geologically-constrained predictive maps exclusive of the remotely-detected hydrothermal alteration evidence (Figures 7.4b and 10.1b) are superior to the predictive maps inclusive of this spatial evidence.
- In all the geologically-constrained predictive maps, portions of the predicted favourable zones show spatial coincidence with the geochemical anomalies;

these portions of the predicted geologically-favourable zones are probably sources of the geochemical anomalies.

- Among the different methods, the application of weights of evidence modeling and the theory of evidential belief generally produced the geologically-constrained predictive maps with the highest prediction rates for the 'model' deposits. The application of weights of evidence modeling and the theory of evidential belief are therefore optimum for data-driven geologically-constrained predictive mapping of porphyry copper potential in Benguet province. A data-driven method is optimum for geologically-constrained predictive mapping of porphyry copper potential because of the high number (i.e., 23) of known porphyry copper deposits in the province used in the predictive modeling of mineral potential.
- The high prediction rates of 68-71% for the 'validation deposits' of the geologically-constrained predictive maps based on the wildcat method indicate that the wildcat method is useful for geologically-constrained predictive mapping of porphyry copper potential in areas with a similar geological setting to Benguet province but where porphyry copper deposits are unknown.

11.6.2 Epithermal gold potential of Baguio district

Tables 11.11 and 11.12 show the geoinformation characteristics of the different predictive maps, inclusive and exclusive of the remotely-detected hydrothermal alteration evidence, respectively, of epithermal gold potential of Baguio district based on the different methods of predictive mapping of mineral potential.

Table 11.11. Spatial geoinformation characteristics of predictive maps (inclusive of hydrothermal alteration evidence) of epithermal gold potential based on different methods of predictive mapping of mineral potential, Baguio district.

Method	Simple map algebra		Weights of evidence	Evidential belief	Fuzzy sets	Logistic regression		Wildcat mapping
Predictive map	Fig. 5.13a[1]	Fig. 5.14a[2]	-	Fig. 7.10a	Fig. 8.11a	Fig. 9.4a	Fig. 9.4b	Fig. 10.2a
% predicted favourable zones	33	22	-	19	23	20	20	23
% predicted 'model' deposits	79	79	-	68	68	79	73	-
% predicted 'validation' deposits	76	82	-	60	78	76	60	58 (63)[3]
% geochemical anomaly 'predicted'	65	81	-	40	54	57	53	35

[1]geologically-constrained predictive map; [2]integrated geochemical-geological predictive map
[3]values outside parentheses pertain to prediction rate for large-scale gold-deposits; values in parentheses pertain to prediction rate for small-scale gold deposits.

- On average, about 23% of Baguio district has potential for epithermal gold deposits. On average, the geologically-constrained predictive maps have prediction rates of about 72% for the 'model' deposits. On average, the geologically-constrained predictive maps have prediction rates of about 69% for the 'validation' deposits.
- The usefulness of the remotely-detected hydrothermal alteration evidence is indicated by the predictive maps inclusive of this spatial evidence (Figures 5.14a, 7.10a, 8.10a, 9.4a, 9.4b, 10.2a), which have an average prediction rate of about 71% for the 'model' deposits and an average prediction rate of about 67% for the 'validation' deposits based on the application of simple map algebra, the theory of evidential belief, the theory of fuzzy sets, logistic regression modeling and the wildcat mapping method (Table 11.11).
- The predicted favourable zones in most of the geologically-constrained predictive maps spatially coincide with at least 40% of the geochemical anomalies (Tables 11.11 and 11.12). The similar prediction rates of the geologically-constrained predictive maps (Figures 5.13a and 5.13b) with the prediction rates of the integrated geochemical-geological predictive maps (Figures 5.14a and 5.14b) for the 'model' deposits indicate that the geologically-constrained predictive maps are as useful as integrated geochemical-geological predictive maps.

Table 11.12. Spatial geoinformation characteristics of predictive maps (exclusive of hydrothermal alteration evidence) of epithermal gold potential based on different methods of predictive mapping of mineral potential, Baguio district.

Method	Simple map algebra		Weights of evidence		Evidential belief	Fuzzy sets	Logistic regression	Wildcat mapping
Predictive map	Fig. 5.13b[1]	Fig. 5.14b[2]	Fig. 6.9a[3]	Fig. 6.9b[4]	Fig. 7.10c	Fig. 8.13a	-	Fig. 10.2b
% predicted favourable zones	22	20	24	29	18	25	-	25
% predicted 'model' deposits	68	68	74	72	68	68	-	-
% predicted 'validation' deposits	62	79	78	74	56	76	-	58 (68)[5]
% geochemical anomaly 'predicted'	51	75	60	60	42	59	-	43

[1]geologically-constrained predictive map; [2]integrated geochemical-geological predictive map;
[3]based on large-scale gold deposits; [4]based on small-scale gold deposits;
[5]values outside parentheses pertain to prediction rate for large-scale gold-deposits; values in parentheses pertain to prediction rate for small-scale gold deposits.

- Among the different methods, the application of the theory of fuzzy sets produced the geologically-constrained predictive maps with the highest prediction rates for the 'validation' deposits. The application of the theory of fuzzy sets is therefore optimum for a combined data-driven and knowledge-driven geologically-constrained predictive mapping of epithermal gold potential of the district. The application of fuzzy sets is a combined data-driven and knowledge-driven method and is optimum for geologically-constrained predictive mapping of epithermal gold potential because of the marginally-adequate number of deposits (i.e., 19) used in the predictive modeling of mineral potential.
- The high prediction rates of 58-68% for the 'validation deposits' of the geologically-constrained predictive maps based on the wildcat method indicate that the wildcat method is useful for geologically-constrained predictive mapping of epithermal gold potential in areas with similar geological settings to Baguio district province but where epithermal gold deposits are unknown.

11.6.3 Porphyry copper potential of Abra area

Table 11.13 shows the geoinformation characteristics of the different predictive maps of porphyry copper potential of Abra area based on the different methods of predictive mapping of mineral potential.

Table 11.13. Spatial geoinformation characteristics of predictive maps of porphyry copper potential based on different methods of predictive mapping of mineral potential, Abra area.

Method	Simple map algebra		Weights of evidence	Evidential belief		Fuzzy sets		Logistic regression		Wildcat mapping	
Predictive map	Fig. 5.8b[1]	Fig. 5.9b[2]	Fig. 6.14c[1]	Fig. 7.14a[1]	Fig. 7.14b[2]	Fig. 8.18a[2]	Fig. 8.18b[1]	Fig. 9.6a[2]	Fig. 9.6b[1]	Fig. 10.3a[2]	Fig. 10.3b[1]
% predicted favourable zones	25	27	29	20	20	25	23	19	19	19	25
% predicted 'model' deposits	75	75	75	58	58	50	58	67	67	-	-
% predicted 'validation' deposits	61	64	59	62	66	68	65	54	53	58 (35)[3]	58 (61)[3]
% geochemical anomaly 'predicted'	58	-	57	46	-	-	60	-	40	-	61

[1]geologically-constrained predictive map; [2]integrated geochemical-geological predictive map.
[3]Values outside parentheses pertain to prediction rate for known porphyry copper deposits; values in parentheses pertain to prediction rate for known mineralised zones.

- On average, about 23% and 22% of Abra area has potential for porphyry copper deposits based on the geologically-constrained predictive maps and the integrated geochemical-geological predictive maps, respectively. On average, the geologically-constrained predictive maps and the integrated geochemical-geological predictive maps have prediction rates for the 'model' deposits of about 65% and about 57%, respectively. On average, the geologically-constrained predictive maps and the integrated geochemical-geological predictive maps have prediction rates for the 'validation' deposits of about 60% and about 57%, respectively.
- On average, the predicted geologically-favourable zones spatially coincide with about 54% of the geochemical anomalies. This indicates that, together with the higher average prediction rates of the geologically-constrained predictive maps as compared to the average prediction rates of the integrated geochemical-geological predictive maps for the 'model' and the 'validation' deposits, the geologically-constrained predictive maps are generally equal to or superior to the integrated geochemical-geological predictive maps.
- Among the different methods, simple map algebra (i.e., based on the criteria provided by conceptual deposit models) and weights of evidence modeling produced the geologically-constrained predictive maps with the highest prediction rates for the 'model' deposits. Among the different methods, the application of the theory of fuzzy sets produced the geologically-constrained predictive map with the highest prediction rates for the 'validation' deposits. These indicate that a combined data-driven and knowledge-driven method, like simple map algebra and the application of the theory of fuzzy sets, is optimum for geologically-constrained predictive mapping of porphyry copper potential in Abra area. A combined data-driven and knowledge-driven predictive method, rather than only a data-driven method like weights of evidence modeling, is optimum for Abra area because of the low number of known deposits (i.e., 12) used in the predictive modeling of mineral potential.
- The prediction rates of 58-61% for the 'validation' deposits of the geologically-constrained wildcat predictive maps indicates the usefulness of the wildcat predictive method for mapping porphyry copper potential in areas with similar geological settings to Abra area but where porphyry copper deposits are unknown.

11.6.4 Gold-copper vein deposit potential of Catanduanes Island

Table 11.14 shows the geoinformation characteristics of the different predictive maps of gold-copper vein deposit potential of Catanduanes Island based on the different methods of predictive mapping of mineral potential.

- On average, about 22% and 17% of Catanduanes Island has potential for gold-copper vein deposits based on the geologically-constrained predictive maps and the integrated geochemical-geological predictive maps,

respectively. On average, the geologically-constrained predictive maps and the integrated geochemical-geological predictive maps have prediction rates for the 'model' deposits of about 68% and about 66%, respectively.

- On average, the predicted geologically-favourable zones spatially coincide with about 45% of the geochemical anomalies. This indicates that, together with the higher average prediction rates of the geologically-constrained predictive maps as compared to the average prediction rates of the integrated geochemical-geological predictive maps for the 'model' and the 'validation' deposits, the geologically-constrained predictive maps are generally equal to or superior to the integrated geochemical-geological predictive maps.
- Among the different methods, simple map algebra (i.e., based on the criteria provided by conceptual deposit models) and logistic regression modeling produced the geologically-constrained predictive maps with the highest prediction rates for the 'model' deposits. This indicates that a combined data-driven and knowledge-driven method, like the simple map algebra, and a data-driven method, like logistic regression modeling, is optimum for geologically-constrained predictive mapping of gold-copper vein deposit potential in Catanduanes Island. A data-driven or a combined data-driven and knowledge-driven predictive method is optimum for Catanduanes Island because the number of known gold-copper deposits is marginally-adequate (i.e., 17).
- The prediction rate of 59% for the 'validation deposits' of the geologically-constrained predictive map based on the wildcat method indicates that the wildcat method is useful for geologically-constrained predictive mapping of gold-copper vein deposit potential in areas with similar geological settings to Catanduanes Island and where gold-copper vein deposits are unknown.

Table 11.14. Spatial geoinformation characteristics of predictive maps of gold-copper vein deposit potential based on different methods of predictive mapping of mineral potential, Catanduanes Island.

Method	Simple map algebra		Weights of evidence	Evidential belief		Fuzzy sets		Logistic regression		Wildcat mapping	
Predictive map	Fig. 5.16a[1]	Fig. 5.16b[2]	Fig. 6.18[1]	Fig. 7.18a[1]	Fig. 7.18b[2]	Fig. 8.23b[1]	Fig. 8.24b[2]	Fig. 9.8a[1]	Fig. 9.9b[2]	Fig. 10.4a[2]	Fig. 10.4b[1]
% predicted favourable zones	24	15	22	20	20	18	19	20	18	9.5	25
% predicted 'model' ('validation'[3]) deposits	76	52	60	71	76	65	85	71	76	47	59
% geochemical anomaly 'predicted'	49	-	42	37	-	39	-	40	-	-	47

[1]geologically-constrained predictive map; [2]integrated geochemical-geological predictive map.
[3]'validation' deposits apply to wildcat mapping method only as the deposits were not used in the predictive modeling.

11.6.5 Nickeliferous-laterite potential of Isabela area

- The nickeliferous-laterite potential of Isabela area is, for the most part, unknown. Nickeliferous-laterite deposits have been reported in the southern part of the ultramafic terrane but appropriate mineral deposit data are unavailable for predictive modeling and/or validation purposes.
- Attempts have been made to classify the nickeliferous-laterite potential of the area based on criteria provided by conceptual deposit models and by knowledge-driven methods for geologically-constrained predictive mapping of mineral potential such as simple map algebra, the application of the theory of evidential belief, the application of the theory of fuzzy sets and the application of the wildcat method.
- The methods applied indicate that it is mostly the ultramafic terrane that has high potential for nickeliferous-laterite.
- Among the three methods used, simple map algebra (i.e., based on the criteria provided by conceptual nickeliferous-laterite model) indicates that 20% of the ultramafic terrane has high potential for nickeliferous-laterite, 8% of the section with reported nickeliferous-laterite has high potential for this type of deposit. The areas of high potential delineated in the section with reported nickeliferous-laterite coincide with 9% of the area of a catchment basin with >2500 ppm Ni in stream sediments (Table 11.15).
- The application of the theory of fuzzy sets and the evidential belief theory result in predictive maps with the same geoinformation characteristics about the nickeliferous-laterite potential of the ultramafic terrane and the section with reported nickeliferous-laterite (Table 11.15). Both predictive methods indicate that 62% of the ultramafic terrane has high potential for nickeliferous-laterite, 45% of the section with reported nickeliferous-laterite has high potential for this type of deposit. The areas delineated as having high potential in the section with reported nickeliferous-laterite coincide with 67% of the area of a catchment basin with >2500 ppm Ni in stream sediments.
- The application of the wildcat method produced similar results to the application of the theory of evidential belief and the theory of fuzzy sets but with lower estimates of nickeliferous-laterite potential.
- The section with reported nickeliferous-laterite has lower percentage of predicted high potential zones than several other sections in the ultramafic terrane. However, the other sections with higher percentage of predicted high potential are situated in portions of the Isabela area where mineral resources development is prohibited. The prohibition on mineral resources development in certain portions of Isabela area, which was imposed before the predictive classification of nickeliferous-laterite was generated, is not being disputed. Nevertheless, the results demonstrate that mineral potential classification is an important factor in land-use decision-making so that land areas likely to contain mineral deposits are not alienated to mineral resources development.

- In the absence of appropriate validation data, the nickeliferous-laterite potential of Isabela area remains uncertain.

Table 11.15. Spatial geoinformation characteristics of predictive maps of nickeliferous-laterite potential based on different methods of predictive mapping of mineral potential, Isabela area.

Method	Simple map algebra	Evidential belief	Fuzzy sets	Wildcat mapping
Predictive map	Figure 5.18a	Figure 7.20	Figure 8.28	Figure 10.5
% of ultramafic terrane classified as high potential	20	62	62	58
% of section with known nickeliferous-laterite deposits classified as high potential	8	45	45	36
% of catchment basin with >2500 ppm Ni in stream sediments classified as high potential	9	67	67	64

11.6 RECOMMENDATIONS FOR APPLYING GEOLOGICALLY-CONSTRAINED MINERAL POTENTIAL MAPPING ELSEWHERE

Deciding which method or methods to apply to a given geological area depends on how comfortable the users are with the conceptual aspects of each method. In general, a data-driven method such as weights of evidence modeling, the data-driven application of Dempster-Shafer theory of evidential belief and/or logistic regression is possible only when suitable training data are available (i.e., presence of a number of representative deposits of a given type), from which the weighting of the evidential data layers are calculated. However, any data-driven method can benefit from clearly-defined conceptual deposit exploration models in the choice of datasets and extraction of useful spatial evidences for mineral potential prediction. On the other hand, a knowledge-driven method such as simple map algebra, knowledge-driven application of Dempster-Shafer theory of evidential belief, application of the theory of fuzzy sets and or wildcat mapping is appropriate when training data are unavailable and when a conceptual deposit exploration model is clearly-defined. The conceptual deposit exploration model is vital to the assignment of weights to map classes with evidential data layers and to the way the evidential data layers are combined. Although the weighting of evidences in knowledge-driven approaches depends on clearly-defined conceptual deposit exploration models, it is controlled entirely by a mineral deposit expert. When expert opinion is lacking, the essentially knowledge-driven methods of simple map algebra, knowledge-driven application of Dempster-Shafer theory of evidential belief and application of theory of fuzzy sets can be applied when suitable training data are available, from which 'a quantitative expert opinion' of weighting of evidences can be calculated as shown in this thesis.

From the inspection of the performances of the different methods in the different study areas presented in the previous sections, the following empirical guidelines are proposed, yet are open for further testing, in order to answer the fundamental question put forth above in sub-section 11.4.1.

- For areas where systematic and comprehensive geoexploration data are lacking but where known mineral deposits can be represented as points (e.g., porphyry copper, epithermal gold, gold-copper vein deposits) and number at least 20, data-driven methods such as weights of evidence modeling, data-driven application of the theory of evidential belief or logistic regression can be more effective than knowledge-driven methods particularly when expert opinion is lacking.
- For areas where systematic and comprehensive geoexploration data are lacking but where known mineral deposits can be represented as points (e.g., porphyry copper, epithermal gold, gold-copper vein deposits) and number at most 20, knowledge-driven methods such as simple map algebra and the application of the theory of fuzzy sets can be more effective data than data-driven methods.
- For areas where systematic and comprehensive geoexploration data are lacking and where mineral deposits are unknown, knowledge-driven methods such as simple map algebra, the knowledge-driven application theory of evidential belief, the application of the theory of fuzzy sets and wildcat mapping is appropriate.

In the first two cases given above, the distance correlation method, can be applied to quantify spatial associations between known mineral deposits and curvi-linear or point geological features. In addition, remotely-sensed spectral data can be used to extract indications of mineralisation for input into the predictive modeling of mineral potential. In all the different cases given above, appropriate validation data are required to properly evaluate the reliability and usefulness of the geologically-constrained predictive maps of mineral potential. Because it is not always possible to have validation data in situations with relatively small training sets (as in Abra and Catanduanes), mineralisation-related geoinformation (e.g., significant geochemical anomalies, etc.) can be valuable in assessment of reliability of predictive models.

11.7 RECOMMENDATIONS FOR FURTHER RESEARCH

- The methodologies presented here are tested for porphyry copper, epithermal gold vein, gold-copper vein and nickeliferous-laterite mineralisation. There is a need to test further these methodologies on other deposit types; if found unsatisfactory, there is a need to develop new methodologies for these other styles of mineralisation.
- The methodologies presented here are demonstrated for areas with rugged landscape, from which structural geological data can be extracted interpretively and adequately from DEMs to augment available geological

map data. Development of methodologies for geologically-constrained predictive mapping of mineral potential in areas with non-rugged landscape needs investigation.

- The methodologies presented here are demonstrated for areas where the geological evidences of mineralisation are not covered or buried by post-mineralisation geological processes. Development of methodologies for geologically-constrained predictive mapping of mineral potential in such areas is another problem for further research.

References

Abrams, M.J., 2000. The Advanced Spaceborne Thermal Emission and Reflection Radiometer (ASTER): data products for the high resolution imager on NASA's Terra platform. International Journal of Remote Sensing, vol. 21, no. 5, pp. 847-859.

Abrams, M.J., Ashley, R.P., Rowan, L.C., Goetz, A.F.H. and Kahle, A.B., 1977. Mapping of hydrothermal alteration in the Cuprite mining district, Nevada, using aircraft scanner images for spectral region 0.46-2.36 μm. Geology, vol. 5, pp. 713-718.

Abrams, M.J., Brown, D, Lepley, L. and Sadowski, R., 1983. Remote sensing for porphyry copper deposits in southern Arizona. Economic Geology, vol. 78, pp. 591-604.

Adams, J.B. and Adams, J.D., 1984. Geologic mapping using Landsat MSS and TM images: removing vegetation by modelling spectral mixtures. Proceedings of the 3rd International Symposium on Remote Sensing for Exploration Geology, Colorado Springs, Colorado, 16-19 April 1984, pp. 615-622.

Adams, M.L., Philpot, W.D. and Novell, W.A., 1999. Yellowness index: an application of spectral second derivatives to estimate chlorosis of leaves in stressed vegetation. International Journal of Remote Sensing, vol. 20, no. 18, pp. 3663-3675.

Agterberg, F.P., 1974. Automatic contouring of geological maps to detect target areas for mineral exploration. Mathematical Geology, vol. 6, no. 4, p.. 373-395.

Agterberg, F.P., 1988. Application of recent developments of regression analysis in regional mineral resource evaluation. In: C.F. Chung, A.G. Fabbri and R. Sinding-Larsen (Eds.), Quantitative Analysis of Mineral and Energy Resources, D. Reidel Publishing Company, Dordrecht, pp. 1-28.

Agterberg, F.P., 1989. Systematic approach to dealing with uncertainty of geoscience information in mineral exploration. Proceedings of the 21st APCOM Symposium, Las Vegas, March 1989, Chapter 18, pp. 165-178.

Agterberg F.P., 1992a. Combining indicator patterns in weights of evidence modeling for resource evaluation. Nonrenewable Resources, vol. 1, no. 1, pp. 39-50.

Agterberg, F.P., 1992b. Estimating the probability of occurrence of mineral deposits from multiple map patterns. In: D.F. Merriam and H. Kurzl (Eds.), The Use of Microcomputers in Geology, Plenum Press, New York, pp. 73-92.

Agterberg, F.P. and Fabbri, A.G., 1972. Harmonic analysis of copper and gold occurrences in the Abitibi area of the Canadian Shield. Proceedings of the 10th International Symposium on Applications of Computers in the Mineral Industry (APCOM), pp. 193-201.

Agterberg, F.P., Bonham-Carter, G.F. and Wright, D.F., 1990. Statistical pattern integration for mineral exploration. In: Gaál, G. and Merriam, D.F. (Eds.),

Computer Applications in Resource Estimation, Pergamon Press, Oxford, pp. 1-21.

Agterberg, F.P., Bonham-Carter, G.F., Cheng, Q. and Wright, D.F., 1993. Weights of evidence modeling and weighted logistic regression in mineral potential mapping. In: J.C. Davis and U.C. Herzfeld (Eds.), Computers in Geology, Oxford University Press, New York, pp. 13-32.

Akman, A.Ü., Sanga, T., Narui, E. and Oikawa, N., 2001. Development of a new technique for geological investigation using DTM data: an example in western Turkey. International Journal of Remote Sensing, vol. 22, no. 5, pp. 851-859.

Almeida-Filho, R. and Vitorello, I., 1997. Remote sensing and field data integration in the definition of hydrothermally altered areas in vegetated terrain, central Brazil. International Journal of Remote Sensing, vol. 18, no. 8, pp. 1835-1842.

Amos, B.J. and Greenbaum, D., 1989. Alteration detection using TM imagery: the effects of supergene weathering in arid climate. International Journal of Remote Sensing, vol. 10, pp. 515-527.

An, P., Moon, W.M. and Rencz, A., 1991. Application of fuzzy set theory for integration of geological, geophysical and remote sensing data. Canadian Journal of Exploration Geophysics, vol. 27, p. 1-11.

An, P., Moon, W.M. and Bonham-Carter, G.F., 1992. On knowledge-based approach on integrating remote sensing, geophysical and geological information. Proceedings of International Geoscience and Remote Sensing Symposium (IGARSS) 1992, pp. 34-38.

An, P., Moon, W.M. and Bonham-Carter, G.F., 1994a. An object-oriented knowledge representation structure for exploration data integration. Nonrenewable Resources, vol. 3, no. 2, pp. 132-145.

An, P., Moon, W.M. and Bonham-Carter, G.F., 1994b. Uncertainty management in integration of exploration data using the belief function. Nonrenewable Resources, vol. 3, no. 1, pp. 60-71.

Anderson, J.R., Hardy, E.E., Roach, J.T. and Witner, R.E., 1976. A land use and land cover classification system for use with remote sensor data. USGS Professional Paper 964.

Ashley, R.P., 1990a. The Goldfield gold district, Esmeralda and Nye Counties, Nevada. U.S. Geological Survey Bulletin 1857-H, H1-H7.

Ashley, R.P., 1990b. The Tonopah precious metal district, Esmeralda and Nye Counties, Nevada. U.S. Geological Survey Bulletin 1857-H, H8-H13.

Ashley, R.P. and Abrams, M.J., 1980. Alteration mapping using multi-spectral images – Cuprite mining district, Esmeralda County, Nevada. U.S. Geological Survey Open-File Report 80-367, 17 pp.

Ashley, R.P. and Berger, B.R., 1985. Precious Metals in Volcanic Terranes, U.S. Geological Survey, Circular.

Aspinall, P.J. and Hill, A.R., 1983. Clinical inferences and decision – Part I. Diagnosis and Bayes' Theorem. Ophthalmic and Physiological Optics, vol. 3, pp. 295-304.

Aurelio, M.A., 1992. Tectonics of the central segment of the Philippine Fault: structures, kinematics and geodynamic evolution. Ph.D. thesis (2 vols.), Université Pierre et Marie Curie, Paris 500 pp.

Aurelio, M.A., Hauchon, P., Barrier, E. and Gaulon, R., 1994. Displacement rates along the Philippines Fault estimated from slip vectors and regional kinematics. Journal of the Geological Society of the Philippines, vol. 49, no. 2, pp. 65-77.

Aurelio, M.A., Barrier, E., Gaulon, R. and Rangin, C., 1997. Deformation and stress states along the central segment of the Philippines Fault: implications to wrench fault tectonics. Journal of Asian Earth Sciences, vol. 15, nos. 2-3, pp. 107-119.

Bagby, W.C. and Berger, B.R., 1985. Geologic characteristics of sediment-hosted, disseminated precious-metal deposits in the western United States. In: B.R. Berger and P.M. Bethke (Eds.), Geology and Geochemistry of Epithermal Systems. Review in Economic Geology, Vol. 2, Society of Economic Geologists, pp. 169-202.

Balce, G.R., Encina, R.Y., Momongan, A., and Lara, E., 1980. Geology of the Baguio district and its implications on the tectonic development of the Luzon Central Cordillera. Geology and Paleontology of Southeast Asia, vol. 21, pp. 265-287.

Baldwin, J.T., Swain, H.D. and Clark, G.H., 1978. Geology and grade distribution of the Paguna porphyry copper deposit, Territory of Papua and New Guinea. Economic Geology, vol. 73, pp. 690-702.

Baluda, R.P. and Galapon, J.B., 1998. Ore reserve, production history and geologic characteristics of the Sto. Tomas II copper-gold mine, Padcal, Tuba, Benguet, Philippines. Unpublished company report, Philex Mining Corporation, 7 pp.

Bárdossy, G. and Aleva, G.J.J., 1990. Lateritic Bauxites. Elsevier, Amsterdam, 624 pp.

Baret, F., Jacquemoud, S. and Guyot, G., 1992. Modeled analysis of the biophysical nature of spectral shift and comparison with information content of broad bands. Remote Sensing of Environment, vol. 41, pp

Barniak, V.J., Vincent, R.K., Mancuso, J.S. and Ashbaugh, T.J., 1996. Comparison of a gold prospect in Churchill County, Nevada with a known gold deposit in Mineral County, Nevada from laboratory measurements and Landsat TM images. Proceedings of the 11th Thematic Conference on Geologic Remote Sensing, Las Vegas, Nevada, 27-29 February 1996, Environmental Research Institute of Michigan, Ann Arbor, pp. II188-II197.

Barton, P.B., Jr., 1986. User-friendly deposit models. U.S. Geological Survey Circular 980, pp. 94-110.

Bateman, A.M., 1951a. Economic Mineral Deposits. Wiley and Sons, New York, 916 pp.

Bateman, A.M., 1951b. The Formation of Mineral Deposits. Wiley and Sons, New York, 371 pp.

Beane, R.E. and Titley, S.R., 1981. Porphyry copper deposits – Part II: Hydrothermal alteration and mineralization. Economic Geology 75th Anniversary Volume, pp. 235-269.

Bennett, S.A., 1993. Integration of Thematic Mapper data, field mapping and ARCINFO to delineate sediment-hosted disseminated gold projects in the Santa Teresa district, Sonora, Mexico. Proceedings of the 9th Thematic Conference on Geologic Remote Sensing, Pasadena, California, 8-11 February 1993, Environmental Research Institute of Michigan, Ann Arbor, pp. 779-790.

Beratan, K.K., Peer, B., Dunbar, N.W. and Blom, R., 1997. A remote sensing approach to alteration mapping: AVIRIS data and extension-related potassium metasomatism, Socorro, New Mexico. International Journal of Remote Sensing, vol. 18, no. 17, pp. 3595-3609.

Berger, B.R. and Eimon, P.I., 1983. Conceptual models of epithermal precious-metal deposits. In: Shanks III, W.C. (Ed.), Cameron Volume on Unconventional Mineral Deposits, Society of Mining Engineers, pp. 191-205.

Berger, B.R. and Henley, R.W., 1989. Advances in the understanding of epithermal gold-silver deposits – with special reference to deposits of the western United States. In: R. Keays, R. Ramsay and Groves, D. (Eds.), The Geology of Gold Deposits: The Perceptive in 1988. Economic Geology Monograph 6, Economic Geology Publishing Company, New Haven, Connecticut, pp. 405-423.

Berman, M., 1977. Distance distributions associated with Poisson processes of geometric figures. Journal of Applied Probability, vol. 14, pp. 195-199.

Bernardo, J.M. and Smith, A.F.M., 1996. Bayesian Theory. Wiley, Chichester, 586 pp.

Besag, J.E., 1974. Spatial interaction and the statistical analysis of lattice systems. Journal of the Royal Statistical Society, Series B, vol. 36, pp. 192-225.

Bishop, M.M., Feinberg, S.E. and Holland, P.W., 1975. Discrete Multivariate Analysis: Theory and Practice. MIT Press, Cambridge, Massachusetts, 587 pp.

Blackburn, G.A., 1998. Spectral indices for estimating photosynthetic pigments concentrations: a test using senescent tree leaves. International Journal of Remote Sensing, vol. 19, no. 4, pp. 657-675.

Boardman, J.W., 1993. Automating spectral unmixing of AVIRIS data using convex geometry concepts, Summaries of the 4th Annual JPL Airborne Geoscience Workshop, Jet Propulsion Laboratory, Pasadena, California, JPL Publication 93-26, vol. 1, pp. 11-14.

Boardman, J.W. and Kruse, F.A., 1994. Automated spectral analysis; a geological example using AVIRIS data, north Grapevine Mountains, Nevada. Proceedings of the 10th Thematic Conference on Geologic Remote Sensing, Environmental Research Institute of Michigan, Ann Arbor, pp. I-407 - I-418.

Bølviken, B., Honey, F., Levine, S.R., Lyon, R.J.P. and Prelat, A., 1977. Detection of naturally heavy-metal-poisoned areas by Landsat-1 digital data. Journal of Geochemical Exploration, vol. 8, pp. 457-471.

Bonham, H.F., 1986. Models for volcanic-hosted epithermal deposits. In: International Volcanological Congress, Proceedings of Symposium 5: Volcanism, Hydrothermal Systems and Related Mineralisation, Australian Institute of Mining and Metallurgy, University of Auckland, pp. 13-18.

Bonham-Carter, G.F., 1985. Statistical association of gold occurrences with Landsat – derived lineaments, Timmins-Kirkland Lake area, Ontario. Canadian Journal of Remote Sensing, vol. 11, no. 2, pp. 195-211.

Bonham-Carter, G.F., 1988. Numerical procedures and computer programs for fitting an inverted Gaussian model to vegetation reflectance data. Computers and Geosciences, vol. 14, pp. 339-356.

Bonham-Carter, G.F., 1991. Integration of geoscientific data using GIS. In: D.J. Maguire, M.F. Goodchild and D.W. Rhind (Eds.), Geographic Information Systems: Principles and Applications, Longman, London, vol. 2, pp. 171-184.

Bonham-Carter, G.F., 1994. Geographic Information Systems for Geoscientists, Modelling with GIS, Pergamon, Ontario, 398 pp.

Bonham-Carter, G.F., 1997. GIS methods for integrating exploration data sets. In: A.G. Gubins (Ed.), Proceedings of Exploration 97: 4th Decennial International Conference on Mineral Exploration, Toronto, Canada, 14-18 September 1997, pp. 59-64.

Bonham-Carter, G.F. and Agterberg, F.P., 1990. Application of a microcomputer-based geographic information system to mineral potential mapping. In: T. Hanley and D.F. Merriam (Eds.), Microcomputers in Geology, vol. 2, Pergamon Press, Oxford, pp. 49-74.

Bonham-Carter, G.F. and Agterberg, F.P., 1999. Arc-WofE: a GIS tool for statistical integration of mineral exploration datasets. Proceedings of the 52nd Session of the International Statistical Institute (http://www.stat.fi/isi99/proceedings.html), 10-18 August 1999, Helsinki.

Bonham-Carter, G.F. and Chung, C.F., 1983. Integration of mineral resource data for Kasmere Lake area, Northwest Manitoba, with emphasis on uranium. Computers and Geosciences, vol. 15, pp. 25-45.

Bonham-Carter, G.F., Rencz, A.N., and Harris, J.R., 1985. Spatial relationship of gold occurrences with lineaments derived from Landsat and Seasat imagery, Meguma

Group, Nova Scotia. Proceedings of the 4th Thematic Conference on Remote Sensing for Exploration Geology, San Francisco, April 1985, pp. 755-768.

Bonham-Carter, G.F., Agterberg, F.P. and Wright, D.F., 1988. Integration of geological datasets for gold exploration in Nova Scotia. Photogrammetric Engineering and Remote Sensing, vol. 54, no. 11, pp. 1585-1592.

Bonham-Carter, G.F., Agterberg, F.P. and Wright, D.F., 1989. Weights of evidence modelling: a new approach to mapping mineral potential. In F.P. Agterberg and G.F. Bonham-Carter (Eds.), Statistical Applications in the Earth Sciences, Geological Survey of Canada, Paper 89-9, pp. 171-183.

Boochs, F., Kupfer, G., Dockter, K. and Kuhbauch, W., 1990. Shape of the red edge as vitality indicator for plants. International Journal of Remote Sensing, vol. 11, pp. 1741-1753.

Boots, B.N. and Getis, A., 1988. Point Pattern Analysis. Sage University Scientific Geography Series No. 8, Sage Publications, Beverly Hills, 93 pp.

Borengasser, M.X. and Taranik, J.V., 1985. Evaluation of SPOT simulator data for the detection of alteration in Goldfield/Cuprite, Nevada. Photogrammetric Engineering and Remote Sensing, vol. 51, pp. 1109-1114.

Botbol, J.M., 1971. An application of characteristic analysis to mineral exploration. Proceedings of 9th International Symposium on Techniques for Decision-making in the Mineral Industry, Special Volume 12, Canadian Institute of Mining and Metallurgy, Montreal, Canada, pp. 92-99.

Botbol, J.M., Sinding-Larsen, R., McCammon, R.B. and Gott, G.B., 1978. A regionalized multivariate approach to target area selection in geochemical exploration. Economic Geology, vol. 73, pp. 534-546.

Brivio, P.A., Giardino, C. and Zilioli, E., 2001. Determination of chlorophyll concentration changes in Lake Garda using image-based radiative transfer code for Landsat TM images. International Journal of Remote Sensing, vol. 22, nos. 2 & 3, pp. 487-502.

Brooks, R.R., 1972. Geobotany and Biogeochemistry in Mineral Prospecting, Harper and Row, New York, 290 pp.

Bryner, L. 1968. Notes on the geology of the porphyry copper deposits of the Philippines. Mineral Engineering Magazine, Manila, vol. 19, no. 1, pp. 12-23, 56.

Bryner, L., 1969. Ore deposits of the Philippines – an introduction to their geology. Economic Geology, vol. 64, pp. 644-666.

Buchanan, F., 1807. In: A Journey from Madras through the Countries of Mysore, Kanara and Malabar, Volume 2 and 3. East India Co., London, Volume 2: pp. 436-461, 559; Volume 3: pp. 66, 89, 251, 258, 378.

Buckingham, W.F. and Sommer, S.E., 1983. Mineralogical characterization of rock surfaces formed by hydrothermal alteration and weathering – application to remote sensing. Economic Geology, vol. 78, pp. 664-674.

Bureau of Mines, 1976. Geology and mineral resources of Abra province. Report of Investigation No. 85, Bureau of Mines, Manila, April 1976, 14 pp.

Bureau of Mines and Geosciences, 1982. Geology and Mineral Resources of the Philippines, Volume 1 – Geology. BMG, Manila, 406 pp.

Bureau of Mines and Geosciences, 1986. Geology and Mineral Resources of the Philippines, Volume 2 – Mineral Resources. BMG, Manila, 446 pp.

Buschman, C. and Nagel, E., 1993. In vivo spectroscopy and internal optic of leaves as basis for remote sensing of vegetation. International Journal of Remote Sensing, vol. 14, no. 4, pp. 711-722.

Caculitan, P.R., 1987. Geological and mineral verification of the "R" and "MSV" group of claims of AVR Mining Company for lease application located in Ampasungan, Bakun, Benguet. Unpublished report, Mines and Geosciences Bureau, Manila.

Carlisle, D. and Berry, W.L., 1986. Mineral Exploration: Biological Systems and Organic Matter, Prentice Hall, Englewood Cliffs, California, 465 pp.

Campbell, J.B., 1981. Spatial correlation effects upon accuracy of supervised classification of land cover. Photogrammetric Engineering & Remote Sensing, vol. 47, no. 3, pp. 355-363.

Cannon, H.L., 1960. Botanical prospecting for ore deposits. Science, vol. 132, no. 3427, pp. 591-598.

Carranza, E.J.M. and Hale, M., 1997. A catchment basin approach to the analysis of reconnaissance geochemical-geological data from Albay province, Philippines. Journal of Geochemical Exploration, vol. 60, pp. 157-171.

Carranza, E.J.M., Mangaoang, J.C. and Hale, M., 1999a. Application of mineral exploration models and GIS to generate mineral potential maps as input for optimum land-use planning in the Philippines. Natural Resources Research, vol. 8, no. 2, pp. 165-173.

Carranza, E.J.M. and Hale, M., 1999b. Geologically constrained probabilistic mapping of gold potential, Baguio district, Philippines. On-line Proceedings of IV International Conference on GeoComputation, Mary Washington College, Fredericksburg, VA, USA, 25-28 July 1999. Paper No. 13, CD-ROM and Website: http://www.geovista.psu.edu/geocomp/geocomp99/Gc99/013/gc_013.htm.

Carranza, E.J.M. and Hale, M., 1999c. Image processing and GIS for hydrothermal alteration mapping, Baguio district, Philippines. Proceedings of the 1999 IEEE International Geoscience and Remote Sensing Symposium, Hamburg, Germany, 28 June - 2 July 1999. CD-ROM.

Carranza, E.J.M. and Hale, M. 1999d. Porphyry copper deposits and strike-slip faults, Central Cordillera, Philippines. Proceedings of the 5th Biennial SGA Meeting and the 10th Quadrennial IAGOD Meeting, London, UK, 22-25 August 1999, pp. 1307-1310.

Carranza, E.J.M. and Hale, M. 1999e. Spatial relationships of porphyry copper deposits and strike-slip fault discontinuities and plutons, Benguet, Philippines. Proceedings of the 5th Annual Conference of the International Association for Mathematical Geology, Trondheim, Norway, 6-11 August 1999, pp. 157-162.

Carranza, E.J.M. and Hale, M., 2000. Geologically constrained probabilistic mapping of gold potential, Baguio district, Philippines. Natural Resources Research, vol. 9, no. 3, pp. 237-253.

Carranza, E.J.M. and Hale, M., 2001a. Evidential belief functions for geologically-constrained predictive mapping of gold mineralization potential, Baguio district, Philippines. Ore Geology Reviews (in review).

Carranza, E.J.M. and Hale, M., 2001b. Geologically constrained fuzzy mapping of gold mineralization potential, Baguio district, Philippines. Natural Resources Research, vol. 10, no. 2, pp. 125-136.

Carranza, E.J.M. and Hale, M., 2001c. Logistic regression for geologically-constrained mapping of gold mineralization potential, Baguio district, Philippines. Exploration and Mining Geology Journal (in review).

Carranza, E.J.M. and Hale, M., 2001d. Mineral imaging with Landsat TM data for hydrothermal alteration mapping. International Journal of Remote Sensing (in press).

Carranza, E.J.M. and Hale, M., 2001e. Remote detection of mineralization-related vegetation stress using Landsat TM data, Catanduanes Island, Philippines. Remote Sensing of Environment (in review).

Carranza, E.J.M. and Hale, M., 2001f. Remote detection of vegetation stress for mineral exploration. Proceedings of the 1999 IEEE International Geoscience and Remote Sensing Symposium, Sydney, Australia, 9-13 July 2001. CD-ROM.

Carranza, E.J.M. and Hale, M., 2001g. Spatial association of mineral occurrences and curvi-linear geological features. Mathematical Geology (in press).

Carranza, E.J.M. and Hale, M., 2001h. Where are porphyry copper deposits spatially localized? A case study in Benguet province, Philippines, Natural Resources Research (in press).

Carranza, E.J.M. and Hale, M., 2001i. Wildcat mapping of gold potential, Baguio district, Philippines, Transactions of Institution of Mining and Metallurgy, Section B - Applied Earth Science (in review).

Carter, G.A., 1994a. Ratios of leaf reflectance in narrow wavebands as indicators of plant stress. International Journal of Remote Sensing, vol. 15, no. 3, pp. 697-703.

Carter, G.A., 1994b. Early detection of plant stress by digital imaging within narrow stress-sensitive wavebands. Remote Sensing of the Environment, vol. 50, pp. 459-479.

Chang, S.-H., and Collins, W., 1980. Toxic effect of heavy metals on plants. Proceedings of the 6th Annual Pecora Symposium, Sioux Falls, April, pp. 122-124.

Chang, S.-H. and Collins, W., 1983. Confirmation of the airborne biogeophysical mineral exploration technique using laboratory methods. Economic Geology, vol. 78, pp. 723-736.

Chavez, P.S., Jr., 1988. An improved dark-object subtraction technique for atmospheric scattering correction of multispectral data. Remote Sensing of Environment, vol. 24, pp. 459-479.

Chen, Z. and Elvidge, C.D., 1993. Description of derivative-based high spectral-resolution (AVIRIS) green vegetation index. Proceedings of the SPIE Conference on Imaging Spectrometry in terrestrial Environment, vol. 1937, pp. 43-54.

Cheng, Q. and Agterberg, F.P., 1999. Fuzzy weights of evidence and its application in mineral potential mapping. Natural Resources Research, vol. 8, no. 1, pp. 27-35.

Chinn, G.T. and Ascough, G.L., 1997. Mineral potential mapping using an expert system and GIS. In: A.G. Gubins (Ed.), Proceedings of Exploration 97: 4th Decennial International Conference on Mineral Exploration, Toronto, Canada, 14-18 September 1997, pp. 105-114.

Chung, C.F., 1978. Computer program for the logistic model to estimate the probability of occurrence of discrete events. Geological Survey of Canada, Paper 78-11, 23 pp.

Chung, C.F. and Agterberg, F.P., 1980. Regression models for estimating mineral resources from geological map data. Mathematical Geology, vol. 12, no. 5, pp. 472-488.

Chung, C.F. and Agterberg, F.P., 1988. Poisson regression analysis and its application. In: C.F. Chung, A.G. Fabbri and R. Sinding-Larsen (Eds.), Quantitative Analysis of Mineral and Energy Resources, D. Reidel Publishing Company, Dordrecht, pp. 29-36.

Chung, C.F. and Fabbri, A.G., 1993. The representation of geoscience information for data integration. Nonrenewable Resources, vol. 2, no. 2, pp. 122-139.

Chung, C.F. and Moon, W.M., 1991. Combination rules of spatial geoscience data for mineral exploration. Geoinformatics, vol. 2, no. 2, pp. 159-169.

Clark, R.N., Swayze, G.A., Gallagher, A., King, T.V.V. and Calvin, W.M., 1993. The U.S. Geological Survey Digital Spectral Library, Version 1: 0.2 to 3.0 μm, U.S. Geological Survey Open File Report 93-592, 1326 pp.

Clark, R.N., King, T.V.V., Ager, C. and Swayze, G.A., 1995. Initial vegetation species and senescence/stress mapping in the San Luis Valley, Colorado using imaging spectrometer data. In: H.H. Posey, J.A. Pendleton and D. Van Zyl (Eds.), Proceedings of Summitville Forum '95, Colorado Geological Survey Special Publication 38, pp. 64-69.

Clarke, D.S. and Govett, G.J.S., 1990. Southwest Pacific epithermal gold: a rock-geochemistry perspective. In: J.W. Hedenquist, N.C. White and G. Siddeley (Eds.), Epithermal Gold Mineralization of the Circum-Pacific: Geology, Geochemistry, Origin and Exploration. Journal of Geochemical Exploration, vol. 35, pp. 225-240.

Cliff, A. and Ord, J.K., 1981. Spatial Processes; Models and Applications. Pion, London, 266 pp.

Cohen, J., 1960. A coefficient of agreement for nominal scales. Education and Psychological Measurement, vol. 20, pp. 37-45.

Cohen, P.R., 1985. Heuristic Reasoning About Uncertainty: An Artificial Intelligence Approach, Pitman, London, 204 pp.

Collins, A., 1989. Thermal infrared spectra of altered volcanics in the Virginia Range, Nevada. Proceedings of the 7th Thematic Conference on Geologic Remote Sensing, Calgary, Alberta, 2-6 October 1989, Environmental Research Institute of Michigan, Ann Arbor, pp. 1335-1349.

Collins, W., 1978. Remote sensing of crop type and maturity. Photogrammetric Engineering and Remote Sensing, vol. 44, pp. 43-55.

Collins, W.E. and Chang, S.-H., 1990. Commercial spectroscopy with the Geophysical Research Imaging Spectrometer (GERIS). Proceedings of the Technical Symposium on Optical Engineering and Photonics in Aerospace Sensing, Society of Photo-Optical Instrumentation Engineers (SPIE), vol. 1298, pp. 61-72.

Collins, W.E., Chang, S.H. and Kuo, J.T., 1981. Infrared airborne spectroradiometer survey results in the western Nevada area. Columbia University, Aldridge Laboratory of Applied Geophysics, Final Report to NASA, Contract JPL 955832, 61 pp.

Collins, W., Chang, S.-H., Raines, G., Canney, F., and Ashley, R., 1983. Airborne biogeophysical mapping of hidden mineral deposits. Economic Geology, vol. 78. pp. 737-749.

Concepcion, R.A. and Cinco, J.C., Jr., 1989. Geology of the Lepanto Far Southeast gold-rich porphyry copper deposits, Mankayan, Benguet, Philippines. Proceedings of the 28th International Geological Congress, Washington D.C., 9-19 July 1989, pp. 319-320.

Congalton, R.G., 1988. Using spatial autocorrelation analysis to explore the errors in maps generated from remotely sensed data. Photogrammetric Engineering & Remote Sensing, vol. 54, no. 5, pp. 587-592.

Congalton, R.G., 1991. A review of assessing the accuracy of classifications of remotely sensed data. Remote Sensing of Environment, vol. 43, pp. 1671-1678.

Congalton, R.G. and Green, K., 1999. Assessing the Accuracy of Remotely Sensed Data: Principles and Practices. Lewis Publishers, Boca Raton, FL, 137 pp.

Cooke, D.R. and Bloom, M.S., 1990. Epithermal and subjacent porphyry mineralization, Acupan, Baguio district, Philippines: a fluid-inclusion and paragenetic study. Journal of Geochemical Exploration, vol. 35, pp. 341-362.

Cooke, D.R., McPhail, D.C. and Bloom, M.S., 1996. Epithermal gold mineralization, Acupan, Baguio district, Philippines: geology, mineralization, alteration and the thermochemical environment of ore deposition. Economic Geology, vol. 91, pp. 243-272.

Cox, D.P., 1982. A generalized empirical model for porphyry copper deposits. In: R.L. Erickson (Compiler), Characteristics of Mineral Deposit Occurrences, U.S. Geological Survey Open-File Report 82-795, pp. 27-32.

Cox, D.R. and Snell, E.J., 1989. Analysis of Binary Data, 2nd Ed., Chapman and Hall, London, 236 pp.

Cressie, N.A.C., 1993. Statistical for Spatial Data, Wiley, New York, 900 pp.

Crósta, A.P. and Moore, J.M., 1989. Enhancement of Landsat Thematic Mapper imagery for residual soil mapping in SW Minas Gerias State, Brazil: a prospecting case history in Greenstone belt terrain. Proceedings of the Seventh Thematic conference on Remote Sensing for Exploration Geology, Calgary, Alberta, Canada, 2-6 October 1989, pp. 1173-1187.

Crósta, A.P. and Rabelo, A., 1993. Assessing Landsat TM for hydrothermal alteration mapping in central-western Brazil. Proceedings of the Ninth Thematic Conference on Geologic Remote Sensing, Pasadena, California, USA, 8-11 February 1993, pp. 1053-1061.

Crósta, A.P., Sabine, C. and Taranik, J.V., 1996. High-spatial resolution remote sensing for mineral mapping in the Bodie and Paramount mining districts, California. International Archives of Photogrammetry and Remote Sensing, vol. 31, B7, pp. 161-166.

Curico, J.A., 1961. Evaluation of atmospheric aerosol particle size distribution from scattering measurement in the visible and infrared. Journal of the Optical Society of America, vol. 51, pp. 548-551.

Curran, P.J., Dungan, J.L. and Gholz, H.L., 1991. Exploring the relationship between reflectance red edge and chlorophyll content in slash pine. Remote Sensing of Environment, vol. 35, pp. 69-76.

Curran, P.J., Dungan, J.L., Macler, B.A., Plummer, S.E. and Peterson, D.L., 1992. Reflectance spectroscopy of fresh whole leaves for the estimation of chemical concentration. Remote Sensing of Environment, vol. 39, pp. 153-166.

Curtiss, B. and Maecher, A.G., 1991. Changes in forest canopy reflectance associated with chronic exposure to high concentrations of soil trace metals. Proceedings of the 8th Thematic Conference on Geologic Remote Sensing, Denver, Colorado, 29 April – 2 May, 1991, Environmental Research Institute of Michigan, Ann Arbor, pp. 337 –347.

Danson, F.M. and Plummer, S.E., 1995. Red edge response to forest leaf area index. International Journal of Remote Sensing, vol. 16, pp. 183-188.

Darch, J.P. and Barber, J., 1983. Multitemporal remote sensing of geobotanical anomaly. Economic Geology, vol. 78. pp. 770-782.

Datt, B., 1999. Visible/near infrared reflectance and chlorophyll content in Eucalyptus leaves. International Journal of Remote Sensing, vol. 20, no. 14, pp. 2741-2759.

Davis, J.C., 1973. Statistics and Data Analysis in Geology, 2nd Edition. John Wiley and Sons, Singapore, 646 pp.

Dawson, T.P., 2000. the potential for estimating chlorophyll content from a vegetation canopy using the Medium Resolution Imaging Spectrometer (MERIS). International Journal of Remote Sensing, vol. 21, no. 10, pp. 2043-2051.

Dawson, T.P. and Curran, P.J., 1998. A new technique for interpolating the reflectance red edge position. International Journal of Remote Sensing, vol. 19, no. 11, pp. 2133-2139.

Dekker, A.G. and Peters, S.W.M., 1993. The use of Thematic Mapper for the analysis of eutrophic lakes: a case study in the Netherlands. International Journal of Remote Sensing, vol. 14, pp. 799-821.

Demetriades-Shah, T.H., Steven, M.D. and Clark, J.A., 1990. High resolution derivative spectra in remote sensing. Remote Sensing of Environment, vol. 33, pp. 55-64.

Dempster, A.P., 1967. Upper and lower probabilities induced by a multivalued mapping. Annals of Mathematical Statistics, vol. 38, pp. 325-339.

Dempster, A.P., 1968. A generalization of Bayesian inference. Journal of the Royal Statistical Society, series B, vol. 30, pp. 205-247.

D'Ercole, C. and Knox-Robinson, C.M., 1997. Application of a geographic information system for assessing MVT mineralisation potential of the southeastern Lennard Shelf, Western Australia. In: H. Papunen (Ed.), Mineral Deposits: Research and Exploration, Where do they Meet? Proceedings of the 4th Biennial SGA Meeting, Turku, Finland, 11-13 August 1997, pp. 855-857.

Diggle, P.J., 1983. Statistical Analysis of Spatial Point Patterns, Academic Press, London, 148 pp.

Diggle, P.J., Besag, J.E. and Gleaves, 1976. Statistical analysis of spatial point patterns by means of distance methods. Biometrics, vol. 32, pp. 659-667.

Divis, A.F., 1983. The geology and geochemistry of the Philippine porphyry copper deposits. In: D.E. Hayes (Ed.), The Tectonic and Geologic Evolution of Southeast Asian Seas and Islands, Part 2. Geophysical Monograph Series No. 27, pp. 173-216.

Domingo, E.G., 1993. The Philippine mining industry: status and trends in mineral resources development. Journal of Southeast Asian Earth Sciences, vol. 8, pp. 25-36.

Drury, S.A., 1993. Image Interpretation in Geology, 2nd Edn., Chapman & Hall, London, 283 pp.

Duchemin D., Guyon, D. and Lagouarde, J.P., 1999. Potential and limits of NOAA-AVHRR temporal composite data for phenology and water stress monitoring of temperate forest ecosystems. International Journal of Remote Sensing, vol. 20, no. 5, pp. 895-917.

Duda, R.O., Hart, P.E., Nilsson, N.J. and Sutherland, G.L., 1978. Semantic network representations in rule-based interference systems. In: D.A. Waterman and F. Hayes-Roth (Eds.), Pattern-Directed Inference systems, Academic Press, London, pp. 203-221.

Einaudi, M.T., 1982a. Description of skarns associated with porphyry copper plutons. In: S.R. Titley (Ed.), Advances in Geology of the Porphyry Copper Deposits, Southwestern North America, University of Arizona Press, Tucson, pp. 139-184.

Einaudi, M.T., 1982b. General features and origin of skarns associated with porphyry copper plutons. In: S.R. Titley (Ed.), Advances in Geology of the Porphyry Copper Deposits, Southwestern North America, University of Arizona Press, Tucson, pp. 185-209.

Einaudi, M.T. and Burt, D.M., 1982. Introduction, terminology, classification and composition of skarn deposits. Economic Geology, vol. 77, pp. 745-754.

Einaudi, M.T., Meinert, L.D. and Newberry, J.R., 1981. Skarn deposits. Economic Geology 75th Anniversary Volume, pp. 317-391.

Elvidge, C.D., 1982. Effect of vegetation on airborne Thematic Mapper imagery of the Kalamazoo porphyry copper deposit, Arizona, Proceedings of the International Symposium on Remote Sensing of Environment, 2nd Thematic Conference on Remote Sensing for Exploration Geology, vol. 2, pp. 661-667.

Elvidge, C.D., Chen, Z. and Groenveld, D.P., 1993. Detection of trace quantities of green vegetation in 1990 AVIRIS data. Remote Sensing of Environment, vol. 44, pp. 271-279.

Evans, M.E., 1987. An Introduction to Ore Geology. Blackwell Scientific Publications, Oxford, 358 pp.

Evans, M.E., 1993. Ore Geology and Industrial Minerals; An Introduction. Blackwell Scientific Publications, Oxford, 390 pp.

Evans, M.E. (Ed.), 1995. Introduction to Mineral Exploration. Blackwell Scientific Publications, Oxford, 396 pp.

Farrand, W.H., 1997. Identification and mapping of ferric oxide and oxyhydroxide minerals in imaging spectrometer data of Summitville, Colorado, U.S.A., and the surrounding San Juan Mountains. International Journal of Remote Sensing, vol. 18, no. 7, pp. 1543-1552.

Feldman, S. and Taranik, J.V., 1986. Identification of hydrothermal alteration assemblage using airborne imaging spectrometer data. Proceedings of 2nd Airborne Imaging Spectrometer Data Analysis Workshop, 6-8 May 1986, JPL Publication 86-35, Jet Propulsion Laboratory, Pasadena, California, pp. 96-101.

Fernandez, H.E. and Damasco, F.V., 1979. Gold deposition in the Baguio gold district and its relationship to regional geology. Economic Geology, vol. 74, pp. 1852-1868.

Field, C.W., Jones, M.G. and Bruce, W.R., 1974. Porphyry copper-molybdenum deposits of the Pacific northwest. Society of Mining Engineers AIME Transactions, vol. 256, pp. 9-22.

Fitter, A.H. and Hay, R.K.M., 1987. Environmental Physiology of Plants, 2nd Edn. Academic Press, London, 423 pp.

França, H. and Setzer, A.W., 1998. AVHRR temporal analysis of a savanna site in Brazil. International Journal of Remote Sensing, vol. 19, no. 16, pp. 3127-3140.

Fraser, A., Huggins, P., Rees, J. and Cleverly, P., 1997. A satellite remote sensing technique for geological structure horizon mapping. International Journal of Remote Sensing, vol. 18, no. 7, pp. 1607-1615.

Fraser, S.J., 1991. Discrimination and identification of ferric oxides using satellite Thematic Mapper data: a Newman case study. International Journal of Remote Sensing, vol. 12, pp. 635-641.

Fraser, S.J. and Green, A.A., 1987. A software defoliant for geological analysis of band ratios. International Journal of Remote Sensing, vol. 8, no. 3, pp. 525-532.

Freund, R., 1974. Kinematics of transform and transcurrent fault. Tectonophysics, vol. 21, pp. 93-134.

Garcia, J.S. Jr., 1991. Geology and mineralization of the Mankayan mineral district, Benguet, Philippines. Geological Survey of Japan Report, no. 277, pp. 21-30.

Garcia, J.S. Jr., and Bongolan, B.B., 1989. Developments in enargite ore research at Lepanto, Mankayan, Benguet, Philippines. Proceedings of the Symposium on Mineral Resources Development, Philippine Mine Safety Association, Manila, 24-25 November 1989.

Garrett, R.G., Kane, V.E. and Ziegler, R.K., 1980. The management and analysis of geochemical data. Journal of Geochemical Exploration, vol. 13, pp. 115-152.

Gates, D.M., Keegan, H.J., Schleter and Weidner, V.R., 1965. Spectral properties of plants. Applied Optics, vol. 4, no. 1, pp. 11-20.

George, H. and Bonham-Carter, G.F., 1989. Spatial modelling of geological data for gold exploration, Star Lake area, Saskatchewan. In: F.P. Agterberg and G.F. Bonham-Carter (Eds.) Statistical Applications in the Earth Sciences. Geological Survey of Canada, Paper 89-9, pp. 157-169.

Gettings, M.E. and Bultman, M.W., 1993. Quantifying favorableness for occurrence of a mineral deposit type using fuzzy logic – an example from Arizona. U.S. Geological Survey Open-File Report 93-392, 23 pp.

Gitelson, A. and Merzlyak, M.N., 1994. Spectral reflectance changes associated with autumn senescence of Aesculus hippocastanum L. and Acer platanoides L. leaves, spectral features and relation to chlorophyll estimation. Journal or Plant Physiology, vol. 143, pp. 286-292.

Gitelson, A. and Merzlyak, M.N., 1996. Signature analysis of leaf reflectance spectra: algorithm development for remote sensing of chlorophyll. In: H.K. Lichtenhaler (Ed.), Vegetation Stress, Special Edition of Journal of Plant Physiology, vol. 148, nos. 1-5, pp. 494-500.

Gitelson, A. and Merzlyak, M.N., 1997. Remote estimation of chlorophyll content in higher plant leaves. International Journal of Remote Sensing, vol. 18, no. 12, pp. 2691-2697.

Gitelson, A., Merzlyak, M.N. and Lichtenhaler, H.K., 1996. Detection of red edge position and chlorophyll content by reflectance measurements near 700 nm. In: H.K. Lichtenhaler (Ed.), Vegetation Stress, Special Edition of Journal of Plant Physiology, vol. 148, nos. 1-5, pp. 501-508.

Gladwell, D.R., Lett, R.E. and Lawrence, P., 1983. Application of reflectance spectroscopy to mineral exploration. Economic Geology, vol. 78, pp. 699-710.

Goetz, A.F.H. and Srivastava, V., 1985. Mineralogical mapping in the Curpite mining district. Proceedings of the Airborne Imaging Spectrometer (AIS) Data analysis Workshop, 8-12 April 1985, JPL Publication 85-41, Jet Propulsion Laboratory Pasadena, California, pp. 22-29.

Goetz, A.F.H., Rock, B.N. and Rowan, L.C., 1983. Remote sensing for exploration: an overview. Economic Geology, vol. 78, pp. 573-590.

Goetz, A.F.H., Vane, G., Solomon, J.E. and Rock, B.N., 1985. Imaging spectrometry for earth remote sensing. Science, vol. 228, pp. 1147-1153.

Gold, T., and Soter, S., 1985, Fluid ascent through solid lithosphere and its relation to earthquakes: Pure and Applied Geophysics, v. 122, nos. 2-4, pp. 492-530.

Golightly, J.P., 1979. Nickeliferous laterites: a general description. In: D.J.I. Evans, R.S. Shoemaker and H. Veltman (Eds.), International Laterite Symposium. Soc. Min. Engrs., Am. Inst. Min. Met. Petr., Inc., New York, pp. 3-23.

Golightly, J.P., 1981. Nickeliferous laterite deposits. Economic Geology 75th Anniversary Volume, pp. 710-735.

Goodacre, A.K., Bonham-Carter, G.F., Agterberg, F.P. and Wright, D.F., 1993. A statistical analysis of the spatial association of seismicity with drainage patterns and magnetic anomalies in western Quebec. Tectonophysics, vol. 217, pp. 285-305.

Goodman, L.P., 1954. Kolmogorov-Smirnov test for psychological research, Psychological Bulletin, vol. 51, no. 2, pp. 160-168.

Green, A.A., Berkman, M., Switzer, P. and Craig, M.A., 1988. A transformation for ordering multispectral data in terms of image quality with implications for noise removal. IEEE Transactions on Geoscience and Remote Sensing, vol. 26, no. 1, pp. 65-74.

Griffith, D.A., 1988. Advanced Spatial Statistics; Special Topics in the Exploration of Quantitative Spatial Data Series, Kluwer, Dordrecht, 273 pp.

Grimmet, G. and Welsh, D., 1983. Probability: An Introduction. Clarendon, Oxford, 211 pp.

Guilbert, J.M., 1986. Recent advances in porphyry base metal deposit research. In: G.H. Friedrich, A.D. Genkin, A.J. Naldrett, J.D. Ridge, R.H. Sillitoe and F.M. Vokes (Eds.), Geology and Metallogeny of Copper Deposits, Geological Society of Applied Mineral Deposits Special Publication 4, pp. 196-208.

Guilbert, J.M. and Lowell, J.D., 1974. Variations in zoning patterns in porphyry ore deposits. Canadian Institute of Mining and Metallurgy Bulletin, vol. 67, pp. 99-109.

Guyot, G., Baret, F. and Jacquemoud, S., 1992. Imaging spectroscopy for vegetation studies. In: F. Toselli and J. Bodecthel (Eds.), Imaging Spectrometry: Fundamentals and Perspective Applications, Kluwer Academic, Dordrecht, pp. 145-165.

Harris, D.P., 1984. Mineral Resources Appraisal – Mineral Endowment, Resources and Potential Supply: Concept, Methods and Cases, Oxford University Press, New York, 445 pp.

Harris, D.P. and Pan, G.C., 1991. Consistent geological areas for epithermal gold-silver deposits in the Walker Lake quadrangle of Nevada and California delineated by quantitative methods. Economic Geology, vol. 86, pp. 142-165.

Hartigan, J.A., 1983. Bayes Theory. Springer, New York, 145 pp.

Hawking, S.W., 1988. A Brief History of Time: From the Big Bang to Black Holes., Bantam, New York, p. 174.

Hayba, D.O., Bethke, P.M. Heald, P. and Foley, N.K., 1985. Geologic, mineralogic and geochemical characteristics of volcanic-hosted epithermal precious-metal deposits. In: B.R. Berger and P.M. Bethke (Eds.), Geology and Geochemistry of Epithermal Systems. Review in Economic Geology, Vol. 2, Society of Economic Geologists, pp. 129-168.

Heald, P., Foley, N. K. and Hayba, D.O., 1987. Comparative anatomy of volcanic-hosted epithermal deposits: acid-sulfate and adularia-sericite types. Economic Geology, vol. 82, pp. 1-26.

Hedenquist, J.W., 1986. Geothermal systems in the Taupo Volcanic Zone: their characteristics and relation to volcanism and mineralization. In: I.E.M. Smith (Ed.), Late Cenozoic Volcanism in New Zealand, Royal Society of New Zealand Bulletin, vol. 23, pp. 134-168.

Hedenquist, J.W., 1987. Mineralization associated with volcanic-related hydrothermal systems in the circum-Pacific basin. In: M.K. Horn (Ed.), Transactions of the Fourth Circum-Pacific Energy and Mineral Resources Conference, American Association of Petroleum Geologists, Singapore, pp. 513-524.

Hedenquist, J.W., Arribas, A.A., Jr., and Reynolds, J.T., 1998. Evolution of an intrusion-centered hydrothermal system: Far Southeast-Lepanto porphyry and epithermal Cu-Au deposits, Philippines. Economic Geology, vol. 93, no. 4, pp. 373-404.

Henley, R.W., 1990. Epithermal gold deposits in volcanic terranes. In: R.P. Foster (Ed.), Gold Metallogeny and Exploration, Blackie, Glasgow, p. 133-164.

Hewson, R.D., Cudahy, T.J. and Huntington, J.F., 2001. Geologic and alteration mapping at Mt. Fitton, South Australia, using ASTER satellite-borne data. Proceedings of the 1999 IEEE International Geoscience and Remote Sensing Symposium, Sydney, Australia, 9-13 July 2001. CD-ROM.

Hodcroft, A.J.T. and Moore, J. McM., 1988. Remote sensing of vegetation – a promising exploration tool. Mining Magazine, October 1988, pp 274-279.

Hollister, V.F., 1974. Regional characteristics of porphyry copper deposits of South America, Society of Mining Engineers AIME Transactions, vol. 255, pp. 45-53.

Hollister, V.F., 1975. An appraisal of the nature of some porphyry copper deposits. Mineralogical and Science Engineering, vol. 7, pp. 225-233.

Hollister, V.F., 1978. Geology of the Porphyry Copper Deposits of the Western Hemisphere. Society of Mining Engineers AIME, New York, 219 pp.

Horler, D.N.H., Barber, J. and Barringer, A.R., 1980. Effects of heavy metals on the absorbance and reflectance spectra of plants. International Journal of Remote Sensing, vol. 1, no. 2, pp. 121-136.

Horler, D.N.H., Dockray, M. and Barber, J., 1983. The red edge of plant leaf reflectance. International Journal of Remote Sensing, vol. 4, pp. 273-288.

Horton, D.J., 1978. Porphyry-type copper-molybdenum mineralization belts in eastern Queensland, Australia. Economic Geology, vol. 73, pp. 904-921.

Howarth, R.J. (Ed.), 1983. Statistics and Data Analysis in Geochemical Prospecting. Handbook of Exploration Geochemistry, Volume 2, Elsevier, Amsterdam, 230 pp.

Huckberby, J.A., Magee, R., Moore, J.M. and Coates, P., 1986. Thematic Mapper applied to alteration zone mapping for gold exploration in southeast Spain. Proceedings of the 5th Thematic Conference on Remote Sensing for Exploration Geology, Reno Nevada, pp. 597-599.

Huete, A.R., 1988. A soil adjusted vegetation index (SAVI). Remote Sensing of Environment, vol. 25, pp. 259-309.

Hunt, G.R., 1979. Near-infrared (1.3-2.4 μm) spectra of alteration minerals – potential for use in remote sensing. Geophysics, vol. 44, pp. 1974-1986.

Hunt, G.R. and Ashley, R.P., 1979. Spectra of altered rocks in the visible and near infrared. Economic Geology, vol. 74, pp. 1613-1629.

Huntington, J.F., 1998. Space dependent technologies – remote sensing in mineral exploration. Online Proceedings: Technology – Australia's Future: New technology for Traditional Industries, November 1998, The Australian Academy for Technological Sciences and Engineering (http://www.atse.org.au/publications/symposia/proc-1998p6.htm).

Huntington, J.F. and Green, A.A., 1978. Relationship between lineaments and mineral deposits (abstract). Proceedings of International Association for the Genesis of Ore Deposits Symposium, 1978, Snowbird, Utah.

Hutchison, C.S., 1983. Economic Deposits and their Tectonic Setting, MacMillan, London, 315 pp.

JICA, 1980. Report on the Geological Survey of Northwestern Luzon, Phase II. Unpublished report, Japan International Cooperating Agency, Tokyo.

JICA-MMAJ, 1987. Report on the Mineral Exploration: Mineral Deposits and Tectonics of Two Contrasting Geologic Environments in the Republic of the Philippines, Phase II (Part 1), Northern Sierra Madre. Unpublished report, Japan International Cooperating Agency and Metal Mining Agency of Japan, Tokyo, 403 pp.

JICA-MMAJ, 1994. Report on the Mineral Exploration in the Catanduanes Area, Phase I. Unpublished report, Japan International Cooperating Agency and Metal Mining agency of Japan, Tokyo.

JICA-MMAJ, 1996. Report on the Mineral Exploration in the Catanduanes Area, Phase III. Unpublished report, Japan International Cooperating Agency and Metal Mining agency of Japan, Tokyo.

John, D.A. and Leventhal, J.S., 1995. Bioavailability of metals. In: E.A. du Bray (Ed.), Preliminary Compilation of Descriptive Geoenvironmental Mineral Deposit Models, U.S. Geological Survey Open-File Report 95-831, pp. 10-18.

John, D.A., Nash, J.T., Clark, C.W. and Wulftange, W.H., 1991. Geology, hydrothermal alteration and mineralization at the Paradise Peak gold-silver-mercury deposit, Nye County, Nevada. Symposium Proceedings: Geology and Ore Deposits of the Great Basin, Geological Survey of Nevada, 1-5 April 1990, vol. 2, pp. 1020-1050.

Johnson, D.J., 1992. Dynamics of magma storage in the summit reservoir of Kilauea Volcano, Hawaii, Journal of Geophysical Research, vol. 97, pp. 1807-1820.

Johnson, R.A. and Wichern, D.W., 1998. Applied Multivariate Statistical Analysis, 4th Edn. Prentice-Hall, Upper Saddle River, 816 pp.

Journel, A.G. and Huijbregts, C.J., 1978. Mining Geostatistics, Academic Press, London, 600 pp.

Kahle, A.B., Palluconi, F.D., Hook, S.J., Realmuto, V.J. and Bothwell, G., 1991. The Advanced Spaceborne Thermal Emission and Reflectance Radiometer (ASTER). International Journal of Imaging Systems and Technology, vol. 3, pp. 144-156.

Karig, S.E., 1983, Accreted terranes in the northern part of the Philippine archipelago: Tectonics, v. 2, no. 2, pp. 211-236.

Karr, A.F., 1993. Probability. Springer, New York, 282 pp.

Kasischke, E.S. and French, N.H.F., 1997. Constraints on using AVHRR composite index imagery to study patterns of vegetation cover in boreal forests. International Journal of Remote Sensing, vol. 18, no. 11, pp. 2403-2426.

Katz, S.S., 1991. Emulating the Prospector expert system with a raster GIS. Computers and Geosciences, vol. 17, no. 7, pp. 1033-1050.

Kauth, R.J. and Thomas, G.S., 1976. The tasselled cap – a graphic description of the spectral-temporal development of agricultural crops as seen by Landsat. Proceedings, Symposium of Machine Processing of Remotely Sensed Data, Purdue University, West Lafayette, pp. 41-51.

Kearey, P. and Brooks, M., 1984. An Introduction to Geophysical Prospecting, 2nd Edn., Blackwell Scientific Publications, Oxford, 254 pp.

Kendall, M.G. and Buckland, W.R., 1982. A Dictionary of Statistical Terms, 4th Ed. Longmans, London, 213 pp.

Kepper, J.C., Lugaski, T.P. and MacDonald, J.S., 1986. Discrimination of lithologic units, alteration patterns and major structural block in Tonopah, Nevada area using Thematic Mapper data. Proceedings of the 5th Thematic conference on Geologic Remote Sensing, Reno Nevada, 29 September – 2 October 1986, Environmental Research Institute of Michigan, Ann Arbor, pp. 349-359.

Kierein-Young, K.S., 1997. The integration of optical and radar data to characterize mineralogy and morphology of surfaces in Death Valley, California, U.S.A. International Journal of Remote Sensing, vol. 18, no. 7, pp. 1517-1541.

Kierein-Young, K.S. and Kruse, F.A., 1989. Proceedings of the International Geoscience and Remote Sensing Symposium (IGARSS) '89, 12th Canadian Symposium on Remote Sensing, vol. 2, pp. 961-964.

Kim, H. and Swain, P.H., 1989. Multisource data analysis in remote sensing and geographic information systems based on Shafer's theory of evidence. Proceedings of 1989 International Geoscience and Remote Sensing Symposium (IGARSS), pp. 829-832.

Knipling, E.B., 1970. Physical and physiological basis for the reflectance of visible and near-infrared radiation from vegetation. Remote Sensing of Environment, vol. 1, pp. 155-159.

Knox-Robinson, C.M., 2000. Vectorial fuzzy logic: a novel technique for enhanced mineral prospectivity mapping with reference to the orogenic gold mineralisation potential of the Kalgoorlie Terrane, Western Australia. Australian Journal of Earth Sciences, vol. 47, no. 5, pp. 929-942.

Koch, G.S., Jr., and Link, R.F., 1970. Statistical Analysis of Geological Data, John Wiley and Sons, Inc., New York, 375 pp.

Krohn, M.D., Milton, N.M. and Segal, D., 1981. Discrimination of a chestnut forest unit for geologic mapping by means of a principal component enhancement of Landsat multispectral scanner data. Geophysical Research Letters, vol. 8, pp. 151-154.

Kruse, F.A., 1988. Use of airborne imaging spectrometer data to map minerals associated with hydrothermally altered rocks in Northern Grapevine Mountains, Nevada and California. Remote Sensing of Environment, vol. 24, pp. 31-51.

Kruse, F.A. and Hauff, P.L., 1989. Identification of illite polytype zoning in disseminated gold deposits using reflectance spectroscopy and X-ray diffraction – potential for mapping with imaging spectrometers. Proceedings of the International Geoscience and Remote Sensing Symposium (IGARSS) '89, 12th Canadian Symposium on Remote Sensing, vol. 2, pp. 965-968.

Kruse, F.A. and Taranik, D.L., 1989. Mapping hydrothermally altered rocks with the Airborne Imaging Spectrometer (AIS) and the Airborne Visible/Infrared Imaging Spectrometer (AVIRIS). Proceedings of the International Geoscience and Remote

Sensing Symposium (IGARSS) '89, 12th Canadian Symposium on Remote Sensing, vol. 2, pp. 952-956.

Kruse, F.A., Kierein-Young, K.S. and Boardman, J.W., 1990. Mineral mapping at Cuprite, Nevada with a 63-channel imaging spectrometer. Photogrammetric Engineering and Remote Sensing, vol. 56, pp. 83-92.

Lahren, M.M., Schweickert, R.A. and Taranik, J.V., 1988. Analysis of the northern Sierra accreted terrain, California, with airborne thermal infrared multispectral scanner data. Geology, vol. 16, pp. 525-528.

Landis, J. and Koch, G., 1977. The measurement of observer agreement for categorical data. Biometrics, vol. 33, pp. 159-174.

Laznicka, P., 1976. Porphyry copper and molybdenum deposits of the USSR and their plate tectonic settings. American Institute of Mining, Metallurgical and Petroleum Engineers Transactions, vol. 82, pp. B14-b32.

Learned, R.E. and Boissen, R., 1973. Gold – a useful pathfinder in the search for porphyry copper deposits in Puerto Rico. In: M.J. Jones (Ed.) Geochemical Exploration 1972, Proceedings of the 4th International Geochemical Exploration Symposium, London, 17-20 April 1972. The Institute of Mining and Metallurgy, London, pp. 93-103.

Lee, K., 1985. Interactive digital image analysis of Landsat image for mapping hydrothermal limonite. Proceedings of the International Symposium on Remote Sensing of Environment, 4th Thematic Conference on Remote Sensing for Exploration Geology, Environmental Research Institute of Michigan, Ann Arbor, pp. 293-307.

Lee, K. and Raines, G.L., 1984. Reflectance spectra of some alteration minerals – a chart compiled from published data 04-2.5 μm. U.S. Geological Survey Open-File Report 84-96, 6 pp., 1 chart.

Lee, P.M., 1997. Bayesian Statistics: An Introduction, 2nd Ed., Arnold, London, 344 pp,

Lee, T., Richards, J.A. and Swain, P.H., 1987. Probabilistic and evidential approaches for multisource data analysis. IEEE Transactions on Geoscience and Remote Sensing, vol. GE-25, no. 3, pp. 283-293.

Lehmann, F., Rothfuss, H. and Werner, K., 1991. Imaging spectroscopy data used for geological and environmental analysis in Europe. Proceedings of the Third Airborne Visible/Infrared Imaging Spectrometer (AVIRIS) Workshop, JPL Publication 91-28, pp. 62-71.

Le Pichon, X., Francheteau, J. and Bonnin, J., 1973. Plate Tectonics. Developments in Geotectonics 6, Elsevier, Amsterdam, 300 pp.

Lepp, N.W. (Ed.), 1981. Effect of Heavy Metal Pollution on Plants, Volume 1: Effects of Trace Metals on Plant Function. Applied Science Publishers, London, U.K., 352 pp.

Leprieur, C.E., 1989. Red edge measurements and canopy structure: a first look with AVIRIS data. Proceedings of the International Geoscience and Remote Sensing Symposium (IGARSS) '89, 12th Canadian Symposium on Remote Sensing, 10-14 July 1989, Vancouver, Canada, pp. 2093-2096.

Levinson, A.A., 1974. Introduction to Exploration Geochemistry. Applied Publishing Ltd., Calgary, 612 pp.

Lewis, P., 1997. A review of GIS techniques for handling geoscience data within Australian Geological Surveys. In: A.G. Gubins (Ed.), Proceedings of Exploration 97: 4th Decennial International Conference on Mineral Exploration, Toronto, Canada, 14-18 September 1997, pp. 81-86.

Lichtenhaler, H.K., Gitelson, A. and Lang, M., 1996. Non-destructive determination of chlorophyll content of leaves of a green and an aurea mutant of tobacco by reflectance measurements. In: H.K. Lichtenhaler (Ed.), Vegetation Stress, Special Edition of Journal of Plant Physiology, vol. 148, nos. 1-5, pp. 483-493.

Lindgren, W., 1922. A suggestion for the terminology of certain mineral deposits. Economic Geology, vol. 17, pp. 202-294.

Lindgren, W., 1933. Mineral Deposits, 4th Ed., McGraw-Hill, New York, 930 pp.

Livingston, C.W., 1939. Mechanics of vein formation in the northern half of Baguio district. Engineering and Mining Journal, vol. 140, no. 9, Sept. 1939, pp. 38-51.

Loughlin, W.P., 1991. Principal components analysis for alteration mapping. Photogrammetric Engineering and Remote Sensing, vol. 57, no. 9, pp. 1163-1169.

Lowell, J.D., 1974. Regional characteristics of porphyry copper deposits of the Southwest. Economic Geology, vol. 69, pp. 601-617.

Lowell, J.D., 1991. The discovery of the La Escondida Orebody. In: R.W. Hutchinson and R.I. Grauch (Eds.), Historical Perspectives of Genetic concepts and Case Histories of Famous Discoveries, Economic Geology Monograph 8, Economic Geology Publishing Company, pp. 300-313.

Lowell, J.D. and Guilbert, J.M., 1970. Lateral and vertical alteration-mineralization zoning in porphyry ore deposits. Economic Geology, vol. 65, pp. 373-408.

Lundén, B., Wang, G. and Wester, K., 2001. A GIS based analysis of data from Landsat TM, airborne geophysical measurements, and digital maps for geological remote sensing in the Stockholm region, Sweden. International Journal of Remote Sensing, vol. 22, no. 4, pp. 517-532.

Luo, J., 1990. Statistical mineral prediction without defining a training area. Mathematical Geology, vol. 22, no. 3, pp. 253-260.

Lusted, L.B., 1968. Introduction to Medical Decision Making, Charles Thomas, Springfield, 271 pp.

Lyday, T.Q., The mineral industry of the Philippines – 1998. U.S. Geological Survey Minerals Information, http://minerals.usgs.gov/minerals/pubs/country/9326096.pdf.

Magee, R.W., Moore, J.M. and Brunner, S., 1986. Thematic Mapper data applied to mapping hydrothermal alteration in southwest Mexico. Proceedings of the 5th Thematic conference on Remote Sensing for Exploration Geology, Reno, Nevada, pp. 373-382.

Major, D.J., Baret, F. and Guyot, G., 1990. A ratio vegetation index adjusted for soil brightness. International Journal of Remote Sensing, vol. 11, pp. 727-740.

Mandl, G., 1988. Mechanics of Tectonic Faulting. Elsevier, Amsterdam, 407 pp.

Mangaoang, J.C., 1997. GIS for management and development of mineral resources, Isabela province, Philippines. Masters Thesis. International Institute for Aerospace Survey and Earth Sciences, Delft, The Netherlands, 86 pp.

Marsh, S.E. and McKeon, J.B., 1983. Integrated analysis of high-resolution field and airborne spectroradiometer data for alteration mapping. Economic Geology, vol. 78, pp. 618-632.

Mason, G.T., Jr., and Arndt, R.E., 1996, Mineral Resources Data System, U.S. Geological Survey Digital Data Series DDS-20, Release 1. [Published on CD-ROM.].

Matheron, G., 1963. Principles of geostatistics. Economic Geology, vol. 58, pp. 1246-1266.

Matsuoka, E.J., Labovitz, M.L., Bell, R., Nelson, P.W. Broderick, P.W. and Ludwig, R.W., 1982. The application of remote sensing in geobotanical exploration for metal sulfides. Proceedings of the International Symposium on Remote Sensing of Environment, 2nd Thematic Conference on Remote Sensing for Exploration Geology, vol. 2, pp. 669-677.

Mazzarini, F., Pareschi, M.T., Sbrana, A., Favalli, M. and Fulignati, P., 2001. Surface hydrothermal alteration mapping at Vulcano Island using MIVIS data. International Journal of Remote Sensing, vol. 22, no. 11, pp. 2045-2070.

McCammon, R.B., 1989a. Prospector II – The redesign of Prospector. Proceedings of AI Systems in Government, March 27-31, 1989, Washington, D.C., pp. 88-92.

McCammon, R.B., 1989b. Prospector III – Towards a map-based expert system for regional mineral resource assessment. In: In F.P. Agterberg and G.F. Bonham-Carter (Eds.), Statistical Applications in the Earth Sciences, Geological Survey of Canada, Paper 89-9, pp. 395-404.

McCammon, R.B. and Briskey, J.A. Jr., 1992. A proposed national mineral-resource assessment. Nonrenewable Resources, vol. 1, no. 4, pp. 259-266.

McCammon, R.B., Botbol, J.M., Sinding-Larsen, R. and Bowen, R.W., 1983a. Characteristics analysis – 1981: final program and a possible discovery. Mathematical Geology, vol. 15, pp. 59-83.

McCammon, R.B., Botbol, J.M., McCarthy, J.H., Jr., and Gott, G.H., 1983b. Characteristic analysis applied to multiple geochemical anomalies over a concealed porphyry copper prospect, Rowe Canyon, Nevada. AIME Transactions, vol. 272, pp. 1998-2002.

McCammon, R.B., Botbol, J.M., Sinding-Larsen, R. and Bowen, R.W., 1984. The new CHARaracteristic Analysis (NCHARAN) program: U.S. Geological Survey Bulletin 1621, 27 pp.

McColl, J.H., 1995. Probability. Arnold, London, 182 pp.

McFarlane, M.J., 1976. Laterite and Landscape. Academic Press, London, 151 pp.

McKinney, J. and Rogers, R., 1992. Metal bioavailability. Environmental Science and Technology, vol. 26, pp. 1298-1299.

McLaren, G.P., 1992. Classifying mineral potential in support of land-use policy decisions in British Columbia, Canada. Nonrenewable Resources, vol. 1 no. 1, pp. 85-96.

McMillan, W.J. and Panteleyev, A., 1980. Ore deposit models. 1. Porphyry copper deposits. Geoscience Canada, vol. 7, pp. 52-63.

McMillan, W.J. and Panteleyev, A., 1988. Porphyry copper deposits. In: R.G. Roberts and P.A. Sheahan (Eds.), Geoscience Canada, Reprint Series 3, pp. 45-58.

Menard, S., 1995. Applied logistic regression analysis. Thousand Oaks, CA: Sage Publications. Series: Quantitative Applications in the Social Sciences, No. 106, 98 pp.

Mendoza, C.V. and Viaga, R.G., 1993. Initial report on the detailed geological survey of Palansa Cu-Au prospect. Unpublished report, Mines and Geosciences Bureau, Baguio.

Miller, J.R., Hare, E.W., and Wu, J., 1990. Quantitative characterisation of the vegetation red edge reflectance I. An inverted-Gaussian reflectance model. International Journal of Remote Sensing, vol. 11, pp. 1755-1773.

Milton, N.M., 1983. Use of reflectance spectra of native plant species for interpreting airborne multispectral data in the East Tintic Mountains, Utah. Economic Geology, vol. 78, pp. 761-769.

Milton, N.M. and Mouat, D.A., 1984. Spatial and spectral resolution in geobotany. Proceedings of the International Symposium of Remote Sensing of Environment, 3rd Thematic Conference on Remote Sensing for Exploration Geology, 16-19 April 1984, Colorado Springs, Colorado, pp. 173-182.

Milton, N.M. and Mouat, D.A., 1989. Remote sensing of vegetation responses to natural and cultural environmental conditions. Photogrammetric Engineering and Remote Sensing, vol. 55, no. 8, pp. 1167-1173.

Milton, N.M., Collins, W., Chang, S.-H. and Schimdt, R.G., 1983. Remote detection of metal anomalies on Plot Mountain, Randolph County, North Carolina. Economic Geology, vol. 78, pp. 605-617.

Miranda, F.E. and Vargas, B.S., 1967. Geology and mineral resources of Catanduanes province. Philippine Bureau of Mines, Report of Investigation No. 62.

Mitchell, A.H.G. and Balce, G.R., 1990. Geological features of some epithermal gold systems, Philippines. In: J.W. Hedenquist, N.C. White and G. Siddeley (Eds.), Epithermal Gold Mineralization of the Circum-Pacific: Geology, Geochemistry, Origin and Exploration. Journal of Geochemical Exploration, vol. 35, pp. 241-296.

Mitchell, A.H.G. and Garson, M.S., 1981. Mineral Deposits and Global Tectonic Settings. Academic Press, London, 405 pp.

Mitchell, A.H.G., Hernandez, F. and de la Cruz, A.P., 1986. Cenozoic evolution of the Philippine archipelago. Journal of Southeast Asian Earth Sciences, vol. 1, no. 1, pp. 3-22.

Mitchell, A.H.G. and Leach, T.M., 1991. Epithermal Gold in the Philippines: Island Arc Metallogenesis, Geothermal Systems and Geology. Academic Press Ltd., London, 457 pp.

MMAJ, 1996. Gold and copper deposits of the Southwestern Pacific. Metal Mining Agency of Japan (MMAJ), Tokyo, 11 pp.

MMAJ-JICA, 1977. Report on the Geological Survey of Northeastern Luzon, Phase III. Metal Mining Agency of Japan (MMAJ) and Japan International Cooperating Agency, Tokyo, 280 pp.

Moon, C.J., 1999. Towards a quantitative model of downstream dilution of point source geochemical anomalies. Journal of Geochemical Exploration, vol. 65, pp. 111-132.

Moon, W.M., 1989. Integration of remote sensing and geological/geophysical data using Dempster-Shafer approach. Proceedings of International Geoscience and Remote Sensing Symposium (IGARSS) 1989, pp. 838-841.

Moon, W.M., 1990. Integration of geophysical and geological data using evidential belief function. IEEE Transactions on Geoscience and Remote Sensing, vol. 28, no. 4, pp. 711-720.

Moon, W.M., Chung, C.F. and An, P., 1991. Representation and integration of geological, geophysical and remote sensing data. Geoinformatics, vol. 2, no. 2, pp. 177-188.

Mouat, D.A., 1982. The response of vegetation to geochemical conditions. Proceedings of the International Symposium on Remote Sensing for Exploration Geology, Fort Worth, Texas, 6-10 December 1982, pp. 75-84.

Mouat, D.A., Myers, J.S. and Miller, N.L., 1986. An integrated approach to the use of Landsat TM data for gold exploration in west central Nevada. Proceedings of the 5th Thematic Conference on Geologic Remote Sensing, Reno, Nevada, 28 September – 2 October 1986, Environmental Research Institute of Michigan, Ann Arbor, pp. 615-626.

Nahon, D. and Tardy, Y., 1992. The ferruginous laterites. In: C.R.M. Butt and H. Zeegers (Eds.), Regolith Exploration Geochemistry in Tropical and Subtropical Terrains, Handbook of Exploration Geochemistry Volume 4, Elsevier, Amsterdam, pp. 41-55.

NAMRIA, 1989. Forest resources condition map of Benguet province, Cordillera administrative region. National Mapping and Resource Information Authority (NAMRIA), Philippines.

NAMRIA, 1990a. Atok 1:50,000 scale topographic map sheet 7176-III. National Mapping and Resource Information Authority, Philippines. Reprinted Dec. 1990.

NAMRIA, 1990b. Bagamanoc 1:50,000 scale topographic map sheet 3861-I. National Mapping and Resource Information Authority, Philippines. Reprinted July 1990.

NAMRIA, 1990c. Baguio City 1:50,000 scale topographic map sheet 7175-IV. National Mapping and Resource Information Authority, Philippines. Reprinted Dec. 1990.

NAMRIA, 1990d. Binalonan 1:50,000 scale topographic map sheet 7175-III. National Mapping and Resource Information Authority, Philippines. Reprinted Dec. 1990.

NAMRIA, 1990e. Calolbon 1:50,000 scale topographic map sheet 3860-IV. National Mapping and Resource Information Authority, Philippines. Reprinted July 1990.

NAMRIA, 1990f. Caramoran 1:50,000 scale topographic map sheet 3861-IV. National Mapping and Resource Information Authority, Philippines. Reprinted July 1990.

NAMRIA, 1990g. Cervantes 1:50,000 scale topographic map sheet 7176-IV. National Mapping and Resource Information Authority, Philippines. Reprinted Dec. 1990.

NAMRIA, 1990h. Gigmoto 1:50,000 scale topographic map sheet 3861-II. National Mapping and Resource Information Authority, Philippines. Reprinted July 1990.

NAMRIA, 1990i. Hitoma 1:50,000 scale topographic map sheet 3861-III. National Mapping and Resource Information Authority, Philippines. Reprinted July 1990.

NAMRIA, 1990j. Kabayan 1:50,000 scale topographic map sheet 7176-II. National Mapping and Resource Information Authority, Philippines. Reprinted Dec. 1990.

NAMRIA, 1990k. Kayapa 1:50,000 scale topographic map sheet 7175-I. National Mapping and Resource Information Authority, Philippines. Reprinted Dec. 1990.

NAMRIA, 1990l. Licuan 1:50,000 scale topographic map sheet 7178-II. National Mapping and Resource Information Authority, Philippines. Reprinted Dec. 1990.

NAMRIA, 1990m. Mankayan 1:50,000 scale topographic map sheet 7176-I. National Mapping and Resource Information Authority, Philippines. Reprinted Dec. 1990.

NAMRIA, 1990n. Nagumbuaya Point 1:50,000 scale topographic map sheet 3860-I. National Mapping and Resource Information Authority, Philippines. Reprinted July 1990.

NAMRIA, 1990o. Pandan 1:50,000 scale topographic map sheet 3862-III. National Mapping and Resource Information Authority, Philippines. Reprinted July 1990.

NAMRIA, 1990p. Salegseg 1:50,000 scale topographic map sheet 7278-I. National Mapping and Resource Information Authority, Philippines. Reprinted Dec. 1990.

NAMRIA, 1990q. Sal-Lapadan 1:50,000 scale topographic map sheet 7177-I. National Mapping and Resource Information Authority, Philippines. Reprinted Dec. 1990.

NAMRIA, 1990r. San Nicolas 1:50,000 scale topographic map sheet 7175-II. National Mapping and Resource Information Authority, Philippines. Reprinted Dec. 1990.

NAMRIA, 1992a. Ilagan 1:200,000 scale topographic map sheet S-2506. National Mapping and Resource Information Authority, Philippines.

NAMRIA, 1992b. Solano 1:200,000 scale topographic map sheet S-2508. National Mapping and Resource Information Authority, Philippines.

Nash, G.D. and Hernandez, M.W., 2001. Cost-effective vegetation anomaly mapping for geothermal exploration. Proceedings of the 26th Workshop on Geothermal Reservoir Engineering, 29-30 January 2001, Stanford University, Stanford, California.

Nash, G. and McCoy, R., 1993. The use of high resolution spectroscopy in the determination of geobotanical anomalies associated with gold placers, La Sal Mountains area, Utah. Proceedings of the 9th Thematic Conference on Geologic Remote Sensing, 8-11 February 1993, Pasadena, California, Environmental Research Institute of Michigan, Ann Arbor, pp. 767-777.

Nichol, I., Garrett, R.G., and Webb, J.S., 1969. The role of some statistical and mathematical methods in the interpretation of regional geochemical data. Economic Geology, vol. 64, pp. 204-220.

Odhiambo, B.D.O., Gaciri, J. and Falconer, A., 1989. Geobotanical anomalies over a fluorite mineralization in Kerio Valley, Kenya. Proceedings of the 9th International Geoscience and Remote Sensing Symposium (IGARSS) '89, 10-14 July, Vancouver, Canada, pp. 2514-2517.

Odhiambo, B.D.O. and Howarth, P.J., 1993. Geobotanical anomaly over the Sekerr chromite mineralization in West Pokot district, Kenya. Proceedings of the 9th

Thematic Conference on Geologic Remote Sensing, 8-11 February 1993, Pasadena, California, Environmental Research Institute of Michigan, Ann Arbor, pp. 791-800.

Östensson, O., 1996. The role of UNCTAD in international mineral development. Geoscience and Development, no. 3, January 1993, pp. 12-14.

Palacharla, P. and Nelson, P.C., 1994. Understanding relations between fuzzy Logic and evidential reasoning methods. Proceedings of 3rd IEEE International Conference on Fuzzy Systems, Orlando, Florida, June 1994, pp. 1933-1938.

Pan, G.C., 1993a. Indicator favorability theory for mineral potential mapping. Nonrenewable Resources, vol. 2, no. 4, pp. 292-311.

Pan, G.C., 1993b. Canonical favourability model for data integration and mineral potential mapping. Computers and Geosciences, vol. 19, pp. 1077-1100.

Pan, G.C., 1993c. Regionalized favorability theory for information synthesis in mineral exploration. Mathematical Geology, vol. 25, no. 5, pp. 603-631.

Pan, G.C. and Harris, D.P., 1992a. Decomposed and weighted characteristic analysis for the quantitative estimation of mineral resources. Mathematical Geology, vol. 24, pp. 807-823.

Pan, G.C. and Harris, D.P., 1992b. Estimating a favourability equation for the integration of geodata and selection of mineral exploration targets. Mathematical Geology, vol. 24, no. 2, pp. 177-202.

Pan, G.C. and Harris, D.P., 2000. Information Synthesis for Mineral Exploration, Oxford University Press, Inc., New York, 461 pp.

Pan, G.C. and Portefield, B., 1995. Large-scale mineral potential estimation for blind precious metal ore deposits. Nonrenewable Resources, vol. 4, no. 2, pp. 187-207.

Park, C.F. and MacDiarmid, R.A., 1975. Ore Deposits, 3rd Ed., Freeman, San Francisco, 529 pp.

Payás, A., Schmidt, R.G. and Bonet, A., 1993. The effects of hydrothermally altered bedrock on natural forest vegetation in the Snow Camp - Saxapahaw area, North Carolina, and the resulting expression in Landsat TM imagery. In: Scott, R.W., Jr., Detra, D.S. and Berger, B.R. (Eds.), Advances Related to the United States and International Mineral Resources: Developing Frameworks and Exploration Technologies, U.S. Geological Survey Bulletin 2039, pp. 189-200.

Peña, R.E., 1970. Brief geology of a portion of the Baguio mineral district. Journal of the Geological Society of the Philippines, vol. 24, no. 4, pp. 41-43.

Perry, C.R., Jr., and Lautenschlager, L.F., 1984. Functional equivalence of spectral vegetation indices. Remote Sensing of Environment, vol. 14, pp. 169-182.

Pinar, A. and Curran, P.J., 1996. Grass chlorophyll and the reflectance red edge. International Journal of Remote Sensing, vol. 17, pp. 351-357.

Pirajno, F., 1992. Hydrothermal Mineral Deposits, Principles and Fundamental Concepts for the Exploration Geologists, Springer-Verlag, Berlin, 709 pp.

Podwysocki, M.H., Segal, D.B. and Abrams, M.J., 1983. Use of multispectral scanner images for assessment of hydrothermal alteration in the Marysvale, Utah, mining area. Economic Geology, vol. 78, pp. 675-687.

Podwysocki, M.H., Power, M.S., Salisbury, J.W. and Jones, O.D., 1984. Evaluation of low-sun illuminated Landsat-4 Thematic Mapper data for mapping hydrothermally altered rocks in southern Nevada. Proceedings of the International Symposium on Remote Sensing of Environment, 3rd Thematic Conference on Remote Sensing for Exploration Geology, Colorado Springs, Colorado, Environmental Research Institute of Michigan, Ann Arbor, pp. 541-545.

Porter, W.M. and Enmark, H.T., 1987. A system overview of the Airborne Visible/Infrared Imaging Spectrometer (AVIRIS). Proceedings of the 31st Annual International Technical Symposium, 16-21 August 1987, Society of Photo-Optical Instrumentation Engineers (SPIE), vol. 834, pp. 22-31.

Prost, G., 1983. Mineral exploration with Skylab photography in Central Colorado. Economic Geology, vol. 78, pp. 633-640.

Quebral, R.D., 1994. Tectonics of the southern segment of the Philippines Fault: transition from strike-slip to a collision zone. Ph.D. thesis, Université Pierre et Marie Curie, Paris, 350 pp.

Railyan, V.Y. and Korobov, R.M., 1993. Red edge structure of canopy reflectance spectra of tricale. Remote Sensing of Environment, vol. 46, pp. 173-182.

Raines, G.L., and Wynn, J.C., 1982. Mapping of ultramafic rocks in a heavily vegetated terrain using Landsat data. Economic Geology, vol. 77, pp. 1755-1769.

Raines, G.L., 1997. Data, evidence, and the silver bullet. In: A.G. Gubins (Ed.), Proceedings of Exploration 97: 4th Decennial International Conference on Mineral Exploration, Toronto, Canada, 14-18 September 1997, pp. 87-88.

Rangin, C., 1991. The Philippine mobile belt: a complex plate boundary. Journal of Southeast Asian Earth Sciences, vol. 6, nos. 3 and 4 pp. 209-220.

Rao, C.R., 1973. Linear Statistical Inference and Its Applications, 2nd Ed. Wiley, New York, pp. 366-374 (chapter 5).

Rast, M., Bézy, J.L. and Bruzzi, S., 1999. The ESA Medium Resolution Imaging Spectrometer MERIS – a review of the instrument and its mission. International Journal Remote Sensing, vol. 20, no. 9, pp. 1681-1702.

Reddy, R.K.T., Agterberg, F.P. and Bonham-Carter, G.F., 1991. Application of GIS-based logistic models to base-metal potential mapping in Snow Lake area, Manitoba.

Proceedings of the Canadian Conference on GIS, Ottawa, Canada, 18-22 March 1991, pp. 607-618.

Reddy, R.K.T., Bonham-Carter, G.F. and Galley, A.G., 1992. Developing a geographic expert system for regional mapping of volcanogenic massive sulphide (VMS) deposit potential. Nonrenewable Resources, vol. 1, no. 2, pp. 112-124.

Reddy, R.K.T., Bonham-Carter, G.F. and Wright, D.F., 1990. GIS for mapping mineral resource potential: preliminary results of base-metal study, Snow Lake area, Manitoba. Proceedings of GIS for the 1990s Conference, Ottawa, Canada, 5-8 march 1990, pp. 384-400.

Reeves, C.V., Westerhof, A.B., Botman, L.G., Dessauvagie. T.F.J. and Dijkstra, S., 1990. Systematic mineral resource development in the '90s and the next century: new techniques, old challenges. ITC Journal 1990-2, pp. 92-101.

Resh, H.M. 1983. Hydroponic Food Production, 2nd Edn. Woodbridge Press Publishing Co., Santa Barbara, CA., pp. 335.

Resmini, R.G., Kappus, M.E., Aldrich, W.S., Harsanyi, J.C. and M. Anderson., 1997. Mineral mapping with Hyperspectral Digital Imagery Collection Experiment (HYDICE) sensor data at Curpite, Nevada, U.S.A. International Journal of Remote Sensing, vol. 18, no. 7, pp. 1553-1570.

Ricchetti, E., 2001. Visible-infrared and radar imagery fusion for geological application: a new approach using DEM and sun-illumination model. International Journal of Remote Sensing, vol. 22, no. 11, pp. 2219-2230.

Richards, J.A., 1999. Remote Sensing Digital Image Analysis, An Introduction, 3rd Edn.,. Springer-Verlag, Berlin, 363 pp.

Richardson, A.J. and Wiegand, C.L., 1977. Distinguishing vegetation from soil background information. Photogrammetric Engineering and Remote Sensing, vol. 43, pp. 1541-1552.

Ricklefs, R.E., 1990. Ecology, 3rd Edn., Freeman, New York, 896 pp.

Ringenbach, J.C., 1992. La faille Philippine et les chaînes en décrochement associées (centre et nord Luzon): évolution Cénozique et cinématique des déformation Quaternaires. Ph.D. thesis, Université de Nice-Sophia Antipolis, France, 316 pp.

Ringenbach, J.C., Stephan, J.F., Maleterre, P. and Bellon, H., 1990. Structure and geologic history of the Lepanto-Cervantes releasing bend on the Abra River Fault, Luzon Central Cordillera, Philippines. Tectonophysics, vol. 183, pp. 225-241.

Ripley, B.D., 1981. Spatial Statistics, Wiley, New York, 252 pp.

Rock, B.N., Hoshizaki, T. and Miller, J.R., 1988. Comparison of in situ and airborne spectral measurements of the blue shift associated with forest decline. Remote Sensing of Environment, vol. 24, pp. 109-127.

Rock, N.M.S., 1988. Numerical Geology. Springer-Verlag, Berlin, 427 pp.

Rockwell, B.W., 1989. Hydrothermal alteration mapping in spectral ratio feature space using TM reflectance data: Aurora mining district, Mineral County, Nevada. Proceedings of the 7th Thematic Conference on Exploration Geology, Calgary, Alberta, 2-6 October 1989, Environmental Research Institute of Michigan, Ann Arbor, pp. 1189-1203.

Rogers, R. and McKee, C., 1990. Geology, volcanism and mineral deposits of Papua New Guinea. In: F.E. Hughes (Ed.), Geology of the Mineral Deposits of Australia and Papua New Guinea, vol. 2, Australasian Institute of Mining and Metallurgy Monograph 14, pp. 1689-1701.

Rose, A.W., Hawkes, H.E. and Webb, J.S., 1979. Geochemistry in Mineral Exploration, 2nd Ed., Academic Press, London, 657 pp.

Rosenfield, G.H. and Fitzpatrick-Lins, K., 1986. A coefficient of agreement as a measure of thematic classification accuracy. Photogrammetric Engineering & Remote Sensing, vol. 52, no. 2, pp. 223-227.

Rouse, J.W., Hass, R.H., Schell, J.A., Deering, D.W. and Harlan, J.C., 1974. Monitoring the vernal advancement of retrogration (greenwave effect) of natural vegetation (Type III Final Report), NASA Goddard Space Flight Center, Greenbelt, Maryland, 371 pp.

Ruiz-Armenta, J.R. and Prol-Ledesma, R.M., 1998. Techniques for enhancing the spectral response of hydrothermal alteration minerals in Thematic Mapper images of Central Mexico. International Journal of Remote Sensing, vol. 19, no. 10, pp. 1981-2000.

Rush, P.M. and Seegers, H.J., 1990. Ok Tedi copper-gold deposits. In: F.E. Hughes (Ed.), Geology of the Mineral Deposits of Australia and Papua New Guinea, vol. 2, Australasian Institute of Mining and Metallurgy Monograph 14, pp. 1747-1754.

Ryan, M.P., 1990. The physical nature of the Icelandic magma transport system. In: M.P. Ryan (Ed.), Magma Transport and Storage, John Wiley and Sons, Chichester, pp. 175-224.

Rybach, L., 1985. Heat Flow and Geothermal Processes. Special volume of Journal of Geodynamics (vol. 4, nos. 1-4), Geophysical Press, Amsterdam, 352 pp.

Sabine, C., Realmuto, V.J. and Taranik, J.V., 1994. Quantitative estimation of granitoid composition from Thermal Infrared Multispectral Scanner (TIMS) data, Desolation Wilderness, northern Sierra Nevada, California. Journal of Geophysical Research, vol. 99, pp. 4261-4271.

Sabins, F.F., 1996. Remote Sensing: Principles and Interpretation, 3rd Edn., W.H. Freeman and Company, New York, 494 pp.

Salisbury, F.B. and Ross, C., 1969. Plant Physiology. Wadsworth, Belmont, CA., 422 pp.

Salisbury, J.W., Walter, L.S. and Vergo, N., 1987. Mid-infrared spectra of minerals. U.S. Geological Survey Open-File Report 87-263, USGS, Reston, Virginia.

Sangster, D.F., 1986. Application of mineral deposit models to regional assessments: discussion. U.S. Geological Survey 980, pp. 287-292.

Saraf, A.K. and Choudhury, P.R., 1998. Integrated remote sensing and GIS for groundwater exploration and identification of artificial recharge sites. International Journal of Remote Sensing, vol. 19, no. 10, pp. 1825-1841.

Sawkins, F.J., 1989. Metal Deposits in Relation to Plate Tectonics, 2nd Edn., Springer-Verlag, Berlin, 461 pp.

Sawkins, F.J., O'Neil, J.R. and Thompson, J.M., 1979. Fluid inclusion and geochemical studies of vein gold deposits, Baguio district, Philippines. Economic Geology, vol. 74, pp. 1420-1434.

Schmidt, R.G., Payás, A., Gumiel, P. and D'Agostino, J.P., 1987. The Saxapahaw, North Carolina, gold occurrence – search for a deposit model and new remote sensing technologies. In: Sachs, J.S. (Ed.), U.S. Geological Survey Research on Mineral Resources – 1987, Programs and Abstracts, U.S. Geological Survey Circular 995, pp. 62-63.

Schwaller, M.R., 1982. Discrimination of metal stressed and non-stressed vegetation in simulated soil-vegetation ensembles. Proceedings of the International Symposium on Remote Sensing of Environment, 2nd Thematic conference on Remote Sensing for Exploration Geology, Fort Worth Texas, 6-10 December, pp. 679-692.

Schwartz, M.D. and Reed, B. C., 1999. Surface phenology and satellite sensor-derived onset of greenness: an initial comparison.

Seber, G.A.F., 1984. Multivariate Observations. John Wiley and Sons, New York 686 pp.

Segal, D.B., 1983. Use of Landsat multispectral scanner data for the definition of limonitic exposures in heavily vegetated areas. Economic Geology, vol. 78, pp. 711-722.

Segall, P. and Pollard, D.D., 1980. Mechanics of discontinuous faults. Journal of Geophysical Research, vol. 85, no. B8, pp. 4337-4350.

Shafer, G., 1976. A Mathematical Theory of Evidence. Princeton University Press, Princeton, N.J., 297 pp.

Shaulis, L. and Lancaster, J., 1994. Changes in Plant Spectra as an Indicator of Environmental Contamination, Desert Research Institute Publication, Nevada, 29 pp.

Shutt, J.B., Rowland, R.R. and Heartly, W.H., 1984. A laboratory investigation of a physical mechanism for extended infrared absorption ('red shift') in wheat. International Journal of Remote Sensing, vol. 5, pp. 92-102.

Sibson, R.H., 1981. Fluid flow accompanying faulting: field evidence and models. In: D.W. Simpson and P.G. Richards (Eds.), Earthquake Prediction: an International Review, American Geophysical Union Monograph, Maurice Ewing Series 4, pp. 593-603.

Sibson, R.H., 1987, Earthquake rupturing as a mineralizing agent in hydrothermal systems: Geology, v. 15, no. 8, pp. 701-704.

Sibson, R.H., 1990. Conditions for fault-valve behavior. In: R.J. Knipe and E.H. Rutter (Eds.), Deformation Mechanisms, Rheology and Tectonics, Geological Society Publication No. 54, The Geological Society of London, pp. 15-28.

Siegal, B.S. and Gillespie, A.R., 1980. Remote Sensing in Geology, John Wiley and Sons, New York, 702 pp.

Siegal, B.S. and Goetz, A.F.H., 1977. Effect of vegetation on rock and soil discrimination. Photogrammetric Engineering and Remote Sensing, vol. 43, no. 2, pp. 191-196.

Siegel, S., 1956. Non-Parametric Statistics for the Behavioral Sciences, McGraw-Hill, New York, 312 pp.

Sillitoe, R.H., 1972. A plate tectonic model for the origin of porphyry copper deposits. Economic Geology, vol. 67, pp. 184-197.

Sillitoe, R.H., 1973. Tops and bottoms of porphyry copper deposits. Mining Magazine, vol. 142, pp. 550-553.

Sillitoe, R.H., 1976. Andean mineralization: a model for the metallogeny of convergent plat margins. In: D.F. Strong (Ed.), Metallogeny and Plate Tectonics, Geological Association of Canada Special Paper 14, pp. 59-100.

Sillitoe, R.H., 1981. Regional aspects of the Andean porphyry copper belt in Chile and Argentina. Transactions of the Institute of Mining and Metallurgy, vol. 90, pp. B15-B36.

Sillitoe, R.H., 1986. Space-time distribution, crustal setting and Cu/Mo Ratios of central Andean porphyry copper deposits: metallogenic implications. In: G.H. Friedrich, A.D. Genkin, A.J. Naldrett, J.D. Ridge, R.H. Sillitoe and F.M. Vokes (Eds.), Geology and Metallogeny of Copper Deposits, Geological Society of Applied Mineral Deposits Special Publication 4, pp. 235-250.

Sillitoe, R.H., 1992. The Porphyry-epithermal transition. In: Magmatic Contributions To Hydrothermal Systems, Geological Survey of Japan, Report No. 279, pp. 156-160.

Sillitoe, R.H., 1993. Epithermal models: genetic types, geometric controls and shallow features. Geological Association of Canada, Special Volume 40, pp. 403-417.

Sillitoe, R.H. and Angeles, C.A., Jr., 1985. Geological characteristics and evolution of a gold-rich porphyry copper deposit at Guinaoang, Luzon, Philippines. Asian Mining '85, London, Institution of Mining and Metallurgy, pp. 15-26.

Sillitoe, R.H. and Bonham, H.F., 1984. Volcanic landforms and ore deposits. Economic Geology, vol. 79, pp. 1286-1298.

Sillitoe, R.H. and Gappe, I.M., Jr., 1984. Philippine porphyry copper deposits: geological setting and characteristics. CCOP Technical Publication 14, Bangkok, 89 pp.

Simmons, G., 1992. Calculus Gems: Brief Lives and Memorable Mathematics, McGraw-Hill, New York, 355 pp.

Simpson, C.J., Huntington, J.F., Leishman, J. and Green, A.A., 1980. A study of the Pine Creek Geosyncline using integrated Landsat and aeromagnetic data. In: J. Ferguson and A. Goleby (Eds.), Uranium in the Pine Creek Geosyncline, International Atomic Energy Agency, Vienna, pp. 141-155.

Singhroy, V., Kenny, F. and Springer, J., 1989. Reflectance spectra of vegetation growing on mine sites in the Canadian Shield. Proceedings of the 12th Canadian Symposium on Remote Sensing, International Geoscience and Remote Sensing Symposium 1989, Vancouver, British Columbia, Canada, pp. 665-669.

Smith, M.O., Johnston, P.E. and Adams, J.B., 1985. Quantitative determination of mineral types and abundances from reflectance spectra using principal components analysis. Journal of Geophysical Research, vol. 90, pp. 797-804.

Smith, K.S., Plumlee, G.S. and Ficklin, W.H., 1994. Predicting water contamination from metal mines and mining wastes. U.S. Geology Survey Open-File Report 94-264, U.S. Geological Survey, 112 pp.

Snedecor, G.W. and Cochran, W.G., 1967. Statistical Methods, 6th Edn., Iowa State University Press, Ames, Iowa, 593 pp.

Spatz, D.M., 1997. Remote Sensing characteristics of the sediment- and volcanic-hosted precious metal system: imagery selection for exploration and development. International Journal of Remote Sensing, vol. 18, no. 7, pp. 1413-1438.

Spiegelhalter, D.J., 1986. Uncertainty in expert systems. In: W.A. Gale (Ed.), Artificial Intelligence and Statistics, Addison-Wesley, Reading, Massachusetts, pp. 17-55.

Spiegelhalter, D.J. and Knill-Jones, R.P., 1984. Statistical and knowledge-based approaches to clinical decision-support systems, with an application to gastroenterology. Journal of the Royal Statistical Society, A, Part 1, pp. 35-77.

Stein, A., Varekamp, C., Van Egmond, C. and Van Zoest, R., 1995. Interactive GIS for environmental risk assessment. International Journal of Geographical Information Systems, vol. 5, pp. 509-525.

Story, M. and Congalton, R., 1986. Accuracy assessment: a user's perspective. Photogrammetric Engineering & Remote Sensing, vol. 52, no. 3, pp. 397-399.

Swain, P.H. and Davis, S.M., 1979. Remote Sensing: The Quantitative Approach, McGraw-Hill, New York, 396.

Tanaka, S.M. and Segal, D.B., 1989. Integrated remote sensing / vector based GIS technology for gold exploration, Round Mountain district, Nevada. Proceedings of the 7th Thematic Conference for Exploration Geology, Calgary, Alberta, Environmental Research Institute of Michigan, Ann Arbor, pp. 1269-1283.

Taranik, J.V. and Crósta, A.P., 1996. Remote sensing for geological and mineral resources, an assessment of tools for geoscientists in the future. International Archives of Photogrammetry and Remote Sensing, vol. 31, B7, pp. 689-698.

Thomas, J.R. and Gausman, H.W., 1977. Leaf reflectance vs. leaf chlorophyll and carotenoid concentrations for eight crops. Agronomy Journal, vol. 69, pp. 799-802.

Titley, S.R., 1981. Geologic framework of southeastern Arizona porphyry copper deposits. In: S.R. Titley (Ed.), Advances in Geology of the Porphyry Copper Deposits of Southwestern North America, University of Arizona Press, Tucson, pp. 93-116.

Titley, S.R. and Beane, R.E., 1981. Porphyry copper deposits – Part I: Geological settings, petrology and tectogenesis. Economic Geology 75th Anniversary Volume, pp. 214-235.

Titley, S.R. and Heidrick, T.L., 1978. Intrusion and fracture styles of some mineralized porphyry systems of the southwestern Pacific and their relationship to plate interactions. Economic Geology, vol. 73, pp. 891-903.

Tolbert, G.E., Tremaine, J.W., Melcher, G.C. and Gomes, G.B., 1971. The recently discovered Serra dos Carajas iron deposits, northern Brazil. Economic Geology, vol. 66, pp. 985-994.

Tucker, C.J., 1979. Red and photographic infrared linear combinations for monitoring vegetation. Remote Sensing of Environment, vol. 8, pp. 127-150.

Turner, D.D., 1997. Predictive GIS model for sediment-hosted gold deposits, North-Central Nevada, U.S.A. In: A.G. Gubins (Ed.), Proceedings of Exploration 97: 4th Decennial International Conference on Mineral Exploration, Toronto, Canada, 14-18 September 1997, pp. 115-126.

UNDP, 1987a. Geochemical nature of epithermal gold mineralization and related anomalies in the Philippines. Technical Report No. 4, DP/UN/PHI-85-001/6, United Nations Development Programme, New York, 151 pp.

UNDP, 1987b. Geology and mineralisation in the Baguio area, Northern Luzon. Technical Report No. 5, DP/UN/PHI-85-001/5, United Nations Development Programme, New York, 82 pp.

USGS, 1998. USGS Spectroscopy Library. http://speclab.cr.usgs.gov. United States Geological Survey.

Van Assche, F. and Clijsters, H., 1990. Effects of metals on enzyme activity in plants. Plant, Cell and Environment, vol. 13, pp. 195-206.

Vanderbilt, V.C., Grant, L. Biehl, L.L. and Robinson, B.F., 1985. Specular, diffuse, and polarized light scattered by two wheat canopies. Applied Optics, vol. 24, pp. 2408-2418.

Vanderbilt, V.C., Ustin, S.L. and Clark, J., 1988. Canopy geometry changes due to wind cause red edge spectral shift. Proceedings of the International Geoscience and Remote Sensing Symposium (IGARSS) '88, Edinburgh, Scotland, 13-16 September 1988, pp. 835.

Van der Meer, F., 1995. Imaging Spectrometry and the Ronda Peridotites, Ph.D. Thesis, Agricultural University of Wageningen, The Netherlands, 309 pp.

Van der Meer, F., 1996. Spectral unmixing: a new tool in geologic image processing. Proceedings of the SIRDC Conference on the Application of Remotely Sensed Data and GIS in Environment and Natural Resource Assessment in Africa, 15-22 March 1996, Harare, Zimbabwe, pp. 131-134.

Van der Meer, F. and De Jong, S.M., 2000. Improving the results of spectral unmixing of Landsat Thematic Mapper imagery by enhancing the orthogonality of end-members. International Journal of Remote Sensing, vol. 21, no. 15, 2781-2797.

Van der Meer, F., Bakker, W., Scholte, K. Skidmore, A., De Jong, S., Clever, J. and Epema, G., 2000. Vegetation indices, above ground biomass estimates and the red edge from MERIS. International Archives of Photogrammetry and Remote Sensing, vol. 33, part B7, pp. 1580-1587.

Vane, G., Goetz, A.F.H. and Wellman, J.B., 1983. Airborne imaging spectrometer: a new tool for remote sensing. IEEE Transactions of Geoscience and Remote Sensing, vol. GE-22, no. 6, pp. 546-549.

Walker, P.A. and Lev, J., 1953. Statistical Inference. Holt, Rhinehart and Winston, New York, 510 pp.

Walley, P., 1987. Belief function representations of statistical evidence. The Annals of Statistics, vol. 15, no. 4, pp. 1439-1465.

Watson, G.P. and Rencz, A.N., 1989. Data integration studies in northern New Brunsiwck. In: F.P. Agterberg and G.F. Bonham-Carter (Eds.), Statistical Analysis in the Earth Sciences, Geological Survey of Canada, Paper 89-9, pp. 185-191.

White, F.M., 1974. Viscous Fluid Flow, McGraw-Hill, New York, 725 pp.

White, N.C. and Hedenquist, J.W., 1990. Epithermal environments and styles of mineralization; variations and their causes, and guidelines for exploration. In: J.W. Hedenquist, N.C. White and Siddeley, G. (Eds.), Epithermal Gold Mineralization of the Circum-Pacific: Geology and Geochemistry, Origin and Exploration II, Journal of Geochemical Exploration, vol. 36, pp. 454-474.

Whitney, G., Abrams, M.J. and Goetz, A.F.H., 1983. Mineral discrimination using a portable ratio-determining radiometer. Economic Geology, vol. 78, pp. 688-698.

Whitten, D.G.A. and Brooks, J.R.V., 1972. Dictionary of Geology, Penguin Books Ltd., Middlesex, England, 516 pp.

Wickham, J., Chesley, M., Lancaster, J. and Mouat, D., 1993. Remote Sensing for the Geobotanical and Biogeochemical Assessment of Environmental Contamination. Publication No. 45111, Desert Research Institute, University and Community College System of Nevada, Reno, Nevada, 76 pp.

Wilkinson, L., Harris, J. and Kjarsgaard, B., 1999. Searching for kimberlite: preliminary weights of evidence modeling of the Lac de Gras area, NWT, using GIS technology. Proceedings of the 13th International Conference on Applied Geologic Remote Sensing, Vancouver, British Columbia, Canada, 1-3 March 1999, vol. 1, pp. 263-270.

Willats, E.C., 1970. Maps and maidens. Cartographic Journal, vol. 7, no. 1, p. 50.

Wolfe, J.A., 1981. Philippines geochronology. Journal of the Geological Society of the Philippines, vol. 35, pp. 1-30.

Wolfe, J.A., 1988. Arc magmatism and mineralization in North Luzon and its relationship to subduction at the East Luzon and North Manila Trenches. Journal of Southeast Asian Earth Sciences, vol. 2, no. 2, pp. 79-93.

Wright, D.F. and Bonham-Carter, G.F., 1996. VHMS favourability mapping with GIS-based integration models, Chisel Lake – Anderson Lake area. In: G.F. Bonham-Carter, A.G. Galley and G.E.M. Hall (Eds.), EXTECH I: A Multidisciplinary Approach to Massive Sulphide Research in the Rusty Lake – Snow Lake Greenstone Belts, Manitoba. Geological Survey of Canada, Bulletin 426, pp. 339-376, 387-401.

Wrigley, N. and Dunn, R., 1986. Graphical diagnostics for logistic oil exploration models. Mathematical Geology, vol. 18, no. 4, pp. 356-374.

Yamaguchi, Y., Fujisada, H., Kahle, A.B., Tsu, H., Sato, I., Kato, M., Watanabe, H. and Kudoh, M., 2001. ASTER instrument performance, operation status and application to Earth sciences. Proceedings of the 1999 IEEE International Geoscience and Remote Sensing Symposium, Sydney, Australia, 9-13 July 2001. CD-ROM.

Yang, H., Zhang, J., van der Meer, F. and Kroonenberg, S.B., 2000. Imaging spectrometry data correlated to hydrocarbon microseepage. International Journal of Remote Sensing, vol. 21, no. 1, 197-202.

Yoder, B.J. and Waring, R.H., 1994. The normalised difference vegetation index of small Douglas-fir canopies with varying chlorophyll concentrations. Remote Sensing of Environment, vol. 49, pp. 81-91.

Yumul, G.P., Jr, 1980. Cordillera central region: it's geology and mineral resources – Benguet province. Unpublished report, Mines and Geosciences Bureau, Manila.

Zadeh, L.A., 1965. Fuzzy sets. IEEE Information and Control, vol. 8, pp. 338-353.

Zadeh, L.A., 1973. Outline of a new approach to the analysis of complex systems and decision processes. Institute of Electric and Electronic Engineering, Transactions on Systems, Man and Cybernetics, vol. 3, pp. 28-44.

Zadeh, L.A., 1983. The role of fuzzy logic in the management of uncertainty. Fuzzy Sets and Systems, vol. 11, pp. 199-227.

Zadeh, L.A., 1986. A simple view of the Dempster-Shafer theory of evidence and its implication for the rule of combination. AI Magazine, vol. 7, no. 2, pp. 85-90.

Zagolski, F., Pinel, V., Romier, J., Alcayde, D., Fontanar, J., Gastellu-Etchegorry, J.P., Giordano, G., Marty, G., Mougin, E. and Joffre, R., 1996. Forest canopy chemistry with high spectral resolution remote sensing. International Journal of Remote Sensing, vol. 17, 1107-1128.

Zimmerman, H.-J., 1991. Fuzzy Set Theory – and Its Applications, 2nd Edition. Kluwer Academic Publisher, Dordrecht, 399 pp.

Zimmerman, H.-J. and Zysno, P., 1980. Latent connectives in human decision making. Fuzzy Sets and Systems, vol. 4, pp. 37-51.

Curriculum Vitae

EMMANUEL JOHN MUICO CARRANZA was born on 8 October 1962 in the city of Legazpi, Bicol Region, Philippines. He completed his secondary education at the Science-Oriented High School of Aquinas University of Legazpi in March 1979. He won a university scholarship from the Bureau of Mines (BM) of the Philippines to study geology. He received his Bachelor of Science degree in Geology from Adamson University in Manila in March 1983. He joined the BM Regional Office in Bicol Region in May 1983. In his early years with the Bureau of Mines, he took part in various projects involving geological mapping and stratigraphic studies, evaluation of industrial rocks and minerals, and geological exploration for gold. He undertook a post-graduate diploma course in Mineral Exploration at the International Institute for Aerospace Survey and Earth Sciences (ITC) in Delft, The Netherlands in August 1989, with a scholarship from the Netherlands Fellowship Program (NFP). He earned his post-graduate diploma in Mineral Exploration in July 1990. Back to his work at the Bureau of Mines and Geosciences (BMG), he applied exploration geochemistry to map gold potential in Quaternary volcanic areas. His work led to the recognition of a previously unknown potentially gold-mineralised zone in the municipality of Bulan in Sorsogon province of the Bicol Region. He returned to ITC-Delft to undertake the Master of Science (MSc) degree course in Mineral Exploration in September 1993 with another scholarship from NFP. He earned his MSc degree (with distinction) in Mineral Exploration in November 1994, with a thesis entitled A Catchment Basin Approach to the Analysis of Reconnaissance Geochemical-Geological Data from Albay Province, Philippines. He continued to apply exploration geochemistry in the various mineral exploration projects of the BMG. He returned to ITC-Delft to undertake the present doctoral research in June 1997, with a joint scholarship from ITC and DGIS (Dutch Agency for International Cooperation). He received the 1998 ITC Research Award for a scientific paper published in the Journal of Geochemical Exploration (vol. 60), which bears the same title as his MSc thesis and which he co-authored with his supervisor Professor Martin Hale. Concerning his doctoral research, he presented scientific papers in seven international conferences/symposia and published fifteen scientific papers in international peer-reviewed journals and in the proceedings of the international conferences/symposia in which he participated. During his doctoral research, he also co-authored two other scientific papers on GIS-based mineral potential mapping but not related to his doctoral research and reviewed four scientific papers that were submitted for publication in international peer-reviewed journals – Journal of Applied Earth Observation and Geoinformation (formerly ITC Journal), Computers and Geosciences, and Natural Resources Research. He will defend his doctoral thesis on 04 February 2002.

List of ITC PhD Dissertations

1. Akinyede, 1990, Highway cost modelling and route selection using a geotechnical information system
2. Pan He Ping, 1990, 90-9003757-8, Spatial structure theory in machine vision and applications to structural and textural analysis of remotely sensed images
3. Bocco Verdinelli, G., 1990, Gully erosion analysis using remote sensing and geographic information systems: a case study in Central Mexico
4. Sharif, M, 1991, Composite sampling optimization for DTM in the context of GIS
5. Drummond, J., 1991, Determining and processing quality parameters in geographic information systems
6. Groten, S., 1991, Satellite monitoring of agro-ecosystems in the Sahel
7. Sharifi, A., 1991, 90-6164-074-1, Development of an appropriate resource information system to support agricultural management at farm enterprise level
8. Zee, D. van der, 1991, 90-6164-075-X, Recreation studied from above: Air photo interpretation as input into land evaluation for recreation
9. Mannaerts, C., 1991, 90-6164-085-7, Assessment of the transferability of laboratory rainfall-runoff and rainfall - soil loss relationships to field and catchment scales: a study in the Cape Verde Islands
10. Ze Shen Wang, 1991: 90-393-0333-9, An expert system for cartographic symbol design
11. Zhou Yunxian, 1991, 90-6164-081-4, Application of Radon transforms to the processing of airborne geophysical data
12. Zuviria, M. de, 1992, 90-6164-077-6, Mapping agro-topoclimates by integrating topographic, meteorological and land ecological data in a geographic information system: a case study of the Lom Sak area, North Central Thailand
13. Westen, C. van, 1993, 90-6164-078-4, Application of Geographic Information Systems to landslide hazard zonation
14. Shi Wenzhong, 1994, 90-6164-099-7, Modelling positional and thematic uncertainties in integration of remote sensing and geographic information systems
15. Javelosa, R., 1994, 90-6164-086-5, Active Quaternary environments in the Philippine mobile belt
16. Lo King-Chang, 1994, 90-9006526-1, High Quality Automatic DEM, Digital Elevation Model Generation from Multiple Imagery
17. Wokabi, S., 1994, 90-6164-102-0, Quantified land evaluation for maize yield gap analysis at three sites on the eastern slope of Mt. Kenya
18. Rodriguez, O., 1995, Land Use conflicts and planning strategies in urban fringes: a case study of Western Caracas, Venezuela
19. Meer, F. van der, 1995, 90-5485-385-9, Imaging spectrometry & the Ronda peridotites
20. Kufoniyi, O., 1995, 90-6164-105-5, Spatial coincidence: automated database updating and data consistency in vector GIS
21. Zambezi, P., 1995, Geochemistry of the Nkombwa Hill carbonatite complex of Isoka District, north-east Zambia, with special emphasis on economic minerals
22. Woldai, T., 1995, The application of remote sensing to the study of the geology and structure of the Carboniferous in the Calañas area, pyrite belt, SW Spain
23. Verweij, P., 1995, 90-6164-109-8, Spatial and temporal modelling of vegetation patterns: burning and grazing in the Paramo of Los Nevados National Park, Colombia

24. Pohl, C., 1996, 90-6164-121-7, Geometric Aspects of Multisensor Image Fusion for Topographic Map Updating in the Humid Tropics
25. Jiang Bin, 1996, 90-6266-128-9, Fuzzy overlay analysis and visualization in GIS
26. Metternicht, G., 1996, 90-6164-118-7, Detecting and monitoring land degradation features and processes in the Cochabamba Valleys, Bolivia. A synergistic approach
27. Hoanh Chu Thai, 1996, 90-6164-120-9, Development of a Computerized Aid to Integrated Land Use Planning (CAILUP) at regional level in irrigated areas: a case study for the Quan Lo Phung Hiep region in the Mekong Delta, Vietnam
28. Roshannejad, A., 1996, 90-9009284-6, The management of spatio-temporal data in a national geographic information system
29. Terlien, M., 1996, 90-6164-115-2, Modelling Spatial and Temporal Variations in Rainfall-Triggered Landslides: the integration of hydrologic models, slope stability models and GIS for the hazard zonation of rainfall-triggered landslides with examples from Manizales, Colombia
30. Mahavir, J., 1996, 90-6164-117-9, Modelling settlement patterns for metropolitan regions: inputs from remote sensing
31. Al-Amir, S., 1996, 90-6164-116-0, Modern spatial planning practice as supported by the multi-applicable tools of remote sensing and GIS: the Syrian case
32. Pilouk, M., 1996, 90-6164-122-5, Integrated modelling for 3D GIS
33. Duan Zengshan, 1996, 90-6164-123-3, Optimization modelling of a river-aquifer system with technical interventions: a case study for the Huangshui river and the coastal aquifer, Shandong, China
34. Man, W.H. de, 1996, 90-9009-775-9, Surveys: informatie als norm: een verkenning van de institutionalisering van dorp - surveys in Thailand en op de Filippijnen
35. Vekerdy, Z., 1996, 90-6164-119-5, GIS-based hydrological modelling of alluvial regions: using the example of the Kisaföld, Hungary
36. Pereira, Luisa, 1996, 90-407-1385-5, A Robust and Adaptive Matching Procedure for Automatic Modelling of Terrain Relief
37. Fandino Lozano, M., 1996, 90-6164-129-2, A Framework of Ecological Evaluation oriented at the Establishment and Management of Protected Areas: a case study of the Santuario de Iguaque, Colombia
38. Toxopeus, B., 1996, 90-6164-126-8, ISM: an Interactive Spatial and temporal Modelling system as a tool in ecosystem management: with two case studies: Cibodas biosphere reserve, West Java Indonesia: Amboseli biosphere reserve, Kajiado district, Central Southern Kenya
39. Wang Yiman, 1997, 90-6164-131-4, Satellite SAR imagery for topographic mapping of tidal flat areas in the Dutch Wadden Sea
40. Asun Saldana-Lopez, 1997, 90-6164-133-0, Complexity of soils and Soilscape patterns on the southern slopes of the Ayllon Range, central Spain: a GIS assisted modelling approach
41. Ceccarelli, T., 1997, 90-6164-135-7, Towards a planning support system for communal areas in the Zambezi valley, Zimbabwe; a multi-criteria evaluation linking farm household analysis, land evaluation and geographic information systems
42. Peng Wanning, 1997, 90-6164-134-9, Automated generalization in GIS
43. Lawas, C., 1997, 90-6164-137-3, The Resource Users' Knowledge, the neglected input in Land resource management: the case of the Kankanaey farmers in Benguet, Philippines
44. Bijker, W., 1997, 90-6164-139-X, Radar for rain forest: A monitoring system for land cover Change in the Colombian Amazon

45. Farshad, A., 1997, 90-6164-142-X, Analysis of integrated land and water management practices within different agricultural systems under semi-arid conditions of Iran and evaluation of their sustainability
46. Orlic, B., 1997, 90-6164-140-3, Predicting subsurface conditions for geotechnical modelling
47. Bishr, Y., 1997, 90-6164-141-1, Semantic Aspects of Interoperable GIS
48. Zhang Xiangmin, 1998, 90-6164-144-6, Coal fires in Northwest China: detection, monitoring and prediction using remote sensing data
49. Gens, R., 1998, 90-6164-155-1, Quality assessment of SAR interferometric data
50. Turkstra, J., 1998, 90-6164-147-0, Urban development and geographical information: spatial and temporal patterns of urban development and land values using integrated geo-data, Villaviciencia, Colombia
51. Cassells, C., 1998, Thermal modelling of underground coal fires in northern China
52. Naseri, M., 1998, 90-6164-195-0, Characterization of Salt-affected Soils for Modelling Sustainable Land Management in Semi-arid Environment: a case study in the Gorgan Region, Northeast, Iran
53. Gorte B.G.H., 1998, 90-6164-157-8, Probabilistic Segmentation of Remotely Sensed Images
54. Tenalem Ayenew, 1998, 90-6164-158-6, The hydrological system of the lake district basin, central main Ethiopian rift
55. Wang Donggen, 1998, 90-6864-551-7, Conjoint approaches to developing activity-based models
56. Bastidas de Calderon, M., 1998, 90-6164-193-4, Environmental fragility and vulnerability of Amazonian landscapes and ecosystems in the middle Orinoco river basin, Venezuela
57. Moameni, A., 1999, Soil quality changes under long-term wheat cultivation in the Marvdasht plain, South-Central Iran
58. Groenigen, J.W. van, 1999, 90-6164-156-X, Constrained optimisation of spatial sampling: a geostatistical approach
59. Cheng Tao, 1999, 90-6164-164-0, A process-oriented data model for fuzzy spatial objects
60. Wolski, Piotr, 1999, 90-6164-165-9, Application of reservoir modelling to hydrotopes identified by remote sensing
61. Acharya, B., 1999, 90-6164-168-3, Forest biodiversity assessment: A spatial analysis of tree species diversity in Nepal
62. Akbar Abkar, Ali, 1999, 90-6164-169-1, Likelihood-based segmentation and classification of remotely sensed images
63. Yanuariadi, T., 1999, 90-5808-082-X, Sustainable Land Allocation: GIS-based decision support for industrial forest plantation development in Indonesia
64. Abu Bakr, Mohamed, 1999, 90-6164-170-5, An Integrated Agro-Economic and Agro-Ecological Framework for Land Use Planning and Policy Analysis
65. Eleveld, M., 1999, 90-6461-166-7, Exploring coastal morphodynamics of Ameland (The Netherlands) with remote sensing monitoring techniques and dynamic modelling in GIS
66. Yang Hong, 1999, 90-6164-172-1, Imaging Spectrometry for Hydrocarbon Microseepage
67. Mainam, Félix, 1999, 90-6164-179-9, Modelling soil erodibility in the semiarid zone of Cameroon

68. Bakr, Mahmoud, 2000, 90-6164-176-4, A Stochastic Inverse-Management Approach to Groundwater Quality
69. Zlatanova, Z., 2000, 90-6164-178-0, 3D GIS for Urban Development
70. Ottichilo, Wilber K., 2000, 90-5808-197-4, Wildlife Dynamics: An Analysis of Change in the Masai Mara Ecosystem
71. Kaymakci, Nuri, 2000, 90-6164-181-0, Tectono-stratigraphical Evolution of the Cankori Basin (Central Anatolia, Turkey)
72. Gonzalez, Rhodora, 2000, 90-5808-246-6, Platforms and Terraces: Bridging participation and GIS in joint-learning for watershed management with the Ifugaos of the Philippines
73. Schetselaar, Ernst, 2000, 90-6164-180-2, Integrated analyses of granite-gneiss terrain from field and multisource remotely sensed data. A case study from the Canadian Shield
74. Mesgari, Saadi, 2000, 90-3651-511-4, Topological Cell-Tuple Structure for Three-Dimensional Spatial Data
75. Bie, Cees A.J.M. de, 2000, 90-5808-253-9, Comparative Performance Analysis of Agro-Ecosystems
76. Khaemba, Wilson M., 2000, 90-5808-280-6, Spatial Statistics for Natural Resource Management
77. Shrestha, Dhruba, 2000, 90-6164-189-6, Aspects of erosion and sedimentation in the Nepalese Himalaya: highland-lowland relations
78. Asadi Haroni, Hooshang, 2000, 90-6164-185-3, The Zarshuran Gold Deposit Model Applied in a Mineral Exploration GIS in Iran
79. Raza, Ale, 2001, 90-3651-540-8, Object-oriented Temporal GIS for Urban Applications
80. Farah, Hussein, 2001, 90-5808-331-4, Estimation of regional evaporation under different weather conditions from satellite and meteorological data. A case study in the Naivasha Basin, Kenya
81. Zheng, Ding, 2001, 90-6164-190-X, A Neural - Fuzzy Approach to Linguistic Knowledge Acquisition and Assessment in Spatial Decision Making
82. Sahu, B.K., 2001, Aeromagnetics of continental areas flanking the Indian Ocean; with implications for geological correlation and Gondwana reassembly
83. Alfasatwi, Y., 2001, 90-6164-198-5, The structural, paleogeographical and hydrocarbon systems analysis of the Ghadamis and Murzuq Basins, West Libya, with emphasis on their relation to the intervening Al Qarqaf Arch
84. Liu, Xuehua, 2001, 90-5808-496-5, Mapping and Modelling the Habitat of Giant Pandas in Foping Nature Reserve, China
85. Oindo, Boniface Oluoch, 2001, 90-5808-495-7, Spatial Patterns of Species Diversity in Kenya

ISBN 90-6164-203-5
ITC Publication No. 86